From Boron to Nitrogen Based Pincer Complexes: Bonding and Reactivity Patterns

Kumulative Dissertation

Zur Erlangung des akademischen Grades eines

Doktors der Naturwissenschaften

(Dr. rer. nat.)

dem Fachbereich Chemie der Philipps-Universität Marburg

vorgelegt von

Lisa Vondung, M.Sc.

aus Ludwigshafen am Rhein

Erstgutachterin: Prof. Dr. Stefanie Dehnen

Zweitgutachter: Dr. Robert Langer

Einreichungstermin: 27.10.2017

Prüfungstermin: 11.12.2017

Marburg (Lahn) 2017

Hochschulkennziffer 1180

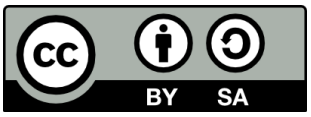

A scientist in his laboratory is not a mere technician: he is also a child confronting natural phenomena that impress him as though they were fairy tales.

– *Marie Skłodowska Curie*

Erklärung

Ich erkläre, dass eine Promotion noch an keiner anderen Hochschule als der Philipps-Universität Marburg, Fachbereich Chemie, versucht wurde. Weiterhin versichere ich, dass ich meine vorgelegte Dissertation "From Boron to Nitrogen Based Pincer Complexes: Bonding and Reactivity Patterns" selbst und ohne fremde Hilfe verfasst, nicht andere als die in ihr angegebenen Quellen oder Hilfsmittel benutzt, alle vollständig oder sinngemäß übernommenen Zitate als solche gekennzeichnet sowie die Dissertation in der vorliegenden oder einer ähnlichen Form noch bei keiner anderen in- oder ausländischen Hochschule anlässlich eines Promotionsgesuchs oder zu anderen Prüfungszwecken eingereicht habe.

Marburg, den 27. Oktober 2017

Lisa Vondung

Einreichungstermin: 27.10.2017
Vom Fachbereich Chemie als Dissertation angenommen: 08.12.2017
Prüfungstermin: 11.12.2017

Die vorliegende Arbeit wurde am Fachbereich Chemie der Philipps-Universität Marburg unter Anleitung von Frau Prof. Dr. Stefanie Dehnen und Dr. Robert Langer in der Zeit von Mai 2014 bis Oktober 2017 angefertigt.

Contents

Chapter 1

Introduction

1.1 Pincer complexes

Three-dentate ligands that coordinate to the metal center in a meridonal fashion are called pincer ligands (Fig. 1.1). The central donor atom D^2 can be boron or a group 4-6 element.[1] The other two donor atoms, D^1 and D^3, are situated *trans* to each other and can be different elements. The backbone between the donor atoms is usually made up of one- or two-atom bridges, such as methyl, ethyl or amines. The central donor D^2 can be part of an aromatic system or a cluster, such as carboranes.
Pincer ligands provide manifold possibilities for electronic and steric fine-tuning of complexes and furthermore enable the incorporation of unusual and often very reactive donor groups.

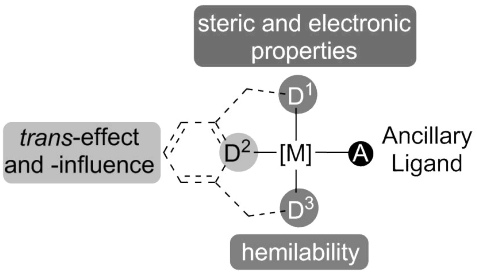

Figure 1.1: General structure of a pincer complex and tunable properties.

Pincer ligands can also enable hemilabile behaviour, i.e. reversible dissociation of one of the donor arms and thus generation of vacant coordination sites. All these properties of pincer-ligands and their complexes make them ideal for catalytic applications and many studies have been published on this topic in the last years.

1.1.1 Boron based tridentate ligands

One emerging class of pincer ligands contains a boron atom at the central donor position. Compared to the widely used amine- and carbene-based pincer ligands, boron-based pincer ligands show interesting different electronic properties. Since the development of boron-based pincer ligands is still in its infancy, it is also of interest to first give a more general overview on tridentate boron-based ligands.

Classification

Ligands for transition metal complexes can be classified according to the *Covalent Bond Classification* method proposed by *Green* in 1995.[2] Depending on the origin of the electrons in a two-electron two-center bond between a ligand and a metal atom, the ligand is either classified as Z- (electron accepting), L- (electron donating) or X-type (electron sharing/covalent) ligand (Fig. 1.2).

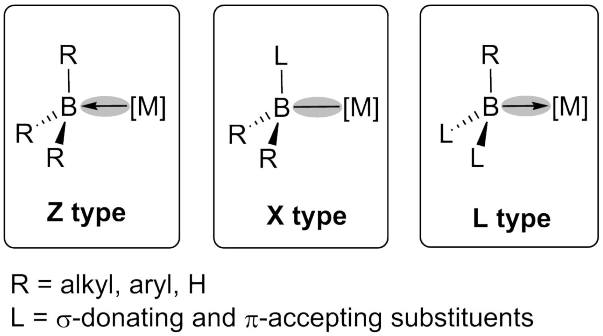

Figure 1.2: Ligand types in tricoordinate boron based ligands and their classficiation according to the *Covalent Bond Classification* in Z-, X- and L-type.

Boron-based ligands can accordingly be expressed in these terms as well. In ligands with tricoordinate boron atoms, the boron-moiety can therefore be expressed either as BR_3 (borane, Z-type), R_2LB (boryl, X-type) or L_2RB (borylene, Z-type).

Borane based ligands

The first and thus best explored tridentate ligands based on tricoordinate boron are borane or boratrane ligands. They are Lewis acidic ligands and thus classified as Z-type ligands. The group of *Hill* reported the first such example with a ruthenium boratrane complex that was synthesized from a poly(azolyl)borate via B-H activation at a ruthenium precursor (Fig. 1.3).[3] Following this seminal work, metallaboratranes were explored

further with similar ligand scaffolds (for a detailed review see [4]). In 2007, *Bourissou*, *Maron* and co-workers found the first borane-based pincer-type ligand, whose central BR_3-group acts as a Z-type ligand for gold(I) chloride (Fig. 1.3).[5] Interestingly, the formed complex exhibits a square-planar coordination geometry and, at the same time, the formal oxidation state of the gold atom was demonstrated to be +I. This shows the unusual bonding modes which are possible with borane-ligands.

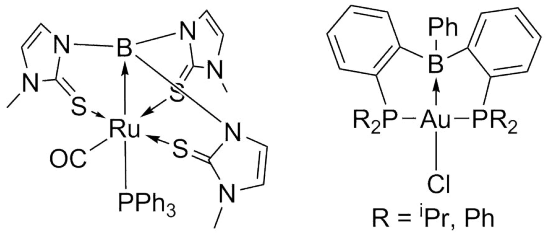

Figure 1.3: First example of a metallaboratrane by *Hill* (left) and first pincer borane complex by *Bourissou* (right).[3, 5]

In these complexes, the metal atom donates electron density towards the boron atom, which exhibits a pyramidalized coordination sphere. Since the borane does not have any electrons left for bonding with the metal, the metal-boron bond is solely a donor bond from the metal to the borane atom, which is in line with the description of a σ-accepting ligand.[4]

Boryl based ligands

Pincer ligands based on boryl groups of the general formula BR_2^- have been developed since 2009. The groups of *Nozaki* and *Yamashita* first reported on the now widely used design of an amido-stabilized boryl group (**I**, see Fig. 1.4).[6] After this initial finding, the groups of *Yamashita*, *Nozaki*, *Murakami*, *Hill*, *Peters*, *López-Serrano* and *Rodriguez* reported complexes with different transition metals and numerous ancillary ligands.[7–20] Until mid 2017, only one more type of boryl based pincer ligands was reported: The group of *Ozerov* employed *Bourissou*'s borane-based pincer ligand in the reaction with iridium precursors, which resulted in oxidative C-B-addition and formation of complex **II** (Fig. 1.4).[21]

The reactivity of these complexes has also been explored. The group of *Peters* found that their cobalt boryl pincer complex can react with two equivalents of H_2, forming a

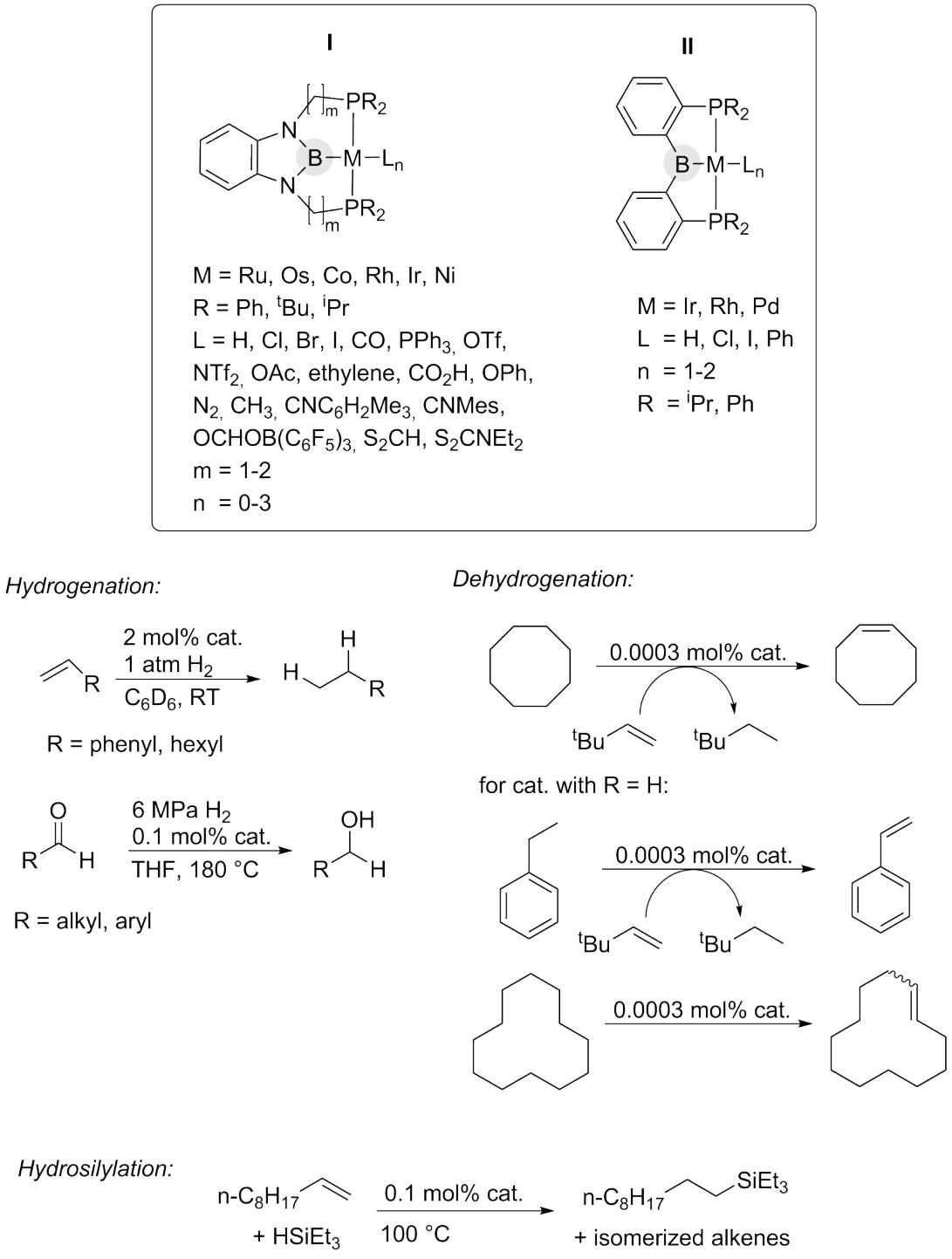

Figure 1.4: Known types of boryl-based pincer ligands and their application in homogeneous catalysis.

dihydrido borato cobalt dihydride complex.[10] This reactivity can be used in catalytic olefin hydration or amine-borane dehydrogenation catalysis. The remaining Lewis acidity at the boron atom in the coordinated boryl ligand is believed to be responsible for this reactivity.

Encouraged by these results, several boryl pincer complexes were tested and optimized for catalytic reactions (Fig. 1.4). Examples include hydrogenation, dehydrogenation and hydrosilylation reactions.[10, 11, 17–19]

Borylene based ligands

For the third complex type, the L-type borylenes, only few examples are known so far. This is mostly owed to the high reactivity of borylenes.

Free borylenes in the form of :BR have not yet been isolated at ambient conditions. A few examples were observed in the gas-phase or with matrix isolation techniques at low temperatures.[22–25] Only when σ-donating and π-accepting substituents are installed at the boron atom, borylenes can be isolated in significant amounts. The first example was reported by *Bertrand* and co-workers with cyclic (alkyl)(amino)carbenes.[26] In 2014, the group of *Kinjo* was able to isolate the first borylene complex (with chromium), using an oxazol-2-ylidenes to stabilize a :BPh fragment.[27]

Because of their filled p_z-orbital, borylenes act as strong σ-donors in transition metal complexes. For the incorporation of borylenes in pincer ligands, so far only one ligand type is known. Recently, our group showed that phosphine-stabilized borylenes can be employed in PBP-pincer complexes for iron and palladium (Fig. 1.5).[28, 29] The donor groups in these complexes are isoelectronic to the central donors in amine- and protonated carbodiphosphorane based pincer ligands. Their reactivity, however, is quite different, which will be discussed in the first publication. This reactivity enables new routes for catalytic processes.

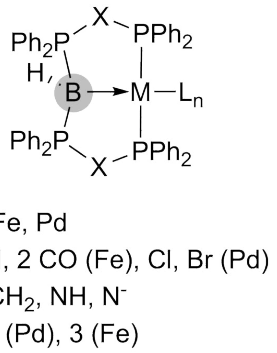

Figure 1.5: Borylene-based pincer ligands in transition metal complexes.

1.1.2 Carbon based pincer ligands

Pincer ligands with a central carbon donor atom can be based on sp^3 or sp^2 hybridized carbon atoms, such as alkyls, aryls, carbenes or carbodiphosphoranes (CDP).[30, 31] Carbenes, that are isoelectronic to boryl-ligands, such as *N*-heterocyclic carbenes (NHC) are mostly employed in the terminal donor positions to replace phosphines as more stable and stronger donors.[32] Nonetheless, NHCs are also being used as central donor groups.[33–37]

The application of carbon-based pincer complexes in homogeneous catalysis is far less explored than that of their amine-based analogues. Still, for alkyl-based pincer complexes,

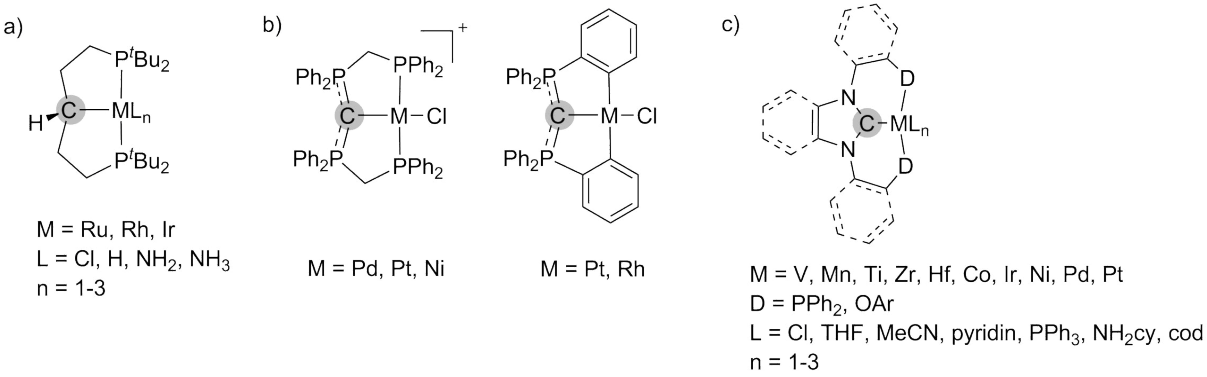

Figure 1.6: General motifs for carbon-based pincer ligands in transition-metal complexes. a) Alkyl-based pincer complexes,[30, 31] b) Carbodiphosphorane-based complexes,[30] c) N-heterocyclic carbene-based complexes.[33–37]

examples of catalytic H/D exchange are known.[38] NHC-based pincer complexes are reported to be active in Heck- and Suzuki-couplings.[33] For CDP-based pincer complexes, so far only few examples are known and only their reactivity concerning protonation and deprotonation reactions has been reported.[30]

1.1.3 Nitrogen based pincer ligands

Nitrogen as the central donor atom is usually employed as amine. These ligands are isoelectronic to borylenes, but much better explored.[39] Numerous applications in homogeneous catalysis, especially (de)hydrogenations, show their ability to be adapted to varying environments. Some typical examples of amine-based pincer complexes and their application are shown in Fig. 1.7. Possible substrates for hydrogenation and dehydrogenation also include more challenging compounds, such as carbamates, amides, esters and ureas.[28, 40–55] The amine can be embedded in an aryl group or bound to alkyls. The other two donor groups can vary from tertiary phosphines to carbenes, olefines, silylenes, heterocycles and thioethers.

Recently, nitrenium based pincer ligands were successfully synthesized by the group of *Gandelman* (Fig. 1.7b).[56–58] They are isoelectronic to carbenes, but much harder to stabilize due to their positive charge and thus coulomb repulsion to the positively charged metal center.

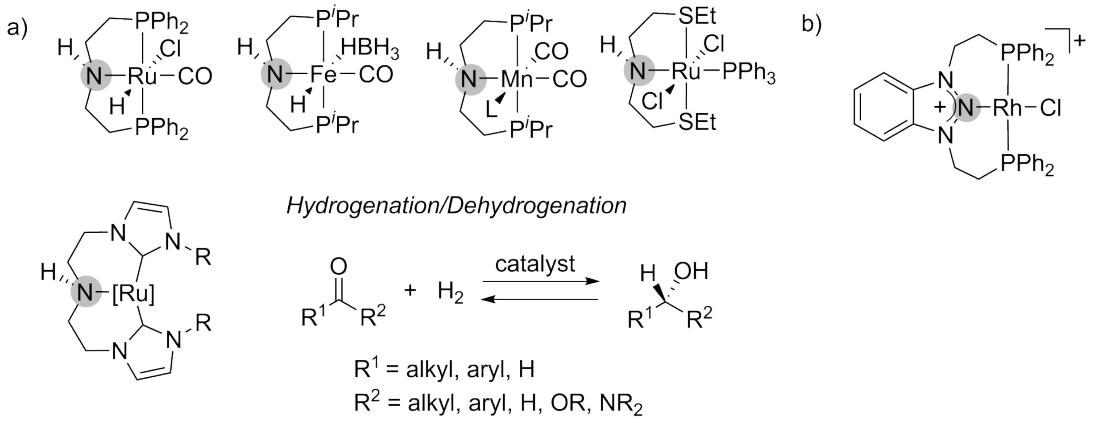

Figure 1.7: a) Examples for amine-based pincer complexes that are highly active in hydrogenation and dehydrogenation reactions.[28, 40–55] b) First example of a nitrenium-based pincer ligand by *Gandelman*.[56]

1.2 Relativistic effects

For elements heavier than cesium, an influence of relativistic effects on their properties and reactivities can be observed and thus needs to be taken into account when performing quantum chemical calculations on these systems.[59] Furthermore, unexpected experimental observations are often owed to relativistic effects when heavy elements are present. The origin of these effects lies in the fact that for heavier elements, the inner electrons possess a higher speed.[60] The relationship between the radial velocity and the atomic number for 1s-electrons is linear and for mercury, the velocity of the 1s-electrons already is 58 % of the speed of light. According to the special theory of relativity, the mass increases and is given by

$$m = \frac{m_0}{\sqrt{1 - \left(\frac{v}{c}\right)^2}} \tag{1.1}$$

with m_0 being the stationary mass, v the speed of the particle and c the speed of light. For mercury, the mass of an 1s-electron is approximately 1.2 m_0. This has a direct effect on the *Bohr* radius, which is given by

$$a_0 = \frac{4\pi\,\varepsilon_0\,\hbar^2}{m\,2e^2} \tag{1.2}$$

with ε_0 the electric constant, $\hbar$ the reduced Planck constant, m the mass of the electron and e the charge of the electron. The contraction of the 1s-orbital (and subsequent s-orbitals) for mercury is about 20 %. This effect is called the *relativistic contraction* and is responsible for the inertness of the s-orbitals in the heavier elements. The p-orbitals

are also contracted, but not at the same magnitude for the $p_{1/2}$ and $p_{2/3}$. This is due to another relativistic effect, the *spin-orbit splitting*: The quantum numbers l and s are no "good quantum numbers" anymore, only the vector sum $\vec{j} = \vec{l} + \vec{s}$ is. Therefore for $l \neq 0$ the p-orbitals split up into two sets. As a result of the contraction of s- and p-orbitals, the nucleus charge is shielded better and the d- and f-orbitals expand, which is the so called *relativistic expansion*.

One of the most pronounced example for the influences of relativistic effects is the element gold. Without relativistic effects, its colour would be silver like its lighter homologue, but the changes in the orbital structure and energies, and therefore the band structure, result in a shifted absorption in the blue/violet range and thus the golden colour. Another example is mercury, which has baffled scientists for hundreds of years, due to its liquid state at ambient conditions. Recently, *Schwerdtfeger* and co-workers found, that relativistic effects are responsible for the liquid nature of mercury; without relativity, mercury would be a solid at room temperature as the other metals.[61]

1.3 Bonding analysis

A valuable tool for the understanding of novel molecules and their bonding situation are quantum chemical calculations. These can be either wave-function based or density functional theory (DFT) based. The concept of bonds between atoms is solely a model that chemists use to understand molecules better and has no physical equivalent which could be observed directly, making bonding analysis a highly-discussed field. Different approaches exist for the evaluation of bonding situations by quantum chemical methods and while they all have their limitations, they can provide valuable information on chemical interpretation of the obtained data. Especially the combination of different methods often helps to complete the picture of how a molecule can be explained by common concepts in chemistry.

1.3.1 Quantum Theory of Atoms in Molecules

The Quantum Theory of Atoms in Molecules (QTAIM) was developed by *Richard Bader* in the 1990s and connects the physical observable of the electron density $\rho(\vec{r})$ with the concept of bonds between atoms.[62]

The electron density shows maxima at the cores and drops from there in all directions. Therefore the gradient of the electron density $\nabla\rho(\vec{r})$ is zero at the surface between two

atoms. These surfaces are so-called *zero-flux surfaces* and describe the boundary of atomic basins, which usually contain one atom. The trajectories of the density gradient originates in infinity and ends at the critical points, where $\nabla\rho = 0$. For a better differentiation between the critical points, the Laplace operator is applied to the electron density:

$$\Delta\rho(\vec{r}) = \nabla^2\rho(\vec{r}) = \left(\frac{\partial^2}{\partial x^2} + \frac{\partial^2}{\partial y^2} + \frac{\partial^2}{\partial z^2}\right)\rho(\vec{r}) \tag{1.3}$$

Depending on the sum of the signs, the critical points can be categorized:

- Core critical point: The sum of the signs equals -3, the electron density drops in all three spatial directions and a maximum is observed.
- Bond critical point (bcp): The sum of the signs equals -1. The electron density rises in one direction (the one of the core critical points) and drops in both other directions. The appearance of a bond critical point is usually taken as an indicator for a chemical bond, but does not necessarily mean the existence of a bond.[63]
- Ring critical point (rcp): The sum of the signs equals +1. The electron density drops only in one direction and rises in the other two directions. This point lies within a ring molecule. The gradient rises within the ring plane and drops orthogonal to the ring plane.
- Cage critical point (ccp): The sum of the signs equals +3. The electron density rises in all directions, because this point lies within a cage of atoms. The cage critical point therefore signifies a local minimum in the electron density.

Inspection of a topological Laplace map shows at which points electron density is accumulated (negative sign) or removed (positive sign). With this, non-bonding electron pairs can be characterized.
The connecting line between two atoms along the path of maximum electron density via the bcp is the so-called bond path. This path is not necessarily the shortest connection between two atoms (e.g. in constrained ring systems). In contrast to the bond itself, the bond path is an observable, due to its direct correlation with the electron density. The bond path therefore describes, which atoms interact with each other, but does not always mean a bond in the classical sense of chemistry.[63]

1.3.2 Energy Decomposition Analysis

Already in the 1970s *Morokuma*, *Ziegler* and *Rauk* developed the Energy Decomposition Analysis (EDA, also sometimes called ETS, Extended Transition State method).[64, 65] In this framework, quantum mechanical descriptions are connected to the interpretation within chemical models of bonding. The basic idea is to seperate the total interaction energy ΔE_{int} between two molecular fragments A and B of the molecule A-B into three parts, which can be interpreted chemically:

$$\Delta E_{\text{int}} = \Delta E_{\text{Elstat}} + \Delta E_{\text{Pauli}} + \Delta E_{\text{Orb}} \tag{1.4}$$

ΔE_{Elstat}: electrostatic interaction
ΔE_{Pauli}: Pauli repulsion
ΔE_{Orb}: orbital interaction

During an EDA, all three interaction terms are obtained.
The molecule A-B has the wave function Ψ_{AB} and the energy E_{AB} in its ground state. Before interacting, the fragments A^0 and B^0 (with wave functions Ψ^0_{A} and Ψ^0_{B}) have the ground state energies E^0_{A} and E^0_{B}. During the EDA, the fragments are excited into their geometries and electronic structures as in the molecule to give fragments A and B with wave functions Ψ_{A} and Ψ_{B} and energies E_{A} and E_{B}.
The necessary energy for this excitation is called preparation energy Δ_{prep} (formula 1.5). Together with the interaction energy ΔE_{int}, the dissociation energy D_{e} is obtained as in formula 1.6:

$$\Delta_{\text{prep}} = E_{\text{A}} + E_{\text{B}} - E_{\text{A}^0} - E_{\text{B}^0} \tag{1.5}$$

$$-D_{\text{e}} = \Delta E_{\text{int}} + \Delta_{\text{prep}} \tag{1.6}$$

The excited fragments are now brought together from an infinite distance. In this state, the electrostatic or Coulomb interaction between the charges of fragments A and B can be calculated as follows:

$$\Delta E_{\text{Elstat}} = \sum_{\alpha\in\text{A}}\sum_{\beta\in\text{B}} \frac{Z_\alpha Z_\beta}{R_{\alpha\beta}} - \int \sum_{\alpha\in\text{A}} \frac{Z_\alpha}{|r-R_\alpha|}\rho_{\text{B}}(r)\,\mathrm{d}r - \int \sum_{\beta\in\text{B}} \frac{Z_\beta}{|r-R_\beta|}\rho_{\text{A}}(r)\,\mathrm{d}r + \int\int \frac{\rho_{\text{A}}(r_1)\,\rho_{\text{B}}(r_2)}{r_{12}}\,\mathrm{d}r_1\,\mathrm{d}r_2 \tag{1.7}$$

Together, the fragments form the so-called "pre-molecule", which is described as the Hartree product $\Psi_A\Psi_B$ with the energy E^0_{AB}. To obtain the Pauli repulsion, this intermediate wave function is normalized and the anti-symmetrization operator $\hat{A}$ is applied to form the anti-symmetric wave function Ψ^0 with the energy E^0:

$$\Psi^0 = N\hat{A}\{\Psi_A\Psi_B\} \tag{1.8}$$

The Pauli repulsion is obtained as the difference between the energy of the non-anti-symmetrical state E^0_{AB} and the energy of the anti-symmetrical state E^0:

$$\Delta E_{\text{Pauli}} = E^0_{AB} - E^0 \tag{1.9}$$

Finally, the excited molecule is being relaxed back to the ground state. The energy that is released during this process is the so-called orbital interaction energy ΔE_{Orb}:

$$\Delta E_{\text{Orb}} = E_{AB} - E^0_{AB} \tag{1.10}$$

The last relaxation can also be described as the change $\Delta\rho$ in the electron density between the excited state Ψ^0 with the density ρ^0 in the ground state with the density ρ:

$$\Delta\rho = \rho - \rho^0 = \sum_{\mu\nu}(P_{\mu\nu} - P^0_{\mu\nu})\chi_\mu\chi_\nu = \sum_{\mu\nu}\Delta P_{\mu\nu}\chi_\mu\chi_\nu \tag{1.11}$$

$\mathbb{P}$ and $\mathbb{P}^0$ are the density matrices before and after relaxation and χ_μ are the basis functions from the Linear Combination of Atomic Orbitals (LCAO) ansatz.
In symmetrical molecules, the difference density matrix $\Delta\mathbb{P}$ contains blocks of irreducible representations Γ and thus the orbital interaction can also be described as the sum of the orbital contributions of these blocks:

$$\Delta E_{\text{Orb}} = \sum_\Gamma \Delta E_{\text{Orb}}(\Gamma) \tag{1.12}$$

For non-symmetrical molecules, an extension of the EDA scheme has been developed, which combines the decomposition of charges and bond energies. For this, the Natural Orbitals for Chemical Valence (NOCV) are used and the method is called EDA-NOCV.[66] The NOCVs are used to break down the total orbital interaction between the fragments into pairwise interactions.
The deformation density $\Delta\rho$ is expressed as the sum of pairs of complimentary eigen-

functions ϕ_{-k}, ϕ_k which correspond to the eigenvalues $-\nu_k$ and ν_k (k goes over the pairs of NOCVs):

$$\Delta\rho(r) = \sum \Delta\rho_k(r) = \sum \nu_k \left(-\Psi_k^2(r) + \Psi_k^2(r)\right) \tag{1.13}$$

The deformation density $\Delta\rho$ can be plotted to provide for visual analysis of the fragment interaction. Usually the number of interactions that contribute significantly to the total orbital energy is rather low.

The orbital interaction term ΔE_{Orb} in the NOCV framework is expressed as follows:

$$\Delta E_{\mathrm{Orb}} = \sum \Delta E_k^{\mathrm{Orb}} = \sum \nu_k \left(-F_{-k}^{\mathrm{TS}} + F_k^{\mathrm{TS}}\right) \tag{1.14}$$

$-F_{-k}^{\mathrm{TS}}$ and F_k^{TS} are the diagonal transition-state Kohn-Sham matrix elements which correspond to the NOCVs with the eigenvalues of $-\nu_k$ and ν_k.

Chapter 2

Project scope and motivation

Approximately 85-90 % of all reactions in the chemical industry are catalyzed.[67] Within these processes, homogeneous catalysis plays a major role in the production of fine chemicals and especially pharmaceuticals.[68] In academic laboratories, homogeneous catalysis is also a highly active area of research, because of its ability to enable precise reactions at milder conditions than with its heterogeneous counterparts. So far, the vast majority of widely applied homogeneous catalysts are based on precious metals. Because of their limited abundancy and therewith already high and further rising prices, the search for more inexpensive, catalytically active transition metal complexes began. One of the most abundant and thus cheapest options is iron. As the lighter homologue of ruthenium, a metal employed in highly active hydrogenation- and dehydrogenation catalysts, it shows a lot of promise.[69] Due to its different redox-reactivity compared to ruthenium (one electron vs. two electron redox steps), the replacement of ruthenium by iron is usually not directly possible. Therefore, new reaction pathways need to be explored.

In this dissertation, new cooperative processes in iron complexes with boron-based ligands were to be explored and extended to other metals and donor-groups as well. The project consists of several subtopics, which will be explained in the following.

Previous work in the *Langer* group by *Nicolas Frank* in the course of his master thesis resulted in the formation of a η^2-phosphine-borane iron complex,[70] which, under carbon monoxide atmosphere, rearranges to give the PBP-pincer complex **1** (Scheme 2.1). In a NOESY-NMR spectrum, a signal for chemical exchange between the Fe-H and B-H had been observed. This kind of rearrangement, ligand-structure and intramolecular exchange process was entirely new and promising for the development of new catalytic pathways. This was the starting point for my work.

The first project of this dissertation involved investigating the formation of **1**, clarification of the bonding mode between the boron and iron atoms and mechanistic investigations on

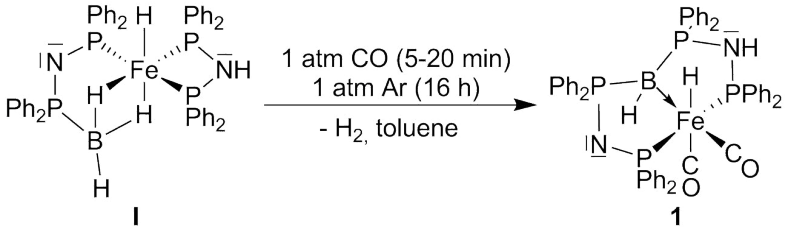

Scheme 2.1: Rearrangement of phosphino-borane complex **I** to PBP-pincer complex **1**

the observed exchange between the Fe-H and B-H. Built on the understanding of complex **1**, its application in catalytic dehydrogenation reactions was to be tested.

In the next step, a new route for the direct synthesis of the PBP-ligand was to be developed to enable variation of the metal center. To achieve this, two different routes seemed possible (Scheme 2.2). Route A should give the protonated PBP-ligand, which could either be reacted directly with metal precursors (preferably carbonyl complexes, which can lose CO ligands under UV light irradiation) or treated with a base first. The second route should give only part of the PBP ligand, which would have to assemble itself fully during coordination to a metal precursor. A suitable precursor for route B seemed, for example, $[Fe(N\{SiMe_3\}_2)_2(thf)]$.

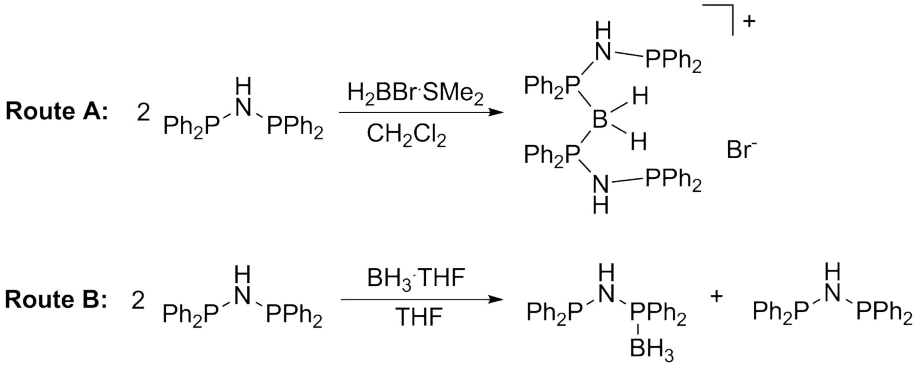

Scheme 2.2: Possible routes for the formation of the PBP-ligand.

Another question that was to be addressed in the course of this work, was the modification of the PBP-pincer complex **1**. Therefore it was supposed to be tested if CO could be replaced by similar small σ-donor/π-acceptor ligands and how this influences the complex formation (Scheme 2.3a).

The obtained complexes were to be fully characterized by NMR, mass spectrometry, IR, and single crystal x-ray diffraction, if possible. Furthermore, the activity in catalytic processes, such as hydrogenation/dehydrogenation or C-H bond activation was to be investigated. When applicable, bonding situations were to be examined by means of

quantum chemistry (DFT and Coupled Cluster (CC) calculations and bonding analysis). Furthermore, investigations on the effect of replacing the boron moiety by aluminium or (protonated) carbodiphosphorane and exchanges of the iron metal center to ruthenium, osmium, manganese and cobalt were to be carried out (Scheme 2.3b). This part was to be performed by quantum chemical methods (EDA-NOCV and Natural Bond Orbital (NBO) analysis), to get a better insight in the applicability of the unique reactivity of **1** to other systems.

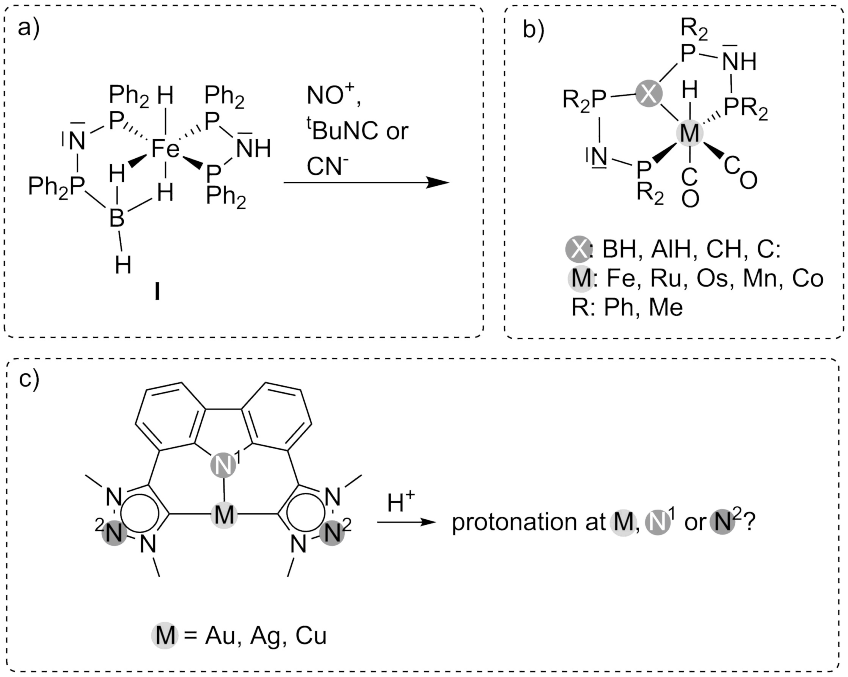

Scheme 2.3: a) Reaction of **I** with other ancillary ligands; b) Possible variations of **1** which were to be investigated quantum chemically; c) Protonation of CNC-pincer coinage metal complexes.

Adding to the investigations of reactivities of transition-metal pincer complexes, the influence of relativistic effects on the proton affinity of coinage metal complexes with a carbene-/carbazole-based CNC-pincer ligand was to be investigated (Scheme 2.3c). This was to be done by DFT and CC calculations.

Chapter 3

Cumulative part

This dissertation consists of five publications, to which I contributed the majority and one publication (no. 3) which contains results of my work as well. In this chapter, these publications will be discussed in the following order:

1. "Phosphine-Stabilized Borylenes and Boryl-Anions as Ligands? Redox Reactivity in Boron-Based Pincer Complexes"
   Lisa Vondung, Nicolas Frank, Maximilian Fritz, Lukas Alig, Robert Langer, *Angew. Chem. Int. Ed.* **2016**, *55*, 14450-14454, DOI: 10.1002/anie.201605838; *Angew. Chem.* **2016**, *128*, 14665-14670, DOI: 10.1002/ange.201605838.

2. "Ambireactive $(R_3P)_2BH_2$-groups facilitating temperature-switchable bond activation by an iron complex"
   Lisa Vondung, Lars E. Sattler, Robert Langer, *Chem. Eur. J.*, DOI: 10.1002/chem.201704018.

3. "Donor ligands based on tricoordinated boron formed by B-H- activation of bis(phosphine)boronium salts"
   Maik Grätz, Andreas Bäcker, Lisa Vondung, Leon Maser, Arian Reincke, Robert Langer, *Chem. Commun.* **2017**, *53*, 7230-7233, DOI: 10.1039/C7CC02335A.

4. "Ancillary Ligand Induced H_2-Liberation from Phosphine-Borane Complexes: Fe-B-Bond Formation vs. Hydride Protonation "
   Lisa Vondung, Lukas Alig, Monika Ballmann, Robert Langer, *submitted*.

5. "Pincer-Type Complexes Based on Phosphine-Stabilized Aluminum(I), Borylene and Carbon(0)"
   Lisa Vondung, Paul Jerabek, Gernot Frenking, Robert Langer, *manuscript in preparation*.

6. “Tipping the Balance between Ligand and Metal Protonation due to Relativistic Effects: The Case of the Coinage Metal(I) Pincer Complexes”
   Lisa Vondung, Paul Jerabek, Peter Schwerdtfeger, *manuscript in preparation.*

3.1 Phosphine-Stabilized Borylenes and Boryl-Anions as Ligands? Redox Reactivity in Boron-Based Pincer Complexes

Lisa Vondung, Nicolas Frank, Maximilian Fritz, Lukas Alig, Robert Langer, *Angew. Chem. Int. Ed.* **2016**, *55*, 14450-14454; *Angew. Chem.* **2016**, *128*, 14665-14670.

Abstract: Stabilized borylenes (L_2BH:) with weakly π-accepting substituents L, such as phosphines, were previously believed to be unstable. In the current manuscript, we describe a series of complexes formally containing a phosphine-stabilized borylene or boryl anion. In contrast to common trivalent boron compounds, the boron-based ligands in this study act as electron-donating ligands. The reported iron hydride complexes exhibit a unique reactivity pattern, undergoing a reversible B-H reductive elimination concomitant with oxidation of the boron(I) center.

Contents: Due to their vacant p_z orbital, ligands based on tricoordinate boron usually act as Lewis bases or electron accepting ligands. A few examples are known where this behaviour can be changed by installing strong σ-donors/π-acceptors at the boron atom. The resulting borylenes show Lewis acidic or electron donating character in complexes.

In this work, we investigated an unusual ligand rearrangement that leads to a PBP pincer ligand with a phosphine-stabilized borylene as central donor group (Fig. 3.1a). The boryl complex **I** first reacts with one equivalent of CO, forming the short-lived intermediate **2**, in which the hapticity of the borane ligand changed from 2 to 1. Reaction with a second equivalent of CO and loss of H_2 leads to the formation of boryl-complex **3**. In solution, this complex slowly isomerizes to borylene-complex **1**. Experimental (X-ray and NMR spectroscopy) and quantum chemical (Molecular Orbitals, Natural Population Analysis, Wiberg Bond Indices, QTAIM) data both show the electron donating character of the boron atom.

In solution, **1** shows an intramolecular exchange between the iron and boron bound hydrogen atoms, as observed by ^{1}H NOESY NMR spectroscopy. Kinetic and thermodynamic data, deuteration experiments and quantum chemical calculations on possible mechanisms showed that the exchange proceeds via a reversible reductive elimination/oxidative addition mechanism (Fig. 3.1b). The iron bound hydrogen atom is reductively eliminated, resulting fomally in an Fe(0)/B(III) species with both hydrogen atoms bound to boron. Then, the other boron bound hydrogen atom is oxidatively added to iron and the Fe(II)/B(I) complex is formed again.

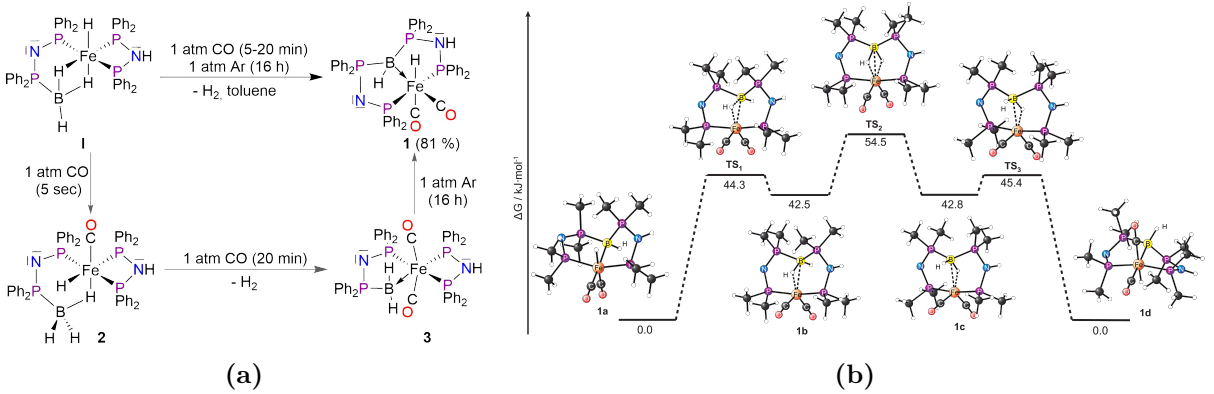

(a) (b)

Figure 3.1: (a) Formation of PBP pincer complex **1** via borane complex **2** and boryl complex **3**. (b) Exchange mechanism for intramolecular H-H exchange in **1**, as calculated with B97D/def2-TZVPP.

Reactivity studies on complex **1** show that (de)protonation takes place selectively at the amines in the ligand backbone. The (de)protonation affects the exchange rate and barriers significantly, which was rather unexpected.

In order to probe whether the formal Fe^0L_4 intermediate can be employed in catalytic bond activation processes, we tested **1** in the catalytic dehydrogenation of benzyl alcohol. We found it to be active under the condition that an external base was added. The deprotonated complex is also active without additional base, suggesting that the lower exchange barrier in the deprotonated complex does play a role for the catalytic process.

Own contribution: The first synthesis of **1** was done by Nicolas Frank in the course of his master thesis under Robert Langer's supervision. I optimized the syntheses of **1** and **5** and carried out the synthesis of the deprotonated complex **4**. Maximilian Fritz did the first synthesis of **5** during a research project under Robert Langer's and my supervision. Lukas Alig did some of the catalytic experiments during a research project under my supervision. All $^{31}P\{^1H\}$ NMR experiments were recorded by myself. ^1H and ^{13}C NMR spectroscopy was done by me on automated spectrometers and temperature dependent and ^{11}B, NOESY and ^{31}P and ^{11}B decoupled spectra were measured by the NMR core facility. Mass spectrometric and elemental analyses were performed by the Mass Spectrometry core facility. All IR spectra were measured by myself. All analytical data was evaluated by myself. X-ray diffraction analysis and structure solving and refinement was done by Robert Langer and me. I planned, performed and evaluated all DFT calculations. Robert Langer and I co-wrote the manuscript.

3.2 Ambireactive $(R_3P)_2BH_2$-groups facilitating temperature-switchable bond activation by an iron complex

Lisa Vondung, Lars E. Sattler, Robert Langer, *Chem. Eur. J.* **2017**, DOI: 10.1002/chem.201704018.

Abstract: An iron pincer complex containing a hemi-labile $(R_3P)_2BH_2$-group exhibits temperature-switchable reactivity patterns: a reversible B-H-activation concomitant with a P-B-bond cleavage is observed at room temperature. Below 4 °C, intra- and intermolecular C-H-activation pathways are becoming faster and dominating. Mechanistic investigations reveal that the lability of the $(R_3P)_2BH_2$-group in combination with the exothermic formation of σ-bonded complexes are responsible for the switchable bond activation. Finally, a protocol for an iron-catalysed H/D-exchange of organic solvents in the absence of oxidants has been developed.

Contents: Complexes of boron-based tridentate ligands show multiple types of metal-ligand cooperativity. Usually, hydrido-borates are formed either by insertion of a hydride ligand in the M-B bond (borane complexes), by addition of H_2 across the M-B bond (boryl complexes) or by reductive elimination of a Fe-H/oxidative addition to B (borylene complexes). Depending on the ligand at the boron-atom or oxidation state of the metal, different reactivities can be observed.

In an attempt to synthesize the previously reported PBP pincer complex (see section 3.1), we reacted *N,N*-bis(diphenylphospino)amine (dppa) with $BH_3 \cdot THF$ to obtain the phosphino-borane adduct **1** (Scheme 3.1). Addition of two more equivalents of dppa and an iron(II) precursor led to the formation of a bis(phosphino)borate-based tridentate ligand in an iron hydride complex (**2**, Scheme 3.1). We further showed, that two different reactivity patterns are present in **2**. NOESY NMR spectra at room temperature and at 260 K revealed the different processes. Using line-shape analysis on temperature-dependent ^1H NMR spectra and subsequent Eyring analysis, the activation parameters for both processes could be obtained. Deuteration experiments and quantum chemical calculations werde performed in order to understand the activation processes. At temperatures above 4 °C, a reversible B-H activation process between the borane and the iron atom dominates. Below 4 °C, this process is hardly observable and an inter- and intramolecular C-H activation process between the *ortho*-phenyl hydrogen atoms at the phosphines or hydrogen atoms of solvent molecules and the metal atom takes place.

The observed C-H activation led to the development of a protocol for the use of complex **2** in catalytic D/H exchange in deuterated solvents.

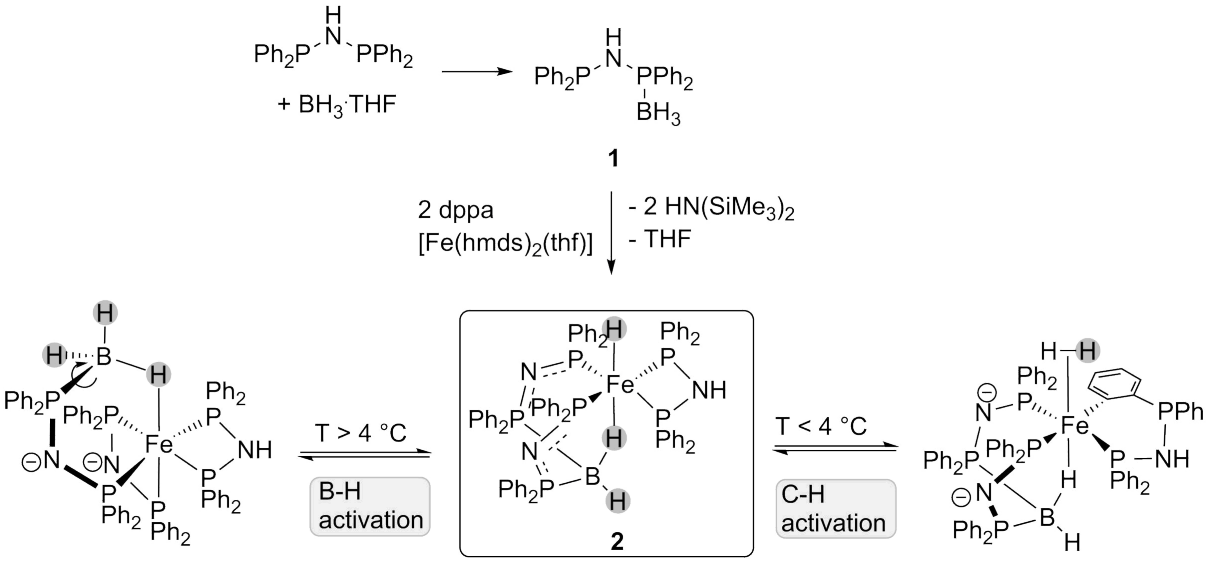

Scheme 3.1: Formation of the phosphino-borane adduct **1** and subsequent reaction with $[Fe(N\{SiMe_3\}_2)_2(thf)]$ to the bis(phosphino)borate complex **2**.

Own contribution: The first synthesis of **1** and **2** was done by Lars E. Sattler during his research project in the group under Robert Langer's and my supervision. I optimized the syntheses of **1** and **2**, planned and performed the synthesis of all other compounds and developed the protocol for the catalytic reactions. All $^{31}P\{^1H\}$ NMR spectra were recorded by myself, ^1H and ^{13}C NMR spectra were recorded on automated spectrometers and all other spectra and variable temperature measurements were recorded by the NMR core facility. Mass spectrometric and elemental analyses were performed by the mass spectrometry core facility. Analytical results were evaluated by myself, with the help of Robert Langer for the kinetic measurements. I planned, performed and evaluated all DFT calculations. Robert Langer and I co-wrote the manuscript.

3.3 Donor ligands based on tricoordinated boron formed by B-H-activation of bis(phosphine)boronium salts

Maik Grätz, Andreas Bäcker, Lisa Vondung, Leon Maser, Arian Reincke, Robert Langer, *Chem. Commun.* **2017**, *53*, 7230-7233.

Abstract: We report a novel method for the preparation of PBP-pincer complexes from bis(phosphine)boronium salts. The central $(R_3P)_2HB$-moiety in a palladium complex is demonstrated to be a L-type ligand, therewith completing a series of pincer-type complexes with Z-, X- and L-type boron-based ligands, respectively.

Contents: The stabilization of a borylene by phosphines in a PBP pincer ligand has been reported by our group before (see section 3.1). Because of the unusual intramolecular rearrangement to form this ligand, we set out to develop a different synthetic approach to obtain transition metal complexes with a phosphine-stabilized borylene pincer ligand. In the previous report on this ligand type, a bis(phosphine)boronium was found as an intermediate. Therefore, the synthesis was attempted via such a species. 1,1-bis(diphenylphosphino)methane (dppm) was reacted with $BH_2Br \cdot SMe_2$ to give the bis(phosphine)boronium salt **1** (Scheme 3.2). Reaction with $[Pd(MeCN)_2Cl_2]$ yielded the palladium PBP-pincer complex **3**. Reaction with other palladium and nickel-precursors did not lead to M-B bond formation. Comparison of Pd-B bond lenghts and $^{11}B\{^1H\}$-NMR shifts of **3** with X- and Z-type palladium complexes with a tricoordinate boron as ligand showed a clear distinction to these compound classes. Quantum chemical calculations by means of NBO and QTAIM confirmed the assignment of the boron moiety in **3** as L-type ligand. For the three ligand types, significant differences in the spectroscopic and quantum chemical data could be made out.

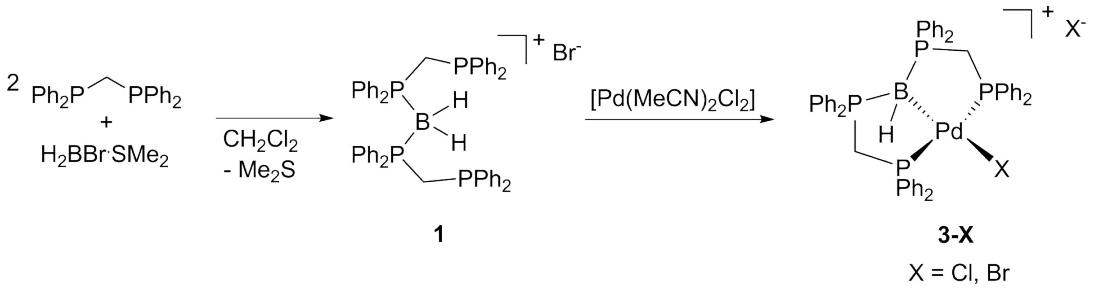

Scheme 3.2: Formation of the bis(phosphine)boronium salt **1** and subsequent reaction to the palladium PBP-pincer complex **3**.

Own contribution: I suggested the synthetic approach to the formation of the bis-(phosphine)boronium salts and planned, performed and analyzed the DFT calculations and bond analysis of the discussed complexes and wrote some of the computational parts of the manuscript. Maik Grätz and Andreas Bäcker performed the syntheses and analyzed the products as part of their Diploma/Master theses. Leon Maser did the first synthesis of the bis(phosphine)boronium salt and helped with the DFT calculation of the literature compounds. Arian Reincke helped with the syntheses as part of his project work in the group. Robert Langer had the project idea, supervised the project, did the x-ray crystallographic analyses and wrote the main part of the manuscript.

3.4 Ancillary Ligand Induced H_2-Liberation from Phosphine-Borane Complexes: Fe-B-Bond Formation vs. Hydride Protonation

Lisa Vondung, Lukas Alig, Monika Ballmann, Robert Langer, *submitted*.

Abstract: η^2-coordinated phosphine-borane ligands are demonstrated to undergo dehydrocoupling reactions and simultaneous P-B-bond formation upon treatment with different σ-donor/π-acceptor ligands (CO, ^{t}BuNC, NO^+, CN^-). The general reaction scheme proceeds via coordination of the ancillary ligand and change of the hapticity of the phosphino-borane to a η^1-mode. A second equivalent of the ancillary ligand induces hydrogen liberation from the η^1-coordinated key-intermediate **B**, which depending on the type of ligand results in different products. Formation of a phosphine-stabilized boryl-ligand is observed with carbon monoxide as ancillary ligand, whose subsequent re-arrangement yields a pincer-type ligand with a phosphine-stabilized borylene as central donor group. With *tert*-butylisonitrile as ancillary ligand hydrogen liberation takes place η^1-phosphino-borane moiety is initially maintained, but decomposes further to give a hydride complex with a pending bisphosphino-borate group.

Contents: Phosphine-boranes as ligands for transition metal complexes have been investigated in different contexts previously. Initially, their isoelectronic relationship with alkanes, but at the same time much higher stability as ligands, was the focus of research. More recently, the catalytic dehydrocoupling/dehydropolymerization processes of phosphine-boranes drew attention to the corresponding transition metal complexes in order to understand the elementary steps of these reactions. Since the, previously by our group reported, formation of the iron PBP-pincer complex involves several rearrangement and dehydrocoupling steps of the initial phosphine-borane, we were interested in investigating the influence of other ancillary ligands than CO on these reaction steps. Therefore, we reacted the phosphine-borane complex **I** with NO^+, CN^- and ^{t}BuNC. Reaction with NO^+ did not yield any complexes, but for the reaction with CN^- and ^{t}BuNC, several intermediates could be observed and partially isolated (Scheme 3.3). The reaction with the cyanido ligand proceeds via the same intermediates as with carbon monoxide. Albeit, the stability of the intermediates is different: The η^1-phosphine-borane complex **1-CN** crystallizes easily, whereas for CO, it is only a short-lived intermediate. On the other hand, the boryl-complex **2-CN** can not be observed, while it can be crystallized for CO. Addition of carbon monoxide gas to a solution of **1-CN** leads to the formation of the

borylene pincer complex **3b-CN** with two CO and one CN^- ligand (Scheme 3.3).

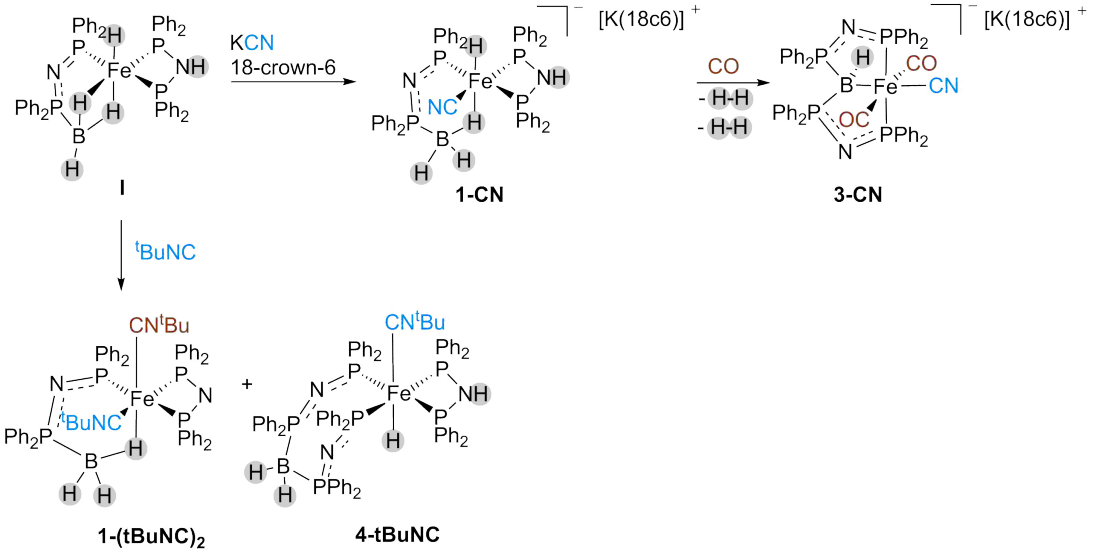

Scheme 3.3: Isolated products from the reactions of **I** with CN^- and ^{t}BuNC.

The reaction of **I** with the isocyanide ^{t}BuNC yielded different products: A mixture of **1-(tBuNC)$_2$** and **4-tBuNC** was obtained (Scheme 3.3). Monitoring the reaction by $^{31}P\{^1H\}$ NMR spectroscopy showed that initially the known η^1-phosphino-borane complex **1-tBuNC** as well as the boryl complex **2-tBuNC** are formed. At the same time, **4-tBuNC** can already be observed and **1-(tBuNC)$_2$** is starting to be formed within the first hour.

Combination of these results enables the formulation of a general reaction scheme for the investigated ligand-induced rearrangement processes (Scheme 3.4). From this scheme, it becomes clear that the stability of **1-L** determines where the first H_2-elimination takes place and therefore which reaction route is followed. Furthermore, the relative Gibbs energies for the different intermediates were calculated. From these results, the experimental observation of different stabilities for the intermediates could be explained. Overall, it can be concluded that the ancillary ligand influences the stability of the intermediates greatly and is therefore an important aspect in the design of transition metal complexes with boron containing ligands.

Own contribution: The project was planned by Robert Langer and me. I performed and evaluated all calculations and supervised all experiments. The first syntheses of **1-CN** and **3-CN** were performed by Lukas Alig during a research project under my supervision.

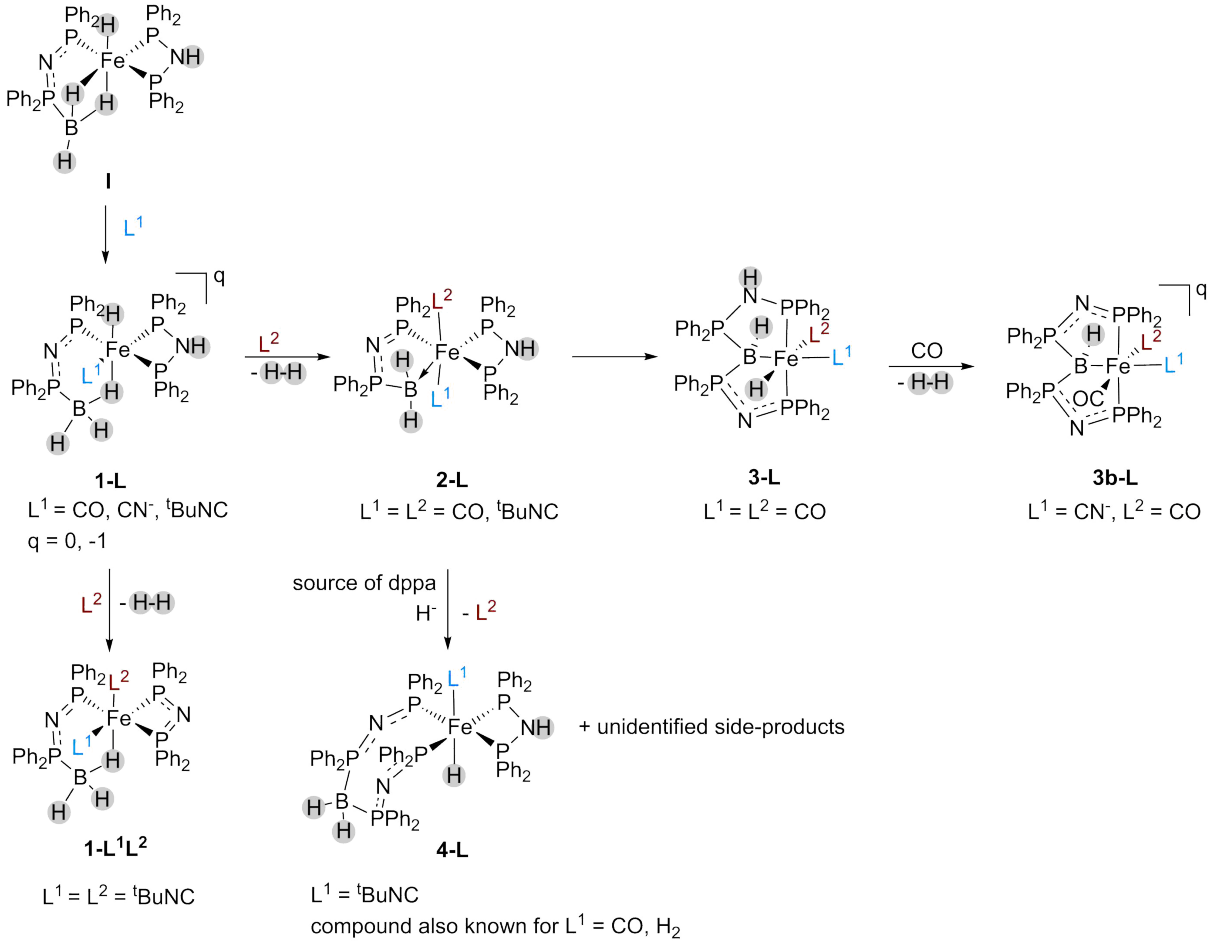

Scheme 3.4: General reaction path for the rearrangement processes induced by ancillary ligands in the phosphino-borane complex **I**.

The first synthesis of **1-(tBuNC)$_2$** was done by Monika Ballmann in a research project under my supervision. I did the synthesis of **4-tBuNC** and the characterization of all products. All $^{31}P\{^1H\}$ NMR spectra were recorded by myself, ^1H and ^{13}C NMR spectra were recorded on automated spectrometers and all other NMR spectra and low temperature measurements were recorded by the NMR core facility. Mass spectrometric measurements were performed by the mass spectrometry core facility. Analytical results were evaluated by myself. Lukas Alig and Monika Ballmann grew the single crystals of **1-CN** and **3-CN** for single crystal x-ray diffraction and Robert Langer did the diffraction experiments. The diffraction experiments on **4-tBuNC** were done by the central x-ray crystallography core facility. All x-ray structures were solved and refined by me and Robert Langer. I wrote the manuscript and Robert Langer corrected the manuscript, provided general support and helpful discussions.

3.5 Pincer-Type Complexes Based on Phosphine-Stabilized Aluminum(I), Borylene and Carbon(0)

Lisa Vondung, Paul Jerabek, Gernot Frenking, Robert Langer, *manuscript in preparation.*

Abstract: A systematic quantum chemical study of the bisphosphine-stabilized main group element fragments AlH, BH, CH^+ and C as ligands in transition metal complexes is reported. The interaction of five different metal ion fragments with (pincer-)ligands containing the four different donor groups is analysed by Energy Decomposition Analysis combined with the Natural Orbitals for Chemical Valence extension for three different fragmentation variants. These results show, that the aluminium(I)-based ligand is not sufficiently stabilized by the phosphine substituents, while the analogous boron(I)-based ligand can be isolated as a ligand coordinated to a transition metal centre. Isoelectronic ligands based on carbon(0), carbodiphosphoranes (CDPs), give rise to strong metal ligand interactions as well, but protonation of the $(R_3P)_2C$-moiety leads to significant destabilization for cationic metal fragments. This is due to repulsion between the cationic ligand and the cationic metal fragment. These findings explain the commonly observed reactivity of CDP-complexes, which often dissociate upon protonation. Finally, we demonstrate for iron(II) complexes that different reactivity patterns are expected for the four donor groups: the experimentally observed reversible E-H-reductive elimination of the borylene-based ligand (E = B) exhibits significantly higher barriers for the protonated CDP-ligand (E = C) and would proceed via different intermediates and transition states. For aluminium, such reaction pathways are not feasible. Moreover, we demonstrate that the metal hydrido complexes with CDP-ligands might not be stable towards reduction and isomerisation to a protonated CDP-ligand and a reduced metal centre.

Contents: In the past, several examples for carbodiphosphorane-based ligands and their protonated analogues were reported. Recently, it was also possible to isolate the isoelectronic borylene-moiety as a donor group for transition metal complexes. This was achieved by strongly donating ligands at the boron atom or incorporation in a pincer ligand, as shown in our previous work. Both CDP- and borylene-complexes exhibit interesting bonding situations. In this work, we investigated how the bonding situation is influenced by changing the donor moiety in the ligand from BH to AlH, CH^+ and C and also varying the metal from iron to ruthenium, osmium, manganese and cobalt. In order

to evaluate and compare the bonding situations, EDA-NOCV was employed and three different cutting schemes were used (Figure 3.2). The first variant cuts the PXP-pincer ligand from the metal with its ancillary ligands. This fragmentation leads to negatively charged ligand fragments (neutral for X = CH^+) and positively charged metal fragments for group 8 and neutral/dicationic fragments for manganese and cobalt, respectively. The charges induce a bias in the EDA-NOCV and thus, we analyzed the complexes with a second fragmentation variant which leads to neutral fragments for the isoelectronic X = BH, AlH and C and group 8 metals. For X = CH^+, this fragment is charged positively and the Mn and Co fragments carry a negative and positive charge accordingly. The first and second variant both cut the M-X bond, but cut the phosphine-metal interaction for variant 1 and the phosphine-X interaction for variant 2. In order to get a clear picture of only the M-X bond, a third variant was employed, in which the amine-bridge was removed and the phosphine-groups were saturated with methoxy-groups. In this variant, the ligand is neutral for BH, AlH and C and positively charged for CH. The metal fragment is positively charged for group 8, neutral for manganese and dicationic for cobalt.

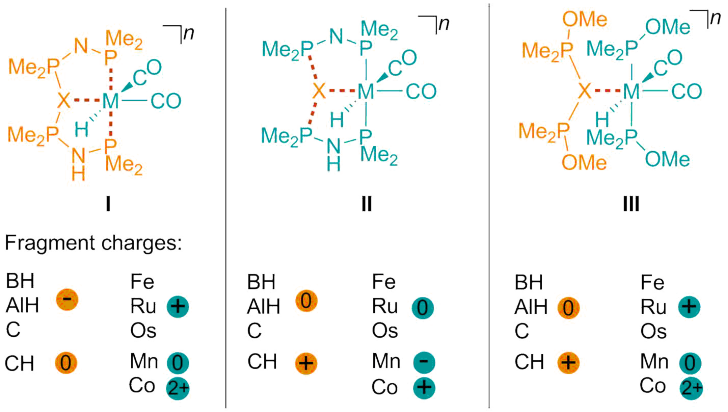

Figure 3.2: Fragmentation variants used for EDA-NOCV and resulting fragment charges for the different donor groups X and metals M.

Comparison of the partial charges, as derived from NBO analysis, shows already that AlH as donor group is rather different to the other donor groups, as the aluminium carries a positive partial charge and the H_{Al} is negatively charged. For the other donor groups, this is exactly the opposite.

The EDA-NOCV results show, that in all combinations of metal and donor group, the donor group does donate electron density towards the metal atom. For the BH and CDP, a similar situation is observed, with the phosphine-groups at X stabilizing it sufficiently to enable donation towards the metal atom and overall large interaction energies. From

cutting variant II, it becomes clear that the AlH fragment is stabilized significantly worse by the phosphine groups compared to the other donor groups. This can be observed in the fact that no electron density is accumulated at the AlH group in the plots of the highest deformation densities, whereas the other X-groups show accumulation of electron density (Figure 3.3).

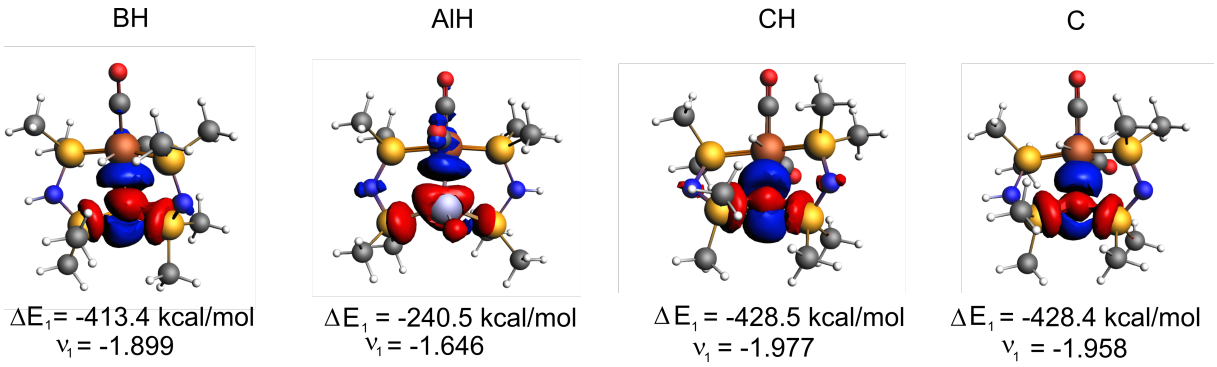

Figure 3.3: Deformation densities with the highest contribution for Fe-X complexes in cutting variant II and corresponding orbital interaction energy contributions ΔE_1 and eigenvalues ν_1. The contour value is $|\Delta\rho| = 0.003$ a.u. The charge flow is from red to blue.

The third cutting variant finally revealed that the electrostatic interaction between the Fe- and CH^+-fragments is very weak, resulting in an overall very weak interaction energy. This can be attributed the positive charges of both fragments and, most probably, the larger s-character of the CH-carbon atom due to the protonation. This also explains why protonated CDP-groups are only isolable for metals in low oxidation states and protonation of CDP ligands often leads to dissociation of the complexes.

For the other group 8 metals, the same observations are made. For manganese and cobalt, the results for variants I and II are also very similar. In Variant III, the 2+ charge of the cobalt fragment and 1+ charge of the CH^+ fragment result formally in a positive interaction energy. Accordingly, this complex is not expected to be stable.

Furthermore, we investigated whether the in the original PBP-pincer iron complex observed Fe-H/B-H exchange can be expected for the other iron complexes as well. To achieve this, we calculated possible transition states and intermediates. For the Fe-AlH complex, an intermediate analogous to the one in Fe-BH was found, but the found transition states did not connect the intermediate to the starting complex. For Fe-CH, the found structure was a transition state that is directly connected with the starting complex and the η^2-isomer, which for Fe-BH is a transition state. Accordingly, the reductive elimination/oxidative addition mechanism found in Fe-BH should be present in Fe-CH^+

as well, although the activation barriers are higher. For Fe-C, we found that the isomer with an Fe(0) and protonated CDP is lower in energy. This suggests that the CDP-ligand probably exhibits a basicity too high for this iron-hydrido complex.

Own contribution: The project was planned by Robert Langer and me. The calculations were planned, performed and evaluated by me. Paul Jerabek introduced me to EDA-NOCV calculations and helped with the interpretation of the results. Gernot Frenking provided the ADF program and helped with the interpretation of the results. Robert Langer supervised the project, helped with the interpretation of the results and co-wrote the manuscript with me.

3.6 Tipping the Balance between Ligand and Metal Protonation due to Relativistic Effects: The Case of the Coinage Metal(I) Pincer Complexes

Lisa Vondung, Paul Jerabek, Peter Schwerdtfeger, *manuscript in preparation*

Abstract: Quantum theoretical studies show that the unusually high proton affinity of the unusual T-shaped (LXL)Au(I)-pincer complex with a carbazole framework and two mesoionic carbenes by *Kleinhans et al.* is due to relativistic effects. This brings the basicity of the Au(I) center in line with the other electron-rich nitrogens in the ligand ring system.

Contents: Proton transfer reactions play an important role in many areas of chemistry, such as catalytic processes, but also other organic reactions, solvation processes or in biomolecular processes. The understanding of these protonation processes is crucial for the design of new molecules with specific properties. *Kleinhans et al.* reported recently on the synthesis and unusual protonation process in a CNC pincer gold(I) complex. In contrast to expectations, protonation occurs at the gold atom and not the electron-rich nitrogen atoms in the ligand.

In this work, we investigated if this unusually high basicity of gold in these (LXL)Au(I) pincer complexes is due to relativistic effects. Therefore, the proton affinity for all three different possible protonation sites (at the metal, at the carbazolide nitrogen atom and the triazole nitrogen atom; see 3.4a) was calculated for the respective copper, silver and gold complexes with and without inclusion of relativistic effects. To ensure if any solvent effects are present, proton affinities were also calculated including the COSMO solvent model for THF. Including the solvation model led to higher proton affinities overall, but did not have any other effect. The proton affinities were rather high in general (between 915 and 1233 kJ/mol, depending on the model and protonation site). For copper and silver protonation is clearly favoured at the carbazolide nitrogen atoms. Without relativistic effects, the same is true for gold, but including them leads to very similar proton affinities for the gold atom and carbazolide nitrogen site. This can also be observed in plots of the electrostatic potential surface (ESP) maps. For copper and silver, no difference can be observed between relativistic and non-relativistic calculations. In the case of gold, the ESP becomes more positive at the gold atom when computed relativistically (Fig. 3.4b and 3.4c). The changes in the Natural Charge, population of ns and np orbitals and

electron localization functions (ELF) for relativistic gold compared to non-relativistic gold explain this observation further.

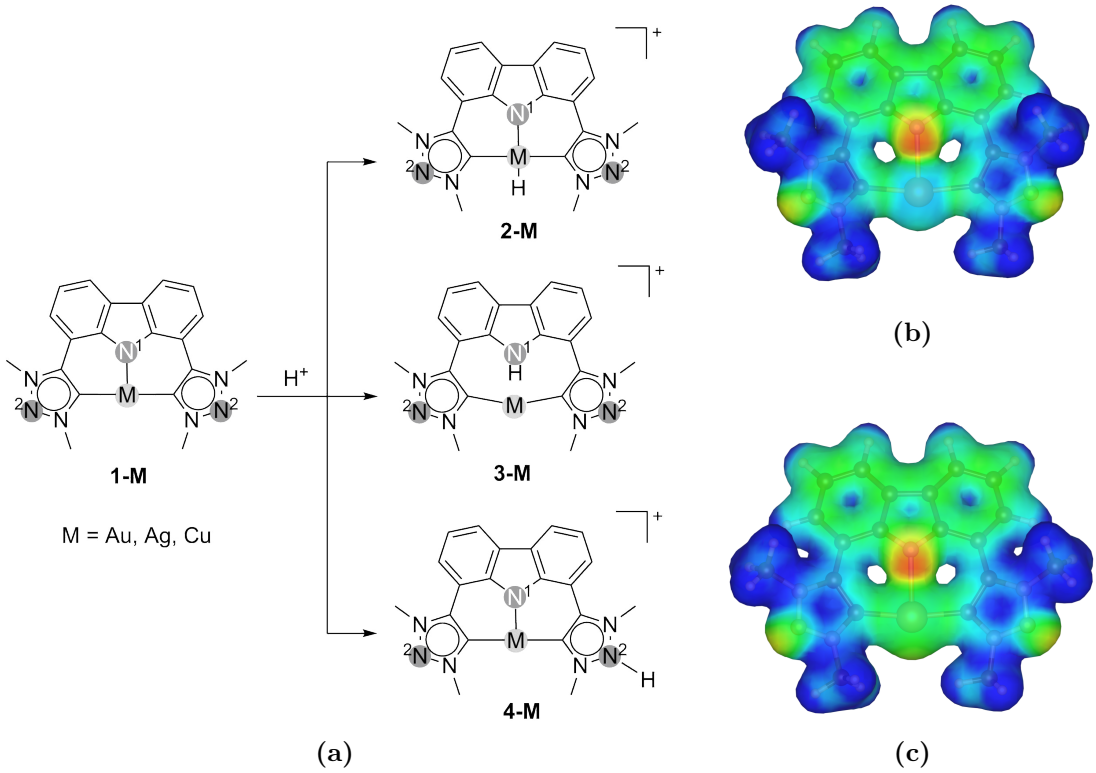

Figure 3.4: (a) Possible protonation sites in (LXL)M(I) coinage metal pincer complexes. (b) Electrostatic potential surface plot for non-relativstic Au-pincer complex. (c) Electrostatic potential surface plot for relativstic Au-pincer complex. Deep blue, green and red areas correspond to ESP values of -0.1, 0.0 and +0.1 a.u., respectively

Own contribution: Peter Schwerdtfeger had the project idea. I designed the calculations with Paul Jerabek and performed the calculations and evaluated the results. Paul Jerabek did the all-electron calculations for the electrostatic potential surface figures and ELF analysis. Paul Jerabek, Peter Schwerdtfeger and I co-wrote the manuscript.

Chapter 4

Summary

The aim of this work was the investigation of novel tridentate boron-based ligands and their complexes. The focus was to be laid on understanding their formation, bonding situation, intramolecular exchange processes, reactivity towards other ancillary ligands, acids and bases and potential as catalysts for homogeneous dehydrogenation and C-H activation reactions. Furthermore, the effects of varying the metal, the central donor-group of the ligand and the ancillary ligands was to be evaluated. The second task of this dissertation was the investigation of the influence of relativistic effects on the proton affinities of CNC-pincer complexes of the coinage metals.

In order to answer these questions, first, the iron PBP-pincer complex **A** (**1***) was investigated. It was shown that the novel formation sequence proceeds via the phosphine-borane complex **B** (**2***), dehydrocoupling to phoshpine-boryl complex **C** (**3***) and subsequent P-B bond formation and B-H activation to form **A** (Scheme 4.1). The iron-boron bond in **A** was characterized as a donor-acceptor bond from boron to iron, making the central donor group the first phosphine-stabilized borylene which has been characterized and reported. The exchange mechanism between the Fe-H and B-H was shown to proceed formally via a reversible reductive elimination/oxidative addition of the Fe-H and B-H. The (de)protonation of the amines in the ligand backbone influences the barrier and rate of this exchange process significantly. **A** was also shown to be active in catalytic dehydrogenation of benzyl alcohol.

Attempts to directly synthesize the PBP ligand led to the formation of a novel iron-hydride complex **D** (**2***) with a tridentate bis(phosphino)borate ligand (Scheme 4.1). The central $(R_3P)_2BH_2$-group exhibits ambireactive behavior, in that it undergoes different bond activation processes depending on the temperature: Below 4 °C, intra- and inter-

*numbering in the corresponding publication

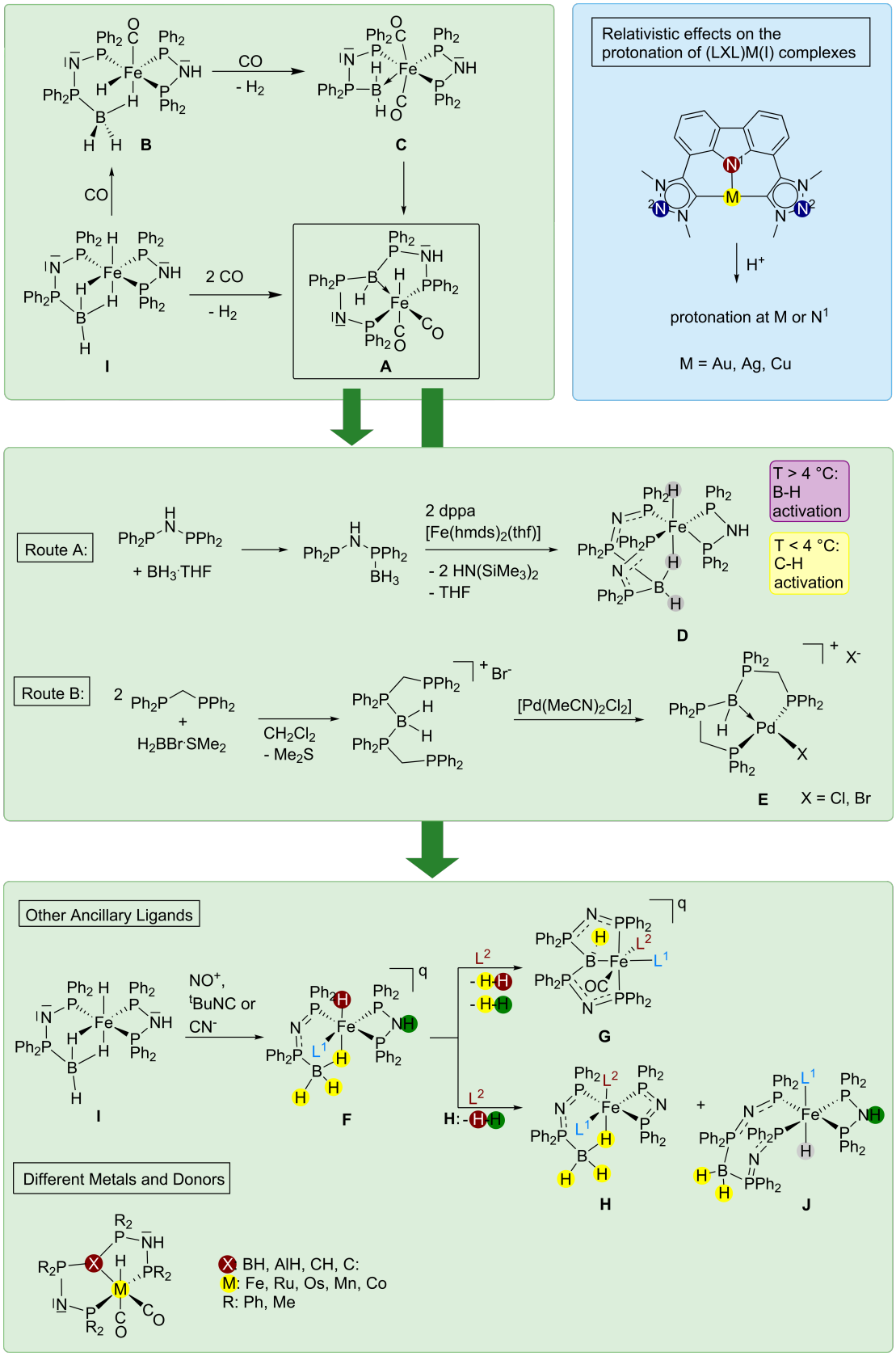

Scheme 4.1: Overview on the different investigations and results in this work.

molecular C-H activation reactions were observed, while above 4 °C, B-H activation and P-B bond cleavage occur. These processes were characterized by temperature dependent 1D- and 2D NMR spectroscopy, deuteration experiments and quantum chemical calculations. Furthermore, complex **D** was also shown to be highly active in the catalytic H/D exchange of deuterated solvents.

The second synthetic approach to the PBP-ligand proved successful and a novel palladium complex **E** (**3-X***) with the PBP pincer ligand was synthesized (Scheme 4.1). Quantum chemical calculations confirmed that the boron moiety can also be described as phosphine-stabilized borylene. Comparison with palladium complexes that contain tricoordinate boron based X- and Z-type ligands showed, that a clear distinction between these three ligand classes is possible.

Next, the variation of different aspects in the iron PBP-pincer complex were investigated. First, the influence of different ancillary ligands other than CO on the complex formation was tested. It was found that, for *tert*-butyl isonitrile and cyanide, in principle the same intermediates as for carbon monoxide can be observed. The stability of these intermediates, especially the η^1-phosphine-borane complex **F** (**1-L***), however, is strongly influenced by the ancillary ligands. They also determine, where the first H_2-elimination takes place and thus, if the PBP-pincer complex **G** (**3/3b-L***) is formed, or if a different phosphine-borane complex **H** (**1-L$_1$L$_2$***) and hydrido complex **J** (**4-L***) are the products.

After clarification of the influence of the ancillary ligand, the variation of the metal atom from iron to ruthenium, osmium, manganese and cobalt and at the same time variation of the central donor moiety from BH to AlH, CH and C was investigated. In order to ascertain if those complexes should be accessible and how the bonding situation can be described in each of these complexes, quantum chemical calculations were performed. Variation of the metal within group 8 did not lead to any changes in the bonding situation and all corresponding complexes with BH, CH and C should be stable. For manganese, the same applies, while the higher oxidation state of the corresponding d^6 cobalt atom leads to an instable complex with the positively charged CH-based ligand. Within the donor groups, it was found that AlH is not sufficiently stabilized by the phosphines and thus the corresponding complexes are rather unstable, which has also been observed experimentally. The complexes with a CDP-based donor groups on the other hand should be accessible and can be described as L-type ligands as expected. For CH as a donor group, a similar intramolecular exchange-pathway as observed for Fe-BH should be possible, while for the AlH based complexes no suitable transition states could be found. Isolation of the

CDP iron complex might not be possible, as the CH-Fe(0) isomer resulting from reductive proton transfer lies lower in energy than the CDP-Fe(II) complex.
In the second part of this work, the investigations on unusual reactivities in transition-metal pincer complexes were extended to a series of copper, silver, and gold complexes with a carbene-/carbazole-based CNC-pincer ligand. Experimentally, a similar gold complex had already been isolated by another group. This complex showed a rather unusual behavior, as it was protonated at the gold(I) atom and not at one of the electron-rich nitrogen atoms. High-level quantum chemical calculations with and without inclusion of relativistic effects showed that for the copper and silver complexes, protonation should occur at the nitrogen atom, as expected. In the gold complex, however, relativistic effects influence its charge, population and electron distribution enough to raise the proton affinity of the gold site to approximately the same value as the carbazole nitrogen. Experimentally, it had been observed that those two protonation sites are both accessible and through the reversibility of the reaction, eventually all complexes are protonated at the gold atom.

Kapitel 5

Zusammenfassung

Das primäre Ziel dieser Arbeit war die Untersuchung neuer dreizähniger Bor-basierter Liganden und deren Komplexe. Der Fokus sollte dabei auf das Verständnis der Bildungsmechanismen, Bindungssituation, intramolekularen Austausch-Prozesse und der Reaktivität gegenüber anderen Hilfsliganden, Säuren und Basen gelegt werden. Neue Komplexe sollten weiterhin auf das Potentials als Katalysatoren für homogene Dehydrierungen und C-H Aktivierungen untersucht werden. Weiterhin sollten die Auswirkungen durch Austausch des Metalls, der zentralen Donor-Gruppe des Liganden und der Hilfsliganden untersucht werden. Ein weiteres Ziel dieser Dissertation war die Untersuchung des Einflusses relativistischer Effekte auf die Protonenaffinität von CNC-Pinzetten-Komplexen der Münzmetalle.

Um diese Fragestellungen zu bearbeiten, wurde zunächst der PBP-Pinzetten-Komplex **A** (**1***) untersucht. Es konnte gezeigt werden, dass die Reaktion zur Bildung von **A** über den Phosphino-Boran-Komplex **B** (**2***) mit anschließender Dehydrokupplung zum Phosphino-Boryl-Komplex **C** (**3***) und schlussendlich einer P-B Bindungsknüpfung und B-H Aktivierung abläuft (Schema 5.1). Die Eisen-Bor-Bindung in **A** wurde mittels quantenchemischer und spektroskopischer Methoden als Donor-Akzeptor-Bindung von Bor zu Eisen klassifiziert, was die zentrale Donor-Gruppe zum ersten charakterisierten und publizierten Phosphan-stabilisierten Borylen macht. Weiterhin wurde gezeigt, dass der Austausch-Mechanismus zwischen dem Fe-H und B-H formal über einen reversiblen reduktiven Eliminierungs-/oxidativen Additions-Mechanismus verläuft. Die (De)protonierung der Aminfunktionen im Liganden-Rückgrat beeinflusst die Austauschbarriere und -rate der Eisen- und Bor-gebundenen Wasserstoffatome signifikant. **A** wurde außerdem in ersten Untersuchungen als Katalysator in der katalytischen Dehydrierung von Benzylalkohol

*Nummerierung in der Originalpublikation

eingesetzt.

Die Versuche, den PBP-Liganden auf direktem Wege zu synthetisieren, resultierten zunächst in der Bildung eines neuen Eisen-Hydrid-Komplexes **D** (**2***) mit einem dreizähnigen Bis(phosphino)borat-Liganden (Schema 5.1). Die zentrale $(R_3P)_2BH_2$-Gruppe ist ambireaktiv, was sich in unterschiedlichen Bindungsaktivierungsprozessen bei verschiedenen Temperaturen äußert: Unter 4 °C wurden intra- und intermolekulare C-H-Aktivierung beobachtet, während oberhalb von 4 °C B-H-Aktiverung und P-B-Bindungsspaltung stattfinden. Diese Prozesse wurden mittels temperaturabhängiger 1D- und 2D-NMR-Spektroskopie, Deuterierungsexperimenten und quantenchemischen Rechnungen charakterisiert. Zusätzlich konnte nachgewiesen werden, dass Komplex **D** in katalytischen H/D-Austauschreaktionen von deuterierten Lösungsmitteln aktiv ist.

Die zweite Syntheseroute zum PBP-Liganden über ein Bisphosphinoboroniumsalz war erfolgreich und ein neuer Palladium-Komplex **E** (**3-X***) mit dem PBP-Liganden wurde isoliert (Schema 5.1). Quantenchemische Rechnungen bestätigten, dass die Bor-Einheit ebenfalls als Phosphan-stabilisiertes Borylen zu beschreiben ist. Durch den Vergleich mit anderen Palladium-Komplexen mit X- und L-Typ-Liganden, die auf dreifach koordiniertem Bor basieren, konte gezeigt werden, dass eine klare Unterscheidung zwischen diesen drei Ligandenklassen möglich ist.

Weiterhin wurde versucht, den Eisen-PBP-Pinzetten-Komplex an verschiedenen Stellen zu modifizieren. Zuerst wurde der Einfluss von anderen Hilfsliganden neben CO auf die Komplexbildung untersucht. Für *tert*-Butylisonitril und Cyanid wurden prinzipiell die gleichen Intermediate wie für CO beobachtet. Jedoch ist die Stabilität dieser Intermediate, besonders des η^1-Phosphino-Boran-Komplexes **F** (**1-L***) stark von der Natur des Hilfsliganden beeinflusst. Die Art der Liganden bestimmt außerdem, wo die erste H_2-Eliminierung stattfindet und dementsprechend auch, ob der PBP-Pinzetten-Komplex **G** (**3/3b-L***) oder ein anderer Phosphinoboran-Komplex **H** (**1-L$_1$L$_2$***) und der Eisen-Hydrid-Komplex **J** (**4-L***) gebildet werden.

Nachdem der Einfluss der Hilfsliganden aufgeklärt worden war, wurde in quantenchemischen Untersuchungen das zentrale Metall-Atom von Eisen zu Ruthenium, Osmium, Mangan und Cobalt variiert. Die zentrale Donorgruppe des Liganden wurde in dieser Studie ebenfalls von BH über AlH zu CH und C variiert. Es galt zu klären, ob diese Komplexe überhaupt prinzipiell stabil sein könnten und wie die Bindungssituation in jedem dieser Komplexe beschrieben werden kann. Die Veränderung des Metalls innerhalb der Gruppe 8 führte nicht zu Änderungen in der Bindungssituation und die Komplexe

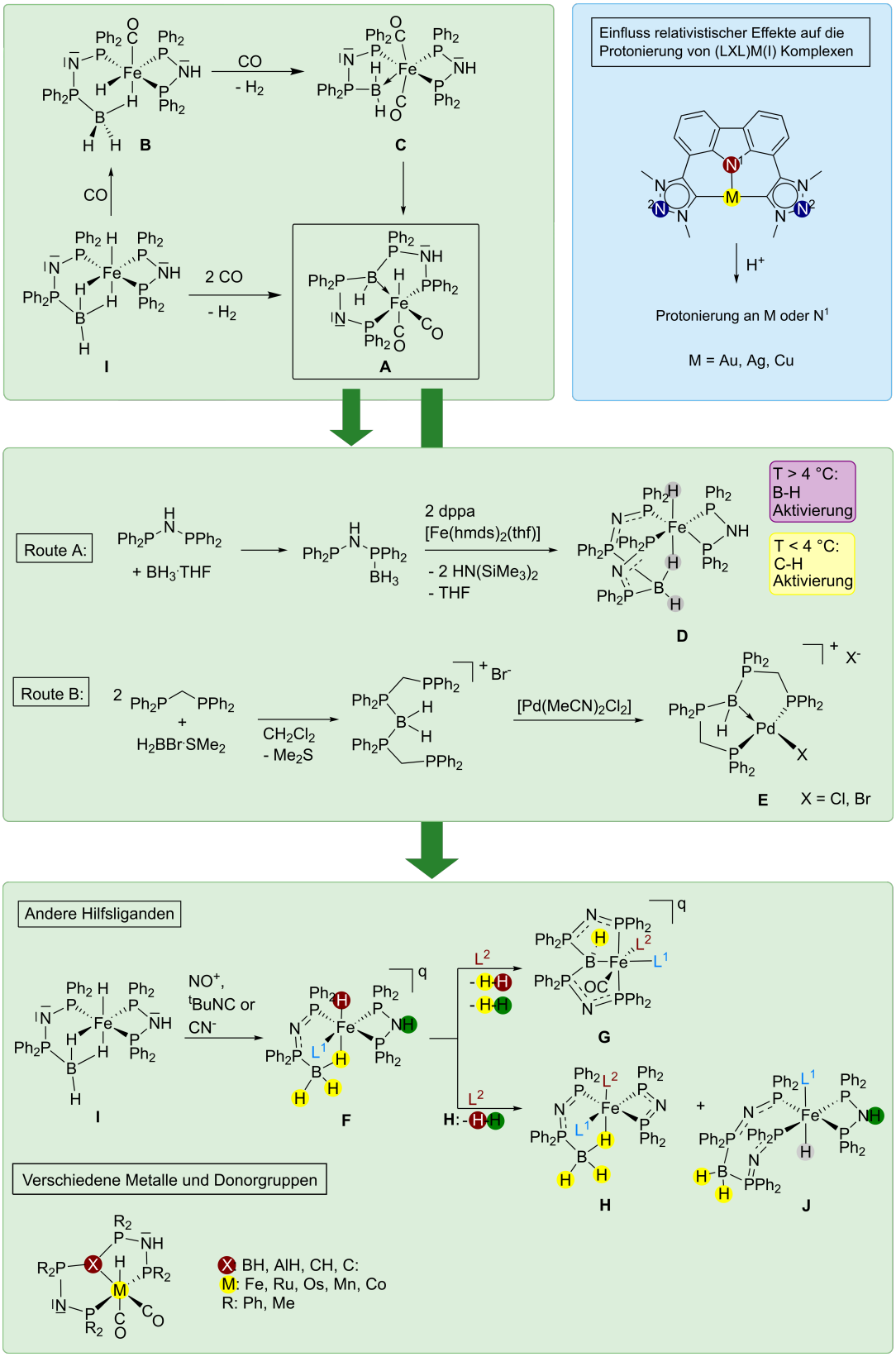

Schema 5.1: Übersicht über die verschiedenen Untersuchungen, die im Rahmen dieser Arbeit durchgeführt wurden und der erhaltenen Ergebnisse.

mit BH, CH und C sollten alle zugänglich sein. Die Funktion der Donorgruppen bleibt ebenfalls als solche erhalten. Für Mangan liegt eine ähnliche Situation vor, während die höhere Oxidationsstufe des entsprechenden d^6-Cobalt-Atoms in Kombination mit dem positiv geladenen CH-basierten Liganden zu keinem stabilen Komplex führt. Bei den Donorgruppen stellte sich heraus, dass AlH durch die Phosphine nur schlecht stabilisiert wird und die entsprechenden Komplexe deshalb nicht stabil sein sollten, was den experimentellen Beobachtungen entspricht. Mit CH als Donorgruppe sollte ein, dem Fe-BH ähnlicher Austauschmechanismus möglich sein, während für die AlH basierten Komplexe keine passenden Übergangszustände gefunden werden konnten. Die Isolierung des Fe-CDP Komplexes könnte schwierig sein, da das Fe(0)-CH Isomer, welches durch reduktiven Protonentransfer gebildet wird, energetisch günstiger ist.

Im zweiten Teil dieser Arbeit wurden die Untersuchungen von ungewöhnlichen Reaktivitäten in Übergangsmetall-Pinzetten-Komplexen auf eine Reihe von Kupfer-, Silber- und Gold-Komplexen mit Carben-/Carbazol-basiertem CNC-Pinzettenligand ausgeweitet. Ein entsprechender Gold-Komplex konnte unlängst von einer anderen Gruppe experimentell charakterisiert werden. Dieser Komplex zeigte ein ungewöhnliches Reaktionsverhalten, da eine Protonierung am Gold(I)-Atom erfolgte und nicht an einem der elektronenreichen Stickstoff-Atome des Liganden. Unsere quantenchemischen Rechnungen zeigten, dass die Ladung, Population und Elektronendichteverteilung durch relativistische Effekte für Gold stark beeinflusst werden. Dies resultiert in einer stark erhöhten Protonenaffinität des Gold-Atoms, sodass diese in etwa den gleichen Wert wie die Protonenaffinität das Carbazol-Stickstoff-Atom besitzt. Experimentell war beobachtet worden, dass diese beiden Protonierungsstellen zugänglich sind. Durch die Reversibilität der Reaktion werden jedoch nach und nach alle Komplexe am Gold-Atom protoniert.

Bibliography

[1] S. Werkmeister, J. Neumann, K. Junge, M. Beller, *Chem. Eur. J.* **2015**, *21*, 12226–12250.

[2] M. Green, *J. Organomet. Chem.* **1995**, *500*, 127–148.

[3] A. Hill, G. Owen, A. White, D. Williams, *Angew. Chem. Int. Ed.* **1999**, *38*, 2759–2761.

[4] H. Braunschweig, R. D. Dewhurst, A. Schneider, *Chem. Rev.* **2010**, *110*, 3924–3957.

[5] M. Sircoglou, S. Bontemps, M. Mercy, N. Saffon, M. Takahashi, G. Bouhadir, L. Maron, D. Bourissou, *Angew. Chem. Int. Ed.* **2007**, *46*, 8583–8586.

[6] Y. Segawa, M. Yamashita, K. Nozaki, *J. Am. Chem. Soc.* **2009**, *131*, 9201–9203.

[7] Y. Segawa, M. Yamashita, K. Nozaki, *Organometallics* **2009**, *28*, 6234–6242.

[8] A. F. Hill, S. B. Lee, J. Park, R. Shang, A. C. Willis, *Organometallics* **2010**, *29*, 5661–5669.

[9] M. Hasegawa, Y. Segawa, M. Yamashita, K. Nozaki, *Angew. Chem. Int. Ed.* **2012**, *51*, 6956–6960.

[10] T. P. Lin, J. C. Peters, *J. Am. Chem. Soc.* **2013**, *135*, 15310–15313.

[11] H. Ogawa, M. Yamashita, *Dalton Trans.* **2013**, *42*, 625–629.

[12] T. Miyada, M. Yamashita, *Organometallics* **2013**, *32*, 5281–5284.

[13] Y. Masuda, M. Hasegawa, M. Yamashita, K. Nozaki, N. Ishida, M. Murakami, *J. Am. Chem. Soc.* **2013**, *135*, 7142–7145.

[14] T. P. Lin, J. C. Peters, *J. Am. Chem. Soc.* **2014**, *136*, 13672–13683.

[15] N. Curado, C. Maya, J. López-Serrano, A. Rodríguez, *Chem. Commun.* **2014**, *50*, 15718–15721.

[16] A. F. Hill, C. M. A. McQueen, *Organometallics* **2014**, *33*, 1977–1985.

[17] T. Miyada, E. Huang Kwan, M. Yamashita, *Organometallics* **2014**, *33*, 6760–6770.

[18] K. Tanoue, M. Yamashita, *Organometallics* **2015**, *34*, 4011–4017.

[19] E. H. Kwan, Y. J. Kawai, S. Kamakura, M. Yamashita, *Dalton Trans.* **2016**, *13*, 15931–15941.

[20] C. M. A. McQueen, A. F. Hill, M. Sharma, S. K. Singh, J. S. Ward, A. C. Willis, R. D. Young, *Polyhedron* **2016**, *120*, 185–195.

[21] W.-C. Shih, W. Gu, M. C. MacInnis, S. D. Timpa, N. Bhuvanesh, J. Zhou, O. V. Ozerov, *J. Am. Chem. Soc.* **2016**, *138*, 2086–2089.

[22] P. L. Timms, *J. Am. Chem. Soc.* **1967**, *89*, 1629–1632.

[23] M. Nomoto, T. Okabayashi, T. Klaus, M. Tanimoto, *J. Mol. Struct.* **1997**, *413-414*, 471–476.

[24] L. Andrews, P. Hassanzadeh, J. M. L. Martin, P. R. Taylor, *J. Phys. Chem.* **1993**, *97*, 5839–5847.

[25] H. F. Bettinger, *J. Am. Chem. Soc.* **2006**, *128*, 2534–2535.

[26] R. Kinjo, B. Donnadieu, M. A. Celik, G. Frenking, G. Bertrand, *Science* **2011**, *333*, 610–3.

[27] L. Kong, Y. Li, R. Ganguly, D. Vidovic, R. Kinjo, *Angew. Chem. Int. Ed.* **2014**, *53*, 9280–9283.

[28] L. Vondung, N. Frank, M. Fritz, L. Alig, R. Langer, *Angew. Chem. Int. Ed.* **2016**, *55*, 14450–14454.

[29] M. Grätz, A. Bäcker, L. Vondung, L. Maser, A. Reincke, R. Langer, *Chem. Commun.* **2017**, 1–4.

[30] L. Maser, L. Vondung, R. Langer, *Polyhedron* **2017**, in press.

[31] D. Gelman, S. Musa, *ACS Catal.* **2012**, *2*, 2456–2466.

[32] R. E. Andrew, L. González-Sebastián, A. B. Chaplin, *Dalton Trans.* **2016**, *45*, 1299–1305.

[33] H. M. Lee, J. Y. Zeng, C. H. Hu, M. T. Lee, *Inorg. Chem.* **2004**, *43*, 6822–6829.

[34] C. Romain, K. Miqueu, J. M. Sotiropoulos, S. Bellemin-Laponnaz, S. Dagorne, *Angew. Chem. Int. Ed.* **2010**, *49*, 2198–2201.

[35] D. R. Weinberg, N. Hazari, J. A. Labinger, J. E. Bercaw, *Organometallics* **2010**, *29*, 89–100.

[36] E. Borré, G. Dahm, A. Aliprandi, M. Mauro, S. Dagorne, S. Bellemin-Laponnaz, *Organometallics* **2014**, *33*, 4374–4384.

[37] C. F. Harris, M. B. Bayless, N. P. van Leest, Q. J. Bruch, B. N. Livesay, J. Bacsa, K. I. Hardcastle, M. P. Shores, B. de Bruin, J. D. Soper, *Inorg. Chem.* **2017**, 12421–12435.

[38] J. Zhou, J. F. Hartwig, *Angew. Chem. Int. Ed.* **2008**, *47*, 5783–5787.

[39] B. Zhao, Z. Han, K. Ding, *Angew. Chem. Int. Ed.* **2013**, *52*, 4744–4788.

[40] D. Spasyuk, S. Smith, D. G. Gusev, *Angew. Chem. Int. Ed.* **2013**, *52*, 2538–2542.

[41] G. A. Filonenko, M. J. B. Aguila, E. N. Schulpen, R. van Putten, J. Wiecko, C. Müller, L. Lefort, E. J. M. Hensen, E. A. Pidko, *J. Am. Chem. Soc.* **2015**, *137*, 7620–7623.

[42] E. A. Bielinski, M. Förster, Y. Zhang, W. H. Bernskoetter, N. Hazari, M. C. Holthausen, *ACS Catal.* **2015**, *5*, 2404–2415.

[43] S. Elangovan, M. Garbe, H. Jiao, A. Spannenberg, K. Junge, M. Beller, *Angew. Chem. Int. Ed.* **2016**, *55*, 15364–15368.

[44] M. B. Widegren, G. J. Harkness, A. M. Slawin, D. B. Cordes, M. L. Clarke, *Angew. Chem. Int. Ed.* **2017**, *56*, 5825–5828.

[45] S. Chakraborty, H. Dai, P. Bhattacharya, N. T. Fairweather, M. S. Gibson, J. A. Krause, H. Guan, *J. Am. Chem. Soc.* **2014**, *136*, 7869–7872.

[46] S. Chakraborty, W. W. Brennessel, W. D. Jones, *J. Am. Chem. Soc.* **2014**, *136*, 8564–8567.

[47] E. A. Bielinski, P. O. Lagaditis, Y. Zhang, B. Q. Mercado, C. Würtele, W. H. Bernskoetter, N. Hazari, S. Schneider, *J. Am. Chem. Soc.* **2014**, *136*, 10234–10237.

[48] P. O. Lagaditis, P. E. Sues, J. F. Sonnenberg, K. Y. Wan, A. J. Lough, R. H. Morris, *J. Am. Chem. Soc.* **2014**, *136*, 1367–1380.

[49] S. Elangovan, C. Topf, S. Fischer, H. Jiao, A. Spannenberg, W. Baumann, R. Ludwig, K. Junge, M. Beller, *J. Am. Chem. Soc.* **2016**, *138*, 8809–8814.

[50] F. Kallmeier, T. Irrgang, T. Dietel, R. Kempe, *Angew. Chem. Int. Ed.* **2016**, *55*, 11806–11809.

[51] N. T. Fairweather, M. S. Gibson, H. Guan, *Organometallics* **2015**, *34*, 335–339.

[52] M. Peña-López, H. Neumann, M. Beller, *ChemCatChem* **2015**, *7*, 865–871.

[53] M. Perez, S. Elangovan, A. Spannenberg, K. Junge, M. Beller, *ChemSusChem* **2017**, *10*, 83–86.

[54] S. Werkmeister, K. Junge, B. Wendt, E. Alberico, H. Jiao, W. Baumann, H. Junge, F. Gallou, M. Beller, *Angew. Chem. Int. Ed.* **2014**, *53*, 8722–8726.

[55] W. Kuriyama, T. Matsumoto, O. Ogata, Y. Ino, K. Aoki, S. Tanaka, K. Ishida, T. Kobayashi, N. Sayo, T. Saito, *Org. Process Res. Dev.* **2012**, *16*, 166–171.

[56] Y. Tulchinsky, M. A. Iron, M. Botoshansky, M. Gandelman, *Nat. Chem.* **2011**, *3*, 525–531.

[57] Y. Tulchinsky, S. Kozuch, P. Saha, M. Botoshansky, L. J. W. Shimon, M. Gandelman, *Chem. Sci.* **2014**, *5*, 1305.

[58] Y. Tulchinsky, S. Kozuch, P. Saha, A. Mauda, G. Nisnevich, M. Botoshansky, L. J. W. Shimon, M. Gandelman, *Chem. Eur. J.* **2015**, *21*, 7099–7110.

[59] P. A. M. Dirac, *Proc. R. Soc. A Math. Phys. Eng. Sci.* **1928**, *117*, 610–624.

[60] P. Pyykkö, J. P. Desclaux, *Acc. Chem. Res.* **1979**, *12*, 276–281.

[61] F. Calvo, E. Pahl, M. Wormit, P. Schwerdtfeger, *Angew. Chem. Int. Ed.* **2013**, *52*, 7583–7585.

[62] R. F. W. Bader, *Accounts of Chemical Research* **1985**, *18*, 9–15.

[63] R. F. W. Bader, *J. Phys. Chem. A* **2009**, *113*, 10391–10396.

[64] K. Morokuma, *J. Chem. Phys.* **1971**, *55*, 1236–1244.

[65] T. Ziegler, A. Rauk, *Theoretica chimica acta* **1977**, *46*, 1–10.

[66] M. P. Mitoraj, A. Michalak, T. Ziegler, *J. Chem. Theory Comput.* **2009**, *5*, 962–975.

[67] Kompetenznetzwerk Katalyse ConneCat, DeCHeMA Gesellschaft für Chemische Technik, Katalyse in Deutschland, `http://www.gecats.de/gecats_media/Urbanczyk/Katalyse_2008_final.pdf`, **2007**.

[68] W. S. Knowles, *Angew. Chem. Int. Ed.* **2002**, *41*, 1999–2007.

[69] S. Enthaler, K. Junge, M. Beller, *Angew. Chem. Int. Ed.* **2008**, *47*, 3317–3321.

[70] N. Frank, K. Hanau, K. Flosdorf, R. Langer, *Dalton Trans.* **2013**, *42*, 11252–11261.

Nomenclature

bcp	bond critical point
CC	Coupled Cluster
ccp	cage critical point
CDP	Carbodiphosphorane
DFT	density functional theory
dppa	*N*,*N*-bis(diphenylphospino)amine
dppm	1,1-bis(diphenylphosphino)methane
EDA	Energy Decomposition Analysis
ELF	electron localization function
ESP	electrostatic potential surface
LCAO	Linear Combination of Atomic Orbitals
NBO	Natural Bond Orbital
NHC	*N*-heterocyclic carbenes
NOCV	Natural Orbitals for Chemical Valence
QTAIM	Quantum Theory of Atoms in Molecules
rcp	ring critical point

Danksagung

Zu guter Letzt möchte ich mich bei den Personen bedanken, die erheblich zum Entstehen dieser Arbeit beigetragen haben: An erster Stelle steht dabei Robert Langer, der mir dieses spannende Thema überlassen hat, mich in den letzten 3,5 Jahren immer unterstützt hat und von dem ich vieles lernen durfte. Schade, dass diese Zeit jetzt schon vorbei ist!
Dann möchte ich mich auch sehr herzlich bei meiner offiziellen Doktormutter Stefanie Dehnen bedanken, die meinen Weg in der Chemie in Marburg seit vielen Jahren begleitet hat und mich ebenfalls in allen Situationen unterstützt hat.
Ein weiteres großes Dankeschön gebührt allen aktuellen und ehemaligen Mitgliedern der AGs Langer, Dehnen und im Nachwuchsbereich für die gute Atmosphäre, außerlaborliche Aktivitäten, gemeinsame Konferenzreisen oder einfach nur Kaffeepausen. Ganz besonders bei Leon möchte ich mich für den guten Zusammenhalt auch in chaotischen Zeiten, den unvergesslichen GRC-Besuch und das Korrekturlesen bedanken! Der ersten AG Langer Truppe Nina, Felix, Weiqin und Leon sei außerdem für den angenehmen Start im AK gedankt.
Bei Peter Schwerdtfeger möchte ich mich sehr herzlich dafür bedanken, dass er es mir ermöglicht hat, einen Teil dieser Arbeit in seiner Gruppe an der Massey University in Auckland anzufertigen und dass ich in dieser Zeit sehr viel lernen dufte. Jan, Andy, Krista, Antony, Lukas, Lukáš, Morten, Odile, Peter, Julius, Steffi, Lotta und Paul sei für die äußerst angenehme Arbeitsatmosphäre, die stets offenen Türen, Frühschwimm- und sonstigen Ausflüge und die tolle Woche auf der WATOC gedankt. Ganz besonders bei Paul möchte ich mich bedanken, dass er mich von den ersten Gehversuchen im TC-Praktikum bis heute begleitet hat, mir unglaublich viel beigebracht hat und ich ihn mit allen Fragen löchern durfte!
Zu dieser Arbeit nicht unerhebliche Teile beigetragen haben außerdem meine Vertiefer Lars, Marc, Vinzent, Lukas, Monika, Yvonne und Franziska, denen an dieser Stelle nochmal für ihre Arbeit gedankt sei!
Ein besonders großer Dank gebührt Reuti, der bei technischen Problemen mit MarC2, Annemarie und diversen Programmen selbst von der anderen Seite der Erde aus eine unglaublich riesige Hilfe war und ohne den ich wahrscheinlich keine einzige Rechnung ab-

geschickt hätte.
Bei den Serviceabteilung des Fachbereichs Chemie, insbesonders der Massenspektrometrie-, NMR- und Kristallographie-Abteilung möchte ich mich ebenfalls für die Messung unzähliger Proben und Sonderwünsche bedanken.
Außerdem möchte ich den Universitätsbibliotheken Kopenhagen und Straßburg und eduroam danken, ohne die das Verfassen dieser Arbeit wesentlich langwieriger und umständlicher gewesen wäre.
Abschließend möchte ich noch die Menschen erwähnen, die mein Leben außerhalb der Chemie bereichert haben: Kerstin, die quasi schon immer ein fester und unverzichtbarer Bestandteil in meinem Leben ist, die Reste der "Box" Marius, Friedrich, Steffen, Robert und Nico, die mit mir das Studium und die Promotion durchgestanden habe, Nina, die ich seit dem 12.12.12 sehr gut kennen und schätzen lernen durfte und den NakNaks oder "os patinhos brancos", die mich sehr effektiv durch beste Ablenkung vor dem Verrücktwerden bewahrt haben und mit denen die #voltadomundo hoffentlich noch lange weiter geht! Zuletzt möchte ich den wichtigsten Menschen danken: Eugen und meiner Familie, dafür, dass ihr immer da wart und seid!

Chapter 6

Appendix

6.1 List of Publications

1. L. Vondung, P. Jerabek, P. Schwerdtfeger, "Tipping the Balance between Ligand and Metal Protonation due to Relativistic Effects: The Case of the Coinage Metal(I) Pincer Complexes", *manuscript in preparation.*

2. L. Vondung, P. Jerabek, G. Frenking, R. Langer, "Pincer-Type Complexes Based on Phosphine-Stabilized Aluminum(I), Borylene and Carbon(0)", *manuscript in preparation.*

3. L. Vondung, L. Alig, M. Ballmann, R. Langer, "Ancillary Ligand Induced H_2-Liberation from Phosphine-Borane Complexes: Fe-B-Bond Formation vs. Hydride Protonation ", *submitted.*

4. L. Vondung, L. E. Sattler, R. Langer, "Ambireactive $(R_3P)_2BH_2$-groups facilitating temperature-switchable bond activation by an iron complex", *Chem. Eur. J.* **2017**, DOI: 10.1002/chem.201704018.

5. L. Maser, L. Vondung, R. Langer, "The ABC in pincer chemistry - from Amine- to Borylene- and Carbon-based Pincer-Ligands", *Polyhedron* **2017**, DOI: 10.1016/j.poly.2017.09.009.

6. M. Grätz, A. Bäcker, L. Vondung, L. Maser, A. Reincke, R. Langer, "Donor ligands based on tricoordinated boron formed by B-H- activation of bis(phosphine)boronium salts", *Chem. Commun.* **2017**, *53*, 7230-7233.

7. L. Vondung, N. Frank, M. Fritz, L. Alig, R. Langer, "Phosphine-Stabilized Borylenes and Boryl-Anions as Ligands? Redox Reactivity in Boron-Based Pincer Complexes", *Angew. Chem. Int. Ed.* **2016**, *55*, 14450-14454; *Angew. Chem.* **2016**, *128*, 14665-14670.

8. L. Vondung, R. Langer, "Ruthenium - weder essentiell noch toxisch, aber katalytisch aktiv!", *Aktuelle Wochenschau* **2016**, Woche 32.

9. G. Thiele, L. Vondung, S. Dehnen, "β-K_2Se_2 and K_2Se_4: Missing links in the binary system K-Se", *Z. Krist.* **2016**, *231*, 257-260.

10. G. Thiele, L. Vondung, S. Dehnen, "About the Syntheses of Chalcogenidometalates by in-situ Reduction with Elemental Alkali Metals", *Z. Anorg. und Allg. Chemie* **2015**, *641*, 247-252.

11. R. Langer, F. Bönisch, L. Maser, C. Pietzonka, L. Vondung, T. P. Zimmermann, "Substitutional Lability of Diphosphine Ligands in Tetrahedral Iron(II) Chloro Complexes", *Eur. J. Inorg. Chem.* **2015**, 141-148.

12. G. Thiele, L. Vondung, C. Donsbach, S. Pulz, S. Dehnen, "Organic Cation and Complex Cation-Stabilized (Poly-)Selenides, $[Cation]_x(Se_y)_z$: Diversity in Structures and Properties", *Z. Anorg. und Allg. Chemie* **2014**, *640*, 2684-2700.

6.2 Reprints of the publications

The publications which are part of this dissertation are presented in their original form in the following in the same order as they were discussed in chapter 3. Permissions for reprint of the already published articles have been obtained from the publisher. Supporting informations are provided as well, except for xyz-coordinates of the calculated structures, which can be found in the supporting informations of the original publications and on CD supplied with this dissertation.

Boron Ligands

International Edition: DOI: 10.1002/anie.201605838
German Edition: DOI: 10.1002/ange.201605838

Phosphine-Stabilized Borylenes and Boryl Anions as Ligands? Redox Reactivity in Boron-Based Pincer Complexes

*Lisa Vondung, Nicolas Frank, Maximilian Fritz, Lukas Alig, and Robert Langer**

Abstract: *Stabilized borylenes (L_2BH:) with weakly π-accepting substituents L, such as phosphines, were previously believed to be unstable. In the current manuscript, we describe a series of complexes formally containing a phosphine-stabilized borylene or boryl anion. In contrast to common trivalent boron compounds, the boron-based ligands in this study act as electron-donating ligands. The reported iron hydride complexes exhibit a unique reactivity pattern, undergoing a reversible B–H reductive elimination concomitant with oxidation of the boron(I) center.*

Trivalent boron compounds are typically electron-deficient and react as electrophiles owing to their vacant p_z orbital. Accordingly, these compounds preferably act as Lewis acids or electron-accepting (Z-type) ligands in transition-metal complexes.[1] Typically, these boron-based Z-type ligands contain σ/π-donating or purely σ-donating substituents. In recent years, increasing effort has been devoted to synthesizing different kinds of nucleophilic boron compounds,[2] including boroles,[3] boryl anions,[4] diazadiborinines,[5] and borylenes[6] as well as metalloborylenes.[7] Most importantly, the utilization of π-accepting substituents, such as N-heterocyclic carbenes (NHCs), cyclic alkyl amino carbenes (CAACs), or cyanides, can stabilize the occupied p_z orbital at the trivalent boron atom.[4n,6b–e,8]

Formally, these nucleophilic boron compounds are isoelectronic to amines and are able to serve as electron-donating or L-type ligands in metal complexes.[4n,9] Bertrand and co-workers, for example, reported a CAAC-stabilized dicyanoboryl anion that readily formed Au^I complex **A** with [(Me_3P)AuCl] (Scheme 1 a).[4n] Kinjo and co-workers used an oxazol-2-ylidene-stabilized phenylborylene as a ligand in several transition-metal complexes (**B**),[9] confirming the nucleophilic nature of these three-coordinated boron compounds.

In this context, it is important to note that quantum-chemical investigations have predicted that ligand-stabilized borylenes (L_2HB:) are stable with σ-donating/π-accepting substituents such as carbenes, and that they can in general serve as electron-donating ligands.[10] Nonetheless, the reactivity of such ligand-stabilized borylenes in transition-metal complexes remains largely unexplored. In comparison, numerous trivalent boron compounds are known whose interaction with a transition-metal fragment is described as a dative bond from an electron-rich metal fragment to a Lewis acidic boron center (Scheme 1 b).[11]

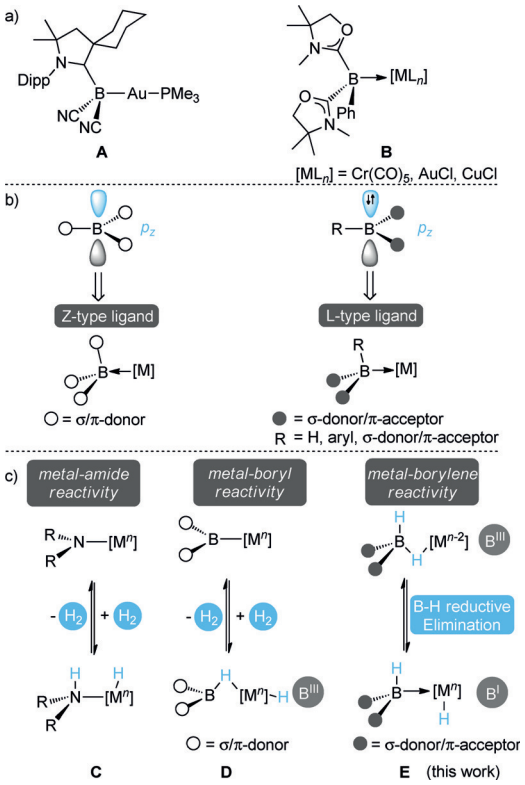

Scheme 1. a) Examples of nucleophilic boron compounds serving as ligands. b) Influence of the substituent properties on the stabilization of tridentate boron species and the relation to the observed ligand type in boron-based ligands. c) Reactivity patterns of metal–amide and metal–boryl complexes in comparison with stabilized borylene and boryl anion complexes.

Although hitherto reported findings showed that a decrease in the π-acceptor ability of the substituents should result in significant destabilization of the borylene (L_2BR:), we were able to synthesize iron complexes containing two phosphines for the stabilization of the :BH fragment, which was then shown to act as an L-type ligand.

The central boron-based donor group in these complexes can be considered as a phosphine-stabilized boryl anion

[*] L. Vondung, N. Frank, M. Fritz, L. Alig, Dr. R. Langer
Department of Chemistry, Philipps-Universität Marburg
Hans-Meerwein-Strasse, 35032 Marburg (Germany)
E-mail: robert.langer@chemie.uni-marburg.de
Dr. R. Langer
Lehn Institute of Functional Material (LIFM)
Sun Yat-Sen University Guangzhou (SYSU)
Xingang Road West, Guangzhou 510275 (PR China)
Supporting information and the ORCID identification number(s) for the author(s) of this article can be found under: http://dx.doi.org/10.1002/anie.201605838.

(LHXB:$^-$ or HX_2B:$^{2-}$, X = anionic phosphine such as $\{Ph_2P–N–PPh_2\}^-$) or as a phosphine-stabilized borylene (L_2HB:). Although such ligands are isoelectronic to amines, we observed fundamentally different reactivity patterns for the new complexes (Scheme 1c). Many hydride complexes with a coordinated secondary amine ligand undergo reversible hydride protonation, which can lead to the formation of an amide complex and dihydrogen liberation (**C**).[12] Like amide complexes, π-donor-stabilized boryl complexes have been reported to heterolytically cleave dihydrogen (**D**).[13] The iron complexes reported herein are to some extent related to these complexes, but they undergo a reversible B–H reductive elimination (**E**). Herein, we demonstrate for the first time that the relative stability of the complexes involved in this redox equilibrium can be strongly influenced by ligand (de)protonation.

Starting from previously reported phosphine–borane complex **I**,[15] we were aiming to modify the reactivity of the coordinated borane group by a change in the hapticity and treated a solution of **I** with one atmosphere of carbon monoxide (Scheme 2). Surprisingly, an unprecedented ligand

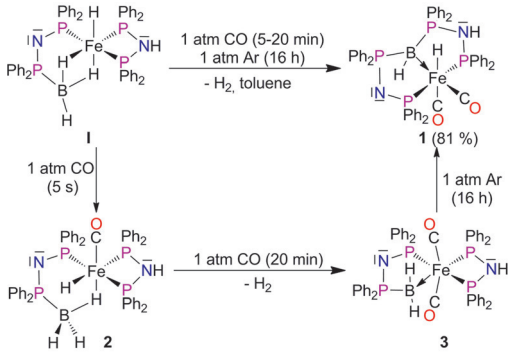

Scheme 2. Synthesis of **1** and its formation via intermediates **2** and **3**.[14]

rearrangement took place, leading to complex **1**. This unique reaction proceeds via two detectable intermediates, **2** and **3** (Scheme 2). The first step indeed involves the coordination of one carbonyl ligand concomitant with a change in the hapticity of the phosphine–borane. The formed η^1-coordinated hydrido phosphine–borane complex **2** subsequently reacts with a second equivalent of carbon monoxide, leading to hydrogen elimination and formation of phosphine-stabilized boryl complex **3**. As phosphine–boranes can be deprotonated,[11b,c,e] it seems likely that in the present case, the η^1-coordinated phosphine–borane in **2** protonates the iron hydride prior to hydrogen liberation. Complex **3** exhibits only limited stability in solution and slowly isomerizes to complex **1**, as determined by ^{1}H and ^{31}P{^{1}H} NMR spectroscopy. Nonetheless, layering a toluene solution containing complex **3** at low temperature with *n*-hexane enabled the isolation of a mixture of single crystals of **1** and **3**.[16]

Although numerous phosphine-stabilized boryl complexes $R_3P{\cdot}BH_2$–[M], such as **3**, have been reported, complexes such as **1** of the type $\{R_3P\}_2{\cdot}B(H)$–[M] are unknown. Complex **3** exhibits typical characteristics of a complex with a dative bond from the central metal atom to the Z-type borane ligand:[11b–k,17] The *trans*-dicarbonyl complex **3** is highly distorted from the idealized octahedral coordination geometry towards a trigonal bipyramid with the boryl group capping an equatorial edge ($\sphericalangle_{C\text{-}Fe\text{-}C} = 150.3°$), which leads to a rather long Fe–B distance in **3** (2.253 Å). The description as an Fe(−)–B(+) bond is further underlined by the shape of the corresponding molecular orbital.[16]

With the two π-accepting phosphine substituents in complex **1**, the situation changes: The broad resonance at −16.7 ppm in the ^{11}B{^{1}H} NMR spectrum of complex **1** is in agreement with transition-metal complexes containing electron-donating or L-type boron-based ligands ($\delta_B = -15.1 \ldots -26.2$ ppm) and is high-field-shifted relative to complex **3** ($\delta_B = -5.8$ ppm) and other Z-type borane complexes.[11f–h,17]

X-ray structure analysis revealed the *trans* arrangement of the iron hydride and the boron-bound hydrogen atom (Figure 1a). Remarkably, the length of the Fe–C bond *trans* to the hydride ligand (1.771 Å), which is considered to have a strong *trans* influence, is very similar to that of the Fe–C bond *trans* to the boron-based donor group (1.773 Å). Further evidence for a changed bonding situation was provided by the Fe–B bond, which is significantly shorter in complex **1** (2.197–2.210 Å) than in complex **3** (2.253 Å). Furthermore, the strong pyramidalization of the boron atom in **1** ($\sphericalangle_{\Sigma P/H\text{-}B\text{-}P} = 322.1°$) indicates a strong Fe–B bond.

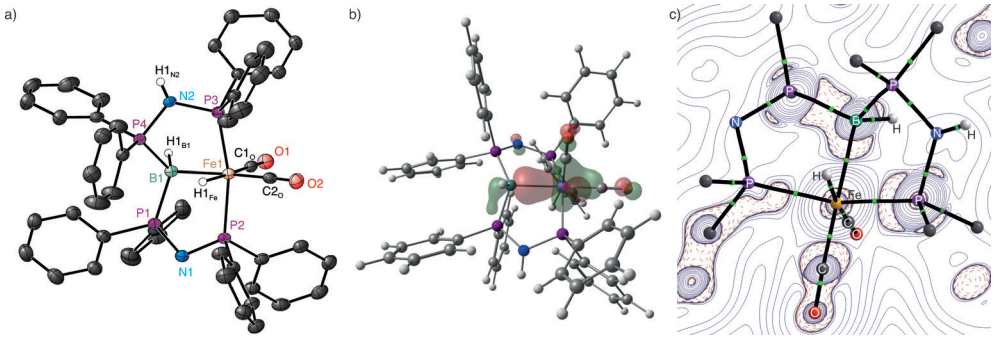

Figure 1. a) Molecular structure of complex **1** in the solid state. Ellipsoids set at 50% probability. Carbon-bound hydrogen atoms are omitted; the shown hydrogen atoms where located in the Fourier difference map. Selected distances [Å] and angles [°]: Fe1–B1 2.200(2), Fe1–P2 2.214(1), Fe1–P3 2.182(1), Fe1–$C1_O$ 1.772(2), Fe1–$C2_O$ 1.769(2), P1–B1 1.941(2), P4–B1 1.914(2); P3-Fe1-P2 164.74(2), $C2_O$-Fe1-B1 169.37(8), $C1_O$-Fe1-B1 88.58(9), $C2_O$-Fe1-$C1_O$ 102.02(9), P3-Fe1-B1 84.63(6), B1-Fe1-P2 86.71(6). b) HOMO−1 of complex **1** (B97D/def2-TZVPP, contour value ±0.05). c) Molecular graph for complex **1** derived from QTAIM analysis with a contour plot of the Laplacian in the B-Fe-P plane. Bond critical points are indicated as green dots. Phenyl groups were omitted, positive values of the Laplacian (charge depletion) are depicted as solid blue lines, and negative values (charge accumulation) as broken red lines.

To further elucidate the bonding situation in complex **1**, we performed quantum-chemical calculations using density functional theory (DFT). The shape of the HOMO−1 in complex **1** suggests a regular σ-bond between the iron and the boron atom (Figure 1b). The Wiberg bond index (WBI) of 0.58 for the Fe−B bond is similar to those found for the Au−B bonds in oxazol-2-ylidene-stabilized phenylborylene complexes.[9a] Natural population analysis revealed a negative charge of −0.56 at the boron atom, which is in agreement with an overall charge transfer of 0.53e relative to the free ligand. A quantum theory of atoms in molecules (QTAIM) analysis showed very similar Laplacians of the electron density for the Fe−B and Fe−P bonds (Figure 1c),[18] clearly indicating that the phosphine-stabilized boron-based ligand acts as an electron-donating ligand. The smaller energy density *H* for the Fe−B bond is in agreement with a weaker bond compared to the Fe−P bonds.

According to the X-ray structure determination and DFT calculations, the bonding situation in the P-N-P moiety is very similar for both arms of the PBP ligand. Moreover, analysis of the molecular orbitals indicates localization of the negative charge at the deprotonated nitrogen atom. Thus all donor groups of the described pincer ligand remain formally neutral and are best described by the resonance structures shown in Scheme 3.[19]

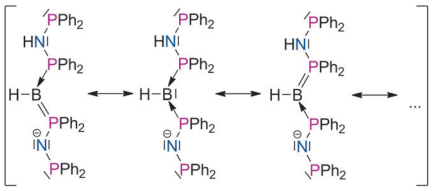

Scheme 3. Possible resonance structures of the ligand in complex **1**.

The new ligand tempted us to investigate the behavior in solution and the reactivity of complex **1** in more detail. Interestingly, the ^{1}H NOESY NMR spectrum of **1** shows exchange correlations between the Fe−H and B−H resonances as well as between the resonances of several *ortho*-phenyl protons, but no exchange with N−H resonances. Based on ^{1}H EXSY NMR spectroscopy and line-shape analysis of ^{1}H NMR spectra recorded at different temperatures, as well as H/D exchange kinetics with D_2 gas, we were able to rule out a σ-bound dihydrogen intermediate for the Fe−H/B−H exchange, suggesting a reversible B−H reductive elimination (Scheme 4; for further details, see the Supporting Information).

Quantum-chemical investigations showed that for the simplified methyl-substituted complex **1a**, a low-energy

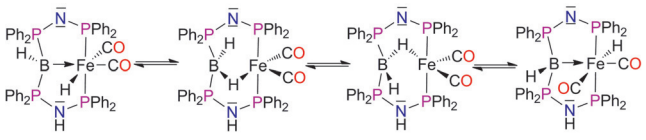

Scheme 4. Exchange pathway of complex **1**.

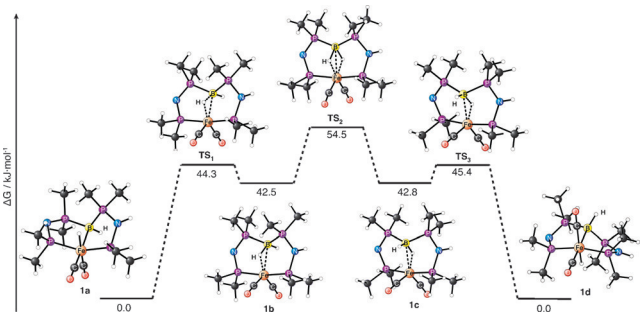

Figure 2. DFT-calculated lowest-energy pathway for the Fe−H/B−H exchange in complex **1a** (B97D/def2-TZVPP).

exchange pathway is accessible (Figure 2). For the identification of the various intermediates, the exchange between two isomeric species **1a** and **1d** was considered (**1d** represents the optimized geometry after exchange of the Fe−H and Fe−CO positions in **1a**). Starting from **1a**, the initial step is indeed a two-electron B−H reductive elimination to give the σ-bound iron(0) species **1b**, which is 42.5 kJ mol^{-1} higher in energy. The two minimum-energy species **1a** and **1b** are connected via transition state $\mathbf{TS_1}$ with a barrier of 44.3 kJ mol^{-1}. The next step includes exchange of the σ-coordinated B−H bond in **1b** with the terminal B−H bond ($\mathbf{TS_2}$). The resulting species **1c** is able to undergo B−H oxidative addition to form the isomeric complex **1d** via transition state $\mathbf{TS_3}$ with a barrier of 45.4 kJ mol^{-1} relative to **1d**. Overall, the calculated barriers are in good agreement with the experimental values and support this unusual sequence of reversible B−H reductive elimination. Owing to the electron-donating character of the boron-based ligand, complex **1a** should be described as an iron(II) complex that is coordinated by a stabilized boryl anion with a formal oxidation state of +I. The discussed reductive elimination yields iron(0) complex **1b** with a σ-coordinated diphosphinoborane in the formal oxidation state +III. The formation of boron(III) species from redox-active metal hydride complexes and oxazol-2-ylidene-stabilized borylene ligands has previously been proposed.[9a] It is noteworthy that the observed exchange equilibrium represents a rare example of an iron complex undergoing two-electron redox processes.[20] Furthermore, the oxidative addition of B−H bonds is assumed to be an important elementary step in some dehydrocoupling reactions of ammonia–boranes as well as in borylation reactions.[11i,21] Whereas examples of B−H oxidative addition with tetravalent boron atoms are rare,[11i,21b] the reversible B−H oxidative addition is unparalleled and may open the possibility to use this reactivity as a protection strategy for L_4Fe^0 fragments.[22]

Next, we investigated the reactivity of complex **1** towards acids and bases (Scheme 5). The reaction with $HBF_4{\cdot}Et_2O$ in Et_2O results in selective protonation of the dppa arm in complex **1**. The reaction of complex **1** with KO*t*Bu in toluene at reflux leads to deprotonation of the dppa arm and formation of the anionic hydride complex **5**. DFT calculations of **1**, **4**, and **5** revealed a very similar bonding situation for all three complexes. The HOMO−1 orbitals representing the main contribution to the iron–boron bonds in **1** and **4** have very similar shapes (Figures 1b and 3a). In the anionic

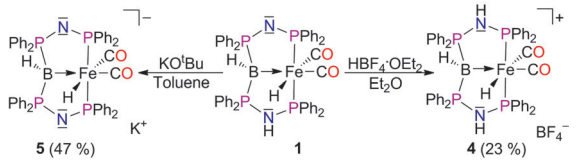

Scheme 5. (De)protonation of complex **1**.

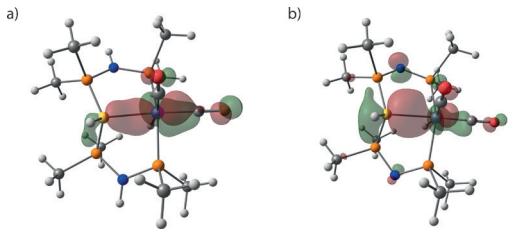

Figure 3. a) HOMO−1 of complex **4**. b) HOMO of complex **5**.

complex **5**, the HOMO represents the iron–boron bond (Figure 3b), which is similar to the HOMO−1 in **1** and **4**.

As the deprotonation of a dppa arm results in an anionic substituent at the :BH fragment, the boron-based pincer ligand could formally be regarded as a phosphine-stabilized borylene in **4** or as phosphine-stabilized boryl anion in **1** and **5**. Nonetheless, although these ligands formally differ in their charge and name, the bonding situation and the formal oxidation state of +I at the boron atom do not change.

Interestingly, we observed intramolecular exchange by reversible B–H reductive elimination for complexes **4** and **5** as well. The rate constants derived from line-shape analysis at 300 K are similar for complexes **1** and **4** ($k = 3.6$–$7.4\ s^{-1}$), whereas for the anionic complex **5**, the reversible B–H reductive elimination is significantly faster (coalescence at 300 K, $k = 3.1 \times 10^3\ s^{-1}$ at 290 K). The corresponding Gibbs enthalpy of activation for the exchange derived from an Eyring analysis for anionic complex **5** ($\Delta G^{\ddagger}_{298} = 51.6\ kJ\,mol^{-1}$) is much smaller than those of complexes **1** and **4** ($\Delta G^{\ddagger}_{298} = 67.4$–$70.6\ kJ\,mol^{-1}$).

As the ligand (de)protonation has a strong impact on the rate of the reversible B–H reductive elimination, we were interested in how the degree of (de)protonation of the ligand arms influences the relative stability of the involved intermediates. Therefore, we performed DFT calculations to determine the relative Gibbs enthalpies of the different redox isomers of the cationic, neutral, and anionic complexes. In agreement with the experimental results, the iron(II) isomer was always found to be the most stable. Interestingly, the relative stability of the reductive-elimination product, the iron(0) isomer, is strongly influenced by the degree of (de)protonation: For the cationic complex, the energy difference (ΔE) is $57.6\ kJ\,mol^{-1}$, for the neutral complex, ΔE is $42.5\ kJ\,mol^{-1}$, and for the anionic complex, ΔE was found to be $26.0\ kJ\,mol^{-1}$. This steadily decreasing energy difference with the degree of deprotonation is a unique example of a ligand (de)protonation reaction influencing the stability of redox isomers.

A brief investigation of the reactivity of those complexes under catalytic conditions revealed that **1** and **5** were active in the oxidation of primary and secondary alcohols with oxygen as the oxidant. For example, the oxidation of benzyl alcohol in the presence of 1 mol% of complex **1** and KO*t*Bu yielded a mixture of carbonyl compounds. In the presence of amines, however, selective imine formation was observed.

In conclusion, we have shown that :BH fragments stabilized by two phosphines can act as electron-donating or L-type ligands. The reported examples formally include a phosphine-stabilized borylene moiety as well as phosphine-stabilized boryl anions, resulting in very similar bonding situations in all cases. Moreover, the reported complexes exhibit unprecedented reactivity as they undergo a reversible B–H reductive elimination. The involved iron(0) intermediates contain a coordinated diphosphinoborane, which is consistent with oxidation of the boron(I) species in complex **1**, **4**, and **5** to a boron(III) species. This unique reactivity indicates the sensitivity of boron(I) ligands to oxidation on the one hand, and represents an unusual example of an iron complex undergoing two-electron redox processes on the other hand. Further investigations of metal complexes containing boron-based L-type pincer ligands and the application of reversible B–H reductive eliminations in cooperative catalysis are currently in progress.

Acknowledgements

This research is supported by the DFG (LA 2830/3-1) and the NSFC (21450110063). L.V. received a fellowship from the Studienstiftung des deutschen Volkes. R.L. is grateful to Prof. S. Dehnen and Prof. C. von Hänisch for their continuous support. We thank Dr. R. Tonner for assistance with the quantum-chemical investigations.

Keywords: boron · density functional theory · iron · pincer ligands · reduction

How to cite: *Angew. Chem. Int. Ed.* **2016**, *55*, 14450–14454
Angew. Chem. **2016**, *128*, 14665–14670

[1] a) H. Braunschweig, R. D. Dewhurst, *Dalton Trans.* **2011**, *40*, 549–558; b) A. Amgoune, D. Bourissou, *Chem. Commun.* **2011**, *47*, 859–871; c) G. Parkin, *Organometallics* **2006**, *25*, 4744–4747.

[2] a) H. Gulyás, A. Bonet, C. Pubill-Ulldemolins, C. Solé, J. Cid, E. Fernández, *Pure Appl. Chem.* **2012**, *84*, 2219; b) L. Weber, *Eur. J. Inorg. Chem.* **2012**, 5595–5609; c) M. Yamashita, *Bull. Chem. Soc. Jpn.* **2011**, *84*, 983–999; d) J. Cid, H. Gulyas, J. J. Carbo, E. Fernandez, *Chem. Soc. Rev.* **2012**, *41*, 3558–3570.

[3] a) R. Bertermann, H. Braunschweig, R. D. Dewhurst, C. Hörl, T. Kramer, I. Krummenacher, *Angew. Chem. Int. Ed.* **2014**, *53*, 5453–5457; *Angew. Chem.* **2014**, *126*, 5557–5561; b) H. Braunschweig, C.-W. Chiu, T. Kupfer, K. Radacki, *Inorg. Chem.* **2011**, *50*, 4247–4249; c) H. Braunschweig, C.-W. Chiu, K. Radacki, T. Kupfer, *Angew. Chem. Int. Ed.* **2010**, *49*, 2041–2044; *Angew. Chem.* **2010**, *122*, 2085–2088; d) W. Lu, H. Hu, Y. Li, R. Ganguly, R. Kinjo, *J. Am. Chem. Soc.* **2016**, *138*, 6650–6661.

[4] a) H. Braunschweig, *Angew. Chem. Int. Ed.* **2007**, *46*, 1946–1948; *Angew. Chem.* **2007**, *119*, 1990–1992; b) M. S. Cheung, T. B. Marder, Z. Lin, *Organometallics* **2011**, *30*, 3018–3028; c) N. Dettenrieder, H. M. Dietrich, C. Schädle, C. Maichle-Mössmer, K. W. Törnroos, R. Anwander, *Angew. Chem. Int. Ed.* **2012**, *51*,

4461 – 4465; *Angew. Chem.* **2012**, *124*, 4537 – 4541; d) N. Dettenrieder, C. O. Hollfelder, L. N. Jende, C. Maichle-Mössmer, R. Anwander, *Organometallics* **2014**, *33*, 1528 – 1531; e) N. Dettenrieder, C. Schädle, C. Maichle-Mössmer, R. Anwander, *Dalton Trans.* **2014**, *43*, 15760 – 15770; f) N. Dettenrieder, C. Schädle, C. Maichle-Mössmer, P. Sirsch, R. Anwander, *J. Am. Chem. Soc.* **2014**, *136*, 886 – 889; g) T. B. Marder, *Science* **2006**, *314*, 69 – 70; h) K. Nozaki, Y. Aramaki, M. Yamashita, S.-H. Ueng, M. Malacria, E. Lacôte, D. P. Curran, *J. Am. Chem. Soc.* **2010**, *132*, 11449 – 11451; i) Y. Okuno, M. Yamashita, K. Nozaki, *Eur. J. Inorg. Chem.* **2011**, 3951 – 3958; j) Y. Okuno, M. Yamashita, K. Nozaki, *Angew. Chem. Int. Ed.* **2011**, *50*, 920 – 923; *Angew. Chem.* **2011**, *123*, 950 – 953; k) A. V. Protchenko, D. Dange, J. R. Harmer, C. Y. Tang, A. D. Schwarz, M. J. Kelly, N. Phillips, R. Tirfoin, K. H. Birjkumar, C. Jones, N. Kaltsoyannis, P. Mountford, S. Aldridge, *Nat. Chem.* **2014**, *6*, 315 – 319; l) Y. Segawa, M. Yamashita, K. Nozaki, *Science* **2006**, *314*, 113 – 115; m) T. Terabayashi, T. Kajiwara, M. Yamashita, K. Nozaki, *J. Am. Chem. Soc.* **2009**, *131*, 14162 – 14163; n) D. A. Ruiz, G. Ung, M. Melaimi, G. Bertrand, *Angew. Chem. Int. Ed.* **2013**, *52*, 7590 – 7592; *Angew. Chem.* **2013**, *125*, 7739 – 7742.

[5] a) D. Wu, R. Ganguly, Y. Li, S. N. Hoo, H. Hirao, R. Kinjo, *Chem. Sci.* **2015**, *6*, 7150 – 7155; b) D. Wu, L. Kong, Y. Li, R. Ganguly, R. Kinjo, *Nat. Commun.* **2015**, *6*, 7340.

[6] a) H. Braunschweig, R. D. Dewhurst, V. H. Gessner, *Chem. Soc. Rev.* **2013**, *42*, 3197 – 3208; b) F. Dahcheh, D. Martin, D. W. Stephan, G. Bertrand, *Angew. Chem. Int. Ed.* **2014**, *53*, 13159 – 13163; *Angew. Chem.* **2014**, *126*, 13375 – 13379; c) R. Kinjo, B. Donnadieu, M. A. Celik, G. Frenking, G. Bertrand, *Science* **2011**, *333*, 610 – 613; d) D. A. Ruiz, M. Melaimi, G. Bertrand, *Chem. Commun.* **2014**, *50*, 7837 – 7839; e) M. Soleilhavoup, G. Bertrand, *Acc. Chem. Res.* **2015**, *48*, 256 – 266.

[7] a) H. Braunschweig, P. Brenner, R. D. Dewhurst, M. Kaupp, R. Müller, S. Östreicher, *Angew. Chem. Int. Ed.* **2009**, *48*, 9735 – 9738; *Angew. Chem.* **2009**, *121*, 9916 – 9919; b) H. Braunschweig, M. Burzler, R. D. Dewhurst, K. Radacki, *Angew. Chem. Int. Ed.* **2008**, *47*, 5650 – 5653; *Angew. Chem.* **2008**, *120*, 5732 – 5735; c) H. Braunschweig, A. Damme, R. D. Dewhurst, T. Kramer, S. Östreicher, K. Radacki, A. Vargas, *J. Am. Chem. Soc.* **2013**, *135*, 2313 – 2320.

[8] a) E. Bernhardt, V. Bernhardt-Pitchougina, H. Willner, N. Ignatiev, *Angew. Chem. Int. Ed.* **2011**, *50*, 12085 – 12088; *Angew. Chem.* **2011**, *123*, 12291 – 12294; b) H. Braunschweig, R. D. Dewhurst, F. Hupp, M. Nutz, K. Radacki, C. W. Tate, A. Vargas, Q. Ye, *Nature* **2015**, *522*, 327 – 330.

[9] a) L. Kong, R. Ganguly, Y. Li, R. Kinjo, *Chem. Sci.* **2015**, *6*, 2893 – 2902; b) L. Kong, Y. Li, R. Ganguly, D. Vidovic, R. Kinjo, *Angew. Chem. Int. Ed.* **2014**, *53*, 9280 – 9283; *Angew. Chem.* **2014**, *126*, 9434 – 9437.

[10] M. A. Celik, R. Sure, S. Klein, R. Kinjo, G. Bertrand, G. Frenking, *Chem. Eur. J.* **2012**, *18*, 5676 – 5692.

[11] a) J. S. Figueroa, J. G. Melnick, G. Parkin, *Inorg. Chem.* **2006**, *45*, 7056 – 7058; b) Y. Kawano, K. Yamaguchi, S.-y. Miyake, T. Kakizawa, M. Shimoi, *Chem. Eur. J.* **2007**, *13*, 6920 – 6931; c) Y. Kawano, T. Yasue, M. Shimoi, *J. Am. Chem. Soc.* **1999**, *121*, 11744 – 11750; d) M. Shimoi, S. Ikubo, Y. Kawano, K. Katoh, H. Ogino, *J. Am. Chem. Soc.* **1998**, *120*, 4222 – 4223; e) T. Yasue, Y. Kawano, M. Shimoi, *Angew. Chem. Int. Ed.* **2003**, *42*, 1727 – 1730; *Angew. Chem.* **2003**, *115*, 1769 – 1772; f) M. E. Moret, J. C. Peters, *Angew. Chem. Int. Ed.* **2011**, *50*, 2063 – 2067; *Angew. Chem.* **2011**, *123*, 2111 – 2115; g) D. L. Suess, J. C. Peters, *J. Am. Chem. Soc.* **2013**, *135*, 4938 – 4941; h) D. L. Suess, J. C. Peters, *J. Am. Chem. Soc.* **2013**, *135*, 12580 – 12583; i) I. R. Crossley, A. F. Hill, A. C. Willis, *Organometallics* **2005**, *24*, 1062 – 1064; j) I. R. Crossley, A. F. Hill, A. C. Willis, *Organometallics* **2010**, *29*, 326 – 336; k) A. F. Hill, S. B. Lee, J. Park, R. Shang, A. C. Willis, *Organometallics* **2010**, *29*, 5661 – 5669; l) M. Sircoglou, S. Bontemps, M. Mercy, N. Saffon, M. Takahashi, G. Bouhadir, L. Maron, D. Bourissou, *Angew. Chem. Int. Ed.* **2007**, *46*, 8583 – 8586; *Angew. Chem.* **2007**, *119*, 8737 – 8740.

[12] a) S. E. Clapham, A. Hadzovic, R. H. Morris, *Coord. Chem. Rev.* **2004**, *248*, 2201 – 2237; b) S. Schneider, J. Meiners, B. Askevold, *Eur. J. Inorg. Chem.* **2012**, 412 – 429; c) H. Grützmacher, *Angew. Chem. Int. Ed.* **2008**, *47*, 1814 – 1818; *Angew. Chem.* **2008**, *120*, 1838 – 1842.

[13] a) W. H. Harman, J. C. Peters, *J. Am. Chem. Soc.* **2012**, *134*, 5080 – 5082; b) T.-P. Lin, J. C. Peters, *J. Am. Chem. Soc.* **2013**, *135*, 15310 – 15313; c) T.-P. Lin, J. C. Peters, *J. Am. Chem. Soc.* **2014**, *136*, 13672 – 13683.

[14] Arrows were used to distinguish more clearly between an electron-donating and an electron-accepting boron ligand. For other bonds, arrows were deliberately not used.

[15] N. Frank, K. Hanau, K. Flosdorf, R. Langer, *Dalton Trans.* **2013**, *42*, 11252 – 11261.

[16] See the Supporting Information for details.

[17] H. Fong, M. E. Moret, Y. Lee, J. C. Peters, *Organometallics* **2013**, *32*, 3053 – 3062.

[18] a) D. Cremer, E. Kraka, *Angew. Chem. Int. Ed. Engl.* **1984**, *23*, 627 – 628; *Angew. Chem.* **1984**, *96*, 612 – 614; b) F. Cortesguzman, R. Bader, *Coord. Chem. Rev.* **2005**, *249*, 633 – 662.

[19] As the negative charge is not located on the donor functionalities of the PBP ligand, the use of donor arrows seems justified in the current case; see: M. L. H. Green, G. Parkin, *J. Chem. Educ.* **2014**, *91*, 807 – 816.

[20] a) C. Cassani, G. Bergonzini, C.-J. Wallentin, *ACS Catal.* **2016**, *6*, 1640 – 1648; b) I. Bauer, H.-J. Knölker in *Iron Catalysis in Organic Chemistry*, Wiley-VCH, Weinheim, **2008**, pp. 1 – 27; c) R. Birk, H. Berke, G. Huttner, L. Zsolnaib, *Chem. Ber.* **1988**, *121*, 1557 – 1564; d) W. D. Jones, G. P. Foster, J. M. Putinas, *J. Am. Chem. Soc.* **1987**, *109*, 5047 – 5048; e) K. H. Karsch, *Chem. Ber.* **1977**, *110*, 2699 – 2711; f) M. V. Baker, L. D. Field, *J. Am. Chem. Soc.* **1987**, *109*, 2825 – 2826; g) W. Lau, J. C. Huffman, J. K. Kochi, *Organometallics* **1982**, *1*, 155 – 169.

[21] a) G. Bénac-Lestrille, U. Helmstedt, L. Vendier, G. Alcaraz, E. Clot, S. Sabo-Etienne, *Inorg. Chem.* **2011**, *50*, 11039 – 11045; b) A. B. Chaplin, A. S. Weller, *Angew. Chem. Int. Ed.* **2010**, *49*, 581 – 584; *Angew. Chem.* **2010**, *122*, 591 – 594; c) A. Rossin, M. Caporali, L. Gonsalvi, A. Guerri, A. Lledós, M. Peruzzini, F. Zanobini, *Eur. J. Inorg. Chem.* **2009**, 3055 – 3059; d) M. V. Câmpian, J. L. Harris, N. Jasim, R. N. Perutz, T. B. Marder, A. C. Whitwood, *Organometallics* **2006**, *25*, 5093 – 5104; e) P. L. Callaghan, R. Fernandez-Pacheco, N. Jasim, S. Lachaize, T. B. Marder, R. N. Perutz, E. Rivalta, S. Sabo-Etienne, *Chem. Commun.* **2004**, 242 – 243.

[22] I. R. Crossley, A. F. Hill, *Dalton Trans.* **2008**, 201 – 203.

Received: June 16, 2016
Revised: August 12, 2016
Published online: October 14, 2016

Angewandte Chemie
Eine Zeitschrift der Gesellschaft Deutscher Chemiker

Supporting Information

Phosphine-Stabilized Borylenes and Boryl Anions as Ligands? Redox Reactivity in Boron-Based Pincer Complexes

*Lisa Vondung, Nicolas Frank, Maximilian Fritz, Lukas Alig, and Robert Langer**

anie_201605838_sm_miscellaneous_information.pdf

Supporting Information

1. **Experimental Details**
2. **NMR spectra**
3. **Variable Temperature NMR Measurements**
4. **X-Ray Crystallography**
5. **DFT Calculations**
6. **Possible Resonance Structures of the PBP-Ligands in Complex 4 and 5**

1. Experimental Details

Material and Methods

All experiments were carried out under an atmosphere of purified argon in a MBraun Labmaster glove box or using standard Schlenk techniques. Et_2O, *n*-hexane and C_6D_6 were dried and distilled from Na/K alloy and stored over molecular sieves. Toluene was dried and distilled from sodium and stored over molecular sieves. CD_3CN was dried and distilled from CaH_2 and stored over molecular sieves. Bis(diphenylphosphino)amine[1] and [$(Ph_2P\text{-}N\text{-}P(BH_3)Ph_2)$(dppa)Fe(H)][2] were prepared according to previously reported procedures. KO^{t}Bu and $HBF_4{\cdot}Et_2O$ were purchased from Sigma-Aldrich and used as received.

^1H, ^{13}C, ^{31}P and ^{11}B NMR spectra were recorded using Bruker DRX 400, DRX 500 and Avance 500 NMR spectrometers. ^1H and $^{13}C\{^1H\}$, ^{13}C-APT (attached proton test) NMR chemical shifts are reported in ppm downfield from tetramethylsilane. The resonance of the residual protons in the deuterated solvent was used as internal standard for ^1H NMR. The solvent peak of the deuterated solvent was used as internal standard for ^{13}C NMR. ^{31}P NMR chemical shifts are reported in ppm downfield from H_3PO_4 and referenced to an external 85% solution of phosphoric acid in D_2O. ^{11}B NMR chemical shifts are reported in ppm downfield from $BF_3{\cdot}Et_2O$ and referenced to an external solution of $BF_3{\cdot}Et_2O$ in $CDCl_3$. The following abbreviations are used for the description of NMR data: br (broad), s (singlet), d (doublet), t (triplet), q (quartet), quin (quintet), m (multiplet), v (virtual).

FT-IR spectra were recorded by attenuated total reflection of the solid samples on a Bruker Tensor IF37 spectrometer. The intensity of the absorption band is indicated as vw (very weak), w (weak), m (medium), s (strong), vs (very strong) and br (broad).

HR-ESI mass spectra were acquired with a LTQ-FT mass spectrometer (Thermo Fisher Scientific). HR-APCI mass spectra were acquired with a LTQ-FT mass spectrometer (Thermo Fisher Scientific). In both cases the resolution was set to 100.000. Elemental analyses were performed on a Vario Micro Cube Elemental Analyzer.

Synthesis of [(Ph-PBP)Fe(H)$(CO)_2$] (1)

[$(Ph_2P\text{-}N\text{-}P(BH_3)Ph_2)$(dppa)Fe(H)] (46 mg, 0.052 mmol) was dissolved in 10 mL toluene. The argon in the Schlenk tube was removed by evacuation until the toluene starts to boil and was refilled with one atmosphere of carbon monoxide. The colour of the solution changes from red to pale yellow after 30 seconds and the mixture was allowed to stir under carbon monoxide atmosphere for further twenty minutes. After this period the tube was evacuated again until the toluene starts to boil and refilled with argon. A $^{31}P\{^1H\}$ NMR spectrum of the reaction mixture confirmed the complex conversion of [$(Ph_2P\text{-}N\text{-}P(BH_3)Ph_2)$(dppa)Fe(H)] (**I**), but does not show any resonances corresponding to **1**. After additional 16 h of stirring at ambient temperature under argon atmosphere the formation of **1** was confirmed by $^{31}P\{^1H\}$ NMR spectroscopy and the pale yellow solution was layered with 30 mL of *n*-hexane. After

complex diffusion (4-6 days) colourless crystals of **1** were isolated. Yield: 37.7 mg (81 %). Anal. Calcd. for $C_{64}H_{58}BFeKN_2O_2P_4$ (**1**·2 toluene, M = 1116.83 g/mol): C 68.83 %, H 5.23 %, N 2.51 %. Found: C 68.80 %, H 5.272 %, N 3.08 %.

$^{31}P\{^1H\}$ NMR (162 MHz, C_6D_6, 27 °C) δ: 46.7 (br, 1P, *P*-B-P), 52.6 (br, 1P, P-B-*P*), 115.7 (vt, 1P, $^2J_{PP}$ = 123.2 Hz, *P*-Fe-P), 129.2 (ddd, 1P, $^2J_{PP}$ = 126.7 Hz, $^2J_{PP}$ = 81.5 Hz, $^2J_{PP}$ = 48.4 Hz, P-Fe-*P*) ppm. ^1H NMR (400 MHz, C_6D_6, 27 °C) δ: -8.89 (td, 1H, $^2J_{PH}$ = 55.9 Hz, J_{PH} = 20.5 Hz, Fe-*H*), 3.13 (t, 1H, $^2J_{PH}$ = 5.0 Hz, N-*H*), 2.70-4.00 (br partly superimposed, 1H, B-*H*), 6.74-7.14 (m, 22H, Phenyl -*H*), 7.18-7.22 m superimposed, 2H, Phenyl -*H*), 7.25 (t, 2H, *J* = 7.7 Hz, Phenyl -*H*), 7.39 (m, 4H, *ortho*-Phenyl-*H*), 7.79 (dd, 2H $^3J_{PH}$ = 11.1 Hz, $^3J_{HH}$ = 7.5 Hz, *ortho*-Phenyl-*H*), 7.90 (dd, 2H, *J* = 10.8 Hz, *J* = 7.3 Hz, *ortho*-Phenyl-*H*), 8.10 (dd, 2H, *J* = 10.8 Hz, *J* = 7.6 Hz, *ortho*-Phenyl-*H*), 8.15 (dd, 2H $^3J_{PH}$ = 10.8 Hz, $^3J_{HH}$ = 7.6 Hz, *ortho*-Phenyl-*H*), 8.23 (vt, 2H, *J* = 9.1 Hz, *ortho*-Phenyl-*H*) ppm. Selectively decoupled $^1H\{^{31}P\}$ NMR spectra were acquired, causing a change in multiplicity for some of the signals. In the following only resonances which are changing upon ^{31}P-decoupling are reported. All other ^1H NMR resonances remained unchanged in comparison to the ^1H NMR spectrum reported above. $^1H\{^{31}P\}$ NMR (400 MHz, C_6D_6, 27 °C, o2p = 129.0 ppm) δ: -8.89 (dd, 1H, J_{PH} = 27.8 Hz, J_{PH} = 19.6 Hz, Fe-*H*), 3.13 (d, 1H, $^2J_{PH}$ = 5.1 Hz, N-*H*), 7.79 (d, 2H, $^3J_{HH}$ = 7.5 Hz, *ortho*-Phenyl-*H*) ppm. $^1H\{^{31}P\}$ NMR (400 MHz, C_6D_6, 27 °C, with selective decoupling on the resonance centred at 116.0 ppm) δ: -8.89 (dd, 1H, J_{PH} = 28.3 Hz, J_{PH} = 19.2 Hz, Fe-*H*),), 3.13 (br, 1H, N-*H*), 8.15 (d, 2H, $^3J_{HH}$ = 7.4 Hz, *ortho*-Phenyl-*H*), 8.23 (d, 2H, $^3J_{HH}$ = 7.6 Hz, *ortho*-Phenyl-*H*) ppm. $^1H\{^{31}P\}$ NMR (400 MHz, C_6D_6, 27 °C, with selective decoupling on the resonance centred at 50.0 ppm) δ: -8.89 (t, 1H, $^2J_{PH}$ = 53.2 Hz, Fe-*H*), 3.14 (d, 1H, $^2J_{PH}$ = 4.4 Hz, N-*H*), 7.89 (d, 2H, $^3J_{HH}$ = 7.1 Hz, *ortho*-Phenyl-*H*), 8.10 (d, 2H, $^3J_{HH}$ = 7.4 Hz, *ortho*-Phenyl-*H*) ppm. ^{13}C-APT NMR (100.6 MHz, C_6D_6, 27 °C) *δ*: 128.3 (s, Aryl-*C*), 129.1 (t, J_{PC} = 19.3 Hz, Aryl-*C*), 129.66 (d, J_{PC} = 12.0 Hz, Aryl-*C*), 130.4 (d, J_{PC} = 12.9 Hz, Aryl-*C*), 130.9 (d, J_{PC} = 7.5 Hz, Aryl-*C*), 131.3 (superimposed, Aryl-*C*), 131.7 (d, J_{PC} = 11.3 Hz, Aryl-*C*), 132.4 (d, J_{PC} = 9.7 Hz, Aryl-*C*), 133.6 (d, J_{PC} = 11.1 Hz, Aryl-*C*), 139.3 (d, J_{PC} = 20.2 Hz, quart. Aryl-*C*), 139.8 (d, J_{PC} = 12.2 Hz, quart. Aryl-*C*), 140.0 (d, J_{PC} = 19.4 Hz, quart. Aryl-*C*), 140.5 (superimposed, quart. Aryl-*C*), 140.8 (s, quart. Aryl-*C*), 141.3 (s, quart. Aryl-*C*), 148.1-148.5 (m, quart. Aryl-*C*), 150.2 (dd, J_{PC} = 60.1, 13.6 Hz, quart. Aryl-*C*), 216.7 (br, Fe-*C*O), 217.6 (br, Fe-*C*O) ppm. $^{11}B\{^1H\}$ NMR (160.5 MHz, C_6D_6, 27 °C) δ: -16.7 (s) ppm. IR (ATR): $\tilde{\vartheta}$ [cm^{-1}] 3353 (w), 3318 (vw), 3053 (br), 2963 (m), 2906 (vw), 2360 (w), 2342 (br), 1969 (m, CO/Fe-H), 1958 (m, CO/Fe-H), 1905 (m, CO/Fe-H), 1860 (w), 1480 (w), 1434 (m), 1413 (br), 1259 (s), 1074 (s), 1012 (vs), 897 (m), 864 (m), 790 (vs), 739 (m), 691 (m), 621 (w), 612 (w), 598 (w), 574 (w), 545 (w), 520 (m), 473 (m, br). High Res. ESI-MS (*m/z, pos.*): 895.1798 (calc. for $[M+H]^+$), 895.1806 (found, Δ = 0.9 ppm).

Formation of [(Ph_2P-N-P(BH_3)Ph_2)(dppa)Fe(H)(CO)] (2)

The synthetic procedure for the formation of complex **2** is identical to the one of complex **1**, except that the starting complex [(Ph_2P-N-P(BH_3)Ph_2)(dppa)Fe(H)] is only exposed for five seconds to one atmosphere of carbon monoxide before the atmosphere was replaced by argon or nitrogen. A $^{31}P\{^1H\}$

NMR spectrum of the reaction mixture confirmed the formation complex **2** as the major product, but significant amounts of the starting complex as well as the complex **3** were present. (As described above complex **3** slowly reacts to complex **1**). Despite several attempts we were unable to crystallize or isolate complex **2**, which usually resulted in the formation unidentified decomposition products. Nevertheless based on 1- and 2-dim. NMR spectroscopy it was possible to assign well separated resonances in the ^{1}H, ^{31}P and ^{13}C NMR spectra, whereas the resonances corresponding to the phenyl rings were superimposed and not unambiguously assignable in the ^{1}H and the ^{13}C-APT NMR spectrum.

^{1}H NMR (400 MHz, C_6D_6, 27 °C) δ: -15.98 (ddd, 1H, $^{2}J_{PH}$ = 56.1 Hz, $^{2}J_{PH}$ = 46.4, $^{2}J_{PH}$ = 37.3 Hz, Fe-*H*), -3.78 (br, 1H, B-*H*), -2.48 (br, 2H, B-*H*), 3.66 (br, NH, N-*H*), 6.50-7.32 (m superimposed, 30H, phenyl-*H*), 7.49 (vt, 2H, *J* = 9.3 Hz, phenyl-*H*), 7.97 (vt, 4H, *J* = 8.8 Hz, phenyl-*H*), 8.42 (vt, 2H, *J* = 8.4 Hz, phenyl-*H*), 8.58 (vt, 2H, J = 8.1 Hz, phenyl-*H*) ppm. $^{31}P\{^{1}H\}$ NMR (101 MHz, C_6D_6, 27 °C) δ: 48.8 (br, 1P, *P*-BH_3-Fe), 85.6 (dd, 1P, $^{2}J_{PP}$ = 89.4Hz, $^{2}J_{PP}$ = 55.5 Hz, Fe-*P*), 98.4 (ddd partly superimposed, 1P, $^{2}J_{PP}$ = 169.2 Hz, $^{2}J_{PP}$ = 81.3 Hz, $^{2}J_{PP}$ = 21.2 Hz, Fe-*P*), 100.4 (ddd partly superimposed, 1P, $^{2}J_{PP}$ = 101.7 Hz, $^{2}J_{PP}$ = 78.6 Hz, $^{2}J_{PP}$ = 53.9 Hz, Fe-*P*) ppm. Selectively decoupled $^{1}H\{^{31}P\}$ NMR spectra were acquired, causing a change in multiplicity for some of the signals. In the following only resonances, which are changing upon ^{31}P-decoupling, are reported. All other ^{1}H NMR resonances remained unchanged in comparison to the ^{1}H NMR spectrum reported above. $^{1}H\{^{31}P\}$ NMR (400 MHz, C_6D_6, 27 °C, o2p = 98.0 ppm) δ: -15.99 (d, 1H, $^{2}J_{PH}$ = 33.2 Hz, Fe-*H*), 6.84 (d, 2H, J_{HH} = 6.8 Hz, phenyl-*H*), 8.58 (d, 2H, J_{HH} = 7.8 Hz, phenyl-*H*) ppm. $^{1}H\{^{31}P\}$ NMR (400 MHz, C_6D_6, 27 °C, o2p = 84.0 ppm) δ: -15.99 (dd, 1H, $^{2}J_{PH}$ = 27.4 Hz, $^{2}J_{PH}$ = 22.5 Hz, Fe-*H*) ppm. $^{1}H\{^{31}P\}$ NMR (400 MHz, C_6D_6, 27 °C, o2p = 47.0 ppm) δ: -15.99 (td, 1H, $^{2}J_{PH}$ = 69.7 Hz, $^{2}J_{PH}$ = 36.8 Hz, Fe-*H*), 8.42 (d, 2H, J_{HH} = 6.8 Hz, phenyl-*H*) ppm. $^{11}B\{^{1}H\}$ NMR (160.5 MHz, C_6D_6, 27 °C) δ: -31,5 (br) ppm.

Formation of [(Ph_2P-N-P(BH_2)Ph_2)(dppa)Fe($CO)_2$] (3)

[(Ph_2P-N-P(BH_3)Ph_2)(dppa)Fe(H)] (25 mg, 0.03 mmol) was dissolved in 10 mL toluene. The argon in the Schlenk tube was removed by evacuation until the toluene starts to boil and was refilled with one atmosphere of carbon monoxide. The colour of the solution changes from red to pale yellow after 30 seconds and the mixture was allowed to stir under carbon monoxide atmosphere for further ten minutes. After this period the tube was evacuated again until the toluene starts to boil and refilled with argon. The solution was immediately layered with *n*-hexane and stored at -24 °C. After two days yellow crystals of **3** formed, which were slightly contaminated with complex **1**. Yield: 7.7 mg (30 %). Anal. Calcd. for $C_{50}H_{43}BFeN_2O_2P_4$ (M = 894.46 g/mol): C 67.14%, H 4.85%, N 3.13%. Found: C 67.87 %, H 5.04 %, N 3.26 %.

^{1}H NMR (400 MHz, C_6D_6, 27 °C) δ: 3.99 (br, 1H, N-*H*), 6.82-7.04 (m, 10H, phenyl-*H*), 7.08 (vt, 2H, *J* = 6.8 Hz, phenyl-*H*), 7.29 (vt, 2H, *J* = 8.8 Hz, phenyl-*H*), 7.61 (vt, 2H, , *J* = 8.8 Hz, phenyl-*H*), 7.69 (vt, 2H, *J* = 7.8 Hz, phenyl-*H*), 8.29 (vt, 2H, *J* = 8.8 Hz, phenyl-*H*) ppm. $^{31}P\{^{1}H\}$ NMR (162 MHz, C_6D_6,

27 °C) δ: 63.8 (br, 1P, *P*-BH_2-Fe), 87.5 (dd, 1P, $^2J_{PP}$ = 53.1 Hz, $^2J_{PP}$ = 31.4 Hz, Fe-*P*), 95.1 (td, 1P, $^2J_{PP}$ = 50.7 Hz, $^2J_{PP}$ = 28.6 Hz, Fe-*P*), 105.4 (ddd, 1P, $^2J_{PP}$ = 109.0 Hz, $^2J_{PP}$ = 49.2 Hz, $^2J_{PP}$ = 30.9 Hz, Fe-*P*) ppm. Selectively decoupled $^1H\{^{31}P\}$ NMR spectra were acquired, causing a changed multiplicity for some of the signals. In the following only resonances which are changing upon ^{31}P-decoupling are reported. All other ^1H NMR resonances remained unchanged in comparison to the ^1H NMR spectrum reported above. $^1H\{^{31}P\}$ NMR (400 MHz, C_6D_6, 27 °C, o2p = 105.0 ppm) δ: 4.00 (vt, 1H, $^2J_{PH}$ = 3.9 Hz, N-*H*), 7.69 (d, 2H, J_{HH} = 5.8 Hz, phenyl-*H*) ppm. $^1H\{^{31}P\}$ NMR (400 MHz, C_6D_6, 27 °C, o2p = 95.2 ppm) δ: 7.29 (br, 2H, phenyl-*H*), 7.61 (d, 2H, J_{HH} = 7.8 Hz, phenyl-*H*), 7.69 (br, 2H, phenyl-*H*) ppm. $^1H\{^{31}P\}$ NMR (400 MHz, C_6D_6, 27 °C, o2p = 87.8 ppm) δ: 7.29 (d, 2H, J_{HH} = 7.8 Hz, phenyl-*H*), 7.61 (br, 2H, phenyl-*H*) ppm. $^{11}B\{^1H\}$ NMR (160.5 MHz, C_6D_6, 27 °C) δ: -5.8 (br) ppm. As complex **3** isomerizes over the course of a few hours to complex **1**, it was not possible to acquire meaningful ^{13}C NMR data. IR (ATR): $\tilde{\nu}$ [cm^{-1}] 2962 (m), 2897 (w), 2862 (vw), 1910 (m, CO), 1731 (m), 1434 (w), 1342 (w), 1259 (s), 1176 (m), 1146 (m), 1092 (vs), 1061 (s), 1014 (s), 963 (m), 862 (w), 842 (m), 792 (s), 741 (m), 691 (m), 624 (w), 582 (w), 530 (m), 511 (m), 497 (m), 475 (m), 464 (m). High Res. FD-MS (*m/z, pos.*): 894.17175 (calc. for $[M]^{+\bullet}$), 894.17118 (found, Δ = 0.64 ppm).

Synthesis of [(Ph-PBP^{+H})Fe(H)(CO)$_2$](BF$_4$) (4)

Complex **1**, [(Ph-PBP)Fe(H)(CO)$_2$] (20 mg, 0.022 mmol) was dissolved in 4 mL diethylether and 0.8 mL of 9.25 mM solution of $HBF_4{\cdot}Et_2O$ in diethylether was added dropwise to the vigorously stirred solution, causing immediate formation of an off-white voluminous precipitate. The supernatant solution was decanted off and the residue was dried *in vacuo* to give **4** as a beige-colored solid. Yield: 5 mg (23 %, M = 982.25 g/mol).

^1H NMR (500 MHz, CD_3CN, 27 °C) δ: -9.59 (td, 1H, $^2J_{PH}$ = 57.5 Hz, Fe-*H*), 2.16 (s, 2H, N*H*), 2.83 (br, 1H, B*H*), 6.98 – 7.75 (m, 40 H, aryl-*H*) ppm. A selectively decoupled $^1H\{^{11}B\}$ NMR spectrum was acquired, causing a sharpening and multiplicity of a triplet of the B-H-signal at 2.83 ppm. All other ^1H NMR resonances remained unchanged in comparison to the ^1H NMR spectrum reported above. $^{31}P\{^1H\}$ NMR (162 MHz, CD_3CN, 27 °C) δ: 54.3 (s, 2P), 129.8 (t, 2P, $^2J_{PP}$ = 54.5 Hz) ppm. $^{11}B\{^1H\}$ NMR (160.5 MHz, CD_3CN, 27 °C) *δ*: -25.0 (br, P-*B*-P), -1.1 (s, *B*F_4^-) ppm. ^{13}C-APT NMR (100.6 MHz, CD_3CN, 27 °C) *δ*: 129.19 (t, J_{PC} = 5.2 Hz, Aryl-*C*), 129.47 (t, 5.20 Hz, Aryl-*C*), 129.74 (t, J_{PC} = 6.07 Hz, Aryl-*C*), 131.05 (s, , Aryl-*C*), 131.29 (br, , Aryl-*C*), 131.58 (s, Aryl-*C*), 131.82 (t, J_{PC} = 6.07 Hz, Aryl-*C*), 132.84 (br, Aryl-*C*), 133.38 (s, Aryl-*C*) ppm. The resonances for the two carbonyl ligands could not be observed in ^{13}C-APT NMR spectrum. IR (ATR): $\tilde{\nu}$ [cm^{-1}] 3059 (vw), 2963 (w), 2361 (vw, B-H), 2324 (vw), 2161 (vw), 2017 (br), 1986 (m, CO/Fe-H), 1936 (CO/Fe-H), 1591 (w), 1574 (vw), 1484 (w), 1438 (m), 1310 (br), 1260 (m), 1189 (br), 1126 (m), 1094 (s), 1053 (s), 1015 (s), 998 (s), 931 (m), 917 (m), 862 (br), 798 (s), 740 (m), 728 (m), 690 (vs), 621 (w). High Res. ESI-MS (*m/z, pos.*): 895.1790 (calc. for $[M]^+$), 895.1800 (found, Δ = 1.1 ppm).

Synthesis of [(Ph-PBP^{-H})Fe(H)(CO)$_2$]K (5)

Complex **1** (75 mg, 0.08 mmol) was dissolved in a solution of 47 mg (0.42 mmol) KO^{t}Bu in 5 mL toluene and heated to reflux for 3 hours. The supernatant solution was decanted off and the remaining light-yellow precipitate was dried *in vacuo* to give **5** as a light-yellow solid. Yield: 35 mg (47%). ^{31}P{^{1}H} NMR (162 MHz, MeCN-d_3, 27 °C) δ: 47.1 (br, 2 P), 109.2 (dd, 2P, $^3J_{PP}$ = 62.4 Hz, $^2J_{PP}$ = 87.2 Hz) ppm. ^{1}H NMR (400 MHz, MeCN-d$_3$, -30 °C) δ: -8.66 (t, 1 H, Fe-*H*, ^{2}J$_{PH}$ = 52.8 Hz), 2.90 (br, 1 H, B-*H*), 7.08-7.29 (br, 40 H, Phenyl-*H*), 7.43 (br, 12 H, *ortho*-Phenyl-*H*), 7.93 (br, 4 H, *ortho*-Phenyl-H) ppm. ^{11}B{^{1}H} NMR (160.5 MHz, MeCN-d$_3$, 27 °C) δ: -11.8 (br) ppm. Selectively decoupled ^{1}H{^{31}P} and ^{1}H{^{11}B} NMR spectra were acquired, causing a sharpening of the B-H-signal at 2.94 ppm for the ^{1}H{^{11}B} NMR spectrum. All other ^{1}H NMR resonances remained unchanged in comparison to the ^{1}H NMR spectrum reported above. At room temperature the Fe-H signal can only be observed as a very broad signal from -8 to 0 ppm. ^{1}H{^{11}B} (400 MHz, MeCN-d$_3$, -30 °C) δ: -8.60 (br, 1 H, Fe-*H*), 2.97 (br, 1 H, B-*H*), 7.14-7.94 (br, m, 40 H, Phenyl-*H*) ppm.^{13}C-APT NMR (100.6 MHz, MeCN-d$_3$, 27 °C) *δ*: 127.3 (t, J_{PC} = 4.1 Hz, Aryl-*C*), 127.6 (d, J_{PC} = 9.8 Hz, Aryl-*C*), 129.0 (br, Aryl-*C*), 131.2 (t, J_{PC} = 5.5 Hz, Aryl-*C*), 132.6 (d, J_{PC} = 10.0 Hz, Aryl-*C*) ppm. IR (ATR): $\tilde{\nu}$ [cm^{-1}] 3052 (w), 2960 (vw), 2340 (w, B-H), 2283 (w), 2216 (w), 2162 (vw), 1956 (m, Fe-H), 1936 (s, Fe-H/CO), 1892 (m, Fe-H/CO), 1841 (m, Fe-H/CO), 1587 (vw), 1572 (vw), 1478 (m), 1433 (s), 1306 (w), 1259 (m), 1194 (m), 1159 (vw), 1123 (m), 1098 (m), 1065 (m), 1048 (s), 1032 (m), 1022 (s), 997 (m), 930 (w), 888 (w), 856 (w), 811 (s), 793 (s), 742 (s), 719 (s), 692 (vs), 617 (m), 600 (w), 573 (s), 564 (s), 536 (s), 517 (s), 506 (s), 494 (s), 479 (s), 451 (m), 424 (w). High Res. ESI-MS (*m/z, pos.*): 893.1643 (calc. for [M]$^-$), 893.1632 (found, Δ = 1.1 ppm).

2. NMR spectra

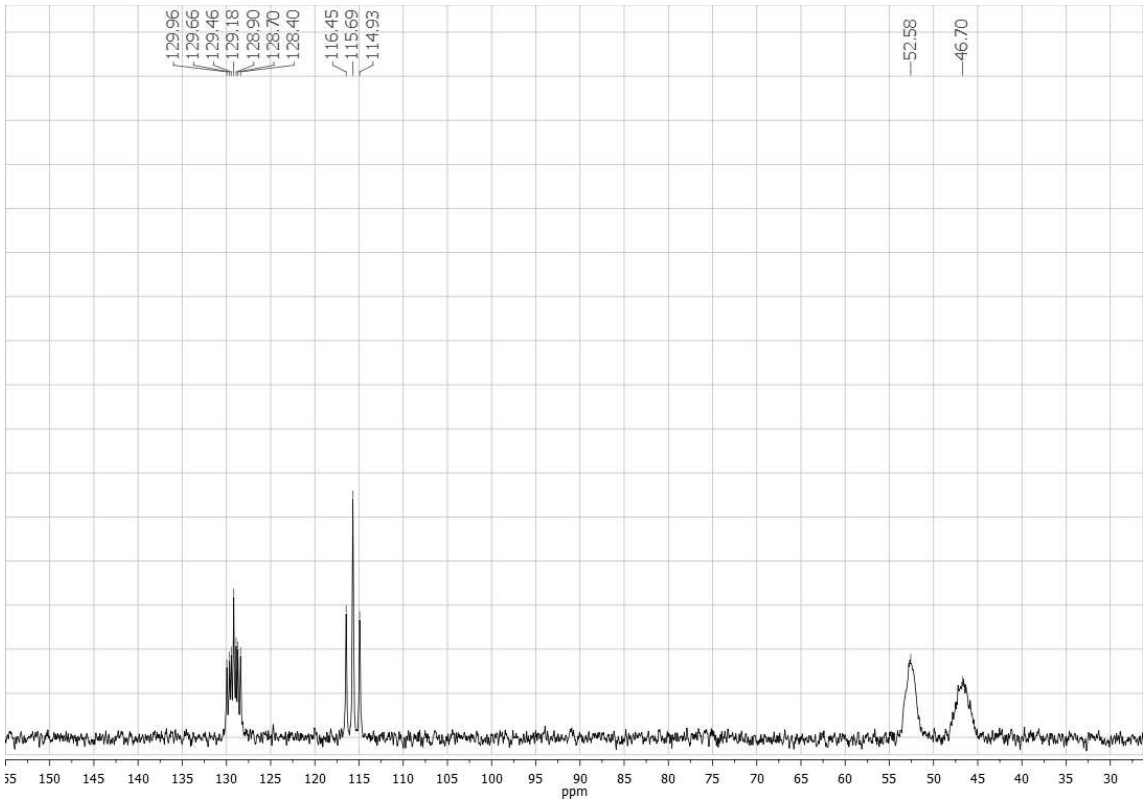

Figure 1 $^{31}P\{^{1}H\}$ NMR spectrum of complex **1** in C_6D_6.

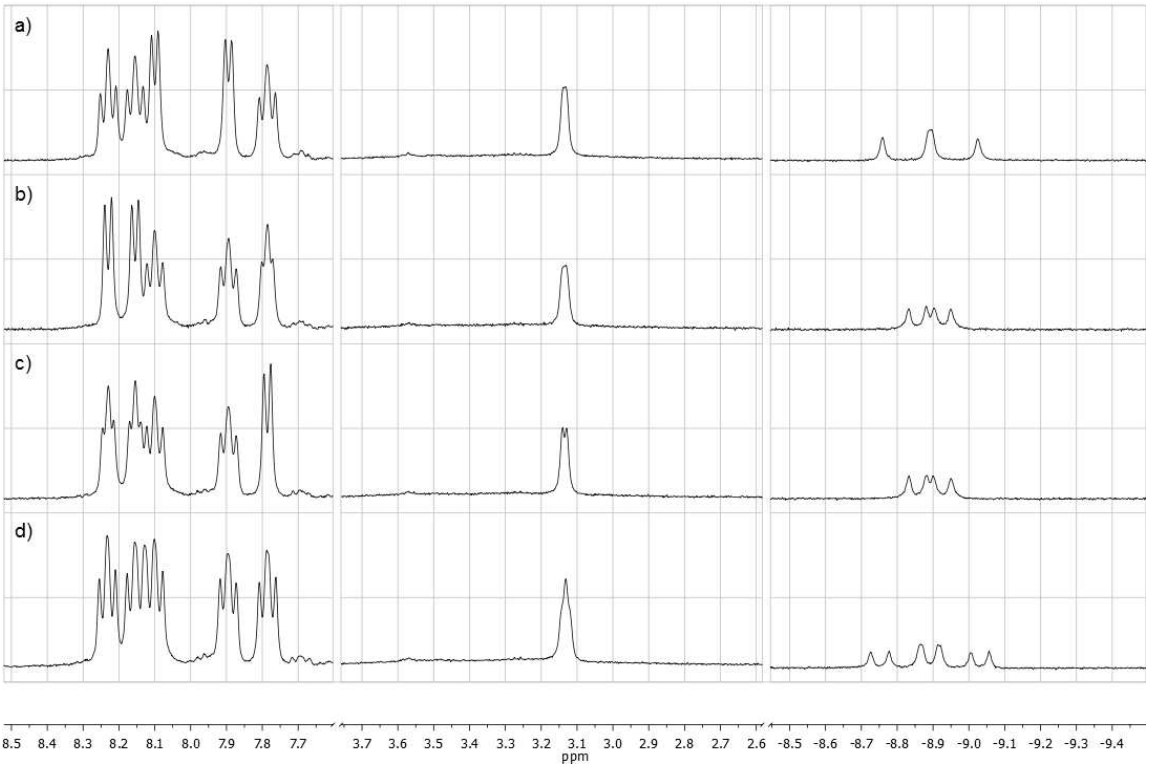

Figure 2 $^{1}H\{^{31}P\}$ NMR (a-c) and ^{1}H NMR spectra (d) of complex **1** in C_6D_6: chemical shift of the decoupling was set to 129.0 (a), 116.0 (b) and 50.0 ppm (c).

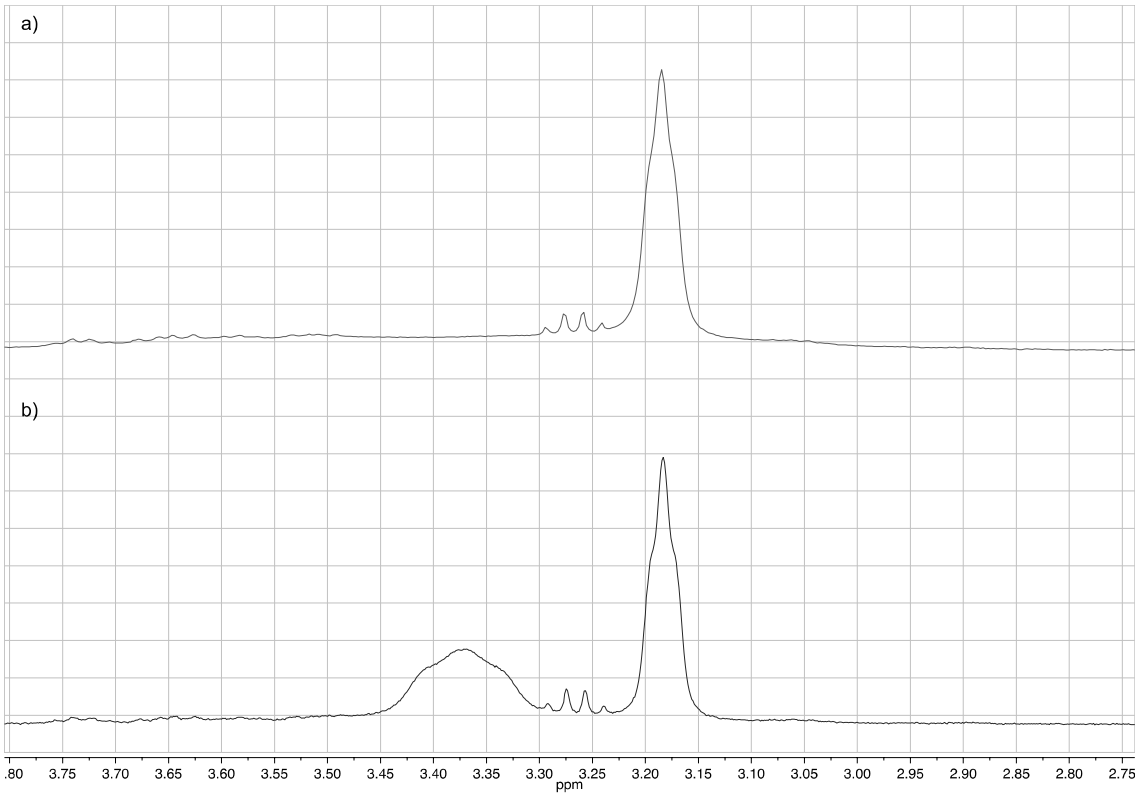

Figure 3 ^{1}H NMR (a) and $^{1}H\{^{11}B\}$ NMR spectrum (b) of complex **1** in C_6D_6.

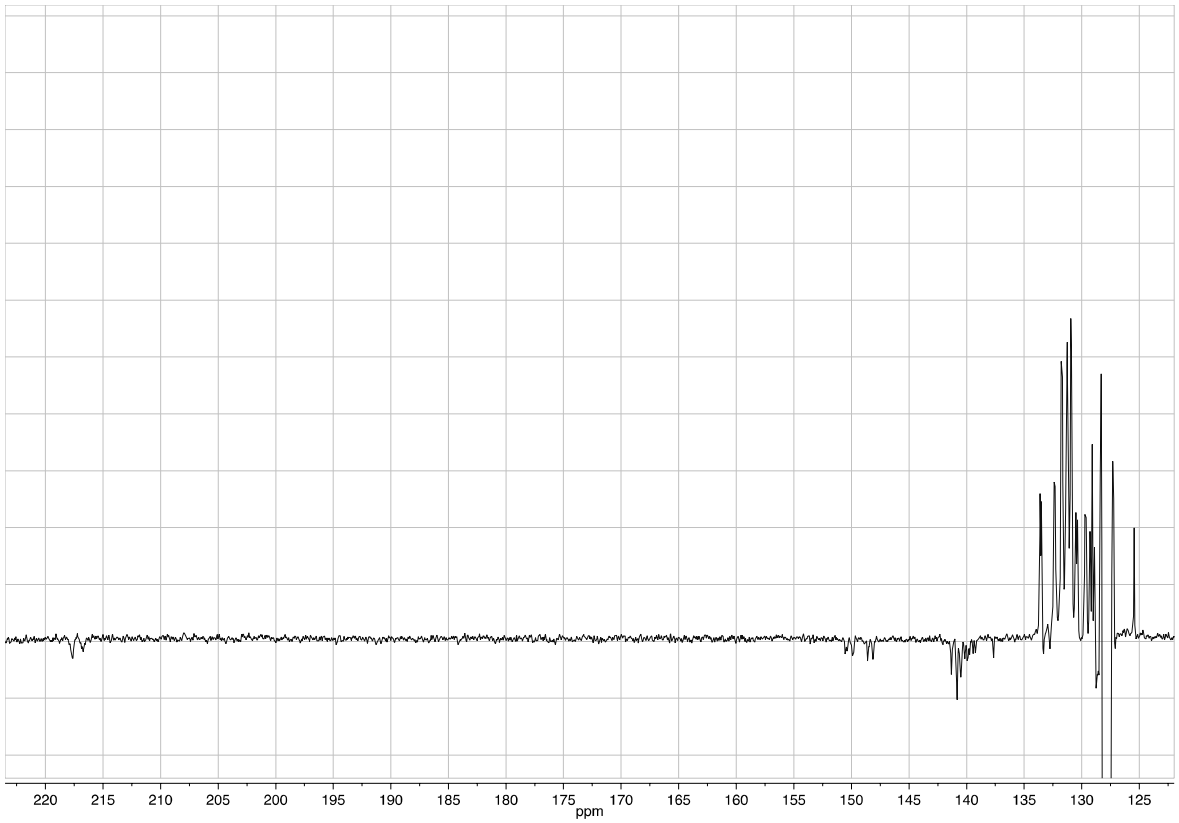

Figure 4 ^{13}C-APT NMR spectrum of complex **1** in C_6D_6.

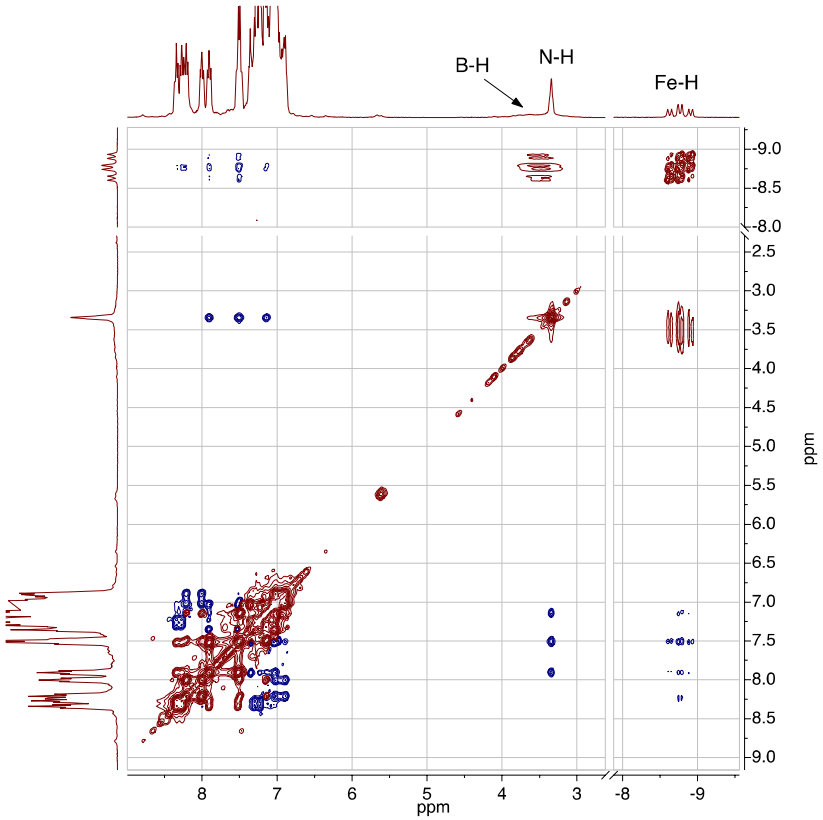

Figure 5 ^{1}H-NOESY NMR spectrum of complex **1** in C_6D_6.

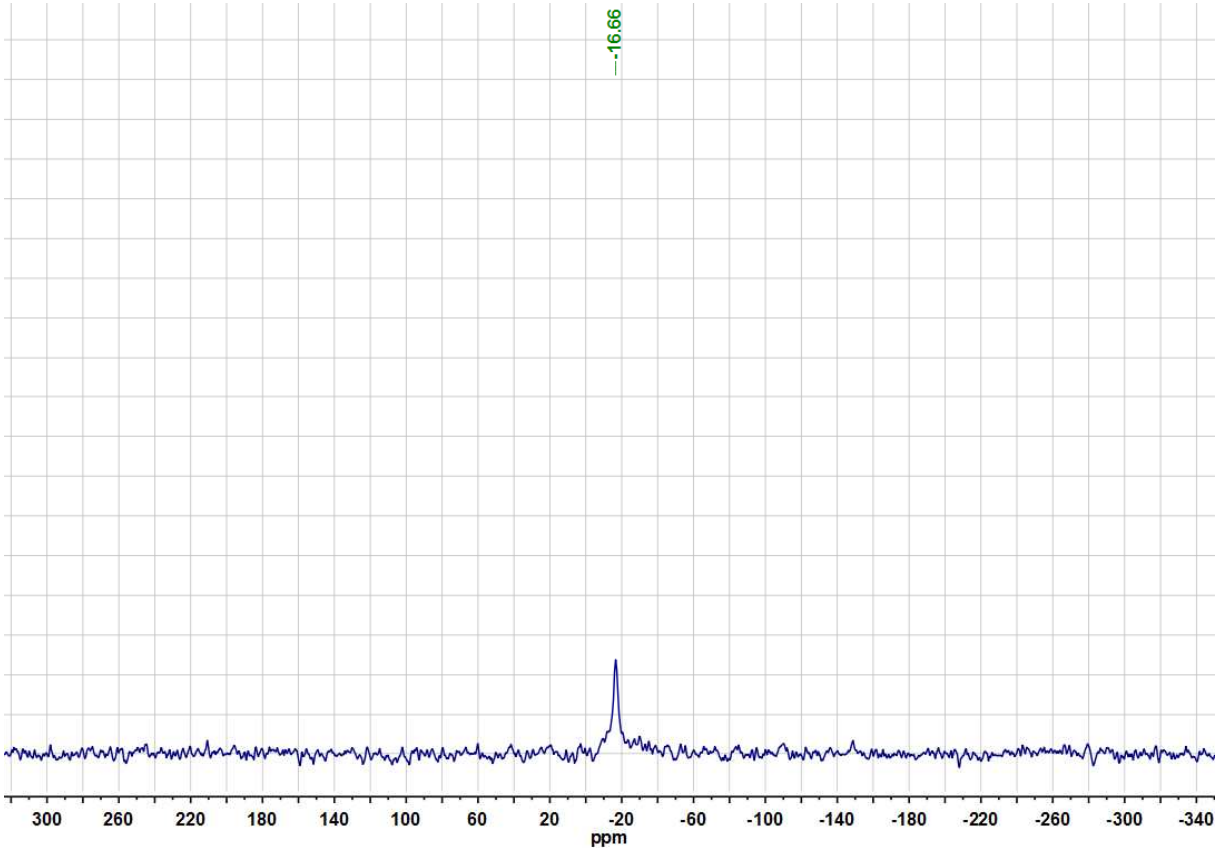

Figure 6 $^{11}B\{^{1}H\}$ NMR spectrum of complex **1** in C_6D_6.

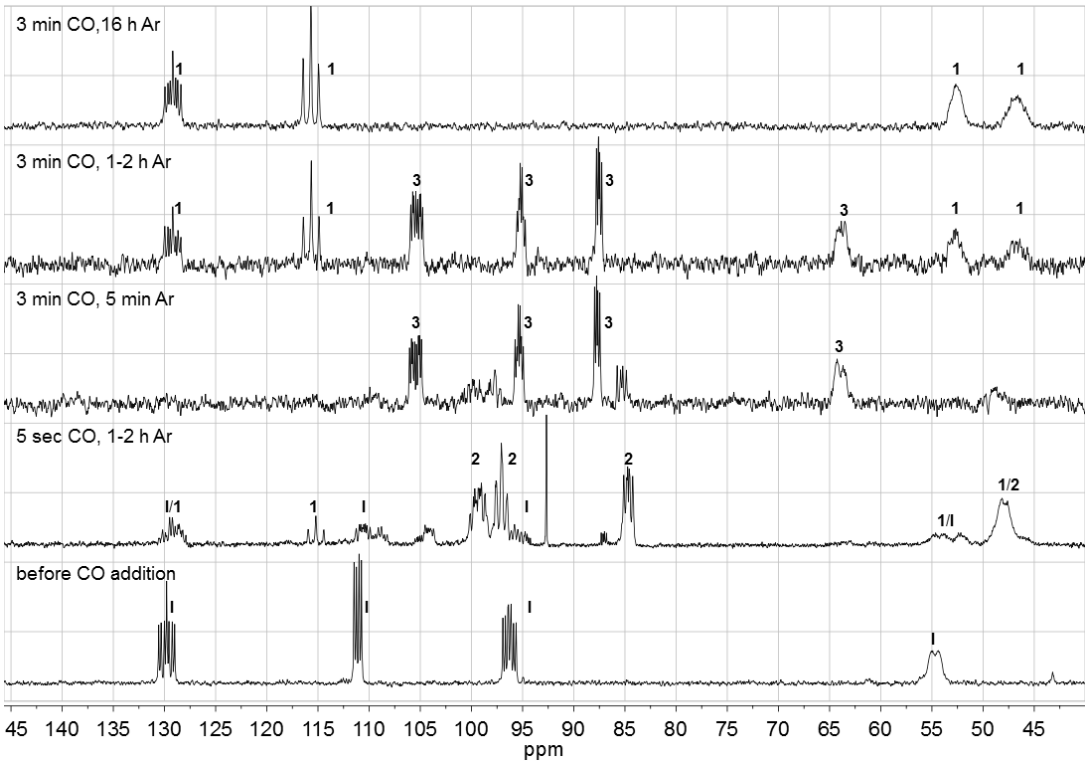

Figure 7 $^{31}P\{^{1}H\}$ NMR spectra of the reaction leading to complex **1** in toluene that shows different detectable intermediates.

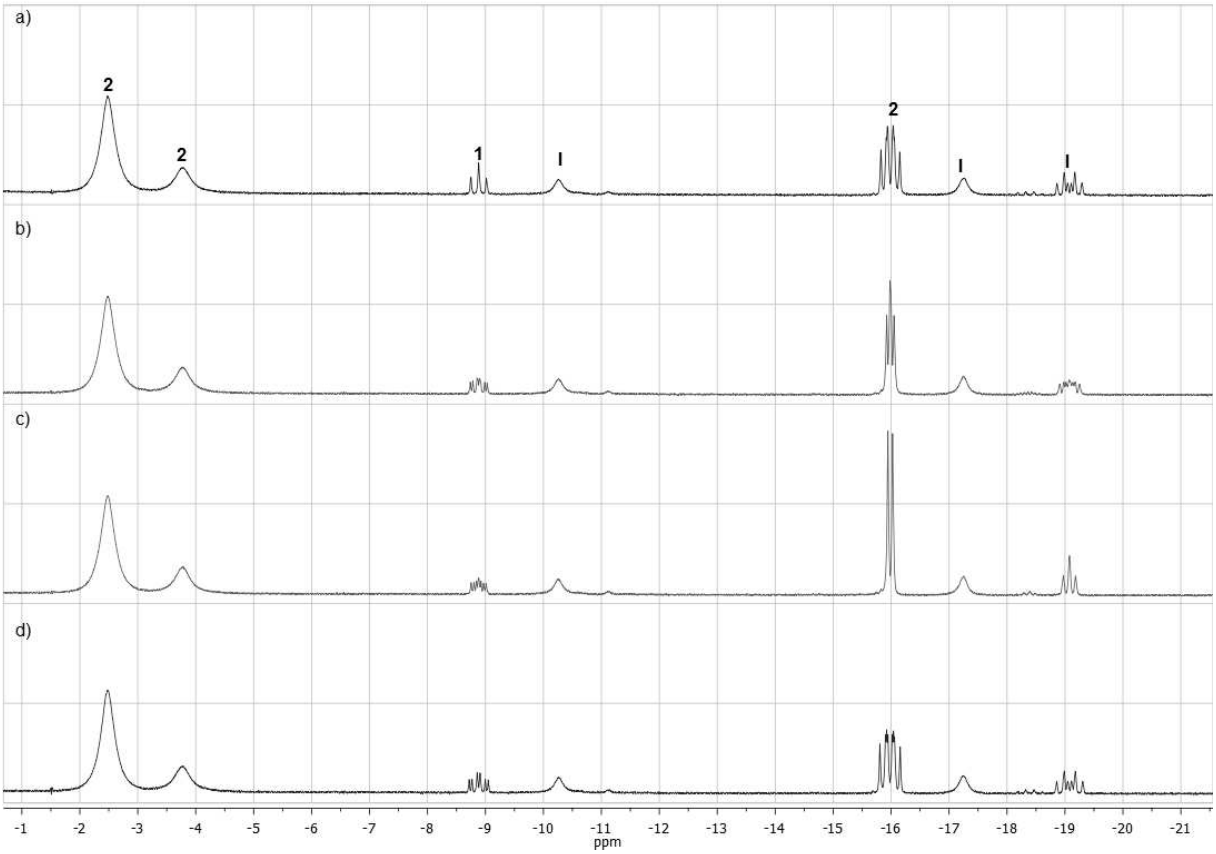

Figure 8 The hydride region in the ^{1}H NMR spectrum of a reaction mixture containing complex **2** as the major species in C_6D_6 (a) and $^{1}H\{^{31}P\}$ NMR spectra with different decoupling frequencies (b-d).

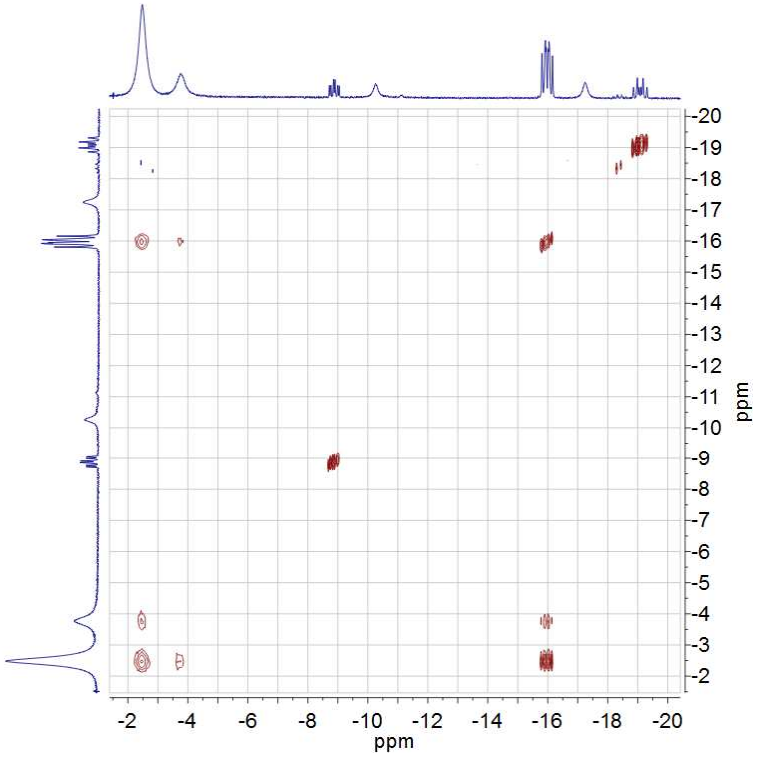

Figure 9 ^{1}H NOESY NMR spectrum of a reaction mixture containing complex **2** as the major species in C_6D_6, indicating chemical exchange between Fe-*H*- and B-*H*-resonances.

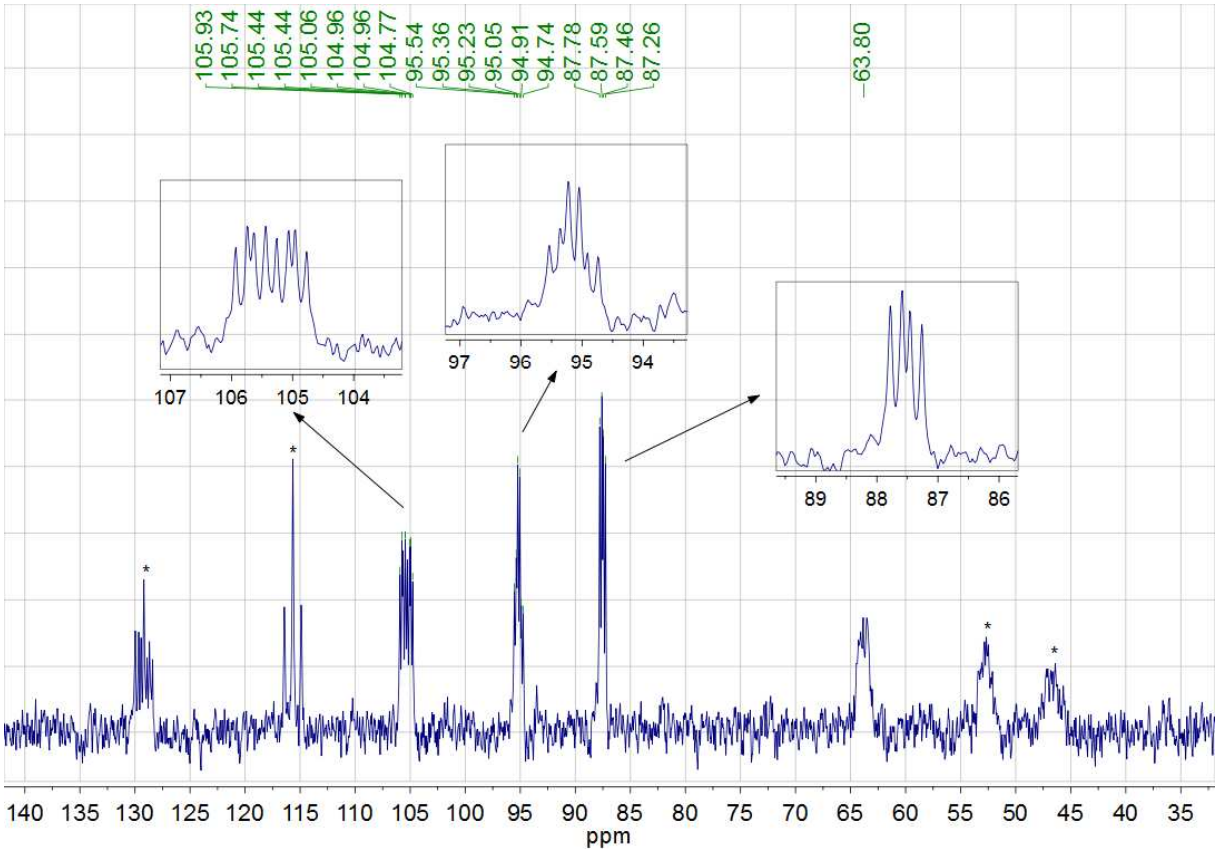

Figure 10 ^{31}P{^{1}H} NMR spectrum of complex **3** in C_6D_6 that isomerizes to complex **1** (marked with *).

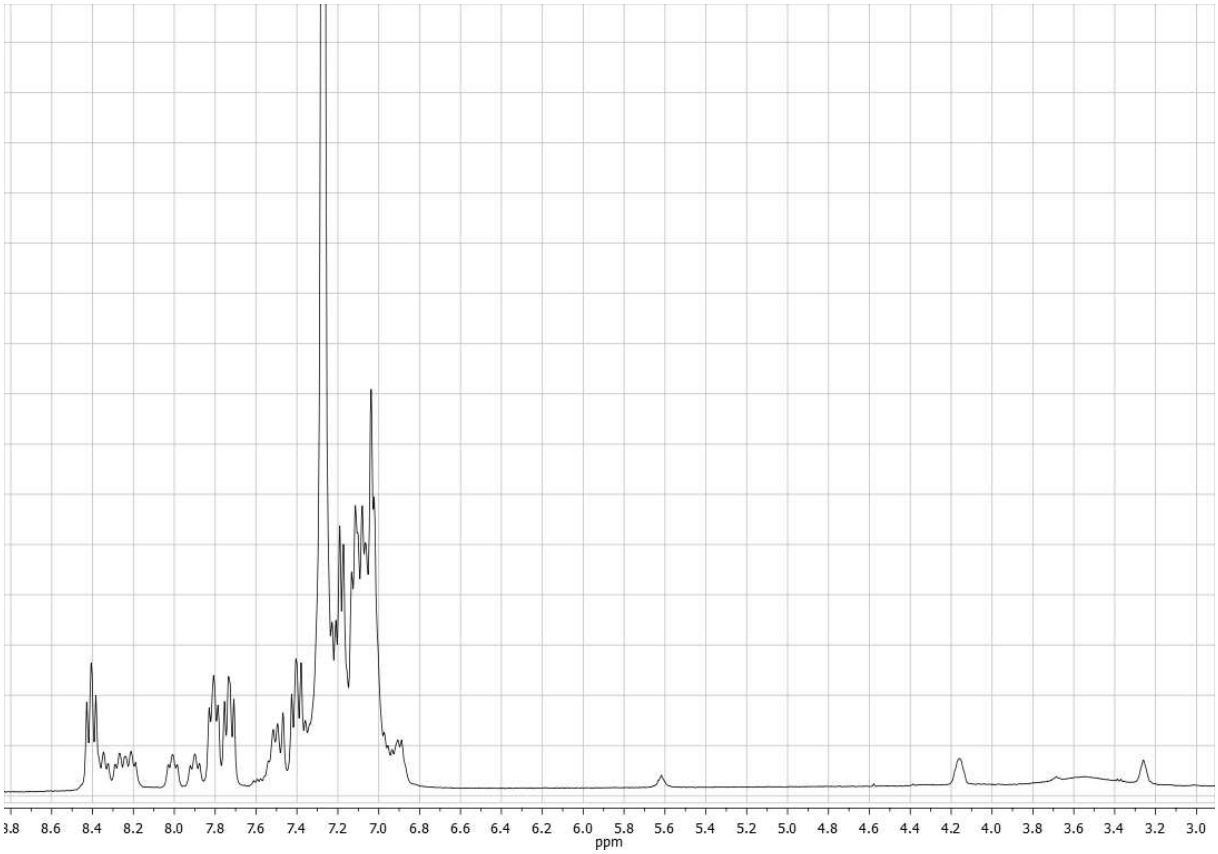

Figure 11 ^{1}H NMR spectrum of complex **3** in C_6D_6 that isomerizes to complex **1**.

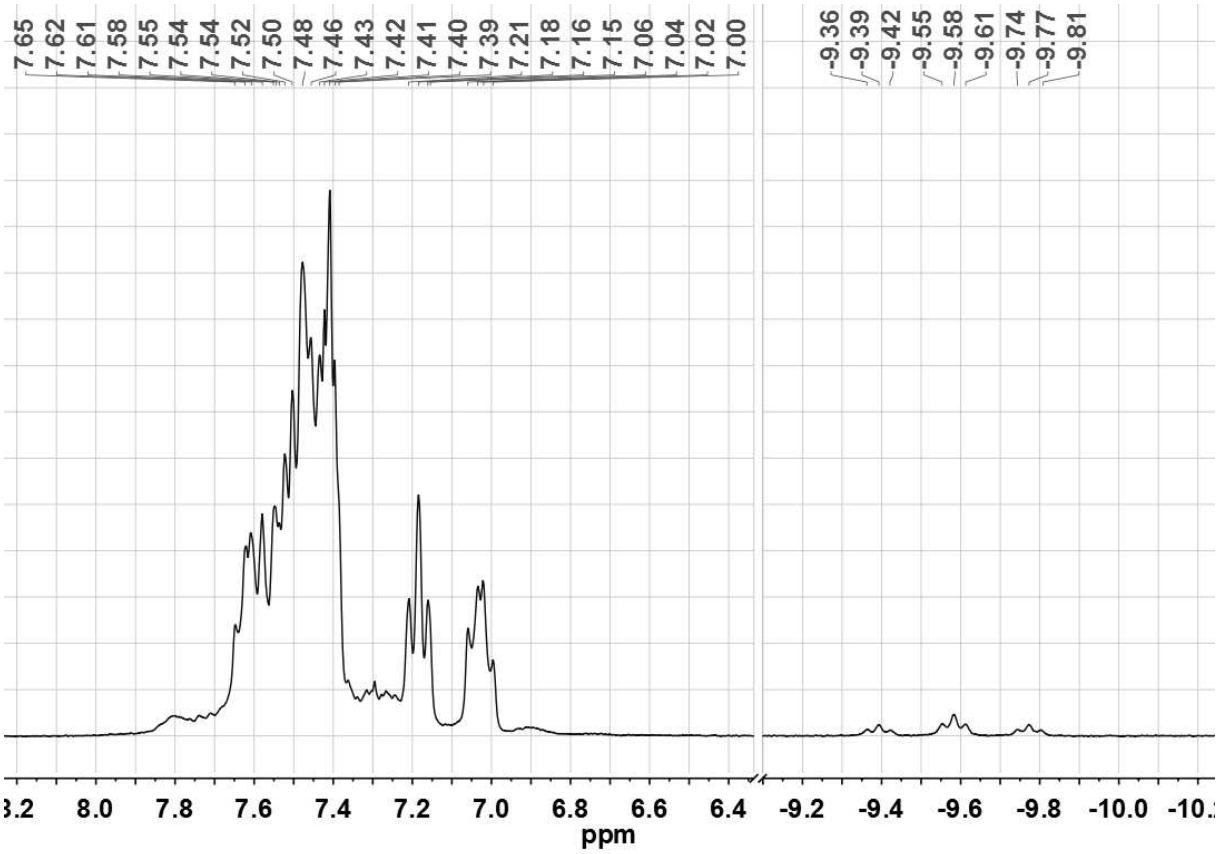

Figure 12 ^{1}H NMR spectrum of complex **4** in MeCN-d_3.

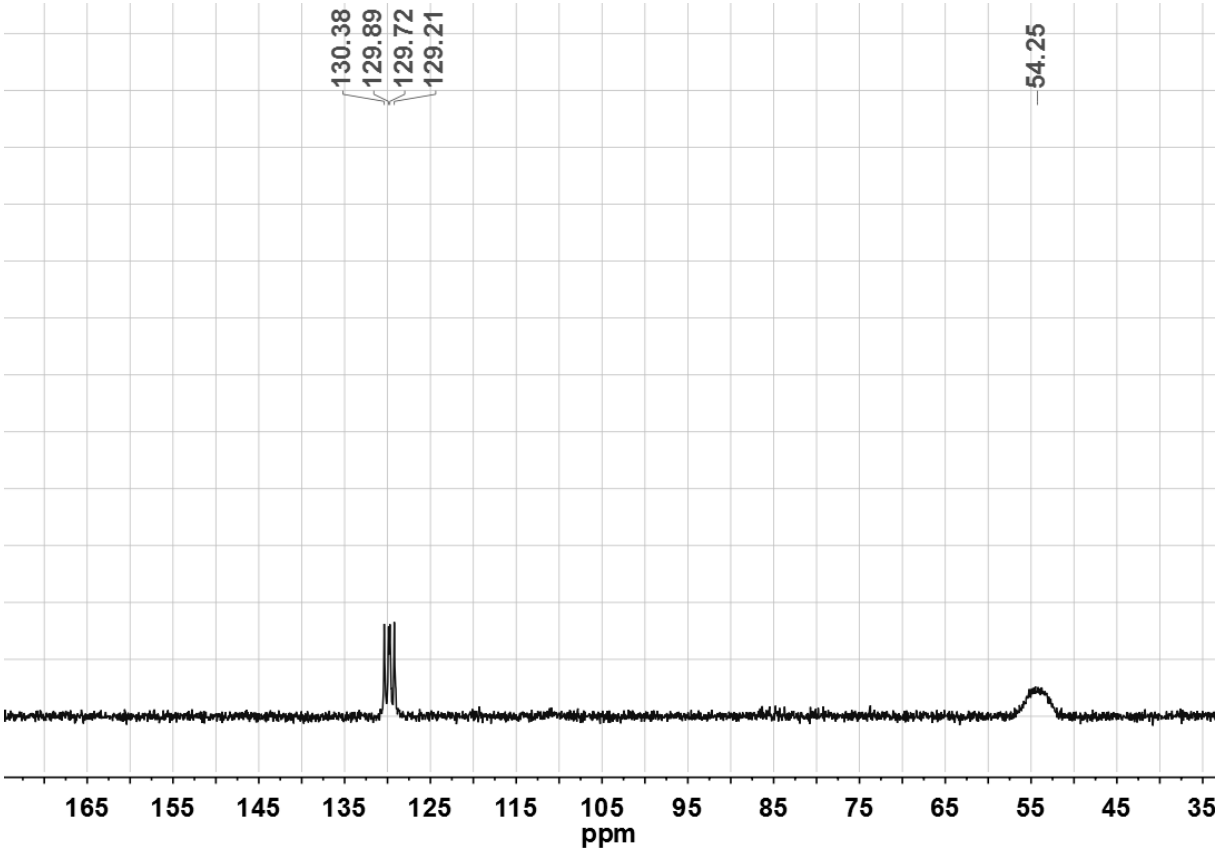

Figure 13 $^{31}P\{^{1}H\}$ NMR spectrum of complex **4** in MeCN-d_3.

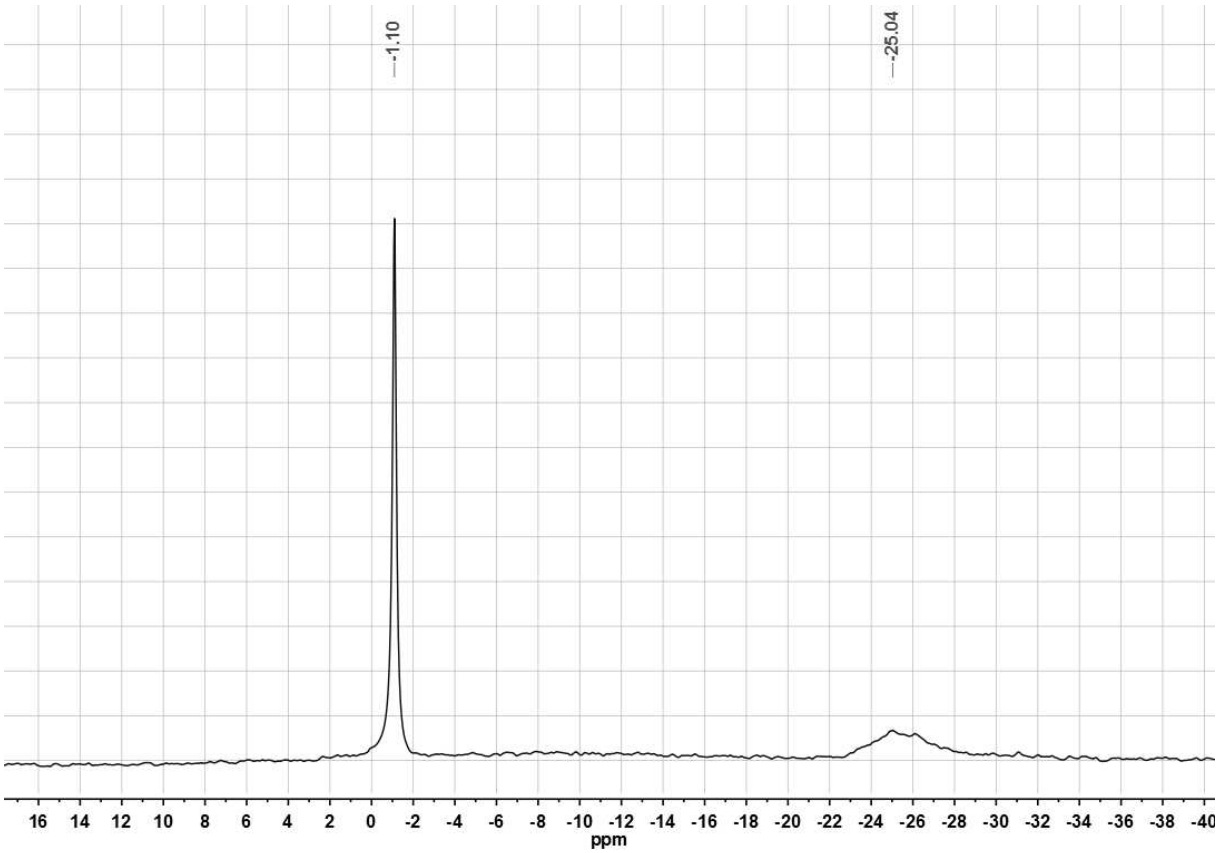

Figure 14 $^{11}B\{^{1}H\}$ NMR spectrum of complex **4** in MeCN-d_3.

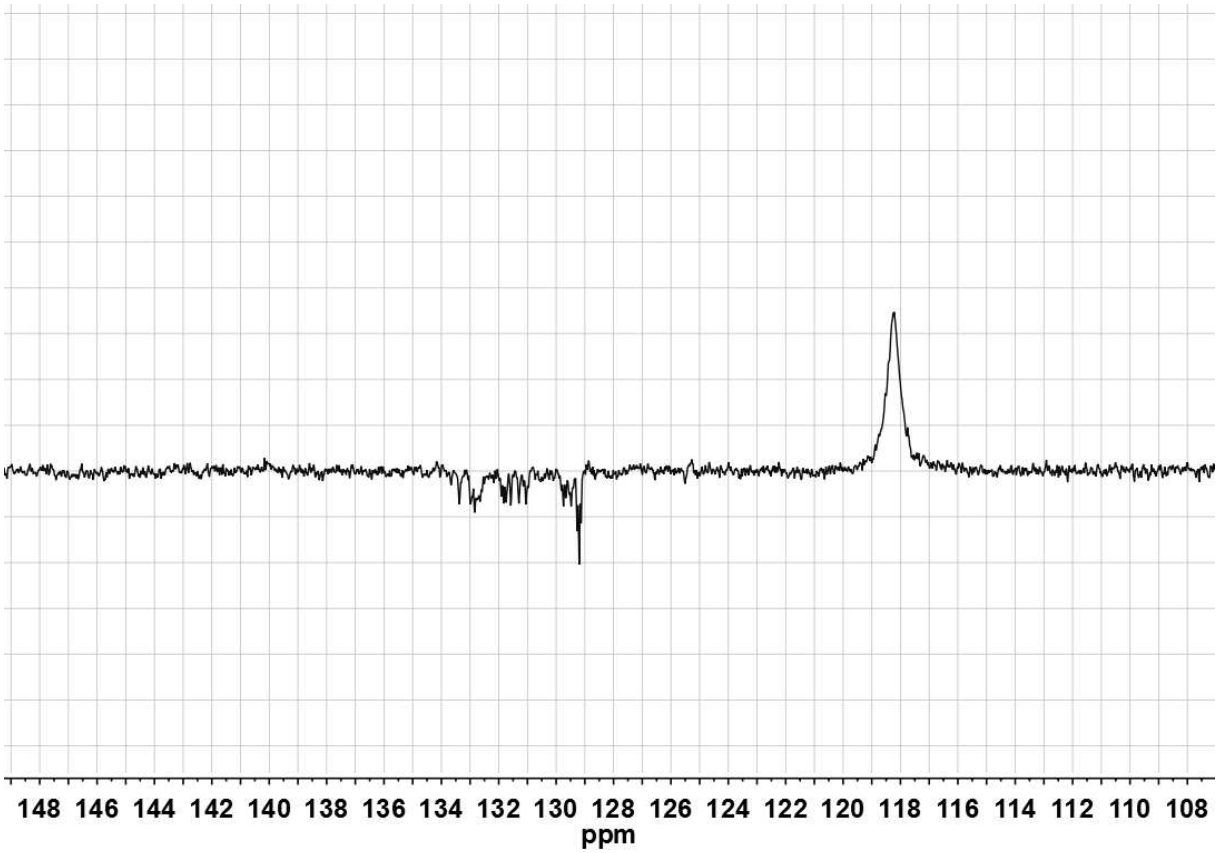

Figure 15 ^{13}C-APT NMR spectrum of complex **4** in MeCN-d_3.

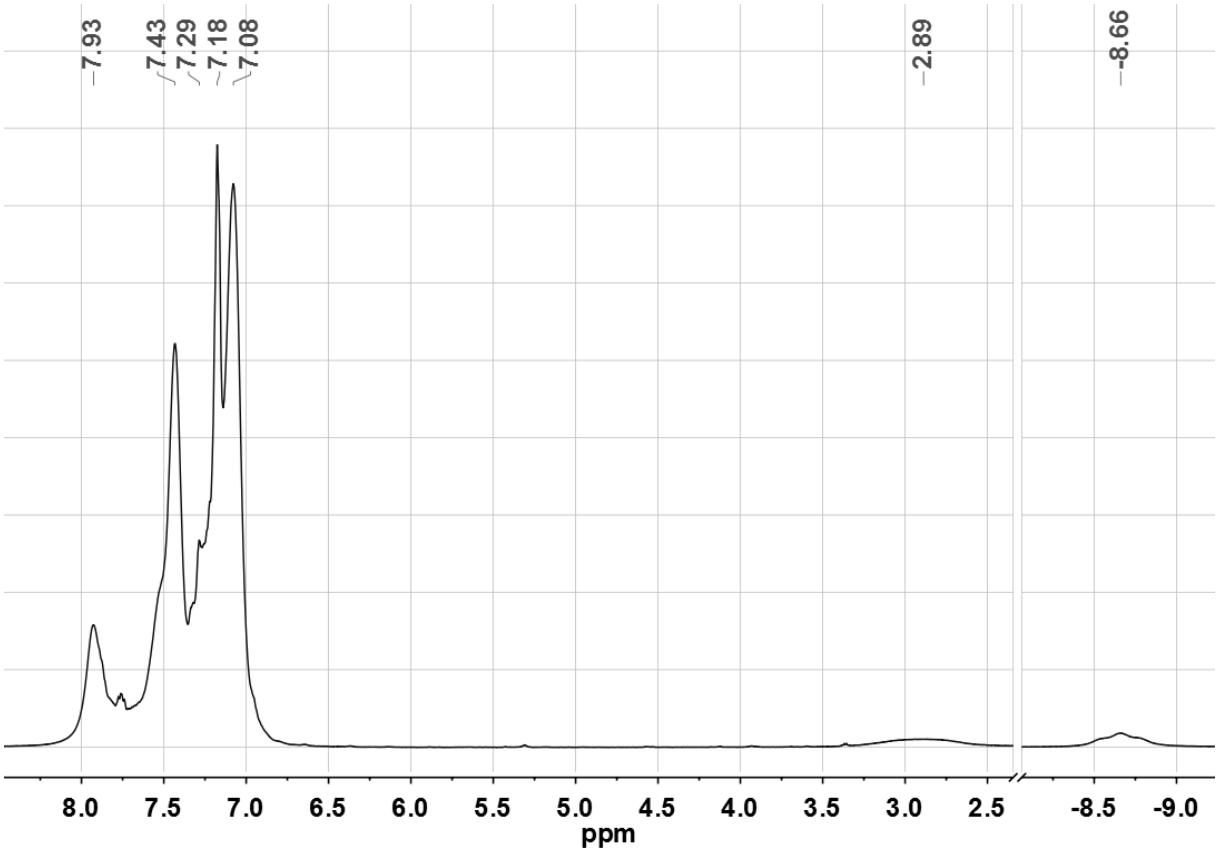

Figure 16 ^{1}H NMR spectrum of complex **5** in MeCN-d_3 at 243 K.

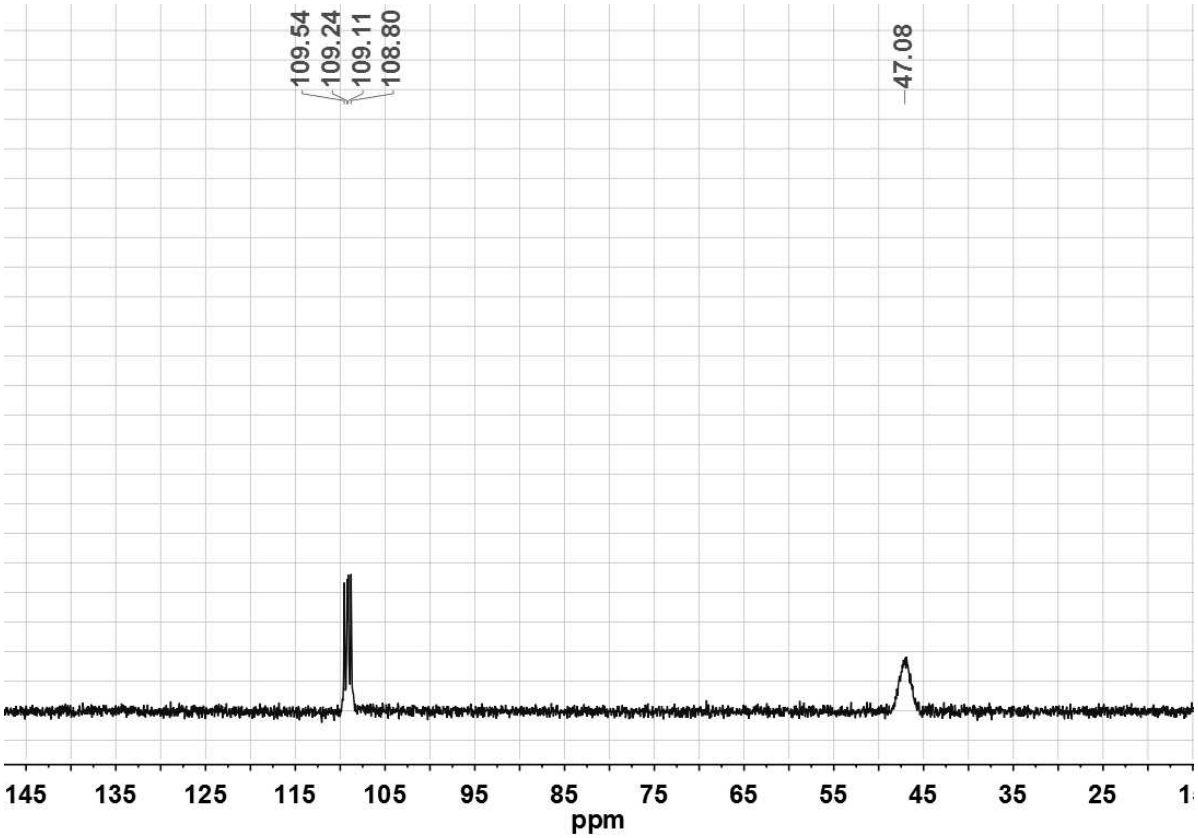

Figure 17 $^{31}P\{^{1}H\}$ NMR spectrum of complex **5** in thf-d_8 at 243 K.

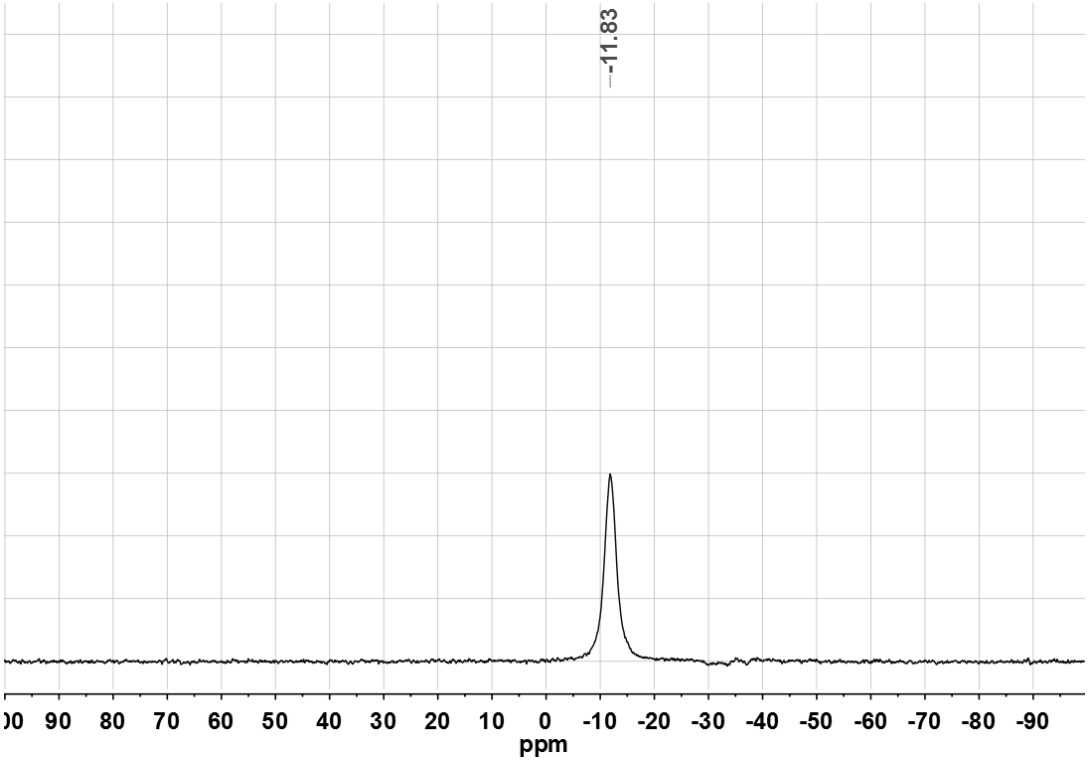

Figure 18 $^{11}B\{^{1}H\}$ NMR spectrum of complex **5** in MeCN-d_3 at 243 K.

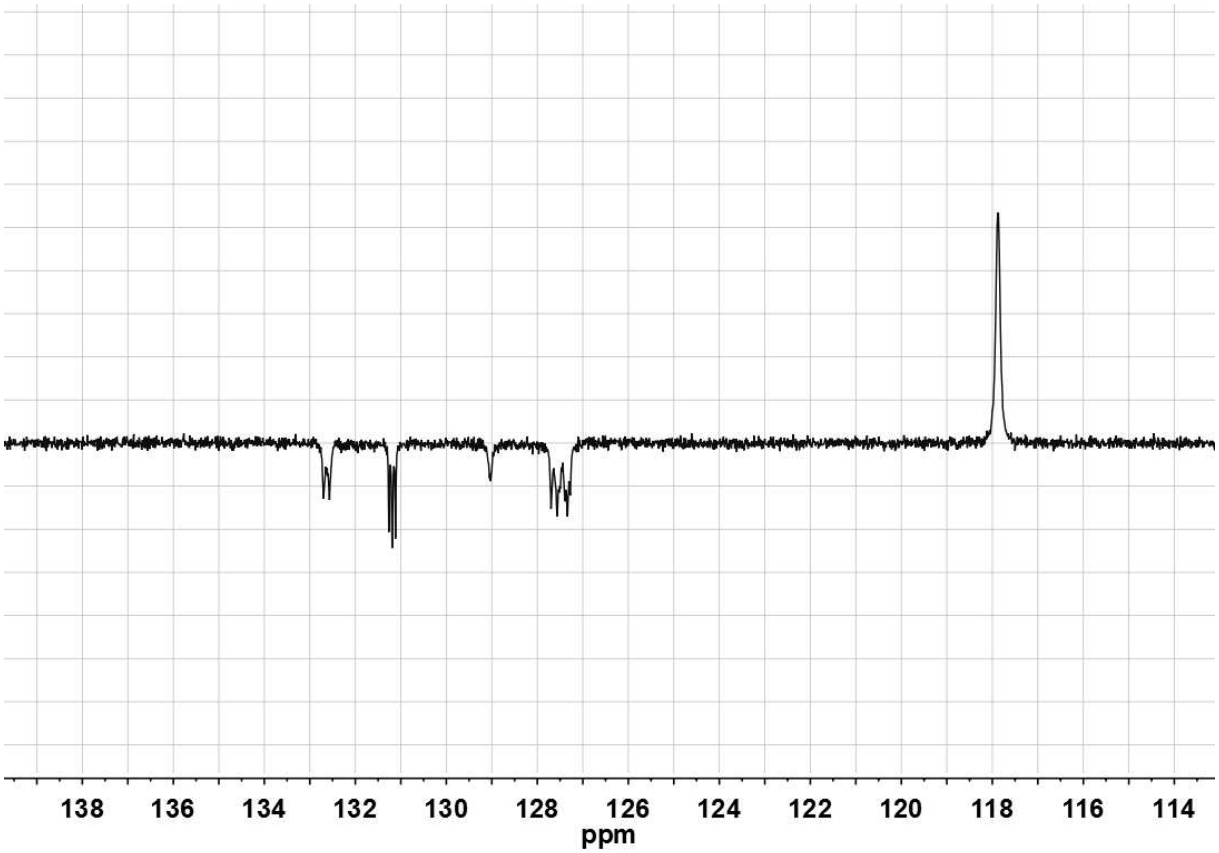

Figure 19 ^{13}C-APT NMR spectrum of complex **5** in MeCN-d_3 at 243 K.

3. Variable Temperature NMR Measurements

The rate constants of the intramolecular exchange in complex **1** were determined by quantitative two dimensional ^{1}H EXSY NMR spectra at different temperatures, using the method described by *Perrin* and *Dwyer*.[3] Therefore the optimal mixing times (τ_{opt}) were calculated for each temperature using equation 1, whereas $k_{AB} = k_{BA}$ for the intra molecular exchange.

$$\tau_{opt} = \frac{1}{\frac{1}{T_1} + k_{AB} + k_{BA}} \quad (1)$$

For the approximation of the exchange rates $k_{AB} = k_{BA}$ in complexes **1**, **4** and **5** a line shape analysis of the resonance of the hydride ligand in the ^{1}H NMR spectra at different temperature was used. To investigate whether the exchange peaks of the *ortho*-phenyl resonances refer to the same process as the cross peaks between the Fe-H and B-H resonances, the analysis of the corresponding rate constants of two well separated *ortho*-phenyl resonances was done as well. For this reason the resonances of interest were analyzed applying deconvolution algorithm at each temperature, from which the half height width was directly obtained. The line broadening due to chemical exchange $\Delta\nu_{1/2}$ of these resonances was obtained as the difference of $\nu_{1/2}$ and the half height width of a reference peak at each temperature. As reference the CH_3-resonance of an uncoordinated solvent molecule was used. The approximate rate constants can be calculated using equation 2. The optimal mixing times for the variable temperature EXSY NMR measurements are summarized in Table 1.

$$k = 2k_{AB} = 2k_{BA} = \pi\Delta\vartheta_{1/2} = \pi(\vartheta_{1/2} - \vartheta_{Ref}) \quad (2)$$

For an intramolecular exchange with the equally populated and exchanging spin systems A and B the exchanging rate constant $k = k_{AB} + k_{BA}$ is given by equation 3 and 4. Thereby, I_{AA} and I_{BB} denote the intensities of the corresponding diagonal cross peaks and I_{AB} and I_{BA} the cross peak intensities in the EXSY NMR spectrum.

$$k = \frac{1}{\tau_{opt}} ln\left(\frac{r+1}{r-1}\right) \quad (3)$$

$$r = \frac{I_{AA}+I_{BB}}{I_{AB}+I_{BA}} \quad (4)$$

Table 1 Rate constants of complex **1** based on line shape analysis of ^{1}H NMR spectra, corresponding mixing times (τ_{opt}) and rate constants based on quant. 2-dim. ^{1}H EXSY NMR spectra at different temperatures.

T / K	k_{ab}/ s^{-1} (line shape, Fe-H)	τ_{opt} / s	k_{ab}/ s^{-1} (EXSY, Fe-H)	k_{ab} / s^{-1} (EXSY, *o*-phenyl)
300	3.63325	0.06652	0.87244	3.38392-4.65654
310	7.04385	0.03314	2.48738	8.7336-12.15248
320	12.80005	0.01880	6.82032	21.14185-25.77555
330	37.4352	0.00659	22.23679	45.95312-69.62359
340	75.3558	0.00330	62.66254	104.11062-190.67542

The *Eyring* analysis of the rate constants obtained via line shape analysis and quantitative 2-dimensional ^{1}H EXSY NMR spectroscopy results in similar parameters of activation for both methods (Fig. 20). Furthermore, the exchange rates of the *ortho*-phenyl resonances give rise to similar free enthalpies of activation $\Delta G^{\ddagger}_{298}$ (Table 3).

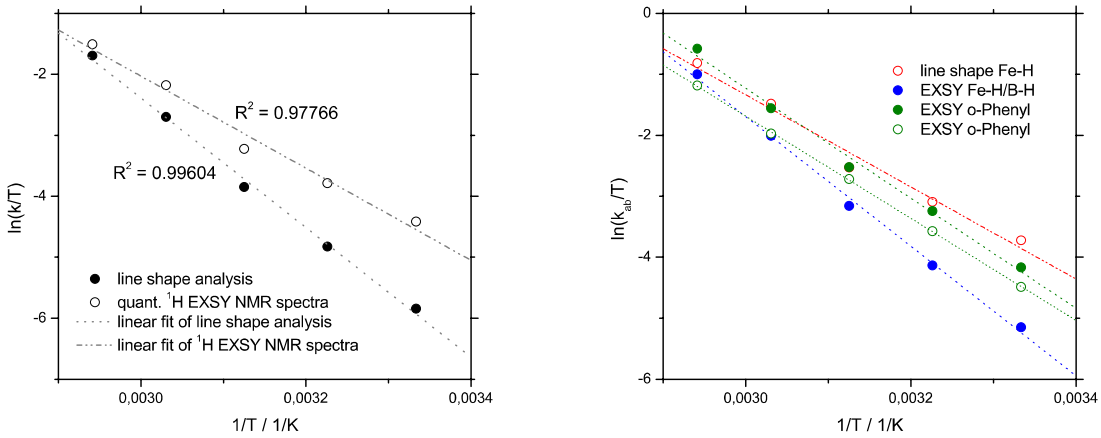

Figure 20 Left: *Eyring* plot of the Fe-H/B-H exchange in complex **1** based on line shape analysis of the ^{1}H NMR spectra and based on ^{1}H-EXSY NMR spectra in C_6D_6; Right: *Eyring* plot comparing Fe-H/B-H- and *o*-phenyl-exchange in complex **1**.

Table 2 Rate constants of complex **1, 4** and **5** in comparison based on line shape analysis of ^{1}H NMR spectra.

T / K	k_{ab}/ s^{-1} (**1**, Fe-H)	k_{ab}/ s^{-1} (**4**, Fe-H)	k_{ab}/ s^{-1} (**5**, Fe-H)
243	-	-	89.52911
250	-	-	163.03138
260	-	-	397.12088
270	-	-	905.03945
280	-	-	1745.3668
290	-	-	3111.55279
300	3.63325	7.41259	coalescence
310	7.04385	9.78763	
320	12.80005	13.50728	
330	37.4352	20.91515	
340	75.3558	29.11000	

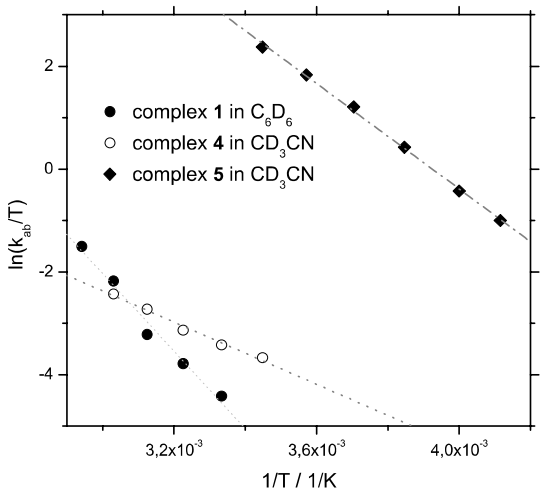

Figure 21 *Eyring* plot of the Fe-H/B-H exchange in complex **1**, **4** and **5** based on line shape analysis of the ^{1}H NMR spectra in C_6D_6 (**1**) or CD_3CN (**4** and **5**).

Table 3 Comparison of exchange rates for Fe-/B-H-exchange and the exchange of *ortho*-phenyl protons.

exchange	$\Delta H^{\ddagger}$ / kJ·mol^{-1}	$\Delta S^{\ddagger}$ / J·mol^{-1}·K^{-1}	$\Delta G^{\ddagger}_{298}$ / kJ·mol^{-1}	R^2
Fe-H/B-H (**1**, EXSY)	88.3 ± 2.8	47.5 ± 8.7	74.1 ± 5.4	0.99604
o-phenyl (**1**, EXSY)	75.0 ± 3.4	17.3 ± 10.8	69.9 ± 6.6	0.99164
o-phenyl (**1**, EXSY)	69.6 ± 0.6	-2.8 ± 1.8	70.4 ± 1.1	0.99971
Fe-H (**1**, line shape)	62.7 ± 4.7	-26.2 ± 14.8	70.6 ± 9.1	0.97766
Fe-H (**4**, line shape)	27.9 ± 1.7	-141.8 ± 5.5	67.4 ± 3.3	0.98231
Fe-H (**5**, line shape)	42.7 ± 0.9	-30.1 ± 3.2	51.6 ± 1.8	0.99801

4. X-Ray Crystallography

The single crystal X-ray diffraction data for the structural analysis has been collected using graphite-monochromated Mo-K_α-radiation ($\lambda_{MoK\alpha}$ = 0.71073) on the imaging plate detector systems STOE IPDS2T (**1**·H_2O·$^1/_2C_7H_8$ and **3**) or on the pixel detector system BRUKER D8-QUEST (**4**·$2CH_2Cl_2$). The structures were solved by direct methods with SHELXS-97 and refined against F^2 by full-matrix-least-square techniques using SHELXL-97.[4] Based on the crystal descriptions, numerical absorption corrections were applied.[5] Crystallographic data for **1, 3** and **4** has been deposited at Cambridge Crystallographic Data Centre (CCDC 1475280-1475284) and can be obtained free of charge via www.ccdc.cam.ac.uk/. Details of the data collection and the refinement can be found in the supporting information.

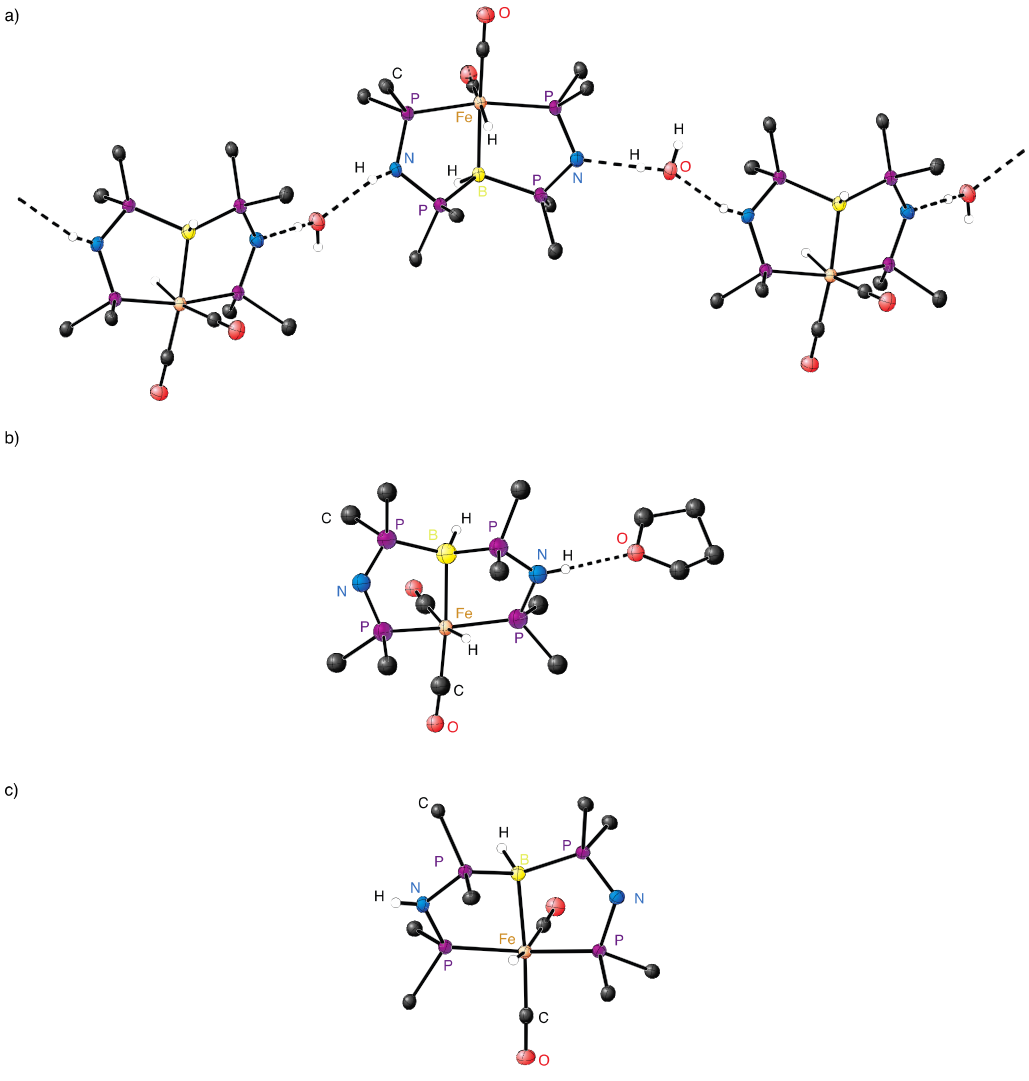

Figure 22 Different interaction of complex **1** in the crystal lattice; a) **1**·H_2O·$^1/_2C_7H_8$, b) **1**·**THF**, c) **1**·$1^1/_2C_7H_8$.

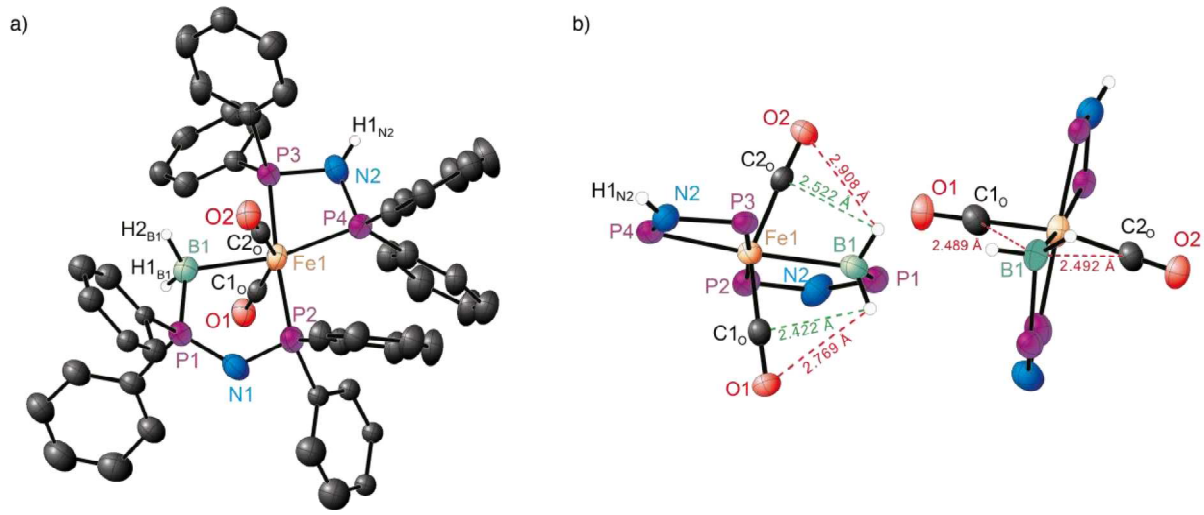

Figure 23 Molecular structure of complex **3** in the solid state, showing the angled coordination of the two carbonyl-ligands in *trans*-position (ellipsoids are drawn at 50% probability, carbon-bound hydrogen atoms are omitted for clarity).

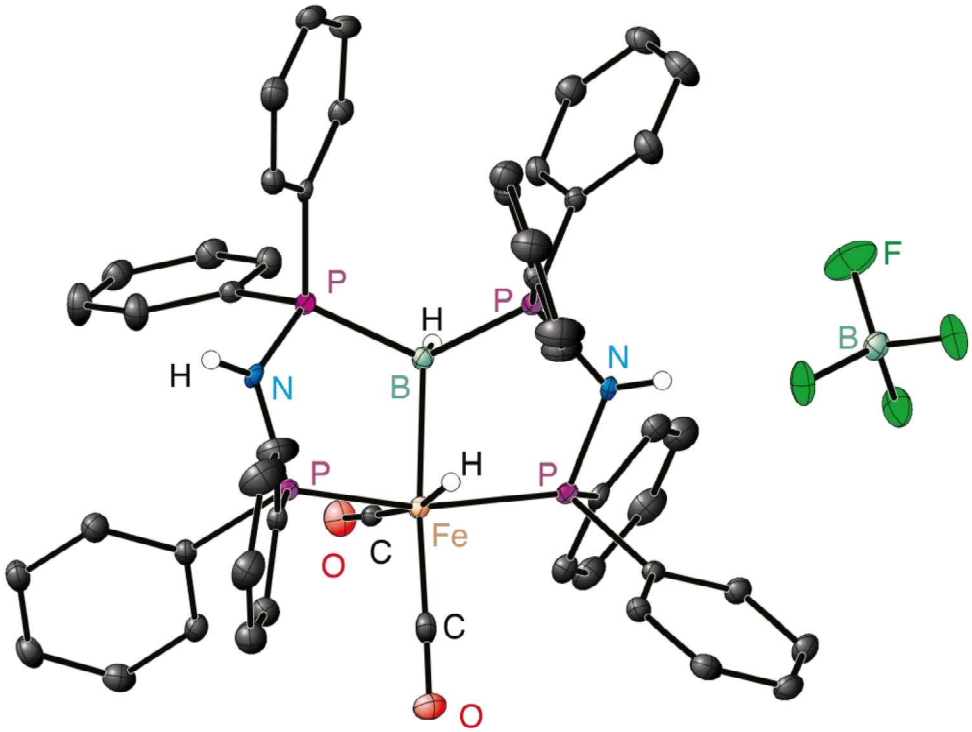

Figure 24 Molecular structure of complex **4** in the solid state (ellipsoids are drawn at 50% probability, carbon-bound hydrogen atoms are omitted for clarity).

Table 4 Crystallographic data for **1-4**.

Compound	**1·1^1/$_2$C$_7$H$_8$**	**1·H$_2$O·^{1}/$_2$C$_7$H$_8$**	**1·THF**	**3**	**4·2CH$_2$Cl$_2$**
Empirical formula	$C_{50}H_{43}BFeN_2O_2P_4 \cdot {}^3/_2C_7H_8$	$C_{50}H_{43}BFeN_2O_2P_4 \cdot H_2O \cdot {}^1/_2C_7H_8$	$C_{50}H_{43}BFeN_2O_2P_4 \cdot C_4H_8O$	$C_{50}H_{43}BFeN_2O_2P_4$	$C_{52}H_{48}B_2Cl_4F_4FeN_2O_2P_4$
Formula weight/g·mol^{-1}	1032.60	958.49	966.51	894.40	1152.07
T/K	100(2)	100(2)	100(2)	100(2)	100(2)
Crystal system	Monoclinic	Monoclinic	Triclinic	Monoclinic	Triclinic
Space group	*C*2/*c*	*P*2$_1$/*c*	$P\bar{1}$	*P*2$_1$/*c*	$P\bar{1}$
a/Å	24.723(5)	12.308(3)	12.222(2)	15.202(3)	12.2566(6)
b/Å	25.112(5)	20.351(4)	12.434(3)	20.180(4)	13.5159(7)
c/Å	18.829(4)	19.333(4)	17.175(3)	18.949(8)	17.1754(9)
α/°	90.00	90.00	78.36(3)	90.00	75.830(2)
β/°	116.39(3)	104.71(3)	75.66(3)	114.22(2)	88.197(2)
γ/°	90.00	90.00	75.20(3)	90.00	69.779(2)
V/Å^3	10471(4)	4684(2)	2418.0(8)	5301(3)	2584.2(2)
Z	8	4	2	4	2
ρ_{calc}/g·cm^{-3}	1.310	1.359	1.328	1.121	1.481
$\mu(MoK_\alpha)$/mm^{-1}	0.456	0.505	0.490	0.441	0.681
F(000)	4312	1996	1008	1856	1180
2θ range/°	3.62-54.44	2.96-53.50	4.96-53.42	3.54-53.64	4.42-52.04
Reflections measured	43861	28638	21995	39837	130120
Independent reflections	11049 (R_{Int} = 0.0747)	9873 (R_{Int} = 0.0448)	10120 (R_{Int} = 0.0525)	11219 (R_{Int} = 0.0880)	10175 (R_{Int} = 0.1363)
Ind. reflections (I>2σ(I))	8970	8026	8093	4204	6932
Parameters/Restraints	681/3	591/0	568/0	541/0	656
R_1 *(I>2σ(I))*	0.0315	0.0387	0.0466	0.0772	0.0313
wR_2 *(all data)*	0.0744	0.0838	0.1256	0.1569	0.0697
GooF (all data)	0.994	1.044	1.063	0.901	0.942
Max. peak/hole/e·Å^{-3}	0.339/-0.260	0.400/-0.429	1.697/-1.351	1.077/-0.238	0.475/-0.404
Min./ max. transmission	0.8387/0.9161	0.8895/0.9288	0.8982/0.9497	0.8916/0.9578	0.5821/0.7456
CCDC	1475281	1475280	1475282	1475284	1475283

5. DFT Calculations

DFT calculations were performed with Gaussian 09, Revision C.01.[6] As functional Grimmes general-gradient approximated and dispersion including B97D functional was used.[7] All geometries were first optimized with the def2-SVP basis set and then reoptimized using the def2-TVPP basis set.[8] Minima and transition states were confirmed with frequency calculations (0 resp. 1 imaginary frequencies). Transition states were connected with their respective minima *via* intrinsic reaction coordinate (IRC) calculations or geometry optimizations starting from the displaced imaginary mode. Geometry optimization of complex **1** was performed starting from the crystal structure. The simplified complex **1a** was then derived by replacing phenyl with methyl groups and subsequent geometry optimization. Bond lengths and selected angles, as well as Mulliken and NBO charges and Mayer-Mulliken and Wiberg bond orders are given in tables 5-9. Comparison of charges between **1** and **1a** shows that the simplified complex **1a** is a suitable model for calculations on this system.

Calculated lowest energy exchange pathway

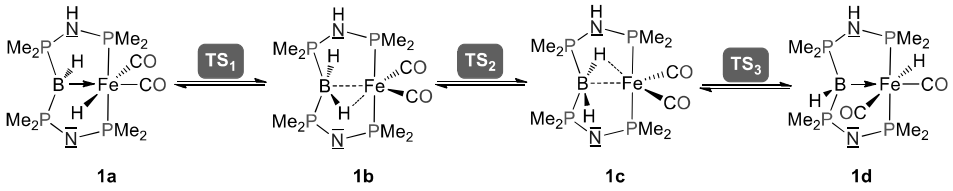

Numbering scheme for atoms

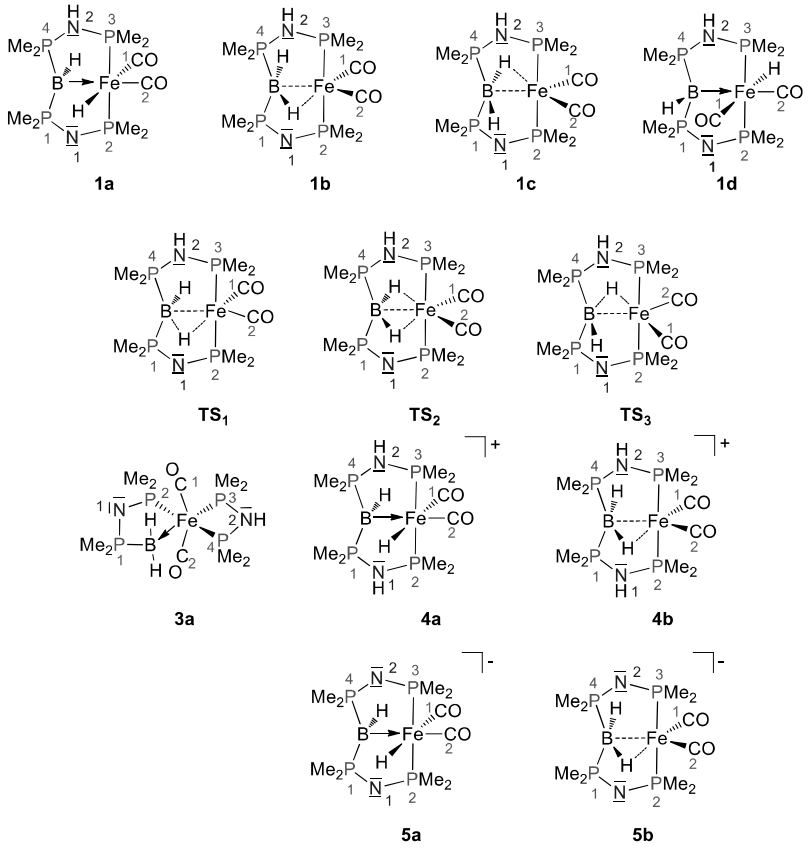

Table 5 Comparison of experimental and calculated geometries for **1** with different solvent molecules and calculated geometries for intermediates. Bond lengths are given in Å and angles in °.

Bond/ Angle	X-ray **1**·H_2O·$^1/_2C_7H_8$	X-ray **1**· 2 C_7H_8	X-ray **1**· C_4H_8O	X-ray **3**	X-Ray **4**·2CH_2Cl_2	DFT **Ph-PBP**	DFT **1a**	DFT **TS_1**	DFT **1b**	DFT **TS_2**	DFT **1c**	DFT **TS_3**	DFT **1d**	DFT **3a**	DFT **4a**	DFT **5a**
Fe-H	1.389	1.41(2)	1.473		1.48(2)	1.524	1.536	1.553	1.618	1.950	1.617	1.552	1.536		1.531	1.543
B-H	1.188	1.117(18)	1.163	0.99(5)- 1.06(4)	1.04(2)	1.209	1.213	1.212	1.202	1.241	1.203	1.211	1.213	1.209	1.209	1.216
Fe-B	2.200(2)	2.1967(17)	2.210(3)	2.254(7)	2.187(2)	2.257	2.289	2.291	2.425	2.370	2.426	2.292	2.289	2.349	2.266	2.299
Fe-C1	1.772(2)	1.7742(16)	1.764(3)	1.762(5)	1.783(2)	1.781	1.774	1.773	1.763	1.758	1.754	1.760	1.774	1.770	1.786	1.763
Fe-C2	1.769(2)	1.7705(16)	1.767(3)	1.795(5)	1.772(2)	1.768	1.762	1.760	1.754	1.758	1.764	1.772	1.762	1.770	1.774	1.753
Fe-P2	2.2143(7)	2.2288(10)	2.2228(9)	2.251(2)	2.1635(6)	2.232	2.240	2.263	2.268	2.279	2.265	2.263	2.240	2.257	2.175	2.214
Fe-P3	2.1823(7)	2.1641(10)	2.1546(9)	2.2248(18)	2.1736(6)	2.152	2.160	2.161	2.155	2.160	2.156	2.160	2.159	2.198	2.187	2.225
P1-B	1.941(2)	1.9153(18)	1.918(3)	1.921(8)	1.921(2)	1.927	1.930	1.945	1.939	1.914	1.940	1.946	1.930	1.952	1.901	1.923
P4-B	1.914(2)	1.9021(18)	1.908(3)		1.905(2)	1.904	1.888	1.912	1.906	1.878	1.907	1.913	1.888		1.900	1.914
P2-N1	1.6560(17)	1.6523(13)	1.649(2)	1.643(5)	1.689(2)	1.656	1.653	1.660	1.666	1.664	1.665	1.660	1.652	1.628	1.737	1.662
N1-P1	1.6198(17)	1.6062(14)	1.612(2)	1.591(5)	1.652(2)	1.615	1.616	1.603	1.599	1.599	1.599	1.603	1.616	1.629	1.684	1.622
P4-N2	1.6633(17)	1.6670(13)	1.669(2)	1.689(5)	1.649(2)	1.690	1.686	1.674	1.673	1.674	1.673	1.675	1.888	1.715	1.678	1.625
N2-P3	1.6924(17)	1.7095(14)	1.710(2)	1.668(6)	1.697(2)	1.737	1.738	1.769	1.782	1.783	1.782	1.768	1.685	1.725	1.732	1.665
N2-H	0.951	0.76(2)	0.833	0.84(4)	0.76(2)	1.015	1.014	1.016	1.017	1.017	1.016	1.016	1.014	1.017	1,014	
Fe-H(B)										1.951						
B-H(Fe)									1.316	1.242	1.318					
N1-H					0.78(3)										1.017	
P-Fe-P	164.74(2)	156.99(2)	152.92(3)		159.33(3)	153.11	155.70	171.39	170.86	171.17	170.77	171.24	155.35		158.29	152.75
C-Fe-C	102.02(9)	101.30(7)	97.06(12)	150.4(2)	99.85(9)	98.03	100.43	117.77	122.92	120.21	122.51	117.66	100.29	153,30	99.315	101.09

Table 6 Mulliken Atomic Charges.

Atom	**1**	**1a/1d**	**TS_1/TS_3**	**1b**	**TS_2**	**1c**	**3a**	**4a**	**5a**
Fe	-0.49	-0.40	-0.08	0.00	-0.02	0.00	-0.36	-0.45	-0.44
B	-0.29	-0.27	-0.21	-0.20	-0.18	-0.20	-0.26	-0.16	-0.39
H(Fe)	-0.18	-0.19	-0.24	-0.17	0.01	-0.18		-0.12	-0.23
H(B)	0.04	0.04	0.05	0.07	0.01	0.07	0.02	0.05	0.03
H(N2)	0.11	0.10	0.10	0.10	0.10	0.09	0.10	0.13	
H(N1)								0.12	
P1	0.73	0.50	0.49	0.49	0.46	0.49	0.51	0.38	0.53
P2	0.65	0.47	0.39	0.38	0.38	0.39	0.40	0.30	0.47
P3	0.59	0.29	0.25	0.24	0.26	0.39	0.33	0.30	0.44
P4	0.62	0.42	0.39	0.39	0.35	0.39	0.32	0.41	0.55
N1	-0.66	-0.57	-0.55	-0.55	-0.57	-0.55	-0.56	-0.30	-0.60
N2	-0.36	-0.33	-0.31	-0.30	-0.32	-0.30	-0.34	-0.31	-0.63
C1	0.36	0.43	0.11	-0.01	0.01	0.07	0.18	0.44	0.47
C2	0.16	0.10	0.11	0.07	0.02	-0.01	0.18	0.10	0.12
O1	-0.13	-0.14	-0.15	-0.16	-0.18	-0.17	-0.15	-0.09	-0.20
O2	-0.13	-0.14	-0.16	-0.17	-0.18	-0.16	-0.15	-0.08	-0.20

Table 7 Charges from Natural Population Analysis for the complexes and the free ligand (Me-PBP).

Atom	**1**	**1a/1d**	**TS_1/TS_3**	**1b**	**TS_2**	**1c**	**3a**	**4a**	**5a**	**Me-PBP**
Fe	-2.51	-2.51	-2.31	-2.08	-2.01	-2.09	-2,40	-2.52	-2.50	
B	-0.56	-0.65	-0.76	-0.83	-0.99	-0.83	-0,40	-0.66	-0.64	-1.18
H(Fe)	0.22	0.19	0.22	0.17	0.19	0.16		0.21	0.17	
H(B)	0.03	0.04	0.08	0.11	0.19	0.11	-0,07	0.07	0.02	0.04
H(N2)	0.41	0.40	0.40	0.40	0.40	0.40	0,39	0.41		0.36
H(N1)								0.41		
P1	1.56	1.57	1.60	1.62	1.62	1.62	1,53	1.55	1.55	1.51
P2	1.71	1.69	1.67	1.63	1.61	1.63	1,68	1.66	1.68	0.92
P3	1.69	1.66	1.62	1.59	1.58	1.59	1,56	1.67	1.68	1.00
P4	1.58	1.57	1.58	1.59	1.59	1.59	1,66	1.57	1.58	1.47
N1	-1.39	-1.37	-1.37	-1.37	-1.36	-1.37	-1,38	-1.25	-1.39	-1.40
N2	-1.25	-1.26	-1.25	-1.25	-1.24	-1.25	-1,25	-1.25	-1.40	-1.27
C1	0.89	0.88	0.81	0.77	0.75	0.76	0,86	0.89	0.87	
C2	0.89	0.88	0.80	0.76	0.75	0.77	0,86	0.89	0.87	
O1	-0.50	-0.52	-0.53	-0.54	-0.54	-0.54	-0,54	-0.48	-0.57	
O2	-0.51	-0.52	-0.54	-0.54	-0.54	-0.54	-0,54	-0.47	-0.56	

Table 8 Mayer-Mulliken bond orders for selected bonds.

Atom	**1**	**1a/1d**	**TS_1/TS_3**	**1b**	**TS_2**	**1c**	**3a**	**4a**	**5a**
Fe-H	0.59	0.57	0.34	0.20	0.09	0.20		0.58	0.60
Fe-B	0.79	0.70	0.31	0.17	0.12	0.17	0.56	0.74	0.71
B-H	0.92	0.94	0.91	0.94	0.83	0.94	0.97	0.95	0.94
B-P1	0.94	0.87	0.87	0.85	0.87	0.85	0.88	0.88	0.88
B-P4	0.84	0.90	0.84	0.82	0.87	0.82		0.90	0.02
Fe-H(B)	0.03	0.03	0.03	0.01	0.09	0.01		0.04	0.03

Table 9 Wiberg bond orders for selected bonds.

Bond	**1**	**1a/1d**	**TS_1/TS_3**	**1b**	**TS_2**	**1c**	**3a**	**4a**	**5a**
Fe-H	0.62	0.66	0.34	0.26	0.13	0.26		0.67	0.66
Fe-B	0.58	0.59	0.31	0.29	0.26	0.29	0.48	0.60	0.59
B-H	0.92	0.94	0.91	0.92	0.76	0.92	0.96	0.93	0.94
B-P1	0.93	0.94	0.87	0.92	0.94	0.92	0.94	1.00	0.95
B-P4	0.97	1.01	0.84	0.98	1.00	0.98		1.00	0.96
Fe-H(B)	0.01	0.01	0.03	0.02	0.13	0.02		0.01	0.01

Molecular Orbitals (Molecular Orbitals are shown with isocontour levels at 0.05)

Complex **1a/1d**

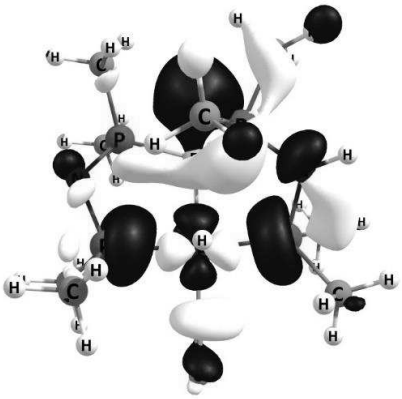

LUMO

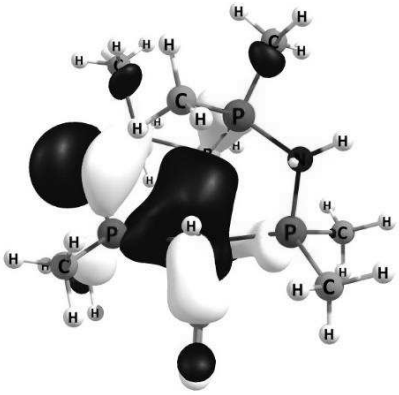

HOMO

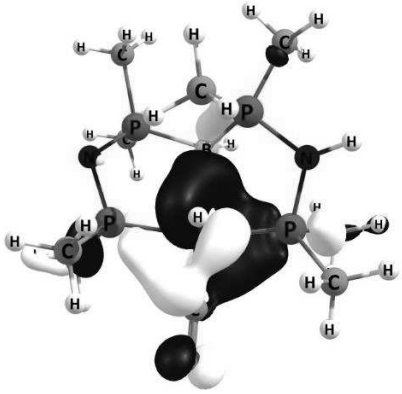

HOMO-1

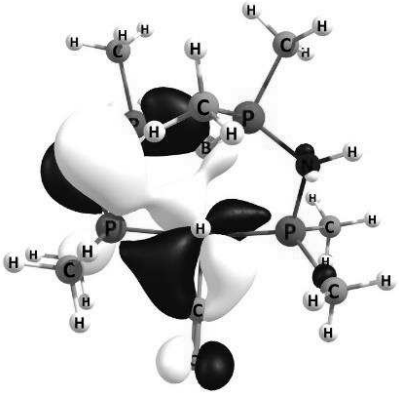

HOMO-2

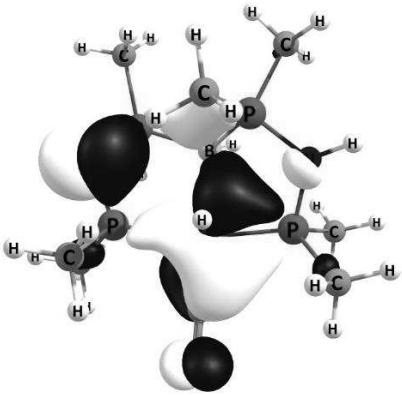

HOMO-3

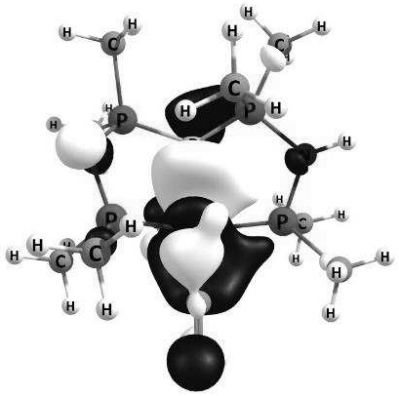

HOMO-4

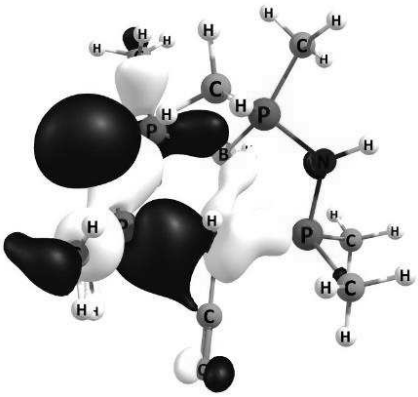

HOMO-5

TS_1/TS_3

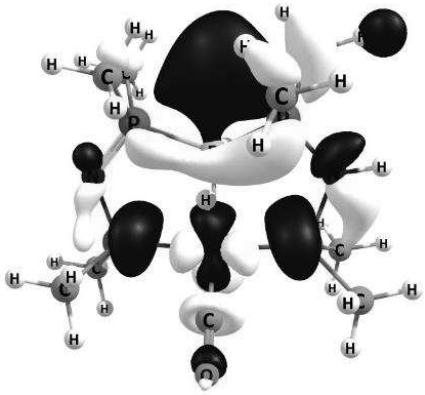

LUMO

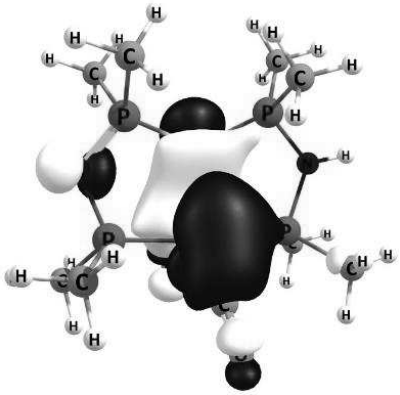

HOMO

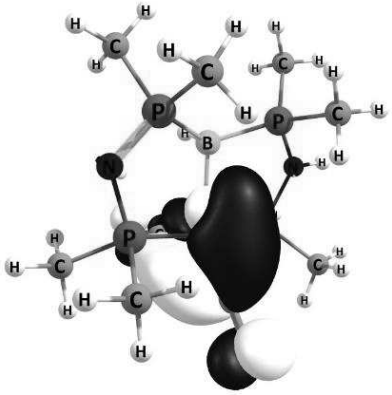

HOMO-1

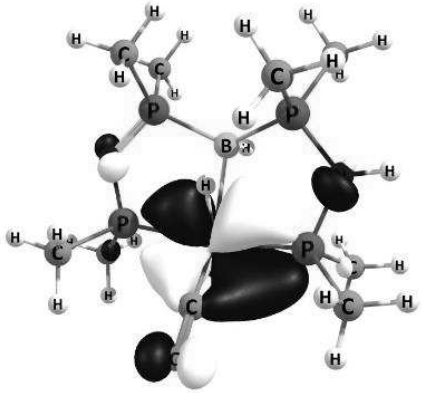

HOMO-2

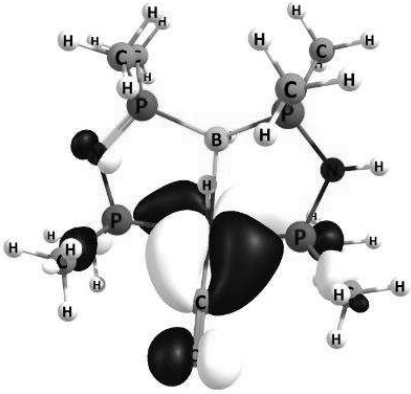

HOMO-3

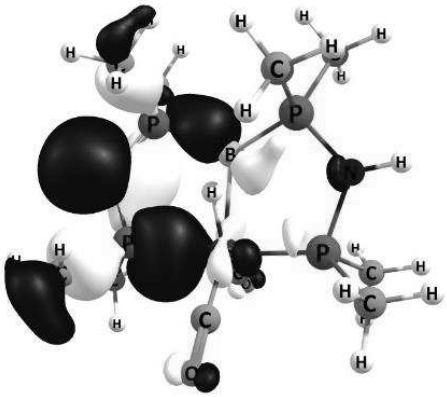

HOMO-4

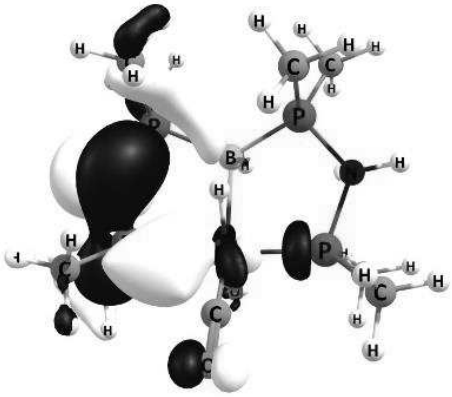

HOMO-5

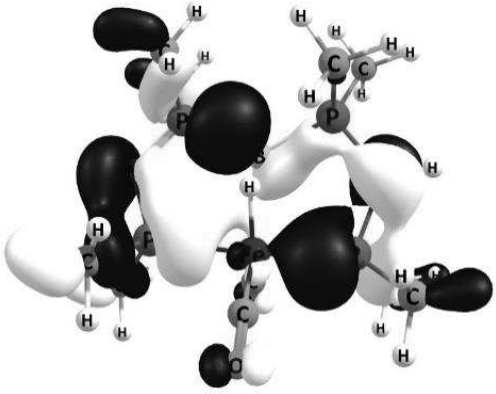

HOMO-6

Complex **1b**

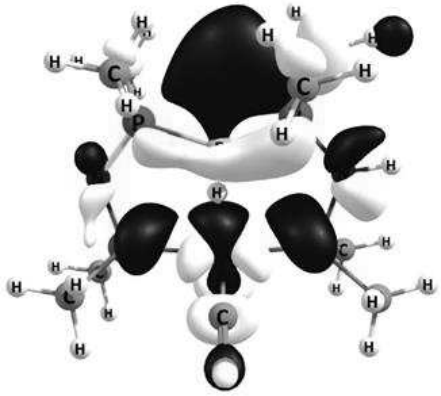

LUMO

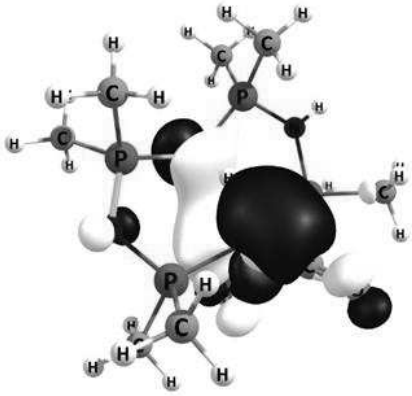

HOMO

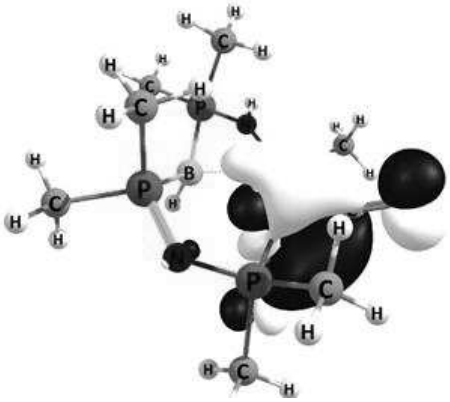

HOMO-1

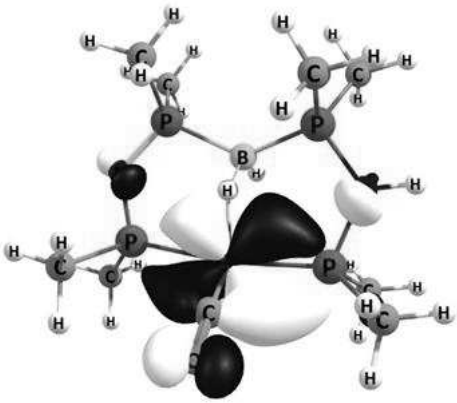

HOMO-2

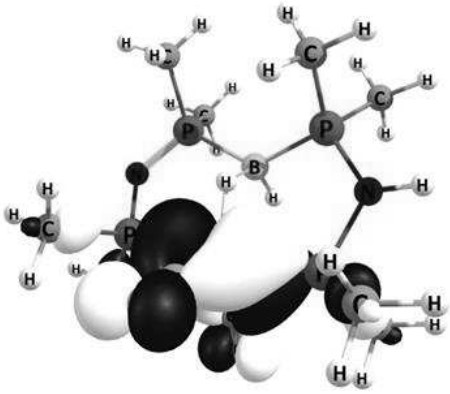

HOMO-3

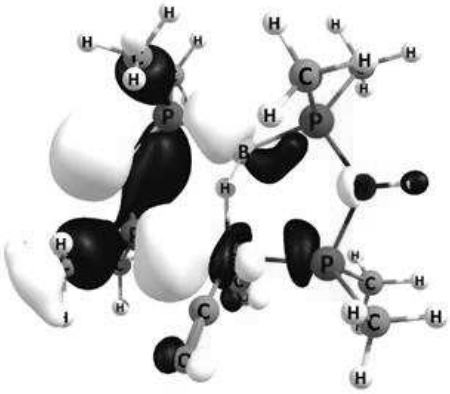

HOMO-4

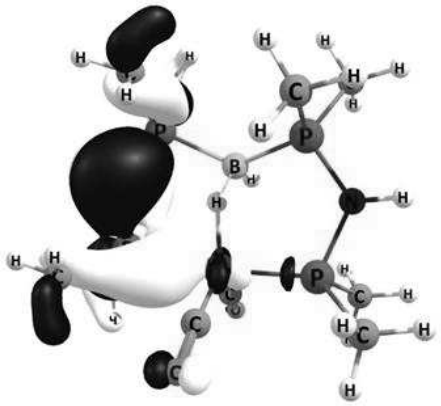

HOMO-5

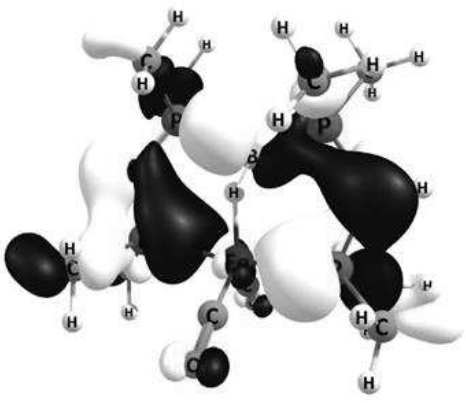

HOMO-6

TS_2

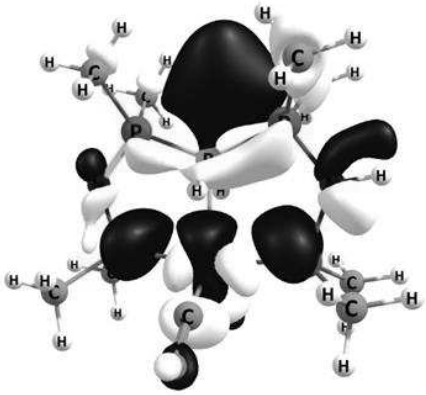

LUMO

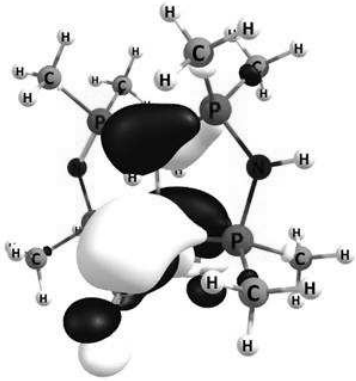

HOMO

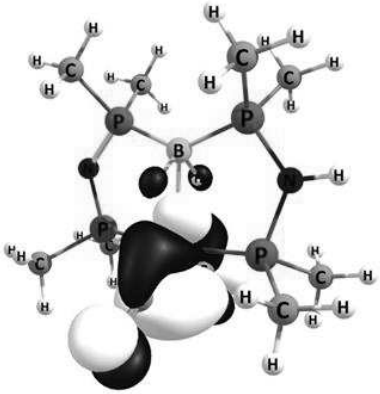

HOMO-1

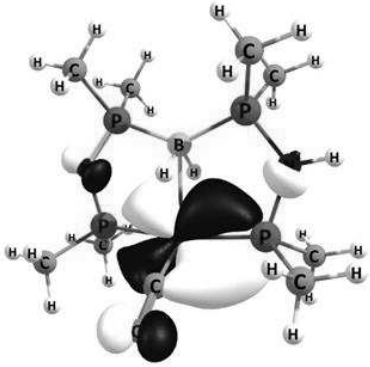

HOMO-2

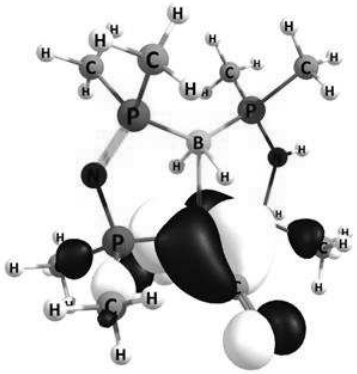

HOMO-3

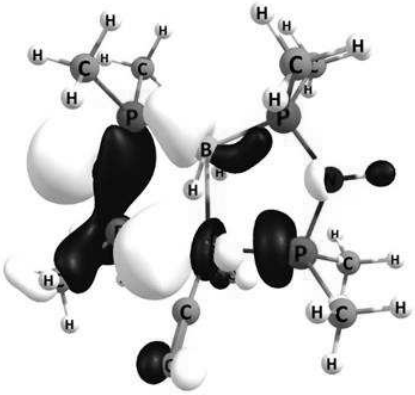

HOMO-4

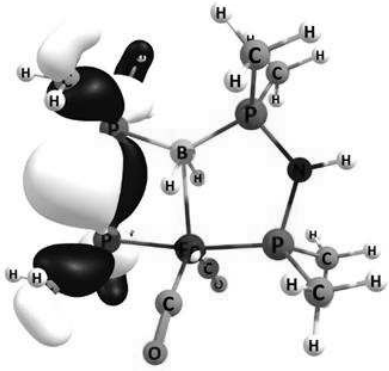

HOMO-5

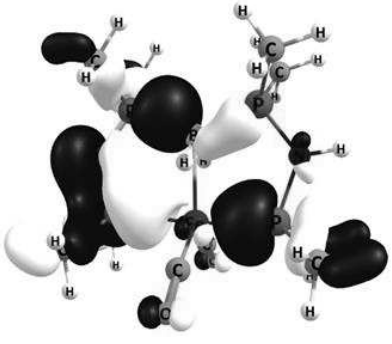

HOMO-6

Complex **1c**

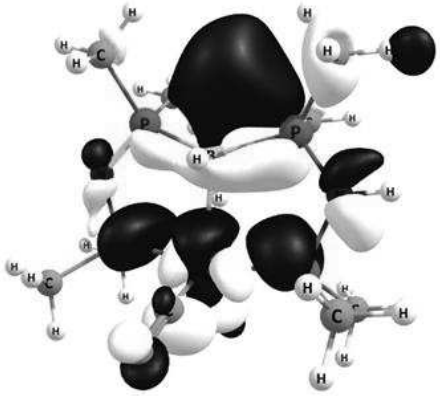

LUMO

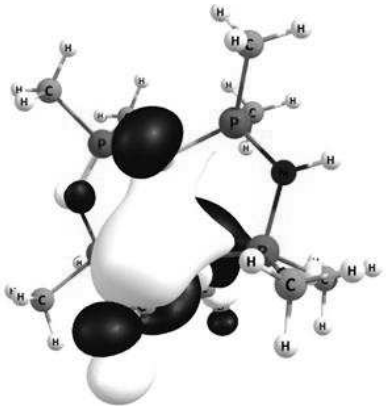

HOMO

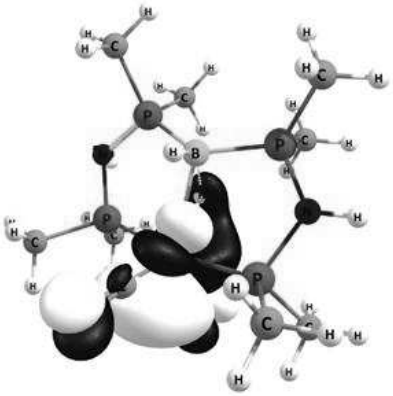

HOMO-1

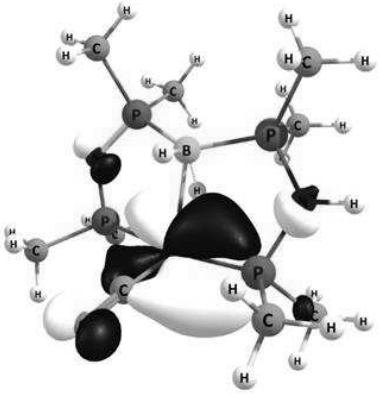

HOMO-2

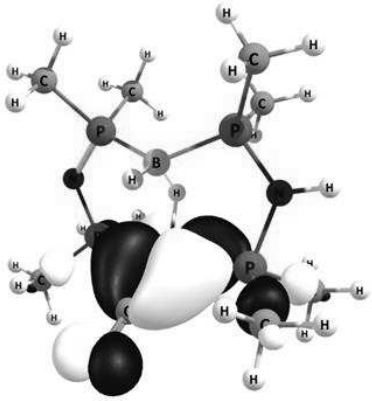

HOMO-3

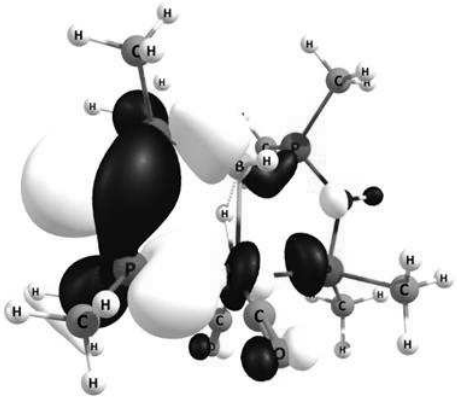

HOMO-4

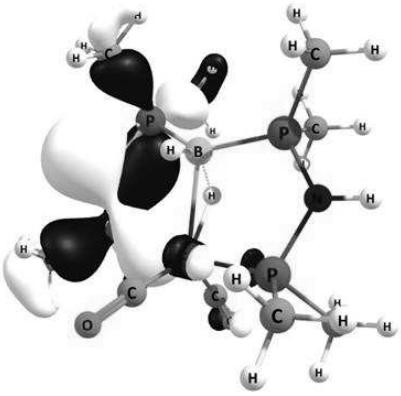

HOMO-5

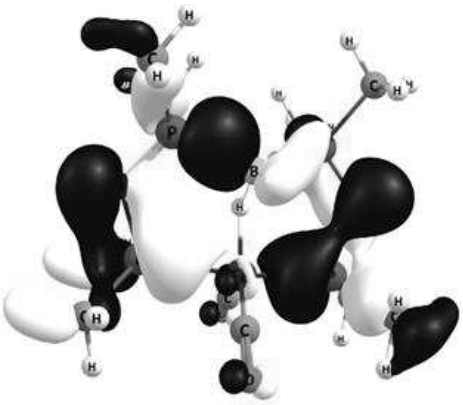

HOMO-6

Complex **1e**

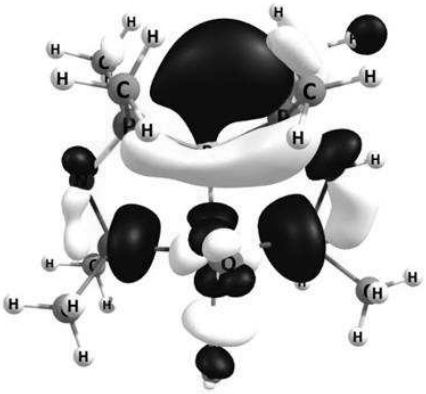

LUMO

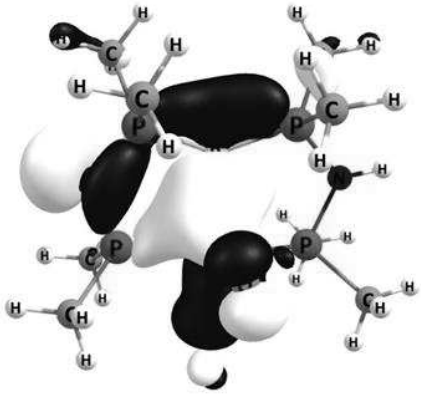

HOMO

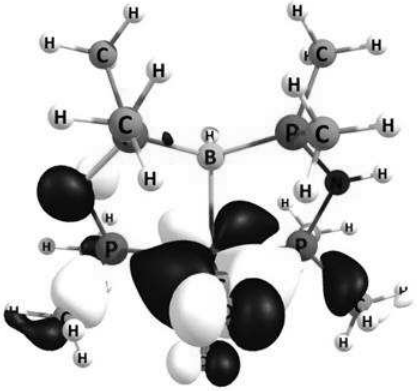

HOMO-1

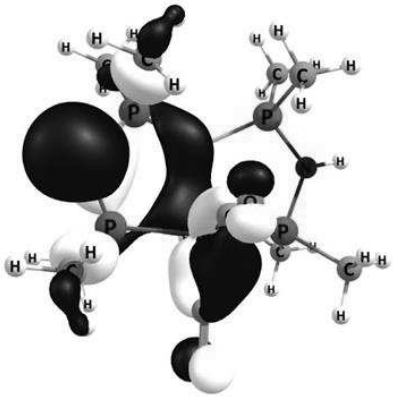

HOMO-2

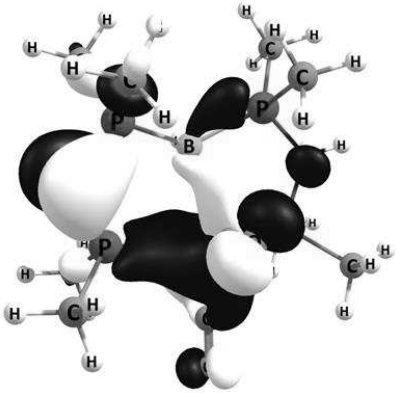

HOMO-3

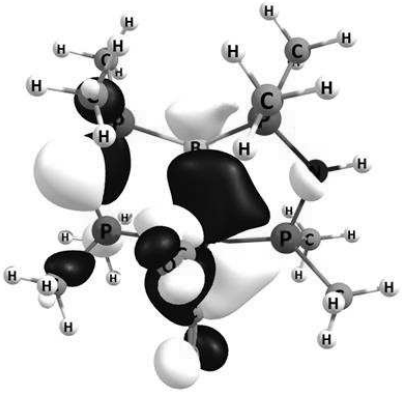

HOMO-4

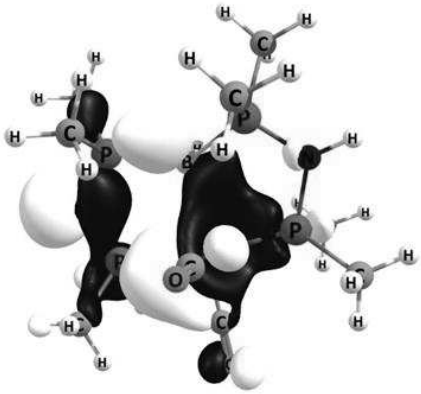

HOMO-5

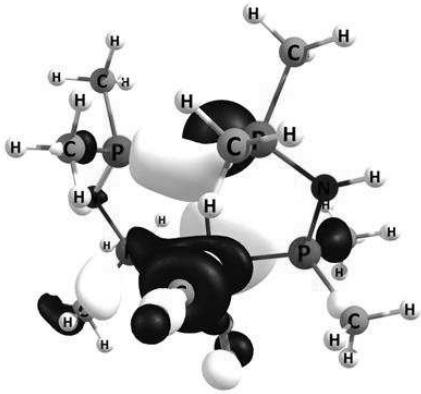

HOMO-6

Complex **3a**

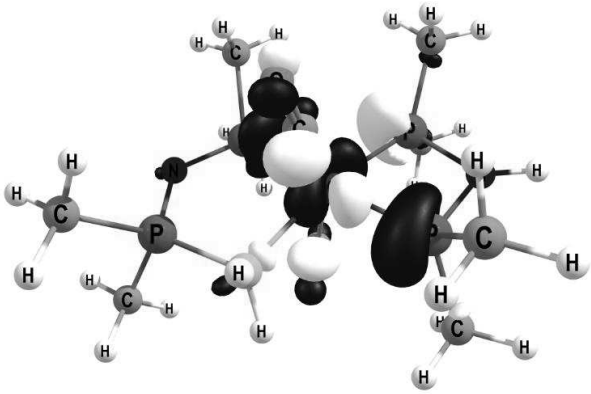

LUMO

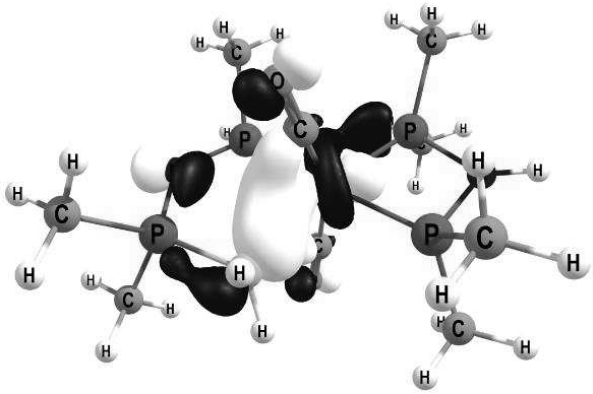

HOMO

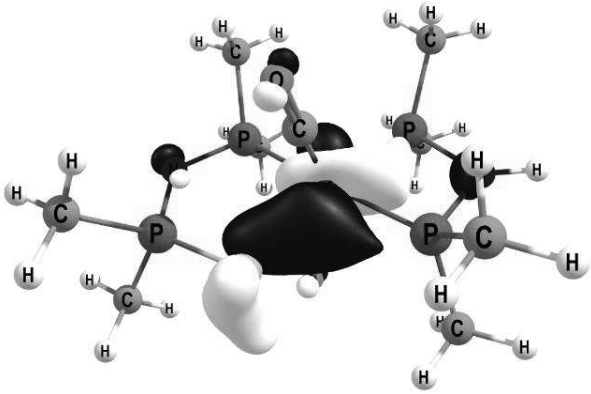

HOMO-1

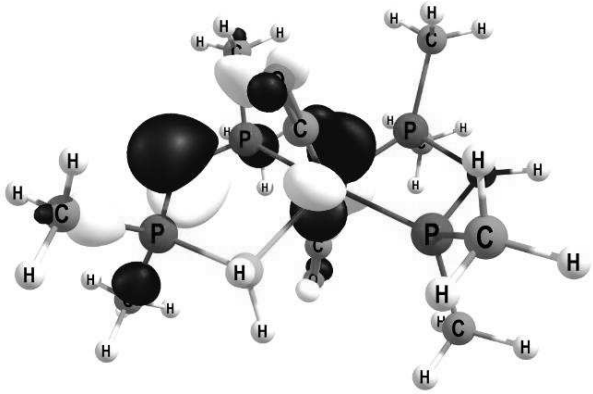

HOMO-2

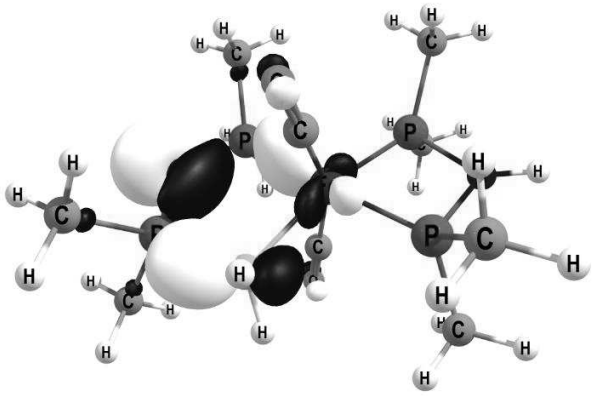

HOMO-3

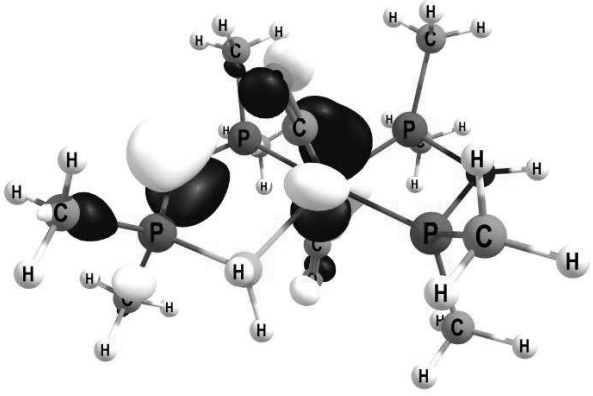

HOMO-4

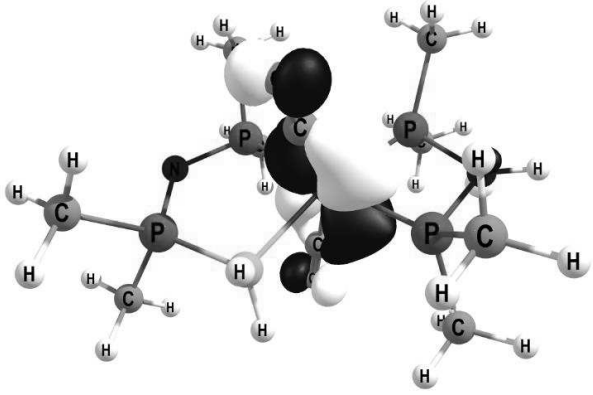

HOMO-5

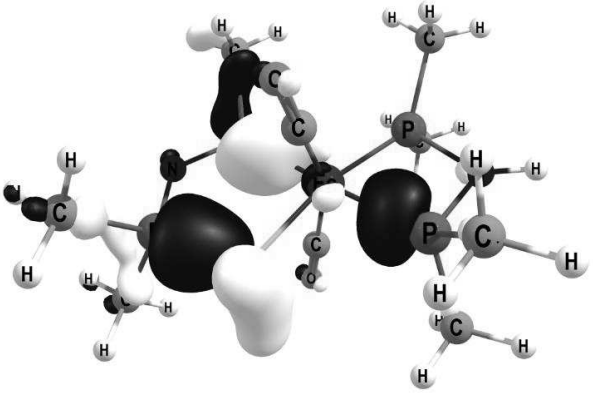

HOMO-6

Complex **4a**

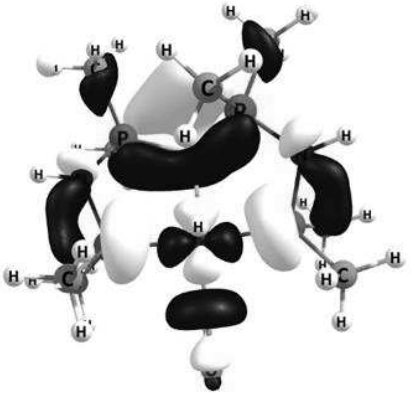

LUMO

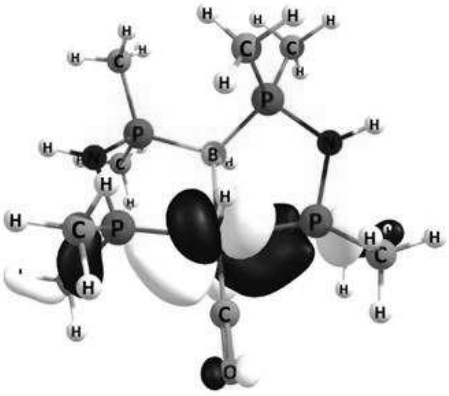

HOMO

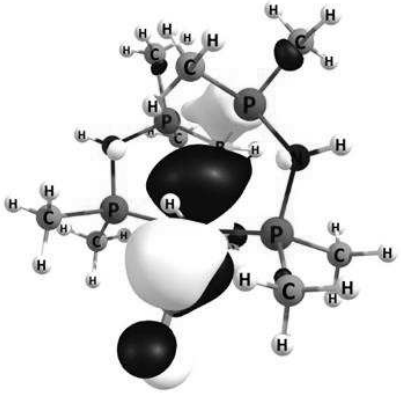

HOMO-1

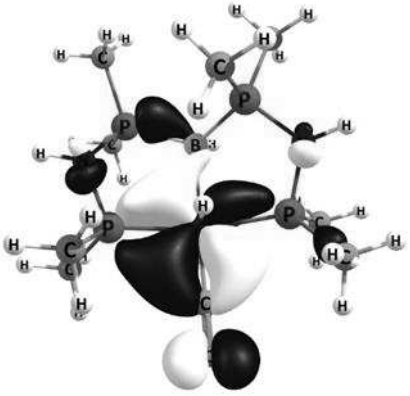

HOMO-2

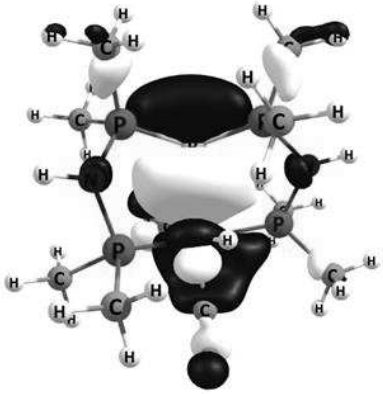

HOMO-3

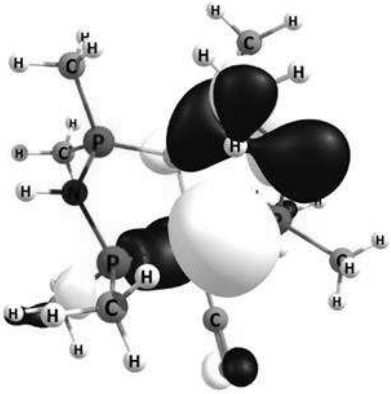

HOMO-4

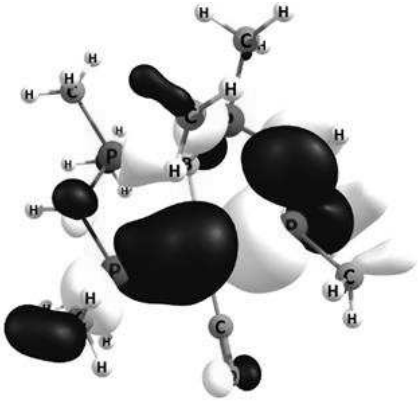

HOMO-5

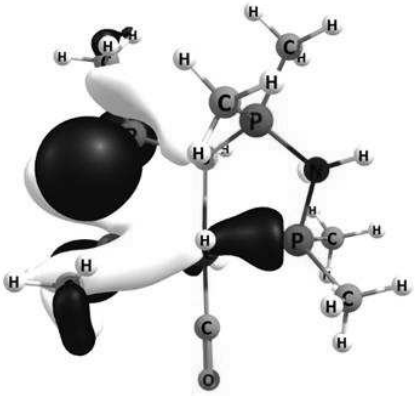

HOMO-6

Complex **5a**

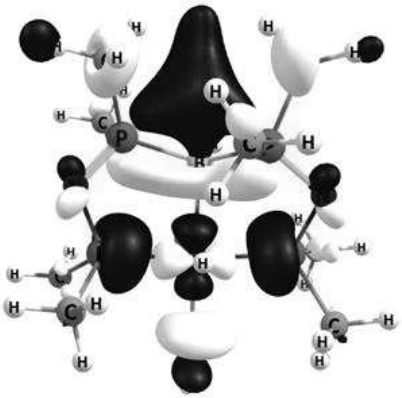

LUMO

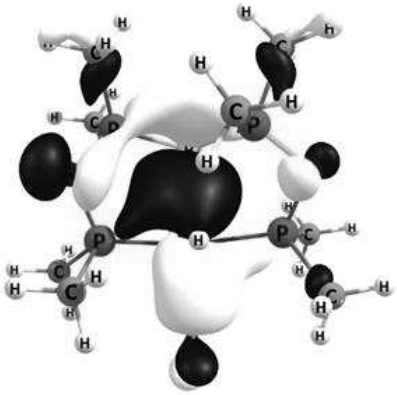

HOMO

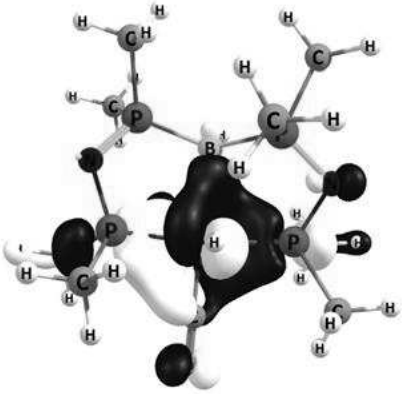

HOMO-1

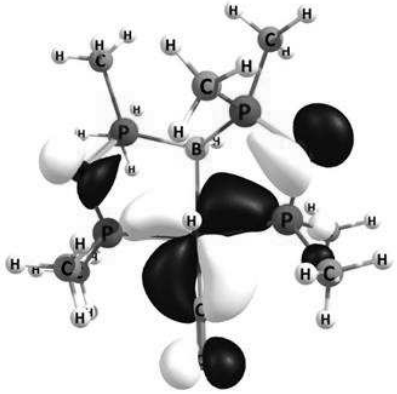

HOMO-2

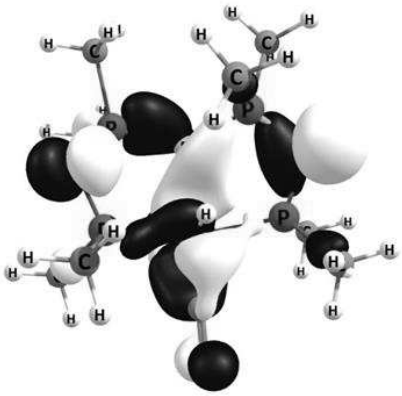

HOMO-3

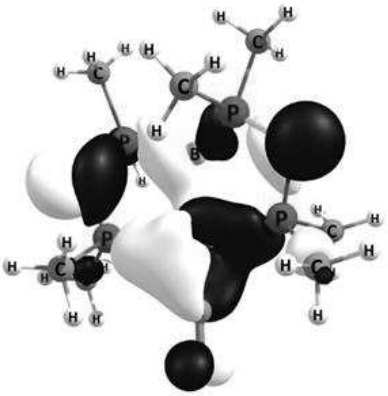

HOMO-4

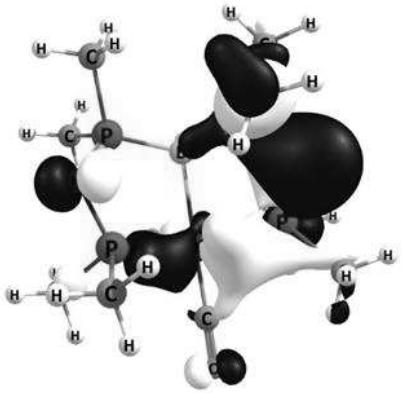

HOMO-5

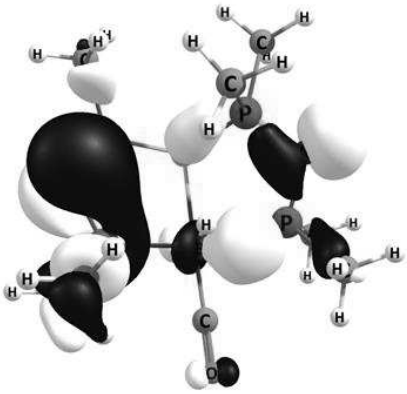

HOMO-6

Alternative Exchange Pathways

An alternative pathway for the Fe-H/B-H-exchange in **1, 4** and **5** has been considered that is shown in scheme 1. Thereby, the B-*H*/Fe-*H*-exchange proceeds *via* a H_2-complex **1e** that allows for rotation of the σ-coordinated H_2-ligand. This possibility was investigated experimentally and by computational methods. The optimized geometry of complex **1e** is shown in figure 25. It was not possible to find a minimum structure for the suggested intermediate as depicted in scheme 1. The relative free Gibbs energy of **1e** lies with 100.8 kJ/mol 45 kJ/mol above the calculated barrier for the reductive elimination exchange mechanism. Based on these findings a mechanism involving H_2-σ-complexes seems unlikely in the present case.

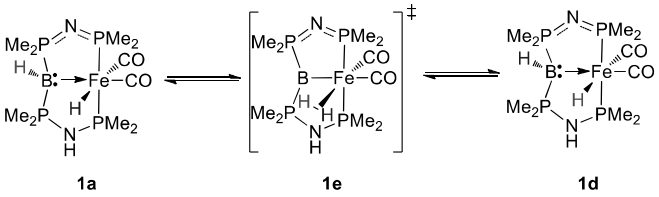

Scheme 1 An alternative exchange pathway for the Fe-H/B-H-exchange.

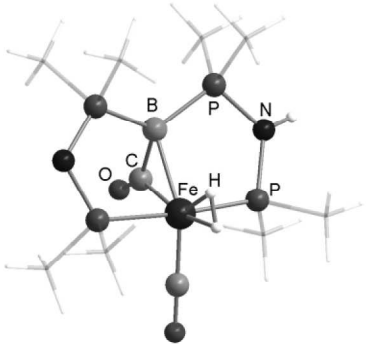

Figure 25 Optimized geometry of the H_2-complex **1e**.

This conclusion is supported by the rate of H/D-exchange of complex **1** or **5** in the presence of one atmosphere of D_2-gas. The reaction shows only in the case of complex **1** measurable progress, whereas the observed rate constant, obtained from a pseudo-first order plot (Fig. 26), is with $6.41 \cdot 10^{-7}$ s^{-1} several orders of magnitudes smaller than the detected Fe-H/B-H-exchange rate.

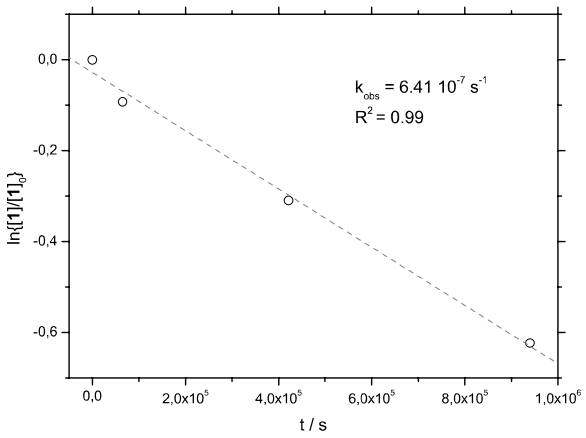

Figure 26 Pseudo-first-order plot for the HD-exchange in complex **1**.

H	-2.698001	-1.685235	-2.961668
C	-3.073388	-1.684692	0.001885
H	-3.992316	-1.791123	-0.589109
H	-2.654556	-2.677282	0.205683
H	-3.296227	-1.199098	0.956875

6. Possible Resonance Structures of the PBP-Ligands in Complex 4 and 5

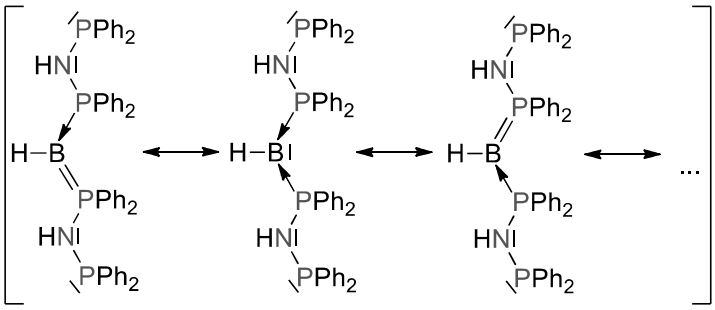

Scheme 2 Possible resonance structures of the ligand in complex **4**.

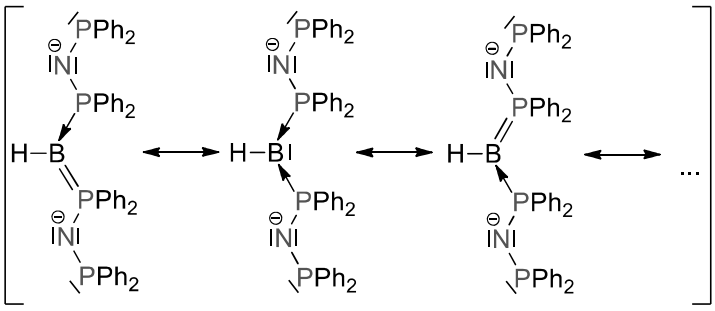

Scheme 3 Possible resonance structures of the ligand in complex **5**.

Literature

[1] H. Nöth, L. Z. Meinel, *Z. Anorg. Allg. Chem.* **1967**, *349*, 225-240.

[2] N. Frank, K. Hanau, K. Flosdorf, R. Langer, *Dalton Trans.* **2013**, *42*, 11252-11261.

[3] C. L. Perrin, T. J. Dwyer, *Chem. Rev.* **1990**, *90*, 935-967.

[4] G. M. Sheldrick, *Acta Crystallogr., Sect. A* **2008**, *64*, 112-122.

[5] a) X.-R. 1.01, *Data Reduction Program, Stoe & Cie GmbH, Darmstadt, Germany, 2001*; b) X.-S. 1.06, *Crystal Optimization for Numerical Absorption Correction Program, Stoe & Cie GmbH, Darmstadt, 1999*.

[6] M. J. Frisch, G. W. Trucks, H. B. Schlegel, G. E. Scuseria, M. A. Robb, J. R. Cheeseman, G. Scalmani, V. Barone, B. Mennucci, G. A. Petersson, H. Nakatsuji, M. Caricato, X. Li, H. P. Hratchian, A. F. Izmaylov, J. Bloino, G. Zheng, J. L. Sonnenberg, M. Hada, M. Ehara, K. Toyota, R. Fukuda, J. Hasegawa, M. Ishida, T. Nakajima, Y. Honda, O. Kitao, H. Nakai, T. Vreven, J. A. Montgomery, J. E. P. Jr., F. Ogliaro, M. Bearpark, J. J. Heyd, E. Brothers, K. N. Kudin, V. N. Staroverov, R. Kobayashi, J. Normand, K. Raghavachari, A. Rendell, J. C. Burant, S. S. Iyengar, J. Tomasi, M. Cossi, N. Rega, J. M. Millam, M. Klene, J. E. Knox, J. B. Cross, V. Bakken, C. Adamo, J. Jaramillo, R. Gomperts, R. E. Stratmann, O. Yazyev, A. J.

Austin, R. Cammi, C. Pomelli, J. W. Ochterski, R. L. Martin, K. Morokuma, V. G. Zakrzewski, G. A. Voth, P. Salvador, J. J. Dannenberg, S. Dapprich, A. D. Daniels, Farkas, J. B. Foresman, J. V. Ortiz, J. Cioslowski, D. J. Fox, *Gaussian 09 Revision C.01, Gaussian Inc. Wallingford CT 2009*.

[7] S. Grimme, *J Comput Chem* **2006**, *27*, 1787-1799.

[8] a) A. Schäfer, H. Horn, R. Ahlrichs, *The Journal of Chemical Physics* **1992**, *97*, 2571; b) F. Weigend, R. Ahlrichs, *Phys Chem Chem Phys* **2005**, *7*, 3297-3305.

ChemPubSoc Europe

DOI: 10.1002/chem.201704018

CHEMISTRY
A European Journal
Full Paper

Bond Activation

Ambireactive $(R_3P)_2BH_2$ Groups Facilitating Temperature-Switchable Bond Activation by an Iron Complex

Lisa Vondung, Lars E. Sattler, and Robert Langer*[a]

Dedicated to Professor David Milstein on the occasion of his 70th birthday

Abstract: An iron pincer complex containing a hemi-labile $(R_3P)_2BH_2$ group exhibits temperature-switchable reactivity patterns: a reversible B–H activation concomitant with a P–B bond cleavage is observed at room temperature. Below 4 °C, intra- and intermolecular C–H activation pathways are becoming faster and more dominant. Mechanistic investigations reveal that the lability of the $(R_3P)_2BH_2$ group in combination with the exothermic formation of σ-bonded complexes are responsible for the switchable bond activation. Finally, a protocol for an iron-catalyzed H/D-exchange of organic solvents in the absence of oxidants has been developed.

Introduction

Reversible reactions between a coordinated ligand and the central metal atom can in principle assist in important reaction steps within a catalytic cycle and facilitate bond activation reactions.[1] In recent years, the concept of metal–ligand cooperativity has successfully been applied to homogenous catalysis, leading to the development of highly active catalysts for atom economical reactions.[2] Most commonly, such cooperative ligand sites act as an internal base/proton source, which, for example, allows for a concerted proton–hydride transfer between the metal complex and the substrate or the reactant.

Boron-based ligands capable of assisting in cooperative bond activation have recently attracted increasing attention, due to their unusual donor/acceptor properties and reactivity patterns.[3] BR_3 groups embedded in multidentate ligands can act as Lewis acidic (Z-type)[4] ligands that are able to stabilize electron-rich metal complexes in low oxidation states and mediate cooperative bond activation reactions.[5] Boryl ligands, in contrast, are very strong σ-donor ligands (X-type),[6] but the remaining Lewis acidity of the trivalent boron atom in R_2B-[M] can be used for unconventional bond activation reactions.[7] Another ligand type is the ligand stabilized borylenes,[8] which are formally boron(I) compounds. They were demonstrated to serve as electron-donating ligands (L-type).[8c,d,9] However, cooperative modes with these different classes of boron-containing groups usually involve the formation of hydrido-borates (Figure 1a). In addition to the metal oxidation state and the nature of the ancillary ligands, the substituents at the boron atom seem to be essential for the observed reactivity patterns. For N- and C-based substituents at boron,[10] hydride-transfer and dihydrogen elimination are observed between the metal and the ligand,[5a,c,7a,b] whereas for phosphine substituents, a pronounced redox reactivity between the metal and boron atom takes place.[11]

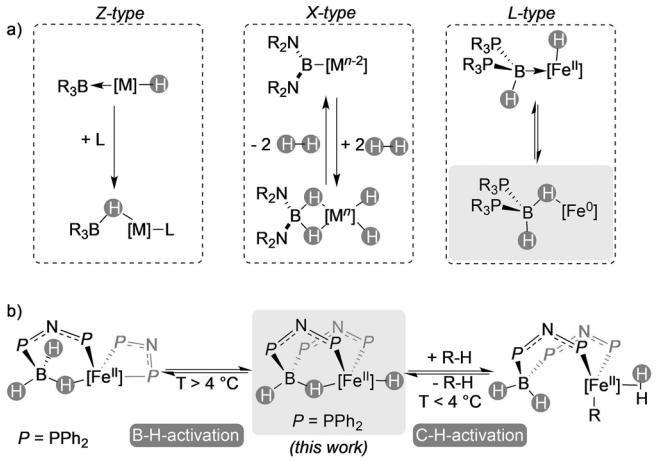

Figure 1. a) Different reactivity patterns of complexes with borane, boryl, and phosphine-stabilized borylene ligands; b) temperature-dependent reactivity of $(R_3P)_2BH_2$ complex.

In the present manuscript, we introduce a new class of tridentate ligands with a central $(R_3P)_2BH_2$ group. In addition to the previously shown redox reactivity of the central bis(phosphine)borate group, we demonstrate that two kinds of intramolecular bond activation reactions are feasible, including reversible B–H and C–H activations. The detailed analysis of these reactivity patterns reveals an unprecedented kinetic scenario for a transition metal complex that allows for the switch of the dominating activation reaction according to tempera-

[a] L. Vondung, L. E. Sattler, Dr. R. Langer
Department of Chemistry
Philipps-Universität Marburg
Hans-Meerwein-Str. 4, 35032 Marburg (Germany)
E-mail: robert.langer@chemie.uni-marburg.de

Supporting information and the ORCID number(s) for the author(s) of this article can be found under https://doi.org/10.1002/chem.201704018.

ture (Figure 1 b). Our study shows that the central $(R_3P)_2BH_2$ group can reversibly react under P–B, B–H, or M–H bond cleavage. Considering that three reversible reactivity patterns are realized within one donor group, we call this donor group ambireactive. Finally, we used this ambireactive nature of the $(R_3P)_2BH_2$ group for catalytic C–H bond activation.

Results and Discussion

In a recent study, we reported the formation of PBP-type pincer complexes through dehydrogenative P–B bond formation of phosphine-borane complexes.[11] In continuation of this work, we investigated the reactivity of other metal precursors in these P–B bond-forming reactions. For this reason, $[Fe(N\{SiMe_3\}_2)_2(thf)]$ was reacted with a 2:1 mixture of bis(diphenylphosphino)amine (dppa) and the borane mono-adduct **1** (Scheme 1), leading to an immediate color change and formation of a deep red solution. The $^{31}P\{^1H\}$ NMR spectrum of the reaction mixture shows three broad resonances at 36.3 ($\nu_{1/2}$ = 303.3 Hz), 84.6 ($\nu_{1/2}$ = 178.4 Hz), and 113.5 ppm ($\nu_{1/2}$ = 285.4 Hz), whereas the $^{11}B\{^1H\}$ NMR spectrum gives rise to a broad resonance at −17.7 ppm. A similar observation can be made in the ^1H NMR spectrum, showing significant broadening of the resonances assignable to the newly formed iron hydride complex **2**. Two broad resonances at −11.68 and 5.02 ppm, each with an integral of one, become sharper upon ^{11}B-decoupling of the ^1H NMR spectrum. These findings suggest the presence of a bridging and a terminal boron-bound hydrogen atom. The identity of complex **2** was finally confirmed by single crystal X-ray diffraction (Figure 2). The central iron atom in **2** is octahedrally surrounded by four phosphine donor groups ($d_{Fe\text{-}P}$ = 2.207–2.291 Å), a hydrido ligand, and a η^1-coordinated $(R_3P)_2BH_2$ group ($d_{Fe\text{-}H}$ = 1.73 Å), which appears to be weakly bound. The corresponding Fe–B distance (2.67 Å) is comparable to the distances in η^1-coordinated tetrahydridoborate iron(II) complexes (2.67–2.86 Å).[12] Along with the formation of a second P–B bond, a unique tridentate ligand is formed in this reaction that coordinates in a *fac*-fashion to the central iron atom. In general, the coordination chemistry of $(R_3P)_2BH_2$ groups is limited to a few examples.[13]

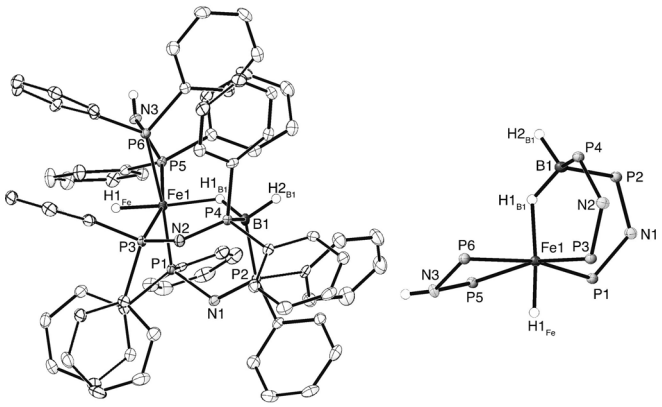

Figure 2. Molecular structure of complex **2** in the solid state (ellipsoids are drawn at 50% probability, carbon-bound hydrogen atoms are omitted). Selected bond length (Å) and angles (°): Fe1–P5 2.207(1), Fe1–P1 2.226(1), Fe1–P3 2.280(1), Fe1–P6 2.291(1), Fe1–$H1_{Fe}$ 1.43(3), Fe1–$H1_{B1}$ 1.73(3), P4–B1 1.929(3), P2–B1 1.976(3), B1–$H2_{B1}$ 1.11(3), B1–$H1_{B1}$ 1.20(3); P5-Fe1-P6 70.43(3), P1-Fe1-P3 94.05(3).

Considering that the formation of complex **2** from **1** involves the cleavage of one B–H and the formation of an additional P–B bond, we tried to gain further insight into the mechanism by utilization of the isotopically labelled phosphine-borane **1-*d*$_3$** (Scheme 1, right). Complex **2-*d*$_3$** is formed with high selectivity in this reaction. **2-*d*$_3$** contains an Fe–D and a BD_2 group, as judged by the absence of the corresponding resonances in the ^1H NMR spectrum. Because the boron- and iron-bound hydrogen atoms showed significant broadening in the ^1H NMR spectrum, we were unable to acquire resonances for the boron- and iron-bound deuterium atoms of **2-*d*$_3$** in the ^2H NMR spectrum. However, the ^2H NMR spectrum of **2-*d*$_3$** in toluene showed the presence of deuterated toluene and other aromatic deuterium atoms. Based on these observations, it seems likely that **1** and dppa are deprotonated in the first step (i), leading to an intermediate such as **3-*d*$_3$** (Scheme 1, right). The hemilability of dppa has previously been demonstrated and would allow for nucleophilic attack of the Ph_2P group to the η^1-coordinated phosphine-borane in **3-*d*$_3$** with the iron hydride as a leaving group step (ii).[14]

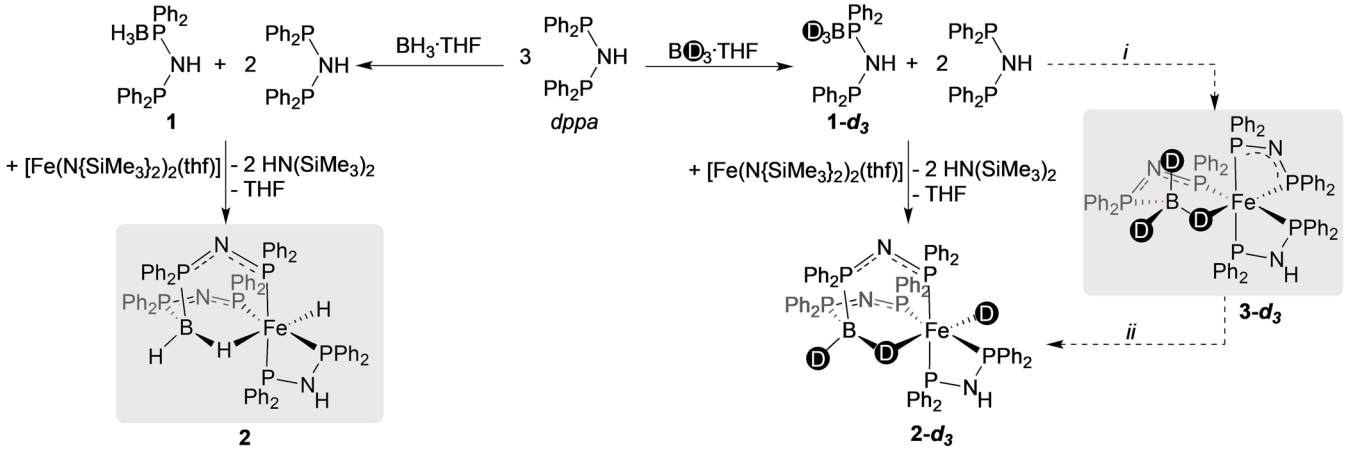

Scheme 1. Left: synthesis of complex **2**; right: possible reaction pathway for the formation of complex **2** based on isotopic labelling of the reactants.

As the line broadening in the NMR spectra indicates dynamic solution behavior of complex **2**, variable temperature ^{1}H NMR measurements were performed. Above 320 K, the resonances of the boron-bound hydrogen atoms and the hydrido ligand vanish. Below 300 K, the broad resonance at −20.78 ppm corresponding to the hydrido ligand starts to split into a virtual quintet ($^2J_{PH}$ = 49.4 Hz). In addition, a broad resonance at −9 ppm appeared at 280 K that remained broadened upon cooling. Further insights are provided by a line shape analysis of the ^{31}P-decoupled ^{1}H NMR resonance of the hydrido ligand at different temperatures, which allows us to estimate average exchange rates k_{ex} for dynamic species ($k_{ex} = {}^1/_2\pi\cdot\Delta\nu_{1/2}$, with $\Delta\nu_{1/2}$ being the difference in half height width of the hydride resonance and a reference peak).[15] An Eyring analysis reveals a linear dependence of $\ln(k_{ex}/T)$ on $1/T$ in a range of 320–280 K (Figure 3). The enthalpy of activation was found to be 59.4 kJ mol^{-1}, whereas the entropy of activation is with −7.5 J mol^{-1} K^{-1} close to zero (Table 1). Below 280 K, a second region of linearity with different activation parameters is detected. The seemingly negative activation enthalpy of −2.1 kJ mol^{-1} is usually explained by a pre-equilibrium with an intermediate, the formation of which is exothermic, followed by reaction steps with lower enthalpies of activation than the initial stabilization of this intermediate.[16] The very large negative entropy of activation (−228.9 J mol K^{-1}) for this process results in a Gibbs enthalpy of activation of 66.1 kJ mol^{-1}. The two linear regions allow for the determination of an inversion temperature of 277.5 K, at which the dominating exchange pathway seems to change (Scheme 2).

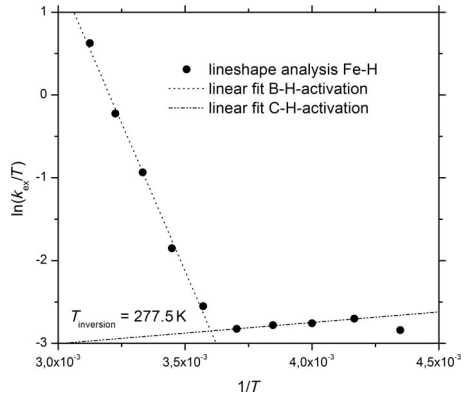

Figure 3. Eyring plot based on line shape analysis of the Fe–H resonance in ^{1}H NMR spectra.

Table 1. Activation parameters based on line shape analysis of **2** in C_7D_8.

Resonance	$\Delta H^{\neq}$ [kJ mol^{-1}]	$\Delta S^{\neq}$ [J mol^{-1} K^{-1}]	$\Delta G^{\neq}_{298}$ [kJ mol^{-1}]	R^2
Fe–H (T > 4 °C)	59.4 ± 2.1	−7.5 ± 7.1	61.6 ± 4.3	0.995
Fe–H (T < 4 °C)	−2.1 ± 0.2	−228.9 ± 0.9	66.1 ± 0.5	0.967

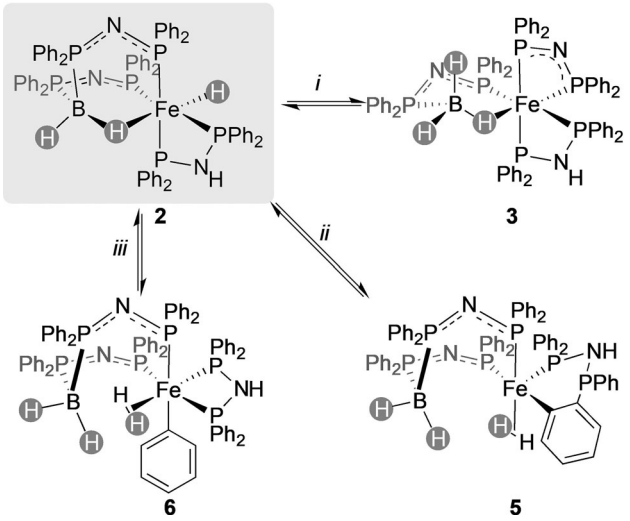

Scheme 2. Exchange pathways of complex **2** at different temperatures: B–H bond formation/activation i) at ambient temperature; intra- (ii) and intermolecular (iii) C–H bond activation dominating below 277.5 K.

To gain insight into the indicated dynamic solution behavior of complex **2**, we performed ^{1}H NOESY NMR experiments (Figure 4). Exchange correlations between the iron-bound hydride, the bridging boron-bound hydrogen atom, and the terminal boron-bound hydrogen atom were detected at 300 K (Figure 4, left). Because a dihydrogen-coordinated intermediate fails to explain the exchange between all three hydrogen atoms, we identified a η^1-coordinated phosphine-borane, such as **3**, as the most likely intermediate. This allows for rotation of the BH_3 group around the P–B bond.

Quantum chemical investigations using density functional theory (DFT) of the methyl substituted complexes reveal that **3-Me** is a minimum structure, which is 18.35 kJ mol^{-1} higher in Gibbs enthalpy relative to **2-Me**. The formation of **3** is assumed to proceed through dissociation of the $(R_3P)_2BH_2$ group, to give the intermediate **4a**. We calculated the relative energy of different penta-coordinated isomers of **4a-Me** using DFT (Figure 5). The isomer with the hydrido ligand pointing towards the $(R_3P)_2BH_2$ group *trans* to the vacant coordination site (**4b-Me**) was found to be 19.03 kJ mol^{-1} higher in ΔG. The isomers with a vacant coordination site *cis* to the hydrido ligand were calculated to be +14.13 kJ mol^{-1} (**4c-Me**) and +20.33 kJ mol^{-1} (**4d-Me**) higher in Gibbs enthalpy. These findings indicate that the different isomers are thermodynamically accessible.

The formation of the assumed phosphinoborane intermediate (**3**) can in principle proceed through nucleophilic attack of the iron hydride in **4b** to the tetra-coordinated boron atom in an S_N2-like reaction step or the $(R_3P)_2BH_2$ group coordinates *cis* to the hydride in **4c** or **4d** prior to the formation of **3** (Scheme 2, path i).

A ^{1}H NOESY NMR spectrum at 260 K with otherwise identical parameters shows new exchange correlations with *ortho*-phenyl protons of the PPh_2-groups and the residual solvent peaks of [D_8]toluene in the aromatic region of the spectrum. This clearly indicates the intra- (ii) and intermolecular (iii) activation of aromatic C–H bonds (Scheme 2). The large entropy of

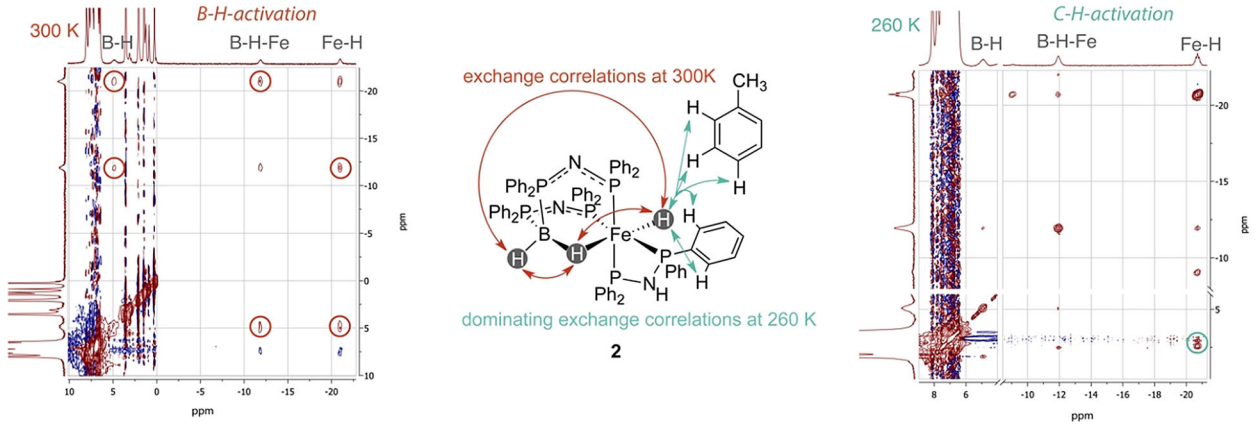

Figure 4. Left: ^{1}H NOESY NMR spectrum of complex **2** in [D$_8$]toluene at 300 K with exchange correlations between the two boron-bound and the iron-bound hydrogen atom; middle: schematic drawing of the observed exchange correlations; right: ^{1}H NOESY NMR spectrum of **2** in [D$_8$]toluene at 260 K with exchange correlations between the iron-bound hydrogen atom and *ortho*-phenyl and toluene hydrogen atoms.

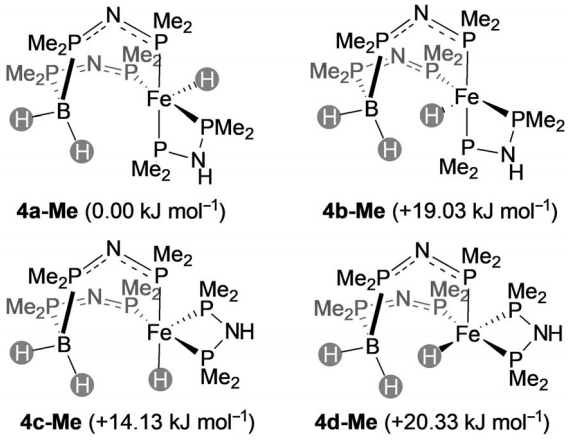

Figure 5. Different isomers as possible intermediates for exchange with the relative ΔG in parenthesis.

activation of $-228.9\ J\,mol^{-1}\,K^{-1}$ derived by line shape analysis as an average of intra- and intermolecular C–H activation pathways at low temperature suggests a bimolecular and therewith an intermolecular pathway to be dominating. Because the iron(II) complex **2** is in an octahedral environment of strong field ligands, it seems unlikely that these activations occur through an oxidative cleavage of the C–H-bond and we rather assume that dihydrogen coordinated intermediates such as **5** and **6** serve as intermediates. Furthermore, an exchange correlation to the low temperature species that gives rise to a broad resonance at approximately −9 ppm is detected, whereas the exchange correlation assignable to the B–H activation exhibits a significantly reduced intensity. The broad resonance at −9 ppm of the new iron species is assumed to be a dihydrogen coordinated complex that is formed upon C–H activation (such as **5** or **6**). The observation of two competing intramolecular reactions in a transition metal complex is already rare, but that both exchange processes are so dominating in different temperature regimes, that the two regions appear virtually linear is highly unusual. More common examples include stereoselective reactions that usually do not show such linearity in Eyring plots and require the analysis of the relative rates of both competing reaction pathways.[17]

To verify the observations from the ^{1}H NOESY NMR spectra, we analyzed a solution of **2-*d*$_3$** in toluene by ^{2}H NMR spectroscopy at 300 K. Although the resonances of the boron- and iron-bound deuterium atoms are too broad to be observed under these conditions, the ^{2}H NMR spectrum clearly shows deuterium incorporation into toluene (all positions) and into *ortho*-phenyl hydrogen atoms of the dppa ligand.[15] These observations are in agreement with the presence of intra- and intermolecular C–H-activations.

Next, we investigated the proposed lability of the $(R_3P)_2BH_2$ group by reactions of **2** with different ancillary ligands (Scheme 3). Using carbon monoxide or dihydrogen, the

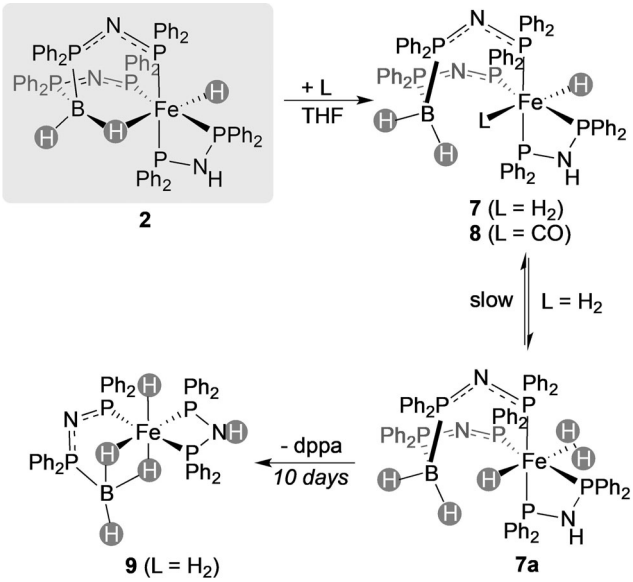

Scheme 3. Reactions of complex **2** with ancillary ligands.

$(R_3P)_2BH_2$ group is easily substituted in the coordination sphere of the central iron(II) atom and remained uncoordinated in the newly formed complexes. The resulting complexes contain a dihydrogen ligand (**7**) or a carbonyl ligand (**8**) in the *trans* position to the hydrido ligand. The hydrido ligand in complex **7** gives rise to a virtual quintet at −7.20 ppm ($^2J_{PH}$ = 48.8 Hz) in the ^{1}H NMR spectrum and a broad resonance for the H_2 ligand at −3.05 ppm. For the corresponding HD-complex, J_{HD} was detected to be 31.8 Hz, clearly indicating the presence of a σ-coordinated H_2-ligand in **7**. A second virtual quintet at −7.30 ppm ($^2J_{PH}$ = 49.0 Hz) slowly evolves in the ^{1}H NMR spectrum of **7**, reaching an approximate 1:1 ratio after three days. This second resonance corresponding to a hydrido ligand is attributed to the isomer **7a**, in which the hydrido ligand is on the same side as the $(R_3P)_2BH_2$ group. Over the course of ten days, complex **7** is slowly converted to the previously reported phosphine-borane complex **9** in solution.[18] The reaction of complex **7** with one atmosphere of D_2 gas in C_6D_6 leads to decreased integrals for the resonances of the hydrido and the dihydrogen ligand, as well as the appearance of a triplet resonance for the coordinated HD-ligand. This observation is in agreement with a facile substitution of the H_2-ligand by D_2 and the deuterium incorporation clearly shows that the hydrido and the dihydrogen ligand are exchanging. The reaction of complex **2** with D_2 gas in C_6H_6 was attempted as well, showing the formation of the isotopologue of **7** in the ^{31}P{^{1}H} NMR spectrum, but the corresponding ^{2}H NMR spectrum in C_6H_6 shows only one resonance for benzene-d_n (n = 1–6).

The facile substitution by weak ligands like dihydrogen underlines the labile nature of the $(R_3P)_2BH_2$ group. DFT calculations on the methyl-substituted complexes indicate that σ-coordination of a H_2-ligand in **7-Me** is exothermic (ΔH = −16.2 kJ mol^{-1}) relative to **2-Me** + H_2. Following this trend, the coordination of a carbonyl ligand leads to a significantly increased stabilization in **8-Me** with an enthalpy difference of −156.4 kJ mol^{-1} relative to **2-Me** + CO. Furthermore, the experimentally observed intramolecular exchange between the hydrido and the dihydrogen ligand in **7** should involve an isomer with a *cis*-arrangement of both ligands, which was calculated to be about 30 kJ mol^{-1} higher in Gibbs enthalpy.[15]

Overall, these findings give rise to the assumption that activation of C–H bonds is more facile at lower temperatures. In agreement with the exothermic coordination of H_2 to **2**, a dihydrogen coordinated intermediate of the C–H activation or even the coordination of a C–H bond concomitant to $(R_3P)_2BH_2$ dissociation might be favored by enthalpy as well. Such a stabilization of a σ-complex can result in an overall negative enthalpy of activation, if the barrier for the actual C–H-cleavage is lower than the stabilization of the σ-complex.

If the observed C–H-activation proceeds through a dihydrogen-bound intermediate, as anticipated from the low temperature ^{1}H NOESY NMR spectrum, an exchange with unbound H_2 in solution should be facile. To proof this hypothesis, we investigated the C–D activation of deuterated solvents in the presence of H_2 gas. A solution of complex **2** in C_6D_6 with an internal standard was analyzed by ^{1}H NMR spectroscopy before and after pressurizing the mixture with H_2 gas (entry 1, Table 2).

Table 2. D/H-exchange of common deuterated solvents with H_2 gas catalyzed by complex **2**.[a]

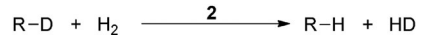

Entry[a]	Solvent-d_n	T [°C]	t [h]	TON
1	C_6D_6	25	18	23
2	[D_8]toluene	25	4	44
3	[D_8]toluene	−10	4	37
4	[D_8]THF	25	4	24
5	[D_6]DMSO	25	4	61

[a] Reaction conditions: 0.01 mmol of complex **2** dissolved in 3 mL of the specified solvent, 10 bar H_2 pressure for the specified time.

This experiment clearly showed an increased integral of the residual solvent peak (C_6D_5H) relative to the internal standard after the reaction with H_2, which is in agreement with a turnover number (TON) of 23.[19] A control experiment showed that in the absence of complex **2** no exchange is observed. The reaction in [D_8]toluene resulted in an increased TON of 44 after four hours (entry 2). In this case, D/H-exchange takes place at all positions, but we observe a slight preference for the C–D activation in *ortho* (TON = 15.5) and *para* positions (TON = 12.5) of the phenyl ring, whereas the methyl group (TON = 8.2) and the *meta* position (TON = 8.1) exhibit lower degrees of hydrogen incorporation. At −10 °C, slightly reduced TONs of 37 are detected (entry 3). Furthermore, we observed a significantly reduced TON at lower hydrogen pressures. Considering that the kinetic measurements indicate an increasing rate for the C–H activation with decreasing temperatures (below 4 °C), these observations suggest that the actual C–H/D activation might not be rate-determining in the catalytic reaction. In addition, the intramolecular exchange reaction is competitive. In line with this, significantly reduced TONs are found with lower hydrogen pressures. Using [D_8]THF, D/H exchange is observed in both positions as well, with an overall TON of 23 (entry 4). The reaction with [D_6]DMSO gave the highest TON of 63 after four hours (entry 5).

The catalytic activation of C–H bonds is an important method that provides an atom-economical strategy for the synthesis of functionalized and labeled organic molecules. In recent years increasing effort has been made to develop homogeneous C–H activation catalysts based on iron.[20] The first example of an iron-catalyzed deuterium or tritium labeling of C–H bonds in pharmaceutically active compounds was just recently reported by the Chirik group.[21]

Due to the fact that our investigations strongly support the involvement of σ-coordinated intermediates, there are at least two possible pathways for the actual C–H bond cleavage (Scheme 4): an oxidative addition/reductive elimination mechanism that would require an iron(IV) intermediate is unlikely in our opinion with such a strong ligand field. An alternative mechanism that avoids the change of oxidation state is the σ-complex assisted metathesis (σ-CAM),[22] which in case of iron has been predicted by DFT calculations to be a viable mechanism.[23] In a possible mechanism, the labile $(R_3P)_2BH_2$ group in

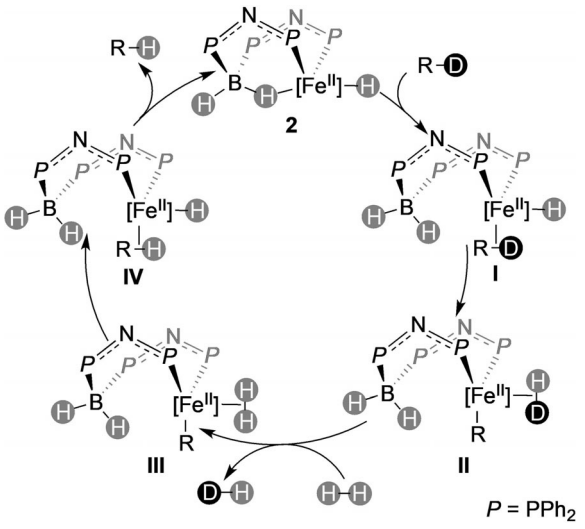

Scheme 4. Proposed mechanism for the catalytic D/H-exchange.

2 allows for the coordination of a C–D bond (**I**), followed by formation of an HD complex (**II**). The exchange of the resulting HD ligand in **II** by H_2 leads to **III**. C–H-bond formation (**IV**) and release of R–D regenerates complex **2**.

Conclusion

In summary, we have shown that three different and completely reversible reactivity patterns are viable for diphosphino borate groups within tridentate ligands. Due to this unusual diversity in reactivity, these donor groups were called ambireactive. In detail the reported iron complex undergoes different bond activation reactions below and above 4 °C, including a reversible P–B bond cleavage that overall represents a B–H activation and a reversible C–H activation. Mechanistic investigations indicate that the labile $(R_3P)_2BH_2$ group allows for the exothermic formation of σ-coordinated complexes. Based on these findings, we developed a protocol for catalytic D/H-exchange of common deuterated solvents in the presence of H_2, which likely proceeds through a σ-CAM mechanism. Currently we are evaluating the possibility of catalytic deuterium labeling for pharmaceutical compounds.

Acknowledgements

We gratefully acknowledge financial support from the Deutsche Forschungsgemeinschaft (LA 2830/3-2), the Erich-Becker-Stiftung (R.L.) and the Studienstiftung des deutschen Volkes (L.V.). R.L. is grateful to Prof. S. Dehnen for her continuous support.

Conflict of interest

The authors declare no conflict of interest.

Keywords: boron · C–H activation · cooperative effects · hydrides · iron

[1] a) H. Grützmacher, *Angew. Chem. Int. Ed.* **2008**, *47*, 1814 – 1818; *Angew. Chem.* **2008**, *120*, 1838 – 1842; b) S. Schneider, J. Meiners, B. Askevold, *Eur. J. Inorg. Chem.* **2012**, *2012*, 412 – 429.

[2] a) C. Gunanathan, D. Milstein, *Acc. Chem. Res.* **2011**, *44*, 588 – 602; b) C. Gunanathan, D. Milstein, *Science* **2013**, *341*, 1229712; c) V. T. Annibale, D. Song, *RSC Adv.* **2013**, *3*, 11432 – 11449; d) D. G. H. Hetterscheid, S. H. Chikkali, B. de Bruin, J. N. H. Reek, *ChemCatChem* **2013**, *5*, 2785 – 2793; e) T. Ikariya, *Bull. Chem. Soc. Japan* **2011**, *84*, 1 – 16; f) J. I. van der Vlugt, *Eur. J. Inorg. Chem.* **2012**, *2012*, 363 – 375; g) T. Zell, D. Milstein, *Acc. Chem. Res.* **2015**, *48*, 1979 – 1994; h) D. G. A. Verhoeven, M.-E. Moret, *Dalton Trans.* **2016**, *45*, 15762 – 15778.

[3] a) H. Braunschweig, R. D. Dewhurst, V. H. Gessner, *Chem. Soc. Rev.* **2013**, *42*, 3197 – 3208; b) J. Cid, H. Gulyas, J. J. Carbo, E. Fernandez, *Chem. Soc. Rev.* **2012**, *41*, 3558 – 3570; c) H. Gulyás, A. Bonet, C. Pubill-Ulldemolins, C. Solé, J. Cid, E. Fernández, *Pure Appl. Chem.* **2012**, *84*, 2219 – 2231; d) L. Weber, *Eur. J. Inorg. Chem.* **2012**, *2012*, 5595 – 5609; e) M. Yamashita, *Bull. Chem. Soc. Jap.* **2011**, *84*, 983 – 999; f) G. R. Owen, *Chem. Commun.* **2016**, *52*, 10712 – 10726.

[4] a) A. Amgoune, D. Bourissou, *Chem. Commun.* **2011**, *47*, 859 – 871; b) S. Bontemps, G. Bouhadir, W. Gu, M. Mercy, C.-H. Chen, B. M. Foxman, L. Maron, O. V. Ozerov, D. Bourissou, *Angew. Chem. Int. Ed.* **2008**, *47*, 1481 – 1484; *Angew. Chem.* **2008**, *120*, 1503 – 1506; c) M. Sircoglou, S. Bontemps, M. Mercy, N. Saffon, M. Takahashi, G. Bouhadir, L. Maron, D. Bourissou, *Angew. Chem. Int. Ed.* **2007**, *46*, 8583 – 8586; *Angew. Chem.* **2007**, *119*, 8737 – 8740.

[5] a) H. Fong, M. E. Moret, Y. Lee, J. C. Peters, *Organometallics* **2013**, *32*, 3053 – 3062; b) S. N. MacMillan, W. Hill Harman, J. C. Peters, *Chem. Sci.* **2014**, *5*, 590 – 597; c) W. H. Harman, J. C. Peters, *J. Am. Chem. Soc.* **2012**, *134*, 5080 – 5082; d) M. A. Nesbit, D. L. M. Suess, J. C. Peters, *Organometallics* **2015**, *34*, 4741 – 4752; e) T. Schindler, M. Lux, M. Peters, L. T. Scharf, H. Osseili, L. Maron, M. E. Tauchert, *Organometallics* **2015**, *34*, 1978 – 1984.

[6] a) M. Hasegawa, Y. Segawa, M. Yamashita, K. Nozaki, *Angew. Chem. Int. Ed.* **2012**, *51*, 6956 – 6960; *Angew. Chem.* **2012**, *124*, 7062 – 7066; b) Y. Segawa, M. Yamashita, K. Nozaki, *Organometallics* **2009**, *28*, 6234 – 6242; c) M. Y. Y. Segawa, K. Nozaki, *J. Am. Chem. Soc.* **2009**, *131*, 9201 – 9203; d) D. Schuhknecht, F. Ritter, M. E. Tauchert, *Chem. Commun.* **2016**, *52*, 11823 – 11826; e) W.-C. Shih, W. Gu, M. C. MacInnis, S. D. Timpa, N. Bhuvanesh, J. Zhou, O. V. Ozerov, *J. Am. Chem. Soc.* **2016**, *138*, 2086 – 2089.

[7] a) T.-P. Lin, J. C. Peters, *J. Am. Chem. Soc.* **2013**, *135*, 15310 – 15313; b) T.-P. Lin, J. C. Peters, *J. Am. Chem. Soc.* **2014**, *136*, 13672 – 13683; c) Y. Li, C. Hou, J. Jiang, Z. Zhang, C. Zhao, A. J. Page, Z. Ke, *ACS Catal.* **2016**, *6*, 1655 – 1662.

[8] a) H. Braunschweig, R. D. Dewhurst, F. Hupp, M. Nutz, K. Radacki, C. W. Tate, A. Vargas, Q. Ye, *Nature* **2015**, *522*, 327 – 330; b) F. Dahcheh, D. Martin, D. W. Stephan, G. Bertrand, *Angew. Chem. Int. Ed.* **2014**, *53*, 13159 – 13163; *Angew. Chem.* **2014**, *126*, 13375 – 13379; c) R. Kinjo, B. Donnadieu, M. A. Celik, G. Frenking, G. Bertrand, *Science* **2011**, *333*, 610 – 613; d) D. A. Ruiz, M. Melaimi, G. Bertrand, *Chem. Commun.* **2014**, *50*, 7837 – 7839; e) E. Bernhardt, V. Bernhardt-Pitchougina, H. Willner, N. Ignatiev, *Angew. Chem. Int. Ed.* **2011**, *50*, 12085 – 12088; *Angew. Chem.* **2011**, *123*, 12291 – 12294.

[9] a) L. Kong, R. Ganguly, Y. Li, R. Kinjo, *Chem. Sci.* **2015**, *6*, 2893 – 2902; b) L. Kong, Y. Li, R. Ganguly, D. Vidovic, R. Kinjo, *Angew. Chem. Int. Ed.* **2014**, *53*, 9280 – 9283; *Angew. Chem.* **2014**, *126*, 9434 – 9437; c) M. Grätz, A. Backer, L. Vondung, L. Maser, A. Reincke, R. Langer, *Chem. Commun.* **2017**, *53*, 7230 – 7233.

[10] a) H. Braunschweig, R. D. Dewhurst, A. Schneider, *Chem. Rev.* **2010**, *110*, 3924 – 3957; b) G. R. Owen, *Chem. Soc. Rev.* **2012**, *41*, 3535 – 3546; c) X.-Y. Wang, Q. Ma, T. Duan, Q. Chen, Q.-F. Zhang, *Inorg. Chim. Acta* **2012**, *384*, 281 – 286; d) A. Al-Harbi, Y. Rong, G. Parkin, *Dalton Trans.* **2013**, *42*, 11117 – 11127; e) R. S. Anju, D. K. Roy, B. Mondal, K. Yuvaraj, C. Arivazhagan, K. Saha, B. Varghese, S. Ghosh, *Angew. Chem. Int. Ed.* **2014**, *53*, 2873 – 2877; *Angew. Chem.* **2014**, *126*, 2917 – 2921; f) R. Rajasekharan-Nair, L. Darby, J. Reglinski, M. D. Spicer, A. R. Kennedy, *Inorg. Chem. Commun.* **2014**, *41*, 11 – 13; g) R. Ramalakshmi, K. Saha, D. K. Roy, B. Var-

ghese, A. K. Phukan, S. Ghosh, *Chem. Eur. J.* **2015**, *21*, 17191 – 17195; h) K. Bakthavachalam, K. Yuvaraj, M. Zafar, S. Ghosh, *Chem. Eur. J.* **2016**, *22*, 17291 – 17297; i) S. Pal, M. W. Drover, B. O. Patrick, J. A. Love, *Eur. J. Inorg. Chem.* **2016**, *15 – 16*, 2403 – 2408.

[11] L. Vondung, N. Frank, M. Fritz, L. Alig, R. Langer, *Angew. Chem. Int. Ed.* **2016**, *55*, 14450 – 14454; *Angew. Chem.* **2016**, *128*, 14665 – 14670.

[12] a) E. Alberico, P. Sponholz, C. Cordes, M. Nielsen, H.-J. Drexler, W. Baumann, H. Junge, M. Beller, *Angew. Chem. Int. Ed.* **2013**, *52*, 14162 – 14166; *Angew. Chem.* **2013**, *125*, 14412 – 14416; b) R. Bau, H. S. H. Yuan, M. V. Baker, L. D. Field, *Inorg. Chim. Acta* **1986**, *114*, L27 – L28; c) S. Chakraborty, H. Dai, P. Bhattacharya, N. T. Fairweather, M. S. Gibson, J. A. Krause, H. Guan, *J. Am. Chem. Soc.* **2014**, *136*, 7869 – 7872; d) S. Elangovan, B. Wendt, C. Topf, S. Bachmann, M. Scalone, A. Spannenberg, H. Jiao, W. Baumann, K. Junge, M. Beller, *Adv. Synth. Catal.* **2016**, *358*, 820 – 825; e) N. Gorgas, B. Stöger, L. F. Veiros, E. Pittenauer, G. Allmaier, K. Kirchner, *Organometallics* **2014**, *33*, 6905 – 6914; f) I. Koehne, T. J. Schmeier, E. A. Bielinski, C. J. Pan, P. O. Lagaditis, W. H. Bernskoetter, M. K. Takase, C. Würtele, N. Hazari, S. Schneider, *Inorg. Chem.* **2014**, *53*, 2133 – 2143; g) R. Langer, M. A. Iron, L. Konstantinovski, Y. Diskin-Posner, G. Leitus, Y. Ben-David, D. Milstein, *Chem. Eur. J.* **2012**, *18*, 7196 – 7209; h) Y. Zhang, A. D. MacIntosh, J. L. Wong, E. A. Bielinski, P. G. Williard, B. Q. Mercado, N. Hazari, W. H. Bernskoetter, *Chem. Sci.* **2015**, *6*, 4291 – 4299.

[13] a) T. N. Hooper, A. S. Weller, N. A. Beattie, S. A. Macgregor, *Chem. Sci.* **2016**, *7*, 2414 – 2426; b) T. A. Shuttleworth, M. A. Huertos, I. Pernik, R. D. Young, A. S. Weller, *Dalton Trans.* **2013**, *42*, 12917 – 12925.

[14] N. Frank, K. Hanau, R. Langer, *Inorg. Chem.* **2014**, *53*, 11335 – 11343.

[15] For further details please see the Supporting Information.

[16] a) K. N. Houk, N. G. Rondan, *J. Am. Chem. Soc.* **1984**, *106*, 4293 – 4294; b) E. I. Kapinus, H. Rau, *J. Phys. Chem. A* **1998**, *102*, 5569 – 5576; c) V. D. Kiselev, J. G. Miller, *J. Am. Chem. Soc.* **1975**, *97*, 4036 – 4039; d) S. M. McCarthy, Y.-C. Lin, D. Devarajan, J. W. Chang, H. P. Yennawar, R. M. Rioux, D. H. Ess, A. T. Radosevich, *J. Am. Chem. Soc.* **2014**, *136*, 4640 – 4650; e) N. J. Turro, D. A. Hrovat, I. R. Gould, A. Padwa, W. Dent, R. J. Rosenthal, *Angew. Chem. Int. Ed. Engl.* **1983**, *22*, 625 – 627; *Angew. Chem.* **1983**, *95*, 647 – 648; f) N. J. Turro, G. F. Lehr, J. A. Butcher, R. A. Moss, W. Guo, *J. Am. Chem. Soc.* **1982**, *104*, 1754 – 1756; g) X.-Q. Zhu, J.-Y. Zhang, J.-P. Cheng, *J. Org. Chem.* **2006**, *71*, 7007 – 7015.

[17] a) H. Buschmann, H.-D. Scharf, N. Hoffmann, P. Esser, *Angew. Chem. Int. Ed. Engl.* **1991**, *30*, 477 – 515; *Angew. Chem.* **1991**, *103*, 480 – 518; b) A. Gypser, P.-O. Norrby, *J. Chem. Soc. Perkin Trans. 2* **1997**, 939 – 944.

[18] N. Frank, K. Hanau, K. Flosdorf, R. Langer, *Dalton Trans.* **2013**, *42*, 11252 – 11261.

[19] The turnover number (TON) was calculated by taking the difference of the integrals of the residual solvent peak before and after the reaction with H_2. The calibration of the integrals was performed by setting the Fe–H resonance in the pre-reaction spectrum to a value of 1 and using the corresponding integral of an internal standard for calibration of the post-reaction spectrum. The final TON was obtained by subtraction of 3 from the calibrated integral difference (for the Fe–H and the BH_2 hydrogen atoms that were incorporated into the deuterated solvent). A control experiment without catalyst was always run in parallel.

[20] R. Shang, L. Ilies, E. Nakamura, *Chem. Rev.* **2017**, *117*, 9086 – 9139.

[21] R. Pony Yu, D. Hesk, N. Rivera, I. Pelczer, P. J. Chirik, *Nature* **2016**, *529*, 195 – 199.

[22] a) A. Di Giuseppe, R. Castarlenas, L. A. Oro, *Comptes Rendus Chim.* **2015**, *18*, 713 – 741; b) R. N. Perutz, S. Sabo-Etienne, *Angew. Chem. Int. Ed.* **2007**, *46*, 2578 – 2592; *Angew. Chem.* **2007**, *119*, 2630 – 2645.

[23] W. H. Lam, G. Jia, Z. Lin, C. P. Lau, O. Eisenstein, *Chem. Eur. J.* **2003**, *9*, 2775 – 2782.

Manuscript received: August 28, 2017

Accepted manuscript online: October 9, 2017

Version of record online: ■■ ■■, 0000

Supporting Information

Ambireactive $(R_3P)_2BH_2$-groups facilitating temperature-switchable bond activation by an iron complex

Lisa Vondung,[a] Lars Erik Sattler,[a] Robert Langer*,[a]

1. **Experimental Details**
2. **NMR spectra**
3. **Variable Temperature NMR Measurements**
4. **X-Ray Crystallography**
5. **DFT Calculations**

[a]*Department of Chemistry, Philipps-Universität Marburg, Hans-Meerwein-Str., 35043 Marburg, Germany, Fax: (+)49-6421-2825617, E-mail: robert.langer@chemie.uni-marburg.de*

1. Experimental Details

Material and Methods

All experiments were carried out under an atmosphere of purified argon in a MBraun Labmaster glove box or using standard Schlenk techniques. *n*-Hexane and C_6D_6 were dried and distilled from Na/K alloy and stored over molecular sieves. Toluene was dried and distilled from sodium and stored over molecular sieves. THF was dried and distilled from potassium and stored over molecular sieves. Bis(diphenylphosphino)amine[1] was prepared according to a previously reported procedure. BD_3·THF was prepared as described by Hossain, Gao and co-workers.[2]

^1H, ^{13}C, ^{31}P and ^{11}B NMR spectra were recorded using Bruker DRX 400, DRX 500 and Avance 500 NMR spectrometers. ^1H and $^{13}C\{^1H\}$, ^{13}C-APT (attached proton test) NMR chemical shifts are reported in ppm downfield from tetramethylsilane. The resonance of the residual protons in the deuterated solvent was used as internal standard for ^1H NMR. The solvent peak of the deuterated solvent was used as internal standard for ^{13}C NMR. ^{31}P NMR chemical shifts are reported in ppm downfield from H_3PO_4 and referenced to an external 85% solution of phosphoric acid in D_2O. ^{11}B NMR chemical shifts are reported in ppm downfield from BF_3·Et_2O and referenced to an external solution of BF_3·Et_2O in $CDCl_3$. The following abbreviations are used for the description of NMR data: br (broad), s (singlet), d (doublet), t (triplet), q (quartet), quin (quintet), m (multiplet), v (virtual).

FT-IR spectra were recorded by attenuated total reflection of the solid samples on a Bruker Tensor IF37 spectrometer. The intensity of the absorption band is indicated as vw (very weak), w (weak), m (medium), s (strong), vs (very strong) and br (broad).

HR-ESI mass spectra were acquired with a LTQ-FT mass spectrometer (Thermo Fisher Scientific). The resolution was set to 100.000.

Formation of bis(diphenylphosphino)amine mono-borane adduct (1)

96 mg (0.25 mmol) Bis(diphenylphosphino)amine were dissolved in 5 mL THF and 0.25 mL (0.25 mmol) of a 1 M solution of BH_3·THF in THF were added at room temperature. Formation of **1** was confirmed by $^{31}P\{^1H\}$ NMR spectroscopy after 15 minutes and the solution was used for the synthesis of **2** without further purification. $^{31}P\{^1H\}$ NMR (162 MHz, THF, 27 °C) δ: 33.6 (d, 2P, *P*-N, J_{PP} = 44.7 Hz), 60.7 (br, 2P, *P*-B).

Formation of Bis(diphenylphosphino)amine mono-borane adduct (1-*d*$_3$)

108 mg (0.28 mmol) Bis(diphenylphosphino)amine were dissolved in 8 mL THF and 0.25 mL (0.25 mmol) of a 1 M solution of BD_3·THF in THF were added at room temperature. Formation of **1** was confirmed by $^{31}P\{^1H\}$ NMR spectroscopy after 10 minutes and the solution was used for the synthesis of **3** without further purification. $^{31}P\{^1H\}$ NMR (162 MHz, THF, 27 °C) δ: 33.5 (d, 2P, *P*-N, J_{PP} = 45.0 Hz), 60.9 (br, 2P, *P*-B).

Synthesis of [({Ph$_2$P-N-PPh$_2$}$_2$BH$_2$)FeH(dppa)] (2)

A THF solution containing 0.25 mmol **1** and 0.5 mmol dppa was added to 112 mg (0.25 mmol) [Fe(hmds)$_2$(thf)]. The solution turned dark red-brown immediately and was stirred at room temperature for one hour. Layering with *n*-hexane and keeping the sample at 4 °C yielded **3** as red crystals. Yield: 159 mg (0.13 mmol, 52 %). Anal. Calcd. for $C_{80}H_{80}BFeN_3O_2P_6$ (**2**•2 THF, M = 1368.04 g/mol): C 70.24 %, H 5.89 %, N 3.07 %. Found: C 70.05 %, H 5.965 %, N 3.03 %. $^{31}P\{^1H\}$ NMR (162 MHz, C_6D_6, 27 °C) δ: 34.6 (br, 2P, *P*-B), 85.3 (br, 2P, *P*-dppa), 111.9 (br, 2P, *P*-Fe) ppm. ^1H NMR (400 MHz, C_6D_6, 27 °C) δ: -20.78 (br, 1H, Fe-*H*), -11.68 (br, 1H, B-*H*-Fe), 5.04 (br, 1H, B-*H*), 6.53-7.03 (m, 38H, Phenyl-*H*), 7.33-7.8.10 (m, 22H, Phenyl -*H*) ppm. Selectively decoupled $^1H\{^{31}P\}$ and $^1H\{^{11}B\}$ NMR spectra were acquired, but didn't cause a change in multiplicity for the observed signals at 300 K. For the $^1H\{^{11}B\}$ NMR spectrum, a sharpening of the signals at -11.68 and 5.04 ppm was observed. Lowering the temperature to 285 K lead to a change of multiplicity for the signal at -20.78 in all ^1H and decoupled spectra ^1H NMR (400 MHz, toluene-*d*$_8$, 12 °C)δ: -20.89 ppm (quin, 1H, J_{PH} = 48.6 Hz). ^{13}C-APT NMR (100.6 MHz, C_6D_6, 27 °C) *δ*: 126.2 (s, Aryl-*C*), 127.1 (s, Aryl-*C*), 128.6 (br, Aryl-*C*), 131.5 (br, Aryl-*C*), 132.0 (br, Aryl-*C*), 132.5 (br, Aryl-*C*) ppm. $^{11}B\{^1H\}$ NMR (160.5 MHz, toluene-*d*$_8$, 27 °C) δ: -17.7 (s) ppm. IR (ATR): $\tilde{\vartheta}$ 3177 (vw, br), 3049 (v), 2963 (m), 2867 (vw), 2385 (w, B-H), 1888 (w, Fe-H), 1586 (vw), 1480 (w), 1433 (m), 1259 (s), 1091 (s, br), 1015 (vs), 911 (w), 866 (m), 790 (vs), 736 (m), 688 (s), 593 (w), 552 (w), 505 (m), 485 (s), 433 (m) [cm^{-1}]. High Res. ESI-MS (*m/z, neg.*): 1222.2896 (calc. for $[M-H]^-$), 1222.2869 (found, Δ = 2.2 ppm).

Synthesis of [({dppa}$_2$BD$_2$)FeD(dppa)] (2-*d*$_3$)

A THF solution containing 0.09 mmol **1-*d*$_3$** and 0.18 mmol dppa was added to 67 mg (0.15 mmol) [Fe(hmds)$_2$(thf)]. The solution turned dark red immediately and was stirred at room temperature for one hour. Filtering, layering with *n*-hexane and keeping the sample at 4 °C

yielded **3-*d*$_3$** as red crystals. Yield: 69 mg (0.06 mmol, 37 %).

$^{31}P\{^1H\}$ NMR (162 MHz, C_6D_6, 27 °C) δ: 34.4 (br, 2P, *P*-B), 85.1 (br, 2P, *P*(dppa)), 111.2 (br, 2P, *P*-Fe) ppm. ^1H NMR (400 MHz, C_6D_6, 27 °C) δ: 6.53-7.00 (m, 38H, Phenyl-*H*), 7.31-7.81 (m, 22H, Phenyl -*H*) ppm. ^2H NMR (400 MHz, toluene, 27 °C) δ: 2.08 (s, 3H, Toluene-C*H*$_3$), 6.98-7.10 (m, 6H, Tolune-o/m/p-*H*), 7.41 (br, **2-*d*$_3$** o-Phenyl-H) ppm.

Synthesis of [{(dppa)$_2$BH$_2$}FeH(H$_2$)(dppa)] (7)

8 mg of **2** were dissolved in 0.7 mL C_6D_6. The argon atmosphere was removed and replaced with one atmosphere of H_2. The red solution changed its color to yellow within a minute. In the absence of the hydrogen atmosphere complex **2** is generated again. All attempts to crystallize complex **7** led to the formation of single crystals of **2**.

$^{31}P\{^1H\}$ NMR (162 MHz, C_6D_6, 27 °C) δ: 24.3 (br, 2P, *P*-B), 90.4-91.0 (m, 2P, *P*(dppa)), 94.0-94.7 (m, 2P, *P*-Fe) ppm. ^1H NMR (400 MHz, C_6D_6, 27 °C) δ: -7.20 (vquin, 1H, Fe-*H,* J_{PH} = 48.8 Hz), -3.05 (br, 2H, Fe-*H*$_2$), 3.27 (br, 1H, B-*H*), 4.53 (br, 1H, B-*H*), 6.28-7.02 (m, 40H, Ph-*H*), 7.33-8.09 (m, 20*H*, Ph-H) ppm. Selectively decoupled $^1H\{^{31}P\}$ and $^1H\{^{11}B\}$ NMR spectra were acquired, which resulted in sharpening and change of multiplicity for some signals. In the following only the changed signals are given. $^1H\{^{31}P\}$ (400 MHz, C_6D_6, 27 °C, O2P = 93.0 ppm) δ: -7.20 (t, 1H, Fe-*H*, J_{PH} = 48.0 Hz), $^1H\{^{31}P\}$ (400 MHz, C_6D_6, 27 °C, O2P = 90.0 ppm) δ: -7.20 (t, 1H, Fe-*H*, J_{PH} = 46.7 Hz) $^1H\{^{11}B\}$ (400 MHz, C_6D_6, 27 °C) δ: 3.16 (br, 1H, B-*H*), 4.54 (br, 1H, B-*H*) ppm. $^{11}B\{^1H\}$ NMR (160.5 MHz, C_6D_6, 27 °C) δ: -32.6 (s) ppm. ^{13}C-APT NMR (100.6 MHz, C_6D_6, 27 °C) δ: 126.5 (br, Aryl-*C*), 128.5 (s, Aryl-*C*), 128.9 (s, Aryl-*C*), 129.3 (s, Aryl-*C*), 129.6 (br, Aryl-*C*), 132.1 (br, Aryl-*C*) ppm. IR (ATR): $\tilde{\vartheta}$ 3053 (w), 2962 (vw), 2918 (vw), 2850 (vw), 2362 (w), 2341 (vw), 1590 (vw), 1574 (w), 1481 (w), 1459 (vw), 1435 (m), 1306 (m), 1205 (s), 1176 (m), 1151 (m), 1121 (s), 1081 (s), 1061 (s), 1025 (m), 997 (m), 984 (m), 799 (m), 744 (m), 721 (s), 690 (vs), 641 (m), 619 (m), 588 (m), 551 (s), 515 (s), 466 (m), 426 (m), 419 (m). High Res. ESI-MS (*m/z, pos.*): 1224.3055 (calc. for $[MH]^+$-H_2), 1224.3034 (found, Δ = 1.7 ppm)

Preparation of [{(dppa)$_2$BH$_2$}FeH(HD)(dppa)] (7-HD)

10 mg of **2** were dissolved in 0.7 mL toluene-d_8. The argon atmosphere was removed and replaced by one atmosphere of HD. The red solution changed its color to orange within a few minutes. Only resonances that different than for complex **7** are reported. ^1H NMR (400 MHz, toluene-d_8, 27 °C) δ: -3.14 (br t, Fe-*HD*, J_{HD} = 31.1 Hz) ppm.

Synthesis of [({dppa}$_2$BH$_2$)FeH(CO)(dppa)] (8)

48 mg of **3** were dissolved in 8 mL toluene. The Argon atmosphere was removed and replaced with 1 atm of CO. After 15 minutes the CO atmosphere was removed and replaced by Argon. The solvent was removed *in vacuo* and **8** was isolated as yellow solid. Despite several attempts under various conditions we were unable to obtain suitable crystals of **8** for single crystal X-ray diffraction.

^{31}P{^{1}H} NMR (162 MHz, C_6D_6, 27 °C) δ: 22.2 (br, 2H, *P*-B), 83.5 (m, 2P, *P*-Fe), 89.3 (m, 2P, *P*-Fe). ^{1}H NMR (400 MHz, C_6D_6, 27 °C) δ: -1.79 (vquin, 1H, Fe-*H*, J_{PH} = 48.3 Hz), 3.00 (br, 1H, N-*H*), 3.51 (br, 2H, B*H*$_2$), 6.49 (t, 2H, *ortho*-Phenyl-*H*, $^3J_{HH}$ = 7.24 Hz), 6.77-7.07 (m, 34H, Phenyl-*H*), 7.33-8.33 (m, 24H, Phenyl-*H*) ppm. A selectively decoupled ^{1}H{^{11}B} NMR spectra was acquired, which resulted in sharpening of signals. In the following only the changed signals are given. ^{1}H{^{11}B} (400 MHz, C_6D_6, 27 °C) δ: 3.24 (br, 1H, B-*H*), 3.61 (br, 1H, B-*H*) ppm. ^{11}B{^{1}H} NMR (160.5 MHz, C_6D_6, 27 °C) δ: -6.6 (s) ppm. ^{13}C-APT NMR (100.6 MHz, C_6D_6, 27 °C) *δ*: 125.7 (s, Aryl-*C*), 126.6 (t, $^1J_{CP}$ = 4.18 Hz, Aryl-*C*), 126.9 (t, $^1J_{CP}$ = 4.58 Hz, Aryl-*C*), 128.5 (s, Aryl-*C*), 128.6 (s, Aryl-*C*), 128.8 (br, Aryl-*C*), 129.0 (br, Aryl-*C*), 129.3 (s, Aryl-*C*), 129.6 (br, Aryl-*C*), 129.9 (br, Aryl-*C*), 131.4 (m, Aryl-*C*), 131.7-132.4 (m, Aryl-*C*), 132.6 (br, Aryl-*C*), 132.8-133.1 (m, Aryl-*C*). IR (ATR): $\tilde{\vartheta}$ 3052 (w), 2962 (vw), 2922 (vw), 2852 (vw), 2377 (w, br), 2030 (vw), 1970 (m), 1954 (m), 1920 (m), 1814 (vw), 1665 (w), 1572 (m), 1480 (m), 1260 (m), 1238 (m), 1211 (m), 1177 (m), 1120 (m), 1086 (s), 1064 (m), 1026 (m), 999 (m), 943 (w, br), 872 (w), 845 (w), 806 (m), 739 (m), 691 (vs), 644 (w), 631 (m), 604 (m), 589 (m), 554 (s), 540 (s), 518 (s), 497 (s), 440 (vw), 427 (w) [cm^{-1}]. High Res. ESI-MS (*m/z, pos.*): 1252.3004 (calc. for [MH]$^+$), 1252.3009 (found, Δ = 0.4 ppm).

Typical procedure for catalytic D/H-exchange

12 mg of complex **2** and a small amount of polydimethylsiloxane were dissolved in 1.6 mL of deuterated solvent. 0.6 mL of this solution were used for acquisition of a ^{1}H NMR spectrum immediately. The remaining solution was placed in a 90 mL Fischer-Porter-tube inside a glovebox. The autoclave was purged with 10 bar H_2 for 5 times and then left under a H_2 pressure of 10 bar. The solution turned from red to yellow within a few seconds and was stirred vigorously at the desired temperature for 4 or 18 hours. Then the pressure was released and a ^{1}H NMR spectrum was measured of the reaction solution.

For obtaining the TON the ^{1}H NMR spectra before and after exposure to H_2 were used as follows: In the before spectrum, the integrals of the Fe-*H*- and B-*H*-resonance of complex **2** were set to equal one. The integral of the reference signal (polydimethylsiloxane) was then used

to set the integrals of the after spectrum. The TON was then calculated using the following formula:

$$\mathrm{TON} = \mathrm{Int(before)\text{-}Int(after)\text{-}3}$$

For toluene-d_8 different TONs were observed for the different positions. The D/H exchange is most favored at the ortho and para positions (5 deuterium exchanged), while the CH_3 group and the meta positions show less exchange than expected (3 deuterium exchanged over both positions) for one molecule.

2. NMR spectra

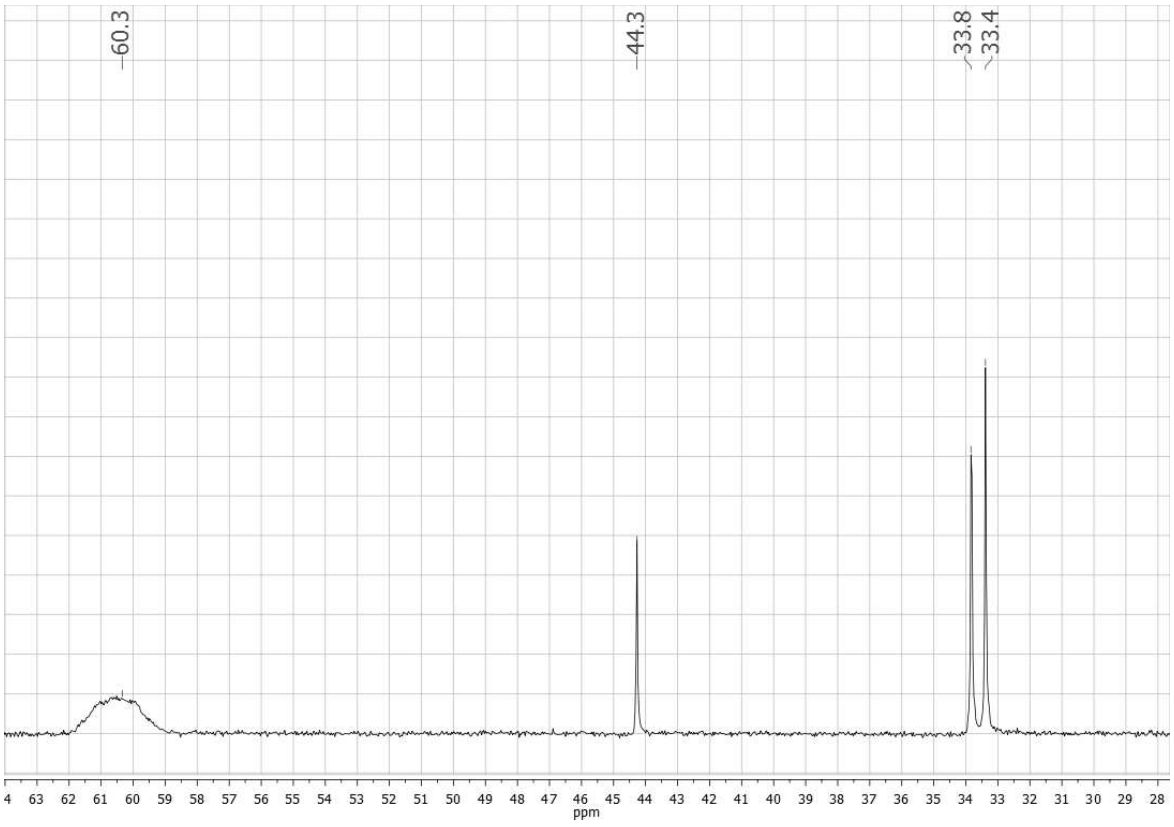

Figure 1 Representative $^{31}P\{^{1}H\}$ NMR spectrum of the reaction of dppa with $BH_3 \cdot THF$, showing a mixture of **1** and *dppa*.

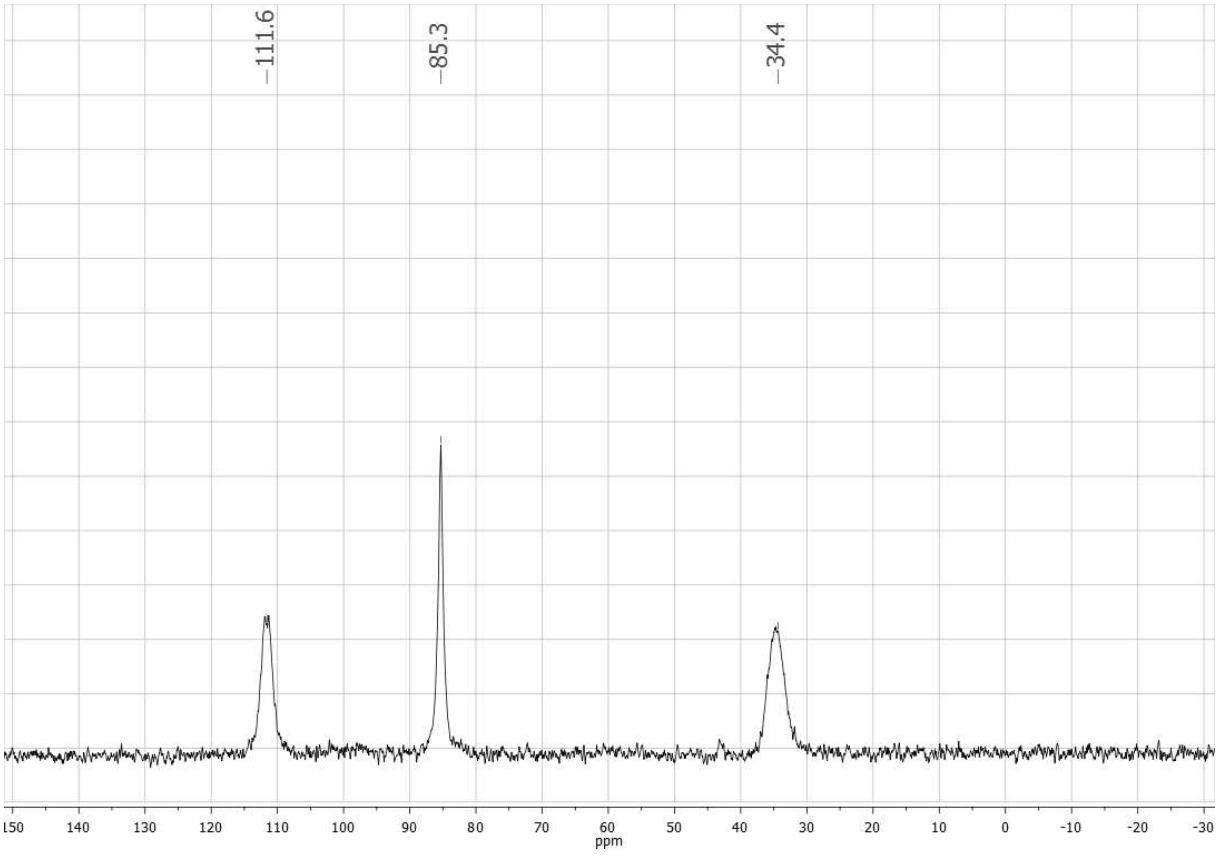

Figure 2 $^{31}P\{^{1}H\}$ NMR spectrum of **2** in C_6D_6.

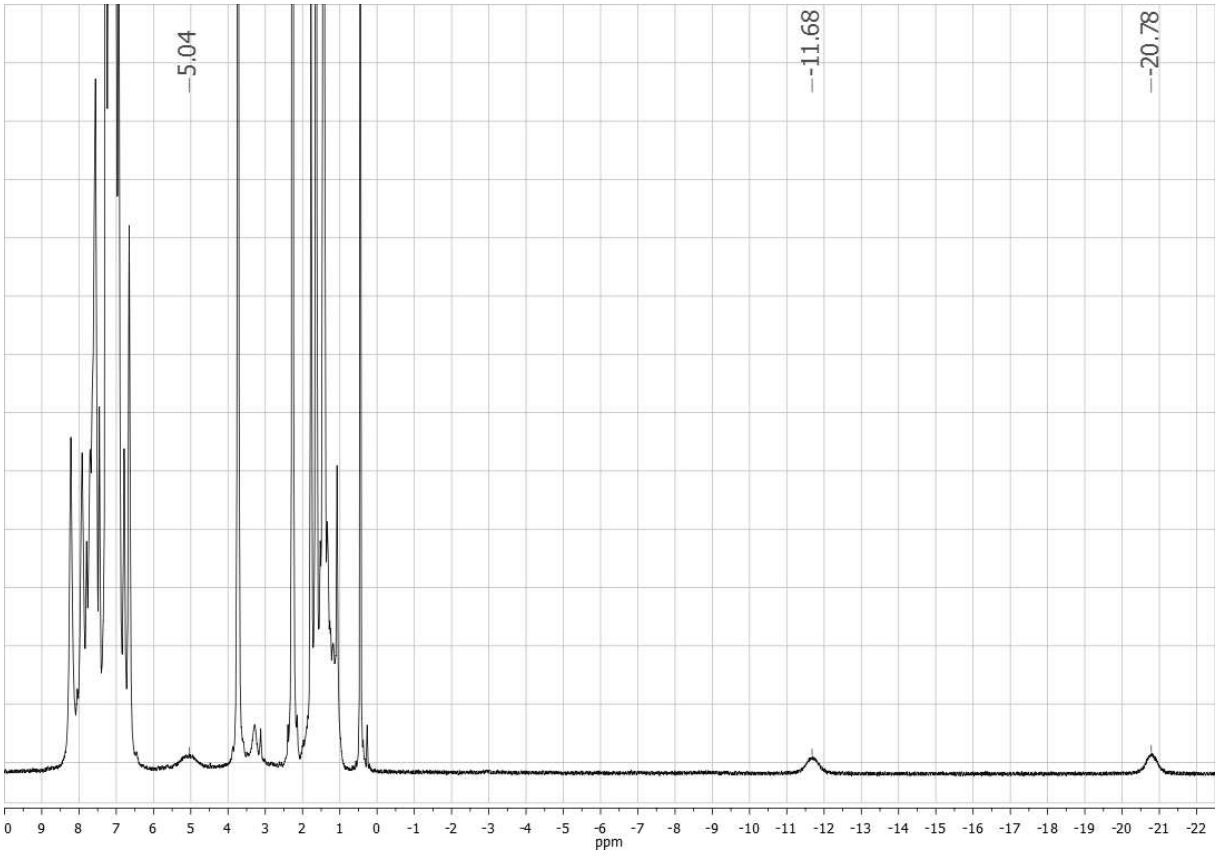

Figure 3 ^{1}H NMR spectrum of **2** in C_6D_6.

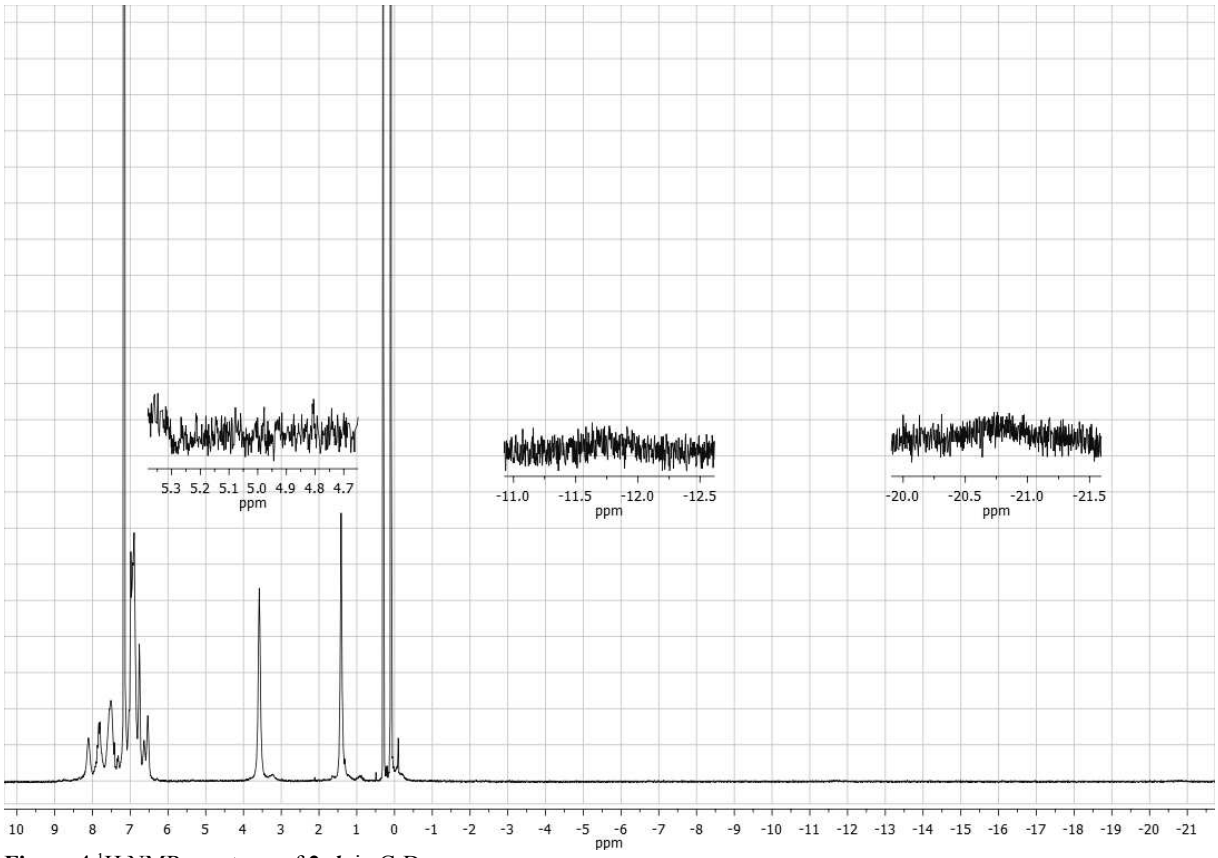

Figure 4 ^{1}H NMR spectrum of **2-*d*$_3$** in C_6D_6.

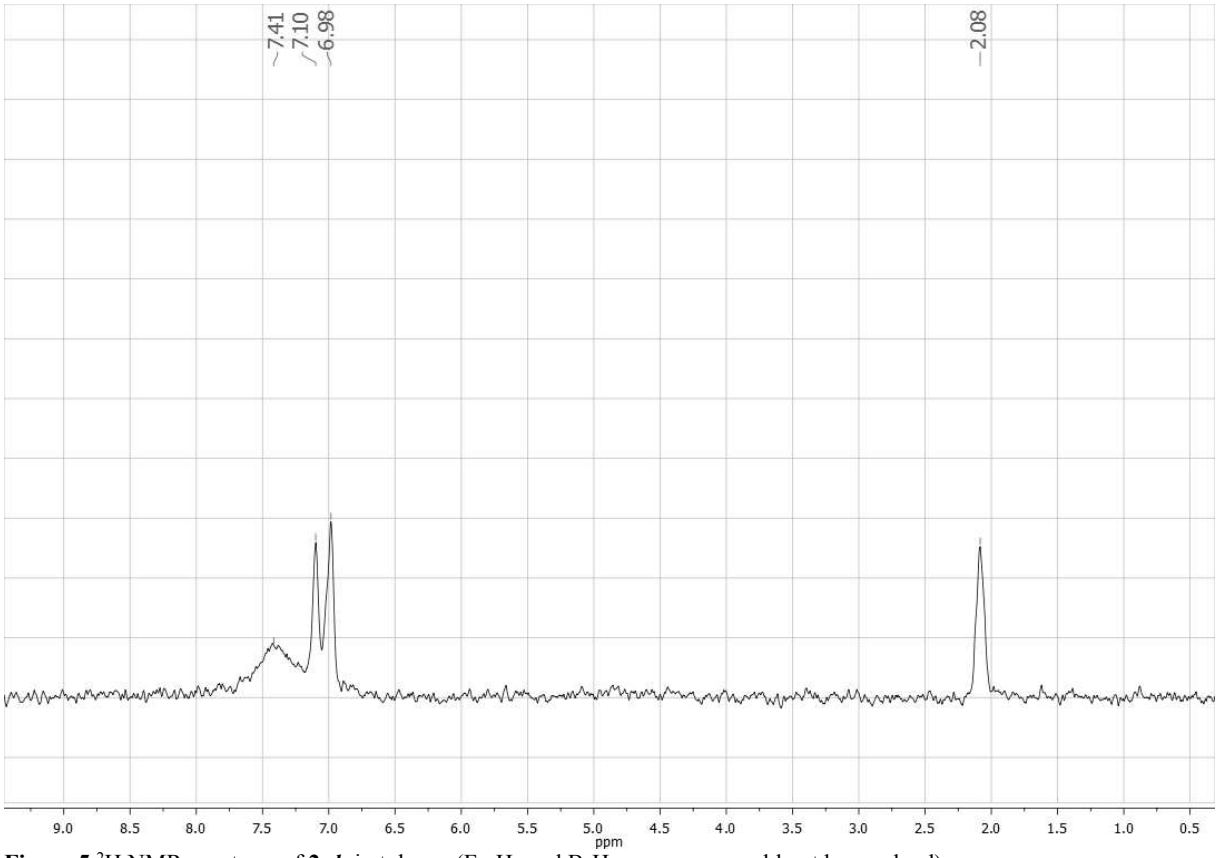

Figure 5 ^{2}H NMR spectrum of **2-*d*$_3$** in toluene (Fe-H- and B-H-resonances could not be resolved).

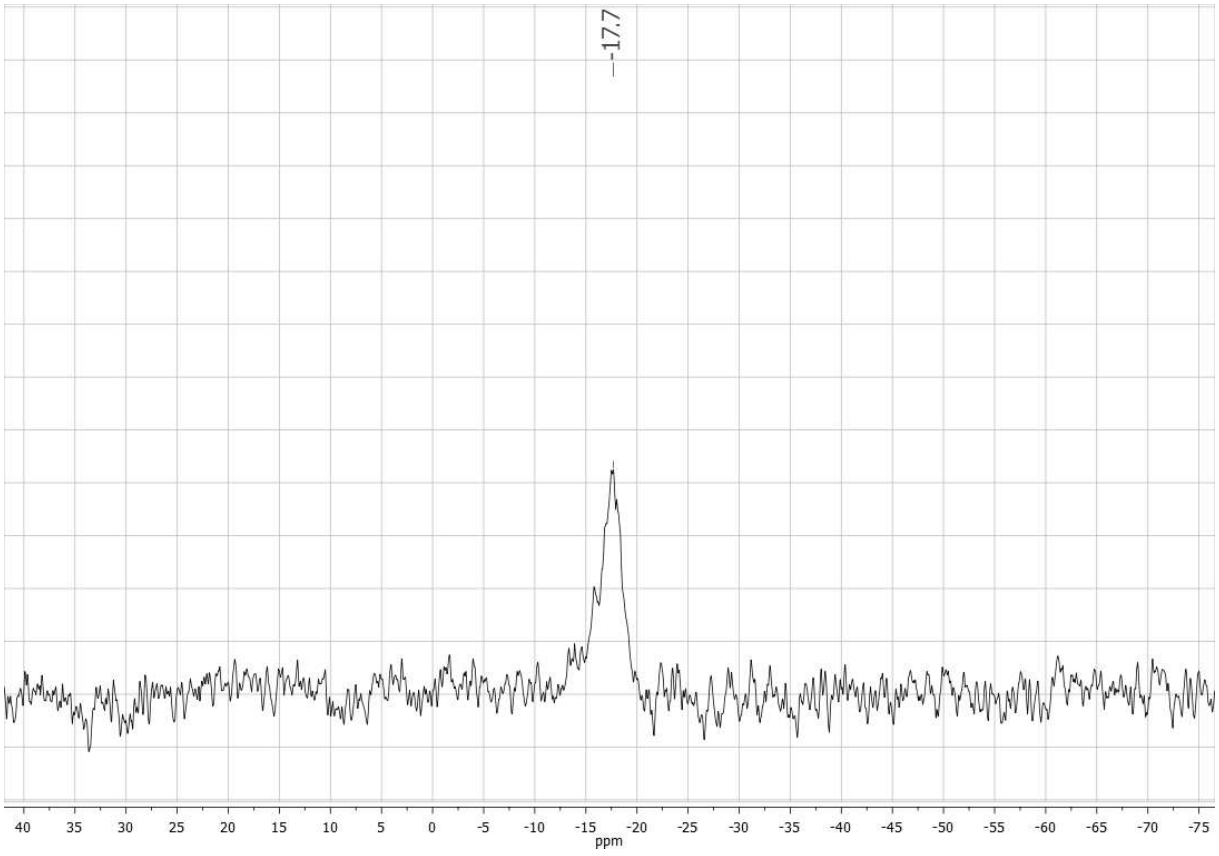

Figure 6 $^{11}B\{^{1}H\}$ NMR spectrum of **2** in C_6D_6.

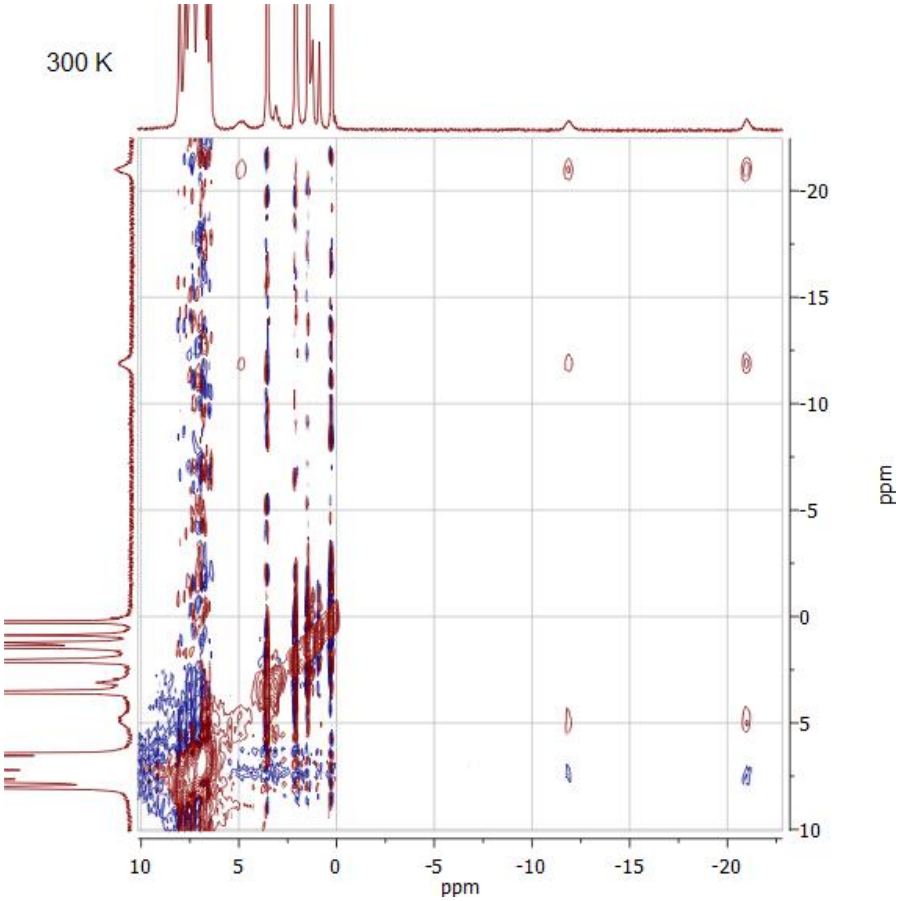

Figure 7 ^{1}H NOESY NMR spectrum of **2** in toluene-d_8 300K.

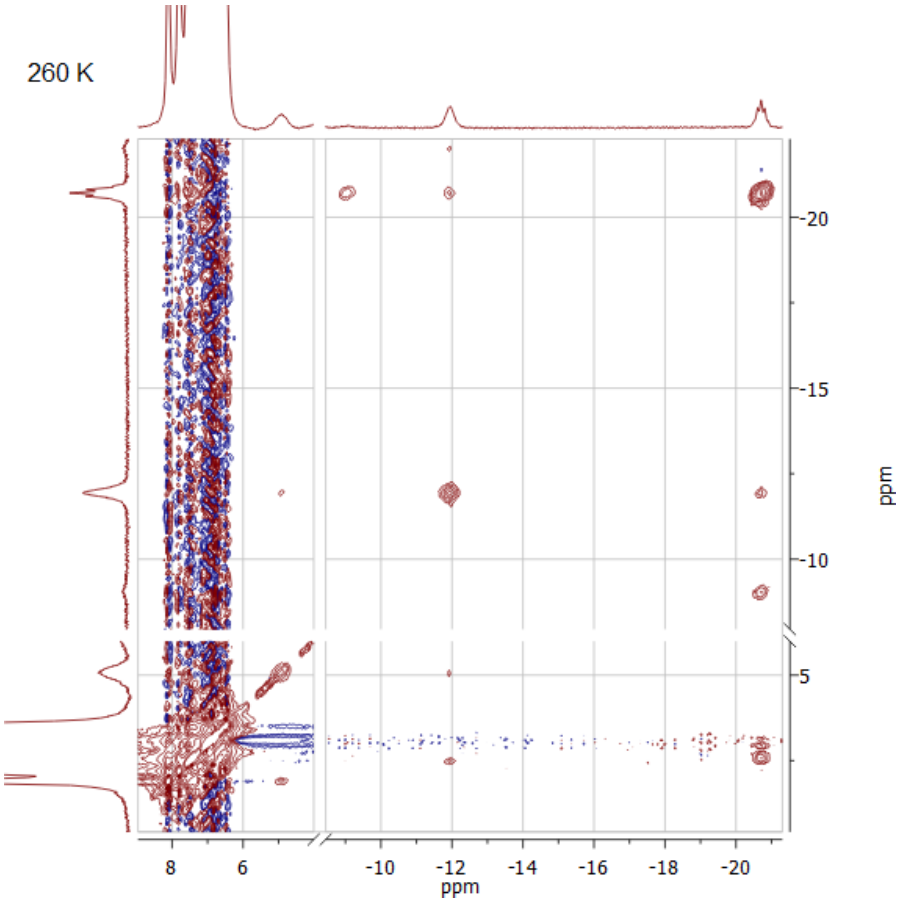

Figure 8 ^{1}H NOESY NMR spectrum of **2** in toluene-d_8 260K.

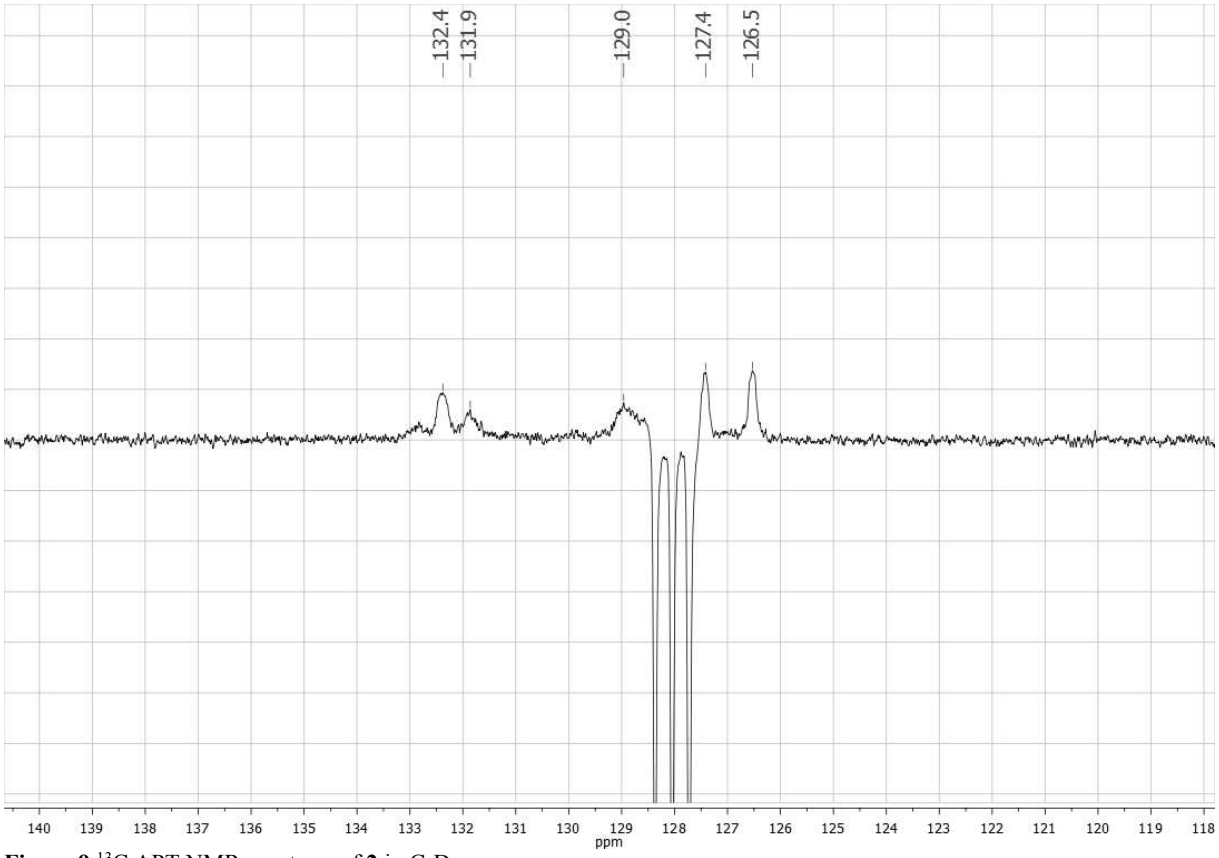

Figure 9 ^{13}C APT NMR spectrum of **2** in C_6D_6.

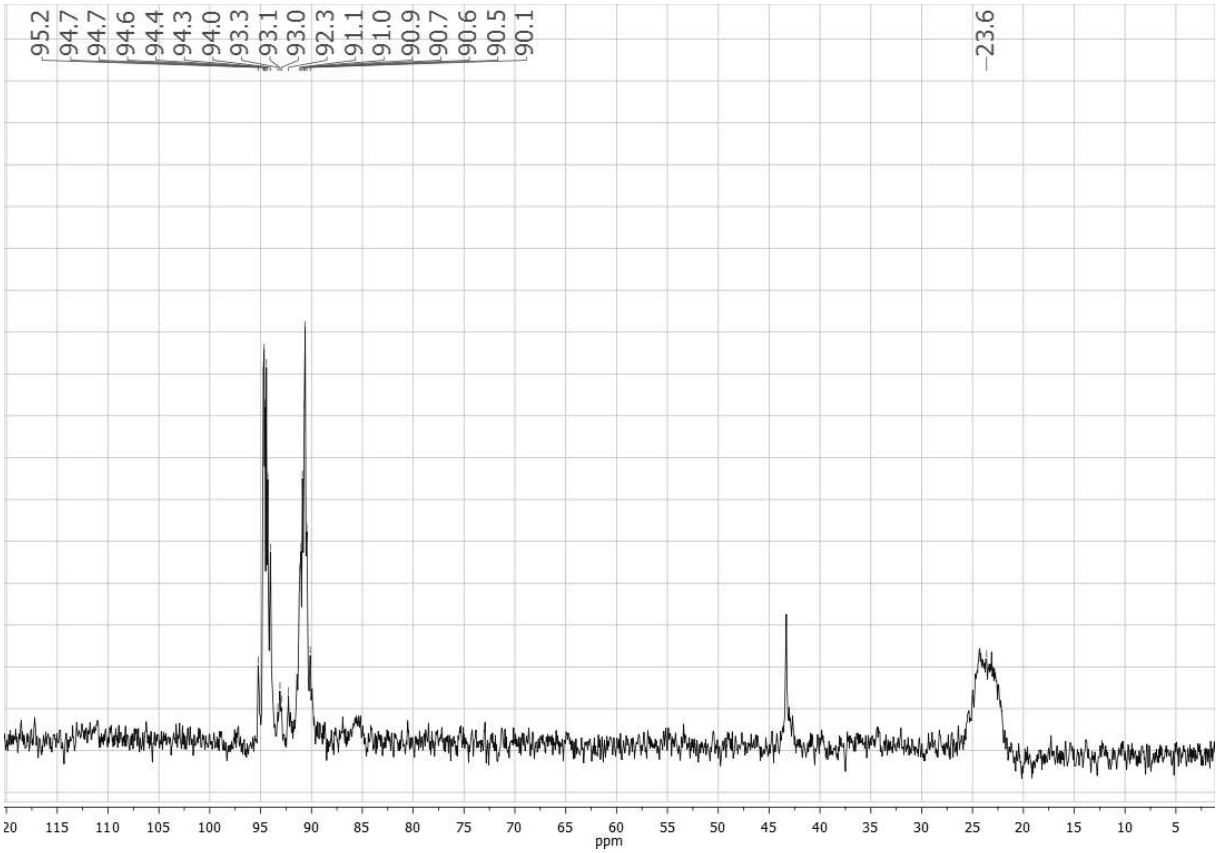

Figure 10 $^{31}P\{^1H\}$ NMR spectrum of **7** in C_6D_6.

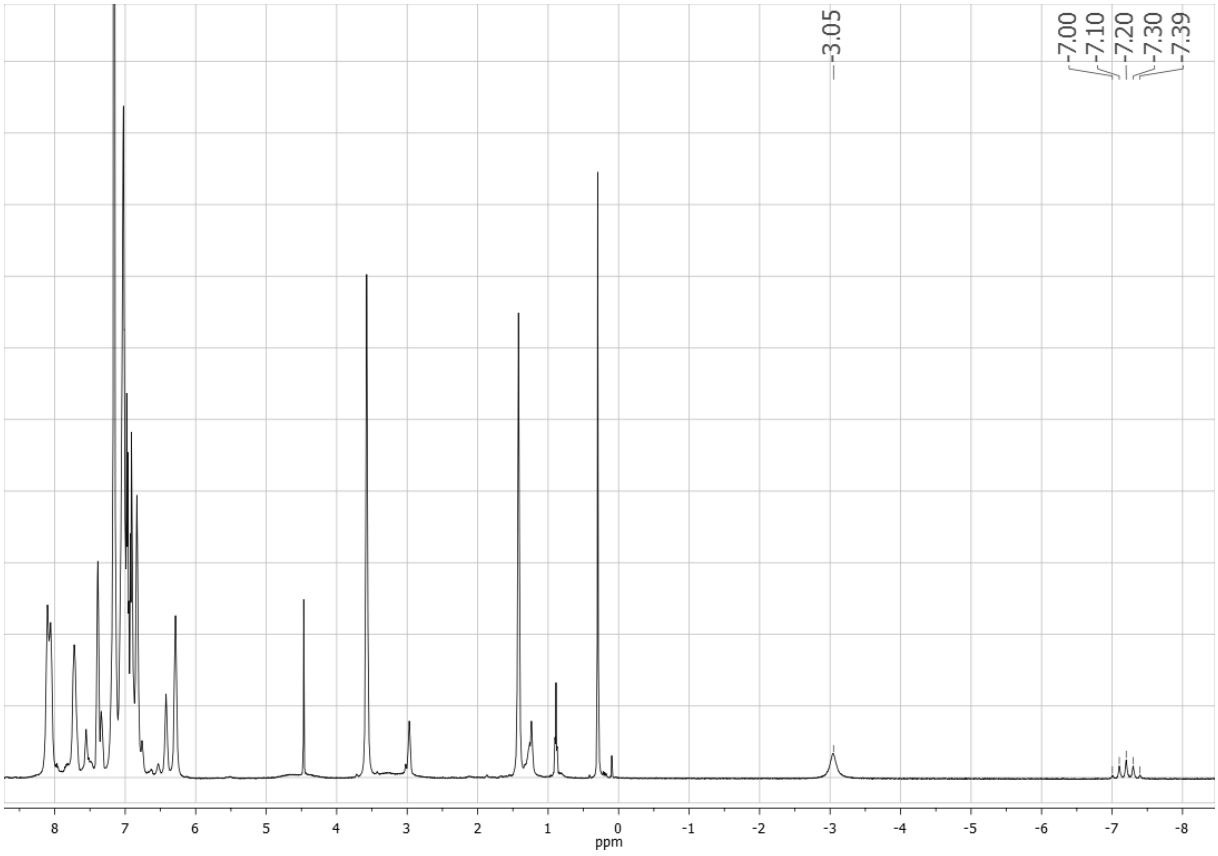

Figure 11 ^{1}H NMR spectrum of **7** in C_6D_6.

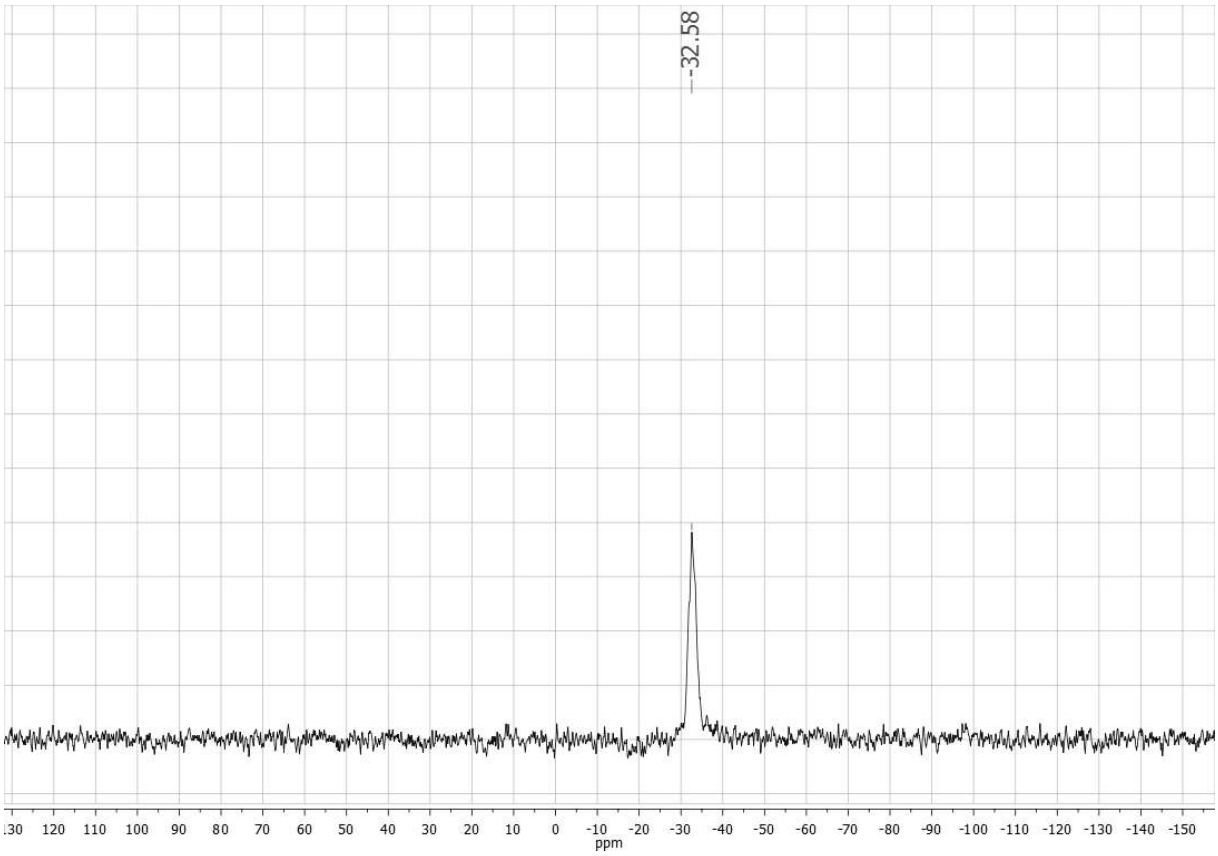

Figure 12 $^{11}B\{^{1}H\}$ NMR spectrum of **7** in C_6D_6.

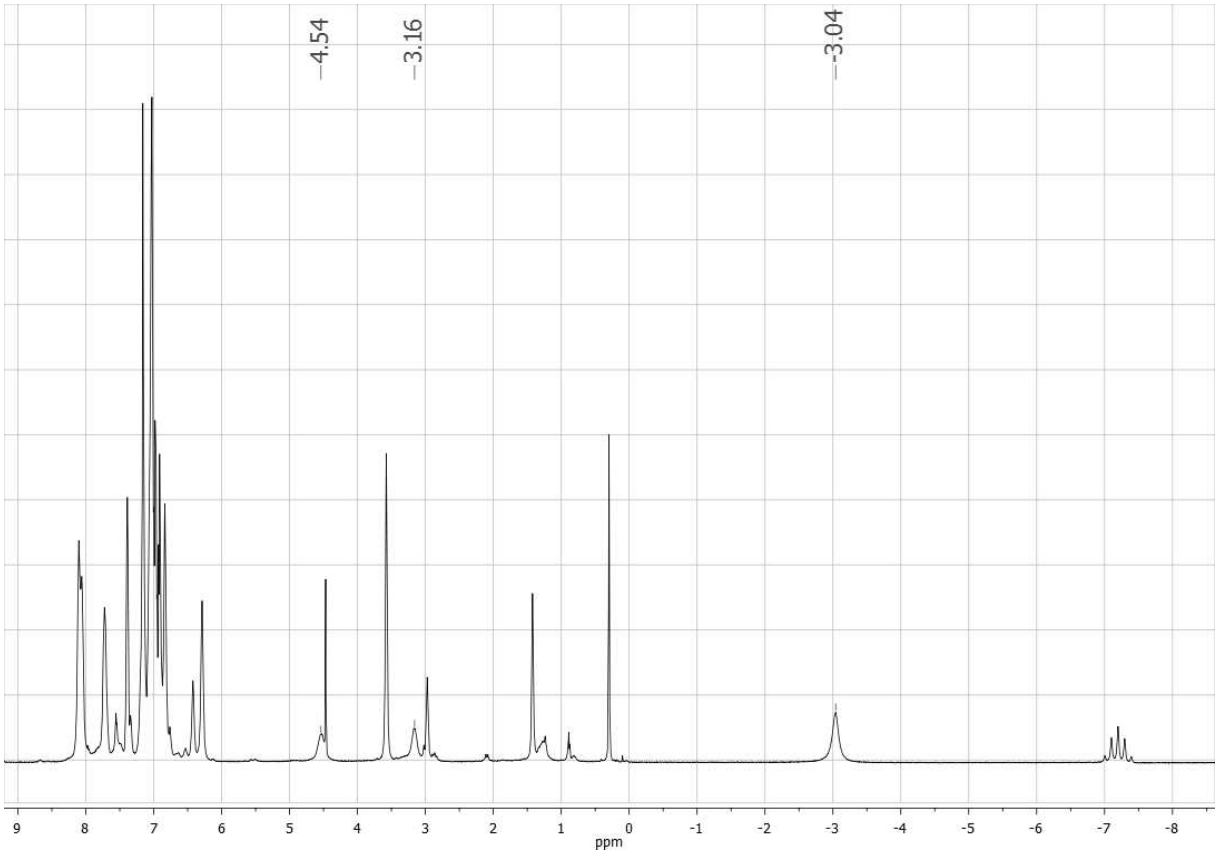

Figure 13 $^{1}H\{^{11}B\}$ NMR spectrum of **7** in C_6D_6.

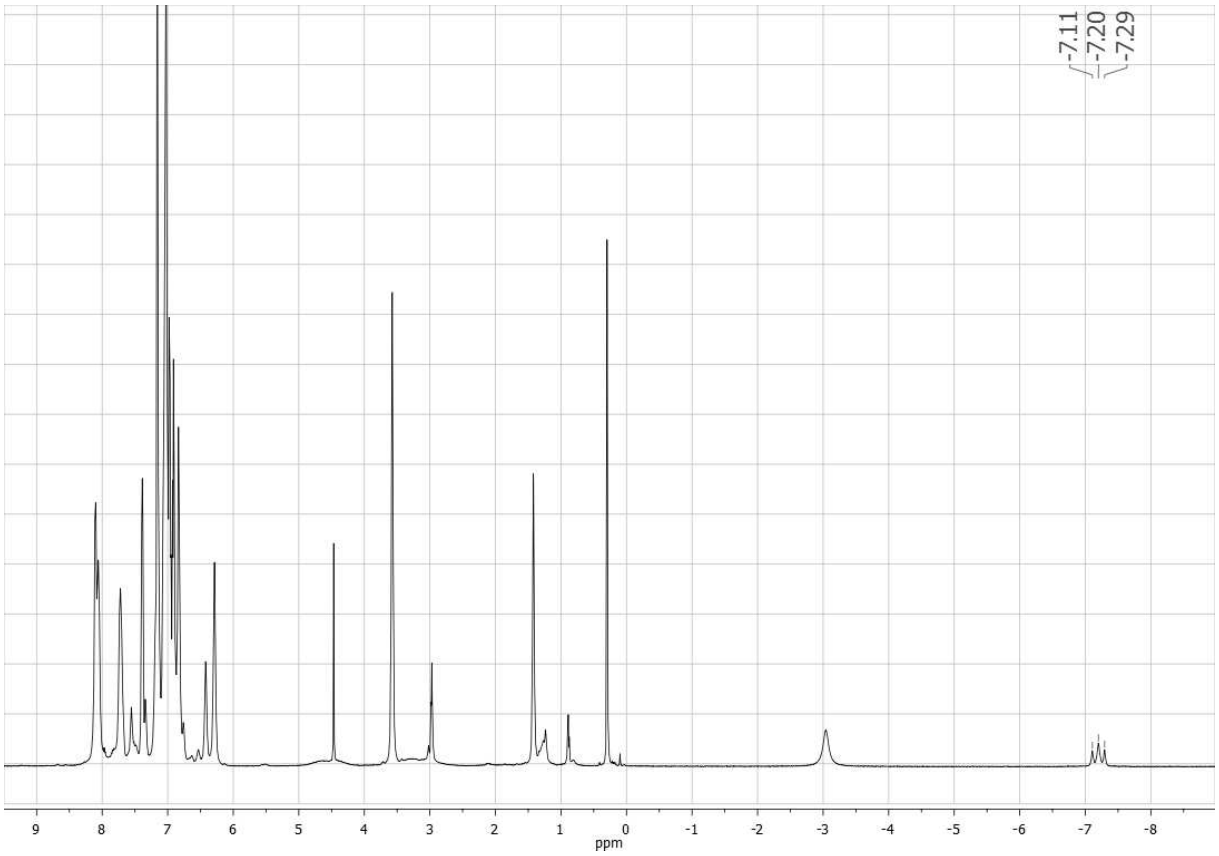

Figure 14 $^{1}H\{^{31}P\}$ NMR spectrum of **7** in C_6D_6.

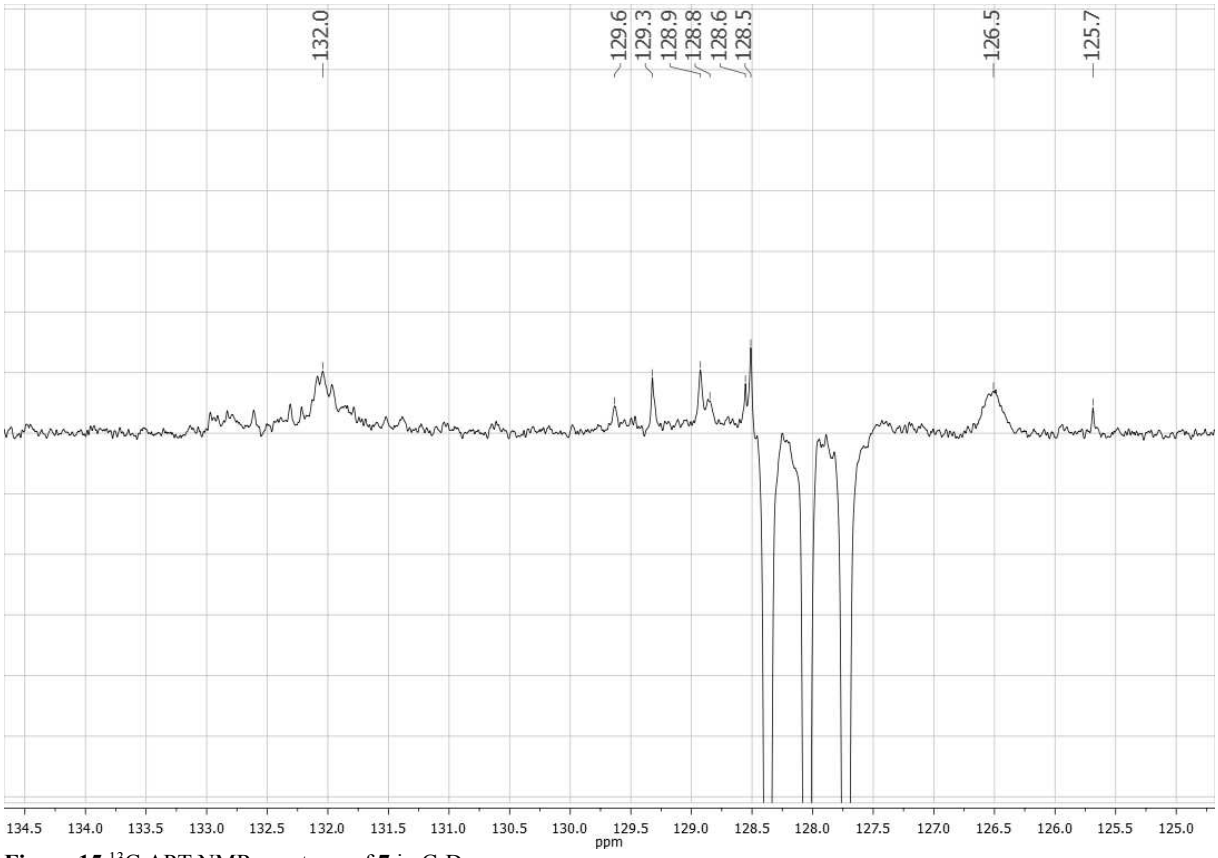

Figure 15 ^{13}C APT NMR spectrum of **7** in C_6D_6.

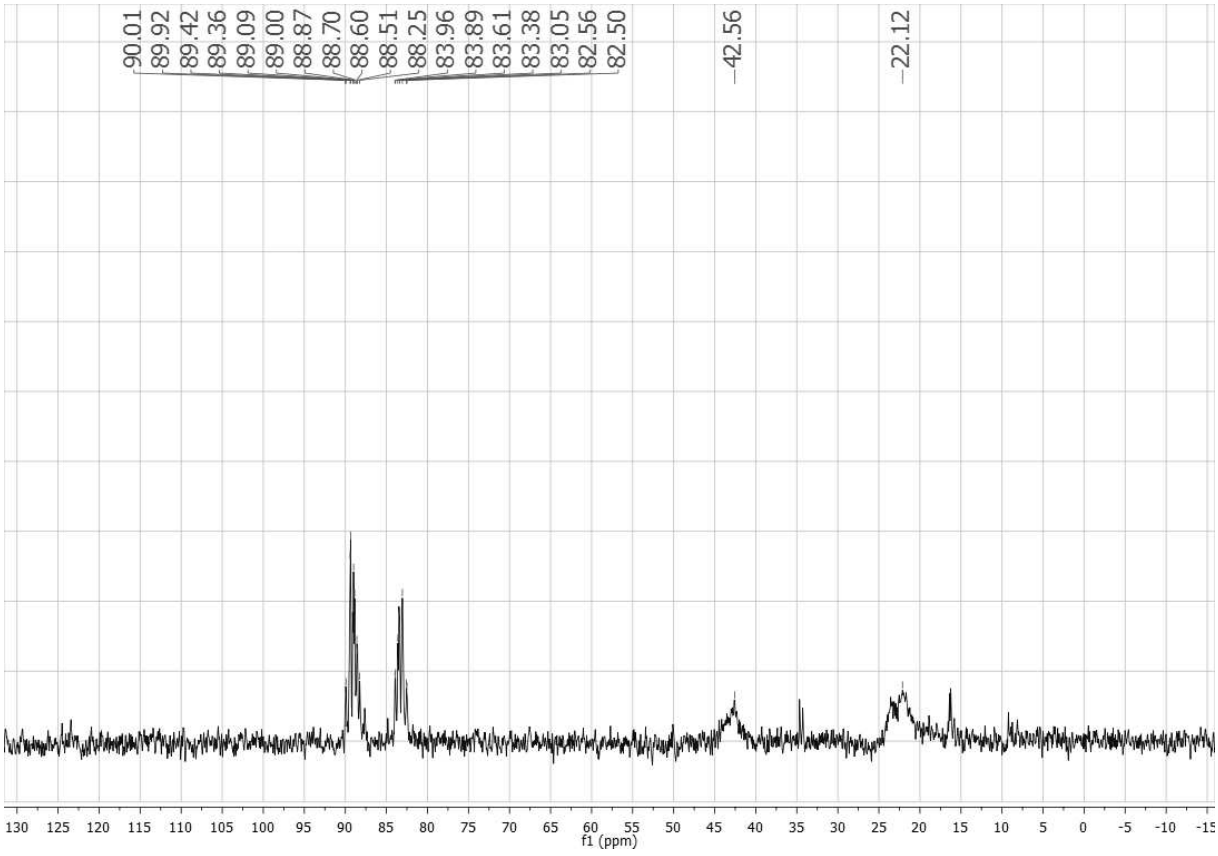

Figure 16 $^{31}P\{^1H\}$ NMR spectrum of **8** in C_6D_6.

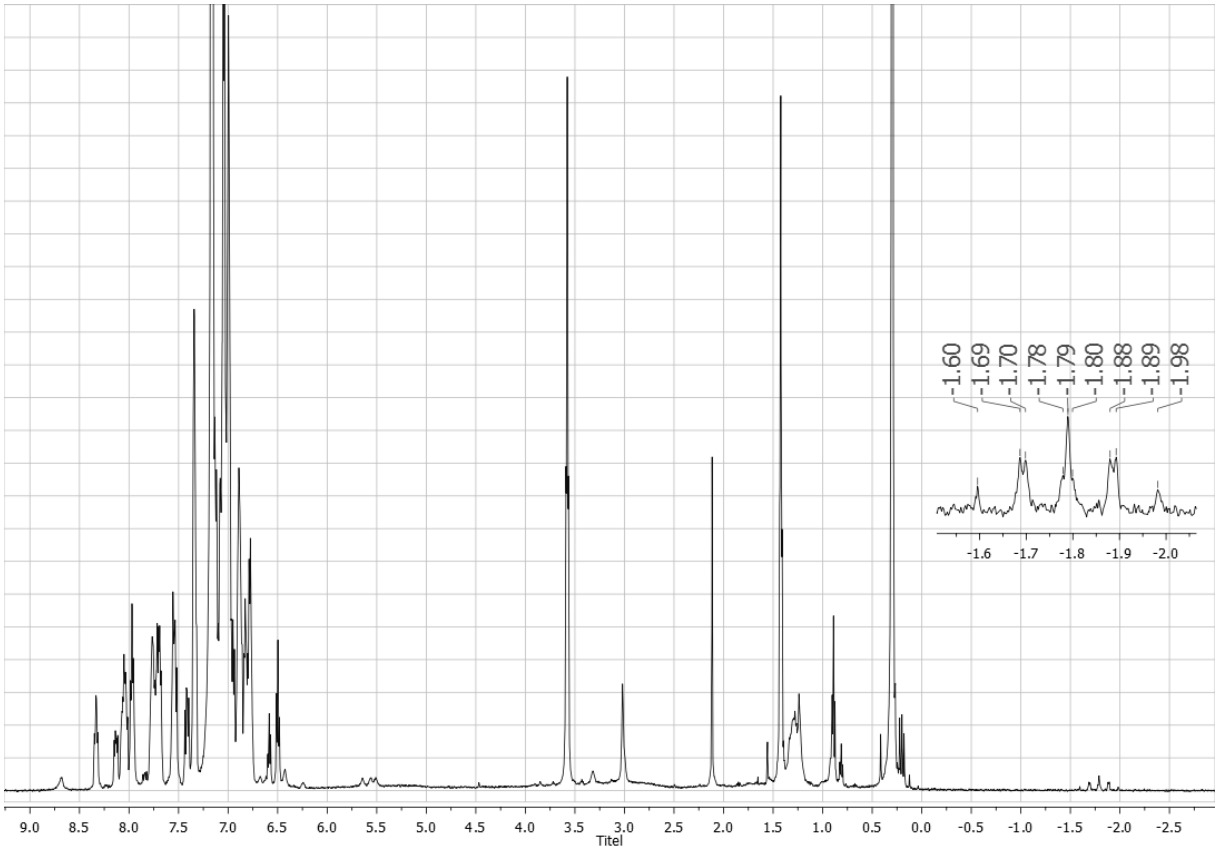

Figure 17 ^{1}H NMR spectrum of **8** in C_6D_6.

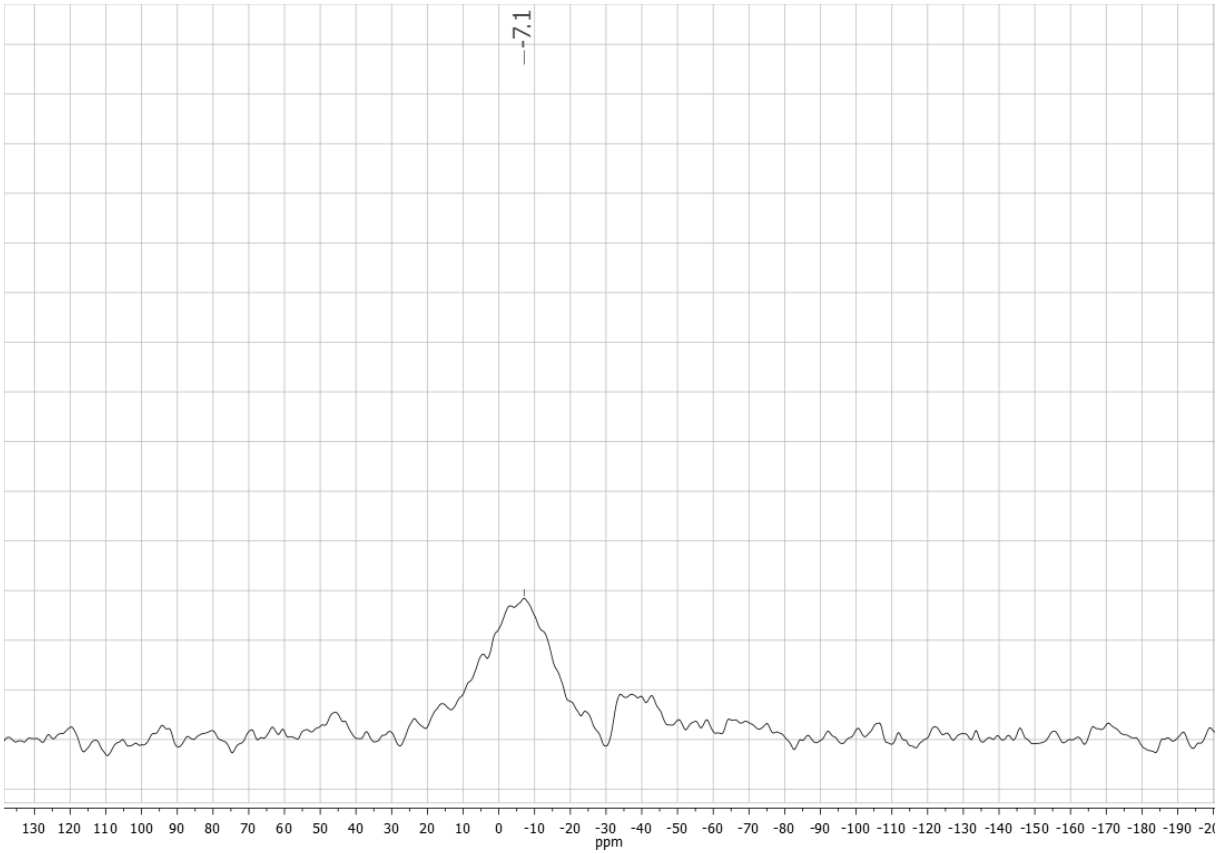

Figure 18 $^{11}B\{^{1}H\}$ NMR spectrum of **8** in C_6D_6.

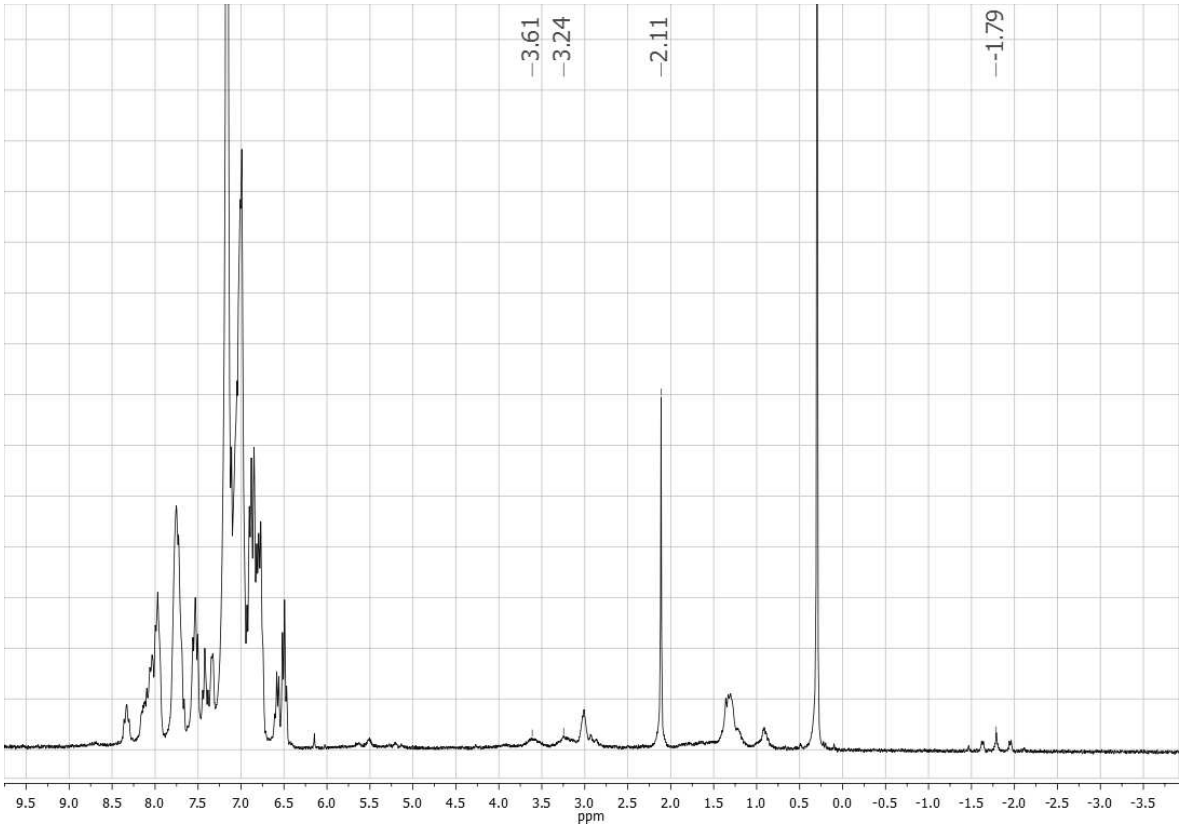

Figure 19 $^{1}H\{^{11}B\}$ NMR spectrum of **8** in C_6D_6.

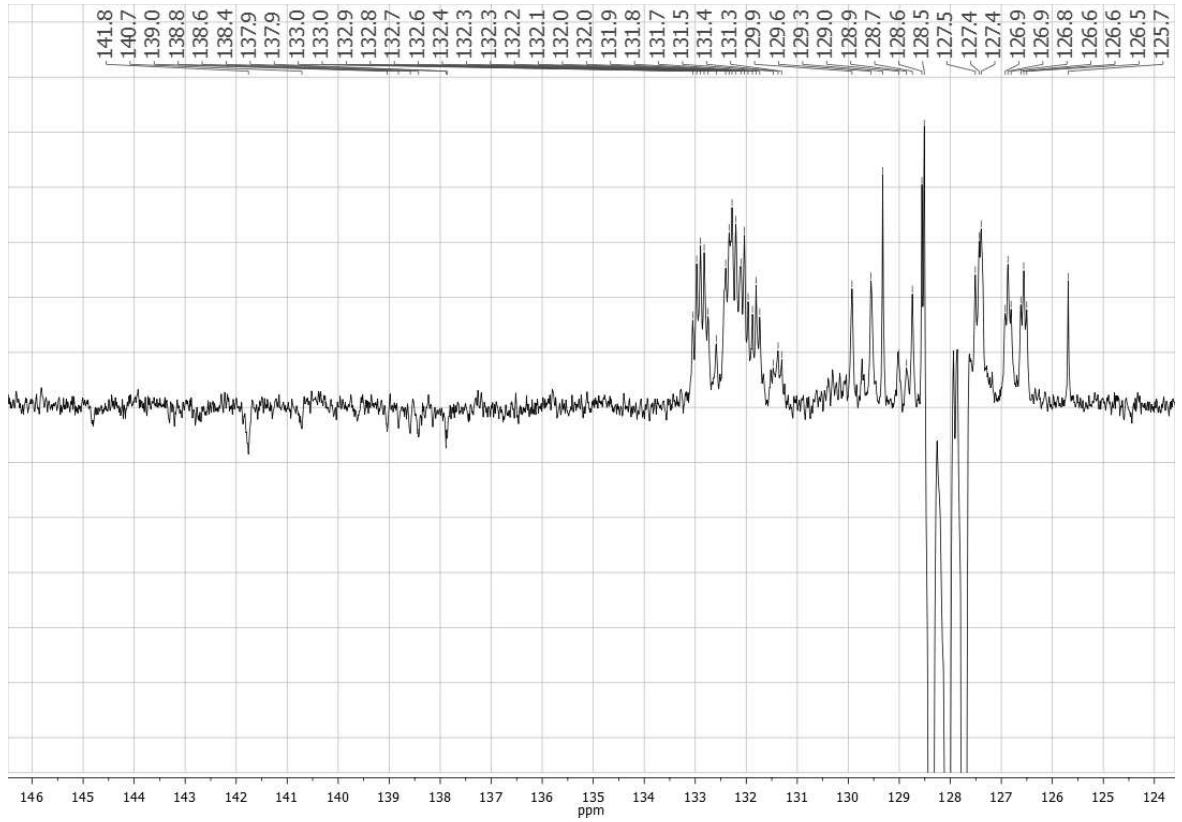

Figure 20 ^{13}C APT NMR spectrum of **8** in C_6D_6.

3. Variable Temperature NMR Measurements

The rate constants of the intramolecular exchange reactions in complex **2** were determined by line shape analysis of the hydride resonance as well as the bridging B-H resonance in the ^{1}H, $^{1}H\{^{11}B\}$ and $^{1}H\{^{31}P\}$ NMR spectra. The line broadening due to chemical exchange $\Delta\nu_{1/2}$ of these resonances was obtained as the difference of $\nu_{1/2}$ and the half height width of a reference peak at each temperature. As reference the CH_3-resonance of silicon grease was used. The approximate rate constants can be calculated using equation 1.

$$k_{ex} = 1/2\pi(\vartheta_{1/2} - \vartheta_{Ref}) \quad (1)$$

Table 1 Rate constants of complex **2** based on line shape analysis of ^{1}H NMR spectra at different temperatures.

T / K	k_{ex}/ s^{-1} (Fe-*H*)	k_{ex}/ s^{-1} (B-H_b)
230	13.4	39.9
240	16.1	59.7
250	15.8	63.7
260	16.1	31.3
270	16.0	22.8
280	21.8	45.2
290	45.6	78.1
300	117.6	135.4
310	247.4	291.8
320	597.6	573.4

4. X-Ray Crystallography

The single crystal X-ray diffraction data for the structural analysis of **2·2THF** has been collected using graphite-monochromated Mo-K_α-radiation ($\lambda_{MoK\alpha}$ = 0.71073) on the pixel detector system BRUKER D8-QUEST. The structures were using the dual-space algorithm of SHELXT.[3] Based on the crystal descriptions, numerical absorption corrections were applied.[4] Crystallographic data for **2** has been deposited at Cambridge Crystallographic Data Centre (CCDC 1551463) and can be obtained free of charge via www.ccdc.cam.ac.uk/. Details of the data collection and the refinement can be found in the supporting information.

Table 2 Crystallographic data for **2**.

Compound	**2·2THF**
Empirical formula	$C_{72}H_{64}BFeN_3O_2P_6 \cdot 2C_4H_8O$
Formula weight/g·mol^{-1}	1367.95
T/K	100(2)
Crystal system	Triclinic
Space group	$P\bar{1}$
a/Å	12.8745(5)
b/Å	12.9582(4)
c/Å	22.3650(8)
α/°	87.1140(10)
β/°	77.1990(10)
γ/°	69.4550(10)
V/Å^3	3405.5(2)
Z	2
ρ_{calc}/g·cm^{-3}	1.334
$\mu(MoK_\alpha)$/mm^{-1}	0.414
F(000)	1436
2θ range/°	4.28-50.60
Reflections measured	38392
Independent reflections	12395 (R_{Int} = 0.0554)
Ind. reflections (I>2σ(I))	9758
Parameters/Restraints	830/0
R_1 *(I>2σ(I))*	0.0461
wR_2 *(all data)*	0.1143
GooF (all data)	1.015
Max. peak/hole/e·Å^{-3}	0.906/-1.331
CCDC	1551463

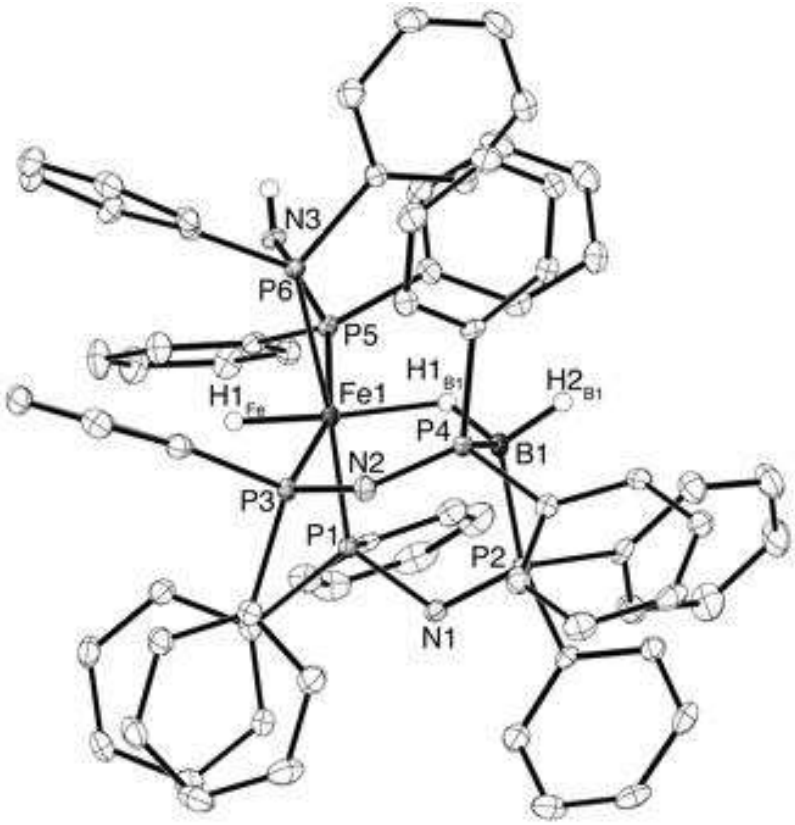

Figure 21 Molecular structure of complex **2** in the solid state (ellipsoids are drawn at 50% probability, carbon-bound hydrogen atoms are omitted). Selected bond length (Å) and angles (°): Fe1-P5 2.207(1), Fe1-P1 2.226(1), Fe1-P3 2.280(1), Fe1-P6 2.291(1), Fe1-H1$_{Fe}$ 1.43(3), Fe1-H1$_{B1}$ 1.73(3), P4-B1 1.929(3), P2-B1 1.976(3), B1-H2$_{B1}$ 1.11(3), B1-H1$_{B1}$ 1.20(3); P5-Fe1-P6 70.43(3), P1-Fe1-P3 94.05(3).

5. DFT Calculations

DFT calculations were performed with Orca 3.0.3 (**3-Me**) and Gaussian 09, Revision C.01 (other structures).[5] As functional Grimmes general-gradient approximated and dispersion including B97D functional was used.[6] All geometries were first optimized with the def2-SVP basis set and then reoptimized using the def2-TVPP basis set.[7] Minima were confirmed with frequency calculations (0 imaginary frequencies). Pictures of optimized structures were created with ChemCraft.[8] Geometry optimization of complex **2** was performed starting from the crystal structure. Natural Bond Orbital Analysis was done with NBO 5.9.[9] The simplified complex **2-Me** was then derived by replacing phenyl with methyl groups and subsequent geometry optimization. Bond lengths and selected angles, as well as Mulliken and NBO charges are given in tables 3-5. Comparison of bond lengths and charges between **2** and **2-Me** shows that the simplified complex **2-Me** is a suitable model for calculations on this system. Quantum Theory of Atoms in Molecules (QTAIM) analysis was done with AIMAll and pictures were created with AIMStudio.[10]

Numbering Scheme for atoms

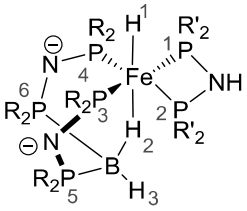

2: R, R' = Ph
2-Me: R, R' = Me
2-Me4Ph: R = Me
R' = Ph

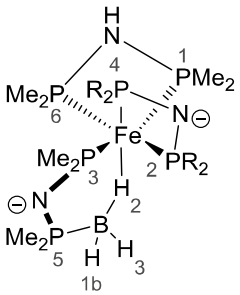

3-Me: R = Me
3-Me4Ph: R = Ph

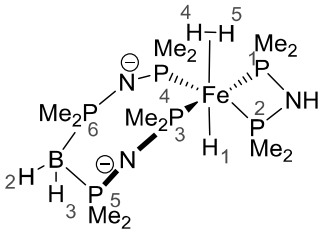

7-Me

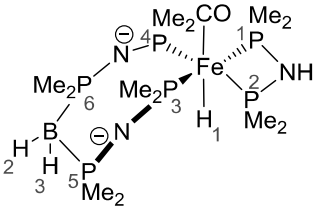

8-Me

Table 3 Comparison of experimental and calculated geometries for **3** and other calculated complexes. Bond lengths are given in Å and angles in °.

Bond/ Angle	X-ray **2**	DFT **2**	DFT **2-Me**	DFT **3-Me**	DFT **7-Me**	DFT **8-Me**
Fe-H1	1.43(3)	1.485	1.497		1.516	1.552
Fe-H2	1.73(3)	1.750	1.775	1.690		
B-H2	1.22(3)	1.266	1.275	1.275	1.219	1.221
B-H3	1.11(3)	1.211	1.218	1.217	1.216	1.216
B-H1b				1.208		
Fe-P1	2.2068(7)	2.184	2.166	2.249	2.198	2.224
Fe-P2	2.2906(8)	2.271	2.224	2.243	2.187	2.214
Fe-P3	2.2798(7)	2.279	2.224	2.275	2.251	2.261
Fe-P4	2.2256(7)	2.233	2.256	2.232	2.250	2.276
Fe-P6				2.206		
B-P5	1.928(3)	1.954	1.950	1.940	1.942	1.936
B-P6	1.976(3)	1.973	1.977		1.945	1.939
Fe-H4/5					1.561	
H4-H5					0.859	
Fe-CO						1.759
P1-Fe-P2	70.43(3)	71.48	70.79	98.69	72.13	72.03
H1-Fe-H2	173.8(14)	173.69	179.08			
P1-Fe-P3	161.72(3)	160.48	156.65	160.09	164.79	164.97
H2-B-H3	100.7(19)	104.38	104.43	103.41	112.60	111.90

Table 4 Mulliken Atomic Charges for the calculated complexes.

Atom	**2**	**2-Me**	**3-Me**	**7-Me**	**8-Me**
Fe	-0.144	-0.222	-0.044	-0.398	-0.437
H1	-0.211	-0.091		-0.150	-0.090
H1b			-0.009		
H2	-0.196	-0.118	-0.038	0.001	-0.001
H3	0.037	0.044	-0.014	0.009	0.001
B	-0.302	-0.268	-0.367	-0.288	-0.238
P1	0.748	0.456	0.346	0.519	0.377
P2	0.579	0.436	0.508	0.515	0.387
P3	0.533	0.454	0.516	0.551	0.498
P4	0.828	0.556	0.463	0.552	0.460
P5	0.643	0.521	0.487	0.528	0.460
P6	0.698	0.490	0.397	0.512	0.463
H4				-0.038	
H5				0.015	

Table 5 Natural Charges for the calculated complexes.

Atom	**2**	**2-Me**	**3-Me**	**7-Me**	**8-Me**
Fe	-2.192	-2.097	-0.830	-2.503	-2.572
H1	0.21	0.169		0.186	0.168
H1b			-0.007		
H2	0.073	0.064	-0.034	0.036	0.04
H3	0.027	0.04	0.014	0.049	0.049
B	-0.673	-0.713	-0.611	-0.903	-0.915
P1	1.617	1.535	1.310	1.588	1.599
P2	1.541	1.48	1.357	1.576	1.596
P3	1.632	1.581	1.377	1.686	1.705
P4	1.682	1.613	1.402	1.673	1.706
P5	1.593	1.585	1.556	1.626	1.62
P6	1.579	1.577	1.319	1.607	1.608
H4				0.184	
H5				0.204	

Possible intermediate for exchange of Fe-H and B-H

In order to better assess the possible exchange pathways, the enthalpy and Gibbs energy differences between **2** and the proposed intermediate **3** were calculated. For the methyl substituted complexes, $\Delta H_{2Me\text{-}3Me}$ is 14.30 kJ/mol and ΔG = 18.35 kJ/mol. Since from the experiments we expected ΔH to be negative, we checked if substitution of the phenyl groups might account for the unexpected value. After replacing methyl groups for phenyl groups, we indeed found ΔH to be negative. For four phenyl groups/methyl otherwise we obtained a ΔH of -10.40 kJ/mol and ΔG = 5.34 kJ/mol. Due to limited resources it was not possible to perform the calculations on the whole systems with all phenyl rings.

QTAIM Analysis

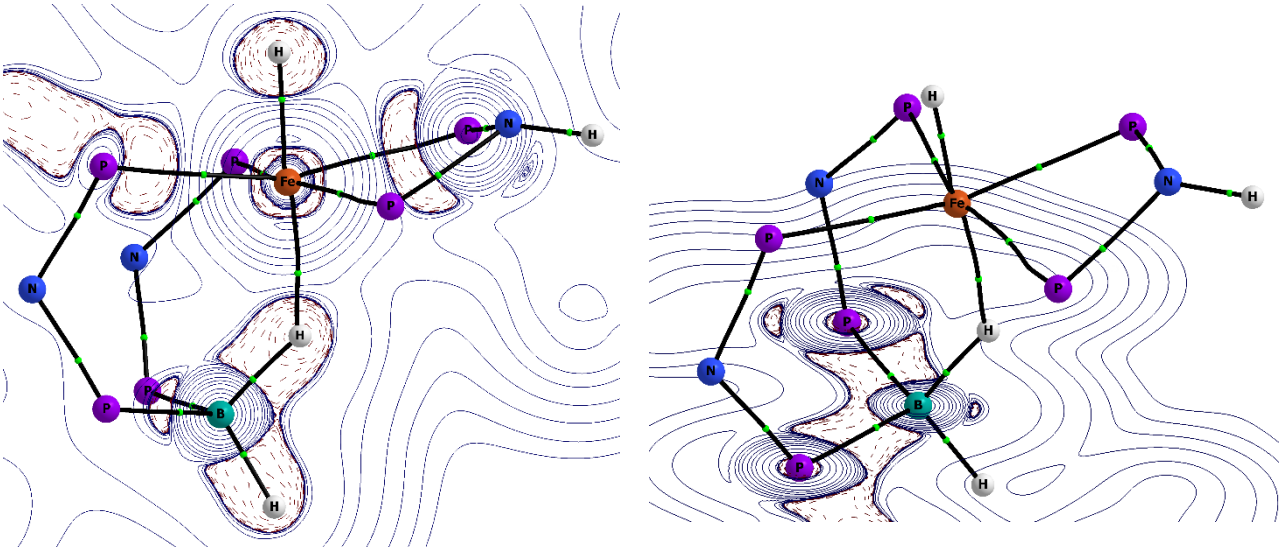

Figure 22 Molecular graph for **2-Me** from QTAIM analysis with contour plot of Laplacian in the H-Fe-H (left) and P-B-P (right) plane. Bond critical points are indicated as green dots. Positive values of the Laplacian (charge depletion) are depicted as solid blue lines and negative values (charge accumulation) as broken red lines. Methyl groups are omitted for clarity.

Table 6 Data (in atomic units) for selected bond critical points (bcp) for **2-Me** as obtained from QTAIM analysis.

BCP	ρ	$\nabla^2\rho$	ε	K_{bcp}	V_{bcp}	H_{bcp}
Fe-H1	0.130	0.117	0.014	0.072	-0.174	-0.102
Fe-H2	0.052	0.207	0.070	0.010	-0.071	-0.062
B-H2	0.134	-0.093	0.056	0.131	-0.239	-0.108
B-H3	0.164	-0.205	0.035	0.175	-0.299	-0.124
B-P5	0.134	-0.286	0.032	0.104	-0.137	-0.033
B-P6	0.128	-0.254	0.034	0.093	-0.122	-0.029
Fe-P1	0.101	0.166	0.115	0.044	-0.129	-0.085
Fe-P2	0.089	0.163	0.159	0.034	-0.110	-0.075
Fe-P4	0.094	0.142	0.044	0.037	-0.109	-0.072
Fe-P3	0.089	0.136	0.049	0.033	-0.100	-0.067

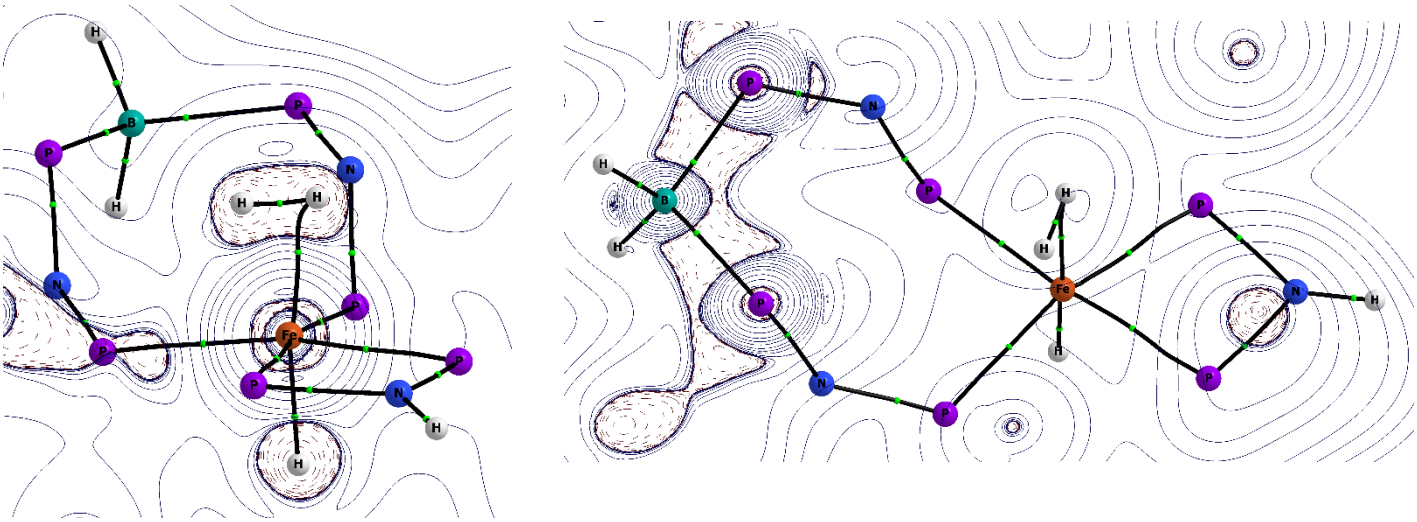

Figure 23 Molecular graph for **7-Me** from QTAIM analysis with contour plot of Laplacian in the H-Fe-H (left) and P-B-P (right) plane. Bond critical points are indicated as green dots. Positive values of the Laplacian (charge depletion) are depicted as solid blue lines and negative values (charge accumulation) as broken red lines. Methyl groups are omitted for clarity.

Table 7 Data (in atomic units) for selected bond critical points (bcp) for **7-Me** as obtained from QTAIM analysis.

BCP	ρ	$\nabla^2\rho$	ε	K_{bcp}	V_{bcp}	H_{bcp}
Fe-H1	0.127	0.101	0.046	0.074	-0.172	-0.099
Fe-H5	0.096	0.387	2.341	0.030	-0.157	-0.127
B-H2	0.162	-0.156	0.004	0.170	-0.300	-0.131
B-H3	0.164	-0.172	0.006	0.174	-0.304	-0.131
B-P5	0.132	-0.262	0.035	0.117	-0.168	-0.051
B-P6	0.131	-0.263	0.019	0.115	-0.164	-0.049
Fe-P1	0.096	0.161	0.075	0.040	-0.121	-0.080
Fe-P2	0.097	0.175	0.119	0.041	-0.126	-0.085
Fe-P4	0.092	0.121	0.044	0.036	-0.103	-0.067
Fe-P3	0.091	0.116	0.015	0.036	-0.101	-0.065

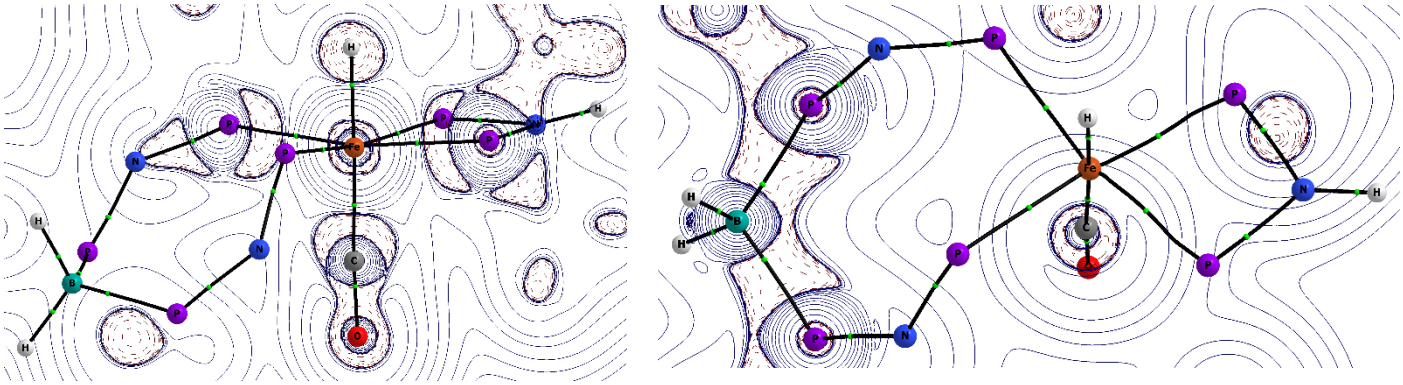

Figure 24 Molecular graph for **8-Me** from QTAIM analysis with contour plot of Laplacian in the H-Fe-H (left) and P-B-P (right) plane. Bond critical points are indicated as green dots. Positive values of the Laplacian (charge depletion) are depicted as solid blue lines and negative values (charge accumulation) as broken red lines. Methyl groups are omitted for clarity.

Table 8 Data (in atomic units) for selected bond critical points (bcp) for **8-Me** as obtained from QTAIM analysis.

BCP	ρ	$\nabla^2\rho$	ε	K_{bcp}	V_{bcp}	H_{bcp}
Fe-H1	0.115	0.123	0.006	0.058	-0.147	-0.089
Fe-C	0.156	0.600	0.032	0.076	-0.302	-0.226
B-H2	0.160	-0.162	0.009	0.168	-0.296	-0.128
B-H3	0.163	-0.179	0.015	0.173	-0.301	-0.128
B-P5	0.132	-0.263	0.038	0.117	-0.168	-0.051
B-P6	0.132	-0.268	0.034	0.114	-0.161	-0.047
Fe-P1	0.091	0.155	0.075	0.035	-0.110	-0.074
Fe-P2	0.162	0.264	0.042	0.132	-0.330	-0.198
Fe-P4	0.088	0.103	0.100	0.033	-0.092	-0.059
Fe-P3	0.090	0.109	0.063	0.034	-0.096	-0.061

Literature

[1] H. Nöth, L. Z. Meinel, *Z. Anorg. Allg. Chem.* **1967**, *349*, 225-240.

[2] R. C. Todd, M. M. Hossain, K. V. Josyula, P. Gao, J. Kuo, C. T. Tan, *Tetrahedron Lett.* **2007**, *48*, 2335-2337.

[3] G. Sheldrick, *Acta Cryst. Sect. A* **2015**, *71*, 3-8.

[4] Bruker, *APEX3, SAINT and SADABS. Bruker AXS Inc* **2015**, Madison , Wisconsin, USA.

[5] a) M. J. Frisch, G. W. Trucks, H. B. Schlegel, G. E. Scuseria, M. A. Robb, J. R. Cheeseman, G. Scalmani, V. Barone, B. Mennucci, G. A. Petersson, H. Nakatsuji, M. Caricato, X. Li, H. P. Hratchian, A. F. Izmaylov, J. Bloino, G. Zheng, J. L. Sonnenberg, M. Hada, M. Ehara, K. Toyota, R. Fukuda, J. Hasegawa, M. Ishida, T. Nakajima, Y. Honda, O. Kitao, H. Nakai, T. Vreven, J. A. Montgomery, J. E. P. Jr., F. Ogliaro, M. Bearpark, J. J. Heyd, E. Brothers, K. N. Kudin, V. N. Staroverov, R. Kobayashi, J. Normand, K. Raghavachari, A. Rendell, J. C. Burant, S. S. Iyengar, J. Tomasi, M. Cossi, N. Rega, J. M. Millam, M. Klene, J. E. Knox, J. B. Cross, V. Bakken, C. Adamo, J. Jaramillo, R. Gomperts, R. E. Stratmann, O. Yazyev, A. J. Austin, R. Cammi, C. Pomelli, J. W. Ochterski, R. L. Martin, K. Morokuma, V. G. Zakrzewski, G. A. Voth, P. Salvador, J. J. Dannenberg, S. Dapprich, A. D. Daniels, Farkas, J. B. Foresman, J. V. Ortiz, J. Cioslowski, D. J. Fox, *Gaussian 09 Revision C.01, Gaussian Inc. Wallingford CT 2009*; b) F. Neese, *WIREs Comput. Mol. Sci.* **2012**, *2*, 73-78.

[6] S. Grimme, *J. Comput. Chem.* **2006**, *27*, 1787-1799.

[7] a) A. Schäfer, H. Horn, R. Ahlrichs, *J. Chem. Phys.* **1992**, *97*, 2571; b) F. Weigend, R. Ahlrichs, *Phys. Chem. Chem. Phys.* **2005**, *7*, 3297-3305.

[8] *Chemcraft version 1.8*, www.chemcraftprog.com.

[9] E. D. Glendening, J.K. Badenhoop, A. E. Reed, J. E. Carpenter, J. A. Bohmann, C. M. Morales, F. Weinhold, *(Theoretical Chemistry Institute, University of Wisconsin, Madison, WI, 2012)* **NBO 5.9**, www.chem.wisc.edu/~nbo5.

[10] Todd A. Keith, *AIMAll (Version 17.01.25)* **2017**, www.aim.tkgristmill.com, TK Gristmill Software, Overland Park KS, USA.

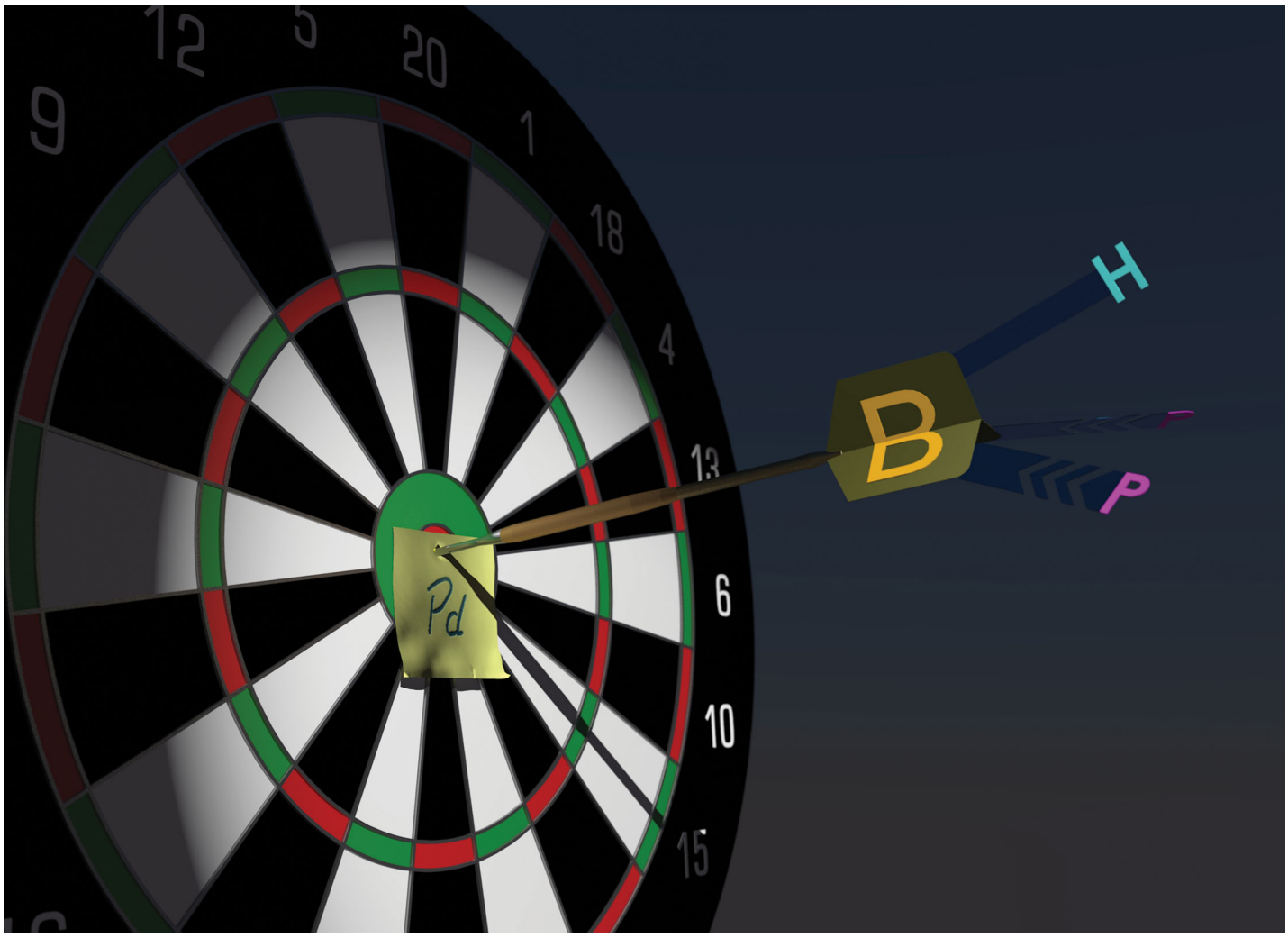

Showcasing research from the group of Robert Langer at the Department of Chemistry, Philipps-University Marburg, Germany

Donor ligands based on tricoordinate boron formed by B–H-activation of bis(phosphine)boronium salts

A novel method for the preparation of PBP-pincer complexes from bis(phosphine)boronium salts is reported. The central $(R_3P)_2HB$-moiety in a palladium complex is demonstrated to be an L-type ligand, therewith completing a series of pincer-type complexes with Z-, X- and L-type boron-based ligands.

As featured in:

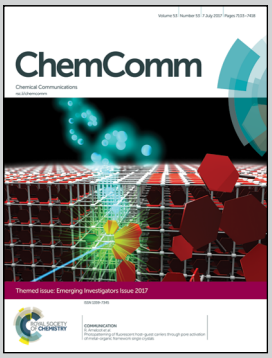

See Robert Langer *et al.*, *Chem. Commun.*, 2017, **53**, 7230.

ROYAL SOCIETY OF CHEMISTRY

rsc.li/chemcomm

Registered charity number: 207890

ChemComm

COMMUNICATION

View Article Online
View Journal | View Issue

Cite this: *Chem. Commun.*, 2017, 53, 7230

Received 27th March 2017,
Accepted 27th April 2017

DOI: 10.1039/c7cc02335a

rsc.li/chemcomm

Donor ligands based on tricoordinate boron formed by B–H-activation of bis(phosphine)boronium salts†‡

Maik Grätz,[a] Andreas Bäcker,[a] Lisa Vondung,[a] Leon Maser,[a] Arian Reincke[a] and Robert Langer *[ab]

We report a novel method for the preparation of PBP-pincer complexes from bis(phosphine)boronium salts. The central $(R_3P)_2HB$-moiety in a palladium complex is demonstrated to be a L-type ligand, therewith completing a series of pincer-type complexes with Z-, X- and L-type boron-based ligands, respectively.

Tricoordinate boron compounds are typically Lewis acids with a vacant p_z-orbital, whose dimerization is often prevented by π-donating substituents such alkoxides or amides. The interaction of such boron-species with electron rich metal complexes is usually described by a dative bond from the central metal atom to the electron deficient BR_3-ligand.[1–18] According to the covalent bond classification these σ-accepting ligands are referred to as Z-type ligands.[19]

The utilization of at least two π-accepting substituents at the boron atom allows for the stabilization of trigonal planar compounds with an occupied p_z-orbital, which are formally construed as boron(I) compounds.[20,21] Examples for these kinds of nucleophilic boron compounds vary from tricyanoborate dianions[22–24] over dicyanoboryl anions[25] to ligand stabilized borylenes.[26–30] Quantum chemical investigations of the latter indicate that species like L_2HB: are sufficiently stabilized by cyclic alkyl amino carbenes (CAAC) and N-heterocyclic carbenes (NHC), but for ligands like carbon monoxide or phosphines the B–L-bond dissociation energy has been calculated to be rather low to expect easily accessible stable compounds.[31] However, experimental studies have shown that nucleophilic boron compounds are reacting with transition metal precursors such as [(L)MCl] (M = Cu, Au; L = phosphine, carbene)[25,32] and $[Cr(CO)_5(thf)]$.[32] Furthermore, quantum chemical investigations predict that reactive borylenes such as $(R_3P)_2HB$: can be stabilized as ligands in gold complexes.[31]

In this context, we recently observed the formation of an iron PBP-complex containing a central $(R_3P)_2HB$-group coordinated to the iron atom.[33,34] Analysis of structural and spectroscopic properties of this compound in combination with a detailed bonding analysis and reactivity studies indicated a L-type donor interaction of the tricoordinate boron-group to the central iron atom. The arm-(de)protonation of this complex results in overall dianionic, anionic and neutral pincer-type ligands without significant change of the bonding situation. However, this iron complex is formed in an odd rearrangement that exclusively occurred in the reported case.

Due to the unexpected "Umpolung" of the ligand properties in combination with the unusual reactivity, we were interested to investigate further transition metals with this pincer-type ligand. Herein we report the formation of such PBP-type pincer complexes by B–H-activation of bis(phosphine)boronium salts. Our study shows that in the case of nucleophilic metal complexes P–B-bond cleavage can be competitive. The obtained palladium(II) complex reported herein nicely illustrates the different coordination modes, ranging from $(R_3P)_2HB$-groups to LR_2B-ligands and typical BR_3-based Z-type ligands (Scheme 1).

Based on the finding that a bis(phosphine)boronium ligand is involved in the reversible B–H-reductive elimination,[34] we supposed that PBP-pincer complexes should generally be accessible by oxidative addition of $(R_3P)_2BH_2$-cations to an unsaturated metal fragment. Starting from the readily available

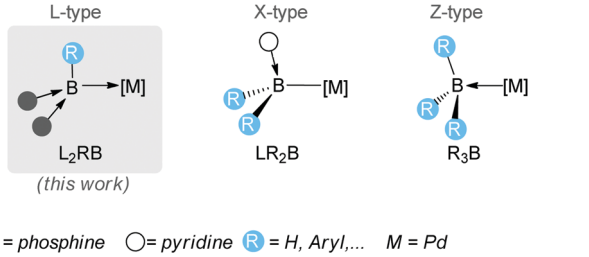

Scheme 1 Comparison of different classes of boron-based ligands.

[a] Department of Chemistry, Philipps-Universität Marburg, Hans-Meerwein-Str., 35032 Marburg, Germany. E-mail: robert.langer@chemie.uni-marburg.de
[b] Lehn Institute of Functional Material (LIFM), Sun Yat-Sen University Guangzhou (SYSU), Xingang Road West, Guangzhou 510275, P. R. China

† Dedicated to Dieter Fenske on occasion of his 75th birthday.

‡ Electronic supplementary information (ESI) available. CCDC 1540277–1540279. For ESI and crystallographic data in CIF or other electronic format see DOI: 10.1039/c7cc02335a

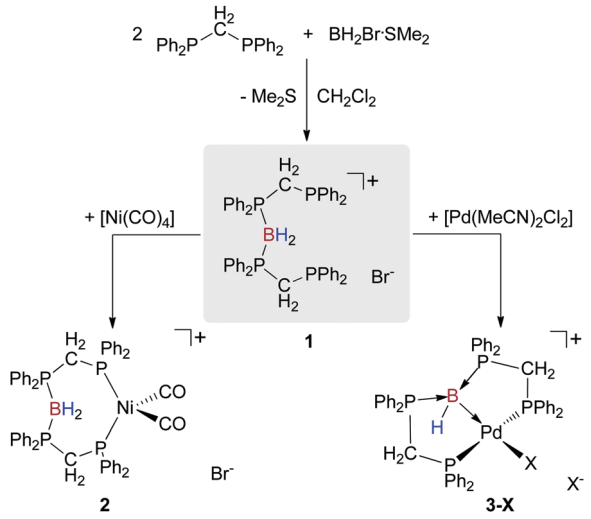

Scheme 2 Synthesis of the bis(phosphine)boronium salt **1** from dppm and its reactivity towards nickel and palladium precursors (X = Cl, Br).

1,1-bis(diphenylphosphino)methane (dppm), we attempted a possible synthesis by the reaction with 0.5 equivalents of $BH_2Br{\cdot}SMe_2$, leading to the formation of a single reaction product according to $^{31}P\{^1H\}$ and $^{11}B\{^1H\}$ NMR spectra (Scheme 2). The appearance of a broad resonance at 8.8 ppm and a doublet resonance at −22.7 ppm ($^2J_{PP}$ = 66.1 Hz) in the $^{31}P\{^1H\}$ NMR spectrum indicates that one phosphorus atom of each dppm unit is bound to boron. The broad resonance at −33.1 ppm in the $^{11}B\{^1H\}$ NMR spectrum is in agreement with previously reported bis(phosphine)boronium cations.[35–39] Upon ^{11}B-decoupling of the ^1H NMR spectrum, a triplet resonance at 2.69 ppm ($^2J_{HP}$ = 20.4 Hz) with an integral of two is observed, which is assigned to the BH_2-group. Finally, we confirmed the formation of the bis(phosphine)-boronium salt **1** by X-ray diffraction of suitable single crystals.[40]

Next, we investigated the reactivity of **1** towards different nickel and palladium precursors. The reaction with one equivalent of [Ni(cod)$_2$] at −78 °C resulted in an orange solution, which subsequently turned darker with continued stirring. The $^{31}P\{^1H\}$ NMR spectra at ambient temperature showed several singlet resonances, indicating that P–B-bond cleavage occurred in a rather unselective reaction. In one case, it was possible to grow suitable crystals for X-ray diffraction from the reaction mixture, which were identified as [(dppm)$_3$Ni$_3$Br$_2$].[40] However, the yield of these crystals was very low and their formation was not completely reproducible. Nonetheless, the formation of such species provides further evidence that P–B-bond cleavage is the preferred reaction pathway with [Ni(cod)$_2$]. The reaction with [Ni(CO)$_4$] leads to a single reaction product without decomposition of the pre-ligand (Scheme 2), as judged by the appearance of a doublet resonance at 20.8 ppm ($^2J_{PP}$ = 33.3 Hz) and a broad resonance at 7.5 ppm. In agreement with the observation of a two-proton-resonance at 4.28 ppm for the BH_2-group, the single crystal X-ray diffraction analysis confirmed the formation of the cationic dicarbonyl complex **2** with an unreacted BH_2-moiety (Fig. 1). The P–B-bond distances (1.918–1.920 Å) in the eight-membered ring formed by the pre-ligand and a Ni(CO)$_2$-fragment

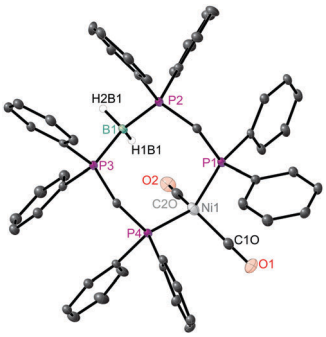

Fig. 1 Molecular structure of the cation in **2** in the solid state (ellipsoids are drawn at 30% probability, carbon-bound hydrogen atoms are omitted); selected distances (Å) and angles (°): Ni1–C2O 1.786(4), Ni1–C1O 1.788(4), Ni1–P4 2.2028(9), Ni1–P1 2.2143(9), B1–P2 1.918(4), B1–P3 1.920(4); P4–Ni1–P1 113.24(3), P2–B1–P3 118.3(2).

are slightly shorter than the distances in **1** (1.927–1.942 Å). With 2.203–2.214 Å the Ni–P-bond distances in **2** are marginally shorter than in related nickel(0)-dicarbonyl complexes with wide bite-angle diphosphine ligands.[41,42]

The reaction of **1** with palladium precursors turned out to be non-uniform as well. With [Pd(PPh$_3$)$_4$], the formation of precipitate is observed and various products are detected in the $^{31}P\{^1H\}$ NMR spectrum, including the palladium(I)-complex [(dppm)PdBr]$_2$.[43] In a similar manner as with [Ni(cod)$_2$], P–B-bond-cleavage seems to be the preferred reaction pathway. In contrast, the reaction of **1** with [Pd(MeCN)$_2$Cl$_2$] leads to the formation of a precipitate, while the $^{31}P\{^1H\}$ NMR spectrum of the supernatant solution lacks any resonances. The $^{31}P\{^1H\}$ NMR spectrum of the precipitate dissolved in DMSO exhibits a doublet of doublets resonance at 81.8 ppm and a broad resonance at 59.3 ppm, indicating the formation of a novel PBP-type pincer complex [(HB{dppm}$_2$)PdCl]$^+$ (**3-Cl**).§ In addition, a triplet resonance at 84.4 ppm of low intensity is observed (ratio 9 : 1) that is assigned to the palladium-bound phosphorus atoms of the corresponding bromido complex [(HB{dppm}$_2$)PdBr]$^+$ (**3-Br**). Meanwhile, the $^{11}B\{^1H\}$ NMR spectrum exhibits only one broad resonance at −24.5 ppm, whose chemical shift is in agreement with previously reported ligand-stabilized borylenes bound to a transition metal.[25,32,44] To confirm the identities of **3**, we tried to grow suitable single crystals for X-ray diffraction, but all attempts resulted in precipitation and the crystallization of minor quantities of [**3-Br**]Br (Fig. 2).

The cationic palladium complex **3-Br** exhibits a direct Pd–B-bond (2.114–2.129 Å)[40] to the central (R$_3$P)$_2$HB-group of the newly formed pincer-ligand. Pd–Br- and Pd–P-distances are in agreement with other square planar palladium(II)–phosphine complexes ($\sum Pd_\alpha$ = 360.42°).[45–48]

Tricoordinate boron compounds bound to a transition metal are usually interpreted as σ-accepting Z-type ligands, which in the present case would result in the formulation of palladium(0) that, in turn, is expected to be non-square planar. However, the square planar coordination geometry and the detected bond length in **3-Br**, as well as the spectroscopic data are in agreement with a palladium(II) complex containing a boron-based donor

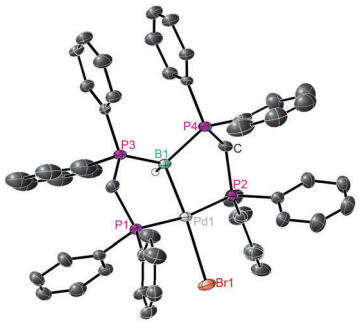

Fig. 2 Molecular structure of the cation in **3-Br** in the solid state (ellipsoids are drawn at 30% probability, carbon-bound hydrogen atoms are omitted). Selected distances (Å) and angles (°): Pd1–B1 2.129(11), Pd1–Br1 2.561(6), Pd1–P1 2.3031(15), Pd1–P2 2.3041(15), P3–B1 1.929(12), 2.005(12); P2–Pd1–P1 170.98(5), B1–Pd1–Br1 168.3(3).

ligand. To get further insight, we performed quantum chemical investigations for the methyl-substituted complexes using density functional theory (DFT). Analysis of the frontier molecular orbitals in $\mathbf{3^{Me}}$**-Cl** reveals that two B–Pd–Cl interactions are relevant for the description of the Pd–B-bond. The HOMO−2 involves a bonding interaction between boron and palladium, which appears to have π-type symmetry (Fig. 3). The HOMO−8 in $\mathbf{3^{Me}}$**-Cl** includes two bonding interactions, Pd–B and Pd–Cl, with a σ-type symmetry. The neutral palladium(II) complex [(κ^{2}P,P′-HB{dmpm}$_2$)PdBrCl] ($\mathbf{4^{Me}}$**-Cl/Br**) with a dissociated B–H-group was found to be an energetic minimum as well ($\Delta E_{3^{Me}-4^{Me}}$ = +80 kJ mol^{-1}). In agreement with previous quantum chemical investigations on phosphine-stabilized borylenes,[31] the boron atom in the dissociated (PR$_3$)$_2$HB-moiety exhibits a trigonal planar environment with a HOMO of π-type symmetry. The occupied p$_z$-orbital at the boron atom in $\mathbf{4^{Me}}$**-Cl/Br**, which is stabilized by π-back bonding to the phosphine substituents, clearly indicates the Lewis-base nature of the dissociated ligand. Natural population analysis revealed a negative charge of −0.85*e* at the boron atom in $\mathbf{3^{Me}}$**-Cl**, which is in agreement with an overall charge transfer of 0.26*e* relative to $\mathbf{4^{Me}}$**-Cl/Br**. This view is further supported by a topological analysis of the electron density within the Quantum Theory of Atoms in Molecules (QTAIM) framework. The Laplacian of the electron density shows that electron density is donated from the boron atom towards the bond critical point (bcp) of the boron palladium bond (Fig. 4).

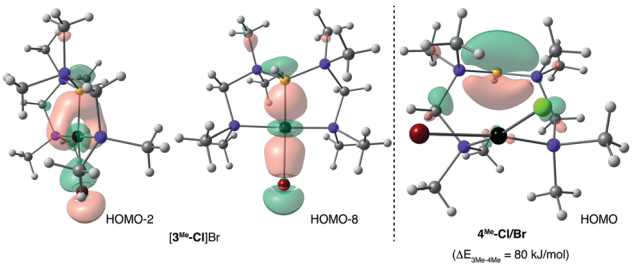

Fig. 3 HOMO−2 and HOMO−8 of complex $\mathbf{3^{Me}}$**-Cl**; HOMO of complex $\mathbf{4^{Me}}$**-Cl/Br** (B97D/def2-TZVPP, contour value 0.05, Pd: black, P: violet, Br: red, Cl: green, B: yellow).

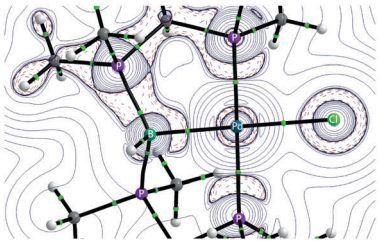

Fig. 4 Molecular graph for complex $\mathbf{3^{Me}}$**-Cl** derived from QTAIM analysis with contour plot of the Laplacian in the B–Pd–P-plane (bcps: green dots; charge depletion ($\nabla^2\rho > 0$): solid blue lines; charge accumulation ($\nabla^2\rho < 0$): dotted red lines).

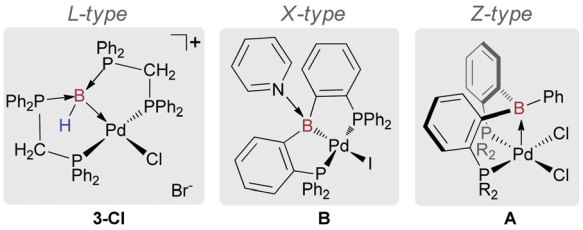

Scheme 3 Representative examples for different boron ligand types in palladium(II) complexes (R = ^{i}Pr).

A look on previously reported palladium PBP-pincer complexes reveals that the three basic ligand types according to the covalent bond classification can formally be realized in palladium(II) complexes (Scheme 3). Using an ambiphilic pincer ligand with a central BR$_3$-group, Bourissou and co-workers reported the square pyramidal palladium(II) complex **A**, in which the central tricoordinate boron atom (BR$_3$) acts as a σ-accepting Z-type ligand in the apical position.[49] Very recently, Tauchert and co-workers described the palladium(II) pincer-type complex **B** with a pyridine-stabilized boryl-group,[50] in which the central LR$_2$B-group can formally be regarded as a X-type ligand. The cationic palladium(II) complex **3** contains a phosphine-stabilized borylene acting as a L-type donor group. In the following, we aimed to identify differences in structural, spectroscopic and quantum chemical data (Table 1).

The long Pd–B-bond and the low pyramidalization of the boron atom in **A** indicate a rather weak interaction, while the interaction in **3** and **B** are found to be significantly stronger. The Pd–P-bond distances, however, are found to be very similar in all three complexes. A clear trend within this series of complexes is observed for the chemical shift in the ^{11}B{^{1}H} NMR spectra: the Z-type ligand exhibits a resonance at 59 ppm, the X-type at 17 ppm and the chemical shift for complex **3** is observed at −24.5 ppm.

We performed quantum chemical calculations of the methyl-substituted complexes $\mathbf{3^{Me}}$**-Cl**, $\mathbf{B^{Me}}$ and $\mathbf{A^{Me}}$ to obtain further information within this series: the natural population analysis reveals a positive charge of +0.90*e* at the boron atom of the Z-type ligand in $\mathbf{A^{Me}}$, which is considerably decreased for $\mathbf{B^{Me}}$ (+0.43*e*) and finally results in a negative charge of −0.85*e* for the boron atom in $\mathbf{3^{Me}}$**-Cl**. Using QTAIM analysis, we identified bcps for the Pd–B-bond in all three complexes. The electron and energy

Table 1 Selected quantum chemical and spectroscopic data, bond distances and angles

	3-X (L-type)	**B** (X-type)[a]	**A** (Z-type)[b]
d_{Pd-B}/Å	2.129	2.196	2.650
d_{Pd-P}/Å	2.203–2.204	2.275–2.284	2.288–2.315
$\sum_{B\alpha}$/°	319–343[c]	330.7	354.9
δ_B/ppm	−24.5	17	59
	3^{Me}-Cl	**B^{Me}**	**A^{Me}**
q_B (NBO)[d]	−0.848	+0.434	+0.902
ρ_{bcp} (Pd–B)[e]	0.091	0.086	0.020
H_{bcp} (Pd–B)[e]	−0.037	−0.029	−0.009

[a] Data taken from ref. 32. [b] Data taken from ref. 31. [c] The BH-group in **3** was disordered and therefor two values are reported; the big discrepancy might be a result of inaccurate location of the hydrogen atoms. [d] Charges from natural bond orbital (NBO) analysis. [e] Electron and energy density at bond critical point (bcp) from QTAIM analysis.

densities at the bcps support this observation as well, although the qualitative interpretation of the orbital shapes and the contour plot of the Laplacians of the electron density appear quite similar for **3^{Me}-Cl** and **B^{Me}**.[40]

In conclusion, we described a synthetic method for the simple preparation of pincer-type complexes containing a phosphine-stabilized borylene as donor group (L-type). Our study shows that P–B-bond cleavage of **1** can be competitive with nucleophilic metal centres. Based on bonding analysis and the comparison of structural and spectroscopic properties, the boron-based ligand in **3** is best described as an electron donating L-type ligand. With this example, it was possible for the first time to compare structurally related palladium(II) complexes with the three different types of boron-based ligands according to the covalent bond classification.

We gratefully acknowledge financial support from the Deutsche Forschungsgemeinschaft (LA 2830/3-2), the Erich-Becker-Stiftung (R. L.) and the Studienstiftung des deutschen Volkes (L. V.). We also thank Dr Paul Jerabek and Prof. Dr Peter Schwerdtfeger for helpful discussions.

Notes and references

§ Further indication for **3-Cl** being the major isomer is provided by ESI-MS.

1 A. F. Hill, G. R. Owen, A. J. P. White and D. J. Williams, *Angew. Chem., Int. Ed.*, 1999, **38**, 2759–2761.
2 H. Braunschweig and R. D. Dewhurst, *Dalton Trans.*, 2011, **40**, 549–558.
3 G. R. Owen, P. H. Gould, A. Hamilton and N. Tsoureas, *Dalton Trans.*, 2010, **39**, 49–52.
4 G. R. Owen, P. Hugh Gould, J. P. H. Charmant, A. Hamilton and S. Saithong, *Dalton Trans.*, 2010, **39**, 392–400.
5 N. Tsoureas, Y.-Y. Kuo, M. F. Haddow and G. R. Owen, *Chem. Commun.*, 2011, **47**, 484–486.
6 J. S. Figueroa, J. G. Melnick and G. Parkin, *Inorg. Chem.*, 2006, **45**, 7056–7058.
7 V. K. Landry, J. G. Melnick, D. Buccella, K. Pang, J. C. Ulichny and G. Parkin, *Inorg. Chem.*, 2006, **45**, 2588–2597.
8 K. Pang, S. M. Quan and G. Parkin, *Chem. Commun.*, 2006, 5015–5017.
9 K. Pang, J. M. Tanski and G. Parkin, *Chem. Commun.*, 2008, 1008–1010.
10 M. E. Moret and J. C. Peters, *Angew. Chem., Int. Ed.*, 2011, **50**, 2063–2067.
11 M. E. Moret and J. C. Peters, *J. Am. Chem. Soc.*, 2011, **133**, 18118–18121.
12 H. Fong, M. E. Moret, Y. Lee and J. C. Peters, *Organometallics*, 2013, **32**, 3053–3062.
13 I. R. Crossley, A. F. Hill and A. C. Willis, *Organometallics*, 2005, **24**, 1062–1064.
14 I. R. Crossley, A. F. Hill and A. C. Willis, *Organometallics*, 2006, **25**, 289–299.
15 I. R. Crossley, M. R. S. J. Foreman, A. F. Hill, G. R. Owen, A. J. P. White, D. J. Williams and A. C. Willis, *Organometallics*, 2008, **27**, 381–386.
16 I. R. Crossley and A. F. Hill, *Dalton Trans.*, 2008, 201–203.
17 I. R. Crossley, A. F. Hill and A. C. Willis, *Organometallics*, 2008, **27**, 312–315.
18 I. R. Crossley, A. F. Hill and A. C. Willis, *Organometallics*, 2010, **29**, 326–336.
19 M. L. H. Green, *J. Organomet. Chem.*, 1995, **500**, 127–148.
20 J. Cid, H. Gulyas, J. J. Carbo and E. Fernandez, *Chem. Soc. Rev.*, 2012, **41**, 3558–3570.
21 H. Gulyás, A. Bonet, C. Pubill-Ulldemolins, C. Solé, J. Cid and E. Fernández, *Pure Appl. Chem.*, 2012, **84**, 2219.
22 E. Bernhardt, V. Bernhardt-Pitchougina, H. Willner and N. Ignatiev, *Angew. Chem., Int. Ed.*, 2011, **50**, 12085–12088.
23 J. Landmann, F. Keppner, D. B. Hofmann, J. A. P. Sprenger, M. Häring, S. H. Zottnick, K. Müller-Buschbaum, N. V. Ignat'ev and M. Finze, *Angew. Chem., Int. Ed.*, 2017, **56**, 2795–2799.
24 J. Landmann, J. A. P. Sprenger, R. Bertermann, N. Ignat'ev, V. Bernhardt-Pitchougina, E. Bernhardt, H. Willner and M. Finze, *Chem. Commun.*, 2015, **51**, 4989–4992.
25 D. A. Ruiz, G. Ung, M. Melaimi and G. Bertrand, *Angew. Chem., Int. Ed.*, 2013, **52**, 7590–7592.
26 H. Braunschweig, R. D. Dewhurst, F. Hupp, M. Nutz, K. Radacki, C. W. Tate, A. Vargas and Q. Ye, *Nature*, 2015, **522**, 327–330.
27 F. Dahcheh, D. Martin, D. W. Stephan and G. Bertrand, *Angew. Chem., Int. Ed.*, 2014, **53**, 13159–13163.
28 R. Kinjo, B. Donnadieu, M. A. Celik, G. Frenking and G. Bertrand, *Science*, 2011, **333**, 610–613.
29 D. A. Ruiz, M. Melaimi and G. Bertrand, *Chem. Commun.*, 2014, **50**, 7837–7839.
30 M. Soleilhavoup and G. Bertrand, *Acc. Chem. Res.*, 2015, **48**, 256–266.
31 M. A. Celik, R. Sure, S. Klein, R. Kinjo, G. Bertrand and G. Frenking, *Chem. – Eur. J.*, 2012, **18**, 5676–5692.
32 L. Kong, R. Ganguly, Y. Li and R. Kinjo, *Chem. Sci.*, 2015, **6**, 2893–2902.
33 N. Frank, K. Hanau, K. Flosdorf and R. Langer, *Dalton Trans.*, 2013, **42**, 11252–11261.
34 L. Vondung, N. Frank, M. Fritz, L. Alig and R. Langer, *Angew. Chem., Int. Ed.*, 2016, **55**, 14450–14454.
35 S. A. Westcott, H. P. Blom, T. B. Marder, R. T. Baker and J. C. Calabrese, *Inorg. Chem.*, 1993, **32**, 2175–2182.
36 M. Sigl, A. Sehier and H. Schmidbaur, *Chem. Ber.*, 1997, **130**, 1411–1416.
37 T. A. Shuttleworth, M. A. Huertos, I. Pernik, R. D. Young and A. S. Weller, *Dalton Trans.*, 2013, **42**, 12917–12925.
38 K. Owsianik, R. Chauvin, A. Balińska, M. Wieczorek, M. Cypryk and M. Mikołajczyk, *Organometallics*, 2009, **28**, 4929–4937.
39 T. Costa and H. Schmidbaur, *Chem. Ber.*, 1982, **115**, 1374–1378.
40 For further details please see ESI‡.
41 S. Wu, X. Li, Z. Xiong, W. Xu, Y. Lu and H. Sun, *Organometallics*, 2013, **32**, 3227–3237.
42 C. F. Czauderna, A. G. Jarvis, F. J. L. Heutz, D. B. Cordes, A. M. Z. Slawin, J. I. van der Vlugt and P. C. J. Kamer, *Organometallics*, 2015, **34**, 1608–1618.
43 R. G. Holloway, B. R. Penfold, R. Colton and M. J. McCormick, *J. Chem. Soc., Chem. Commun.*, 1976, 485–486.
44 L. Kong, Y. Li, R. Ganguly, D. Vidovic and R. Kinjo, *Angew. Chem., Int. Ed.*, 2014, **53**, 9280–9283.
45 A. Naghipour, A. Ghorbani-Choghamarani, H. Babaee and B. Notash, *Appl. Organomet. Chem.*, 2016, **30**, 998–1003.
46 S. Ganguly, J. T. Mague and D. M. Roundhill, *Inorg. Chem.*, 1992, **31**, 3500–3501.
47 H. Braunschweig, K. Radacki, D. Rais and K. Uttinger, *Angew. Chem., Int. Ed.*, 2006, **45**, 162–165.
48 H. Braunschweig, K. Gruss, K. Radacki and K. Uttinger, *Eur. J. Inorg. Chem.*, 2008, 1462–1466.
49 S. Bontemps, M. Sircoglou, G. Bouhadir, H. Puschmann, J. K. Howard, P. W. Dyer, K. Miqueu and D. Bourissou, *Chem. – Eur. J.*, 2008, **14**, 731–740.
50 D. Schuhknecht, F. Ritter and M. E. Tauchert, *Chem. Commun.*, 2016, **52**, 11823–11826.

Supporting Information

Donor ligands based on tricoordinate boron formed by B-H-activation of bis(phosphine)boronium salts

Maik Grätz,[a] Andreas Bäcker,[a] Lisa Vondung,[a] Leon Maser,[a] Arian Reincke,[a] Robert Langer*[,a,b]

1. **Experimental Details**
2. **NMR spectra**
3. **X-Ray Crystallography**
4. **DFT Calculations**

[a]*Department of Chemistry, Philipps-Universität Marburg, Hans-Meerwein-Str., 35043 Marburg, Germany, Fax: (+)49-6421-2825617, E-mail: robert.langer@chemie.uni-marburg.de*

[b]Lehn Institute of Functional Materials (LIFM), Sun Yat-Sen University (SYSU), Xingang Road West, Guangzhou 510275, PR China.

1. Experimental Details

Material and Methods

All experiments were carried out under an atmosphere of purified argon in a MBraun Labmaster glove box or using standard Schlenk techniques. THF and C_6D_6 were dried and distilled from Na/K alloy and stored over molecular sieves. *n*-Hexane was dried and distilled from $LiAlH_4$ and stored over molecular sieves. Toluene was dried and distilled from sodium and stored over molecular sieves. Bis(diphenylphosphino)methane (dppm) was prepared according to a previously reported procedure.[1]

^1H, ^{13}C, ^{31}P and ^{11}B NMR spectra were recorded using Bruker DRX 400, DRX 500 and Avance 500 NMR spectrometers. ^1H and $^{13}C\{^1H\}$, ^{13}C-APT (attached proton test) NMR chemical shifts are reported in ppm downfield from tetramethylsilane. The resonance of the residual protons in the deuterated solvent was used as internal standard for ^1H NMR. The solvent peak of the deuterated solvent was used as internal standard for ^{13}C NMR. ^{31}P NMR chemical shifts are reported in ppm downfield from H_3PO_4 and referenced to an external 85% solution of phosphoric acid in D_2O. ^{11}B NMR chemical shifts are reported in ppm downfield from $BF_3{\cdot}Et_2O$ and referenced to an external solution of $BF_3{\cdot}Et_2O$ in $CDCl_3$. The following abbreviations are used for the description of NMR data: br (broad), s (singlet), d (doublet), t (triplet), q (quartet), quin (quintet), m (multiplet), v (virtual).

FT-IR spectra were recorded by attenuated total reflection of the solid samples on a Bruker Tensor IF37 spectrometer. The intensity of the absorption band is indicated as vw (very weak), w (weak), m (medium), s (strong), vs (very strong) and br (broad).

HR-ESI mass spectra were acquired with a LTQ-FT mass spectrometer (Thermo Fisher Scientific). The resolution was set to 100.000.

Synthesis of $[H_2B(dppm)_2]Br$ (1)

dppm (880 mg, 2.2 mmol) was dissolved in CH_2Cl_2 (6 mL) and a solution of $BH_2Br{\cdot}SMe_2$ in CH_2Cl_2 (1 M, 1.1 mL, 1.1 mmoL) was added. After stirring for 10 d, reaction control via $^{31}P\{^1H\}$ NMR indicated no further conversion of *dppm*. The solvent was removed under reduced pressure and the residue was washed with Et_2O/THF (2:1, 5x 10 mL). The solvent was removed under high vacuum to obtain *$[H_2B(dppm)_2]Br$* (560 mg, 0.65 mmol, 59 %) as

colorless crystalline solid (M = 861.51 g·mol^{-1}). ^{1}H-NMR (300 MHz, THF-d_8, 27 °C) δ = 4.05 (d, 4H, $^{3}J_{HH}$ = 12.3 Hz, CH_2) 7.03-7.16 (m, 16H, phenyl-*H*), 7.19-7.27 (m, 8H, phenyl-*H*), 7.51-7.59 (m, 8H, phenyl-*H*), 7.61-7.72 (m, 8H, phenyl-*H*) ppm. Boron-bound protons were not observed. ^{11}B{^{1}H} NMR (96 MHz, CD_2Cl_2, 27 °C) δ = -34.0 (br) ppm. Only resonances that are changing upon ^{11}B-decoupling are listed in the ^{1}H{^{11}B} NMR spectrum. ^{1}H{^{11}B}NMR (300 MHz, THF-d_8, 27 °C) δ = 2.65 (t, 2H, $^{2}J_{HP}$ = 20.4 Hz, BH_2) ppm. ^{31}P{^{1}H} NMR (122 MHz, CD_2Cl_2, 27 °C) δ = -25.2 (d, $^{2}J_{PP}$ = 67.1 Hz, P-CH_2-*P*), 7.5 (br, *P*-BH_2-*P*) ppm. ^{13}C{^{1}H} NMR (76 MHz, CD_2Cl_2, 27 °C) δ = 22,7 (dd, $^{1}J_{PC}$ = 39.2 Hz, $^{1}J_{PC}$ = 34.2 Hz, P-*C*H_2-P), 124.3 (dd, J_{PC} = 61.6 Hz, J_{PC} = 2.8 Hz, phenyl-*C*), 124.3 (d, J_{PC} = 70.6 Hz, phenyl-*C*), 128.9 (s, phenyl-*C*), 129.1 (s, phenyl-*C*), 129.6 (s, phenyl-*C*), 129.8 (d, J_{PC} = 1.5 Hz, phenyl-*C*), 132.8 (s, phenyl-*C*), 132.9 (s, phenyl-*C*), 133.0 (s, phenyl-*C*), 133.2 (s, phenyl-*C*), 133.3 (d, J_{PC} = 2.8 Hz, phenyl-*C*), 136.3 (d, J_{PC} = 7.3 Hz, phenyl-*C*), 136.5 (d, J_{PC} = 7.3 Hz, phenyl-*C*) ppm. FT-IR (ATR) $\tilde{\upsilon}$/cm^{-1}: 3050 (w), 3008 (w), 2983 (w), 2846 (w), 2440 (w), 2394 (w), 1586 (w), 1482 (w), 1435 (m), 1365 (w), 1314 (w), 1189 (w), 1160 (w), 1106 (m), 1070 (w), 1026 (w) 997 (w), 915 (w), 776 (m), 740 (s), 721 (m), 690 (s), 633 (m). HRMS (ESI^{+}) m/z: 781.2643 (calculated for $C_{50}H_{46}BP_4$), 781.2646 (found, Δ = 0.4 ppm).

Synthesis of [(H_2B{dppm}$_2$)Ni(CO)$_2$]Br (2)

[Ni(CO)$_4$] (24 mg, 0.14 mmol) was added to a solution of **1** (120 mg, 0.14 mmol) in 5 mL THF and the resulting solution was stirred for five hours at ambient temperature. After this period the extent of conversion was checked by ^{31}P{^{1}H} NMR spectroscopy. Addition of 10 mL *n*-hexane resulted in precipitation of **2**. The supernatant solution was decanted off and the precipitate was dried *in vacuo*. Yield: 12 mg (0.012 mmol, 8.5 %). The yield can be increased significantly by removal of all volatiles from the reaction mixture and continuous washing of the residue, but the obtained product contains inseparable byproducts according to the ^{31}P{^{1}H} NMR spectrum. ^{1}H NMR (300 MHz, CD_3CN, 27 °C) δ = 3.82 (br, 4H, CH_2), 7.05-7.14 (m, 10H, phenyl-*H*), 7.19 (dd, 4H, J_{HH} = 7.3 Hz, J_{HH} = 1.1 Hz, phenyl-*H*), 7.24-7.35 (m, 10H, phenyl-*H*), 7.40 (t br, 10H, *J* = 9.0 Hz, phenyl-*H*), 7.62-7.82 (m, 6H, phenyl-*H*) ppm. ^{11}B{^{1}H} NMR (96 MHz, C_6D_6, 27 °C) δ = -35.8 (br) ppm. Only resonances that are changing upon decoupling are listed for the ^{1}H{^{11}B} NMR spectrum. ^{1}H{^{11}B} NMR (300 MHz, C_6D_6, 27 °C) δ = 4.25 (br, 2H, BH_2) ppm. ^{31}P{^{1}H}NMR (122 MHz, $CDCl_3$, 27 °C) δ = 4.9 (br, *P*-B-*P*), 18.1 (ddd, J_{PP} = 38.4 Hz, J_{PP} = 12.0 Hz, J_{PP} = 4.0 Hz, *P*-Ni-*P*) ppm. ^{13}C-APT NMR (76 MHz, CD_3CN, 27 °C) δ = 23.8 (d, $^{1}J_{PC}$ = 36.7 Hz, P-*C*H_2-P), 129.1 (vt, J_{PC} = 4.8 Hz, phenyl-*C*), 129.8 (d, J_{PC} = 11.8 Hz, phenyl-*C*), 130.3 (s, phenyl-*C*), 130.5 (s, phenyl-*C*), 130.6 (s, phenyl-*C*), 133.0 (d, J_{PC} = 9.6 Hz, phenyl-*C*), 133.2 (d, J_{PC} = 2.8 Hz, phenyl-*C*) ppm. The

resonances for carbonyl ligands and for the quaternary carbon atoms of the phenyl rings were not observed. FT-IR (ATR) $\tilde{\upsilon}$/cm^{-1}: 2963 (w) 2905 (w) 2376 (w) 2360 (w) 2349 (w) 2343 (w) 2323 (w) 2298 (w) 2002 (w, ν_{CO}) 1939 (w, ν_{CO}) 1484 (w) 1435 (w) 1413 (w) 1258 (m) 1009 (s) 864 (m) 787 (s) 687 (m) 671 (m) 664 (m) 470 (m) 417 (m). HRMS (ESI$^+$) m/z: 867.1949 (calculated for [(H$_2$B{dppm}$_2$)Ni(CO)]$^+$), 867.1945 (found, Δ = 0.5 ppm); 839.1993 (calculated for [(H$_2$B{dppm}$_2$)Ni]$^+$), 839.1999 ((found, Δ = 0.7 ppm).

Synthesis of [(HB{dppm}$_2$)PdX]X (3, X = Cl, Br)

[H$_2$B(dppm)$_2$]Br (**1**, 40 mg, 0.046 mmol) and [PdCl$_2$(MeCN)$_2$] (12 mg, 0.046 mmol) were dissolved in 5 mL THF and stirred at ambient temperature for 5 hours. During this period, the solution brightened up and precipitate was formed. The supernatant solution was decanted off, the residue was washed with 5 mL THF and dried *in vacuo*. Complex **3** was formed and isolated as a mixture of the two constitutional isomers, with the two cations [[(HB{dppm}$_2$)PdCl]$^+$ (**3-Cl**, ~90 %) and [[(HB{dppm}$_2$)PdBr]$^+$ (**3-Br**, ~10 %). Both isomers are very similar in their spectroscopic properties. In several attempts to grow single crystals with different solvents and under various conditions only single crystals from [**3-Br**]Br could be obtained. Yield: 34.8 mg (0.035 mmol, 76 %). ^{1}H NMR (300 MHz, DMSO-*d*$_6$, 27 °C) δ = 2.52 (partly superimposed, 4H, $^2J_{PH}$ = 4.0 Hz, C*H*$_2$), 7.10-7.20 (m, 8H, phenyl-*H*), 7.36-7.61 (m, 20H, phenyl-*H*), 7.61-7.79 (m, 10H, phenyl-*H*), 8.50 (br t, 2H, J_{HH} = 2.7 Hz, phenyl-*H*) ppm. ^{11}B{^{1}H} NMR (96 MHz, DMSO-*d*$_6$, 27 °C) δ = -24.5 (br) ppm. Only resonances that are changing upon decoupling are listed for the ^{1}H{^{11}B} NMR spectrum. ^{1}H{^{11}B} NMR(300 MHz, DMSO-*d*$_6$, 27 °C) δ = 3.57 (br t, 1H, $^2J_{HP}$ = 17.9 Hz, B*H*) ppm. ^{31}P{^{1}H} NMR (122 MHz, DMSO-*d*$_6$, 27 °C) δ = 59.3 (br, *P*-B-*P*), 81.8 (dd, $^2J_{PP}$ = 76.4 Hz, $^2J_{PP}$ = 68.1 Hz, Ph$_2$*P*-Pd-Cl), 84.4 (t, $^2J_{PP}$ = 71.9 Hz, Ph$_2$*P*-Pd-Br) ppm. ^{13}C{^{1}H} NMR (76 MHz, DMSO-*d*$_6$, 27 °C) δ = 38.5-40.5 (P-*C*H$_2$-P, superimposed by DMSO-*d*$_6$), 128.2-128.6 (superimposed resonances, phenyl-*C*), 128.7 (vt, J_{PC} = 5.7 Hz, phenyl-*C*), 129.3 (vt, J_{PC} = 5.7 Hz, phenyl-*C*), 130.8 (s, phenyl-*C*), 131.0 (s, phenyl-*C*), 131.3-131.8 (superimposed resonances, phenyl-*C*), 132.4 (vt, J_{PC} = 6.2 Hz, phenyl-*C*), 132.7 (s, phenyl-*C*), 132.9 (s, phenyl-*C*), 134.0 (dd, $^1J_{PC}$ = 23.7 Hz, J_{PC} = 2.9 Hz, phenyl-*C*) ppm. FT-IR (ATR) $\tilde{\upsilon}$ / cm^{-1}: 3053 (w), 3015 (w), 2963 (w), 2905 (w), 2586 (w), 2370 (w), 2361 (w), 2349 (w) 2343 (w), 2323 (w), 2298 (w), 1587 (w), 1572 (w), 1483 (w), 1435 (m), 1411 (w), 1307 (m), 1259 (s), 1188 (w), 1086 (s), 1013 (s), 935 (m) 865 (w), 792 (s), 737 (m), 689 (s), 665 (m), 619 (w), 604 (w), 559 (m), 533 (m), 504 (m), 485 (m), 451 (w), 406 (w). HRMS (ESI$^+$) m/z: 921.1303 (calculated for [(HB{dppm}$_2$)PdCl]$^+$), 921.1305 (found, Δ = 0.2 ppm).

2. NMR Spectra

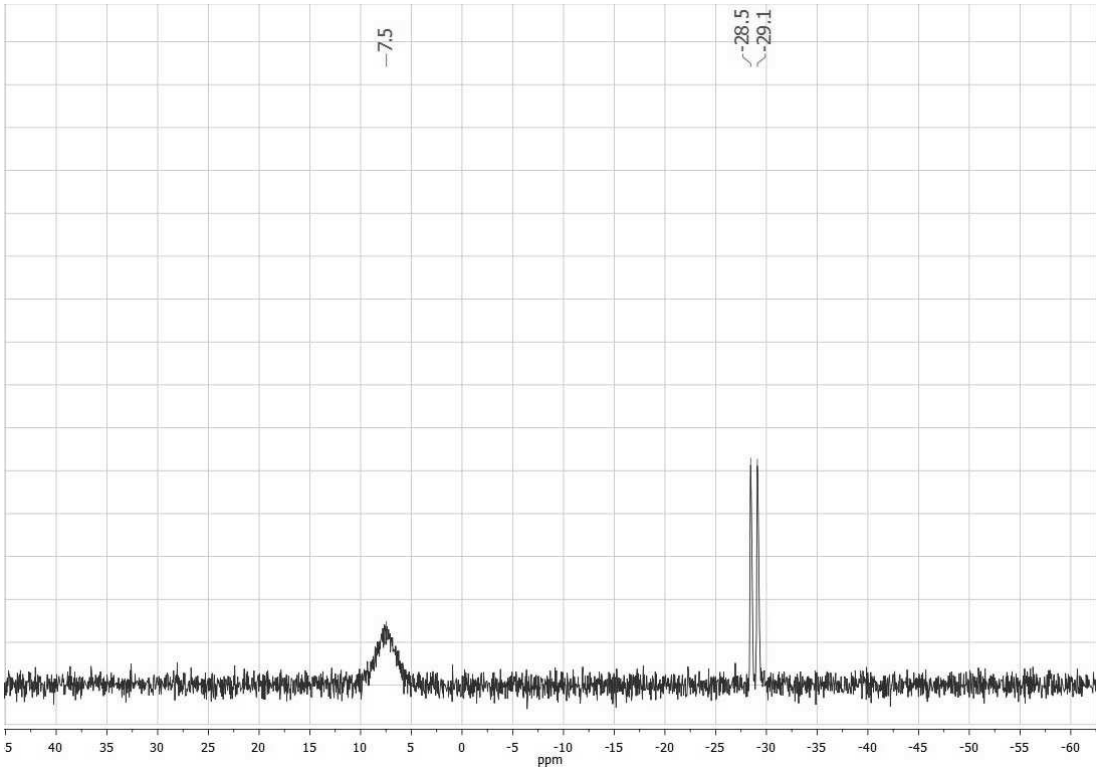

Figure 1 $^{31}P\{^{1}H\}$ NMR spectrum of compound **1** in CD_2Cl_2.

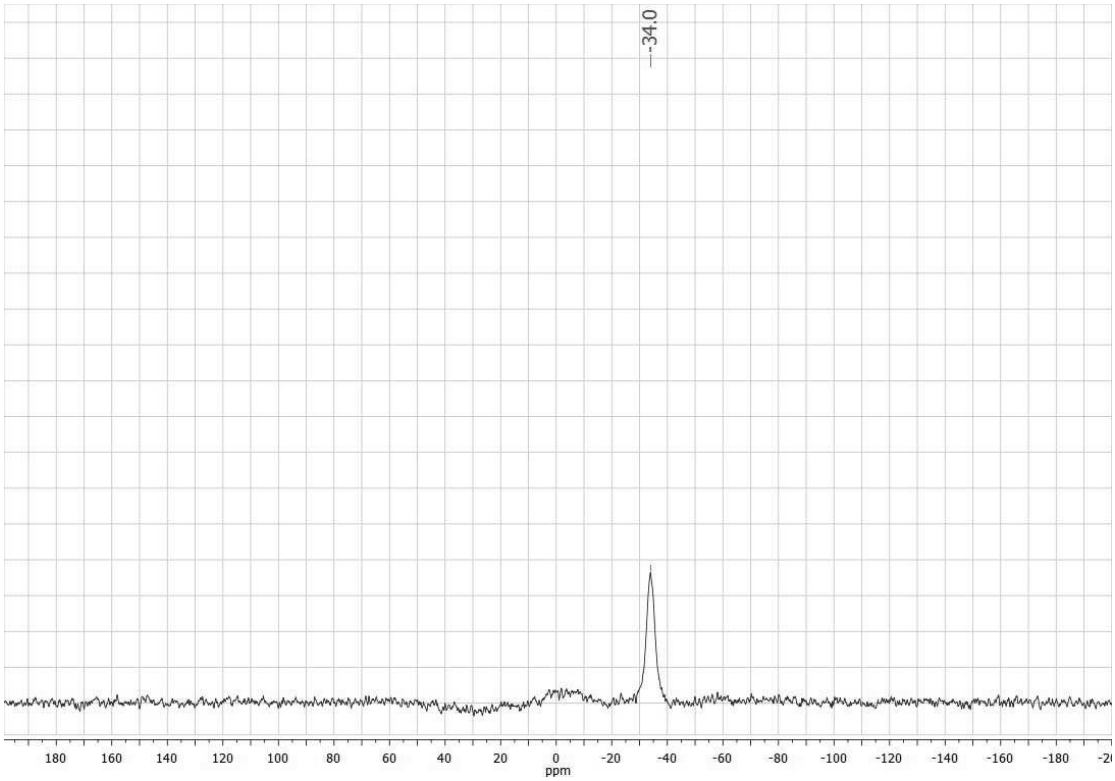

Figure 2 $^{11}B\{^{1}H\}$ NMR spectrum of compound **1** in CD_2Cl_2.

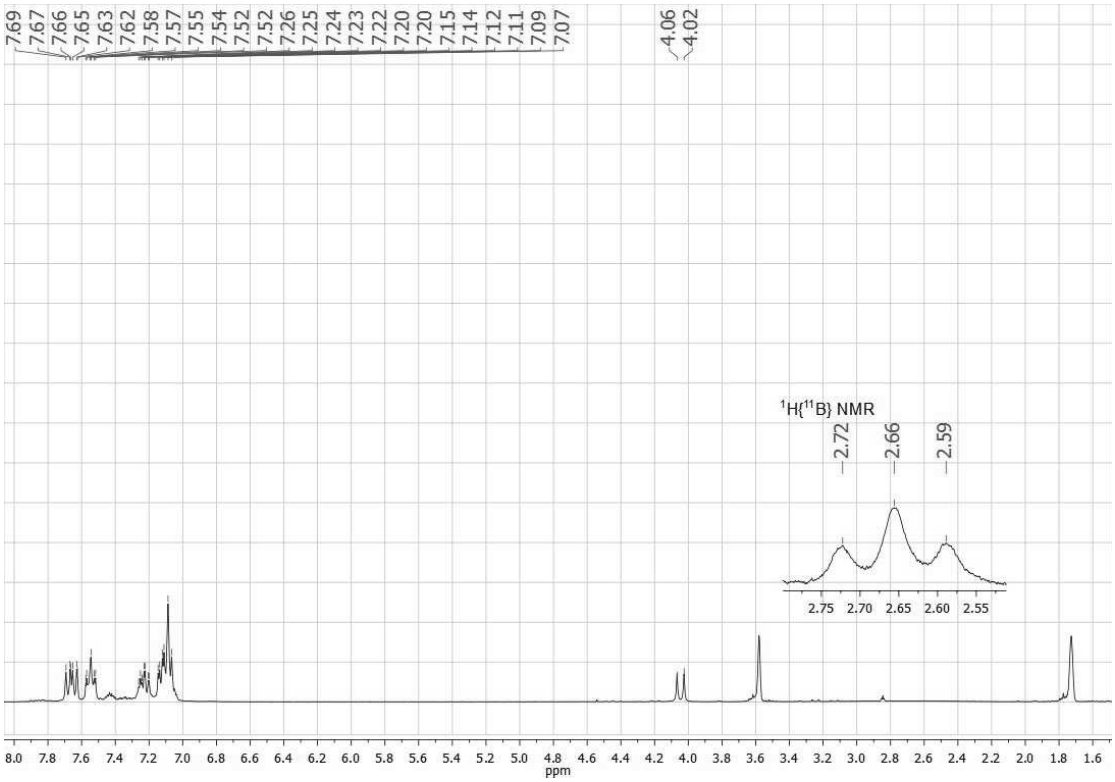

Figure 3 ^{1}H NMR spectrum of compound **1** in THF-d_8, with an inset showing the resonance of the boron-bound H-atoms in the $^{1}H\{^{11}B\}$NMR spectrum .

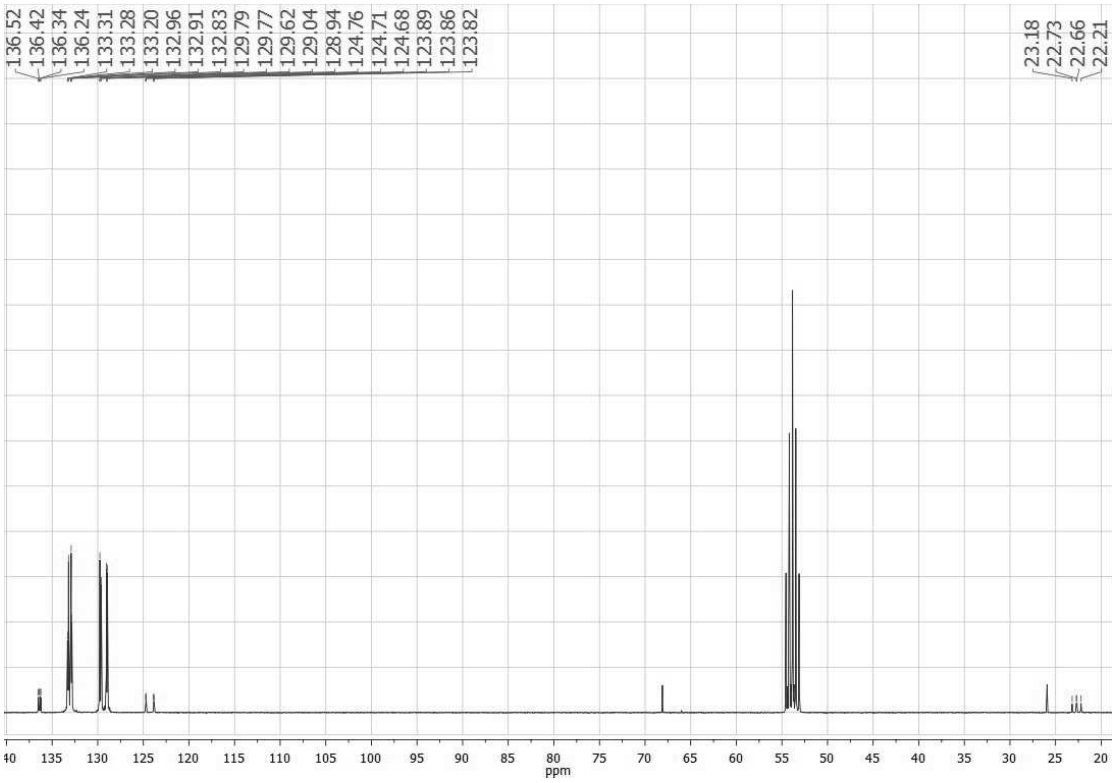

Figure 4 $^{13}C\{^{1}H\}$ NMR spectrum of compound **1** in CD_2Cl_2.

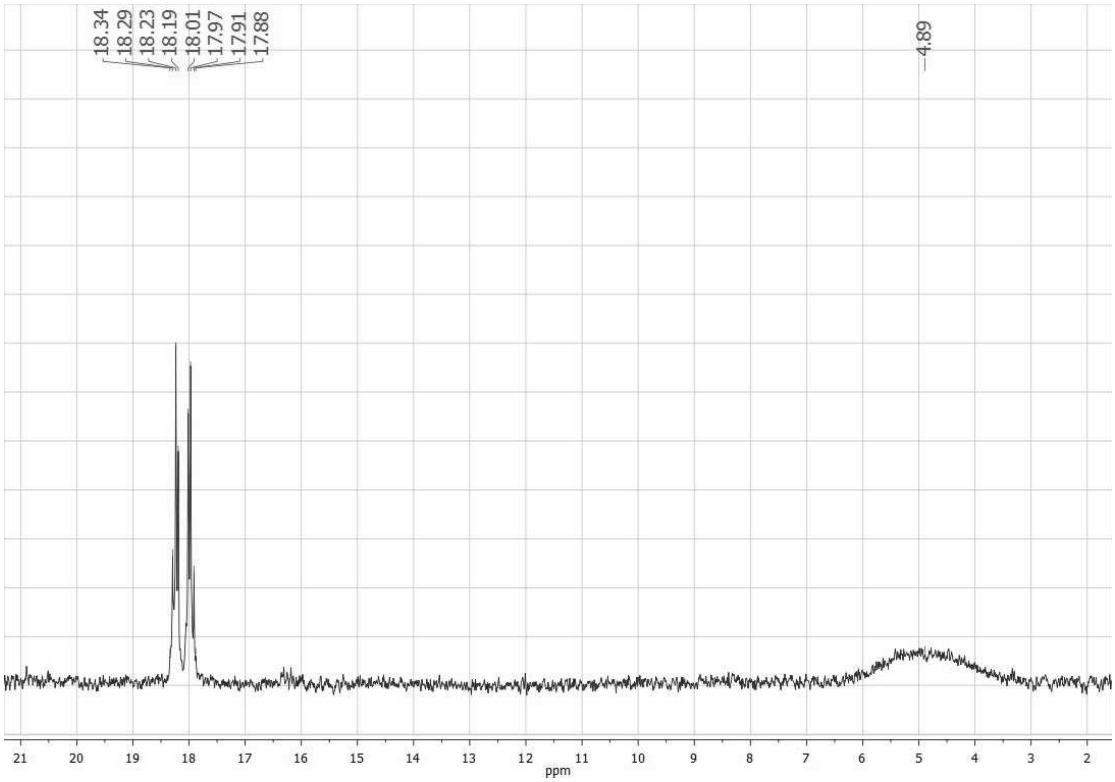

Figure 5 $^{31}P\{^{1}H\}$ NMR spectrum of complex **2** in CD_3CN.

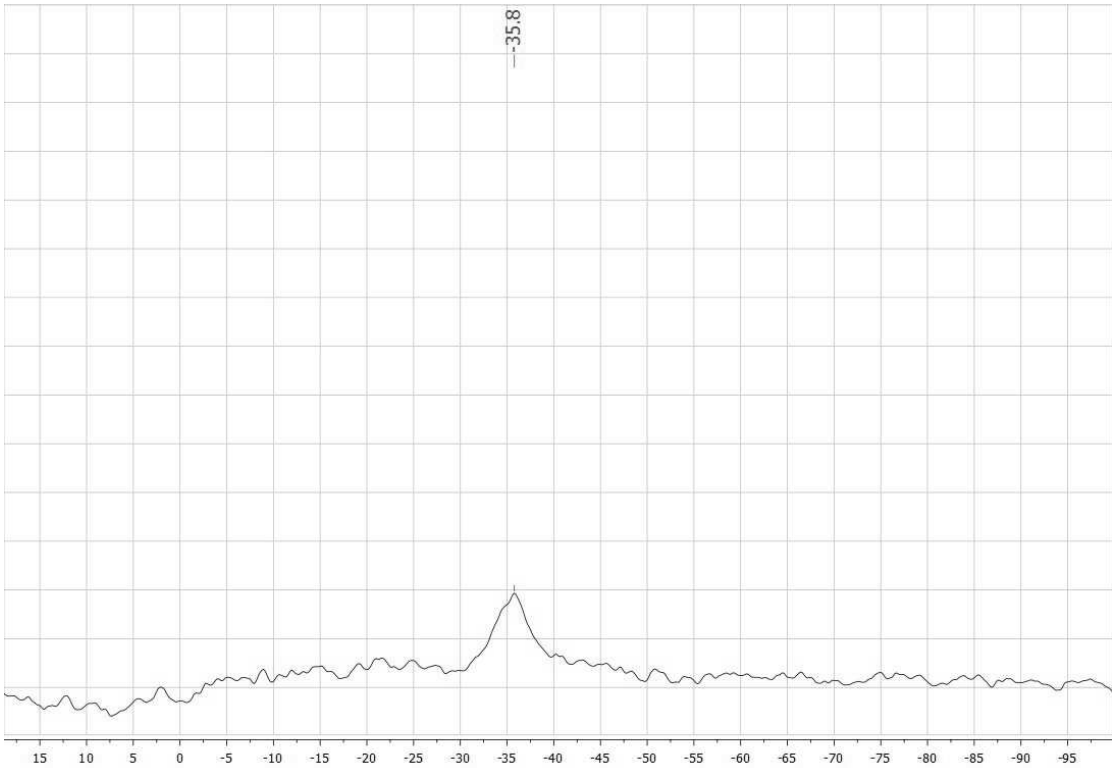

Figure 6 $^{11}B\{^{1}H\}$ NMR spectrum of complex **2** in CD_3CN.

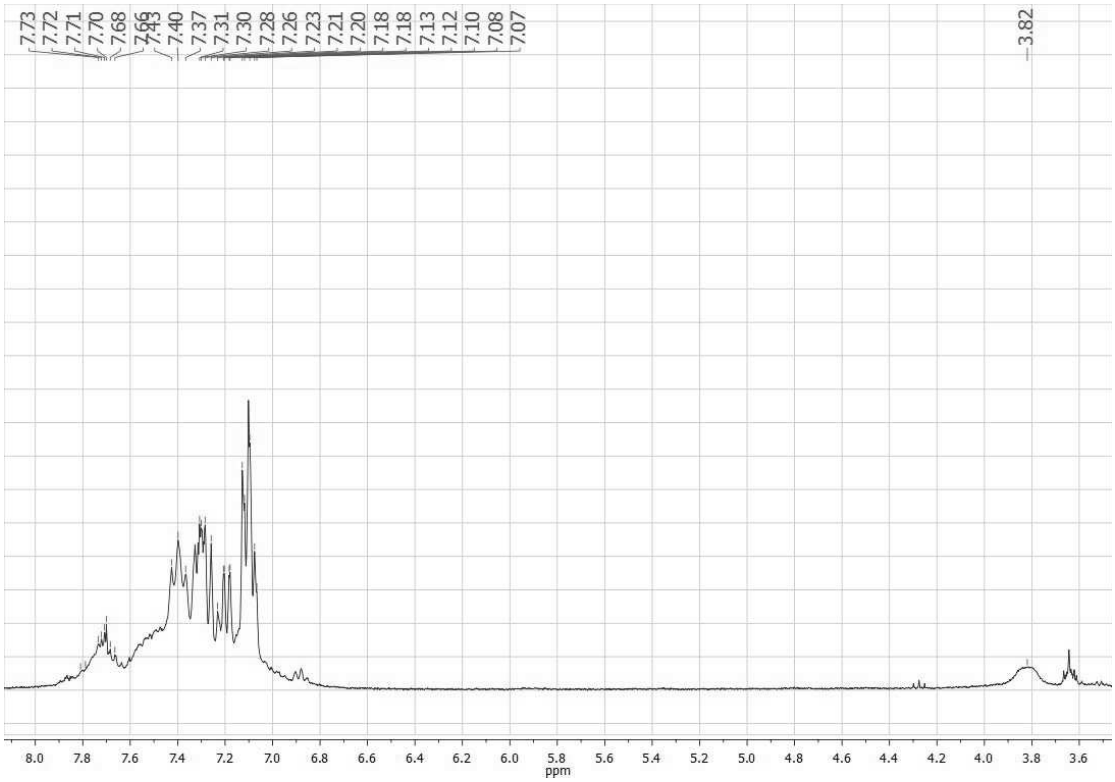

Figure 7 ^{1}H NMR spectrum of complex **2** in CD_3CN.

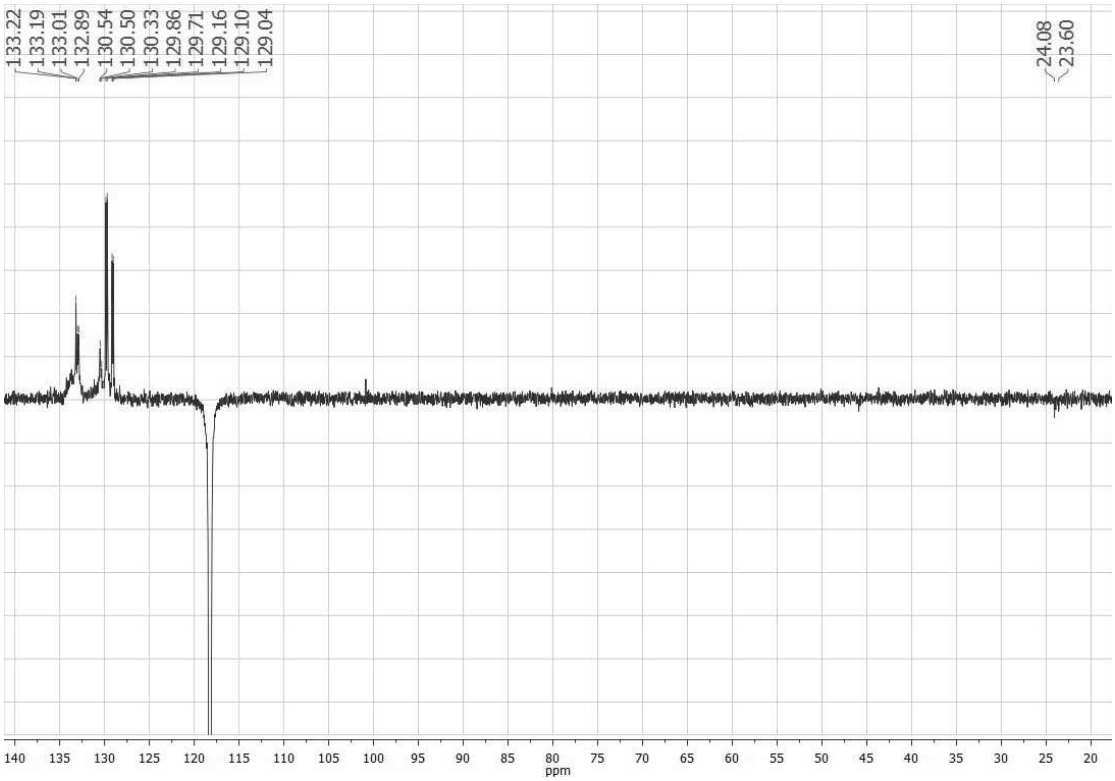

Figure 8 ^{13}C-APT NMR spectrum of complex **2** in CD_3CN.

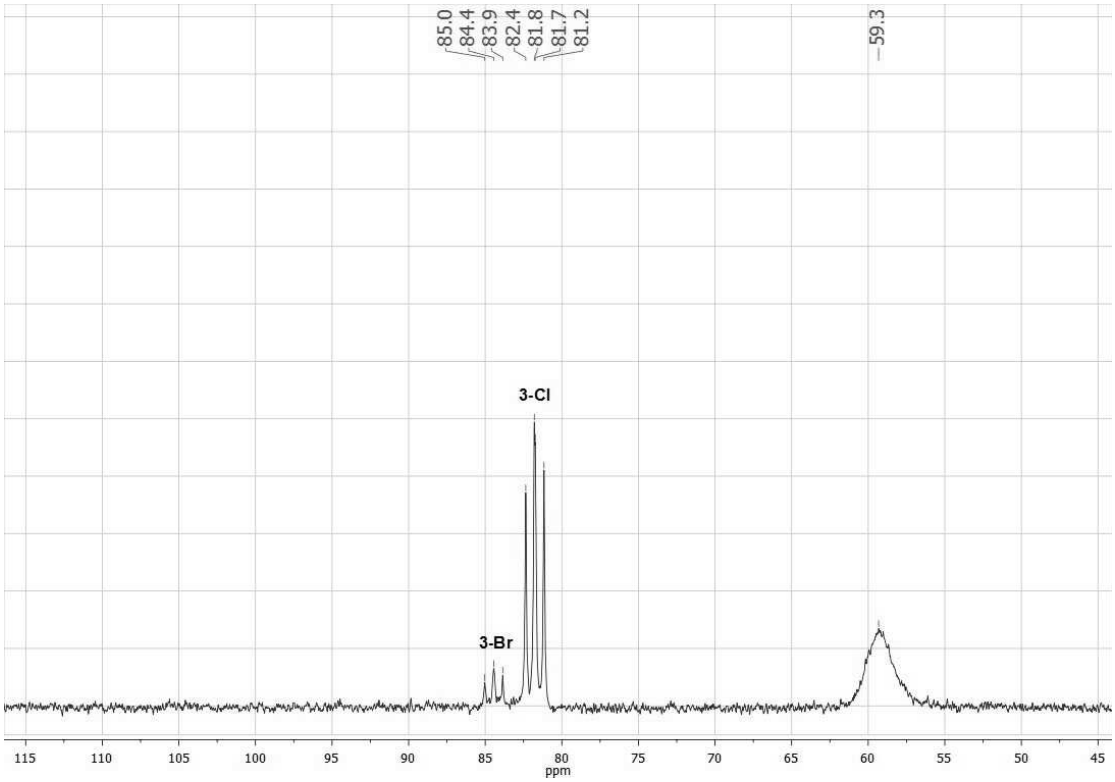

Figure 9 $^{31}P\{^{1}H\}$ NMR spectrum of complex **3** in DMSO-d_6.

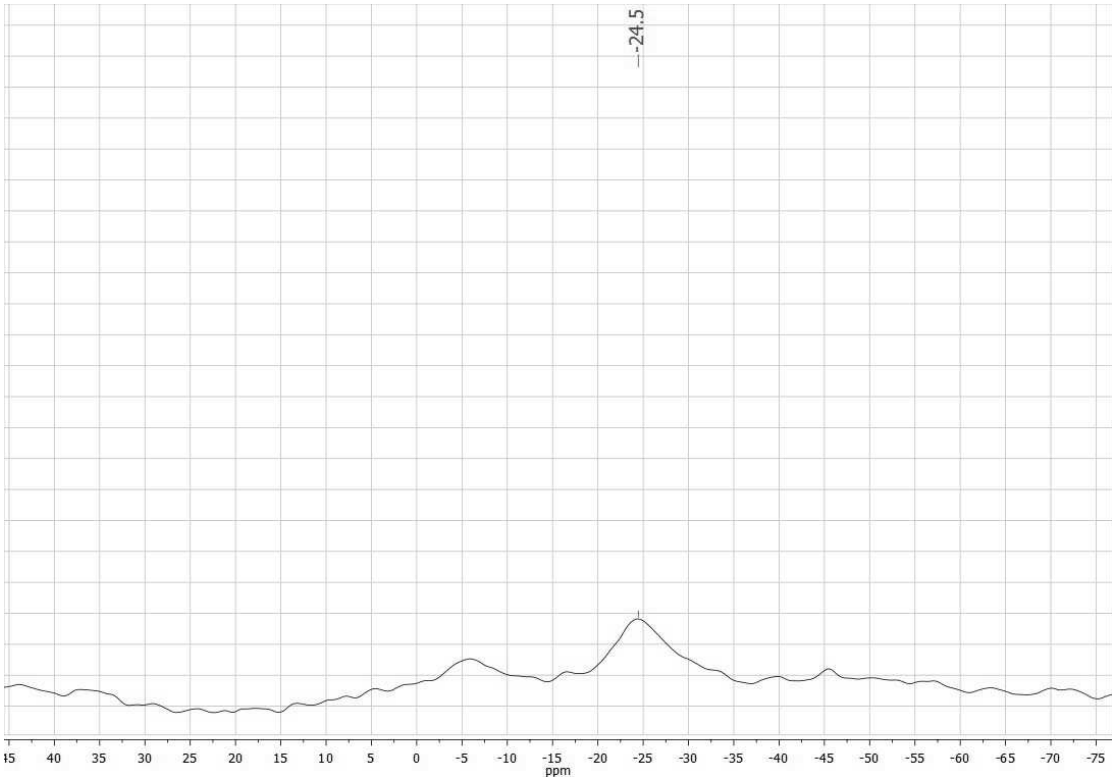

Figure 10 $^{11}B\{^{1}H\}$ NMR spectrum of complex **3** in DMSO-d_6.

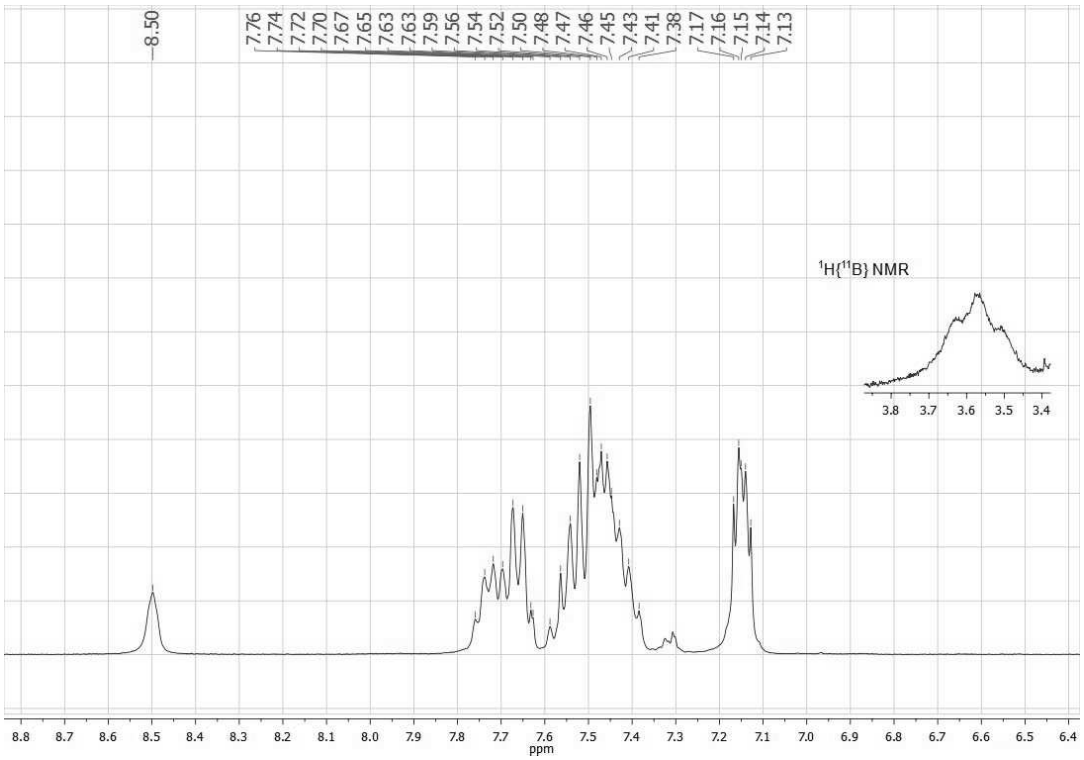

Figure 11 ^{1}H NMR spectrum of complex **3** in DMSO-d_6, with an inset showing the resonance of the boron-bound H-atom in the $^{1}H\{^{11}B\}$NMR spectrum.

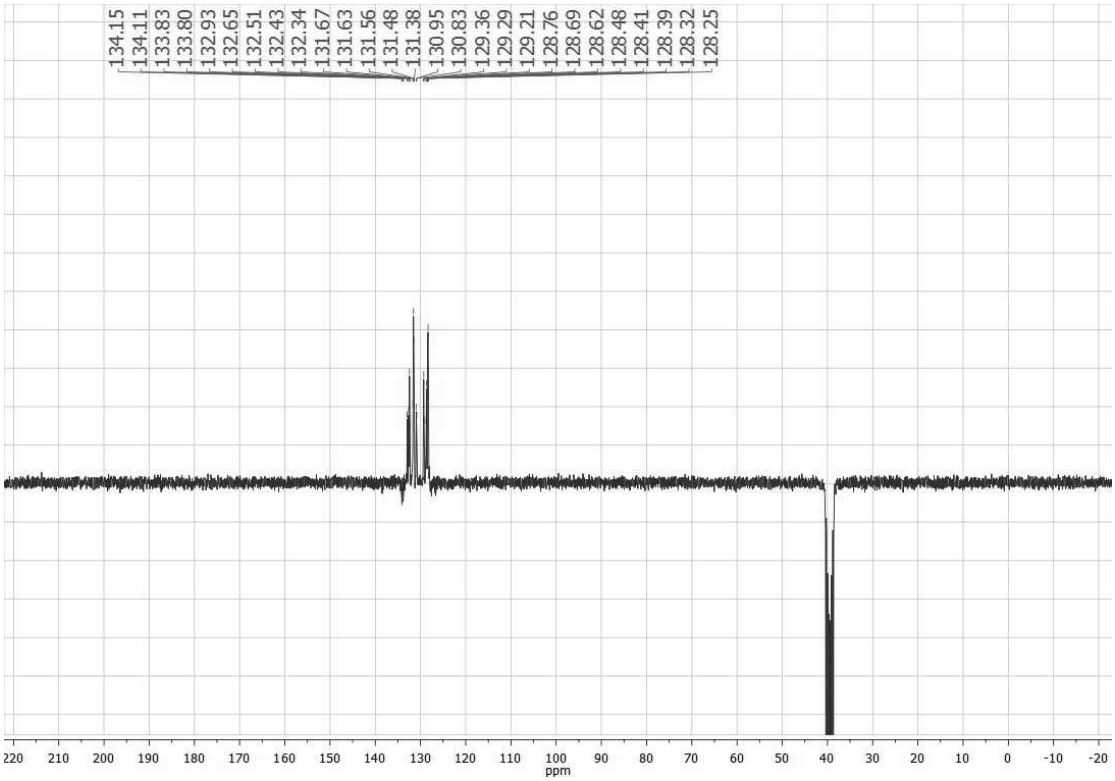

Figure 12 ^{13}C-APT NMR spectrum of complex **3** in DMSO-d_6.

X-Ray Crystallography

The single crystal X-ray diffraction data for the structural analysis of **1** has been collected using graphite-monochromated Mo-K_α-radiation ($\lambda_{MoK\alpha}$ = 0.71073) on the image plate system IPDSII, **2·1^1/$_2$THF** and **[3-Br]Br·1^1/$_4$THF** have been collected using graphite-monochromated Mo-K_α-radiation ($\lambda_{MoK\alpha}$ = 0.71073) on the pixel detector system BRUKER D8-QUEST. The structures were solved by direct methods with SHELXS-97 and refined against F^2 by full-matrix-least-square techniques using SHELXL-97.[2] Based on the crystal descriptions, numerical absorption corrections were applied.[3, 4] Crystallographic data for **1**, **2·1^1/$_2$THF** and **[3-Br]Br·1^1/$_4$THF** have been deposited at Cambridge Crystallographic Data Centre (CCDC 1540277-1540279) and can be obtained free of charge via www.ccdc.cam.ac.uk/. Details of the data collection and the refinement can be found in Table 1. Figure 13 shows the molecular structure of **1** in the solid state.

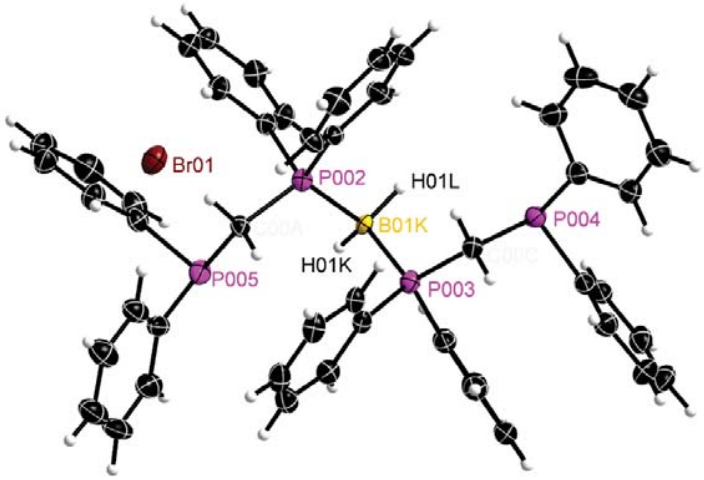

Figure 13 Molecular structure of **1** in the solid state (ellipsoids are drawn at 30 % probability, carbon-bound hydrogen atoms are omitted).

Table 1 Crystallographic data for **1-3**.

Compound	**1**	**2·1^1/$_2$THF**	**[3-Br]Br·1^1/$_4$THF**
Empirical formula	$C_{50}H_{46}BBrP_4$	$C_{52}H_{46}BBrNiO_2P_4 \cdot 1^1/_2C_4H_8O$	$C_{50}H_{45}BBr_2P_4Pd \cdot 1^1/_2C_4H_8O$
Fw/g·mol^{-1}	861.47	1084.35	1136.90
T/K	100(2)	100(2)	110(2)
Crystal system	Orthorhombic	Monoclinic	Monoclinic
Space group	$P2_12_12_1$	$P2_1/c$	$P2_1/n$
a/Å	10.306(2)	16.5199(6)	9.6936(3)
b/Å	13.535(3)	13.4032(6)	24.8956(9)
c/Å	30.934(6)	25.3996(11)	23.1874(10)
α/°	90	90	90
β/°	90	96.7900(10)	91.2630(10)
γ/°	90	90	90
V/Å^3	4315.0(15)	5584.5(4)	5594.4(4)
Z	4	4	4
ρ_{calc}/g·cm^{-3}	1.326	1.290	1.350
$\mu(MoK_\alpha)$/mm^{-1}	1.136	1.220	1.910
F(000)	1784	2248	2304
2θ range/°	2.63-53.44	4.43-53.46	4.51-54.20
Reflections measured	25668	70947	48722
Independent reflections	9087 (R_{Int} = 0.0483)	11812 (R_{Int} = 0.0549)	12151 (R_{Int} = 0.0419)
Ind. reflections (I>2σ(I))	8270	9409	8920
Parameters/Restraints	513/0	624/0	568/39
R_1 *(I>2σ(I))*	0.0350	0.0479	0.0733
wR_2 *(all data)*	0.0840	0.1487	0.2245
GooF (all data)	0.999	0.978	1.047
Max. peak/hole/e·Å^{-3}	0.753/-0.535	2.314/-0.604	1.601/-2.354
CCDC	1540277	1540278	1540279

3. DFT Calculations

DFT calculations were performed with Gaussian 09, Revision C.01.[5] Natural Bond Orbital Analysis was done with NBO 5.9.[6] Grimmes general-gradient approximated and dispersion including B97D functional was used.[7] All geometries were first optimized with the def2-SVP basis set and then reoptimized using the def2-TZVPP basis set.[8, 9] Minima were confirmed with frequency calculations (0 imaginary frequencies). Visualization of molecular orbitals was done with ChemCraft.[10] QTAIM Analysis was performed with AIMAll[11] and pictures were created with Multiwfn.[12] The simplified methyl-substituted complexes **3^{Me}-Br, B^{Me}** and **A^{Me}** were derived by replacing phenyl with methyl groups and subsequent geometry optimization. Bond lengths and selected angles, as well as NBO charges are given in tables 2 and 3.

Table 2 Comparison of experimentally derived bond length and angles of **3-Br** with the results of DFT calculations.

	3-Br (X-Ray)	**3^{Me}-Br** (DFT)	**3^{Me}-Cl** (DFT)
Pd-B	2.129(11)	2.17566	2.17221
Pd-P	2.3031(15)	2.28473	2.28753
Pd-P	2.3041(15)	2.30044	2.29873
P-B	2.005(12)	1.93269	1.92982
P-B	1.929(12)	1.91929	1.91930
P-M-P	170.98(5)	170.37	170.31

Table 3 Charges from Natural Population Analysis for the complexes $\mathbf{3^{Me}}$**-Br**, $\mathbf{B^{Me}}$ and $\mathbf{A^{Me}}$

	$\mathbf{3^{Me}}$**-Cl**	$\mathbf{B^{Me}}$	$\mathbf{A^{Me}}$
Pd	0.116	0.056	0.296
B	-0.848	0.434	0.902
P(Pd)	1.044	1.022	1.15
P(Pd)	1.049	1.01	1.136
P(B)	1.328		
P(B)	1.330		
C(B)		-0.302	-0.368
C(B)		-0.279	-0.367
H(B)	0.051		
N(B)		-0.428	
C(B)			-0.469

Molecular Orbitals (Molecular Orbitals are shown with isocontour values at 0.03; Pd: pale green, P: violet, Cl: green, Br: dark red, C: grey, B: orange)

Complex **3^{Me}-Cl**

LUMO

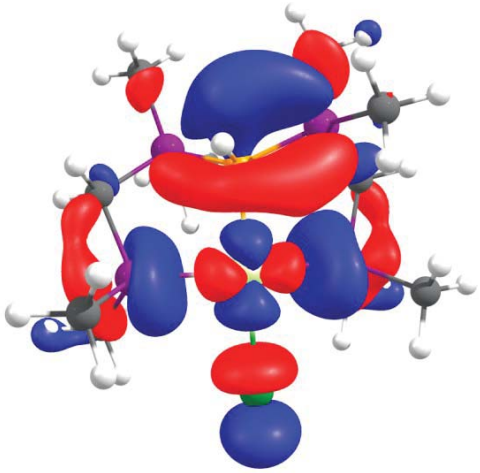

HOMO

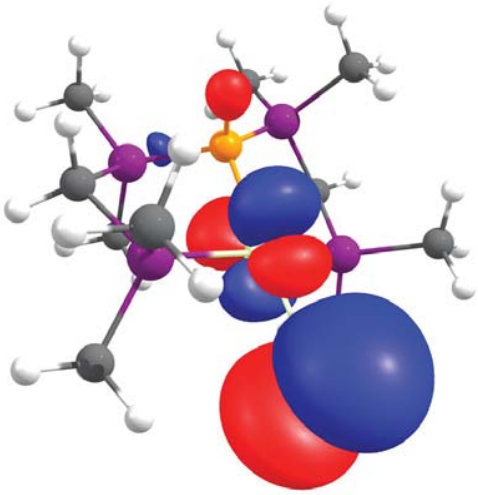

HOMO-1

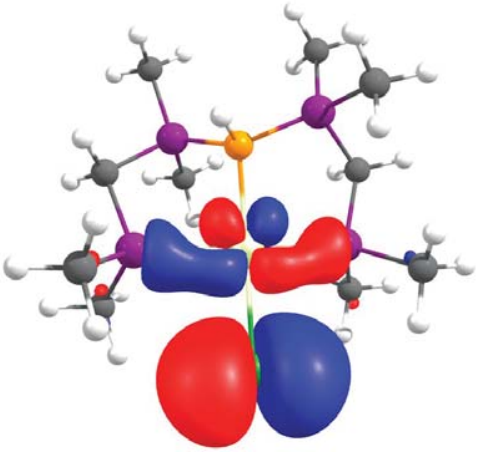

HOMO-2

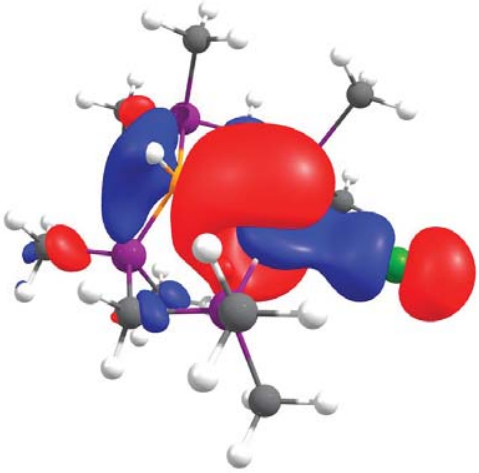

HOMO-3

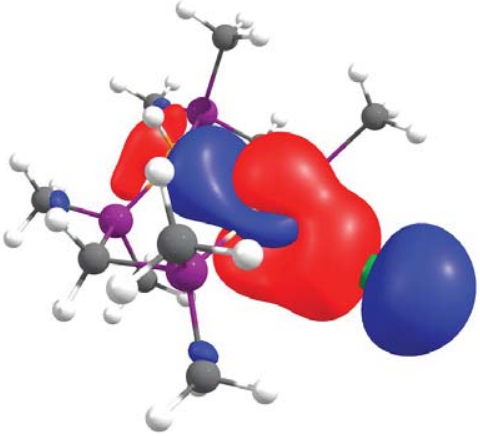

HOMO-4

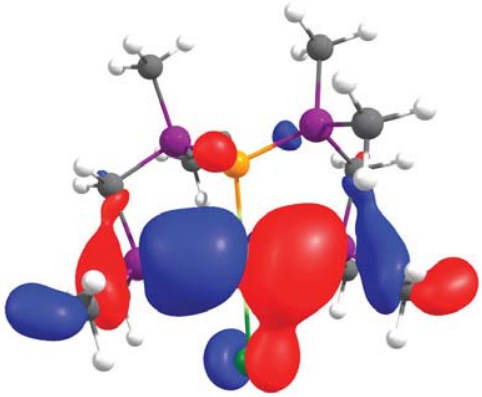

HOMO-5

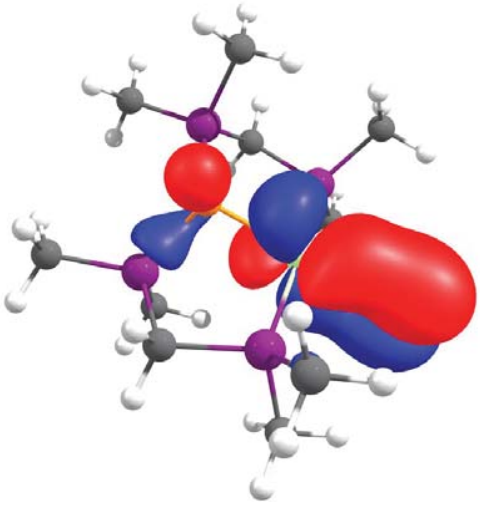

HOMO-8

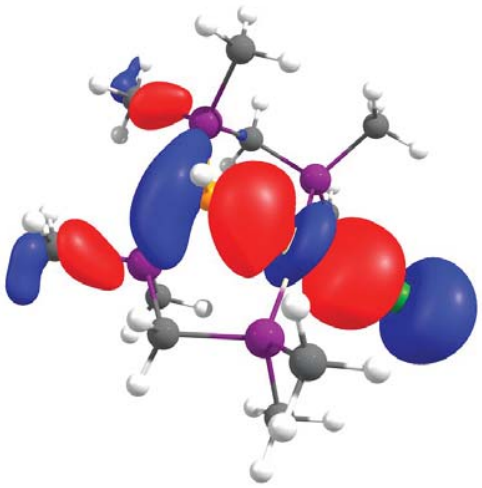

HOMO-9

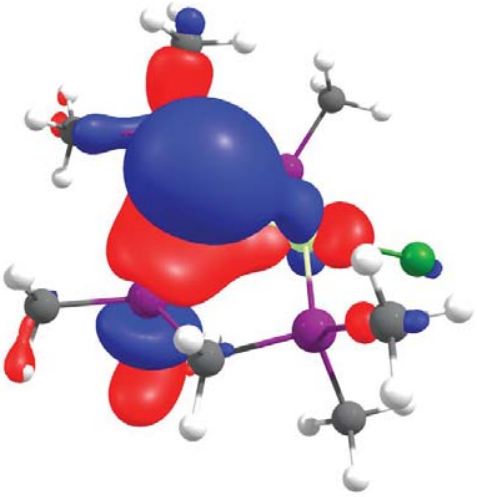

HOMO-10

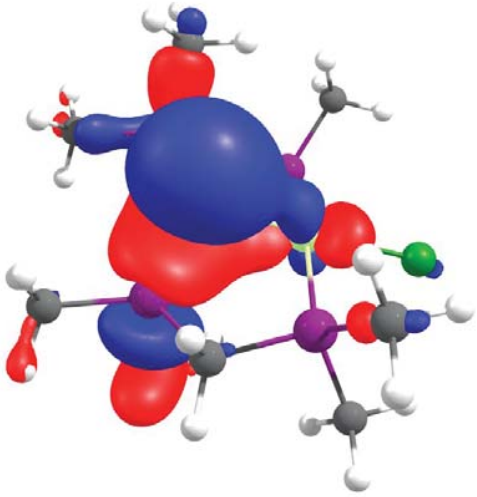

Complex **4^{Me}-Cl/Br**

LUMO

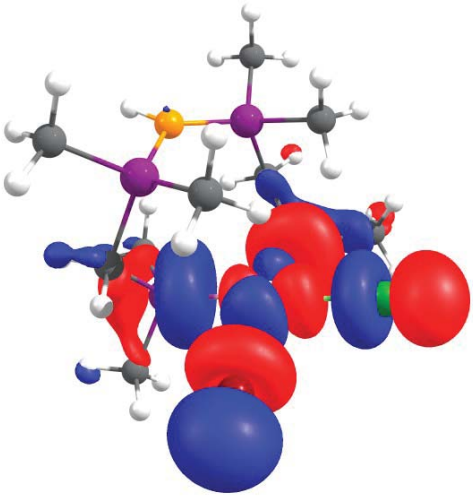

HOMO

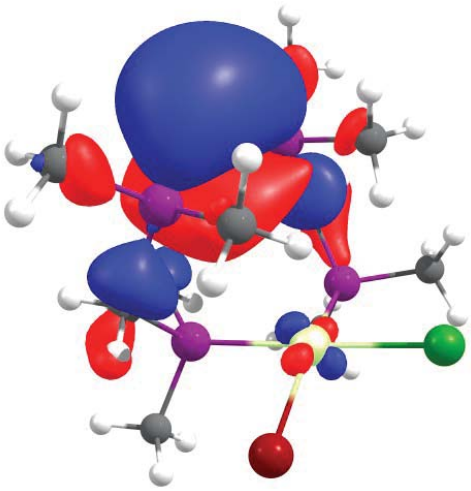

HOMO-1

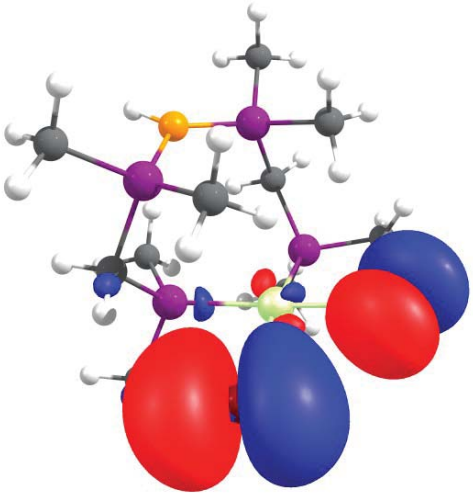

HOMO-2

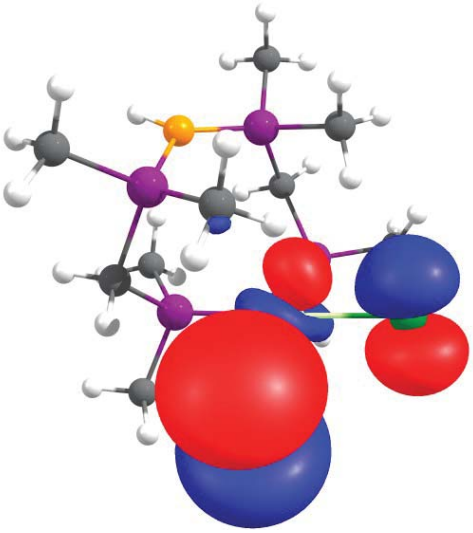

HOMO-3

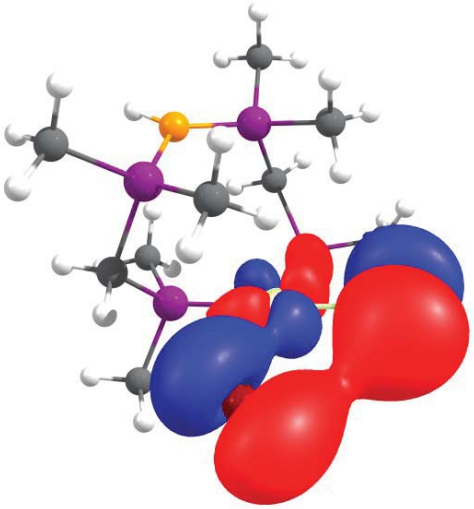

HOMO-4

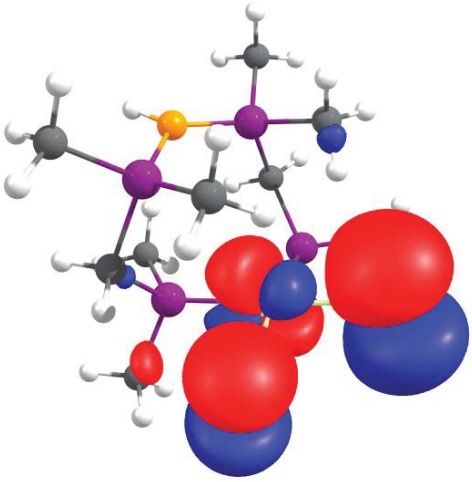

HOMO-10

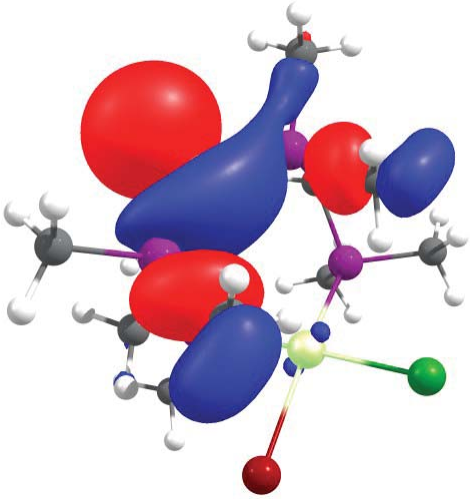

HOMO-11

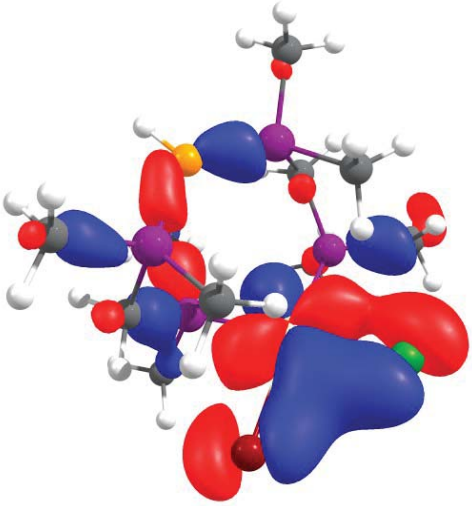

HOMO-12

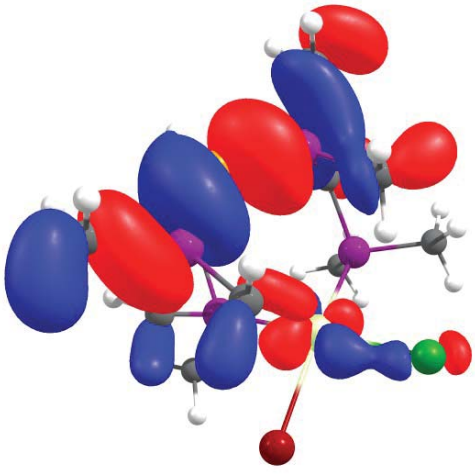

Complex $\mathbf{A}^{\mathbf{Me}}$

LUMO

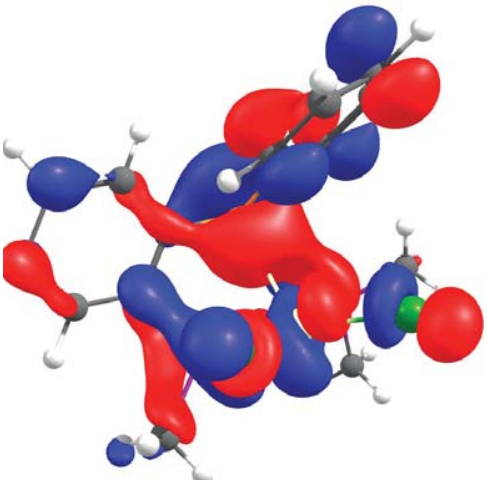

HOMO

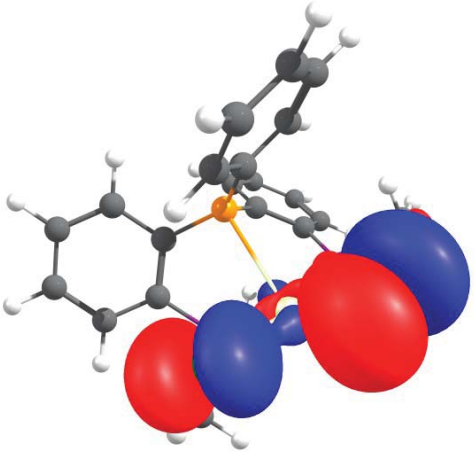

HOMO-1

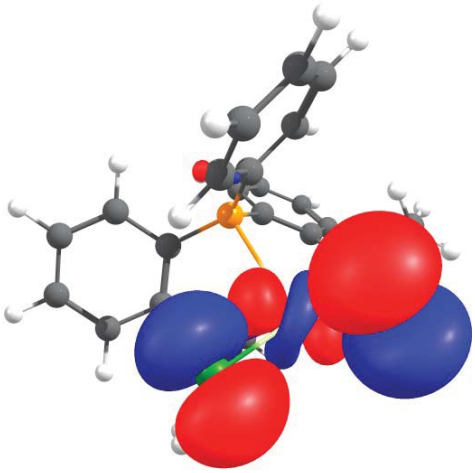

HOMO-2

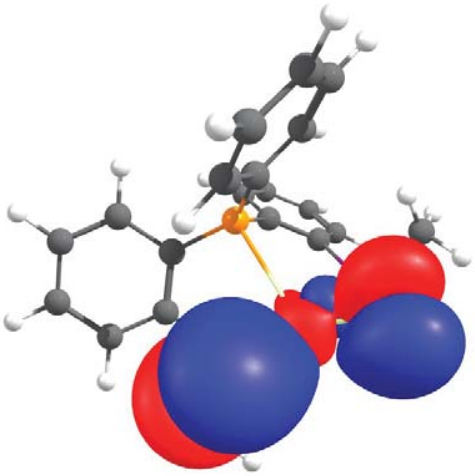

HOMO-3

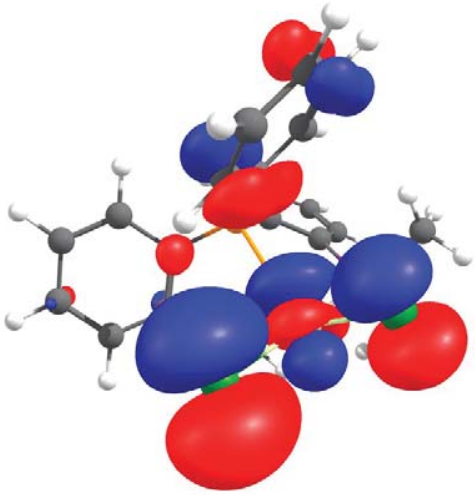

HOMO-4

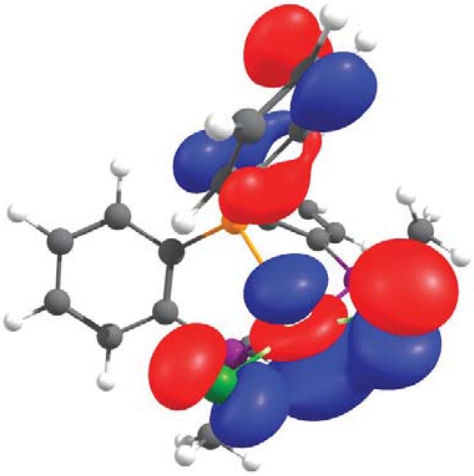

HOMO-5

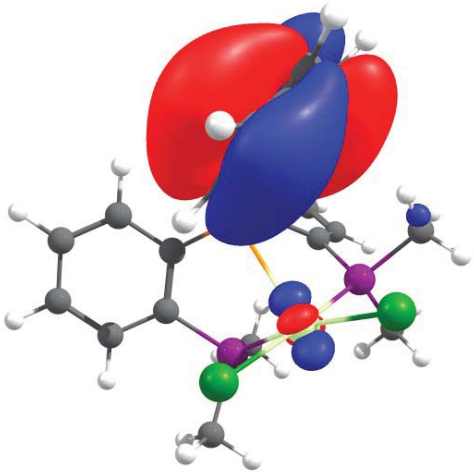

HOMO-6

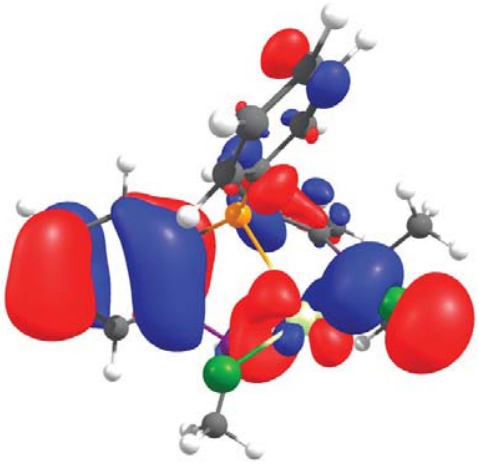

HOMO-12

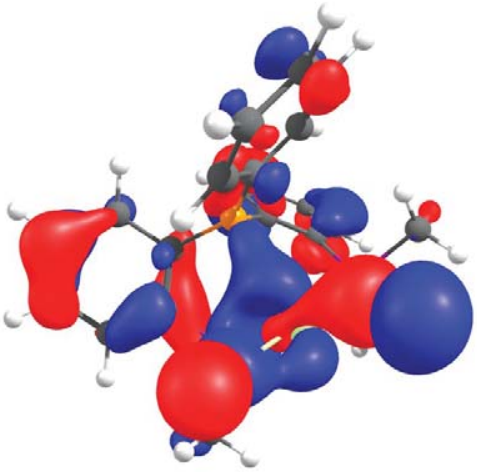

Complex $\mathbf{B}^{\mathbf{Me}}$

LUMO

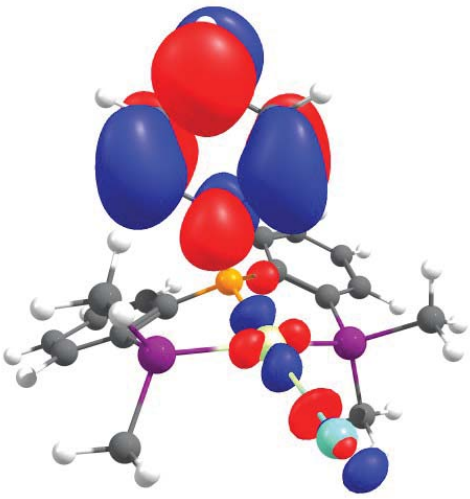

HOMO

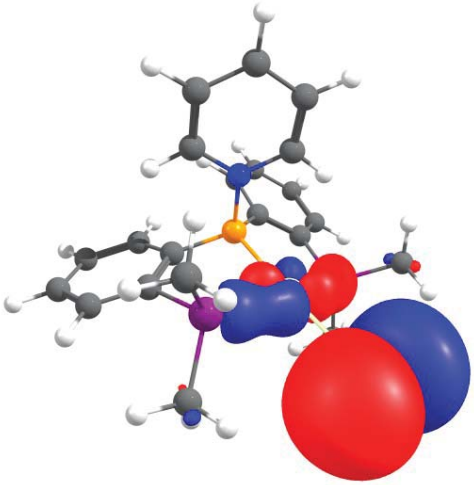

HOMO-1

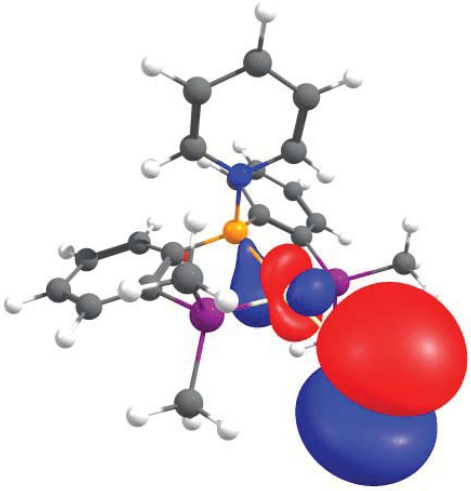

HOMO-2

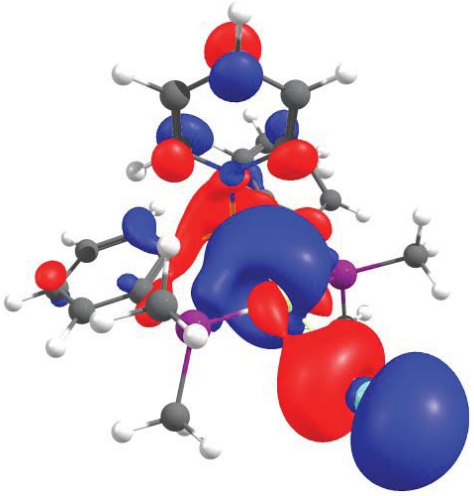

HOMO-3

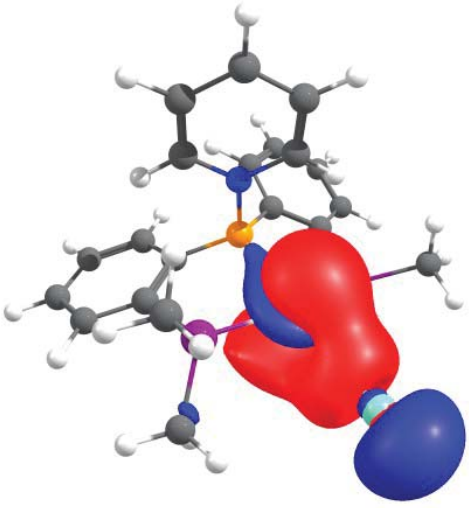

HOMO-4

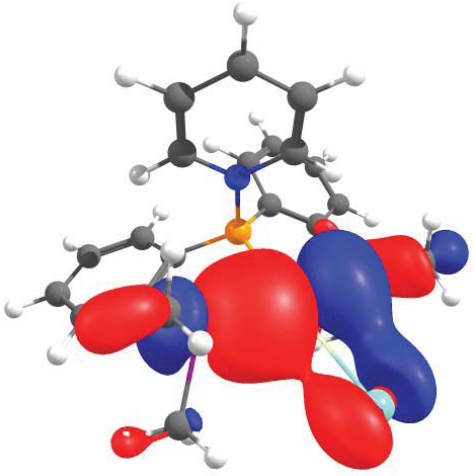

HOMO-5

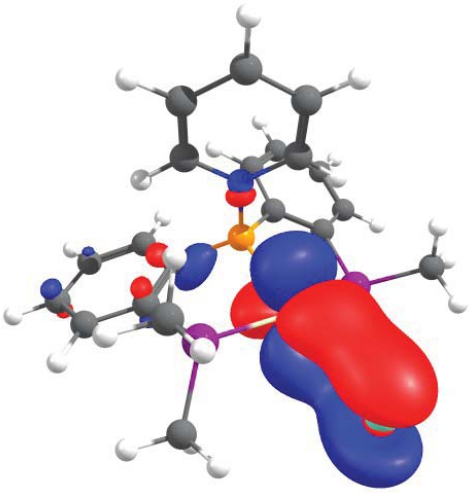

HOMO-12

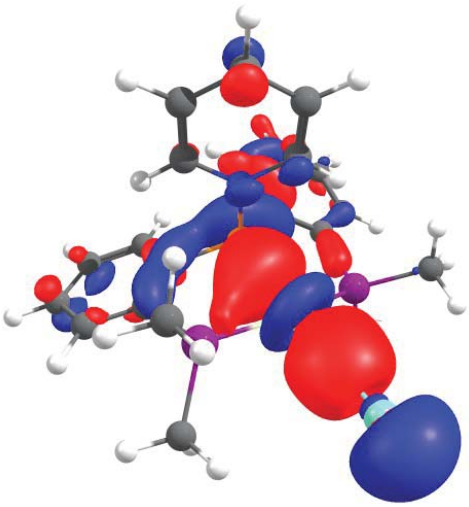

HOMO-15

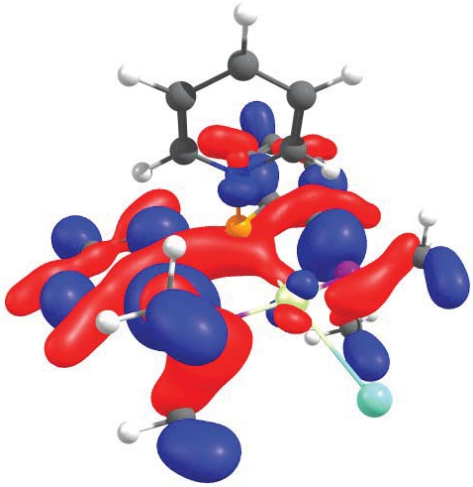

HOMO-17

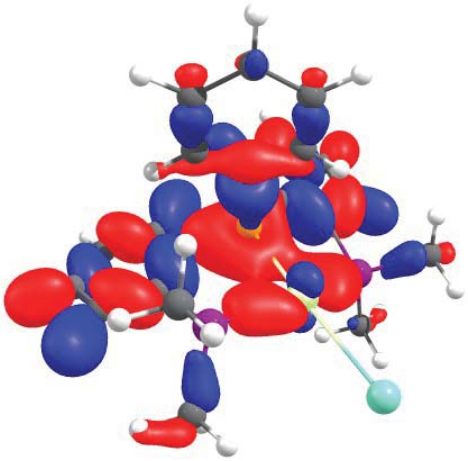

Quantum Theory of Atoms and Molecules (QTAIM)

Table 4 Comparison of bond critical point data in atomic units of the Pd-B-bond in **3^{Me}-Br**, **3^{Me}-Cl**, **A^{Me}** and **B^{Me}**.

	ρ	$\nabla^2\rho$	$\in$	K_{bcp}	V_{bcp}	H_{bcp}
3^{Me}-Br	0.090626	-0.007863	0.063472	0.038974	-0.075977	-0.037003
3^{Me}-Cl	0.091572	-0.008755	0.069699	0.039596	-0.076998	-0.037402
A^{Me}	0.020004	0.029088	0.606243	0.001389	-0.01005	-0.008661
B^{Me}	0.085673	-0.037487	0.026577	0.038215	-0.067059	-0.028844

Table 5 Bond critical point data in atomic units for **3^{Me}-Cl**.

Bond	ρ	$\nabla^2\rho$	∈	K_{bcp}	V_{bcp}	H_{bcp}
Pd1 - Cl2	0.066421	0.187503	0.04863	0.01266	-0.07217	-0.05951
Pd1 - P3	0.103726	0.138338	0.015354	0.040441	-0.115394	-0.074953
Pd1 - B5	0.091572	-0.008755	0.069699	0.039596	-0.076998	-0.037402
Pd1 - P4	0.101723	0.136356	0.025098	0.038802	-0.111626	-0.072824
B5 - P8	0.129748	-0.214093	0.173496	0.120813	-0.188103	-0.06729
B5 - P9	0.128225	-0.217616	0.119375	0.118576	-0.182748	-0.064172
B5 - H14	0.165223	-0.186382	0.012748	0.176202	-0.305809	-0.129607

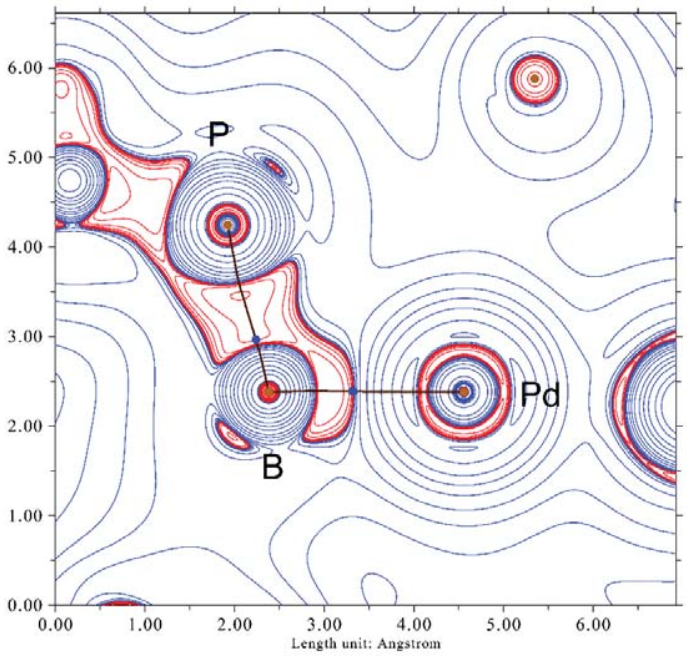

Figure 14 Molecular graph for complex **3^{Me}-Cl** derived from QTAIM analysis with a contour plot of the Laplacian in the P-B-Pd plane. Bond critical points are indicated as blue dots. Positive values of the Laplacian (charge depletion) are depicted as solid blue lines, and negative values (charge accumulation) as red lines.

Table 6 Bond critical point data in atomic units for **3^{Me}-Br**.

Bond	ρ	$\nabla^2\rho$	$\in$	K_{bcp}	V_{bcp}	H_{bcp}
Pd1 - Br2	0.058248	0.137973	0.057183	0.009988	-0.054462	-0.044474
Pd1 - P3	0.103841	0.138583	0.021378	0.04055	-0.115674	-0.075124
Pd1 - P4	0.10133	0.136374	0.027284	0.038493	-0.111015	-0.072522
Pd1 - B5	0.090626	-0.007863	0.063472	0.038974	-0.075977	-0.037003
B5 - P8	0.129942	-0.21554	0.167124	0.121051	-0.188216	-0.067165
B5 - P9	0.127743	-0.217593	0.111006	0.117738	-0.181078	-0.06334
B5 - H14	0.165415	-0.189149	0.016006	0.176547	-0.305807	-0.12926

Table 7 Bond critical point data in atomic units for $\mathbf{A^{Me}}$.

Bond	ρ	$\nabla^2\rho$	∈	K_{bcp}	V_{bcp}	H_{bcp}
Pd1 - Cl2	0.076242	0.19468	0.042741	0.017069	-0.082808	-0.065739
Pd1 - B6	0.020004	0.029088	0.606243	0.001389	-0.01005	-0.008661
Pd1 - Cl3	0.072847	0.190121	0.046568	0.015519	-0.078568	-0.063049
Pd1 - P4	0.111596	0.097202	0.022069	0.048259	-0.120818	-0.072559
Pd1 - P5	0.107013	0.097435	0.029939	0.044407	-0.113174	-0.068767
B6 - C14	0.190579	-0.22681	0.126211	0.211937	-0.367172	-0.155235
B6 - C15	0.180126	-0.225792	0.239159	0.196062	-0.335677	-0.139615

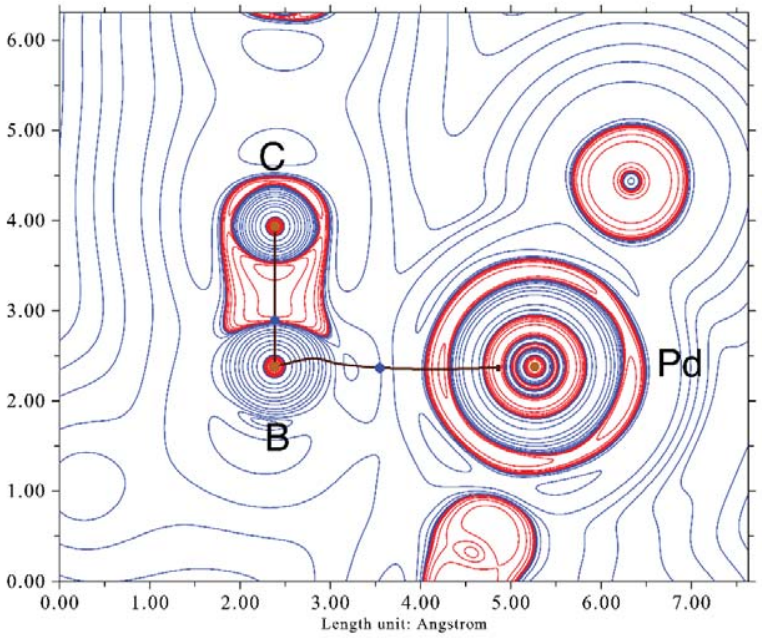

Figure 15 Molecular graph for complex $\mathbf{A^{Me}}$ derived from QTAIM analysis with a contour plot of the Laplacian in the C-B-Pd plane. Bond critical points are indicated as blue dots. Positive values of the Laplacian (charge depletion) are depicted as solid blue lines, and negative values (charge accumulation) as red lines.

Table 8 Bond critical point data in atomic units for $\mathbf{B^{Me}}$.

Bond	ρ	$\nabla^2\rho$	∈	K_{bcp}	V_{bcp}	H_{bcp}
Pd1 - B5	0.085673	-0.037487	0.026577	0.038215	-0.067059	-0.028844
Pd1 - P2	0.108143	0.139611	0.020959	0.044832	-0.124568	-0.079736
Pd1 - P3	0.10403	0.144808	0.025885	0.041348	-0.118898	-0.07755
Pd1 - I4	0.045642	0.087695	0.061059	0.007382	-0.036688	-0.029306
B5 - C12	0.164056	-0.188483	0.08083	0.172342	-0.297562	-0.12522
B5 - C14	0.165549	-0.19283	0.073636	0.174529	-0.300851	-0.126322
B5 - N13	0.116784	0.290182	0.059865	0.089818	-0.252181	-0.162363

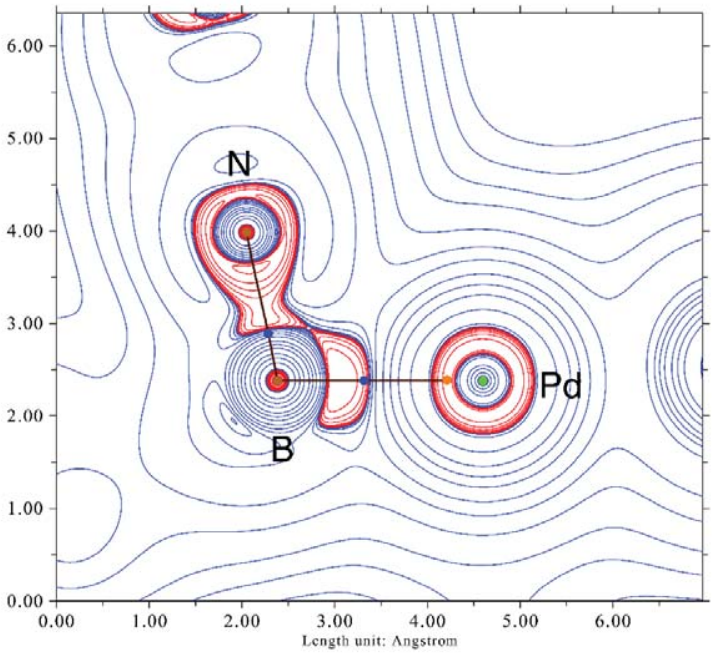

Figure 16 Molecular graph for complex $\mathbf{B^{Me}}$ derived from QTAIM analysis with a contour plot of the Laplacian in the C-B-Pd plane. Bond critical points are indicated as blue dots. Positive values of the Laplacian (charge depletion) are depicted as solid blue lines, and negative values (charge accumulation) as red lines.

H	5.000206000	1.292440000	-5.029903000
H	10.581570000	2.567591000	-1.668892000
C	10.806672000	4.176744000	-3.114771000
H	10.610031000	5.839038000	-4.492053000
H	4.263866000	7.337637000	-5.727563000
H	11.862349000	4.004241000	-3.303802000

Literature

1. K. Sommer, *Z. Anorg. Allg. Chem.*, 1970, **376**, 37-43.
2. G. M. Sheldrick, *Acta Crystallogr., Sect. A*, 2008, **64**, 112-122.
3. X.-R. 1.01, *Data Reduction Program, Stoe & Cie GmbH, Darmstadt, Germany, 2001*.
4. X.-S. 1.06, *Crystal Optimization for Numerical Absorption Correction Program, Stoe & Cie GmbH, Darmstadt, 1999*.
5. M. J. Frisch, G. W. Trucks, H. B. Schlegel, G. E. Scuseria, M. A. Robb, J. R. Cheeseman, G. Scalmani, V. Barone, B. Mennucci, G. A. Petersson, H. Nakatsuji, M. Caricato, X. Li, H. P. Hratchian, A. F. Izmaylov, J. Bloino, G. Zheng, J. L. Sonnenberg, M. Hada, M. Ehara, K. Toyota, R. Fukuda, J. Hasegawa, M. Ishida, T. Nakajima, Y. Honda, O. Kitao, H. Nakai, T. Vreven, J. A. Montgomery, J. E. P. Jr., F. Ogliaro, M. Bearpark, J. J. Heyd, E. Brothers, K. N. Kudin, V. N. Staroverov, R. Kobayashi, J. Normand, K. Raghavachari, A. Rendell, J. C. Burant, S. S. Iyengar, J. Tomasi, M. Cossi, N. Rega, J. M. Millam, M. Klene, J. E. Knox, J. B. Cross, V. Bakken, C. Adamo, J. Jaramillo, R. Gomperts, R. E. Stratmann, O. Yazyev, A. J. Austin, R. Cammi, C. Pomelli, J. W. Ochterski, R. L. Martin, K. Morokuma, V. G. Zakrzewski, G. A. Voth, P. Salvador, J. J. Dannenberg, S. Dapprich, A. D. Daniels, Farkas, J. B. Foresman, J. V. Ortiz, J. Cioslowski and D. J. Fox, *Gaussian 09 Revision C.01, Gaussian Inc. Wallingford CT 2009*.
6. E. D. Glendening, J.K. Badenhoop, A. E. Reed, J. E. Carpenter, J. A. Bohmann, C. M. Morales and F. Weinhold, *(Theoretical Chemistry Institute, University of Wisconsin, Madison, WI, 2012)*, NBO 5.9, **www.chem.wisc.edu/~nbo5**.
7. S. Grimme, *J. Comput. Chem.*, 2006, **27**, 1787-1799.
8. A. Schäfer, H. Horn and R. Ahlrichs, *J. Chem. Phys.*, 1992, **97**, 2571.
9. F. Weigend and R. Ahlrichs, *Phys. Chem. Chem. Phys.*, 2005, **7**, 3297-3305.
10. *Chemcraft version 1.8*, **www.chemcraftprog.com**.
11. Todd A. Keith and O. P. K. TK Gristmill Software, USA, *AIMAll (Version 17.01.25)*, 2017, **www.aim.tkgristmill.com**.
12. Tian Lu and F. Chen, *J. Comp. Chem.*, 2012, **33**, 580-592.

FULL PAPER

Ancillary Ligand Induced H_2-Liberation from Phosphine-Borane Complexes: Fe-B-Bond Formation vs. Hydride Protonation

Lisa Vondung[a], Lukas Alig[a], Monika Ballmann[a], Robert Langer*[a]

Abstract: η^2-coordinated phosphine-borane ligands are demonstrated to undergo dehydrocoupling reactions and simultaneous P-B-bond formation upon treatment with different σ-donor/π-acceptor ligands (CO, ^{t}BuNC, CN^-). The general reaction scheme proceeds via coordination of the ancillary ligand and change of the hapticity of the phosphine-borane to a η^1-mode. A second equivalent of the ancillary ligand induces hydrogen liberation from the η^1-coordinated key-intermediate **B**, which, depending on the type of ligand, results in different products. Formation of a phosphine-stabilized boryl-ligand is observed with carbon monoxide as second ancillary ligand, whose subsequent re-arrangement yields a pincer-type ligand with a central donor group based on tricoordinate boron. With *tert*-butylisocyanide as ancillary ligand two pathways of hydrogen liberation are observed: protonation of the hydrido ligand yields a η^1-phosphine-borane complex, while the competitive formation of a boryl-intermediate finally leads to a complex with a pending bis(phosphine)borate group.

Introduction

Neutral phosphine-boranes as ligands for transition metal complexes have been developed since the 1980's[1–6] and are still attracting attention as potential hydrogen storage materials, metal-free catalysts and ambiphilic ligands. Initially, the interest in this ligand class was triggered by its ability to form B-H-M bridging bonds and its isoelectronic relationship with alkanes.[1,3,7,8] In contrast to the corresponding alkane ligands, phosphine-borane complexes are stable under ambient conditions and thus enable further studies.[3] The $R_3P{\cdot}BH_3$ ligand can bind either in η^1- or in η^2-mode to the metal centre and is often fluxional, due to exchange between the three boron-bound hydrogen atoms.[3,9] It became soon evident that the use of chelating ligands enhances the stability of these complexes enormously.[7,10,11]

The reactivity of the phosphine-borane group in transition metal complexes has been studied in different contexts. An overview of frequently observed reactivity patterns is provided in Scheme 1. *Weller* and co-workers showed for example that addition of CO or PMe_3 to a solution of [Ru(Cp*)(η^2-$H_3B{\cdot}$dppm)](PF_6), [Ru(Cp*)(η^2-$H_2ClB{\cdot}$dppm)]($BAr^F{}_4$) or [Mn(CO)$_3$(η^2-$H_3B{\cdot}$dppm)]($BAr^F{}_4$) leads to a change of the borane binding mode from η^2 (type **A**) to η^1 (type **B**) and coordination of the ancillary ligand.[7,12,13]

From the same group, investigations on the catalytic dehydropolymerization of phosphine-boranes were reported.[14] In these reactions, the formation of a phosphine-stabilized boryl complex of type **C** is observed, which was formed by loss of H_2 from a η^1-phosphine-borane complex of type **B** (with a hydrido ligand as internal base).

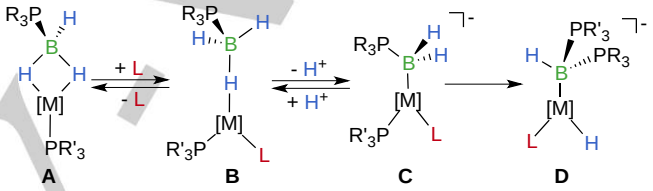

Scheme 1. Reactivity of phosphino-borane ligands with ancillary ligands in coordinatively saturated and unsaturated transition metal complexes.

The reverse reaction from a phosphine-stabilized boryl complex of type **C** to a η^1-phosphine-borane complex of type **B** can be induced by proton addition, as reported for the manganese complexes [Mn(CO)$_4$(PR_3)($BH_2{\cdot}PMe_3$)] (R = PMe_2Ph, PEt_3) by *Shimoi* and co-workers.[15] Alternative reaction pathways of η^1-phosphine-boranes (**B**) are assumed reaction steps in dehydrocoupling/ dehydropolymerization of phosphine-boranes.[14,16] The B-H activation and concomitant P-B coupling of a η^1-phosphine-borane (type **B**) to a bis(phosphine)boronium or –borate complex was proposed by *Manners* and co-workers based on density functional theory (DFT) calculations for the mechanism of [CpFe(CO)$_2$(HP{BH_3}Ph)]-catalysed dehydropolymerization of phosphine-boranes.[16] Our group showed recently, that an iron complex with a phosphine-stabilized boryl ligand of type **C** reacts to a phosphine-stabilized borylene complex (type **D**) via a bis(phosphine)boronium or –borate intermediate.[17] Dihydrogen formation in the coordination sphere of the transition metal and subsequent hydrogen liberation, as well as the concomitant B-E-bond formation are key steps in the catalytic dehydrogenation of phosphine-boranes and amino-boranes (E = N, P). Reactivity patterns of model compounds can provide deeper mechanistic understanding and show competing reaction pathways that potentially lead to catalyst deactivation.[18] In particular, ancillary ligands seem to play an important role for the observed reactivity and can directly induce hydrogen liberation.

Herein, we describe the reactivity of an iron complex with a chelating phosphine-borane towards ancillary ligands. Depending on the ancillary ligand different pathways of hydrogen liberation are realized and subsequent formation of ligand-stabilized

[a] L. Vondung, L. Alig, M. Ballmann, Dr. R. Langer
Fachbereich Chemie
Philipps-Universität
Hans-Meerwein-Str. 4, 35032 Marburg, Germany
E-mail: robert.langer@chemie.uni-marburg.de

Supporting information for this article is given via a link at the end of the document.

borane-, boryl- or borylene intermediates is observed. As all intermediates (**A**-**D**) are involved in the subsequent reactions, the iron complexes reported herein can be regarded as a model system which helps to understand the basic reactivity patterns of phosphine-boranes.

Results and Discussion

Reactivity towards Ancillary Ligands

Starting point of our investigations was the previously observed formation of the boron-based pincer-type complex **3-CO** in the reaction of the η^2-phosphine-borane iron(II) complex **I** with carbon monoxide (Scheme 2).[19,20] This novel rearrangement sequence caught our interest. In continuation of this work, we explored whether this process can also be triggered by other small donor ligands. Therefore, we reacted complex **I** with related ligands, such as ^{t}BuNC, CN^- and NO^+ (Scheme 2). All investigated ancillary ligands are σ-donor/π-acceptor ligands, but vary greatly in their σ-donor and π-acceptor capability: the σ-donor strength is expected to increase in the order $NO^+ < CO < {}^t$BuNC < CN^-, while the π-acceptor ability shows the opposite trend $NO^+ < CO < {}^t$BuNC < CN^-.

Reacting **I** with $NOBF_4$ didn't lead to formation of new NO^+-containing complexes. Only singlet resonances of decomposition products could be observed by $^{31}P\{^1H\}$ NMR spectroscopy of the reaction mixture. The ^1H NMR spectrum showed only very broad resonances, presumably caused by a paramagnetic species. The observed gas evolution hints towards the formation of NO gas by oxidation of Fe^{II} to Fe^{III}. Quantum chemical investigations using DFT showed that the NO^+-ligand containing complexes are distorted with the additional carbonyl ligands in a μ-bridging binding mode.

The cyanido ligand is negatively charged and considered to be a good σ-donor and a poor π-acceptor. The reaction of complex **I** with KCN in the presence of 18-crown-6 leads to the formation of the new complex **1-CN** (Scheme 2). The ^1H NMR spectrum of **1-CN** shows a doublet of triplets at -20.17 ppm for a hydrido ligand that simplifies to a doublet or triplet resonance upon selective ^{31}P-decoupling. The broad resonance at -3.05 ppm sharpens upon ^{11}B decoupling of the ^1H NMR spectrum and can be assigned to a boron bound hydrogen atom. Four resonances are observed in the $^{31}P\{^1H\}$ NMR spectrum: a boron bound phosphorous atom gives rise to a broad resonance at 47.0 ppm. Three resonances with equal integrals appear at 93.6 (ddd), 96.3 (dd) and 115.3 (ddd) ppm. The resonance at -34.6 ppm in the $^{11}B\{^1H\}$ NMR spectrum is in agreement with η^1-phosphine-borane complexes, which typically give rise to high-field shifted resonances compared to the corresponding η^2-complexes.[13] The IR-spectrum of **1-CN** shows a band at 2061 cm^{-1}, which is assigned to the C-N-stretching vibration of one cyanido ligand. Judging from these observations, the reaction of **I** with potassium cyanide led to the formation of a η^1-phosphine-borane complex with a hydride, bis(diphenylphosphino)amine (dppa) and cyanido ligand. Layering a toluene solution of **1-CN** with *n*-hexane yields red crystals that are suitable for single crystal X-Ray diffraction. The determined molecular structure in the solid state confirms the structural assignment (Fig. 1). The Fe-$H1_{B1}$, B-$H1_{B1}$ and B-P bond lengths are in the same range as in related complexes.[3,7,13,14,16,21–28]

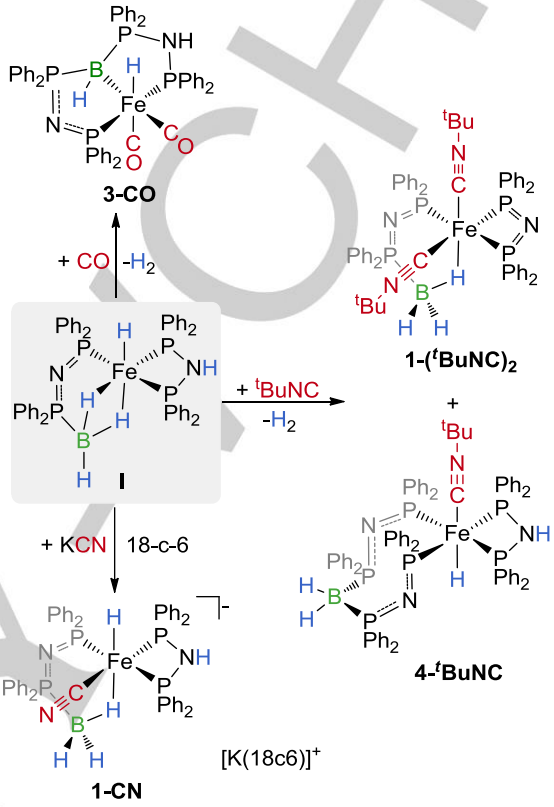

Scheme 2. Reactivity of the η^2-phosphine-borane complex **I** towards different ancillary ligands (18c6 = 18-crown-6 or rather 1,4,7,10,13,16-hexaoxacyclooctadecane).

Isocyanides, such as ^{t}BuNC, are neutral and more bulky than the other ligands, but they are good σ-donor ligands, too. The reaction of **I** with ^{t}BuNC resulted in the formation of a 1:1 mixture of two different products, according to $^{31}P\{^1H\}$ NMR spectroscopy of the reaction mixture (Scheme 2). The products can be separated by precipitating **4-^{t}BuNC** from the reaction solution with *n*-hexane.

Complex **1-(^{t}BuNC)$_2$** shows four resonances with similar integrals in the $^{31}P\{^1H\}$ NMR spectrum: three doublet of doublets at 36.8, 44.5 and 112.2 ppm, respectively, for the iron-bound phosphorus atoms and a broad resonance at 53.7, assignable to a boron-bound phosphorus atom. The $^{11}B\{^1H\}$ NMR spectrum of **1-(^{t}BuNC)$_2$** gives rise to a resonance at -41.1 ppm. Compared to the previously reported η^1-coordinated complex [(Ph_2P-N-PPh_2·BH_3)(dppa)Fe(CO)(H)] (**1-CO**),[20] this resonance is high-field shifted, probably due to the different ligand environment at the iron centre. In the ^1H NMR spectrum of **1-(^{t}BuNC)$_2$**, one broad resonance with a relative integral of one is observed in the hydride region at -13.6 ppm. ^{11}B-decoupling of this resonance results in slight sharpening, but coupling constants remained unresolved, indicating fluxional boron-bound hydrogen atoms. The absence of

a resonance for a nitrogen-bound proton of the initial dppa ligand in the ^{1}H NMR spectrum indicates that the latter was deprotonated in this reaction. Based on the appearance of two resonances in the ^{1}H and the ^{13}C{^{1}H} NMR spectra for the *tert*-butyl groups of the isocyanide ligands, we concluded the coordination of two magnetically non-equivalent isocyanide ligands in **1-(ᵗBuNC)₂**. This view is further confirmed by high resolution mass spectrometry. However, despite several attempts under various conditions we were unable to obtain single crystals for X-Ray diffraction analysis. DFT calculations at B97D/def-TZVPP-level of theory identified **1-(ᵗBuNC)₂** as an energetic minimum. The observation of only one band for C-N and Fe-H stretching vibrations in the IR spectrum is in agreement with the frequency calculations and can be explained by strong coupling of the C-N and Fe-H vibrational modes.

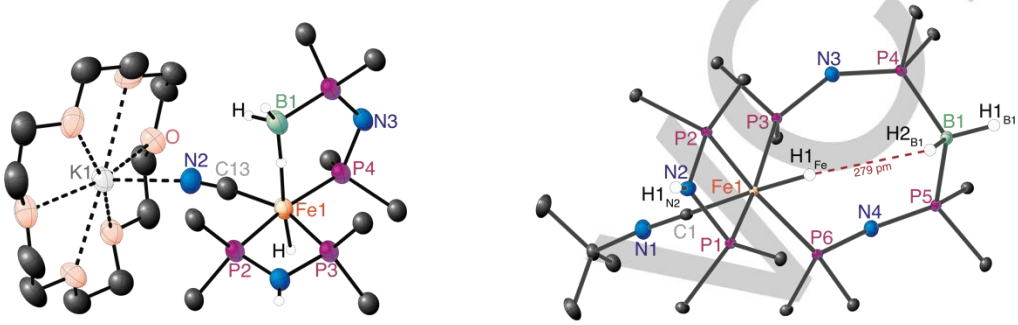

Figure 1. Molecular structure of **1-CN** (left) and **4-ᵗBuNC** (right) in the solid state (ellipsoids are drawn at 30% probability, carbon-bound hydrogen atoms are omitted, only the phosphorus-bound carbon atoms of the phenyl rings are shown for clarity); selected distances (Å) and angles (°) of **1-CN**: Fe1-P2 2.152(2), Fe1-P3 2.183(2), Fe1-P4 2.219(2), Fe1-H1B1 1.5671(9), Fe1-H1Fe 1.48(5), Fe1-C13 1.917(6). Selected distances (Å) and angles (°) of **4-ᵗBuNC**: Fe1-H1Fe1 1.48(2), Fe1-P1 2.2495(6), Fe1-P2 2.2282(6), Fe1-P3 2.2766(6), Fe1-P6 2.2345(5), Fe1-C1 1.844(2), C1-N1 1.171(2), P4-B1 1.934(2), P5-B1 1.922(2), P4-B1-P5 112.28(8), P3-Fe1-P6 93.03(1), P1-Fe1-P2 71.31(1), H1Fe1-Fe1-C1 177.2(9).

For complex **4-ᵗBuNC** only three resonances are observed in the ^{31}P{^{1}H} NMR spectrum (Table 1). One broad resonance appears at 22.0 ppm and two multiplets are observed at 88.8 and 90.8 ppm with similar relative integrals compared the the first resonance. The ^{1}H NMR spectrum of **4-ᵗBuNC** shows a triplet of a triplet resonance at -5.2 ppm for an iron-bound hydride coupling to four phosphorous atoms, indicating an isocyanide ligand in *trans*-position to the hydrido ligand. Furthermore, only one singlet resonance with an integral of nine is observed for the *tert*-butyl group of the isoncyanide, suggesting the coordination of only one isocyanide ligand. In the ^{11}B{^{1}H} NMR spectrum, a resonance at -31.7 ppm is observed for **4-ᵗBuNC**, which corresponds well to the previously reported **4-CO** (Table 1). In the IR spectrum of **4-ᵗBuNC,** only one band is observed for the Fe-H_B and C-N vibrations.

Layering a dichloromethane solution of **4-ᵗBuNC** with *n*-hexane leads to the formation of red crystals that were suitable for single crystal X-Ray diffraction. The obtained structure confirms the formation of an iron(II) complex containing one ᵗBuNC ligand, one hydrido ligand, a dppa ligand and a newly formed dppa-BH_2-dppa ligand (Fig. 1, right). The P-B, Fe-H and Fe-C bond lengths and P-B-P angle are as expected from the literature.[29,30] The determined bond lengths and angles are furthermore in agreement with the optimized structures from DFT calculations. The frequency calculation also showed that the Fe-H_B and C-N vibrations are strongly coupled and therefore give rise to only one band, as already observed for **1-(ᵗBuNC)₂**. High resolution mass spectrometric analysis confirmed the formation of **4-ᵗBuNC** as well.

Table 1. Selected spectroscopic properties of the investigated compounds.

	δ (^{31}P{^{1}H}) / ppm	δ (^{11}B{^{1}H}) / ppm
I[a]	54.3, 96.3, 111.1, 129.0	23.2
1-CO[b]	48.8, 85.6, 98.4, 100.4	-31.5
1-(ᵗBuNC)₂	36.8, 44.7, 63.7, 112.2	-41.1
1-CN	46.9, 93.6, 96.3, 115.3	-34.7
2-CO[b]	63.8, 87.5, 95.1, 105.4	-5.8
3-CO[b]	46.7, 52.6, 115.7, 129.2	-16.7
3b-CN	45.9, 95.3	-37.5
4-CO[c]	22.2, 83.5, 89.3	-32.0
4-ᵗBuNC	21.6, 88.8, 90.8	-31.7

[a] Taken from reference [19]; [b] Taken from reference [17]; [c] Taken from reference [31].

Phosphine-stabilized Borylene vs. Borate

The reaction of **I** with carbon monoxide yields the pincer-type complex **3-CO** with two ancillary carbonyl ligands and a pincer-

type ligand with a central donor group based on tri-coordinated boron.[20] This unusual bonding situation is caused by π-accepting phosphine substituents that enable the stabilization of an occupied p_z-orbital in the uncoordinated form via π-back bonding.

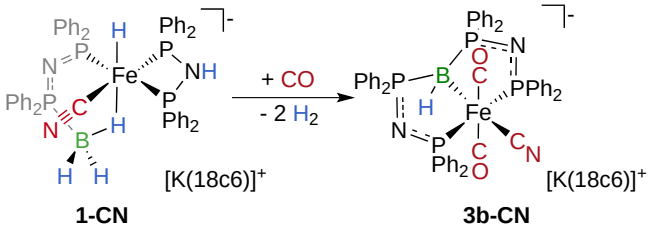

Scheme 3. Reaction of η¹-phosphine-borane cyanido complex **1-CN** with CO to the pincer complex **3b-CN**.

However, the reaction with KCN and crown ether leads to the coordination of one cyanide ligand and **1-CN** does not show any further reactivity, even in the presence of excess cyanide at elevated temperatures. Interestingly, treatment of **1-CN** with carbon monoxide results in an immediate reaction and formation of the new complex **3b-CN** within minutes and no resonances of the starting complex **1-CN** are observed in the $^{31}P\{^1H\}$ NMR spectrum of the reaction mixture after 5 minutes under CO atmosphere. Instead, a broad resonance at 43.9-49.0 ppm and a doublet of doublets resonance at 95.3 ppm (J_{PP} = 45.0 Hz, 75.7 Hz) of low intensity are detected. This is in line with a symmetrisation to a complex with two sets of magnetically equivalent phosphorous atoms. At lower temperatures, the intensity of the resonances rises, indicating a high flexibility of the complex. The ^1H NMR spectrum shows no resonance in the hydridic region. In the $^{11}B\{^1H\}$ NMR spectrum one resonance at -37.5 ppm is observed, which is approx. 21 ppm high-field-shifted compared to **3-CO** (Table 1) and at least 11 ppm high-field-shifted compared to other reported borylene complexes.[32–34] This is probably due to the different charges of the complexes and the different ligands in *trans*-position to the borylene: **3-CO** is neutral and a CO ligand is in *trans*-position to the borylene, whereas in **3b-CN** the complex is anionic and the stronger σ-donor CN^- is *trans*-position to the boron-based donor group.

One band at 2083 cm^{-1} for the stretching mode of the cyanido ligand and two bands at 1922 and 1871 cm^{-1} for the C-O-stretching mode of the carbonyl ligands are observed in the IR spectrum of **3b-CN**. All attempts to prepare suitable crystals for single crystals X-ray diffraction yielded crystals of comparably poor quality that showed only weak diffraction patterns. Nonetheless, it was possible to confirm the connectivity in complex **3b-CN** (Figure 2). In contrast to **3-CO**, no hydride ligand is present in **3b-CN**, as already indicated by the ^1H NMR spectrum. The two carbonyl ligands are situated *trans* to each other and the cyanide ligand occupies the position *trans* to the boron-based donor group. Boron-based donor ligands are expected to show a strong *trans*-influence. However, in **3b-CN** the strongest σ-donor of the ancillary ligands, the cyanido ligand is situated *trans* to the central boron-based donor group. DFT calculations on the Gibbs free energies of the different possible isomers with the [K(18-crown-6)] counter ion show that in the gas phase the *cis*-isomer should be more stable by 23 kJ/mol, indicating that **3b-CN** is a kinetically stabilized isomer.

Both ligand arms (Ph_2P-N-PPh_2) are deprotonated at the nitrogen atoms, resulting in an overall charge of -1 for the complex. $[K(18\text{-crown-6})]^+$ acts as the counter ion with a N···K distance of 2.66 Å. The Fe-B and P-B bond lengths are very similar to those in **3-CO**, while the Fe-CO bond lengths are elongated to 1.860(18) Å compared to 1.764(3) - 1.772(2) Å in **3-CO**. In many cases, a Lewis acid or Z-type ligand is located on an edge of the coordination polyhedron formed by the donor ligands (L- and X-type).[35,36][37] In the current case, the coordination geometry of the five remaining donor groups without the boron-based ligand can help to distinguish between a Z- and a X- or L-type ligand. A trigonal-bipyramidal geometry would indicate a Z-type ligand and a square pyramidal geometry a X- or a L-type ligand. The τ-parameter for the penta-coordinated fragment in **3b-CN** is 0.08, which is in agreement with a boron-based donor ligand.[38]

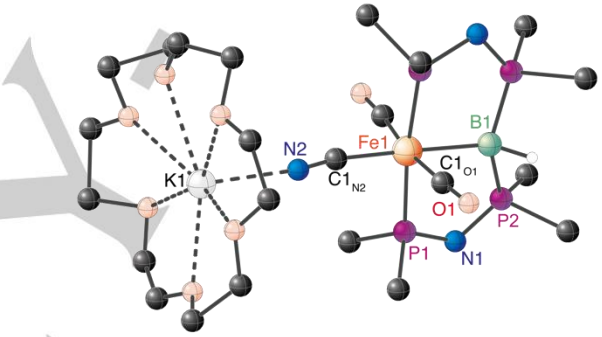

Figure 2. Molecular structure of **3b-CN** in the solid state (carbon-bound hydrogen atoms are omitted, only the phosphorus-bound carbon atoms of the phenyl rings are shown for clarity); selected distances (Å) and angles (°): K1-N3 2.69(1), Fe1-P1 2.260(2), Fe1-B1 2.21(1), Fe1-$C1_{O1}$ 1.71 (2), Fe1-$C1_{N2}$ 1.951(1); $C1_{O1}$'-Fe1-$C1_{O1}$ 167.8(9), P1-Fe1-P1' 172.3(1).

In order to investigate the bonding situation between boron and iron in **3b-CN** we performed DFT calculations. The optimized structure represents an energetic minimum and all bond lengths and angles are in agreement with the experimentally derived structure. Inspection of the molecular orbitals (MOs) reveals that the shape of the HOMO-1 (Fig. 3 left) and HOMO-2 can be attributed to a σ-bond between Fe and B. This is a similar observation as for **3-CO**,[20] but the shape of the HOMO-1 varies slightly, in that a different d-orbital contributes from the iron atom. Subsequently, a topological study based on the Quantum Theory of Atoms in Molecules (QTAIM) was done. The molecular graph with bond critical points (bcps) and the contour plot of the Laplacian of the electron density is shown in Figure 3 (right). In the contour plot of the Laplacian similar bonding situations for the B-Fe and NC-Fe bonds can be observed, which are in line with donor-acceptor bonds from the ligand to the central metal atom. Looking at the electron and energy densities at the Fe-B bcp, very similar values are obtained for **3b-CN** and **3-CO**. These findings

clearly show that the central group in the PBP-type ligand in **3b-CN** is a boron-based donor group.

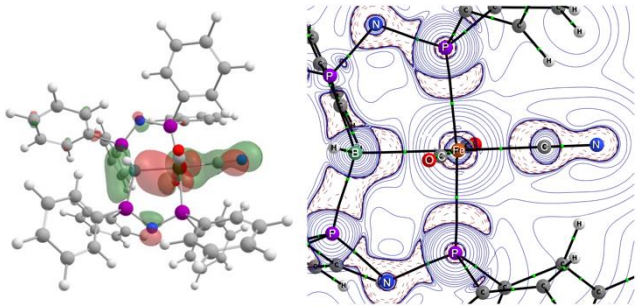

Figure 3. Left: HOMO-1 of **3b-CN.** Right: Molecular graph of **3b-CN** with bcps and contour plot of the Laplacian of the electron density, as derived from QTAIM analysis. Bond critical points are indicated as green dots. Positive values of the Laplacian (charge depletion) are depicted as solid blue lines, and negative values (charge accumulation) as broken red lines.

For the representation of coordination compounds the use of formal charges and donor arrows is uncommon. However, as both arms in **3b-CN** are deprotonated and the entire pincer ligand is a dianion, the actual bonding situation in **3b-CN** is described by several possible resonance structures, which lead to different descriptions of the boron-based donor group. Scheme 4 shows a selection of possible resonance structure.

Based on quantum chemical investigations, the structural parameters and the ^{11}B NMR shifts, we assume the presence of a donor group in **3b-CN** (L- or X-type). A qualitative analysis of molecular orbitals reveals that the lone pair at the nitrogen atoms of the protonated ligand exhibits p-orbital character, which is perpendicular to the plane formed by two phosphorus atoms, the nitrogen atom and the hydrogen atom.[20] Upon deprotonation the second lone pair is mainly located in the P-N-P-plane of the arm, indicating a charge localization at the nitrogen atoms. In such a case the bonding situation is best described by the structures **A** and **B**. Depending on the classification of the P-B-bonds the donor group in **3b-CN** can either be described as a phosphine-stabilized borylene (**B**) or as a bis(phosphine)borate-anion (**A**). However, consideration π-bonding between nitrogen and phosphorus leads to a number of additional resonance structures (e. g. **C** and **D**), in which some of the phosphorus atoms exhibit the formal oxidation state +5.

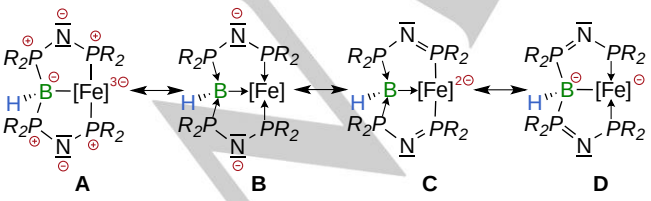

Scheme 4. Selection of possible resonance structures and binding modes for **3b-CN** ([Fe] = {Fe(CN)(CO)$_2$}$^+$).

For **3-CO** it has previously been demonstrated that the partial charges obtained from natural population analysis (NPA) at the boron, the phosphorus and the iron atoms are just slightly changing (Δq = 0.01-0.05*e*) upon deprotonation or protonation,[20] indicating that resonance structures like **C** and **D** only have a minor impact on the actual bonding situation. The partial charges based on NPA in **3b-CN** are very similar to those found in **3-CO** and its (de)protonated analogues. In consequence the bonding situation is expected to be similar in the ligands with protonated and deprotonated nitrogen atoms. Based on reports about carbene- and carbonyl-stabilized borylenes, the uncoordinated ligand with both nitrogen atoms protonated is best described as a phosphine-stabilized borylene. The bonding situation in **3b-CN** can be understood in a similar manner, by a donor acceptor bond between the phosphorus atoms and the central boron atom, as described by resonance structure **B**.

Reaction Pathways

For carbon monoxide as ancillary ligand the rearrangement leading to the boron-based pincer-type complex **3-CO** involves the η^1-intermediate **1-CO** that can be trapped by very short exposure to CO (less than five seconds).[20] Subsequent loss of H_2 is induced by the reaction with a second equivalent of carbon monoxide after a few minutes, yielding the phosphine-stabilized boryl complex **2-CO**. The latter is stable enough to be crystallized at low temperatures, but rearranges at ambient temperature under argon atmosphere to the pincer-type complex **3-CO** over the course of a few hours. In case of potassium cyanide the reaction stops at the η^1-coordinated complex **1-CN**, but a different isomer is formed than with carbon monoxide. For both ancillary ligands the isomer with a *trans*-arrangement of the hydrido ligand and the phosphine-borane was calculated to be the most stable one. However, in both cases the isomer with the ancillary ligand in *trans*-position to the phosphine-borane is only 2-5 kJ/mol higher in Gibbs energy according to DFT calculations. The reaction of **1-CN** with carbon monoxide is also fast and did not allow for the detection of intermediates by NMR spectroscopy. However, the fact that a boron-based pincer-type complex is formed by the reaction of the η^1-coordinated phosphine-borane with carbon monoxide suggests that the reaction proceeds via the same intermediates as the reaction of **I** with carbon monoxide.

In contrast, the reaction of **I** with *tert*-butylisocyanide is less selective and leads to different reaction products than with the other ancillary ligands. The formation of **1-(*t*BuNC)$_2$** must proceed via a competing pathway for hydrogen liberation from the η^1-coordinated phosphine-borane complex. However, formation of **4-*t*BuNC** with three dppa- or Ph_2P-N-PPh_2-building blocks must involve the "decomposition" of one of the intermediates, as the ^{31}P{^{1}H} NMR spectra of the reaction didn't show enough free dppa to explain the origin of the third equivalent of dppa in **4-*t*BuNC**.

In order to gain more insights in the product formation, the reaction was monitored by ^{31}P{^{1}H} NMR spectroscopy (Fig. 4). Directly after addition of the *tert*-butylisocyanide, the resonances of complex **I** completely disappeared in the ^{31}P{^{1}H} NMR spectrum and the formation of two main species was observed (marked in green and violet), whose resonances slowly vanish over the course of several hours. In parallel, resonances

assignable to **4-^{t}BuNC** (marked in brown) are slowly growing with increasing reaction time. After 55 minutes, complex **1-(^{t}BuNC)$_2$** (marked in yellow) starts being formed in detectable concentrations. ^{1}H NMR spectra of the reaction solution after a few hours show five resonances in the hydride region. As discussed in the previous section, the triplet resonance at -5.2 ppm in the ^{1}H NMR spectrum is assigned to the hydrido ligand in **4-^{t}BuNC** and the broad resonance at -13.6 ppm corresponds to the iron-bound hydrogen atom of the BH_3-group in **1-(^{t}BuNC)$_2$**. A broad resonance at -3.6 ppm in the ^{1}H NMR spectrum sharpens upon ^{11}B-decoupling and integrates to 3, while a virtual quartet at -18.5 ppm exhibits a relative integral of 1. These two resonances are assigned to the η^1-phosphine-borane complex **1-^{t}BuNC** that is formed by addition of one equivalent of ^{t}BuNC to **I**. Based on selective ^{31}P-decoupling experiments and comparison with other η^1-phosphine-borane complexes (**1-L^1**), the resonances at 48.1, 88.7, 104.5 and 116.6 ppm in the ^{31}P{^{1}H} NMR spectrum are assignable to **1-^{t}BuNC** (marked in violet). The second intermediate is the boryl complex **2-^{t}BuNC** (marked in green) with a broad resonance at 48.1 (superimposed with **1-^{t}BuNC**) for the boron-bound phosphorus atom, a doublet of doublets resonance at 90.6 ppm, a doublet of triplets resonance 96.4 ppm and doublet of doublets of doublets resonance at 109.7 ppm. The coupling patterns correspond well to the already known **2-CO**.[20] The ratio of **1-^{t}BuNC/2-^{t}BuNC** stays approximately 1:2 over the first two hours of the reaction, while **4-^{t}BuNC** is formed first in a 2:1 ratio compared to **1-(^{t}BuNC)$_2$**. At the end of the reaction, **4-^{t}BuNC** and **1-(^{t}BuNC)$_2$** are obtained in equal amounts, as determined by ^{31}P{^{1}H} NMR spectroscopy. Therefore, it can be assumed that the reaction proceeds via the same intermediates as the reaction with CO (Scheme 5): First, the η^1-phosphine-borane complex **1-^{t}BuNC** is formed, which is in principle energetically accessible, but not very stable for ^{t}BuNC, as judged by DFT calculations. Reaction of **1-^{t}BuNC** with a second equivalent of ^{t}BuNC induces hydrogen liberation, which in this case can proceed via different pathways (Scheme 5): (1) protonation of the hydrido ligand in **1-^{t}BuNC** by the NH-proton and subsequent hydrogen liberation leads to **1-(^{t}BuNC)$_2$**; (2) hydrogen liberation from the η^1-coordinated phosphine-borane and the hydrido ligand in **1-^{t}BuNC** leads to the formation of **2-^{t}BuNC**. The boryl complex **2-^{t}BuNC**, which in contrast to **2-CO** cannot be isolated, reacts to complex **4-^{t}BuNC**. As one equivalent of dppa is consumed in this reaction step, only small but invariant amounts of uncoordinated dppa are detected during the reaction (δ_P = 44.1 ppm). No other species could be detected by ^{31}P{^{1}H} NMR spectroscopy as a result of dppa transfer. Therefore, the dppa transfer is expected to lead to an iron complex, in which all phosphines are replaced by isocyanide ligands. Indeed, several additional resonances of low intensity are observed in the ^{1}H NMR spectra for the *tert*-butyl groups of isocyanide ligands, from which one exhibits the chemical shift of 1.28 ppm, which is known from [Fe(^{t}BuNC)$_5$].[39,40]

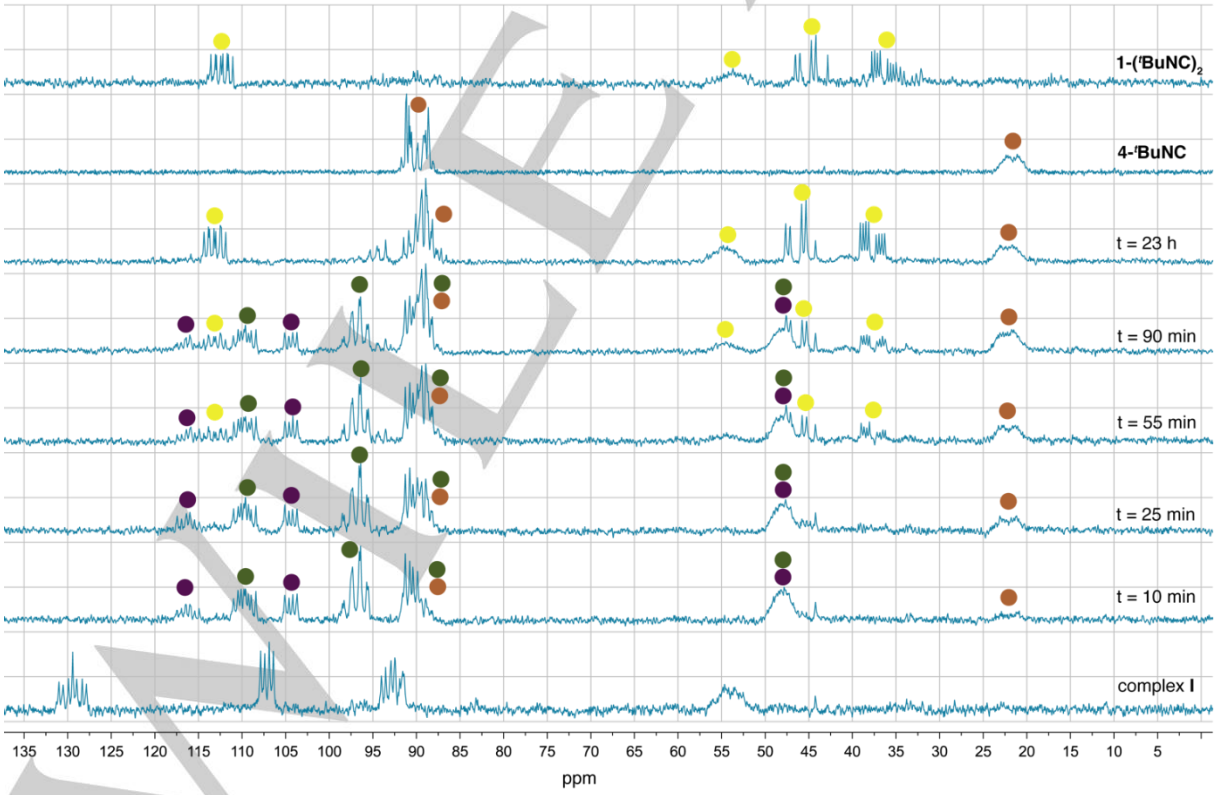

Figure 4. Time dependent ^{31}P{^{1}H} NMR spectra of the reaction solution of **I** in thf-d_8 with 3 equivalents ^{t}BuNC and ^{31}P{^{1}H} NMR spectra of isolated **4-^{t}BuNC** and **1-(^{t}BuNC)$_2$** for comparison. Colour code: violet: **1-^{t}BuNC**, green: **2-^{t}BuNC**, brown: **4-^{t}BuNC**, yellow: **1-(^{t}BuNC)$_2$**.

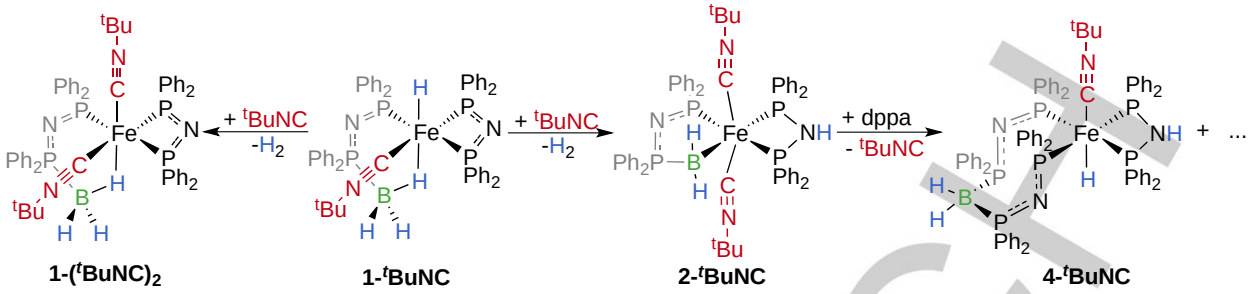

Scheme 5. Reactivity of the detected η^1-coordinated phosphine-borane intermediate **1-^{t}BuNC** towards a second equivalent of ^{t}BuNC.

Complexes of type **4** have previously been observed via a different route for CO and H_2.[31] **4-H₂** slowly reacts back to **I**, showing the accessibility of this reaction path. Formal loss of H_2 from **1-^{t}BuNC** and addition of another equivalent of ^{t}BuNC leads to the formation of **1-(^{t}BuNC)₂**. Leaving a solution of **1-(^{t}BuNC)₂** and **4-^{t}BuNC** under CO atmosphere for up to 24 hours didn't result in any reaction.

Combining these results and the previously described formation and intermediates of **3-CO**, a general reaction pathway can be drawn (Scheme 6). Starting with η^2-phosphine-borane complex **I**, addition of a first equivalent of ancillary ligand leads to the well-known change in hapticity for the borane and formation of **1-L**.

Reaction with a second equivalent of ancillary ligand can result in the formation of different products, depending on which ligand is used: For ^{t}BuNC, H_2 is lost from the amine in dppa and the iron-hydride and the second ^{t}BuNC ligand formally replaces the hydride ligand at the iron atom to form **1-L¹L²**. The second reaction path leads to a phosphine-stabilized boryl complex **2-L¹L²** through hydrogen liberation from a boron-bound hydrogen atom and the hydrido ligand. An intramolecular P-B bond formation and B-H activation step leads to the phosphine-stabilized borylene complex **3-CO** and an additional hydrogen liberation step enables the formation of complex **3b-CN**.

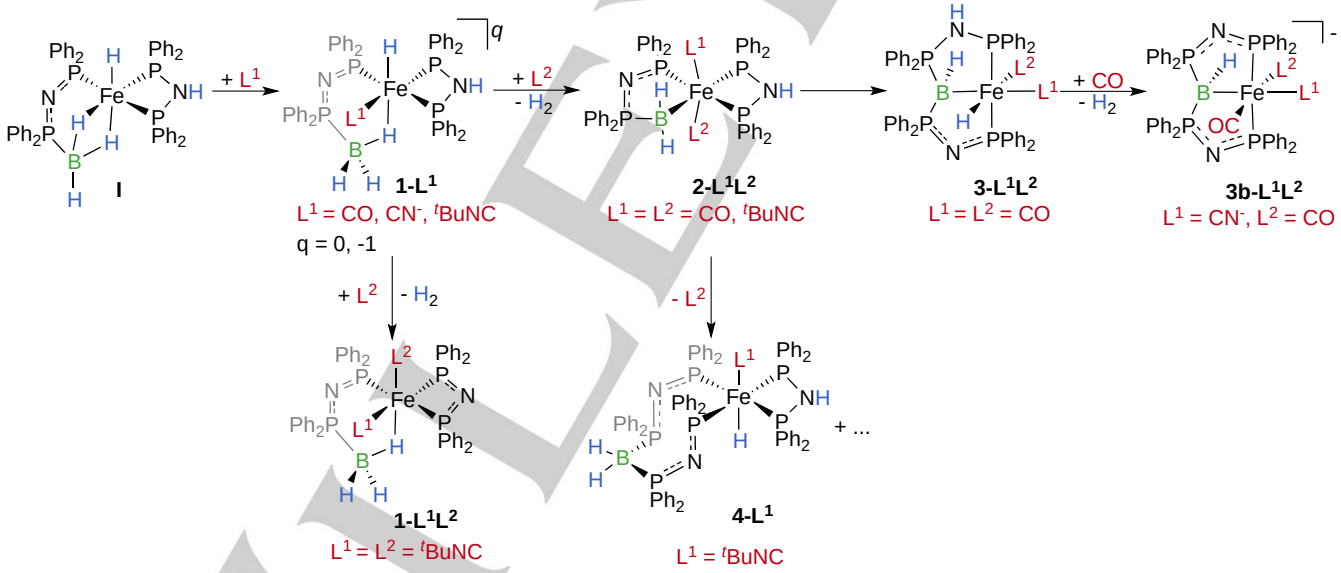

Scheme 6. General reaction pathway for the ancillary ligand induced degradation of phosphine-borane complex **I**. Only isolated or spectroscopically characterized complexes are shown.

In order to understand, why depending on the ancillary ligand different products were obtained, we used DFT methods to calculate the Gibbs free energies of the different possible products for all ligands. Interestingly, for NO^+ only minima could be found in which one carbonyl ligand is in a bridging binding mode between iron and boron (details can be found in the SI).

This explains why no complex formation was observed with $NOBF_4$. Since NO^+ is a poor π-acceptor compared to the other investigated ligands, the π-acidity seems to be a crucial factor for the reaction along the general reaction path to happen. For the other three ligands, we calculated the difference in Gibbs free enthalpy between complex **I** plus the sum of all added ligands and

the complex of interest plus the eliminated equivalents of hydrogen, respectively (Gaussian09, B97D/def2-TZVP). The gradual formation of **3** or **3b** from **I** leads to a subsequent increase in stability.[41]

As the reaction of **I** with ^{t}BuNC yields two complexes in approx. 1:1 ratio, **1-(^{t}BuNC)$_2$** and **4-^{t}BuNC**, the different pathways deserve some further attention. The formation of both complexes was calculated to be thermodynamically favourable relative to **I**. The formation of the detected intermediate **1-^{t}BuNC** from **I** is favourable by 191.7 kJ/mol in Gibbs free energy. The reaction of the key-intermediate **1-^{t}BuNC** with a second equivalent of ^{t}BuNC is assumed to induce hydrogen liberation via two different pathways, either leading to the boryl intermediate **2-^{t}BuNC** or to the η^1-phosphine-borane complex **1-(^{t}BuNC)$_2$**. Both reaction steps are thermodynamically accessible according to DFT calculations, but the formation of **1-(^{t}BuNC)$_2$** is favoured by 42.7 kJ/mol over **2-^{t}BuNC**. However, formation of **2-^{t}BuNC** from **1-^{t}BuNC** must be kinetically favoured, as in the beginning of the reaction of **I** with ^{t}BuNC only **1-^{t}BuNC** and **2-^{t}BuNC** are observed by NMR spectroscopy. Although the formation of **4-^{t}BuNC** is thermodynamically favoured, its formation requires one equivalent of dppa, which is most likely formed by substitution of all dppa-containing ligands by *tert*-butylisocyanide in **2-^{t}BuNC**.

Overall, the η^1-phosphine-borane complex **1-L^1** is the first key intermediate, as hydrogen liberation can proceed via different pathways to different reaction products. In this case the ancillary ligand influences the observed reactivity pattern. The second key intermediate in this sequence is the boryl complex **2-L^{1}L^2**, which is formed by one of the two dehydrogenative pathways observed in this study. The further reactions of this complex involve the formation of a new phosphorous boron bond and an iron boron bond. Depending on the ancillary ligand this can be an intra-molecular reaction, yielding boron-based pincer complexes, or an inter-molecular reaction with uncoordinated diphosphine (dppa). The latter is likely formed by decomposition of the boryl intermediate **2-L^{1}L^2**.

Conclusions

A series of complexes with small σ-donor/π-acceptor ligands (CO, ^{t}BuNC, CN^-) was prepared and characterized. We showed that the ligand-induced rearrangements in these phosphine-borane iron complexes follow a more general reaction sequence. Starting from a η^2-phosphine-borane iron complex, addition of one equivalent of CO, ^{t}BuNC or CN^- leads to a change in hapticity to a η^1-phosphine-borane iron complex. Addition of a second equivalent of the corresponding ligand induces loss of H_2 and formation of a boryl ligand for CO (isolable), ^{t}BuNC (observed, but unstable) and presumably CN^- (not isolated). For the bulky ^{t}BuNC ligand, two products are observed for this reaction step: an iron hydrido complex with a pendant bis(phosphine)borate group and a second η^1-phosphine-borane complex with two equivalents of ^{t}BuNC that was formed by a competitive pathway of H_2-liberation. For the CN^- and CO boryl complexes, a PBP pincer complex based on a phosphine-stabilized borylene is formed in a dehydrocoupling step under CO atmosphere. With the calculated relative Gibbs free energies, the different stabilities and preferred products along the reaction sequence could be explained for the different ligands.

Related dehydrocoupling steps have been observed in the context of dehydropolymerization of phosphine-boranes and thus represent important elementary steps.[14,16] Overall, we were able to show that the choice of ancillary ligands influences the stability of intermediates leading to dehydrocoupling steps greatly. Thus, by the choice of the ancillary ligand, different products are accessible.

Acknowledgements

We gratefully acknowledge financial support from the Deutsche Forschungsgemeinschaft (LA 2830/3-2), the Erich-Becker-Stiftung (R. L.) and the Studienstiftung des deutschen Volkes (L. V.).

Keywords: Boron • Iron • Coordination modes • Pincer ligands • DFT

[1] S. A. Snow, M. Shimoi, C. D. Ostler, B. K. Thompson, G. Kodama, R. W. Parry, *Inorg. Chem.* **1984**, *23*, 511–512.
[2] S. A. Snow, G. Kodama, *Inorg. Chem.* **1985**, *24*, 795–796.
[3] M. Shimoi, S. I. Nagai, M. Ichikawa, Y. Kawano, K. Katoh, M. Uruichi, H. Ogino, *J. Am. Chem. Soc.* **1999**, *121*, 11704–11712.
[4] K. Katoh, M. Shimoi, H. Ogino, *Inorg. Chem.* **1992**, *31*, 670–675.
[5] R. Macías, N. P. Rath, L. Barton, *Angew. Chem. Int. Ed.* **1999**, *38*, 162–164.
[6] D. H. Nguyen, J. Bayardon, C. Salomon-Bertrand, S. Jugé, P. Kalck, J. Daran, M. Urrutigoity, M. Gouygou, *Organometallics* **2012**, *31*, 857–869.
[7] N. Merle, G. Koicok-Köhn, M. F. Mahon, C. G. Frost, G. D. Ruggerio, A. S. Weller, M. C. Willis, *Dalt. Trans.* **2004**, 3883–3892.
[8] M. Shimoi, K. Katoh, Y. Kawano, G. Kodama, H. Ogino, *J. Organomet. Chem.* **2002**, *659*, 102–106.
[9] J. Brugos, J. A. Cabeza, P. García-Álvarez, A. R. Kennedy, E. Pérez-Carreño, J. F. Van Der Maelen, *Inorg. Chem.* **2016**, *55*, 8905–8912.
[10] M. Ingleson, N. J. Patmore, G. D. Ruggiero, C. G. Frost, M. F. Mahon, M. C. Willis, A. S. Weller, *Organometallics* **2001**, *20*, 4434–4436.
[11] O. Volkov, R. Macías, N. P. Rath, L. Barton, *Inorg. Chem.* **2002**, *41*, 5837–5843.
[12] N. Merle, C. G. Frost, G. Kociok-Köhn, M. C. Willis, A. S. Weller, *J. Organomet. Chem.* **2005**, *690*, 2829–2834.
[13] N. Merle, C. G. Frost, G. Kociok-Köhn, M. C. Willis, A. S. Weller, *Eur. J. Inorg. Chem.* **2006**, *2006*, 4068–4073.
[14] T. N. Hooper, A. S. Weller, N. A. Beattie, S. A. Macgregor, *Chem. Sci.* **2016**, *7*, 2414–2426.
[15] T. Yasue, Y. Kawano, M. Shimoi, *Angew. Chem. Int. Ed.* **2003**, *42*, 1727–1730.
[16] A. Schäfer, T. Jurca, J. Turner, J. R. Vance, K. Lee, V. A. Du, M. F. Haddow, G. R. Whittell, I. Manners, *Angew. Chem. Int. Ed.* **2015**, *54*, 4836–4841.
[17] L. Vondung, N. Frank, M. Fritz, L. Alig, R. Langer, *Angew. Chem. Int. Ed.* **2016**, *55*, 14450–14454.
[18] A. B. Chaplin, A. S. Weller, *Angew. Chem. Int. Ed.* **2010**, *49*, 581–584.
[19] N. Frank, K. Hanau, K. Flosdorf, R. Langer, *Dalt. Trans.* **2013**, *42*, 11252.
[20] L. Vondung, N. Frank, M. Fritz, L. Alig, R. Langer, *Angew. Chem. Int. Ed.* **2016**, *55*, 14450–14454.
[21] W. F. McNamara, E. N. Duesler, R. T. Paine, J. V. Ortiz, P. Koelle, H. Noeth, *Organometallics* **1986**, *5*, 380–383.
[22] M. A. Alvarez, M. E. García, R. González, M. A. Ruiz, *Dalt. Trans.* **2012**, *41*, 14498.
[23] M. Blug, D. Grünstein, G. Alcaraz, S. Sabo-Etienne, X.-F. Le Goff,

P. Le Floch, N. Mézailles, *Chem. Commun.* **2009**, 4432.
[24] T. N. Hooper, M. A. Huertos, T. Jurca, S. D. Pike, A. S. Weller, I. Manners, *Inorg. Chem.* **2014**, *53*, 3716–3729.
[25] H. Helten, B. Dutta, J. R. Vance, M. E. Sloan, M. F. Haddow, S. Sproules, D. Collison, G. R. Whittell, C. L. J. Guy, I. Manners, *Angew. Chem. Int. Ed.* **2013**, *52*, 437–440.
[26] Z. Baiko, J. Daniels, D. Gudat, S. Häp, M. Nieger, *Organometallics* **2002**, *21*, 5182–5189.
[27] Y. Kawano, M. Hashiva, M. Shimoi, *Organometallics* **2006**, *25*, 4420–4426.
[28] T. Kakizawa, Y. Kawano, M. Shimoi, *Organometallics* **2001**, *20*, 3211–3213.
[29] H. Fong, M. E. Moret, Y. Lee, J. C. Peters, *Organometallics* **2013**, *32*, 3053–3062.
[30] S. F. Gamper, H. Schmidbaur, *Organometallics* **1992**, *11*, 2863–2867.
[31] L. Vondung, L. E. Sattler, R. Langer, *Chem. - A Eur. J.* **2017**, in press.
[32] L. Kong, Y. Li, R. Ganguly, D. Vidovic, R. Kinjo, *Angew. Chem. Int. Ed.* **2014**, *53*, 9280–9283.
[33] D. A. Ruiz, G. Ung, M. Melaimi, G. Bertrand, *Angew. Chem. Int. Ed.* **2013**, *52*, 7590–7592.
[34] L. Kong, R. Ganguly, Y. Li, R. Kinjo, *Chem. Sci.* **2015**, *6*, 2893–2902.
[35] H. Braunschweig, R. D. Dewhurst, *Dalt. Trans.* **2011**, *40*, 549–558.
[36] A. Amgoune, D. Bourissou, *Chem. Commun.* **2011**, *47*, 859–871.
[37] G. R. Owen, *Chem. Commun.* **2016**, *52*, 10712–10726.
[38] A. W. Addison, T. N. Rao, *J. Chem. Soc. Dalt. Trans.* **1984**, 1349–1356.
[39] J.-M. Bassett, D. E. Berry, G. K. Barker, M. Green, J. A. K. Howard, F. G. A. Stone, *J. Chem. Soc. Dalt. Trans.* **1979**, *20*, 1003.
[40] G. P. Foster, J. M. Putinas, W. D. Jones, *Inorg. Chem.* **1987**, *26*, 2120–2127.
[41] *For Details Please See Supporting Information*, **n.d.**

Entry for the Table of Contents (Please choose one layout)

Layout 1:

FULL PAPER

Catch and release! An iron phosphine borane complex is shown to liberate hydrogen via different reaction pathways upon treatment with ancillary ligands. Depending on the nature of the ancillary ligand, the reaction either leads to the formation of boron-based pincer-type complexes or to deprotonation of the biphosphine.

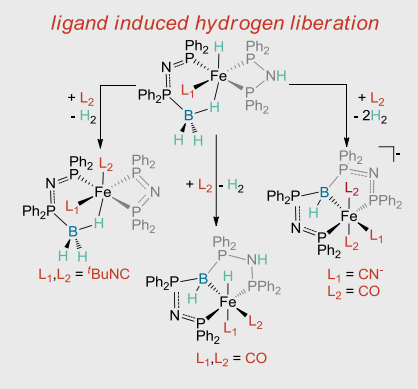

*Lisa Vondung, Lukas Alig, Monika Ballmann, Robert Langer**

Page No. – Page No.

Ancillary Ligand Induced H_2-Liberation from Phosphine-Borane Complexes: Fe-B-Bond Formation vs. Hydride Protonation

Layout 2:

FULL PAPER

*Author(s), Corresponding Author(s)**

Page No. – Page No.

Title

Text for Table of Contents

Supporting Information

Ancillary Ligand Induced H_2-Liberation from Phosphine Borane Complexes: Fe-B-Bond Formation vs. Hydride Protonation

Lisa Vondung,[a] Lukas Alig,[a] Monika Ballmann,[a] Robert Langer*[a]

[a]*Department of Chemistry, Philipps-Universität Marburg, Hans-Meerwein-Str., 35043 Marburg, Germany, Fax: (+)49-6421-2825617, E-mail: robert.langer@chemie.uni-marburg.de*

1. Experimental Details

Material and Methods

All experiments were carried out under an atmosphere of purified argon in a MBraun Labmaster glove box or using standard Schlenk techniques. *n*-Hexane and C_6D_6 were dried and distilled from Na/K alloy and stored over molecular sieves. Toluene was dried and distilled from sodium and stored over molecular sieves. THF was dried and distilled from potassium and stored over molecular sieves. Bis(diphenylphosphino)amine (dppa) was prepared according to a previously reported procedure.[1] ^{1}H, ^{13}C, ^{31}P and ^{11}B NMR spectra were recorded using Bruker HD 250, DRX 400, DRX 500 and Avance 500 NMR spectrometers. ^{1}H and $^{13}C\{^{1}H\}$, ^{13}C-APT (attached proton test) NMR chemical shifts are reported in ppm downfield from tetramethylsilane. The resonance of the residual protons in the deuterated solvent was used as internal standard for ^{1}H NMR. The solvent peak of the deuterated solvent was used as internal standard for ^{13}C NMR. ^{31}P NMR chemical shifts are reported in ppm downfield from H_3PO_4 and referenced to an external 85% solution of phosphoric acid in D_2O. ^{11}B NMR chemical shifts are reported in ppm downfield from $BF_3{\cdot}Et_2O$ and referenced to an external solution of $BF_3{\cdot}Et_2O$ in $CDCl_3$. The following abbreviations are used for the description of NMR data: br (broad), s (singlet), d (doublet), t (triplet), q (quartet), quin (quintet), m (multiplet), v (virtual).

FT-IR spectra were recorded by attenuated total reflection of the solid samples on a Bruker Tensor IF37 spectrometer. The intensity of the absorption band is indicated as vw (very weak), w (weak), m (medium), s (strong), vs (very strong) and br (broad).

HR-ESI mass spectra were acquired with a LTQ-FT mass spectrometer (Thermo Fisher Scientific). The resolution was set to 100.000.

*Synthesis of [(Ph_2P-N-$PPh_2{\cdot}BH_3$)(Ph_2P-N-PPh_2)Fe($CN^tBu)_2$] (***1-(^{t}BuNC)$_2$***) and [({Ph_2P-N-PPh_2}$_2BH_2$)FeH(CN^tBu)(dppa)] (***4-^{t}BuNC***)*

100 mg (0.12 mmol, 1 eq) of [(Ph_2P-N-P(BH_3)Ph_2)(dppa)Fe(H)] (**I**) were dissolved in 5 mL THF. 0.04 mL (0.36 mmol, 3 eq) *tert* butyl cyanide were added, upon which the dark red solution immediately turned orange. Stirring over night at room temperature gives an approximately 1:1 mixture of **1-(^{t}BuNC)$_2$** and **4-^{t}BuNC**. 23 mL *n*-hexane were added and **4-^{t}BuNC** precipitated as a yellow powder. The solution containing **1-(^{t}BuNC)$_2$** was decanted and the solvent was removed in vacuo to give 31 mg (0.03 mmol, 26 %) of **1-(^{t}BuNC)$_2$** as a light yellow powder. All attempts at obtaining single-crystals of **1-(^{t}BuNC)$_2$** only resulted in the formation of precipitate. The residue containing **4-^{t}BuNC** was dissolved in dichloromethane and layered with *n*-hexane. After three days, orange crystals suitable for single-crystal x-ray diffraction were obtained.

1-(^{t}BuNC)$_2$: $^{31}P\{^{1}H\}$ NMR (162 MHz, THF, 27 °C) δ: 36.4 (ddd, 1P, $^{2}J_{PP}$ = 33.2 Hz, $^{2}J_{PP}$ = 65.2 Hz, $^{2}J_{PP}$ = 183.5 Hz, Fe-*P*), 45.4 (ddd, 1P, $^{2}J_{PP}$ = 7.7 Hz, $^{2}J_{PP}$ = 49.8 Hz, $^{2}J_{PP}$ = 184.6 Hz, Fe-*P*), 53.7 (br, 1P, B-*P*), 112.3 (ddd, 1P, $^{2}J_{PP}$ = 50.4 Hz, $^{2}J_{PP}$ = 64.1 Hz, $^{2}J_{PP}$ = 138.9 Hz, Fe-*P*) ppm. ^{1}H NMR (400 MHz, C_6D_6, 27 °C) δ: -13.60 (br, 1H, B-*H*-Fe), 0.51 (s, 9H, C*H*$_3$), 0.58 (s, 9H, C*H*$_3$), 6.73-6.91 (m, 4H,

Aryl-*H*), 7.22-7.42 (m, 12H, Aryl-*H*), 7.68 (m, 4H, Aryl-*H*), 7.87-8.53 (m, 20H, Aryl-*H*) ppm. Selectively decoupled $^{1}H\{^{31}P\}$ and $^{1}H\{^{11}B\}$ NMR spectra were acquired, but no changes compared to the spectrum reported above were observed. ^{13}C-APT NMR (100.6 MHz, C_6D_6, 27 °C) δ: 28.8 (s, CH_3), 29.8 (s, CH_3), 127.3-127.6 (m, Aryl-*C*), 129.5 (s, Aryl-*C*), 130.0 (d, $^{2}J_{CP}$ = 10.7 Hz, Aryl-*C*), 130.24 (br, Aryl-*C*), 131.0 (d, $^{2}J_{CP}$ = 9.1 Hz, Aryl-*C*), 132.4-132.5 (m, Aryl-*C*), 132.9 (d, $^{2}J_{CP}$ = 9.7 Hz, Aryl-*C*) ppm. $^{11}B\{^{1}H\}$ NMR (160.5 MHz, C_6D_6, 27 °C) δ: -41.1 (s) ppm. IR (ATR): $\tilde{\vartheta}$ [cm^{-1}] 3051 (vw), 2963 (m), 2906 (vw), 2361 (B-H, vw), 2338 (B-H, vw), 2105 (CN/Fe-H-B, m), 1544 (vw), 1479 (w), 1434 (m), 1413 (w), 1367 (w), 1259 (s), 1212 (w), 1084 (s), 1012 (vs), 924 (w), 868 (m), 790 (vs), 752 (m), 739 (m), 693 (s), 618 (vw), 553 (m), 529 (s), 511 (m). High Res. ESI-MS (*m/z, pos.*): 1005.3373 (calc. for $[M+H]^+$), 1005.3370 (found, Δ = 0.3 ppm).

4-^{t}BuNC: $^{31}P\{^{1}H\}$ NMR (162 MHz, CD_2Cl_2, 27 °C) δ: 21.6 (br, 2P, *P*-BH_2-*P*), 88.9 (m, 2P), 90.9 (m, 2P) ppm. ^{1}H NMR (400 MHz, CD_2Cl_2, 27 °C) δ: -5.36 (tt, 1H, $^{2}J_{PH}$ = 45.1 Hz, $^{2}J_{PH}$ = 53.1 Hz, Fe-*H*), 1.11 (s, 9H, ^{t}Bu-*H*), 3.59 (s, 1H, N*H*), 6.22 (m, 4H, Aryl-*H*), 6.43 (m, 2H, Aryl-*H*), 6.77-7.28 (m, 42H, Aryl-*H*), 7.60-7.79 (m, 12H, Aryl-*H*) ppm. Selectively decoupled $^{1}H\{^{31}P\}$ and $^{1}H\{^{11}B\}$ NMR spectra were acquired, causing a change in multiplicity for some resonances and for the $^{1}H\{^{11}B\}$ NMR spectrum appearance of two new signals. In the following only resonances which are changing upon ^{31}P-decoupling are reported. All other ^{1}H NMR resonances remained unchanged in comparison to the ^{1}H NMR spectrum reported above. $^{1}H\{^{31}P\}$ NMR (400 MHz, CD_2Cl_2, 27 °C, o2p = 91.1 ppm) δ: -5.36 (s, 1H, Fe-*H*), 7.60 (d, $^{3}J_{PH}$ = 7.1 Hz, *ortho*-Phenyl-*H*), 7.79 (d, $^{3}J_{PH}$ = 7.1 Hz, *ortho*-Phenyl-*H*) ppm. $^{1}H\{^{31}P\}$ NMR (400 MHz, CD_2Cl_2, 27 °C, o2p = 21.0 ppm) δ: 7.68 (d, $^{3}J_{PH}$ = 6.9 Hz, *ortho*-Phenyl-*H*) ppm. $^{1}H\{^{11}B\}$ NMR (400 MHz, CD_2Cl_2, 27 °C, o2p = -31.7 ppm) δ: 2.29 (dd, $^{2}J_{PH}$ = 14.6 Hz, $^{2}J_{PH}$ = 28.7 Hz, B-*H*), 2.95 (dd, $^{2}J_{PH}$ = 18.3 Hz, $^{2}J_{PH}$ = 31.2 Hz, B-*H*) ppm. ^{13}C-APT NMR (100.6 MHz, CD_2Cl_2, 27 °C) δ: 31.0 (s, CH_3), 126.1 (m, Aryl-*C*), 126.6 (m, Aryl-*C*), 127.3 (m, Aryl-*C*), 127.6 (m, Aryl-*C*), 127.8 (m, Aryl-*C*), 128.2 (m, Aryl-*C*), 128.8 (d, $^{2}J_{CP}$ = 18.5 Hz, Aryl-*C*), 129.5 (s, Aryl-*C*), 131.6 (m, Aryl-*C*), 132.1 (m, Aryl-*C*), 133.1 (m, Aryl-*C*), 133.9 (m, Aryl-*C*) ppm. $^{11}B\{^{1}H\}$ NMR (160.5 MHz, THF, 27 °C) δ: -31.7 (s) ppm. IR (ATR): $\tilde{\vartheta}$ [cm^{-1}] 3292 (w), 3044 (w), 2977 (br), 2366 (B-H, br), 2035 (Fe-H/C-N, m), 1844 (Fe-H/C-N, vw), 1586 (m), 1480 (s), 1433 (w), 1365 (w), 1263 (m), 1230 (s), 1194 (s), 1179 (s), 1085 (s), 1027 (s), 848 (m), 809 (m), 733 (s), 690 (vs), 646 (m), 618 (w), 588 (w), 545 (w), 527 (s), 515 (vs), 492 (vs), 452 (m), 433 (m), 423 (m). High Res. ESI-MS (*m/z, pos.*): 1307.3790 (calc. for $[M+H]^+$), 1307.3811 (found, Δ = 1.6 ppm).

*Synthesis of [K(18-crown-6)][(Ph_2P-N-PPh_2·BH_3)(dppa)FeH(CN)] (***1-CN***)*

100 mg (0.12 mmol, 1 eq) of [(Ph_2P-N-P(BH_3)Ph_2)(dppa)Fe(H)] (**I**) were dissolved in 5 mL THF. 23 mg (0.36 mmol, 3 eq) KCN and 95 mg (0.36 mmol, 3 eq) 18-crown-6 were added and the dark red solution was stirred at room temperature overnight. The solution changes colour to orange after a few hours and complete conversion was determined by $^{31}P\{^{1}H\}$ NMR spectroscopy. The solvent was removed *in vacuo* and the residue was dissolved in toluene and layered with *n*-hexane. After 10 days, 1-CN was obtained as red crystals. Yield: 111 mg, 0.095 mmol, 79 %.

$^{31}P\{^{1}H\}$ NMR (162 MHz, C_6D_6, 27 °C) δ: 46.9 (br, 1P , *P*-BH_3), 93.6 (ddd, 1P, $^{3}J_{PP}$ = 17.8 Hz, $^{3}J_{PP}$ = 88.7 Hz, $^{3}J_{PP}$ = 95.4 Hz), 96.3 ppm (dd, 1 P, $^{2}J_{PP}$ = 42.9 Hz, $^{2}J_{PP}$ = 90.0 Hz), 115.3 (ddd, 1P, $^{2}J_{PP}$ = 43.5

Hz, $^{2}J_{PP}$ = 96.9 Hz, $^{2}J_{PP}$ = 128.9 Hz) ppm. ^{1}H NMR (400 MHz, C_6D_6, 27 °C) δ: -20.17 (dt, 1H, $^{2}J_{PH}$ = 45.7 Hz, $^{2}J_{PH}$ = 52.1 Hz, Fe-*H*), -3.05 (br, 1H, P-B*H*$_3$), 3.06 (s, 24 H, C*H*$_2$ in 18-crown-6), 4.36 (dt, 1H, $^{2}J_{PH}$ = 5.7 Hz, $^{4}J_{PH}$ = 2.5 Hz, N*H*), 6.59-7.03 (m, 16H, Aryl-*H*), 7.20-7.44 (m, 12H, Aryl-*H*), 7.85-8.04 (m, 4H, Aryl-*H*), 8.26-8.32 (m, 2H, Aryl-*H*), 8.52-8.62 (m, 4H, Aryl-*H*), 9.10-9.16 (m, 2H, Aryl-*H*) ppm. Selectively decoupled ^{1}H{^{31}P} and ^{1}H{^{11}B} NMR spectra were acquired, causing a change in multiplicity for some of the signals and for the ^{1}H{^{11}B} NMR spectrum a sharpening of the broad singlet resonance at -3.05 ppm. In the following only resonances which are changing upon ^{31}P-decoupling are reported. All other ^{1}H NMR resonances remained unchanged in comparison to the ^{1}H NMR spectrum reported above. ^{1}H{^{31}P} NMR (400 MHz, C_6D_6, 27 °C, o2p = 116.0 ppm) δ: -20.18 (t, 1H, $^{2}J_{PH}$ = 36.5 Hz, Fe-*H*), 4.36 (t, 1H, $^{2}J_{PH}$ = 5.65 Hz, N-*H*) ppm. ^{1}H{^{31}P} NMR (400 MHz, C_6D_6, 27 °C, o2p = 96.5 ppm) δ: -20.17 (d, 1H, $^{2}J_{PH}$ = 38.8 Hz, Fe-*H*), 4.36 (d, 1H, $^{4}J_{PH}$ = 2.5 Hz, N-*H*) ppm. ^{13}C-APT NMR (100.6 MHz, THF-d_8, 27 °C) *δ*: 70.7 (s, 18-crown-6), 124.9 (s, Aryl-*C*), 125.9-126.2 (m, Aryl-*C*), 127.0-128.1 (m, Aryl-*C*), 128.7-128.9 (m, Aryl-*C*), 130.5 (d, $^{2}J_{CH}$ = 10.9 Hz, Aryl-*C*), 131.4 (d, $^{2}J_{CH}$ = 10.8 Hz, Aryl-*C*), 131.8-132.4 (m, Aryl-*C*), 132.8 (d, $^{2}J_{CH}$ = 11.5 Hz, Aryl-*C*), 133.3 (d, $^{2}J_{CH}$ = 10.6 Hz, Aryl-*C*) ppm.^{11}B{^{1}H} NMR (160.5 MHz, THF, 27 °C) δ: -34.6 (s) ppm. IR (ATR): $\tilde{\vartheta}$ [cm^{-1}] 3052 (vw), 2889 (br), 2360 (w, B-H), 2340 (w, B-H), 2061 (w, C-N), 1979 (vw), 1895 (vw, Fe-H), 1821 (vw), 1589 (w), 1473 (m), 1453 (w), 1435 (s), 1351 (m), 1284 (m), 1249 (m), 1209 (m), 1177 (m), 1103 (vs), 1063 (s), 1027 (m), 998 (m), 960 (w), 837 (m), 791 (w), 719 (m), 692 (vs), 619 (vw), 604 (vw), 589 (vw), 548 (m), 514 (s), 466 (m), 431 (m). High Res. ESI-MS (*m/z, neg.*): 866.2022 (calc. for [M]$^{-}$), 866.2018 (found, Δ = 0.5 ppm).

*Synthesis of [(P^{Ph}BP^{Ph})Fe(CO)$_2$(CN)][K(18-crown-6)] (***3-CN***)*

46 mg (0.05 mmol, 1 eq) [K(18-crown-6)][(Ph$_2$P-N-PPh$_2$·BH$_3$)(dppa)FeH(CN)][K(18-crown-6)] (**1-CN**) were dissolved in 5 mL toluene. The argon was replaced by 1 bar carbonmonoxide. The dark red reaction solution was stirred for 12 minutes under the CO atmosphere, during which the colour of the solution turns orange. The CO was removed and replaced by argon. After four days, **3-CN** could be isolated as yellow single crystals suitable for single crystal x-ray diffraction from the reaction solution.

^{31}P{^{1}H} NMR (162 MHz, CH_2Cl_2, 27 °C) δ: 45.9 (br, 2P, *P*-BH$_2$-*P*), 95.4 (dd, 2P, $^{2}J_{PP}$ = 45.0 Hz, $^{2}J_{PP}$ = 75.7 Hz, *P*-Fe) ppm. ^{1}H NMR (400 MHz, CD_2Cl_2, 27 °C) δ: 3.55 (br, 24H, C*H*$_2$ in 18-crown-6), 6.93-8.37 (m, 40H, Aryl-*H*) ppm. Selectively decoupled ^{1}H{^{31}P} and ^{1}H{^{11}B} NMR spectra were acquired, causing the appearance of a broad resonance at 3.53 ppm for the B-*H* in the ^{1}H{^{11}B} NMR spectrum. All other ^{1}H NMR resonances remained unchanged in comparison to the ^{1}H NMR spectrum reported above. ^{1}H{^{11}B} NMR (400 MHz, thf-d_8, -60 °C, o2p = -37.0 ppm) δ: 3.53 (br, 1H, B-*H*) ppm. ^{13}C-APT NMR (100.6 MHz, CD_2Cl_2, 27 °C) *δ*: 70.5 (s, *C* in 18-crown-6), 127.3-129.7 (m, Aryl-*C*), 130.8 (m, Aryl-*C*), 131.2 (d, $^{2}J_{CP}$ = 10.7 Hz, Aryl-*C*), 131.4 (m, Aryl-*C*), 131.5 (m, Aryl-*C*), 131.9-132.1 (m, Aryl-*C*), 132.2 (d, $^{2}J_{CP}$ = 10.3 Hz, Aryl-*C*), 132.4 (d, $^{2}J_{CP}$ = 10.7 Hz, Aryl-*C*). ^{11}B{^{1}H} NMR (160.5 MHz, thf-d_8, -60 °C) δ: -37.5 (s) ppm. IR (ATR): $\tilde{\vartheta}$ [cm^{-1}] 3051 (w), 2962 (m), 2904 (br), 2364 (br, B-H), 2083 (br, Fe-CN), 1922 (w, CO), 1871 (w, CO), 1677 (br), 1604 (br), 1495 (br), 1472 (w), 1453 (w), 1435 (m), 1351 (m), 1259 (s), 1098 (vs), 1020 (vs), 961 (m), 865 (m), 798 (vs), 730 (m), 717 (m), 693 (vs), 634 (w), 611 (w), 591 (w), 551 (s), 529 (s), 517 (s), 465 (m). High Res. ESI-MS (*m/z, neg.*): 918.1587 (calc. for [M-{K(18c6)}]$^{-}$), 918.1607 (found, Δ = 2.2 ppm).

2. NMR spectra

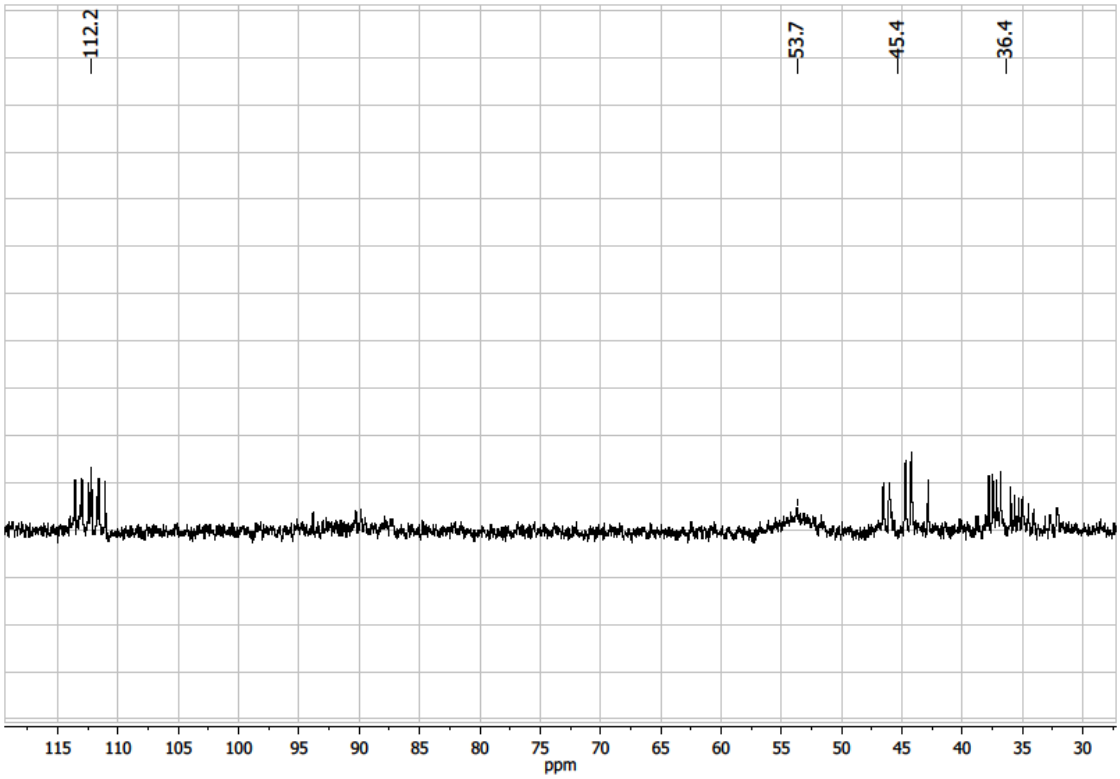

Figure 1. $^{31}P\{^{1}H\}$ NMR spectrum of **1-(ᵗBuNC)₂** in THF.

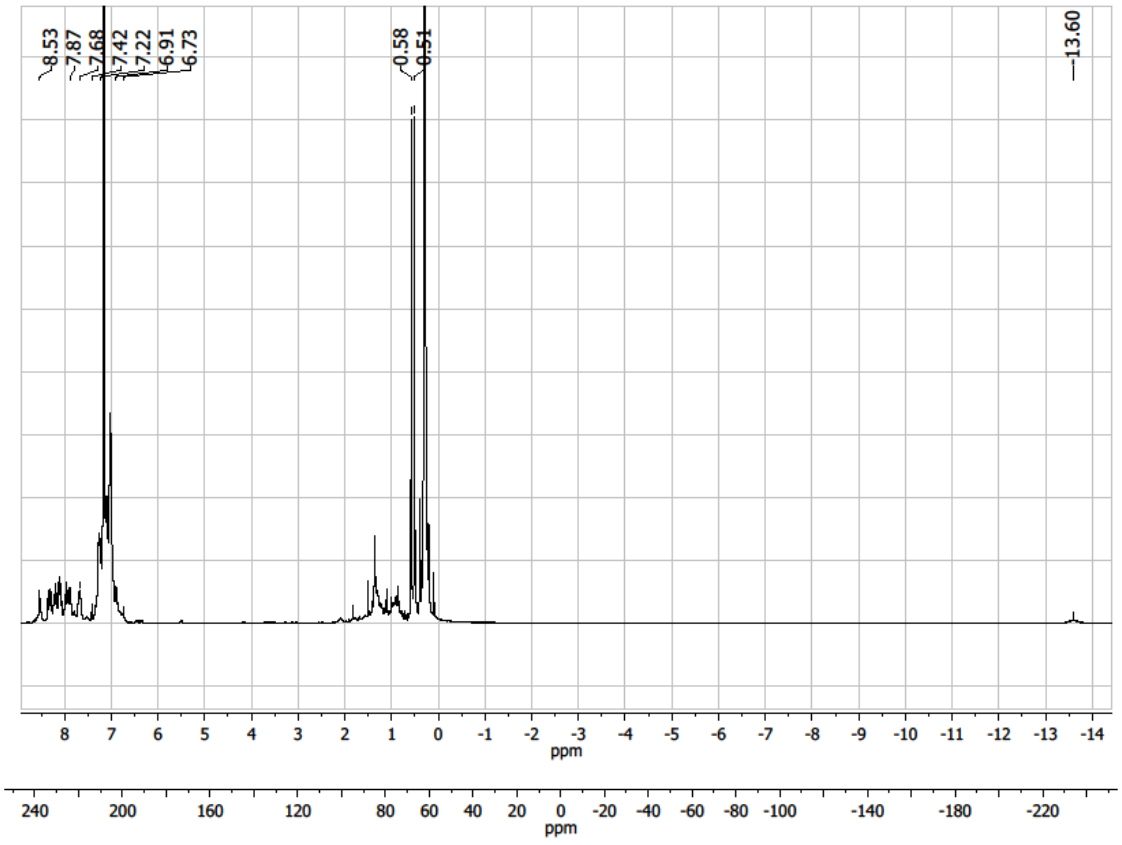

Figure 2. ^{1}H NMR spectrum of **1-(ᵗBuNC)₂** in C_6D_6.

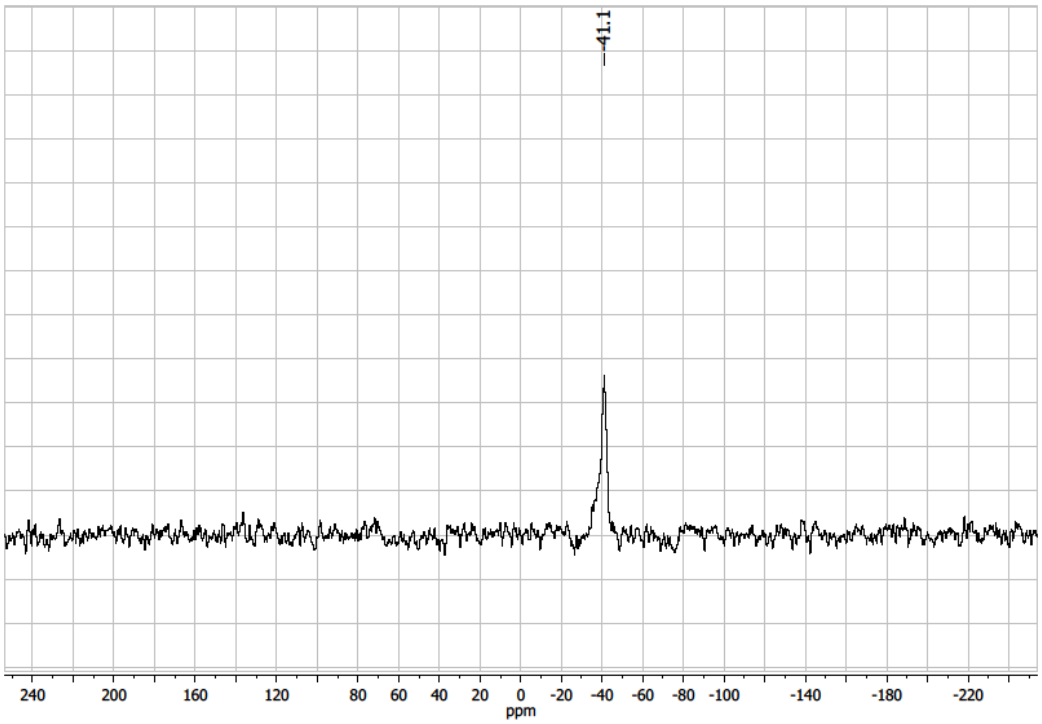

Figure 3. $^{11}B\{^{1}H\}$ NMR spectrum of **1-(ᵗBuNC)₂** in C_6D_6.

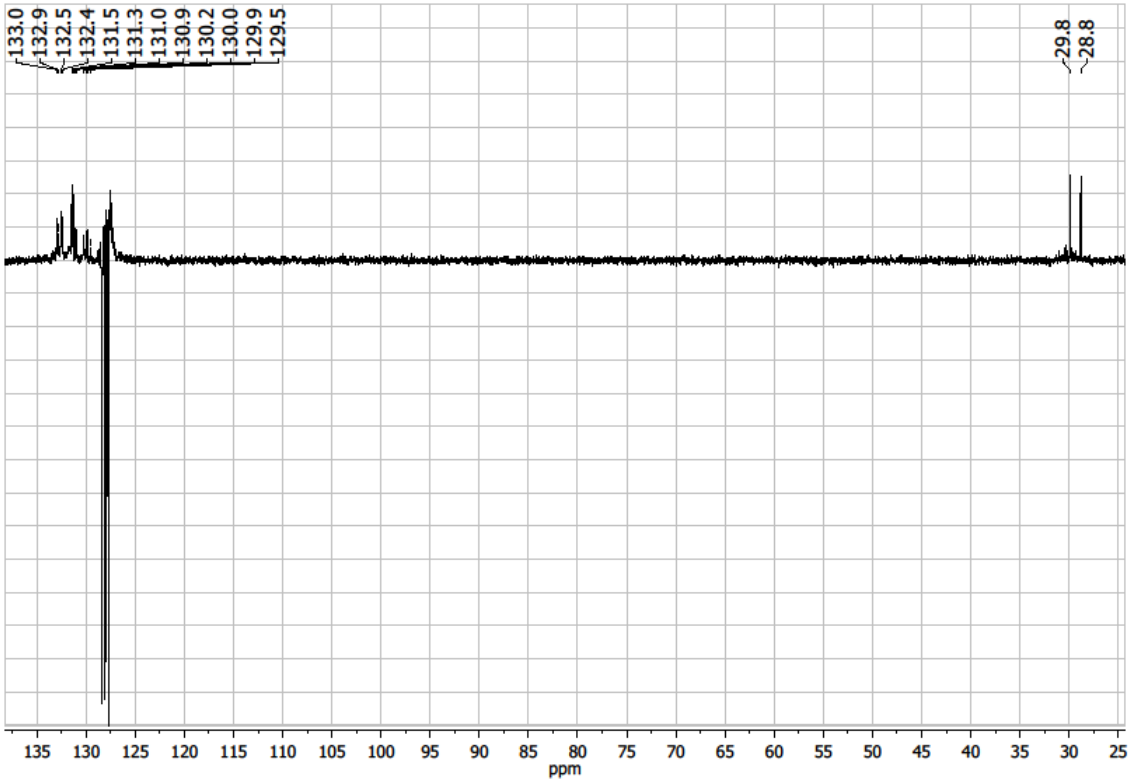

Figure 4. $^{13}C\{^{1}H\}$ NMR spectrum of **1-(ᵗBuNC)₂** in C_6D_6.

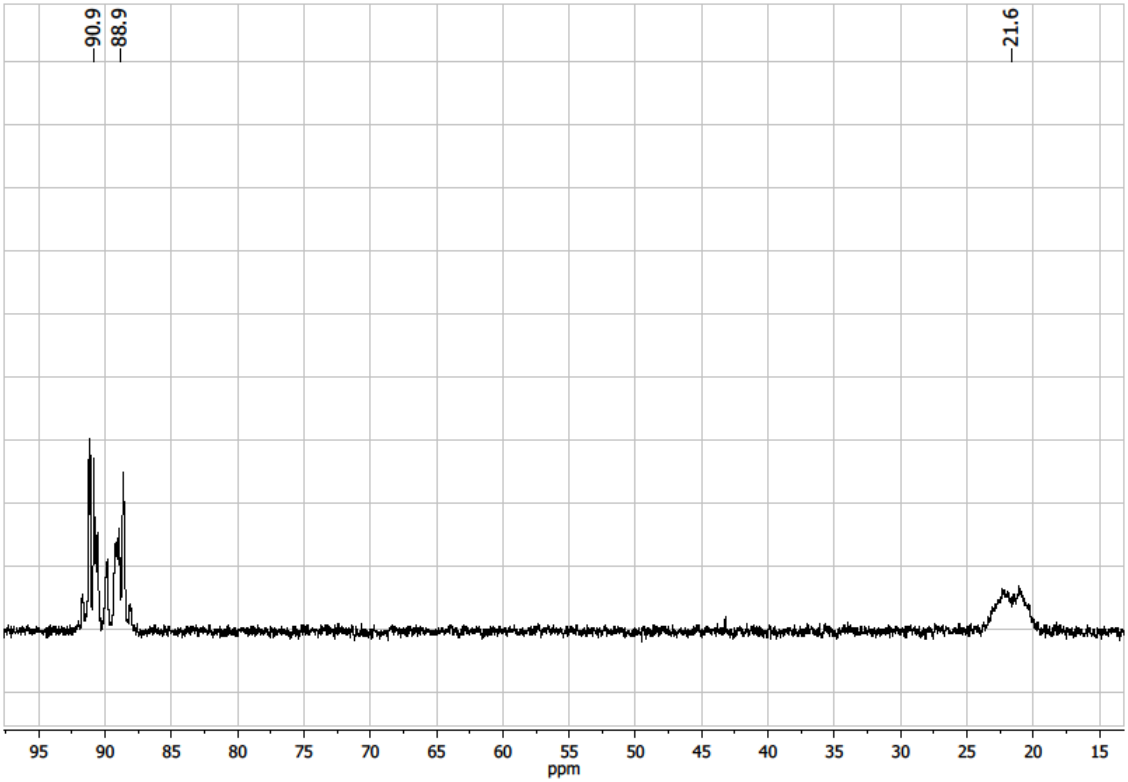

Figure 5. $^{31}P\{^{1}H\}$ NMR spectrum of **4-^{t}BuNC** in CD_2Cl_2.

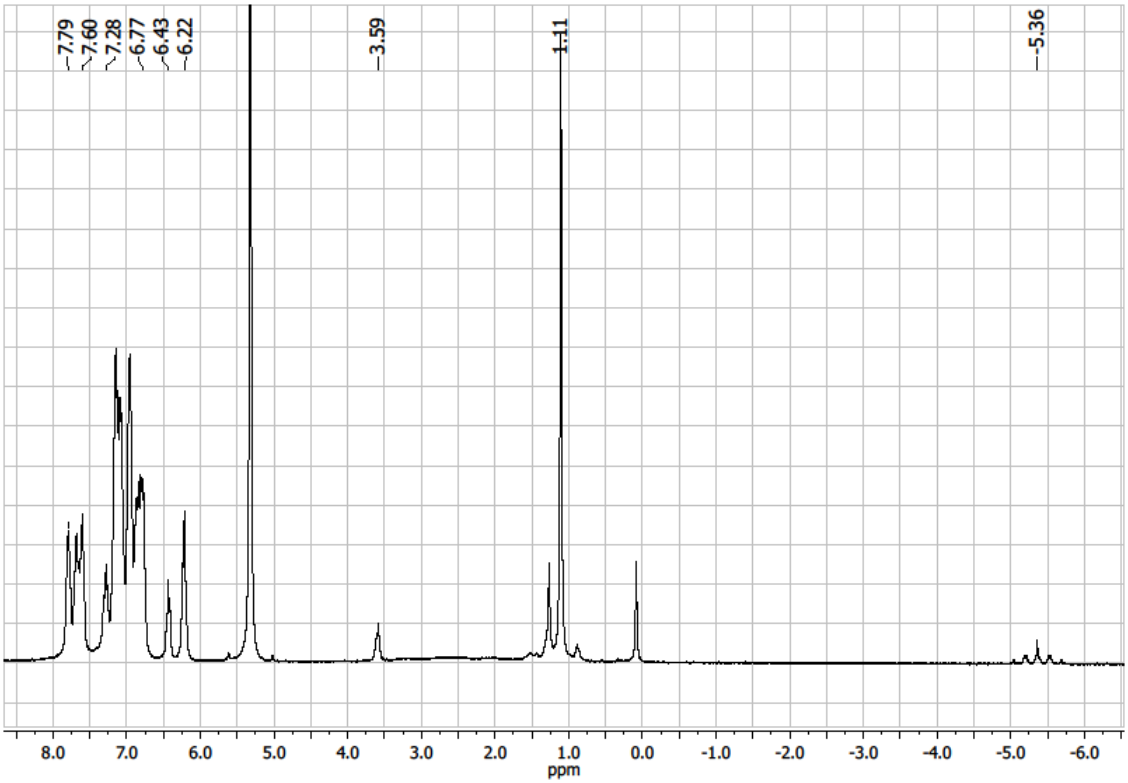

Figure 6. ^{1}H NMR spectrum of **4-^{t}BuNC** in CD_2Cl_2.

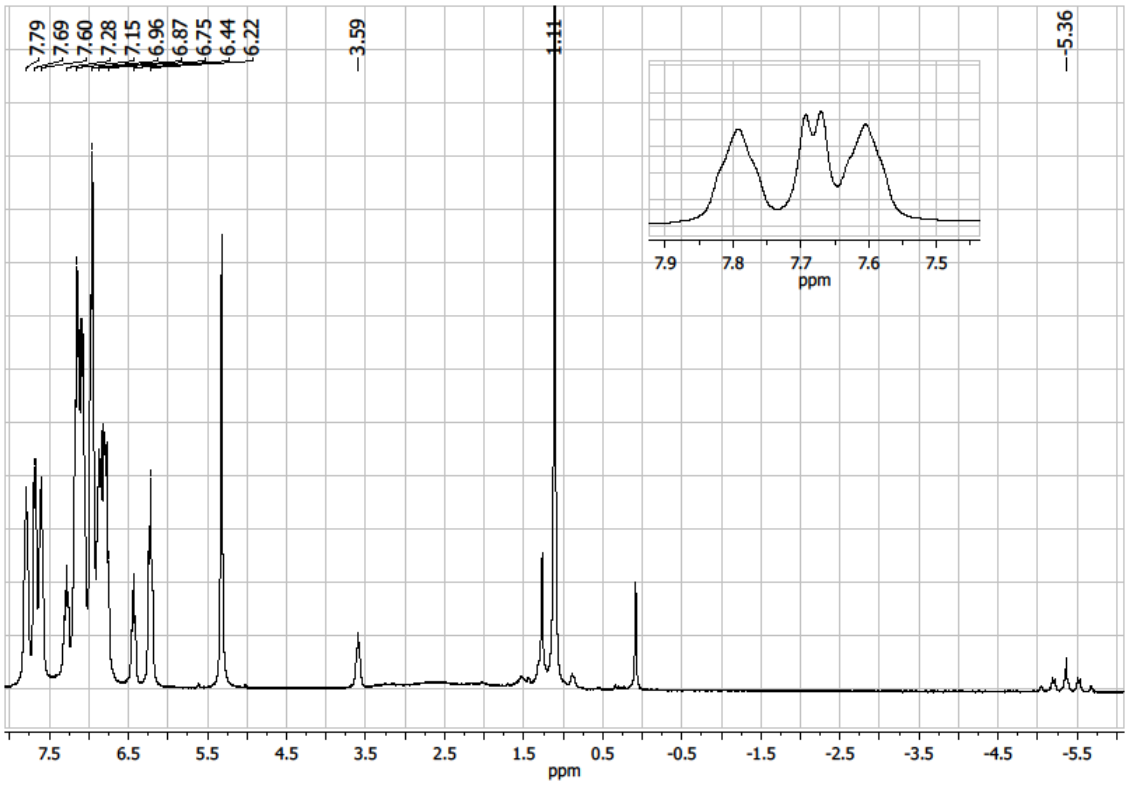

Figure 7. $^{1}H\{^{31}P\}$ NMR spectrum (o2p = 21.0 ppm) of **4-^{t}BuNC** in CD_2Cl_2.

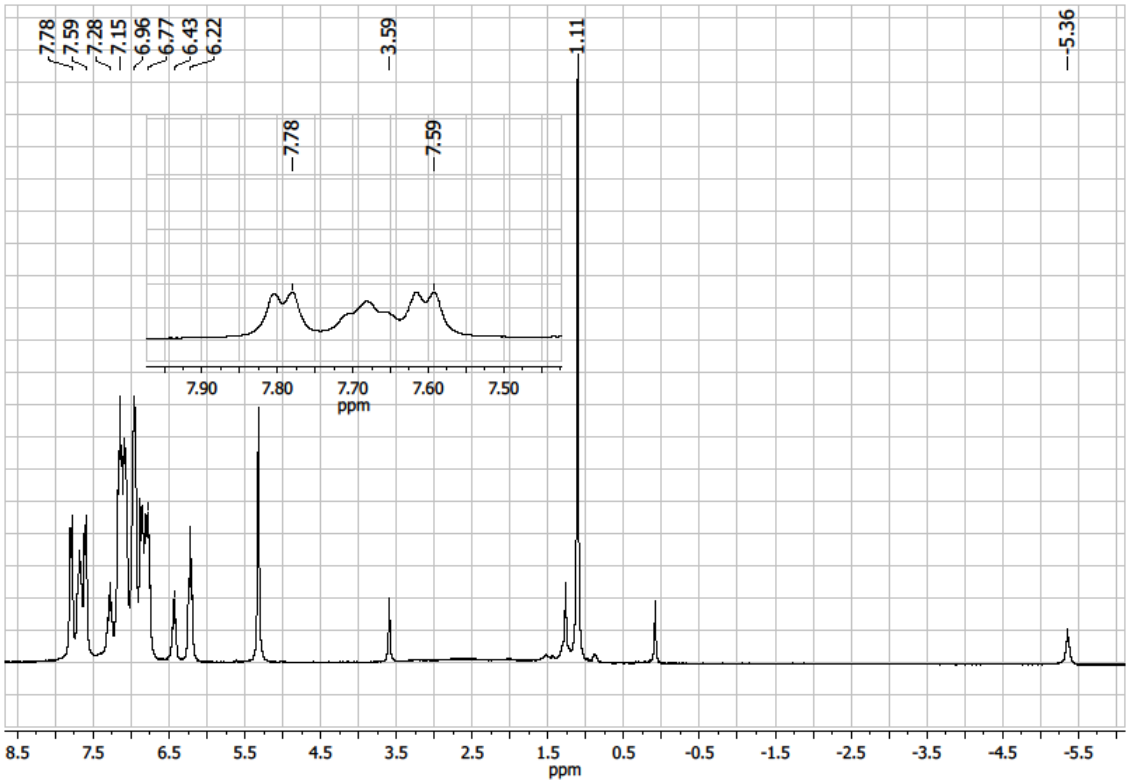

Figure 8. $^{1}H\{^{31}P\}$ NMR spectrum (o2p = 91.1 ppm) of **4-^{t}BuNC** in CD_2Cl_2.

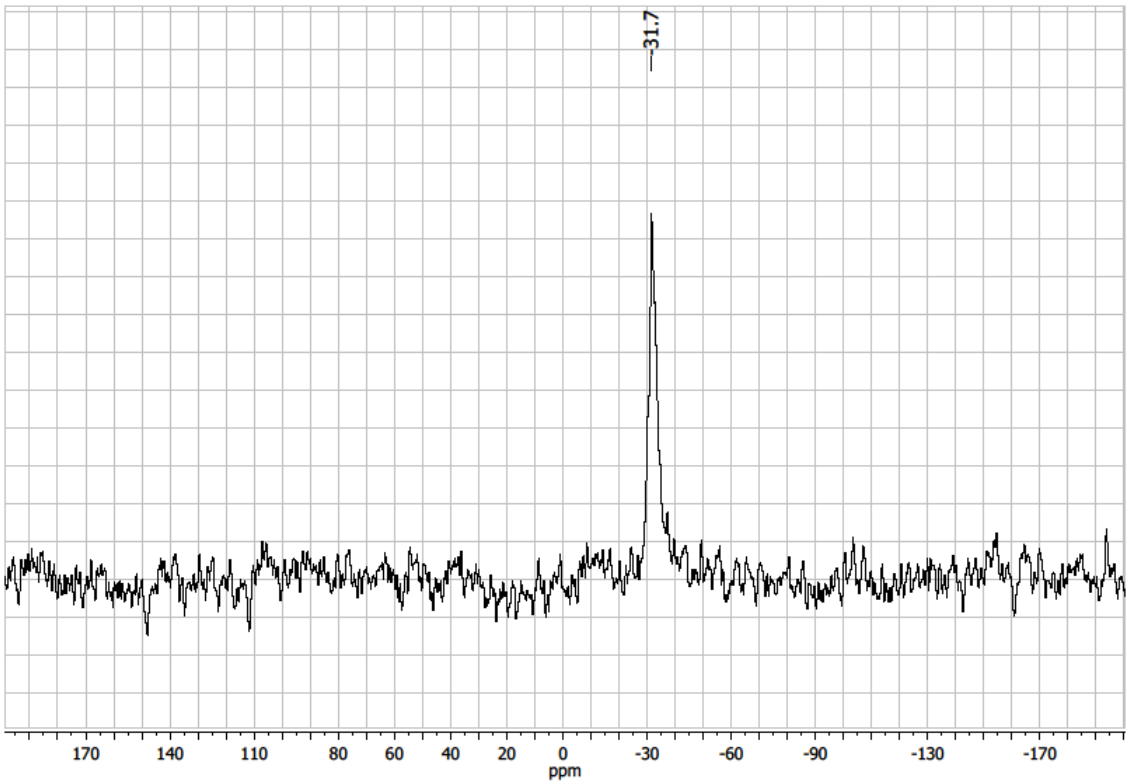

Figure 9. $^{11}B\{^{1}H\}$ NMR spectrum of **4-^{t}BuNC** in CD_2Cl_2.

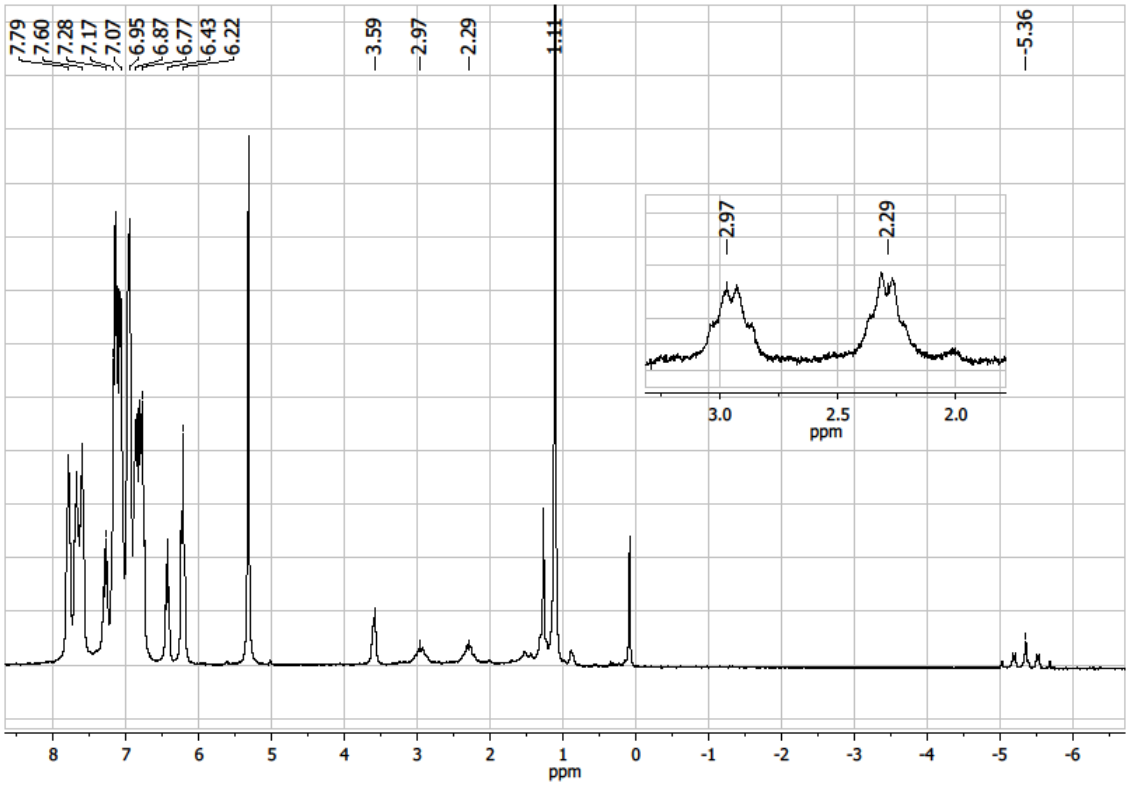

Figure 10. $^{1}H\{^{11}B\}$ NMR spectrum (o2p = -31.7 ppm) of **4-^{t}BuNC** in CD_2Cl_2.

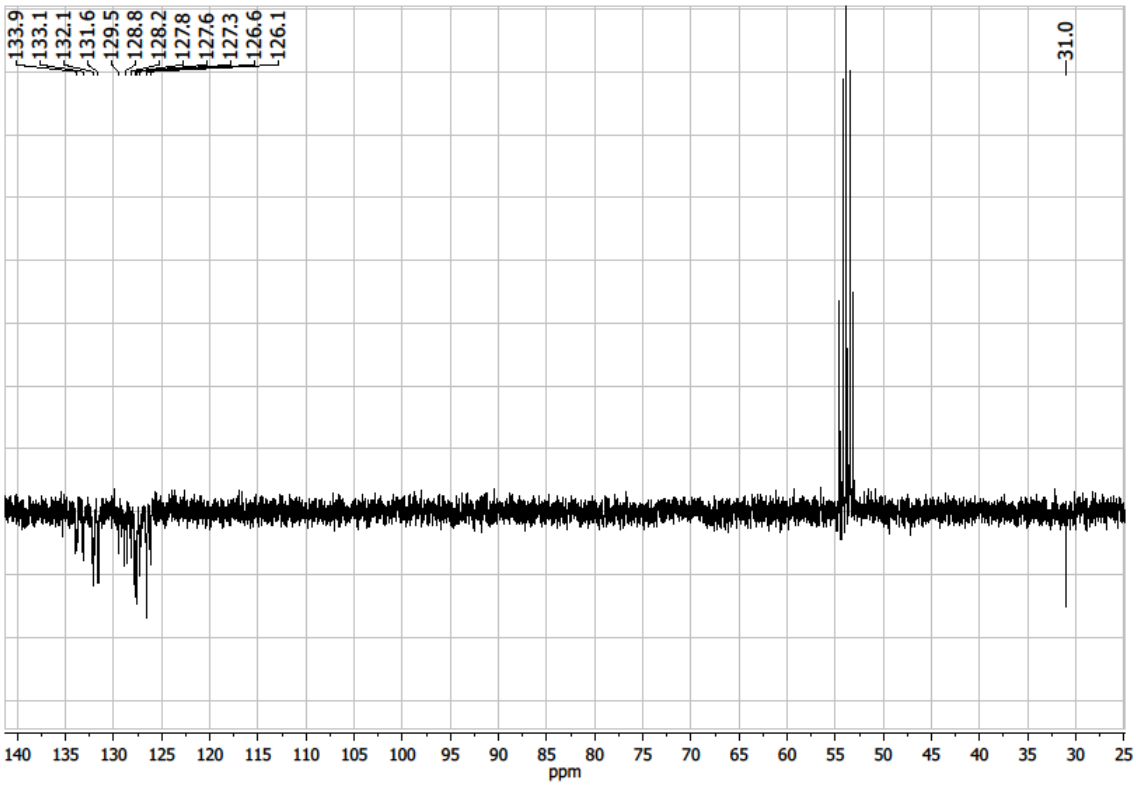

Figure 11. $^{13}C\{^{1}H\}$ NMR spectrum of **4-^{t}BuNC** in CD_2Cl_2.

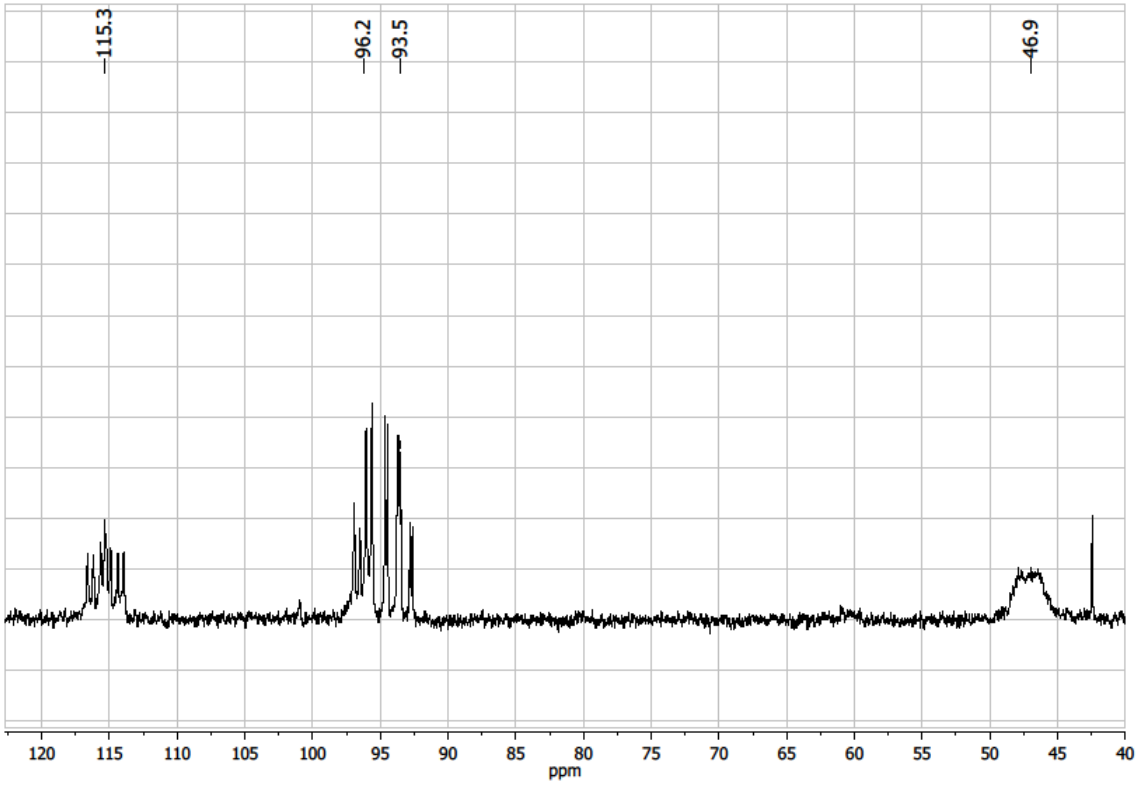

Figure 12. $^{31}P\{^{1}H\}$ NMR spectrum of **1-CN** in C_6D_6.

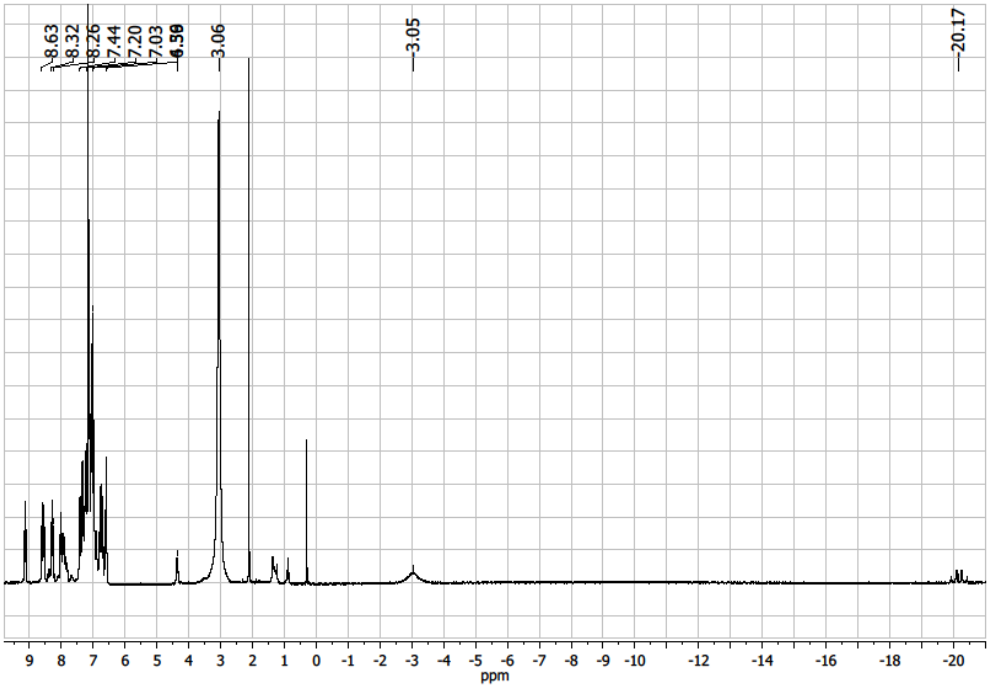

Figure 13. ^{1}H NMR spectrum of **1-CN** in C_6D_6.

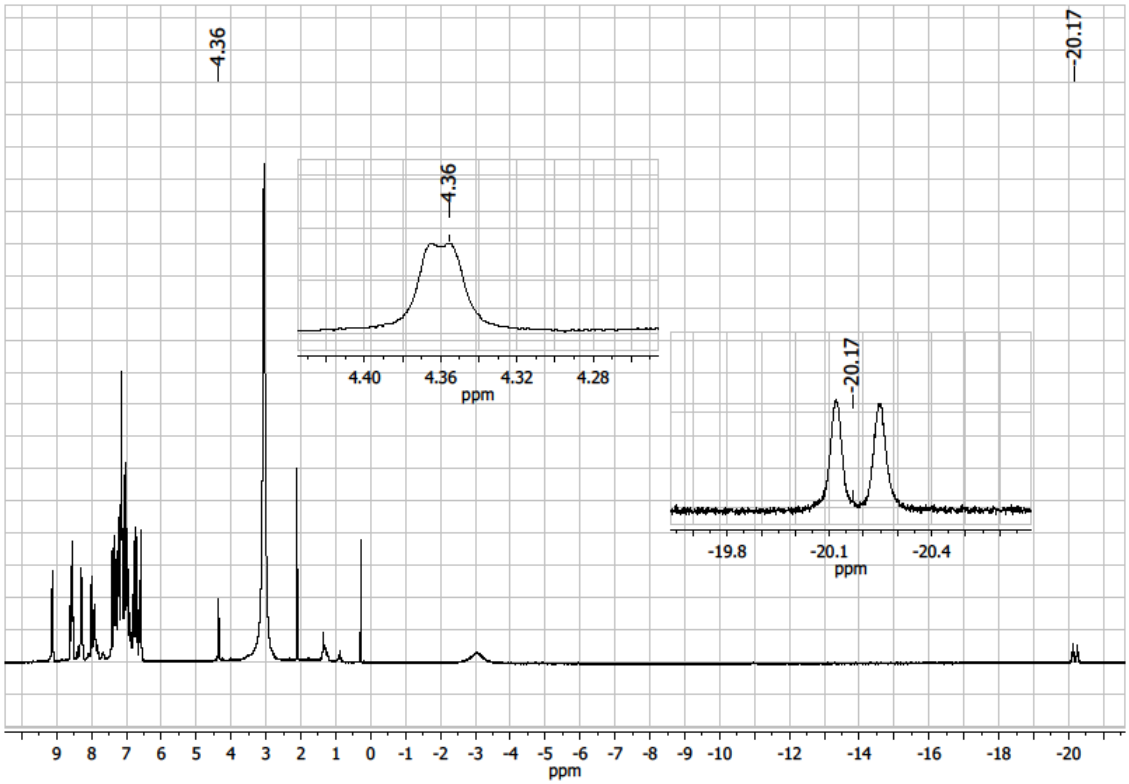

Figure 14. $^{1}H\{^{31}P\}$ NMR spectrum (o2p = 96.5) of **1-CN** in C_6D_6.

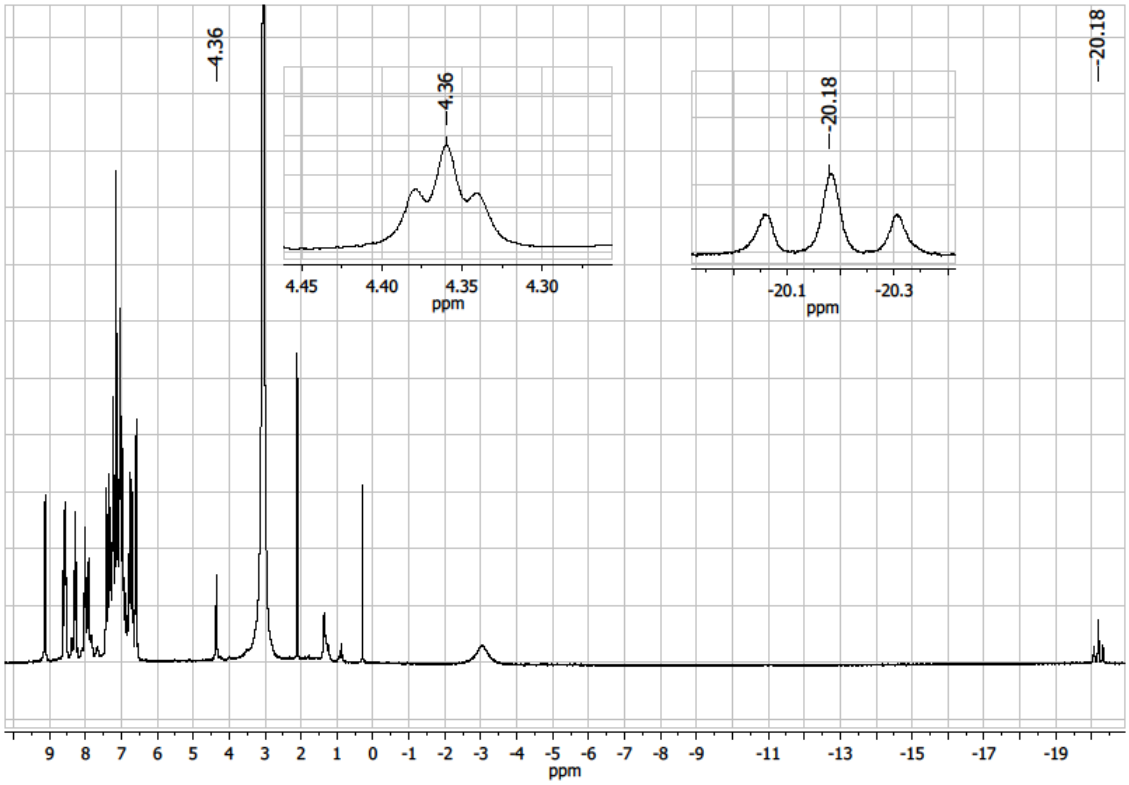

Figure 15. $^{1}H\{^{31}P\}$ NMR spectrum (o2p = 116.0) of **1-CN** in C_6D_6.

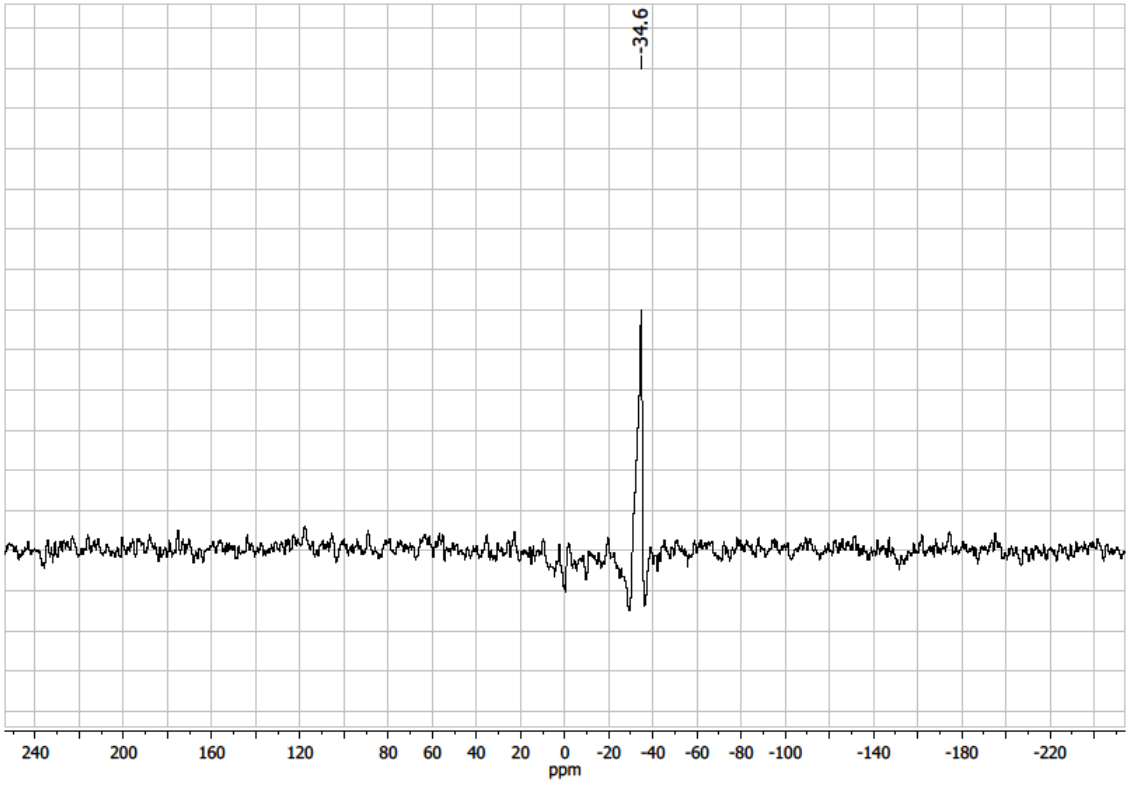

Figure 16. $^{11}B\{^{1}H\}$ NMR spectrum of **1-CN** in THF.

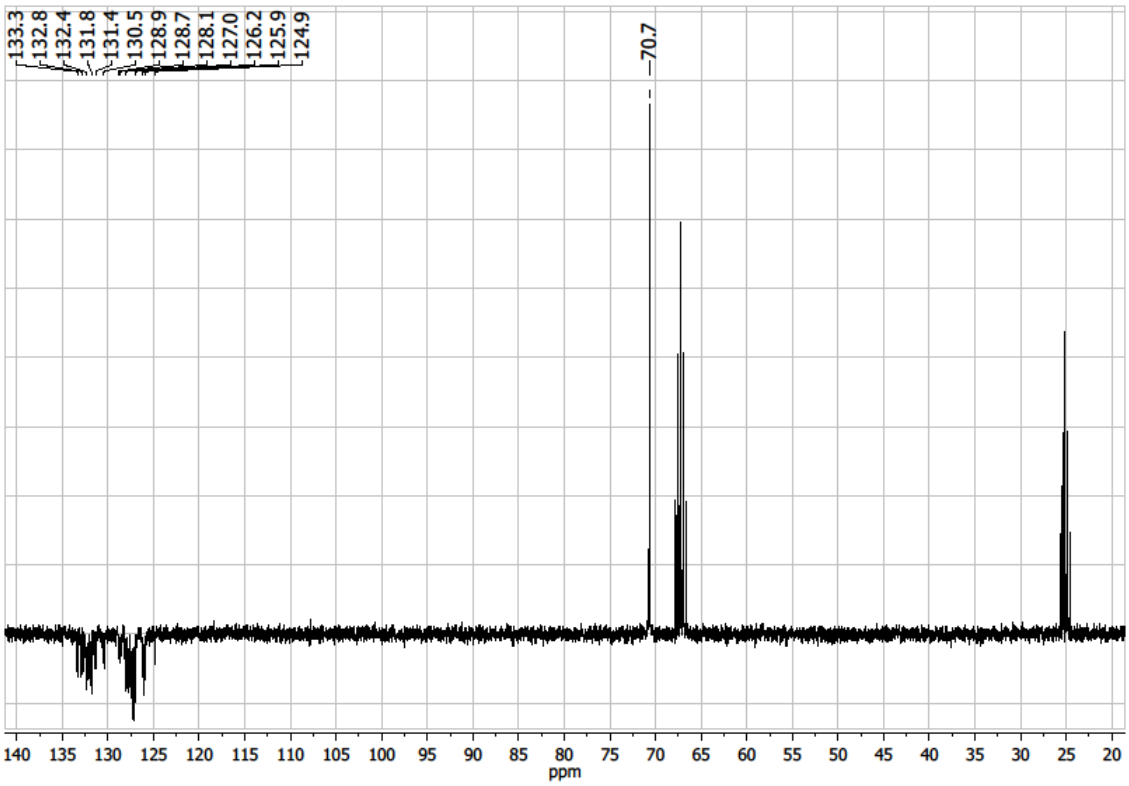

Figure 17. $^{13}C\{^{1}H\}$ NMR spectrum of **1-CN** in THF-d_8.

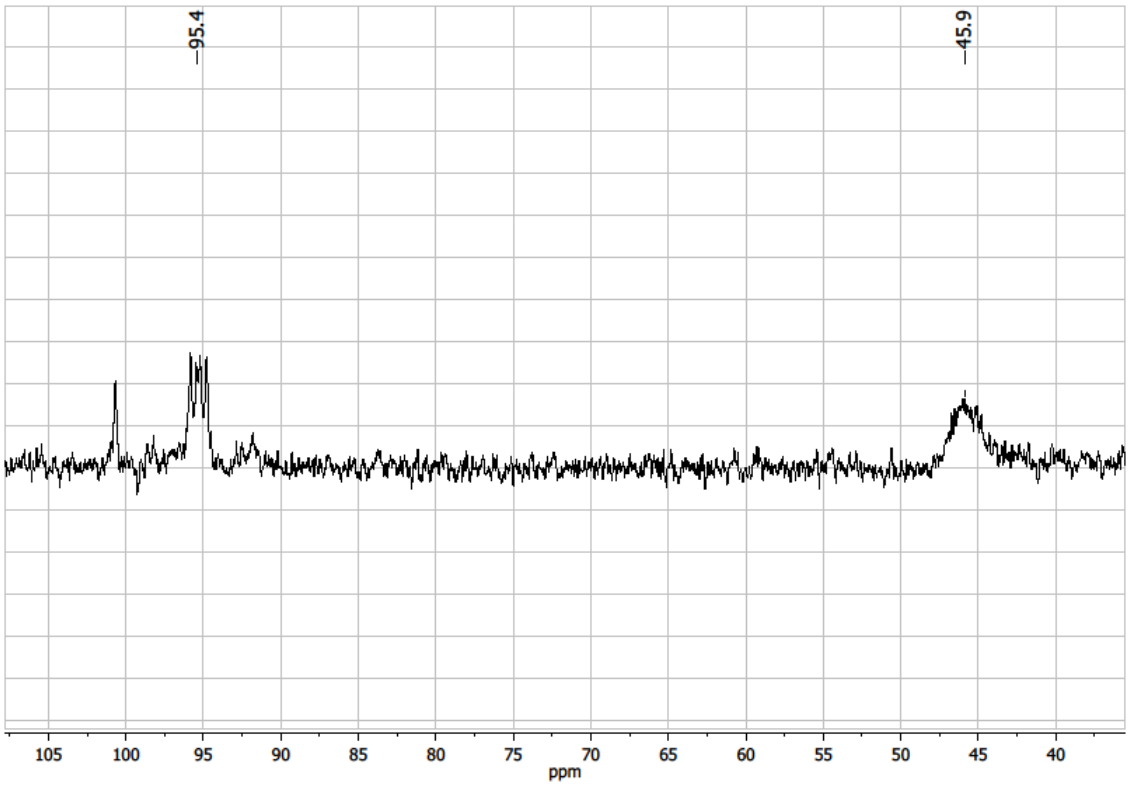

Figure 18. $^{31}P\{^{1}H\}$ NMR spectrum of **3-CN** in CH_2Cl_2.

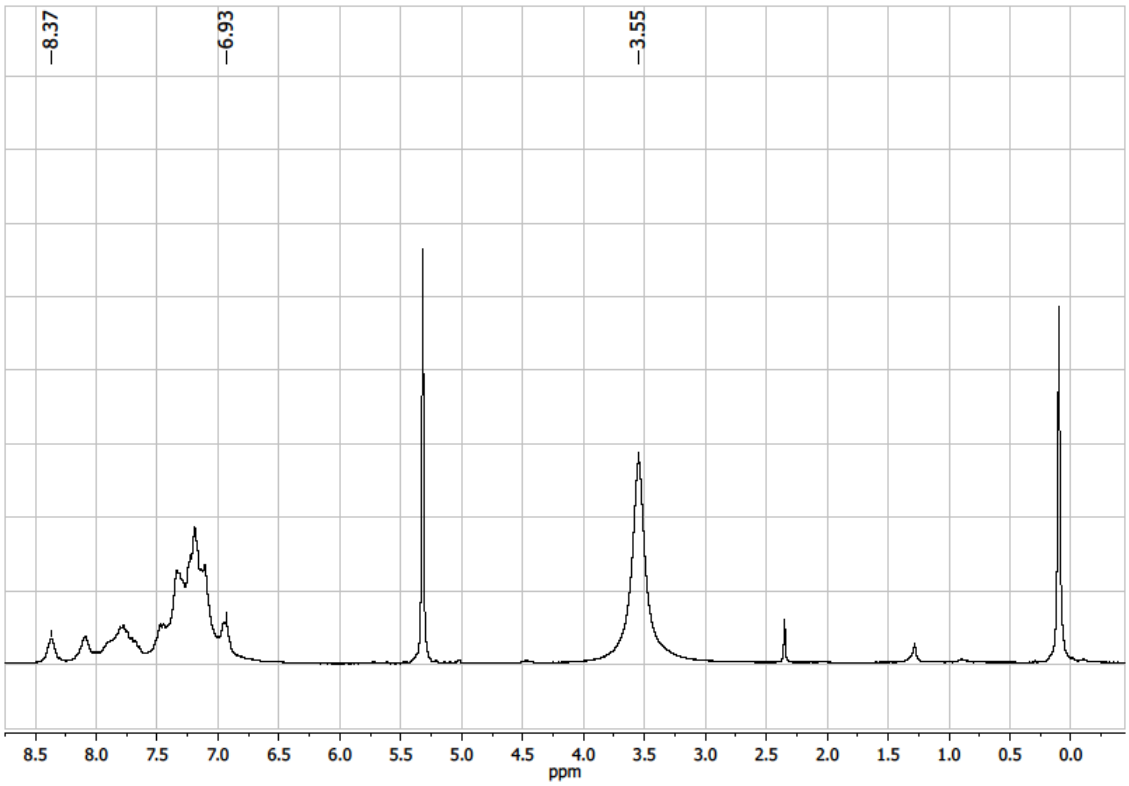

Figure 19. ^{1}H NMR spectrum of **3-CN** in CD_2Cl_2.

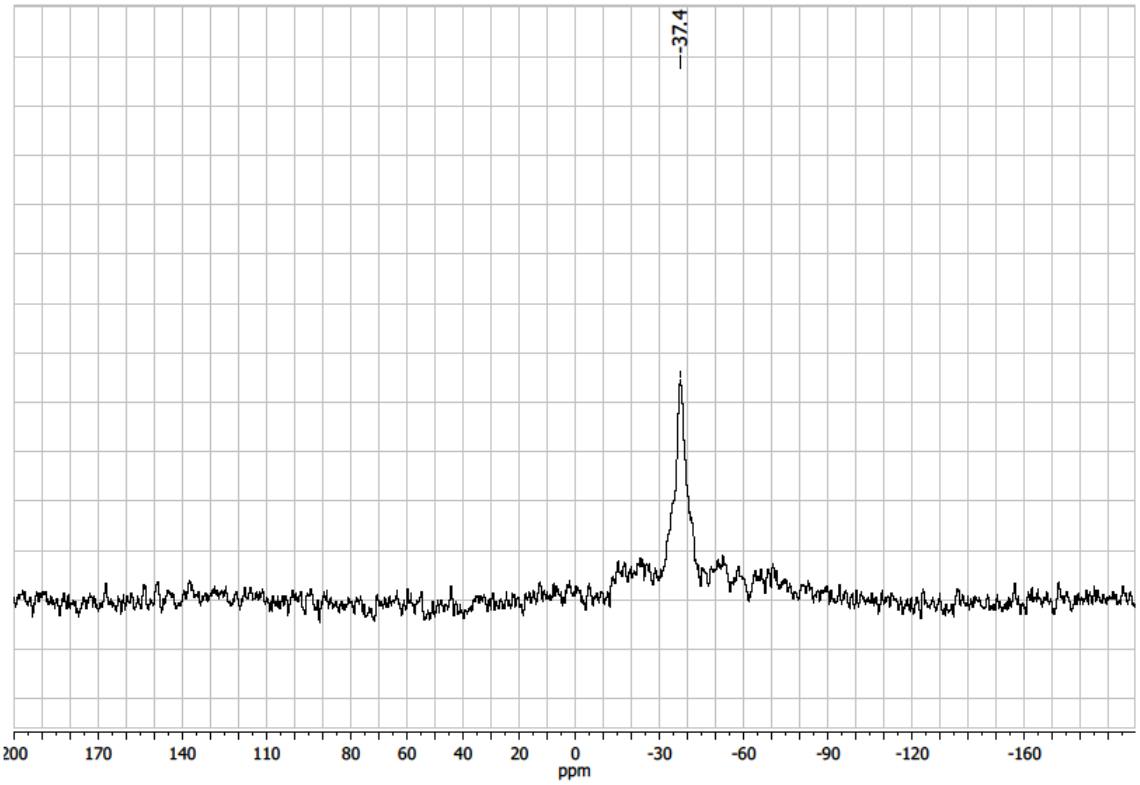

Figure 20. $^{11}B\{^{1}H\}$ NMR spectrum of **3-CN** in THF-d_8.

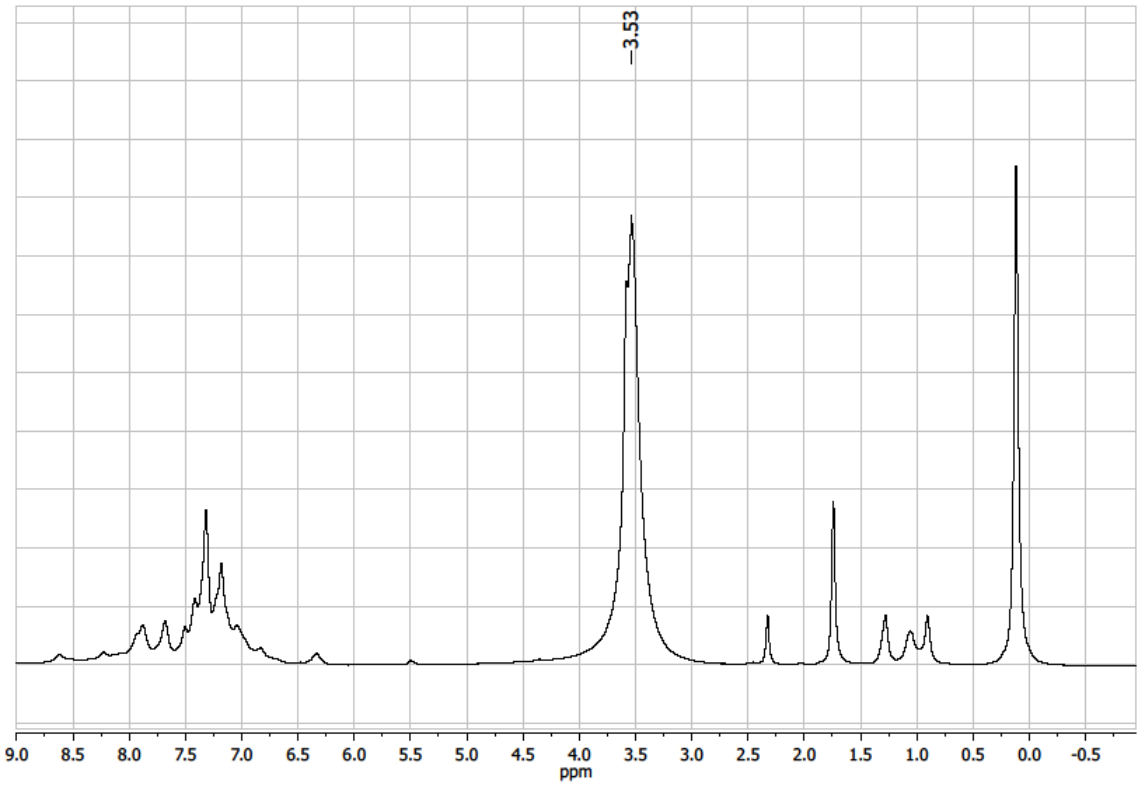

Figure 21. $^{1}H\{^{11}B\}$ NMR spectrum (o2p = -37.4 ppm) of **3-CN** in THF-d_8.

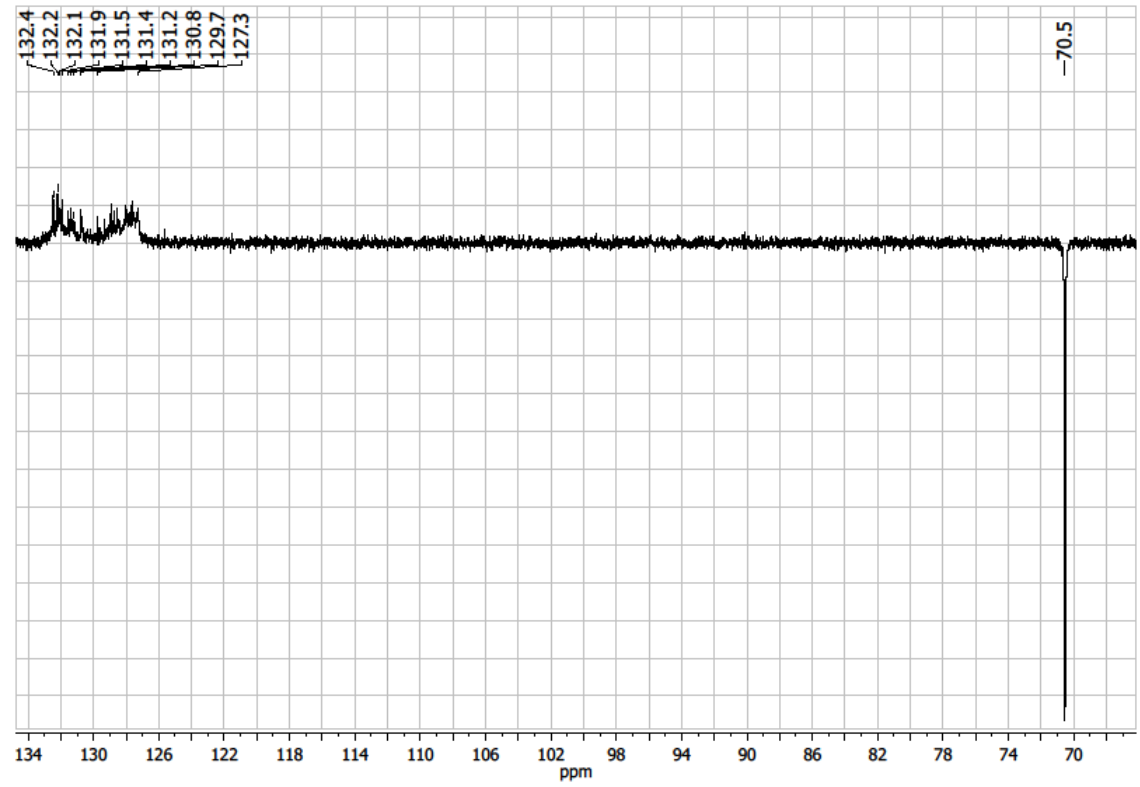

Figure 22. $^{13}C\{^{1}H\}$ NMR spectrum of **3-CN** in CD_2Cl_2.

3. X-Ray Crystallography

The single crystal X-ray diffraction data for the structural analyses has been collected using graphite-monochromated Mo-Kα-radiation (λMoKα = 0.71073) on the pixel detector system BRUKER D8-QUEST. The structures were solved by direct methods with SHELXT and refined against F2 by full-matrix-least-square techniques using SHELXL-2014.[2] Based on the crystal descriptions, numerical absorption corrections were applied.[3] Crystallographic data for **1-CN**, **3-CN** and **4-^{t}BuNC** has been deposited at Cambridge Crystallographic Data Centre (CCDC 1590124-1590126) and can be obtained free of charge via www.ccdc.cam.ac.uk/.

Compound	**1-CN**·C_7H_8	**3-CN**·C_6H_6	**4-^{t}BuNC**·$2CH_2Cl_2$
Empirical formula	$C_{68}H_{77}BFeKN_3O_6P_4$	$C_{69}H_{71}BFeKN_3O_8P_4$	$C_{79}H_{77}BCl_4FeN_4P_6$
Formula weight/g·mol^{-1}	1261.96	1299.92	1476.72
T/K	100(2)	100(2)	100(2)
Crystal system	triclinic	monoclinic	monoclinic
Space group	$P\bar{1}$	*C2/c*	$P2_1/n$
a/Å	13.323(3)	19.049(4)	15.0998(6)
b/Å	13.391(3)	19.040(4)	19.4609(7)
c/Å	19.117(4)	18.357(4)	25.5359(10)
α/°	93.98(3)	90.00	90
β/°	107.59(3)	100.79(3)	102.8950(10)
γ/°	90.07(3)	90.00	90
V/Å^3	3242.5(12)	6540(2)	7314.6(5)
Z	2	4	4
ρ_{calc}/g·cm^{-3}	1.293	1.320	1.341
μ(MoK$_\alpha$)/mm^{-1}	0.448	0.449	0.531
F(000)	1328.0	2720.0	3072.0
2θ range/°	3.05 to 51.362	3.052 to 51.996	4.326 to 54.206
Reflections measured	26798	31193	285847
Independent reflections	12313 (R_{int} = 0.1738)	5759 (R_{int} = 0.1022)	16127 (R_{int} = 0.0563)
Ind. reflections (I>2σ(I))	7853	2176	14778
Parameters/Restraints	773/0	556/965	903/0
R_1 *(I>2σ(I))*	0.0912	0.1172	0.0297
wR_2 *(all data)*	0.2644	0.33348	0.0798
GooF (all data)	0.981	1.099	0.953
Max. peak/hole/e·Å^{-3}	1.23/-0.51	1.032/-0.315	0.75/-0.92
CCDC	1590124	1590125	1590126

Table 1. Selected bond lengths (in Å) and angles (in °) **1-CO**, **1-CN**, **2-CO**, **3-CO** and **3-CN**.

	1-CN	**2-CO**[a]	**3-CO**[a]	**3-CN**
Fe-B	2.646(7)	2.275(7)	2.197(2)-2.210(3)	2.14(3)
Fe-H(B)	1.213(23)			
P-B	1.946(8)	1.914(8)	1.902(2)-1.941(2)	1.910(13)
Fe-CN		-		1.944(19)
Fe-CO		1.759(5)-1.793(5)	1.764(3)-1.772(2)	1.860(18)
OC-Fe-X_{trans}		150.3(2) (X = CO)	164.2(1)-169.1(1) (X = H)	169.3(10) (X = CO)
P-Fe-P	172.37(6)	-	152.9(1)-164.7(1)	171.4(2)

[a] Taken from reference [4].

4. DFT Calculations

DFT calculations were performed with and Gaussian 09, Revision C.01.[5] As functional Grimmes general-gradient approximated and dispersion including B97D functional was used.[6] All geometries were first optimized with the def2-SVP basis set and then reoptimized using the def2-TVP basis set.[7,8] Minima were confirmed with frequency calculations (0 imaginary frequencies). Pictures of optimized structures were created with ChemCraft.[9] Geometry optimizations of complexes **I, 2-CO, 3-CO, 1-CN** and **3-CN** were performed starting from the crystal structures. The simplified complexes (extension "Me" of compound number) were then derived by replacing phenyl with methyl groups and subsequent geometry optimization. Other isomers were derived from the already optimized methyl groups containing structures. Quantum Theory of Atoms in Molecules (QTAIM) analysis was done with AIMAll and pictures were created with AIMStudio.[10]

In the following, the reaction schemes for the different ligands and all calculated isomers are shown, as well as the relative Gibbs Free Energies and Enthalpies, which were calculated in the course of the frequency calculation. For obtaining these values, $\mathbf{I^{Me}}$ was taken as a reference point. In order to be able to compare the energies and enthalpies of the different complexes, the Gibbs Free Energies and the Enthalpies of all ligands that were added to the various complexes during the reactions were calculated and added to the Gibbs Free Energy and Enthalpies of $\mathbf{I^{Me}}$. For each of the other complexes, the Gibbs Free Energies and Enthalpies of the ligands that were not present in the complex were added (or substracted in the case of lost H_2) as well, in order to have the same amount and types of ligands present in each of the complexes and thus be able to compare the Gibbs Free Energies and Enthalpies.

Reaction with CO

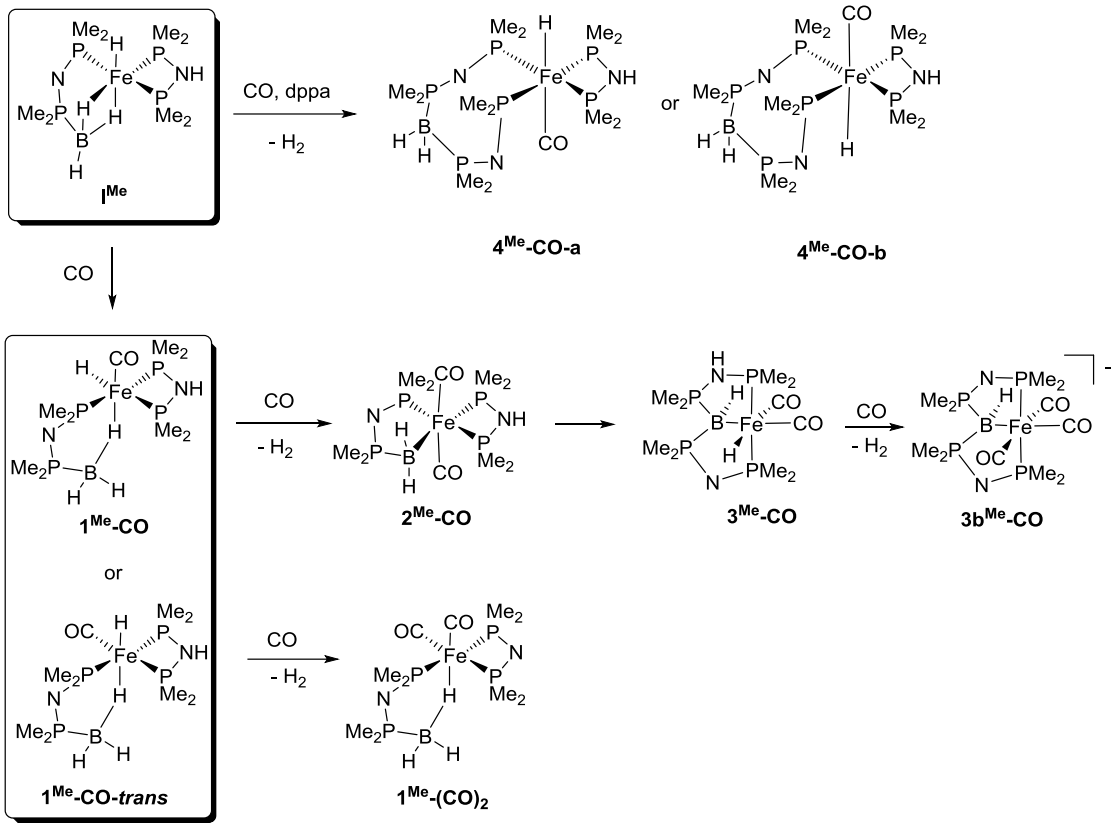

Table 2. Calculated ΔH and ΔG values relative to $\mathbf{I^{Me}}$ which was corrected with the equivalents of CO, dppa and H_2 that reacted with $\mathbf{I^{Me}}$ or were released in this reaction (B97D/def2-TZVP).

	ΔG / kJ/mol	ΔH / kJ/mol
$\mathbf{I^{Me}}$ + ΣCO + Σdppa	0.0	0.0
$\mathbf{1^{Me}}$**-CO**	-160.0	-85.5
$\mathbf{1^{Me}}$**-CO *-trans***	-155.0	-85.6
$\mathbf{1^{Me}}$**-(CO)$_2$** + H_2	-239.0	-498.7
$\mathbf{2^{Me}}$**-CO** + H_2	-239.7	-134.9
$\mathbf{3^{Me}}$**-CO** + H_2	-245.8	-148.8
$\mathbf{3b^{Me}}$**-CO** + 2 H_2	-346.8	-221.0
$\mathbf{4^{Me}}$**-CO-a** + H_2	-324.7	-100.9
$\mathbf{4^{Me}}$**-CO-a** + H_2	-339.1	-116.8

Reaction with CN^-

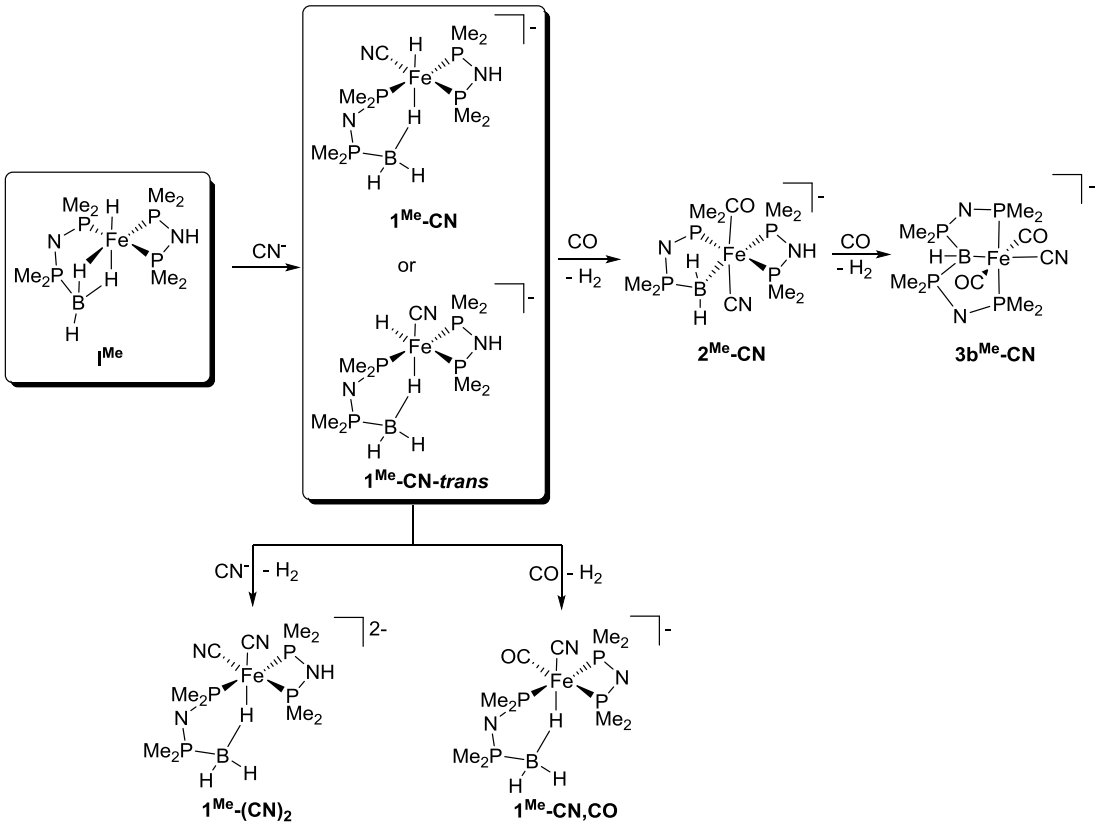

Table 3. Calculated ΔH and ΔG values relative to $\mathbf{I^{Me}}$ which was corrected with the equivalents of CO, CN^- and H_2 that reacted with $\mathbf{I^{Me}}$ or were released in this reaction (B97D/def2-TZVP).

	ΔG / kJ/mol	ΔH / kJ/mol
$\mathbf{I^{Me}}$ + ΣCN^- + ΣCO	0.0	0.0
$\mathbf{1^{Me}}$**-CN**	-192.6	-121.9
$\mathbf{1^{Me}}$**-CN-*trans***	-190.4	-119.5
$\mathbf{1^{Me}}$**-(CN)$_2$** + H_2	-111.0	-11.3
$\mathbf{1^{Me}}$**-CN,CO** + H_2	-344.1	-603.0
$\mathbf{2^{Me}}$**-CN** + H_2	-293.1	-194.6
$\mathbf{3b^{Me}}$**-CN** + 2 H_2	-431.1	-307.8

Reaction with ^{t}BuNC

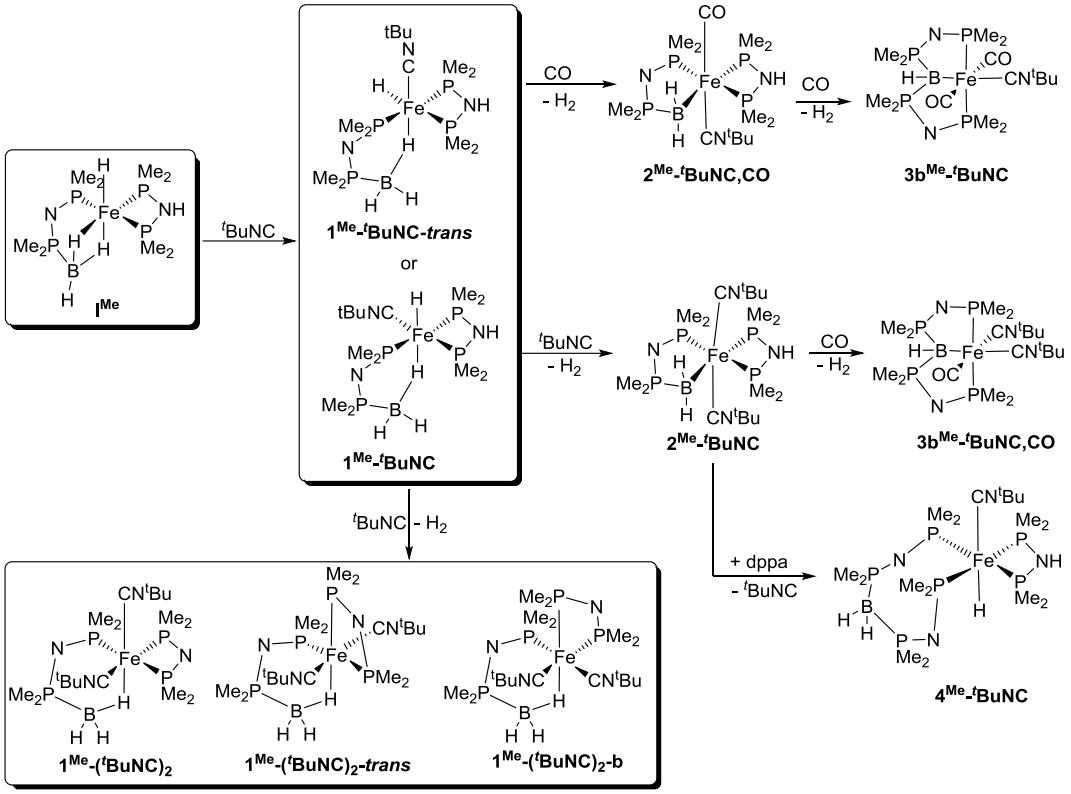

Table 4. Calculated ΔH and ΔG values relative to $\mathbf{I^{Me}}$ which was corrected with the equivalents of CO, ^{t}BuCN, dppa and H_2 that reacted with $\mathbf{I^{Me}}$ or were released in this reaction (B97D/def2-TZVP).

	ΔG / kJ/mol	ΔH / kJ/mol
$\mathbf{I^{Me}}$ + Σ^{t}BuNC + ΣCO + Σdppa	0.0	0.0
$\mathbf{1^{Me}}$-^{t}**BuNC**	-191.7	-29.3
$\mathbf{1^{Me}}$-^{t}**BuNC-*trans***	-169.0	-22.9
$\mathbf{2^{Me}}$-^{t}**BuNC** + H_2	-272.7	-91.3
$\mathbf{1^{Me}}$-(**^{t}BuNC**)$_2$ + H_2	-315.2	-53.1
$\mathbf{1^{Me}}$-(**^{t}BuNC**)$_2$-***trans*** + H_2	-315.4	-53.8
$\mathbf{1^{Me}}$-(**^{t}BuNC**)$_2$-**b** + H_2	-290.9	-29.8
$\mathbf{2^{Me}}$-^{t}**BuNC** + H_2	-288.7	-34.7
$\mathbf{3b^{Me}}$-^{t}**BuNC** + 2 H_2	-382.4	-173.6
$\mathbf{3b^{Me}}$-^{t}**BuNC,CO** + 2 H_2	-417.8	-132.5
$\mathbf{4^{Me}}$-^{t}**BuNC**	-362.1	-58.1

Reaction with NO^+

For the NO complexes, stable compounds were predicted by the calculations. Unfortunately the obtained structures do not match the general scheme, therefore these complexes were omitted in the discussion in the main manuscript. For the sake of completeness, they are shown here.

2^{Me}-NO^+

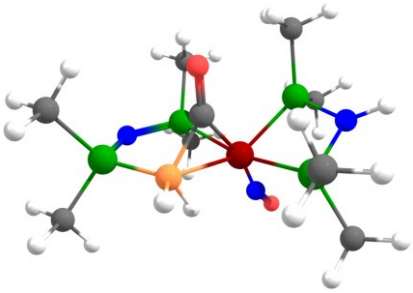

2^{Me}-NO

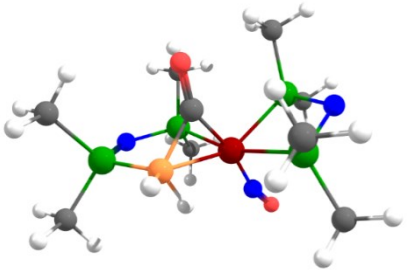

$3b^{Me}$-NO

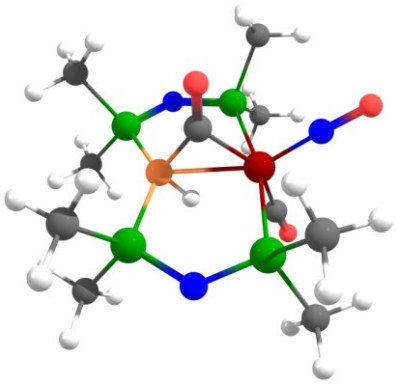

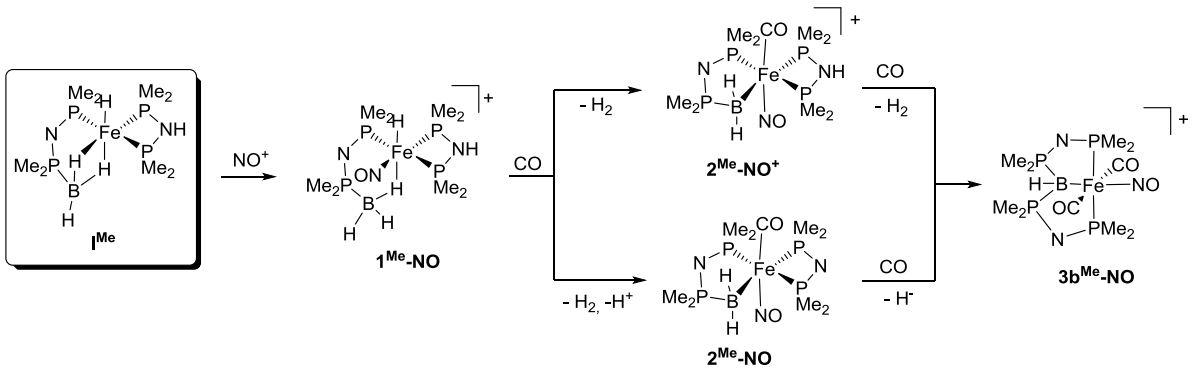

Table 5. Calculated ΔH and ΔG values relative to $\mathbf{I^{Me}}$ which was corrected with the equivalents of CO, NO^+ and H_2 that reacted with $\mathbf{I^{Me}}$ or were released in this reaction (B97D/def2-TZVP).

	ΔG / kJ/mol	ΔH / kJ/mol
$\mathbf{I^{Me}}$ + ΣNO^+ + ΣCO	0.0	0.0
$\mathbf{1^{Me}}$-**NO**	-612.8	-540.4
$\mathbf{2^{Me}}$-$\mathbf{NO^+}$ + H_2	-701.3	-605.8
$\mathbf{2^{Me}}$-**NO** + H_2	383.3	476.4
$\mathbf{3b^{Me}}$-**NO** + 2H_2	-749.5	-621.4

Literature

[1] H. Nöth, L. Meinel, *Z. anorg. allg. Chemie* **1967**, *349*, 225–240.
[2] G. M. Sheldrick, *Acta Cryst. Sect. A* **2015**, *71*, 3–8.
[3] Bruker, *APEX3, SAINT SADABS. Bruker AXS Inc* **2015**, Madison, Wisconsin, USA.
[4] L. Vondung, N. Frank, M. Fritz, L. Alig, R. Langer, *Angew. Chem. Int. Ed.* **2016**, *55*, 14450–14454.
[5] M. J. Frisch, G. W. Trucks, H. B. Schlegel, G. E. Scuseria, M. A. Robb, J. R. Cheeseman, G. Scalmani, V. Barone, B. Mennucci, G. A. Petersson, H. Nakatsuji, M. Caricato, X. Li, H. P. Hratchian, A. F. Izmaylov, J. Bloino, G. Zheng, J. L. Sonnenberg, M. Hada, M. Ehara, K. Toyota, R. Fukuda, J. Hasegawa, M. Ishida, T. Nakajima, Y. Honda, O. Kitao, H. Nakai, T. Vreven, J. A. Montgomery, J. E. P. Jr., F. Ogliaro, M. Bearpark, J. J. Heyd, E. Brothers, K. N. Kudin, V. N. Staroverov, R. Kobayashi, J. Normand, K. Raghavachari, A. Rendell, J. C. Burant, S. S. Iyengar, J. Tomasi, M. Cossi, N. Rega, J. M. Millam, M. Klene, J. E. Knox, J. B. Cross, V. Bakken, C. Adamo, J. Jaramillo, R. Gomperts, R. E. Stratmann, O. Yazyev, A. J. Austin, R. Cammi, C. Pomelli, J. W. Ochterski, R. L. Martin, K. Morokuma, V. G. Zakrzewski, G. A. Voth, P. Salvador, J. J. Dannenberg, S. Dapprich, A. D. Daniels, Farkas, J. B. Foresman, J. V. Ortiz, J. Cioslowski, D. J. Fox, *Gaussian 09 Revision C.01, Gaussian Inc. Wallingford CT* **2009**
[6] S. Grimme, *J. Comput. Chem.* **2006**, *27*, 1787–99.
[7] A. Schäfer, H. Horn, R. Ahlrichs, *J. Chem. Phys.* **1992**, *97*, 2571.
[8] F. Weigend, R. Ahlrichs, *Phys. Chem. Chem. Phys.* **2005**, *7*, 3297–305.
[9] "Chemcraft, Version 1.8," can be found under https://www.chemcraftprog.com**.**
[10] Todd A. Keith, *AIMAll (Version 17.01.25), TK Gristmill Software, Overl. Park KS, USA* **2017**.

Pincer-Type Complexes Based on Phosphine-Stabilized Aluminum(I), Borylene and Carbon(0)

Lisa Vondung,[a,b] Paul Jerabek,[b] Gernot Frenking[a] and Robert Langer*[a]

Abstract: A systematic quantum chemical study of the bisphosphine-stabilized main group element fragments AlH, BH, CH^+ and C as ligands in transition metal complexes is reported. The interaction of five different metal ion fragments with (pincer-)ligands containing the four different donor groups is analysed by Energy Decomposition Analysis combined with the Natural Orbitals for Chemical Valence extension for three different fragmentation variants. These results show that the aluminium(I)-based ligand is not sufficiently stabilized by the phosphine substituents, while the analogous boron(I)-based ligand can be isolated as a ligand coordinated to a transition metal centre. Isoelectronic ligands based on carbon(0), carbodiphosphoranes (CDPs), give rise to strong metal ligand interactions as well, but protonation of the $(R_3P)_2C$-moiety leads to significant destabilization for cationic metal fragments. This is due to repulsion between the cationic ligand and the cationic metal fragment. These findings explain the commonly observed reactivity of CDP-complexes, which often dissociate upon protonation. Finally, we demonstrate for iron(II) complexes that different reactivity patterns are expected for the four donor groups: the experimentally observed reversible E-H-reductive elimination of the borylene-based ligand (E = B) exhibits significantly higher barriers for the protonated CDP-ligand (E = C) and would proceed via different intermediates and transition states. For aluminium, such reaction pathways are not feasible (E = Al). Moreover, we demonstrate that the metal hydrido complexes with CDP-ligands might not be stable towards reduction and isomerisation to a protonated CDP-ligand and a reduced metal centre.

Introduction

Carbodiphosphoranes (CDPs) represent a class of divalent carbon compounds, in which the bonding situation can be understood in terms of a donor-acceptor interaction between a single carbon atom in an exited D^1 state and two ligands with the ability for σ-type donation and π-type back donation.[1] In general, they exhibit a high proton affinity and high tendency to form numerous kinds of adducts and coordination compounds with Lewis-acid or metal fragments. With the two lone pairs, of σ and π symmetry, respectively, CDPs can potentially act as σ- and π-donors and are particularly good ligands for electron-deficient transition metals. Due to the unusual binding properties, increased catalytic activity has been predicted with these ligands (e.g. in olefin metathesis).[2]

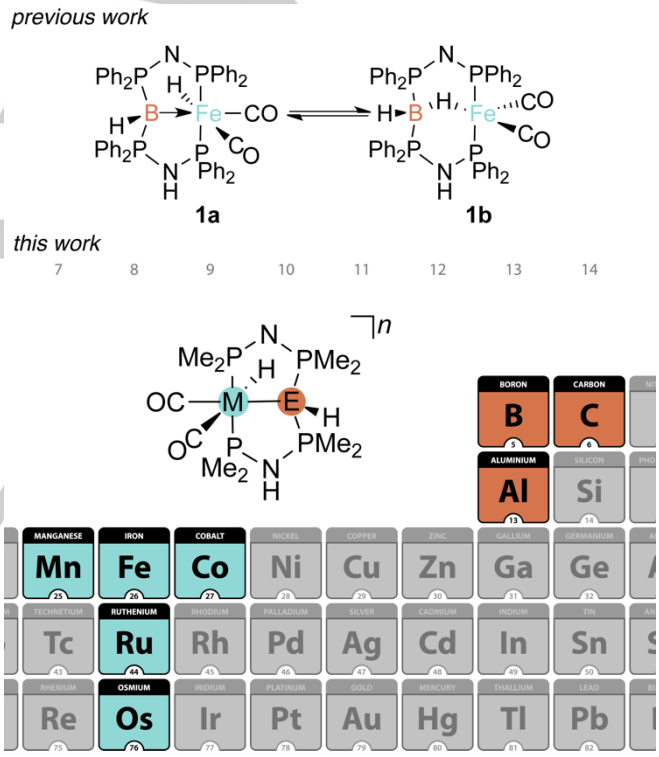

Figure 1. Types of pincer complexes with different central donor groups that are investigated herein.

Recently, preparation of isoelectronic homologues based on boron, namely ligand stabilized borylenes, has been reported. In their initial report *Bertrand* and co-workers were able to stabilize the central borylene fragment in $(CAAC)_2BH$ with two cyclic alkyl amino carbenes (CAACs).[3] Shortly after, *Braunschweig* and co-workers demonstrated that the borylene can be stabilized using simple carbonyl ligands with bulky substituents instead of the hydrogen atom bound to the boron atom.[4] For compounds with the general formula L_2BH quantum chemical investigations suggest that both, N-heterocyclic carbenes (NHCs) and cyclic

[a] L. Vondung, Prof. Dr. G. Frenking, Dr. R. Langer
Department of Chemistry
Philipps-Universität Marburg
Hans-Meerwein-Str. 4, 35032 Marburg, Germany
E-mail: robert.langer@chemie.uni-marburg.de
[b] L. Vondung, Dr. P. Jerabek
Centre for Theoretical Chemistry and Physics,
Institute of Advanced Studies, Massey University Auckland,
Private bag 102904, North Shore Mail Centre, Auckland 0745,
New Zealand

Supporting information for this article is given via a link at the end of the document.

alkyl amino carbenes, should sufficiently stabilize the borylene fragment. For a carbonyl or a triphenyl phosphine ligand on the other hand, the bond dissociation energies are too low to expect an isolable compound.[5] Nonetheless, it is possible to stabilize such species embedded as donor groups in pincer type ligands like in the iron(II) complex **1a**.[6,7] Based on structural parameters, spectroscopic properties, Natural Bond Orbital (NBO) analyses and topological studies based on the Quantum Theory of Atoms in Molecules (QTAIM), it was shown that the tricoordinated boron atom in **1** serves as an electron donating ligand. In consequence, the central donor group is best described as a phosphine-stabilized borylene. However, detailed analysis of these nucleophilic compounds as ligands is missing.

Furthermore, iron complex **1a** with a central phosphine-stabilized borylene as donor group exhibits an unusual reactivity pattern and undergoes reversible reductive B-H-elimination, leading to a bisphosphino boronium or borate group (**1b**, Figure 1 top). Moreover, complex **1a** showed catalytic activity in the oxidation of alcohols.

This work evaluates the bonding situation in a comprehensive quantum chemical investigation of octahedral d^6 metal complexes, containing a pincer-type ligand with central $(R_3P)_2E$- or $(R_3P)_2E(H)$-donor group (E = B, C, Al). This includes a comparative bonding analysis of phosphine-stabilized borylenes, carbodiphosphoranes and their protonated analogues, as well as the analysis of the corresponding aluminium(I)-based pincer ligand.

Results and Discussion

To gain further insight in the bonding situation with these types of ligands, we performed an extensive quantum chemical study of the corresponding methyl-substituted iron(II) complex, using partial charges obtained from NBO analyses and the Energy Decomposition Analysis combined with the Natural Orbitals for Chemical Valence extension (EDA-NOCV). The results were compared with analogue donor groups based on aluminum and carbon.

Table 1 summarizes the partial charges of the methyl-substituted iron(II) complexes. In agreement with the electronegativity of the central donor atom E, the corresponding carbon-based ligands exhibit the most negative partial charge (-1.21*e*), which is further decreased upon deprotonation (-1.41*e*). The partial charge at the boron atom of the phosphine-stabilized borylene is calculated to be -0.84*e*, but the positive partial charge at the corresponding aluminum-based ligand (+0.74*e*) already indicates that the bonding situation is different in the heavier homologue. A closer look on the hydrogen atoms reveals decisive differences in the polarity of the E-H-bond: the positive partial charge of +0.25*e* at the hydrogen atom bound to the negatively charged carbon atom is in line with the experimentally observed facile deprotonation. In comparison, the boron-hydrogen bond is significantly less polar with a partial charge close to zero for the hydrogen atom (+0.03*e*). The negative partial charge of -0.40*e* in combination with the positively charged aluminium atom suggests a hydridic nature of this donor group.

The partial charges at the iron atoms are found to be very similar for CDP (-0.76*e*) and protonated CDP (-0.75*e*), indicating that the donor properties are not significantly changing upon protonation in these complexes. For the boron- and the aluminium-based ligands, the partial charge at the coordinated iron atom is more negative, which might account for stronger donor abilities of the group 13 based ligands. However, the *cis*-influence of the central donor group on the hydrido ligand in *cis*-position is rather small and only small differences are calculated for the four donor groups.

Table 1. NBO partial charges *q* of the central donor group E(H), the central iron atom and the hydrido ligand. Values are given in *e* at B97D/def2-TZVPP level of theory.

E	*q*(Fe)	*q*(H_{Fe})	*q*(E)	*q*(H_E)
BH	-0.84	-0.07	-0.84	+0.03
AlH	-0.92	-0.07	+0.74	-0.40
CH	-0.75	-0.05	-1.21	+0.25
C	-0.76	-0.04	-1.41	

The bonding in the uncoordinated compounds based on boron and carbon is often described by a donor/acceptor interaction of two tertiary phosphines with the central C-atom, the CH^+- or the BH-fragment. However, detailed information about the bonding in the coordinated compounds so far is limited or elusive. EDA-NOCV provides a powerful method to gain deeper understanding of the nature of the chemical bond of interest and its respective components.

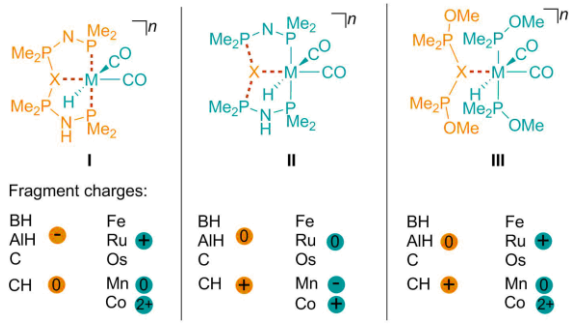

Figure 2. Fragmentation variants considered in this study (X = BH, AlH, CH, C).

To separate the different influences of the three donor groups in the pincer-type ligands, we investigated three different variants of fragmentation by EDA-NOCV analysis (Figure 2). The pincer-type ligands herein can be described as two diphosphines bound to the central fragment X (X = BH, AlH, CH, C). One of the diphosphines, R_2P-N(H)-PR_2 (R = Me, Ph), is deprotonated in the previously reported complex, resulting in an overall anionic ligand

in the case of BH, AlH and C, with the charge being localized at the "arm". For the CH^+-fragment an overall neutral pincer-type ligand is obtained. Given that all three donor groups of the pincer-type ligand are donating one electron pair, we investigated the interaction of a $[Fe(CO)_2H]^+$-fragment with the pincer-type ligands described above in the first step (variant **I**). To gain insights about the nature of the P-X-bond and to eliminate the strong contribution of the two terminal phosphine groups in variant **I**, the interaction of the X- with the $[Fe(CO)_2(R_2P\text{-}N(H)\text{-}PR_2)(R_2P\text{-}N\text{-}PR_2)H]$-fragment is investigated in variant **II**. These two variants include the formation of three bonds upon combination of the fragments and lead to an overlay of different bond properties. With variant **III** the Fe-X-bond will be solely analyzed, by utilization of monodentate ligands instead of a tridentate ligand. Therefore, we use $Me_2(OMe)P$ as ligands and substituents, and analyze the interaction of $(Me_2\{OMe\}P)_2X$ with the $[Fe(CO)_2(Me_2\{OMe\}P)_2H]$-fragment.

Table 2. EDA-NOCV results (BP86/TZ2P+) of iron complexes for different fragmentation variants (**I**-**III**). Energy contributions are given in kcal·mol^{-1}.

	Variant **I**				Variant **II**				Variant **III**			
Interacting fragments	$[Fe(CO)_2H]^+$ and $[PNP\text{-}X\text{-}PN(H)P]^-$				X and $[Fe(CO)_2(R_2P\text{-}N(H)\text{-}PR_2)(R_2P\text{-}N\text{-}PR_2)H]^+$				$[Fe(CO)_2H\{PMe_2(OMe)\}_2]^+$ and $(Me_2\{OMe\}P)_2X$			
X =	BH	AlH	CH	C	BH	AlH	CH	C	BH	AlH	CH	C
ΔE_{int}	-391.2	-447.5	-367.3	-368.3	-193.7	-140.4	-232.6	-250.4	-108.0	-128.8	-7.2	-88.2
ΔE_{Pauli}	276.8	484.3	254.1	252.4	655.7	403.2	1042.0	1331.8	138.7	238.4	83.4	110.2
ΔE_{elstat}[a]	-338.0 (52.5 %)	-400.1 (44.0 %)	-330.1 (55.2 %)	-324.1 (54.3 %)	-302.5 (35.9 %)	-238.6 (44.8 %)	-359.6 (28.3 %)	-443.4 (28.1 %)	-124.8 (56.7 %)	-187.1 (54.4 %)	-8.55 (13.1 %)	-100.4 (59.1 %)
ΔE_{orb}[a]	-306.0 (47.5 %)	-508.3 (56.0 %)	-268.2 (44.8 %)	-273.3 (45.7 %)	-541.0 (64.1 %)	-294.4 (55.2 %)	-910.0 (71.7 %)	-1134.8 (71.9 %)	-95.4 (43.3 %)	-157.0 (45.6 %)	-56.7 (86.9 %)	-69.4 (40.9 %)
ΔE_{disp}	-24.1	-23.3	-23.2	-23.4	-6.0	-10.6	-5.0	-3.9	-26.5	-23.2	-25.3	-28.6
ΔE_{prep}	40.5	95.2	38.0	35.8	61.6	60.4	40.1	60.2	32.8	29.9	48.0	16.3
$-D_e$	-350.7	-352.2	-359.8	-332.5	-132.1	-80.0	-192.5	-190.2	-75.2	-98.9	-31.5	-71.9

[a] The values in parentheses give the percentage contribution to the total attractive interactions $\Delta E_{elstat}+\Delta E_{orb}$.

Table 2 shows the EDA-NOCV results of the different fragmentation variants for iron(II) complexes with different central donor groups. Variant **I** describes the interaction of two tertiary phosphines and one X-group with the central iron(II) fragment. Accordingly, differences in the energy terms should arise from differences in the Fe-X-interaction. The interaction energies (ΔE_{int}) for X = C and CH are almost identical. For X = BH the interaction is approx. 20 kcal·mol^{-1} stronger and even more stronger (80 kcal·mol^{-1}) for X = AlH. Note, how the biggest attractive contribution to bonding for the aluminium-based ligand is the orbital interaction term ΔE_{orb}, while the electrostatic interactions (ΔE_{elstat}) are dominant for the other ligand types. However, the differences in intrinsic bond energies between the boron- and the carbon-based ligands mainly arise from stronger orbital interactions, which are not outweighed by the stronger Pauli repulsion (ΔE_{Pauli}) for X = BH. However, the dominating contributions to the deformation density $\Delta\rho$ are very similar for X = BH, CH and C, showing the donation of the phosphines to the central iron(II) atom, as well as the donation from the central X-group, which leads to a depletion of electron density between P and X. In the case of X = AlH, the highest contributing deformation density shows mainly donation of the phosphines to the iron(II) atom and no donation from the aluminium atom to the iron atom. Only in the second highest deformation density (not shown here), donation from the aluminium to the iron atom is observed. The larger values for the energy contribution and eigenvalues of the deformation densities for X = Al show the larger electron flow compared to the other ligands. Consequently, the orbital interaction is larger as well.

The interaction of the fragments in variant **II** is dominated by the formation of two P-X-bonds in addition to the X-Fe-bond. The interaction energy ΔE_{int} increases in the order AlH > BH > CH > C, giving the strongest interaction for the CDP-based ligand. This can be understood by clear trends for the energy terms: the strong orbital interaction for the CDP-based ligand (ΔE_{orb} = -1138.4 kcal·mol^{-1}) is subsequently decreased in the same order, leading to the weakest interaction for AlH (ΔE_{orb} = -294.4 kcal·mol^{-1}). The same trend with lower absolute values is observed for the electrostatic interaction. The Pauli repulsion shows the reverse trend, giving the strongest repulsion for the CDP-based ligand. However, the attractive interactions predominate the trend of the Pauli repulsion, leading to the described trend for ΔE_{int}. A closer look on the relative contributions to the interaction energy reveals a dominance of orbital (covalent) interactions for the carbon-based ligands (71.7-71.9 %), which subsequently decreases for boron (64.1 %) and aluminum (55.2 %). Inspection of the

corresponding deformation densities shows that in case of X = C, CH, BH electron density is transferred from the phosphines to the boron or carbon atom, and from the latters to the central iron atom. In contrast, almost no accumulation of electron density is observed at the aluminum, which is in line with the weak interaction energies. This indicates that the P-Al interaction is very weak and that the phosphine groups studied herein do not sufficiently stabilize the AlH-fragment with the formal oxidation state +1. However, with carbenes as stabilizing substituents, iron complexes containing a ligand-stabilized aluminum(I) as donor ligand can be isolated.[8]

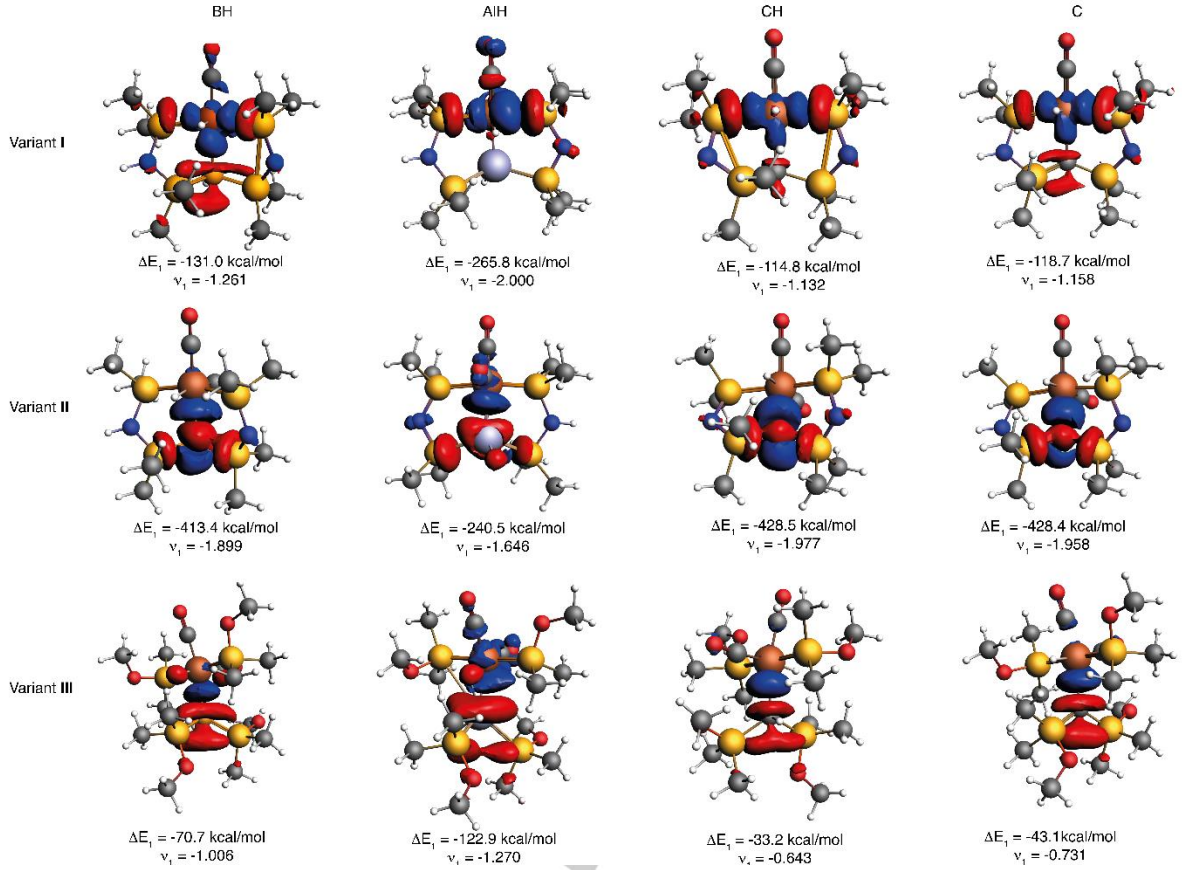

Figure 3. Dominating contributions to the deformation density Δρ for the different fragmentation variants **I**-**III** according to EDA-NOCV analysis. The contour value is |Δρ|=0.003 a.u. The blue contours correspond to accumulation, red contours to depletion of electron density.

The fragmentation variant **III** includes exclusive formation of X-Fe-bond and can help to discriminate the Fe-P- and P-X-interaction from the Fe-X-interaction. The interaction of the cationic CH-based ligand with the cationic metal fragment leads to very small interaction energy (-7.2 kcal·mol^{-1}). A closer look on the energy terms shows that the orbital interaction is smaller than in the other ligands, but the electrostatic interaction is with -8.5 kcal·mol^{-1} significantly smaller than in all other ligands and might be result of a strong repulsion of the two cationic fragments. Although protonation of a coordinated CDP-ligand often results in dissociation of the metal-carbon-bond and formation of protonated CDP, protonated CDPs as ligands coordinated to a transition metal were already isolated.[9–11]

Surprisingly, the aluminium-based ligand gives rise to the strongest interaction energy with the highest absolute values for orbital interaction, electrostatic interaction and Pauli repulsion. The direct comparison of the CDP- and the borylene-based ligand shows a stronger interaction energy for the latter (-88.2 vs. -108.0 kcal·mol^{-1}), which can be understood by stronger orbital and electrostatic interactions, which are not compensated by the stronger Pauli repulsion. Due to the lower preparation energy for the CDP-based ligand (-16.3 kcal·mol^{-1}), the resulting dissociation energies are found to be quite similar for the CDP- (-71.9 kcal·mol^{-1}) and the borylene-based ligand (-75.2 kcal·mol^{-1}).

As previously pointed out, borylenes are likely not sufficiently stabilized by tertiary phosphines to allow for isolation, but as

ligands coordinated to a transition metal these species have been reported. In case of aluminium, the situation is different: although the iron aluminium interaction is rather strong, the AlH-fragment is as coordinated ligand not sufficiently stabilized by the phosphine-substituents. Moreover, findings show that for X = BH, CH and C the bond in these complexes can be interpreted as donor-acceptor-bond from the phosphines to the central group, which itself acts as an electron donating ligand. In consequence, iron(II) complexes containing a CDP-based pincer-type ligand should be isolable. However, transition metal complexes with such ligands are currently limited to rhodium, nickel, palladium, platinum and gold.[9–16]

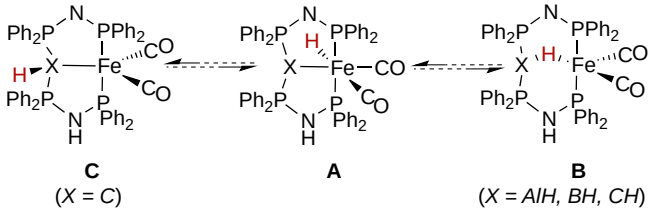

Scheme 1. Possible reductive elimination processes in pincer-type iron(II) complexes.

Next, we evaluated whether the unusual reactivity pattern of a reversible B-H-reductive elimination in the iron(II) complex with the boron-based ligand can be transferred to the other donor groups as well. Therefore, the relative stability of the corresponding isomers was calculated on B97D/def2-TZVPP-level of theory. We considered a reductive proton transfer from **A**, which in case of X = AlH, BH and CH leads to cleavage of the bond from the hydrogen atom to the newly formed iron(0) center in **B**. For X = C the proton transfer yields an iron(0) complex with a protonated CDP as central donor group (isomer **C**). The relative stabilities are summarized in Table 3.

In agreement with the experimental findings,[17] the difference in *Gibbs* enthalpy between the iron(II) complex with a phosphine-stabilized borylene and the iron(0) complex with a bisphosphino-boron(III) species is calculated to be +10.6 kcal·mol^{-1}. The difference for the corresponding isomer of the aluminium based ligand is even smaller with +8.6 kcal·mol^{-1}. The η^1-coordinated species **B** for X = CH turned out to be a transition state (ΔG_{TSB} = 20.1 kcal·mol^{-1}), connecting isomer **A** with the η^2-coordinated isomer **D** (Figure 4). In case of the boron-based ligand, the η^2-coordinated isomer **D** is a transition state (**TS$_D$**), connecting isomer **B** and **B'**. This indicates that a reversible C-H-reductive elimination is a possible reactivity pattern, too, but this pathway is higher in Gibbs enthalpy and proceeds via different intermediates and transition states. The corresponding aluminium species **B** was found to be an energetic minimum as well ($\Delta G_{A\text{-}B}$ = 8.6 kcal·mol^{-1}), but all located transition states did not connect this intermediate with the isomer **A**.

Table 3. Relative stability of isomers at B97D/def2-TZVPP level of theory.

X =	AlH	BH	CH	C
$\Delta G_{A\text{-}B}$ / kcal·mol^{-1}	+8.6[a]	+10.6	+19.1[b]	-
$\Delta G_{A\text{-}C}$ / kcal·mol^{-1}	-	-	-	-7.6

[a] Minimum, but with constraints. [b] The η^2-coordinated complex represents the local minimum for X = CH.

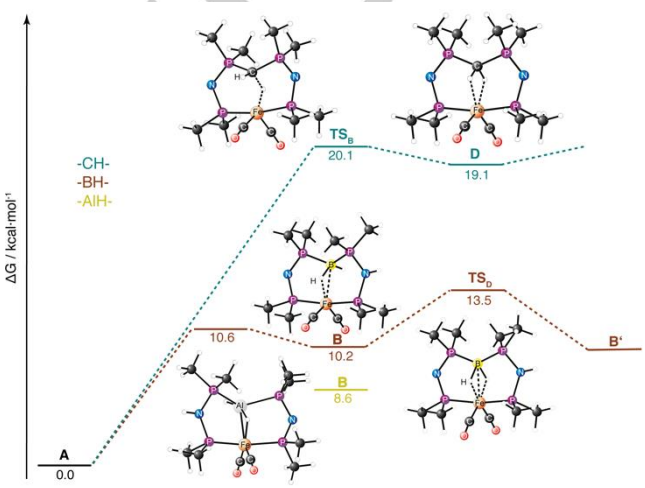

Figure 4. Reversible reductive E-H-elimination of X-based pincer-type iron complexes.

To our surprise, the CDP-based iron(II) complex **A** turned out to be less stable by 7.6 kcal·mol^{-1} than the corresponding iron(0) isomer **C** with a protonated CDP as central donor group. This result indicates that the CDP ligands might be too basic to stabilize transition metal hydrido complexes of high and moderate acidity. Using Morris' increment system, the acidity of the hydrido ligand can be estimated. Assuming the parameter value of an amide donor for the CDP, a *p*K$_a$ value of 7.4 is estimated for the CDP-based complex A.[18]

Next, we investigated whether the insights about bonding in iron complexes are applicable for other transition metals as well (Figure 5). For this reason, analogous complexes with d^6-metal ions were investigated in the three fragmentation variants by EDA-NOCV. This includes the heavier analogues ruthenium(II) and osmium(II), as well as the neighbouring 3d-metals manganese(I) and cobalt(III).

Visual inspection of the results from variant **I** (Figure 5 top) indicates that the differences between the metal ions are rather small compared to the differences between the different donor groups. As with iron(II), the aluminium-based ligand represents an exception and gives rise to the highest absolute values for all energy terms.

The fragmentation variant **II** results in a similar picture with comparably small difference between the metal ions. However, the impact of the formation of two P-X-bonds in this variant results in the lowest interaction energy for the aluminium-based ligand.

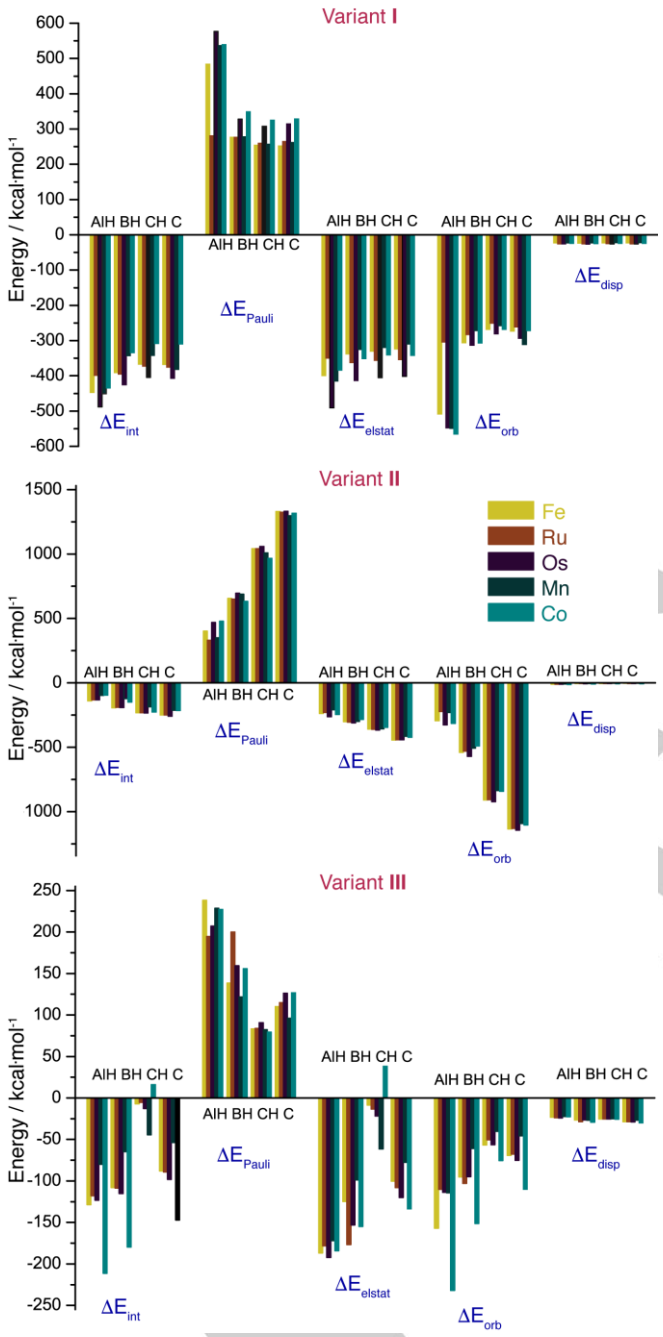

Figure 5. Results of the EDA-NOCV for all investigated combinations of X and M and all cutting variants.

In general, the trends observed for ΔE_{int} in variant **II** confirm the results for iron(II) of $\Delta E_{int}(X = C) < \Delta E_{int}(X = CH) < \Delta E_{int}(X = BH)$. The cobalt(III) represents an exception, in which $\Delta E_{int}(X = C)$ is larger than $\Delta E_{int}(X = CH)$. This small difference in ΔE_{int} is a result of a significantly higher Pauli repulsion for X = C, which is not compensated to the same extent by orbital and electrostatic interaction as for X = CH.

Variant **I** and **II** basically confirmed the findings discussed above for iron(II). The interaction of the mono-dentate ligand with the different metal ions in variant **III** shows differences between the metal ions. Within the group 8 metal ions, the differences in the interaction energy ΔE_{int} remain quite small with slightly stronger interactions for osmium for X = BH, CH, C. The manganese(I) complexes contain the neutral metal fragment $[Mn(CO)_2(Me_2\{OMe\}P)_2H]$ and its interaction with neutral ligands (X = AlH, BH, C) is the weakest of all metals. For the cationic ligand with X = CH, the manganese(I) complexes are more stable than the other metal complexes. This is mainly a result of stronger electrostatic interaction, which is significantly reduced for the interaction of a cationic ligand with a cationic metal fragment. In case of cobalt(III) and the corresponding dicationic metal fragment, this even leads to a positive interaction energy. However, for all other ligands (X = AlH, BH, C) the interaction of the diacationic cobalt(III) fragment with the neutral mono-dentate ligands is the strongest, which is a result of significantly stronger orbital interactions.

Conclusions

In a comprehensive investigation we compared the bonding situation in d^6-metal complexes containing phosphine-stabilized aluminium(I), borylene and carbon(0) as donor groups in a pincer-type ligand. The results from the EDA-NOCV study clearly show that aluminium(I) gives rise to strong interactions with the central metal atom, but is not sufficiently stabilized by the phosphine substituents. Phosphine-stabilized borylenes and carbones(0) in contrast, show strong interactions with transition metal centers and should lead to isolable complexes for both donor groups. However, protonation of the coordinated $(R_3P)_2C$-moiety can lead to strong repulsion between the cationic ligand and a cationic metal fragment. While the CDP donor group with its two lone pairs, one of σ- and one of π-symmetry, can act as a σ-/π-donor and stabilize transition metal ions in high oxidation states, this interaction is significantly weakened upon protonation with increasing oxidation state of the metal. In consequence, protonation of a coordinated CDP-ligand often leads to dissociation and complexes with protonated CDP-groups are only isolable for metals in low oxidation states or with the CDP group in a polydentate ligand.

This investigation further shows that different reactivity patterns can be expected from complexes with the four different donor groups.

The experimentally observed B-H-reductive elimination in the iron(II) complex **1a** proceeds via a η^1-coordinated bisphosphino-boron(III) intermediate. For the corresponding CH^+-based ligand C-H-reductive elimination is facile, too. However, the reaction

barriers are significantly higher and the reaction proceeds via a different intermediate, the η^2-coordinate bisphosphino-boron(III) species. For the aluminium-based ligand, the Al-H-reductive elimination product is an energetic minimum as well, but none of the located transition states connected this intermediate with the investigated aluminium(I)-based ligand. For the iron(II) hydrido complex with a CDP-based pincer-type ligand, reductive proton transfer from the iron-bound hydrido to the CDP-carbon leads to a more stable iron(0) isomer. These findings indicate that CDP-based ligands can exhibit limited stability in the presence of hydrido ligands. In continuation of this study, we are currently investigating the synthesis of the transition metal complexes of this study.

Computational Methods

Geometry optimizations and subsequent analytical frequency calculations for confirmation of minima were carried out with Orca 3.0.3[19] and Gaussian 09 Rev. C.01 (Fe-B complex, NBO calculations).[20] All structures were optimized with the B97D functional and def2-TZVPP basis set.[21,22] Relativistic effects were taken into account for ruthenium and osmium by using the fully relativistic Stuttgart-Köln energy-consistent pseudopotentials.[23,24] For all Orca calculations, RIJCOSX for treatment of the Coulomb term with resolution-of-identity and the exchange term by seminumerical integration was applied.[25] For the Natural Orbital Analysis, NBO 5.0 as implemented in Gaussian 09 Rev. C.01 was used.[26] For the EDA, the BP86 functional with a triple-zeta STO basis set TZ2P+[27] in conjunction with the zero-order regular approximation (ZORA),[28] and Grimme's D3 dispersion correction together with Becke-Johnson damping as implemented in the ADF2016 program package was employed.[29–33]

EDA (also known as extended transition-state method, ETS) was developed independently by Morokuma[34] and Ziegler and Rauk.[35] It analyses the interaction energy ΔE_{int} of a bond in the molecule A-B with fragments A and B in the frozen geometry of AB and the particular electronic reference state. The interaction energy can be described as the sum of three interactions:

$$\Delta E_{\mathrm{int}} = \Delta E_{\mathrm{elstat}} + \Delta E_{\mathrm{Pauli}} + \Delta E_{\mathrm{orb}}$$

ΔE_{elstat} describes the quasiclassical Coulomb interaction between the unperturbed charge distributions of the fragments A and B. ΔE_{Pauli} is the Pauli repulsion, which is destabilizing and describes the interaction between electrons of the same spin between the two fragments. The third interaction ΔE_{orb} is the orbital interaction, which includes the charge transfer and polarization effects. Further details on the EDA method and examples on bond analysis using EDA can be found in the literature.[36–38]

An extension to the EDA scheme is the EDA-NOCV, which combines EDA with decomposition of the natural orbitals for chemical valence (NOCV).[39] Thereby, pairwise energy contributions for each pair of interacting orbitals are provided and ΔE_{orb} can be analyzed by single orbital contributions:

$$\Delta E_{\mathrm{orb}} = \sum \Delta E_k^{\mathrm{orb}} = \sum \nu_k \left(-F_{-k}^{\mathrm{TS}} + F_k^{\mathrm{TS}}\right)$$

$-F_{-k}^{\mathrm{TS}}$ and F_k^{TS} are the diagonal transition-state Kohn-Sham matrix elements that correspond to the NOCVs with eigenvalues $-\nu_k$ and ν_k. This decomposition scheme allows for the interpretation of bonding interactions in molecules without symmetry, as the deformation density is also based on the NOCVs and can be plotted to visualize the single contributions. Additionally, $\Delta E_k^{\mathrm{orb}}$ provides for quantitative interpretation.

Acknowledgements

We gratefully acknowledge financial support from the Deutsche Forschungsgemeinschaft (LA 2830/3-2), the Erich-Becker-Stiftung (R. L.) and the Studienstiftung des deutschen Volkes (L. V.). R. L. is grateful to Prof. S. Dehnen for her continuous support.

Keywords: borylenes • carbones • aluminium • bonding analysis • coordination chemistry

[1] W. Petz, *Coord. Chem. Rev.* **2015**, *291*, 1–27.
[2] R. Tonner, G. Frenking, *Chem. Commun.* **2008**, *1*, 1584.
[3] D. A. Ruiz, G. Ung, M. Melaimi, G. Bertrand, *Angew. Chem. Int. Ed.* **2013**, *52*, 7590–7592.
[4] H. Braunschweig, R. D. Dewhurst, F. Hupp, M. Nutz, K. Radacki, C. W. Tate, A. Vargas, Q. Ye, *Nature* **2015**, *522*, 327–330.
[5] M. A. Celik, R. Sure, S. Klein, R. Kinjo, G. Bertrand, G. Frenking, *Chemistry* **2012**, *18*, 5676–92.
[6] L. Vondung, N. Frank, M. Fritz, L. Alig, R. Langer, *Angew. Chem. Int. Ed.* **2016**, *55*, 14450–14454.
[7] M. Grätz, A. Bäcker, L. Vondung, L. Maser, A. Reincke, R. Langer, *Chem. Commun.* **2017**, 1–4.
[8] G. Tan, T. Szilvási, S. Inoue, B. Blom, M. Driess, *J. Am. Chem. Soc.* **2014**, *136*, 9732–9742.
[9] W. Petz, B. Neumüller, *Polyhedron* **2011**, *30*, 1779–1784.
[10] C. Reitsamer, S. Stallinger, W. Schuh, H. Kopacka, K. Wurst, D. Obendorf, P. Peringer, *Dalt. Trans.* **2012**, *41*, 3503.
[11] C. Reitsamer, W. Schuh, H. Kopacka, K. Wurst, E. P. Ellmerer, P. Peringer, *Organometallics* **2011**, *30*, 4220–4223.
[12] K. Kubo, N. D. Jones, M. J. Ferguson, R. McDonald, R. G. Cavell, *J. Am. Chem. Soc.* **2005**, *127*, 5314–5315.
[13] K. Kubo, H. Okitsu, H. Miwa, S. Kume, R. G. Cavell, T. Mizuta, *Organometallics* **2017**, *36*, 266–274.
[14] S. Stallinger, C. Reitsamer, W. Schuh, H. Kopacka, K. Wurst, P. Peringer, *Chem. Commun.* **2007**, *12*, 510–512.
[15] C. Reitsamer, W. Schuhe, H. Kopacka, K. Wurst, P. Peringer, *Organometallics* **2009**, *28*, 6617–6620.
[16] C. Reitsamer, I. Hackl, W. Schuh, H. Kopacka, K. Wurst, P. Peringer, *J. Organomet. Chem.* **2017**, *830*, 150–154.
[17] L. Vondung, N. Frank, M. Fritz, L. Alig, R. Langer, *Angew. Chem. Int. Ed.* **2016**, *55*, 14450–14454.
[18] R. H. Morris, *J. Am. Chem. Soc.* **2014**, *136*, 1948–1959.
[19] F. Neese, *Wiley Interdiscip. Rev. Comput. Mol. Sci.* **2012**, *2*, 73–78.
[20] M. J. Frisch, G. W. Trucks, H. B. Schlegel, G. E. Scuseria, M. A. Robb, J. R. Cheeseman, G. Scalmani, V. Barone, B. Mennucci, G. A. Petersson, H. Nakatsuji, M. Caricato, X. Li, H. P. Hratchian, A. F. Izmaylov, J. Bloino, G. Zheng, J. L. Sonnenberg, M. Hada, M. Ehara, K. Toyota, R. Fukuda, J. Hasegawa, M. Ishida, T. Nakajima, Y. Honda, O. Kitao, H. Nakai, T. Vreven, J. A. Montgomery Jr., J. E. Peralta, F. Ogliaro, M. Bearpark, J. J. Heyd, E. Brothers, K. N. Kudin, V. N. Staroverov, R. Kobayashi, J. Normand, K. Raghavachari, A. Rendell, J. C. Burant, S. S. Iyengar, J. Tomasi, M. Cossi, N. Rega, J. M. Millam, M. Klene, J. E. Knox, J. B. Cross, V. Bakken, C. Adamo, J. Jaramillo, R. Gomperts, R. E. Stratmann, O. Yazyev, A. J. Austin, R. Cammi, C. Pomelli, J. W. Ochterski, R. L. Martin, K. Morokuma, V. G. Zakrzewski, G. A. Voth, P. Salvador, J. J. Dannenberg, S. Dapprich, A. D. Daniels, O. Farkas, J. B. Foresman, J. V. Ortiz, J. Cioslowski, D. J. Fox, in *Gaussian Inc. Wallingford CT*, Gaussian Inc. Wallingford CT 2009, **2009**.

[21] S. Grimme, *J. Comput. Chem.* **2006**, *27*, 1787–99.
[22] F. Weigend, R. Ahlrichs, *Phys. Chem. Chem. Phys.* **2005**, *7*, 3297–305.
[23] K. A. Peterson, D. Figgen, M. Dolg, H. Stoll, *J. Chem. Phys.* **2007**, *126*.
[24] D. Figgen, K. A. Peterson, M. Dolg, H. Stoll, *J. Chem. Phys.* **2009**, *130*.
[25] F. Neese, F. Wennmohs, A. Hansen, U. Becker, *Chem. Phys.* **2009**, *356*, 98–109.
[26] NBO 5.0, E. D. Glendening, J. K. Badenhoop, A. E. Reed, J. E. Carpenter, J. A. Bohmann, C. M. Morales, F. Weinhold, M. Theoretical Chemistry Institute, University of Wisconsin, **2001**.
[27] E. Van Lenthe, E. J. Baerends, *J. Comput. Chem.* **2003**, *24*, 1142–1156.
[28] E. van Lenthe, E. J. Baerends, J. G. Snijders, *J. Chem. Phys.* **1993**, *99*, 4597–4610.
[29] ADF2016, SCM, Theoretical Chemistry, Vrije Universiteit Amsterdam, The Netherlands, A. E. J. Baerends, T. Ziegler, A.J. Atkins, J. Autschbach, O. Baseggio, D. Bashford, A. Bérces, F.M. Bickelhaupt, C. Bo, P.M. Boerrigter, L. Cavallo, C. Daul, D.P. Chong, D.V. Chulhai, L. Deng, R.M. Dickson, J.M. Dieterich, D.E. Ellis, M. van Faassen, L. Fan
[30] C. Fonseca Guerra, J. G. Snijders, G. Te Velde, E. J. Baerends, *Theor. Chem. Acc.* **1998**, *99*, 391–403.
[31] G. te Velde, F. M. Bickelhaupt, E. J. Baerends, C. Fonseca Guerra, S. J. A. van Gisbergen, J. G. Snijders, T. Ziegler, *J. Comput. Chem.* **2001**, *22*, 931–967.
[32] A. D. Becke, *Phys. Rev. A* **1988**, *38*, 3098–3100.
[33] J. P. Perdew, *Phys. Rev. B* **1986**, *33*, 8822–8824.
[34] K. Morokuma, *J. Chem. Phys.* **1971**, *55*, 1236–1244.
[35] T. Ziegler, A. Rauk, *Theor. Chim. Acta* **1977**, *46*, 1–10.
[36] G. Frenking, K. Wichmann, N. Fröhlich, C. Loschen, M. Lein, J. Frunzke, V. M. Rayón, *Coord. Chem. Rev.* **2003**, *238–239*, 55–82.
[37] F. M. Bickelhaupt, E. J. Baerends, *Rev. Comput. Chem.* **2000**, *238–239*, 55–82.
[38] G. Frenking, F. Matthias Bickelhaupt, in *Chem. Bond* (Eds.: G. Frenking, S. Shaik), Wiley-VCH Verlag GmbH & Co. KGaA, Weinheim, Germany, **2014**, pp. 121–157.
[39] M. P. Mitoraj, A. Michalak, T. Ziegler, *J. Chem. Theory Comput.* **2009**, *5*, 962–975.

Supporting Information

Pincer-Type Complexes Based on Phosphine-Stabilized Aluminum(I), Borylene and Carbon(0)

Lisa Vondung,[a,b] Paul Jerabek,[b] Gernot Frenking[a] and Robert Langer*[a]

[a] *Fachbereich Chemie, Philipps-Universität Marburg, Hans-Meerwein-Str. 4, 35043 Marburg, Germany, Fax: +49-6421-2825617, E-Mail: robert.langer@chemie.uni-marburg.de*
[b] *Centre for Theoretical Chemistry and Physics, The New Zealand Institute for Advanced Study and the Institute for Natural and Mathematical Sciences, Massey University, Albany, New Zealand*

1. EDA-NOCV

a) Cutting Schemes

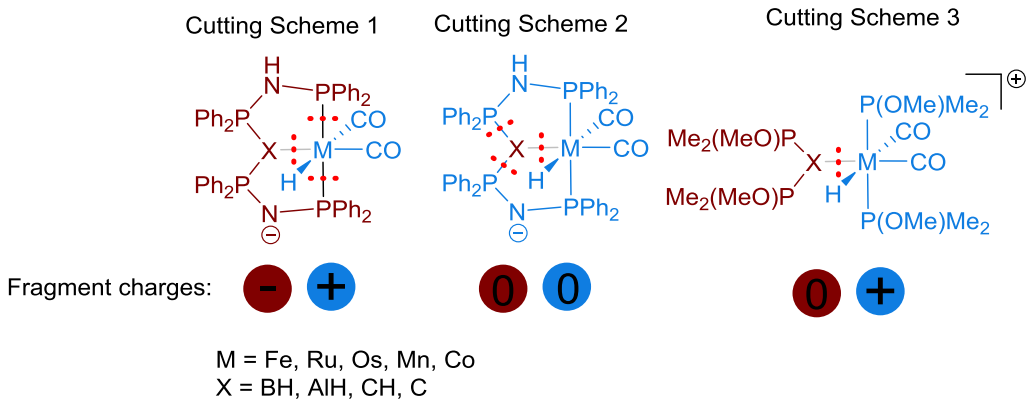

b) Summary of EDA-NOCV results

All energies in kcal/mol

Cutting Scheme 1

	Fe				Ru			
	BH	AlH	CH	C	BH	AlH	CH	C
ΔE_{int}	-391.23	-447.46	-367.26	-368.33	-395.44	-399.12	-373.1	-375.98
ΔE_{Pauli}	276.84	484.26	254.14	252.44	276.98	281.18	259.62	264.83
ΔE_{Elstat}	-338.04	-400.05	-330.06	-324.12	-362.79	-349.99	-356.35	-353.77
ΔE_{Orb}	-305.98	-508.34	-268.18	-273.28	-283.33	-304.35	-250.87	-261.24
ΔE_{Disp}	-24.05	-23.32	-23.16	-23.37	-26.29	-25.96	-25.5	-25.8

	Os				Mn			
	BH	AlH	CH	C	BH	AlH	CH	C
ΔE_{int}	-425.75	-488.55	-404.85	-407.18	-342.71	-450.75	-342.34	-381.86
ΔE_{Pauli}	327.93	577.11	307.94	315.1	278.15	536.44	257.49	262.22
ΔE_{Elstat}	-413.5	-491.22	-405.58	-402.16	-325.21	-414.97	-319.37	-309.97
ΔE_{Orb}	-313.41	-548.14	-281.11	-293.96	-272.15	-549.38	-258.16	-311.52
ΔE_{Disp}	-26.78	-26.3	-26.09	-26.16	-23.49	-22.84	-22.31	-22.59

	Co			
	BH	AlH	CH	C
ΔE_{int}	-334.25	-435.09	-308.3	-309.77
ΔE_{Pauli}	349.17	539.57	325.13	328.91
ΔE_{Elstat}	-351.28	-384.47	-340.95	-342.43
ΔE_{Orb}	-306.89	-565.26	-268.06	-271.77
ΔE_{Disp}	-25.25	-24.92	-24.42	-24.48

Cutting Scheme 2

	Fe				Ru			
	BH	AlH	CH	C	BH	AlH	CH	C
ΔE_{int}	-193.71	-140.38	-232.63	-250.36	-190.24	-131.73	-231.76	-250.15
ΔE_{Pauli}	655.70	403.23	1042.01	1331.76	651.00	331.44	1042.77	1325.84
ΔE_{Elstat}	-302.50	-238.62	-359.61	-443.37	-304.92	-229.97	-360.61	-441.13
ΔE_{Orb}	-540.95	-294.42	-910.04	-1134.82	-530.08	-222.55	-907.99	-1129.81
ΔE_{Disp}	-5.97	-10.58	-5.00	-3.92	-6.24	-10.64	-5.92	-5.04

	Os				Mn			
	BH	AlH	CH	C	BH	AlH	CH	C
ΔE_{int}	-191.55	-132.06	-235.04	-258.49	-123.48	-97.35	-186.02	-213.93
ΔE_{Pauli}	697.41	469.81	1059.64	1333.20	688.71	350.91	1010.24	1298.15
ΔE_{Elstat}	-310.77	-263.40	-366.24	-442.78	-300.57	-209.21	-356.64	-416.08
ΔE_{Orb}	-571.22	-327.17	-922.42	-1144.03	-506.58	-229.79	-835.62	-1093.07
ΔE_{Disp}	-6.96	-11.30	-6.02	-4.88	-5.04	-9.26	-4.00	-2.93

	Co			
	BH	AlH	CH	C
ΔE_{int}	-149.44	-95.90	-226.27	-215.56
ΔE_{Pauli}	633.49	478.98	968.73	1318.51
ΔE_{Elstat}	-283.80	-246.05	-345.25	-423.56
ΔE_{Orb}	-490.11	-315.21	-841.82	-1103.59
ΔE_{Disp}	-9.02	-13.63	-7.92	-6.91

Cutting Scheme 3

	Fe				Ru			
	BH	AlH	CH	C	BH	AlH	CH	C
ΔE_{int}	-107.95	-128.82	-7.16	-88.20	-108.67	-118.02	-5.49	-89.31
ΔE_{Pauli}	138.66	238.36	83.42	110.21	200.10	194.61	83.86	115.06
ΔE_{Elstat}	-124.76	-187.05	-8.55	-100.37	-176.83	-178.26	-13.49	-107.96
ΔE_{Orb}	-95.35	-156.98	-56.73	-69.42	-103.15	-110.33	-50.58	-67.72
ΔE_{Disp}	-26.5	-23.15	-25.29	-28.61	-28.78	-24.03	-25.28	-28.69

	Os				Mn			
	BH	AlH	CH	C	BH	AlH	CH	C
ΔE_{int}	-115.19	-123.19	-12.90	-98.17	-64.84	-79.94	-44.43	-53.72
ΔE_{Pauli}	159.44	207.12	90.67	126.16	121.78	228.82	82.43	96.25
ΔE_{Elstat}	-153.06	-192.38	-21.87	-119.97	-98.70	-171.95	-61.44	-77.51
ΔE_{Orb}	-95.02	-113.85	-56.40	-75.35	-60.91	-114.31	-40.33	-45.62
ΔE_{Disp}	-26.55	-24.09	-25.29	-29.01	-27.02	-22.49	-25.09	-26.84

	Co			
	BH	AlH	CH	C
ΔE_{int}	-179.90	-211.54	16.23	-147.14
ΔE_{Pauli}	155.81	227.32	79.37	126.87
ΔE_{Elstat}	-155.02	-184.09	38.16	-133.71
ΔE_{Orb}	-151.3	-231.98	-75.51	-110.16
ΔE_{Disp}	-29.39	-22.79	-25.78	-30.14

c) Contour plots of deformation densities with energy contribution > 5 kcal/mol for M = Fe, X = BH (charge flow red -> blue)

Deformation densities of other M and X are qualitatively very similar and thus omitted.

a. Cutting Scheme 1

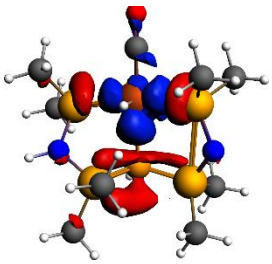

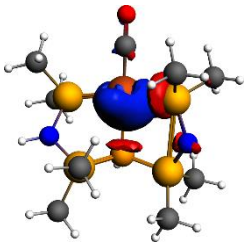

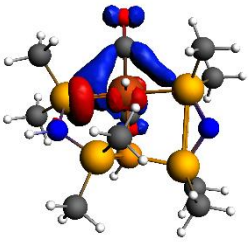

Eigenvalue ν:	-1.26	-0.75	-0.59
Orbital Contribution (ΔE):	-130.96 kcal/mol	-63.48 kcal/mol	-31.23 kcal/mol
Contour Value:	0.003	0.003	0.003

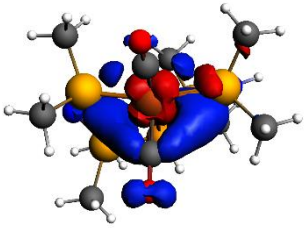

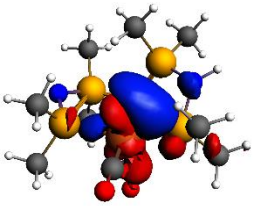

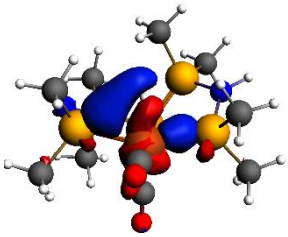

Eigenvalue ν:	-0.46	-0.41	-0.34
Orbital Contribution (ΔE):	-18.83 kcal/mol	-18.19 kcal/mol	-13.89 kcal/mol
Contour Value:	0.001	0.001	0.001

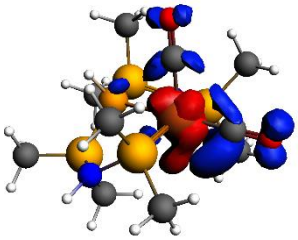

Eigenvalue ν:	-0.24
Orbital Contribution (ΔE):	-7.07 kcal/mol
Contour Value:	0.0008

b. Cutting Scheme 2

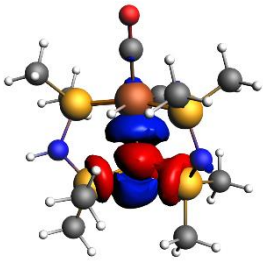
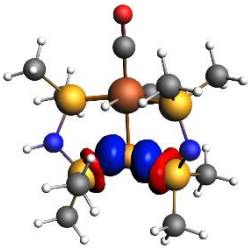
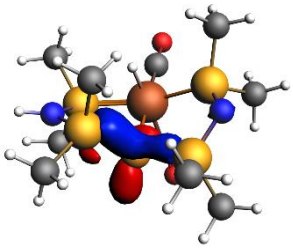

Eigenvalue ν:	-1.90	-0.78	-0.35
Orbital Contribution (ΔE):	-413.40 kcal/mol	-93.04 kcal/mol	-16.91 kcal/mol
Contour Value:	0.005	0.005	0.003

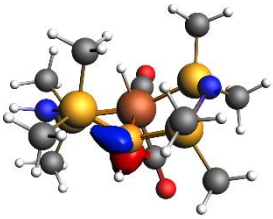
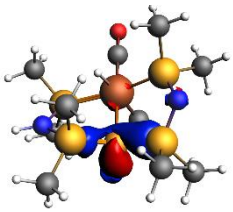

Eigenvalue ν:	-0.23	-0.19
Orbital Contribution (ΔE):	-6.21 kcal/mol	-5.26 kcal/mol
Contour Value:	0.003	0.001

c. <u>Cutting Scheme 3</u>

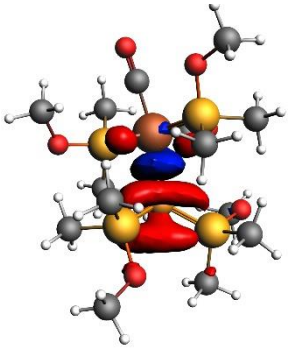

Eigenvalue ν:	-1.01
Orbital Contribution (ΔE):	-70.72 kcal/mol
Contour Value:	0.005

Tipping the Balance between Ligand and Metal Protonation due to Relativistic Effects: Unusual high Proton Affinity in Gold(I) Pincer Complexes

Lisa Vondung,[a,b] Paul Jerabek[b] and Peter Schwerdtfeger*[b]

Abstract: Quantum theoretical studies show that the extremely high proton affinity at the metal center of the unusual T-shaped (LXL)Au(I)-pincer complex, consisting of a carbazole framework and two mesoionic carbenes, is due to relativistic effects. This brings the basicity of the Au(I) center in line with the electron-rich nitrogen atom of the carbazole ring system, resulting in one of the highest proton affinities for a neutral molecule.

Proton transfer reactions are of great importance in almost all areas of chemistry, such as organic reactions,[1] catalytic processes,[2] solvation,[3] or in biomolecular reactions (e.g. in proton-coupled electron transfer reactions),[4] to name but a few. To understand the dynamics of a protonation occurring at specific electron-rich sites is of paramount importance in the design of new molecules and ligands with specific molecular properties. The resulting protonated molecule is often an important activated intermediate in chemical reactions, such as in acid catalyzed organic reactions.[1a] Therefore, knowledge of the basicity of a molecule is central to the understanding of its reactivity.[5]

Studies on proton affinities have mainly focused on "electron-rich" neutral molecules containing non-metallic main-group elements typically used in organic or bio-molecular reactions. Here, proton affinities can range from low values of ~400 kJ/mol (e.g. for H_2) to very high values of ~900-1000 kJ/mol (e.g. for CH_3NH_2 or aza-18-crown-6 ether) for neutral molecules. Anions, on the other hand, can have extremely large electron affinities, as one expects.[6] However, as early as in 1976, *Armentrout* and co-workers pointed out that metal atoms can be very strong bases in the gas phase.[7] In fact, both the coordinated metal and the coordinating ligand in a metal complex may compete for the preferred protonation site.[8] Ligand protonation is mostly preferred, though. This is owed to the fact that these sites are usually more electron rich compared to the positively charged coordinated metal with its formal positive oxidation state.

In a recent paper, *Kleinhans* et al. reported the synthesis and reactivity of unusual T-shaped (LXL)Au(I)-pincer complexes, as shown in Scheme 1.[9] With a the formal oxidation state of +1 at the gold atom, we would naively expect protonation on some of the electron-rich nitrogen sites. However, *Kleinhans* et al. found that the strong electron-donating properties of the ligand makes the Au(I) center reactive towards oxidative addition of electrophiles, such as protons, leading to an unusual cationic Au(III) hydride.[9]

It is well known that relativistic effects substantially increase the electronegativity of gold from 1.9 to 2.4,[10] making gold a pseudohalide with very different properties compared to both copper and silver.[11] The question naturally arises, if the high basicity of gold observed in these (LXL)Au(I)-pincer complexes[9] is due to relativistic effects. In order to answer this interesting question, we decided to perform quantum chemical calculations to determine the proton affinity for the (LXL)M(I)-pincer complexes (M = Cu, Ag and Au) with and without relativity and solvent effects included.

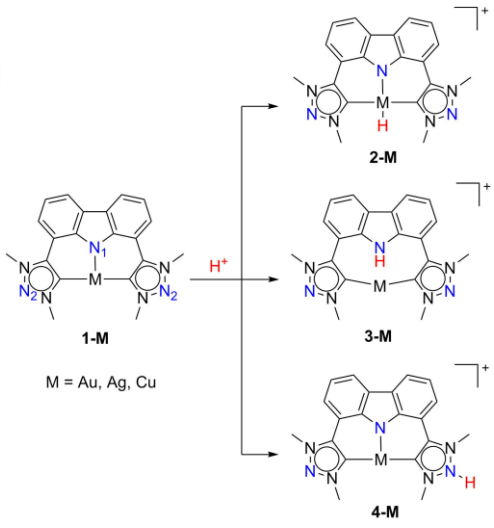

Scheme 1. Investigated model systems and possible protonation products..

The neutral (LXL)Au(I)-pincer complex **1-M** has three different potential protonation sites: at the coinage metal atom (M), the carbazolide nitrogen atom (N-1) and the triazole nitrogen atom (N-2), leading to the respective products **2-M**, **3-M** and **4-M** (Scheme 1).

While the calculated proton affinity on the triazole nitrogen atom is in-line with typical nitrogen containing heterocycles,[12] the proton affinities for the carbazolide nitrogen atom N-1 (resulting complex **3-M)** and the gold atom (resulting complex **2-M**) are

[a] Lisa Vondung
Fachbereich Chemie
Philipps-Universität Marburg
Hans-Meerwein-Str. 4, 35032 Marburg, Germany
[b] Lisa Vondung, Dr. Paul Jerabek, Prof. Dr. Peter Schwerdtfeger
Centre for Theoretical Chemistry and Physics, The New Zealand Institute for Advanced Study and the Institute for Natural and Mathematical Sciences
Massey University, Albany, New Zealand
p.a.schwerdtfeger@massey.ac.nz

Supporting information for this article is given via a link at the end of the document.

unusually high (see Table 1), similar to those of the (gas phase) alkali hydroxides (LiOH: 1000.1 kJ/mol; CsOH: 1117.9 kJ/mol).[5a, 13]

Calculations with a solvent model give proton affinities approximately 100 kJ/mol larger compared to the gas phase values, which is due to the stabilizing effect the polar THF molecules have on the protonated species. However, the solvent does not change the overall trend within the Group 11 species.

For **1-Cu**, **1-Ag** and nonrelativistic **1-Au** the protonation site is clearly the central carbazolide nitrogen atom (N-1), with a difference in proton affinity of 100 kJ/mol compared to the metal center. However, when relativistic effects are switched on, the two protonation sites in **1-Au** compete with each other with a difference of only 25–30 kJ/mol (with/without THF) in the proton affinities. This is in agreement with the observed proton-exchange mechanism between the Au center and the N-1 site.[9] Moreover, in the non-relativistic case, the proton affinities of the coinage metal atom sites follow the trend **1-Ag** < **1-Cu** ≈ **1-Au**. In contrast, relativistic effects enhance the proton affinities of **1-Cu**, **1-Ag** and **1-Au** by around 30 kJ/mol, 65 kJ/mol and 130 kJ/mol, respectively, such that the trend changes to **1-Ag** ≈ **1-Cu** << **1-Au**. Relativistic effects increase ~Z^2, i.e. we get ΔE_R [kJ/mol] = 2.6$(Z\alpha)^2$ + 20, where α is the fine-structure constant.

The M-H bond lengths is also significantly influenced by relativistic effects for gold: in the non-relativistic case, r(Au-H^+)=1.626 Å is obtained, while inclusion of relativistic effects yields r(Au-H^+)=1.557 Å. For copper and silver this effect is far smaller with deviations of 0.012 and 0.007 Å. When a solvent model is employed, the M-H bonds become slightly shorter, although this does not change the overall trends.

In order to understand, why relativistic effects have such an impact on the proton affinity, different bond analysis methods were utilized. A first explanation can be found in the atomic partial charges (Table 2). For copper and silver, relativistic effects don't change them much, but in the case of gold, the partial charge becomes rather large, as expected from the electronegativity. Accordingly, the proton affinity for the gold site rises

The electrostatic potential (ESP) surfaces shown in Figure 1 support this observation, and also demonstrate that protonation at the N-1 site is kinetically driven due to electrostatic effects. The charge on gold is positive, but substantially reduced due to relativistic effects, as seen by comparing the non-relativistic and relativistic ESP surfaces. Nevertheless, the rather large proton affinity at the gold center is also due to the fact that Au(III) prefers a square planar coordination geometry.

The electron localization functions (ELFs) of **1-M** in Figure 2 again illustrate the localization of electron density at the N-1 site. Moreover, the valence shell of relativistic gold (Figure 2d) is far more diffuse and extends over a much larger volume compared to the nonrelativistic case (Figure 2c), offering electron density that can be used to stabilize a proton.

In summary, for the copper and silver complexes, the preferred protonation site is always the carbazolide nitrogen atom, regardless of relativistic effects. In the gold complex, the proton affinities of the gold and carbazolide nitrogen sites are similar and compete in agreement with experimental observations.

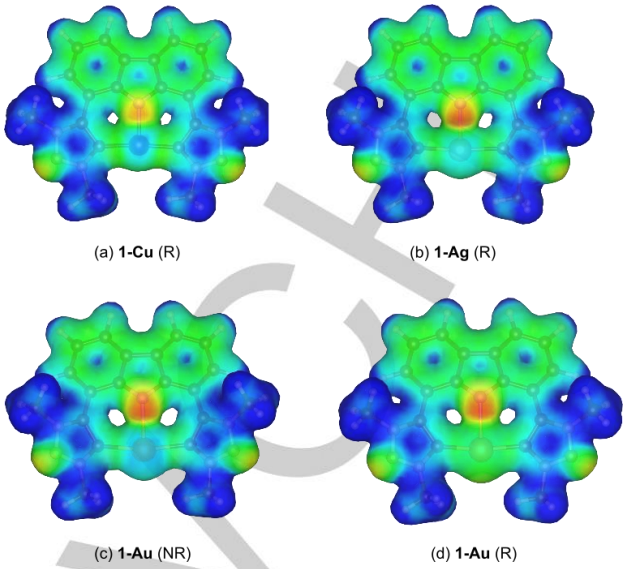

Figure 1. Electrostatic potential (ESP) of **1-M** mapped onto the electron density isovalue surface of 0.02 *e*/Bohr^3 at the B3PW91-D3BJ/def2-SVP level of theory. For gold, both the nonrelativistic (NR) and relativistic (R) ESPs are shown. Deep blue, green, and red areas correspond to ESP values of +0.1, 0.0 and -0.1 a.u., respectively.

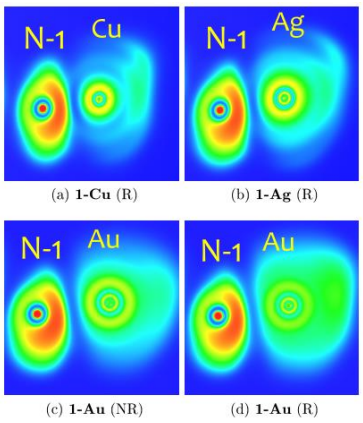

Figure 2. Electron localization function (ELF) of **1-M** calculated at B3PW91-D3BJ/def2-SVP level of theory with (R) and without (NR) inclusion of relativistic effects. Deep blue, cyan, green, yellow and red areas correspond to ELF values of 0.00, 0.25, 0.50, 0.75 and 1.00, respectively.

The reason for this lies in relativistic effects which lead to an increased electronegativity of Au. Consequently, more negative partial charge is accumulated at the gold atom and at the same time more diffuse than for copper and silver. Thus, in the gold complex, the proton is attracted and stabilized much better at the gold atom, compared to the copper and silver species. This makes gold very special within the Group 11 series of elements.

Furthermore, relativistic effects also cause an anomaly in the metal-proton distance, i.e. r(Cu-H$^+$)=1.427 Å, r(Ag-H$^+$)=1.564 Å, and r(Au-H$^+$)=1.557 Å (at the non-relativistic level we obtain r(Au-H$^+$)=1.626 Å).

Table 1. Non-relativistic (NR) and relativistic (R) proton affinities and difference between the two, ΔE_R, at different protonation sites (in kJ/mol) of **1-M** for the gas phase and with THF solvent environment included at the DLPNO-CCSD(T)/def2-TZVPP//B3PW91-D3BJ/def2-TZVPP level of theory.

	1-Cu			**1-Ag**			**1-Au**		
	Cu	N-1	N-2	Ag	N-1	N-2	Au	N-1	N-2
gas phase, NR	974.0	1121.8	915.2	941.5	1147.0	916.5	979.6	1148.9	916.1
gas phase, R	1007.1	1118.4	915.8	1007.3	1143.5	916.3	1117.0	1147.6	908.9
ΔE_R	33.1	-3.4	0.6	65.8	-3.5	-0.2	137.4	-1.3	-7.2
THF, NR	1070.2	1211.0	1038.8	1029.1	1229.2	1036.3	1072.1	1233.2	1036.2
THF, R	1103.1	1206.7	1039.1	1096.5	1227.5	1033.3	1205.8	1231.7	1027.5
ΔE_R	32.9	-4.3	0.3	67.4	-1.7	-3.0	133.7	-1.5	-8.7

Table 2. Natural charges q at different protonation sites (in e) with (R) and without (NR) relativistic effects included, calculated at B3PW91-D3BJ/def2-TZVPP level of theory.

	1-Cu			**1-Ag**			**1-Au**		
	Cu	N-1	N-2	Ag	N-1	N-2	Au	N-1	N-2
q, NR	0.68	-0.63	-0.09	0.62	-0.61	-0.09	0.61	-0.60	-0.10
q, R	0.67	-0.64	-0.09	0.56	-0.61	-0.09	0.44	-0.59	-0.13

Computational Details

For the T-shaped pincer M(I) complexes (M = Cu, Ag and Au),[9] we utilized model systems with less bulky substituents as shown in Figure 1. The structures were optimized with the ORCA 3.0.3 program package,[14] using density function theory (DFT) employing the B3PW91[15] functional together with the def2-TZVPP basis set[16] and D3 dispersion correction including Becke-Johnson damping.[17] To speed up the calculations, the resolution-of-identity (RIJCOSX) approximation was employed.[18] For the coinage metal atoms, we used non-relativistic and relativistic Stuttgart small-core effective core potentials (ECP).[11a, 19] The THF solvent environment was simulated with COSMO.[20] Frequency calculations were performed to ensure that we have found minimum structures and for thermodynamic corrections, in order to obtain proton affinities as enthalpies for the protonation reactions. Natural population analyses (NPA)[21] to obtain atomic partial charges were done with the NBO 5 program,[22] as implemented in Gaussian 09, Rev. C.01.[23] Löwdin population analyses[24] were performed with the built-in functionality of Orca.[25] To improve upon the calculated proton affinities, we used the DFT optimized structures to perform single-point calculations with the domain based local pair natural orbital variant of the coupled-cluster method with excitations from singles, doubles and perturbative triples (DLPNO-CCSD(T))[26] in conjunction with the def2-TZVPP[16] basis set with the above mentioned relativistic and non-relativistic ECPs.[11a, 19] Computations of the electron localization function (ELF)[27] and electrostatic potential (ESP) were carried out with the Multiwfn 3.4 program[28] on the optimized structures, but with a def2-SVP all-electron basis set[29] at the non-relativistic and relativistic level of theory, using the zeroth-order regular approximation (ZORA) for the latter.[30]

Acknowledgements

We acknowledge financial support by the Alexander-von-Humboldt Foundation (Bonn, Germany) and by the Studienstiftung des deutschen Volkes (Bonn, Germany).

Keywords: Proton Affinities • Pincer Complexes • Coinage Metals • Relativistic Effects • Quantum Chemical Calculations

[1] aM. B. Smith, J. March, *March's advanced organic chemistry: reactions, mechanisms, and structure*, John Wiley & Sons, **2007**; bR. W. Nagorski, J. P. Richard, *J. Am. Chem. Soc.* **1996**, *118*, 7432-7433; cE. C. Gentry, R. R. Knowles, *Acc. Chem. Res.* **2016**, *49*, 1546-1556.

[2] aD. K. Bohme, *Int. J. Mass Spectrom. Ion Processes* **1992**, *115*, 95 - 110; bK. B. Schowen, H.-H. Limbach, G. S. Denisov, R. L. Schowen, *Biochimica et Biophysica Acta (BBA) - Bioenergetics* **2000**, *1458*, 43-62; cJ. S. M. Samec, J.-E. Backvall, P. G. Andersson, P. Brandt, *Chem. Soc. Rev.* **2006**, *35*, 237-248; dA. Moser, K. Range, D. M. York, *J. Phys. Chem. B* **2010**, *114*, 13911-13921.

[3] aJ. Tomasi, B. Mennucci, R. Cammi, *Chem. Rev.* **2005**, *105*, 2999-3094; bD. Marx, *ChemPhysChem*, *8*, 209-210.

[4] aM. Eigen, *Angew. Chem. Int. Ed.* **1964**, *3*, 1-19; bS. Hammes-Schiffer, A. A. Stuchebrukhov, *Chem. Rev.* **2010**, *110*, 6939-6960.

[5] aE. P. L. Hunter, S. G. Lias, *J. Phys. Chem. Ref. Data* **1998**, *27*, 413-656; bC. A. Deakyne, *Int. J. Mass spectrom.* **2003**, *227*, 601 - 616.

[6] aW. L. Jolly, *Modern inorganic chemistry*, 2nd ed., McGraw-Hill, Inc., New York, **1991**; bR. R. Julian, J. L. Beauchamp, *J. Am. Soc. Mass Spectr* **2002**, *13*, 493 - 498; cB. L. J. Poad, N. D. Reed, C. S. Hansen, A. J. Trevitt, S. J. Blanksby, E. G. Mackay, M. S. Sherburn, B. Chan, L. Radom, *Chem. Sci.* **2016**, *7*, 6245-6250.

[7] P. Armentrout, R. Hodges, J. L. Beauchamp, *J. Am. Chem. Soc.* **1977**, *99*, 3162-3163.

[8] aG. Eilers, L. Schwartz, M. Stein, G. Zampella, L. de Gioia, S. Ott, R. Lomoth, *Chem. Eur. J.* **2007**, *13*, 7075-7084; bM. Besora, A. Lledos, F. Maseras, *Chem. Soc. Rev.* **2009**, *38*, 957-966.

[9] G. Kleinhans, M. M. Hansmann, G. Guisado-Barrios, D. C. Liles, G. Bertrand, D. I. Bezuidenhout, *J. Am. Chem. Soc.* **2016**, *138*, 15873-15876.

[10] P. Schwerdtfeger, *Chem. Phys. Lett.* **1991**, *183*, 457 - 463.

[11] aP. Schwerdtfeger, M. Dolg, W. H. E. Schwarz, G. A. Bowmaker, P. D. W. Boyd, *J. Chem. Phys.* **1989**, *91*, 1762-1774; bP. Schwerdtfeger, *Heteroatom Chem.* **2002**, *13*, 578-584; cP. Pyykkö, *Chem. Soc. Rev.* **2008**, *37*, 1967-1997.

[12] aS. Kabli, E. S. E. van Beelen, S. Ingemann, L. Henriksen, S. Hammerum, *Int. J. Mass Spect.* **2006**, *249*, 370 - 378; bJ. S. Rao, G. N. Sastry, *Int. J. Quantum Chem* **2006**, *106*, 1217-1224.

[13] I. Džidić, P. Kebarle, *J. Phys. Chem.* **1970**, *74*, 1466-1474.

[14] F. Neese, *Wiley Interdiscip. Rev. Comput. Mol. Sci.* **2012**, *2*, 73-78.

[15] aA. D. Becke, *J. Chem. Phys.* **1993**, *98*, 5648-5652; bJ. P. Perdew, J. A. Chevary, S. H. Vosko, K. A. Jackson, M. R. Pederson, D. J. Singh, C. Fiolhais, *Phys. Rev. B* **1992**, *46*, 4978; cJ. P. Perdew, Y. Wang, *Phys. Rev. B* **1992**, *45*, 13244-13249.

[16] aA. Schäfer, H. Horn, R. Ahlrichs, *J. Chem. Phys.* **1992**, *97*, 2571-2577; bF. Weigend, R. Ahlrichs, *Phys. Chem. Chem. Phys.* **2005**, *7*, 3297-3305.

[17] aS. Grimme, J. Antony, S. Ehrlich, H. Krieg, *J. Chem. Phys.* **2010**, *132*, 154104; bS. Grimme, S. Ehrlich, L. Goerigk, *J. Comp. Chem.* **2011**, *32*, 1456-1465.

[18] F. Neese, F. Wennmohs, A. Hansen, U. Becker, *Chem. Phys.* **2009**, *356*, 98-109.

[19] aD. Andrae, **1989**; bM. Dolg, U. Wedig, H. Stoll, H. Preuss, *J. Chem. Phys.* **1987**, *86*, 866-872; cD. Figgen, G. Rauhut, M. Dolg, H. Stoll, *Chem. Phys.* **2005**, *311*, 227-244.

[20] A. Klamt, G. Schüürmann, *J. Chem. Soc., Perkin Trans. 2* **1993**, 799-805.

[21] A. E. Reed, R. B. Weinstock, F. Weinhold, *J. Chem. Phys.* **1985**, *83*, 735-746.

[22] E. D. Glendening, J. K. Badenhoop, A. E. Reed, J. E. Carpenter, J. A. Bohmann, C. M. Morales, F. Weinhold, **2012**.

[23] M. J. Frisch, G. W. Trucks, H. B. Schlegel, G. E. Scuseria, M. A. Robb, J. R. Cheeseman, G. Scalmani, V. Barone, B. Mennucci, G. A. Petersson, H. Nakatsuji, M. Caricato, X. Li, H. P. Hratchian, A. F. Izmaylov, J. Bloino, G. Zheng, J. L. Sonnenberg, M. Hada, M. Ehara, K. Toyota, R. Fukuda, J. Hasegawa, M. Ishida, T. Nakajima, Y. Honda, O. Kitao, H. Nakai, T. Vreven, J. A. Montgomery Jr., J. E. Peralta, F. Ogliaro, M. Bearpark, J. J. Heyd, E. Brothers, K. N. Kudin, V. N. Staroverov, R. Kobayashi, J. Normand, K. Raghavachari, A. Rendell, J. C. Burant, S. S. Iyengar, J. Tomasi, M. Cossi, N. Rega, J. M. Millam, M. Klene, J. E. Knox, J. B. Cross, V. Bakken, C. Adamo, J. Jaramillo, R. Gomperts, R. E. Stratmann, O. Yazyev, A. J. Austin, R. Cammi, C. Pomelli, J. W. Ochterski, R. L. Martin, K. Morokuma, V. G. Zakrzewski, G. A. Voth, P. Salvador, J. J. Dannenberg, S. Dapprich, A. D. Daniels, O. Farkas, J. B. Foresman, J. V. Ortiz, J. Cioslowski, D. J. Fox, in *Gaussian Inc. Wallingford CT*, Gaussian Inc. Wallingford CT 2009, **2009**.

[24] P.-O. Löwdin, *J. Chem. Phys.* **1950**, *18*, 365-275.

[25] F. Neese, F. Wennmohs, A. Hansen, U. Becker, *Chem. Phys.* **2009**, *356*, 98-109.

[26] aC. Riplinger, F. Neese, *J. Chem. Phys.* **2013**, *138*; bC. Riplinger, B. Sandhoefer, A. Hansen, F. Neese, *J. Chem. Phys.* **2013**, *139*.

[27] A. D. Becke, K. E. Edgecombe, *J. Chem. Phys.* **1990**, *92*, 5397-5403.

[28] T. Lu, F. Chen, *J. Comput. Chem.* **2012**, *33*, 580-592.

[29] D. A. Pantazis, X. Y. Chen, C. R. Landis, F. Neese, *J. Chem. Theory Comput.* **2008**, *4*, 908-919.

[30] C. Van Wüllen, *J. Chem. Phys.* **1998**, *109*, 392-399.

Entry for the Table of Contents (Please choose one layout)

Layout 1:

COMMUNICATION

Relativity tips it over: Relativistic Effects are responsible for changing the proton affinity of Au(I) in a pincer complex of *Kleinhans* et al. enough to compete with the carbazole in the ligand. For the Cu(I) and Ag(I) complexes, protonation occurs only at the ligand.

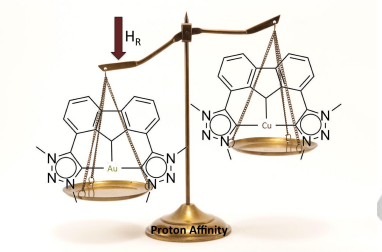

*Lisa Vondung, Paul Jerabek and Peter Schwerdtfeger**

Page No. – Page No.

Tipping the Balance between Ligand and Metal Protonation due to Relativistic Effects: Unusual high Proton Affinity in Gold(I) Pincer Complexes

Layout 2:

COMMUNICATION

((Insert TOC Graphic here))

*Author(s), Corresponding Author(s)**

Page No. – Page No.

Title

Text for Table of Contents

Supporting Information

Tipping the Balance between Ligand and Metal Protonation due to Relativistic Effects: Unusual high Proton Affinity in Gold(I) Pincer Complexes

Lisa Vondung,[a,b] Paul Jerabek[b] and Peter Schwerdtfeger*[b]

[a]*Department of Chemistry, Philipps-Universität Marburg, Hans-Meerwein-Str., 35043 Marburg, Germany*
[b]*Centre for Theoretical Chemistry and Physics, The New Zealand Institute for Advanced Study and the Institute for Natural and Mathematical Sciences, Massey University, Albany, New Zealand, E-Mail: p.a.schwerdtfeger@massey.ac.nz*

Table S1: Löwdin population analysis of valence orbitals of M in 1-M (in *e*) with (R) and without (NR) relativistic effects included, calculated at B3PW91-D3BJ/def2-SVP level of theory.

	1-Cu	**1-Ag**	**1-Au**
*n*s (R)	0.33	0.34	0.60
*n*p (R)	0.83	0.55	0.80
(*n*-1)d (R)	9.67	9.64	9.86
*n*s (NR)	0.31	0.28	0.38
*n*p (NR)	0.80	0.51	0.65
(*n*-1)d (NR)	9.70	9.73	10.09

Table S2: M-H bond lengths in Å, calculated at B3PW91-D3BJ/def2-TZVPP level of theory.

	1-Cu	**1-Ag**	**1-Au**
no solvent, rel	1.427	1.546	1.557
no solvent, non-rel	1.439	1.571	1.626
THF, rel	1.422	1.542	1.553
THF, non-rel	1.433	1.566	1.621

Table S3: NBO partial charges in *e*, calculated at B3PW91-D3BJ/def2-TZVPP level of theory.

		M	N-1	N-2
Cu	rel	0.67	-0.64	-0.09
	non-rel	0.68	-0.63	-0.09
Ag	rel	0.56	-0.61	-0.09
	non-rel	0.62	-0.61	-0.09
Au	rel	0.44	-0.59	-0.13
	non-rel	0.61	-0.60	-0.10

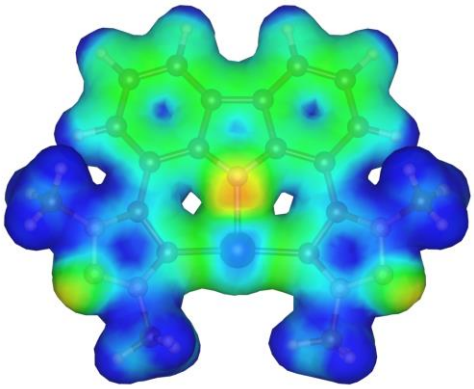

1-Cu (NR)

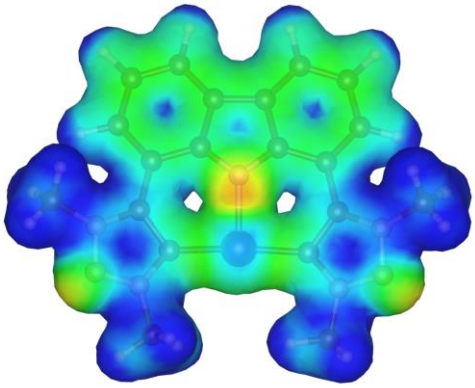

1-Cu (R)

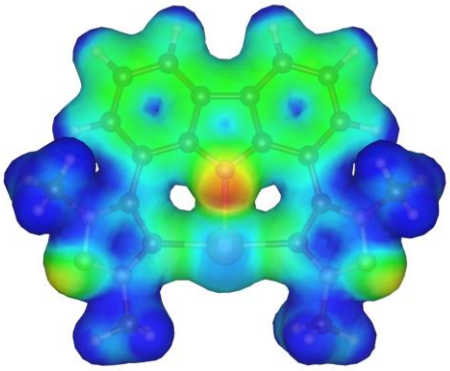

1-Ag (NR)

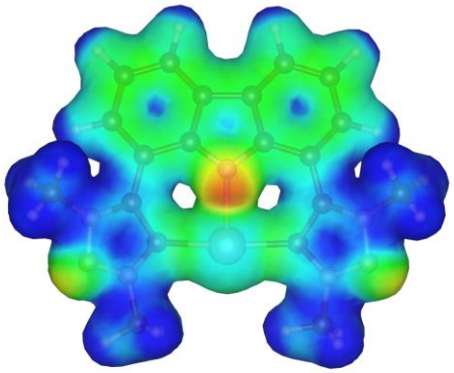

1-Ag (R)

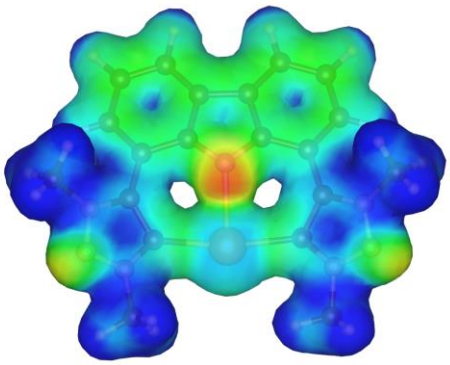

1-Au (NR)

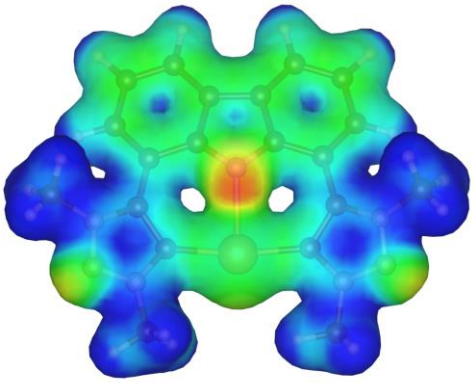

1-Au (R)

Figure S1. Electrostatic potential (ESP) of **1-M** mapped onto the electron density isovalue surface of 0.02 *e*/Bohr^3 at the B3PW91-D3BJ/def2-SVP level of theory. Shown are the nonrelativistic (NR) and relativistic (R) ESPs, respectively. Deep blue, green, and red areas correspond to ESP values of +0.1, 0.0 and -0.1 a.u., respectively.

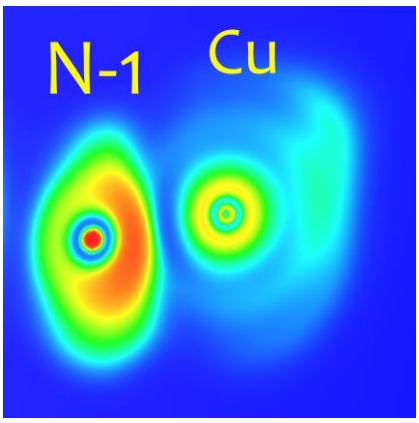

1-Cu (NR)

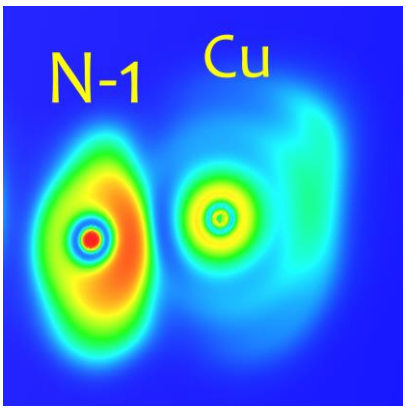

1-Cu (R)

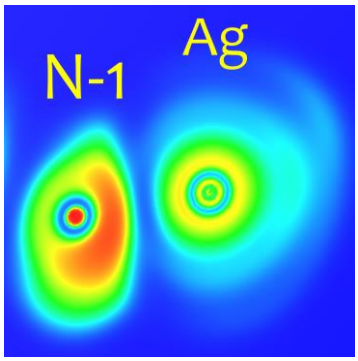

1-Ag (NR)

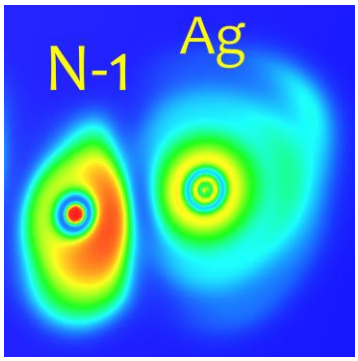

1-Ag (R)

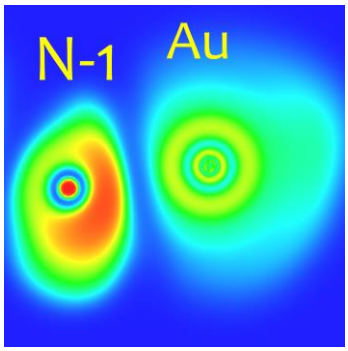

1-Au (NR)

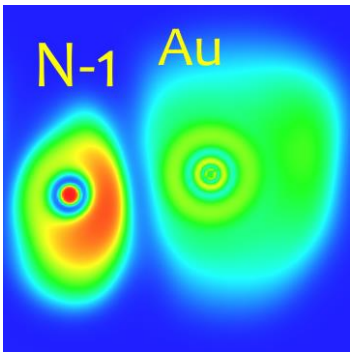

1-Au (R)

Figure S2. Electron localization function (ELF) of **1-M** calculated at B3PW91-D3BJ/def2-SVP level of theory with (R) and without (NR) inclusion of relativistic effects. Deep blue, cyan, green, yellow and red areas correspond to ELF values of 0.00, 0.25, 0.50, 0.75 and 1.00, respectively.

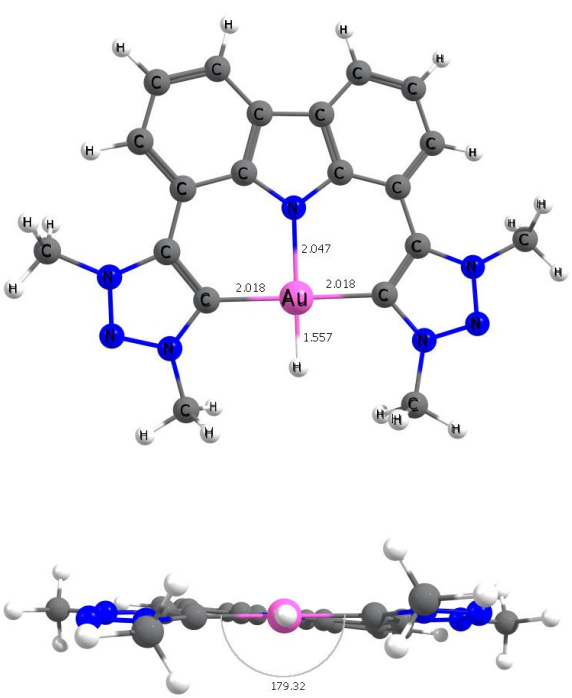

2-Au

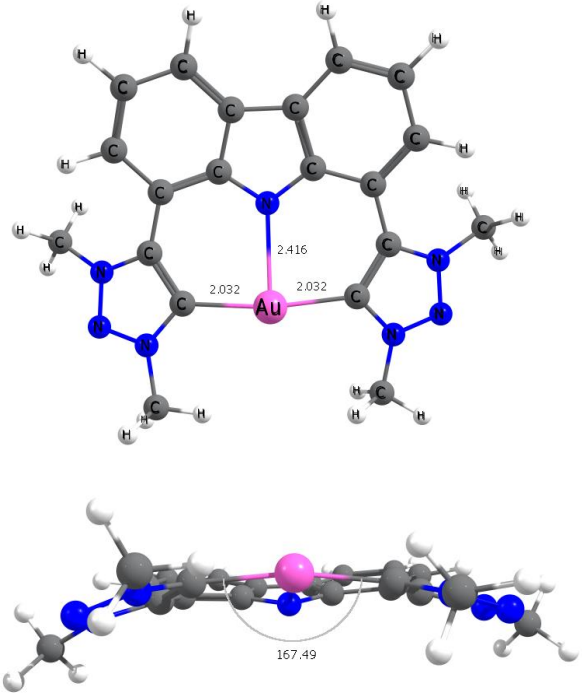

1-Au

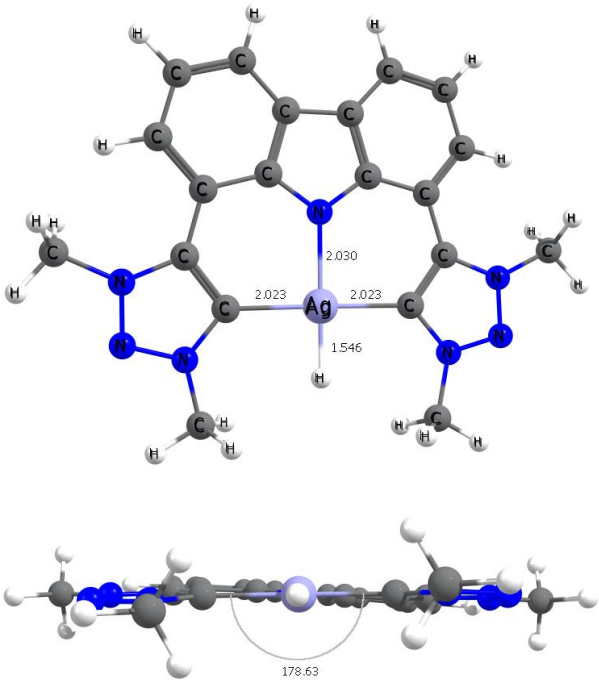

2-Ag

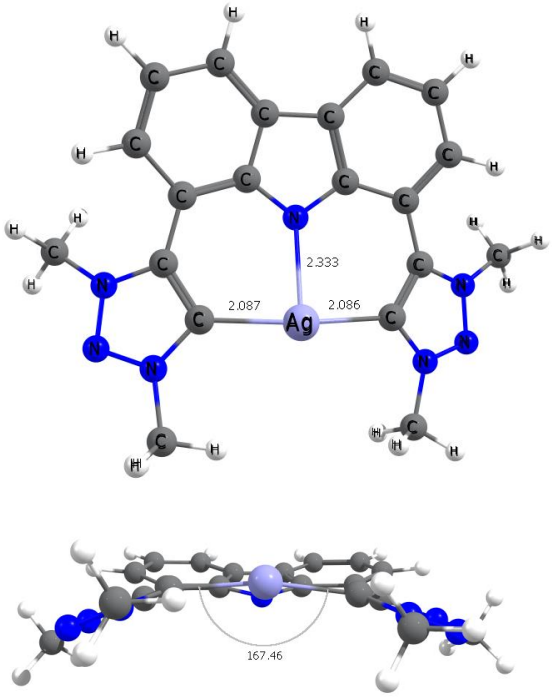

1-Ag

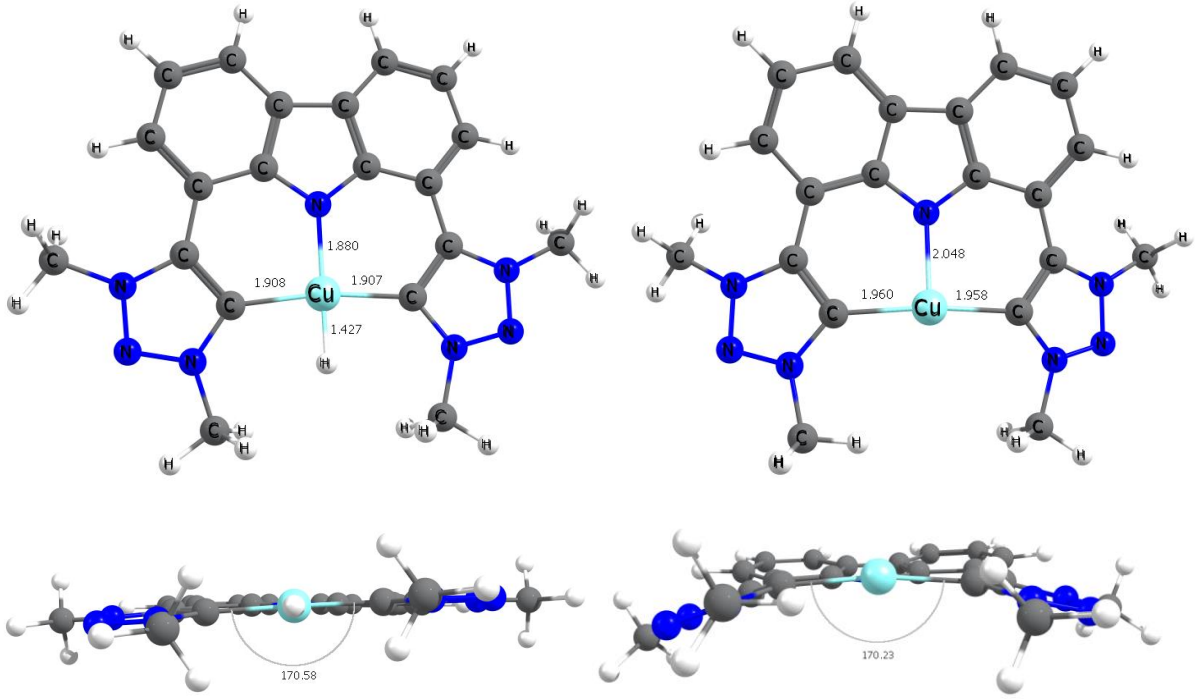

2-Cu **1-Cu**

Figure S2. Optimized structures for **2-M** and **1-M**, B3PW91-D3BJ/def2-TZVPP, relativistic ECPs, gas-phase.